

Space Photovoltaic Research and Technology 1988

*High Efficiency, Space Environment,
and Array Technology*

Proceedings of a conference held at
NASA Lewis Research Center
Cleveland, Ohio
April 19-21, 1988



National Aeronautics and
Space Administration
Office of Management
Scientific and Technical
Information Division

1989

Contents

Foreword

Dennis Flood, Chief, Photovoltaic Branch, NASA Lewis Research Center vii

Overview

Technology Requirements for Advanced NASA Missions

Henry Curtis, Office of Exploration, NASA Headquarters 3

Space Power Technology 21; Photovoltaics

Joseph Wise, Wright-Patterson Air Force Base 10

Session 1-InP Technology

Progress in Indium Phosphide Solar Cell Research

I. Weinberg, C. K. Swartz and R. E. Hart, Jr. 19

InP Shallow-Homojunction Solar Cells

C. Keavney, M. B. Spitzer, S. M. Vernon, V. E. Haven and G. Augustine 28

An Empirical Study of the Performance of APMOVPE

AM0 InP Homojunction Solar Cells as a Function of Emitter Thickness and Doping, and Base Doping

M. W. Wanlass, T. A. Gessert, K. A. Emery and T. J. Coutts 41

N/P InP Homojunction Solar Cells with an $In_{0.53}Ga_{0.47}As$

Contacting Layer by Liquid Phase Epitaxy

C. C. Shen and K. Y. Choi 58

Predicted Performance of InP Solar Cells in Cassegrainian and Slats

Space Concentrator Arrays at 20 to 100 AM0, 80°C to 100°C

C. Goradia, W. Thesling, M. G. Goradia, I. Weinberg and C. K. Swartz 66

Modelling and Design of High Performance Indium Phosphide Solar Cells

S. L. Rhoads and A. M. Barnett 79

Deep Levels and Radiation Effects in P-InP

W. A. Anderson, A. Singh, K. Jiao and B. Lee 90

Encapsulated Diffusion of Sulfur into InP

K. K. Parat, J. M. Borrego and S. K. Ghandhi 99

PRECEDING PAGE BLANK NOT FILMED

Session 2—Lightweight and Ultralightweight PV Technology

<i>The Impact of Solar Cell Technology on Planar Solar Array Performance</i> M. W. Mills and R. M. Kurland	111
<i>Advanced Photovoltaic Solar Array Development</i> R. M. Kurland and P. Stella	122
<i>Development of Tandem Cells Consisting of GaAs Single Crystal and CuInSe₂/CdZnS Polycrystalline Thin Films</i> N. P. Kim, B. J. Stanbery, R. P. Gale and R. W. McClelland	138
<i>Directions for Further Development of GaAs/CuInSe₂ Thin Film Tandem Cells</i> B. J. Stanbery	146
<i>Ultra-Thin, Light-Trapping Silicon Solar Cells</i> G. A. Landis	151
<i>Deployable Aerospace PV Array Based on Amorphous Silicon Alloys</i> J. Hanak, L. Walter, D. Dobias and H. Flaisher	162

Session 3—Heteroepitaxial Cells

<i>High Efficiency GaAs-Ge Tandem Solar Cells Grown by MOCVD</i> S. M. Vernon, S. P. Tobin, C. Bajgar, V. E. Haven, L. M. Geoffroy, D. R. Lillington and R. E. Hart, Jr.	167
<i>Response of Single Junction GaAs/GaAs and GaAs/Ge Solar Cells to Multiple Doses of 1 MeV Electrons</i> D. L. Meier, J. R. Szedon, J. Bartko and M. A. Chung	177
<i>A Three Solar Cell System Based on a Self-Supporting, Transparent AlGaAs Top Solar Cell</i> G. H. Negley, S. L. Rhoads, N. E. Terranova, J. B. McNeely and A. M. Barnett	190

Session 4—GaAs Cells

<i>Investigation of High Efficiency GaAs Solar Cells</i> L. C. Olsen, G. Dunham, F. W. Addis, D. Huber and K. Linden	203
<i>A New Structure for Comparing Surface Passivation Materials of GaAs Solar Cells</i> G. C. DeSalvo and A. M. Barnett	221
<i>Improved Defect Analysis of Gallium Arsenide Solar Cells Using Image Enhancement</i> L. C. Kilmer, C. Honsberg, A. M. Barnett and J. E. Phillips	229

<i>Aging Behavior of Au-Based Ohmic Contacts to GaAs</i>	
N. S. Fatemi	238

<i>Chemical Etching and Organometallic Chemical Vapor Deposition on Varied Geometries of GaAs</i>	
S. G. Bailey, G. A. Landis and D. M. Wilt	250

Session 5—Arrays, Cell Production

<i>Status of GaAs Solar Cell Production</i>	
M. Yeh, F. Ho and P. Iles	267

<i>Flexibility in Space Solar Cell Production</i>	
S. Khemthong and P. Iles	272

<i>Gallium Arsenide Welded Panel Technology for Advanced Space Flight Applications</i>	
D. R. Lillington, M. Gillanders, G. F. J. Garlick, B. T. Cavicchi,	277
G. Glenn and S. Tobin	

<i>Domed Fresnel Lens Concentrator Technology for Space Application</i>	
M. F. Piszczor, Jr. and M. J. O'Neill	286

<i>25% Efficient GaAs Cassegrainian Concentrator Cell</i>	
H. C. Hamaker, M. Grounner, N. R. Kaminar, M. S. Kuryla, M. J. Ladle,	292
D. D. Liu, H. F. MacMillan, L. D. Partain, G. F. Virshup,	
J. G. Werthen and J. M. Gee	

Session 6—Environmental Effects and Measurements

<i>Contamination Effects of GPS Navstar Solar Array Performance</i>	
D. C. Marvin and W. C. Hwang	301

<i>The Experiments of LIPS III</i>	
J. Severns, R. M. Hobbs, N. P. Elliot, R. H. Towsley and G. F. Virshup	306

<i>AM0 Efficiency Measurements</i>	
K. Emery and C. Osterwald	323

<i>A Comparison of the Radiation Tolerance Characteristics of Multijunction Solar Cells With Series and Voltage-Matched Configurations</i>	
J. M. Gee and H. B. Curtis	332

<i>Radiation Resistance Studies of Amorphous Silicon Films</i>	
J. R. Woodyard and J. S. Payson	339

Workshop Summaries

InP Cells	
M. B. Spitzer and S. M. Vernon	351
New Cells-Barriers to Use	
E. Ralph	353
Ultralightweight PV Technology	
P. M. Stella	356
Space Concentrator PV Technology	
J. M. Gee and R. W. Francis	361
Space Environmental Effects	
R. L. Statler	367
Heteroepitaxial Cells for Low Cost, High Performance	
D. R. Lillington and J. Tracy	371

Foreword

Dennis Flood
Chief, Photovoltaic Branch
Power Technology Division
NASA Lewis Research Center
Cleveland, OH 44135

March 17, 1988, marked the 30th anniversary of the first solar array power source launched into orbit in the U.S. space program. Mounted on Vanguard I, it consisted of six panels, each containing 18 p/n silicon solar cells. The cells were 2cm \times 0.5cm in size and averaged 10% efficiency at 28C. The array provided about 1 watt for over 6 years in orbit. Silicon space solar arrays have since become the mainstay power source of the U.S. space program, and will no doubt remain as such for the foreseeable future. Thirty years of development and experience have made it to be the case.

Recent years, however, have seen the rise of significant challenges to that position by alternate power technologies. Indeed, there are a large number of specialized applications for which alternate space power sources may well be the correct answer. It has become critical for the space PV community to regularly and thoroughly examine and respond to such challenges, and to look for those promising new approaches from within space photovoltaics that significantly broaden its applicability to the widest possible range of future missions.

The 9th Space Photovoltaic Research and Technology conference provides ample evidence of exactly that to be the case. The papers and workshop summaries presented in this volume report remarkable progress on a wide variety of approaches in space photovoltaics, for both near and far term applications. Among the former is the recently developed high efficiency GaAs/Ge cell, which formed the focus of a workshop discussion on heteroepitaxial cells. Still aimed at the far term, but with a significant payoff in new mission capability, are InP cells, with their potentially dramatic improvement in radiation resistance. Approaches to near term array specific powers exceeding 130 W/kg are also reported, and advanced concentrator panel technology with the potential to achieve over 250 W/sq.m is beginning to take shape.

Progress over the past few years has been steady, even in the face of constrained budgets and pressure from the "competing" power technologies. New mission opportunities continue to be explored, not only for application, but for new technology demonstration. One of the most significant space PV flight experiments in this decade, LIPS III, has now begun to yield its data, and a preliminary report is contained in this volume.

It is not possible to highlight all of the significant topics and papers discussed at this conference, which, by all accounts, was decidedly very optimistic about the ability of space photovoltaic technology to meet a wide variety of challenges in the years ahead.

The organizer of this year's conference was Dr. Brian Good, of the Photovoltaic Branch at Lewis Research Center. He was ably assisted by several of his colleagues at the Center, and in particular by Pat Nicewander, our Branch secretary, who made sure that things were in the right place at the right time.

Overview

Technology Requirements for Advanced NASA Missions

Henry Curtis
Office of Exploration
NASA Headquarters

Two recent reports, one by the National Commission on Space and the second by the Ride committee, have urged NASA to look at a variety of future missions. Among these are manned missions to Mars and permanent bases on the moon and Mars. This presentation will address a wide variety of technologies needed for such missions as well as areas where power is required. An estimate of power ranges and photovoltaic opportunities will also be presented.

PRECEDING PAGE BLANK NOT FILMED



SPACE STATION EXPLORATION MISSION REQUIREMENTS

- In-space Research Facility
- Assembly Base
- Return Destination

Office of Exploration



IN-SPACE ASSEMBLY TECHNOLOGY ISSUES

- Human Performance
 - Working man's space suit
- Robotic Assistants
 - Demonstrate limited capability
- Compatible Hardware
 - On orbit replacement units
 - Design requirements
- Autonomous Checkout
 - Demonstrate 100% reliability

Office of Exploration



PROPULSION TECHNOLOGY

- Chemical Systems
 - Isp > 480 sec: LOX/LH₂ high chamber pressure
 - Diagnostic instrumentation, health statusing
- High Performance Systems
 - Ion - size (thrust)
 - NPD - life and performance
 - Direct thermal nuclear - cost, commitment, schedule
 - Compatible power system

Office of Exploration



CRYOGENIC FUEL MANAGEMENT TECHNOLOGIES

- Transfer and Management
 - Tank chill-down
 - Vapor condensation/acquisition device integrity
 - Zero-g mass gauging
- Low-loss Containment
 - Insulation
 - Vents
 - Struts
 - Refrigerators

Office of Exploration



AEROBRAKING TECHNOLOGY

- Configuration
 - Validated analysis tools
 - Concepts/capture requirements
 - Mars environment impact
- Navigation, Guidance and Control
 - Autonomous adapting to atmospheric uncertainties
 - Rendezvous error budget
- Thermal Protection Systems
 - Heat load
 - Mars environment
 - In-space assembly

Office of Exploration



ARTIFICIAL GRAVITY TECHNOLOGY

- Human comfort zone - radius, rotation, g-level
- Concept - tethers vs structure
 - Spin-up/spin-down approach
 - Control
 - Aerobrake compatibility
 - Rendezvous techniques

Office of Exploration



CLOSED-LOOP LIFE SUPPORT TECHNOLOGIES

- Process
 - Performance
 - Power
 - Life
 - Fault-tolerant
 - Autonomous operation
- Bioregenerative processes
- Trace contaminant control
- Food production/storage

Office of Exploration



PLANETARY ROVER (UNMANNED) TECHNOLOGIES

- Mobility and navigation
 - Autonomous path recognition
 - Remote driving
 - Hazard recognition and avoidance
- Power
 - 1-5 kW
 - Weight
 - Environment
- Sample selection maintenance
 - In-situ analysis
 - Selection intelligence
 - "Secure" containers
- High-resolution sensors, communication

Office of Exploration



LUNAR BASE TECHNOLOGIES

- Power (30 kW → 100's kW → MW)
- Material processing in reduced gravity
- Closed-loop life support
- Autonomous systems
- Science sensors
- Data/communication systems

Office of Exploration



NEED FOR POWER IS EVERYWHERE

- Electric propulsion
- Earth/Mars and Earth/Lunar vehicles
- Lunar/Mars bases
- Rovers (manned and unmanned)
- Life support
- Assembly at space station
- Permanent manned presence

Office of Exploration

POWER SYSTEM ISSUES

- 0 G 1/6 G (Lunar) 1/3 G (Mars) 0-1 G (variable)
- Surface environment
 - Dust
 - Martian atmosphere
- Recharging rovers
- Man rated nuclear
- 43% AMO at Mars
- Known degradation
- Autonomous operation
- Includes generation, storage, thermal management, conditioning, distribution, and control

Office of Exploration

Space Power Technology 21; Photovoltaics

Joseph Wise
Aero Propulsion Laboratory
Wright-Patterson AFB OH

Abstract

This paper will discuss the Space Power needs for the 21st Century and the program in photovoltaics needed to achieve it. Workshops were conducted in eight different power disciplines involving industry and other government agencies. The Photovoltaics Workshop was conducted at Aerospace Corporation in June 1987. The major findings and recommended program from this workshop are discussed below.

The major finding is that a survivable solar power capability is needed in photovoltaics for critical Department of Defense missions including Air Force and Strategic Defense Initiative. The tasks needed to realize this capability are described in technical, not financial, terms similar to what was presented in the SPT 21 briefing to industry. The paper will also include what efforts are currently being funded and what still needs to be done.

The second finding is the need for lightweight, moderately survivable planar solar arrays especially for SPO future block buys on existing missions where satellite functional requirements are increasing and minimum changes to the basic vehicle structure are desired. High efficiency thin III-V solar cells can meet some of these requirements.

Higher efficiency, longer life solar cells are needed for application to both future planar and concentrator arrays with usable life up to 10 years. Increasing threats are also anticipated and means for avoiding prolonged exposure, retraction, maneuvering and autonomous operation will also be discussed.

In conclusion the potential for nearly doubling the specific power in terms of array weight and area and increasing survivability through higher temperature resistance appear real and highly desirable. Funding is slowly becoming available to make these technical goals achievable.

Description

The objective of the SPT 21 study conducted by the Aerospace Power Division of AFWAL and the Technology Group of the Air Force Space Technology Center was to develop a comprehensive space power research and development program to meet the needs of the Air Force and Department of Defense for the next 10 to 15 years. The schedule for this study is shown in Figure 1. This plan enlisted the best talent in the United States to help us in seven workshops looking at all the disciplines needed to provide power to defense satellite vehicles. Even though projections for power requirements were considerably higher in some cases it was felt that nearly all defense requirements would be met with survivable power in the 10 to 100 kilowatts continuous range. This power range was accordingly made the focus of the study.

The workshops were cochaired by Aerospace Power Division experts plus ones chosen by AFSTC in the following disciplines: Photovoltaics, Energy Storage, Power Conversion and Control, Thermal Management, Solar Dynamic Generation, Nuclear Power, and Advanced Concepts/System Demonstration. Each one of these disciplines conducted a workshop involving potential users, other government agencies and industry expert participation. These workshops were to assess the state of the art and technology readiness of key technology and identify basic research, exploratory development, and advanced development programs needed by the 21st century. The technology readiness levels are shown in Table I. The results of this prioritizing were then presented to industry and government leaders in a symposium at AFSTC Sept 1987. The results will also be published in a technical report to be released soon.

The Photovoltaic Workshop findings and the prioritized program recommended for funding from the SPT 21 study are presented below. The Photovoltaic Workshop was conducted at Aerospace Corporation by the Cochairmen, Joseph Wise of the Aerospace Power Division and Dr. W. Pat Rahilly and Dr. Robert Francis of Aerospace. The latter also graciously made all arrangements for the meeting and supplies. It was attended by 20-25 government and industry representatives. The major findings of this workshop were that developments are needed in high efficiency cells, survivability of solar arrays-planar and concentrator, and increase lifetime and reduce weight and cost to the extent possible within the constraints of survivability. The top priority program in Photovoltaics is outlined in Figure 2. Supporting technology in energy storage, power regulation and control and thermal management accompany the top priority program. The key technology development is the Survivable Concentrating Photovoltaic Array program being pursued by two contractors. Augmentation of these contracts was recommended in more weapon effects testing, development of higher temperature cells, investigating higher g loading, and producibility of the resultant hardware concepts. In addition several high efficiency solar cell programs are recommended to increase specific power of these survivable systems. Basic research is recommended in cell materials and configurations as well as areas incidental to the cells such as passivating and antireflecting coatings and stable high temperature metallization. Advanced survivability is also required since the work on survivability to date has only addressed passive measures and at relatively high levels. Active measures are required as well as a range of levels for those missions where weight or area may be most important and lower levels of weapon threat are a part of the operating scenario. Flexibility in design technology is one of the keys for continued utilization of photovoltaics for Department of Defense space applications. The rationale of recommending survivable photovoltaic systems as the top priority is briefly summarized in Table II. This technology and its admirable heritage make it a prime candidate for future long life high power systems if we can solve the problems of survivability, reliability, lower cost and increased specific power- watts/kg, watts/sq. meter.

The priorities for development of solar dynamic, nuclear and lightweight planar technology were considered by the SPT 21 as approximately equal. These three technologies are being pursued also. The program for lightweight, hardened technology is shown in Figure 3. The technology begins with the development of thin, high efficiency solar cells. The principal candidate at present is the 150 micrometer thick GaAs on Ge solar cell. Since this study was completed more than six months ago this cell has shown dramatic additional improvements and has the potential of better than 20% efficiency in production. This is especially true when we understand and fully exploit the interface between the GaAs and Ge and preserve the apparent boost in efficiency and voltage from the Ge substrate layer. Evaluation of proposals for developing manufacturing technology for this cell is currently underway. Other technology needed to fully utilize photovoltaics for military missions is to minimize the effects of natural particulate radiation. To this end some work is under way in our laboratory investigating annealing effects on GaAs solar cells. This is also where the indium phosphide solar cell appears promising. Understanding of the dynamics of large array subsystems and

their coupling into the vehicle and its attitude control system is vitally important in the application of photovoltaics to mission vehicles which have stringent pointing requirements themselves such as surveillance mission vehicles. The movement of the solar array remains a severe challenge in the development of solar array technology especially in the application of oriented solar arrays.

Program Implementation

How successful have we been in implementing this program? The contracts underway at the time of the study such as SCOPA and thin GaAs solar cells and multibandgap cell development are continuing. The Strategic Defense Initiative Office also recognized late in FY87 the need for nonnuclear baseload power especially for Phase I systems and has provided support for this program. It is indeed fortunate that the planning was conducted so thoroughly that we were able to present a mature plan to SDIO. Much of this program is being supported as illustrated in Figure 4. This includes augmentation of existing programs in photovoltaics and energy storage and the initiation of new efforts both in-house and through PRDAS in multibandgap concentrator cells and advanced hardened solar power technology. Although the latter is open to other than photovoltaic technology, promising photovoltaic proposals are expected to be supported. Similarly the SUPER program, currently on RFP, is to develop power system technology and demonstrate it in flight. Phase I is expected to include photovoltaic technology for power generation among other candidate solar energy conversion concepts. After Phase I there will be a down selection and only the best one or two systems will be continued into Phase II and flight demonstration.

Concluding Remarks

Photovoltaic power technology continues to be the primary candidate for supplying power for military satellites in earth orbit for a variety of missions. The highest priority in the Air Force and SDIO sponsored program is survivability--looking at both active and passive techniques of both avoiding damage and minimizing its effects. Development of higher efficiency and higher temperature solar cells is urgently needed to increase the watts/kg and improve survivability and life. To assist in the development and utilization of photovoltaic technology new facilities are needed to produce the improved hardware and test it from space operation and weapons effects. One recommendation is to develop weapon effects testing capabilities along with the development of the weapons such as lasers, neutral particle beams, pellets and nuclear weapon effects simulation. Basic research is needed to better understand new candidate and existing semiconductors and device concepts, stable high temperature metallization and coatings for passivation and control of absorption and emission from both natural and weapon effects simulation. Modeling is needed both in cell design and performance and solar array dynamics and interactions with vehicle/attitude control systems. Hardened planary array technology is needed in the near term to upgrade the survivability of future versions of existing systems. Ultra lightweight array technology is still enabling technology for very high altitude satellites because of weight limitations and the need for future improved mission capabilities. While higher efficiency solar cells will help somewhat in increasing the watts/kg, development of lightweight solar array blankets and structures are also needed. The photovoltaic industry has a continuing critical role to play in the future US military space missions. I wish to thank all those industry, government and academic experts who assisted in the SPT 21 Workshop on Photovoltaics.

SPT21	MAY	JUN	JUL	AUG	SEPT
<ul style="list-style-type: none"> • KICK OFF MEETING • WORK SHOPS • WORK SHOP REPORTS • INTEGRATION • FINAL SPT21 BRIEFING • ADVOCATE • FINAL REPORT 	▲	(AFWL) —		▲ —	▲ (AFSTC) — DECEMBER

STUDY SCHEDULE
FIG 1

UNCLASSIFIED
(U) TECHNOLOGY MATURITY LEVELS

LEVEL 7	ENGINEERING MODEL TESTED IN SPACE
LEVEL 6	PROTOTYPE/ENGINEERING MODEL TESTED IN RELEVANT ENVIRONMENT
LEVEL 5	COMPONENT/BREADBOARD TESTED IN RELEVANT ENVIRONMENT
LEVEL 4	CRITICAL FUNCTION/CHARACTERISTIC DEMONSTRATION
LEVEL 3	CONCEPTUAL DESIGN TESTED ANALYTICALLY OR EXPERIMENTALLY
LEVEL 2	CONCEPTUAL DESIGN FORMULATED
LEVEL 1	BASIC PRINCIPLES OBSERVED AND REPORTED

UNCLASSIFIED

TABLE I



PHOTOVOLTAIC SURVIVABLE ARRAYS

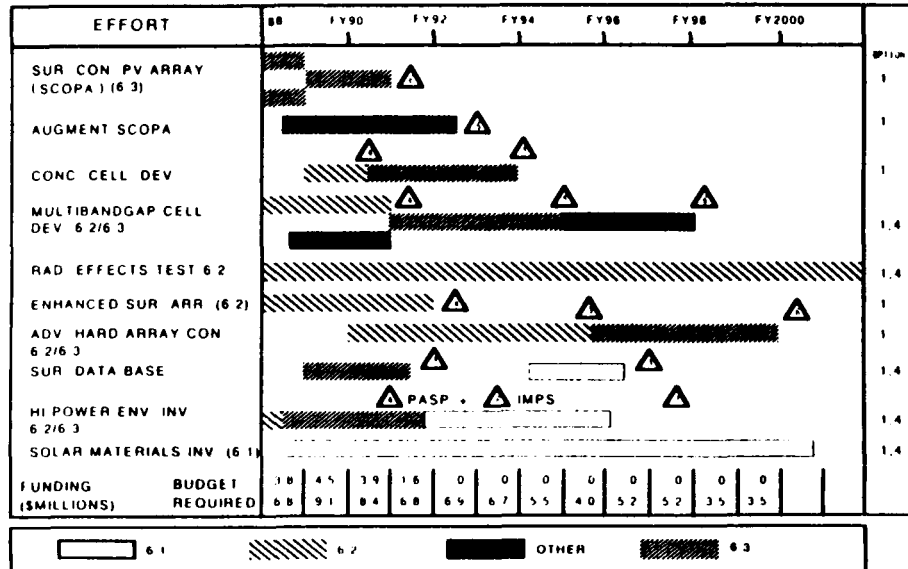


FIG 2

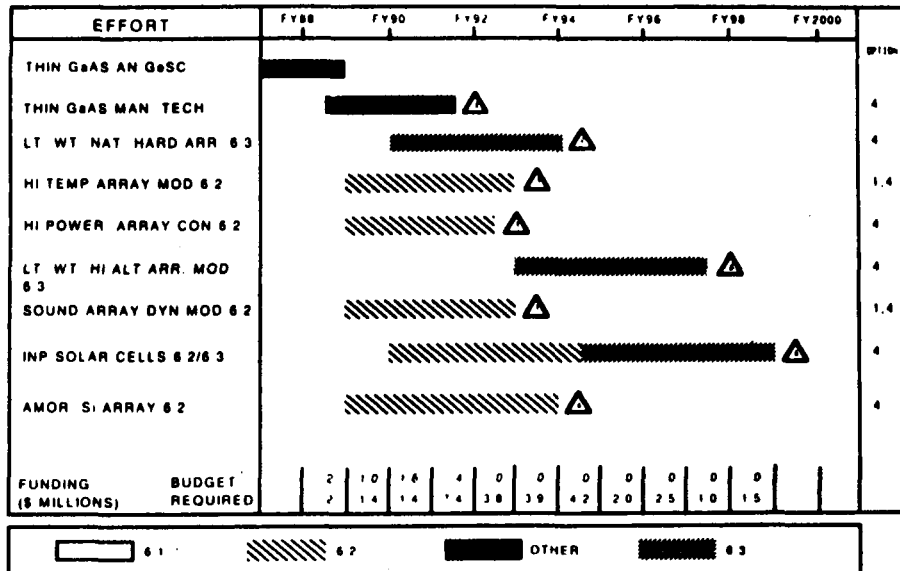
WHY PHOTOVOLTAICS?

- o DEMONSTRATED SPACE RECORD FOR 30 YEARS
- o HIGH RELIABILITY (STATIC)
- o SCALEABILITY/MODULARITY/INHERENT REDUNDANCY
- o COMPACT STOWAGE
- o POTENTIAL FOR SURVIVABILITY, AUTONOMOUS CONTROL/RECONFIGURATION
- o POTENTIALLY LIGHTWEIGHT
- o CAN BE MANEUVERED/RETRACTED/ROTATED/ORIENTED
- o MINIMUM SINGLE POINT FAILURE POINTS
- o PREDICTABLE WEAR OUT MECHANISMS RADIATION DEGRADATION, THERMAL FATIGUE

TABLE II

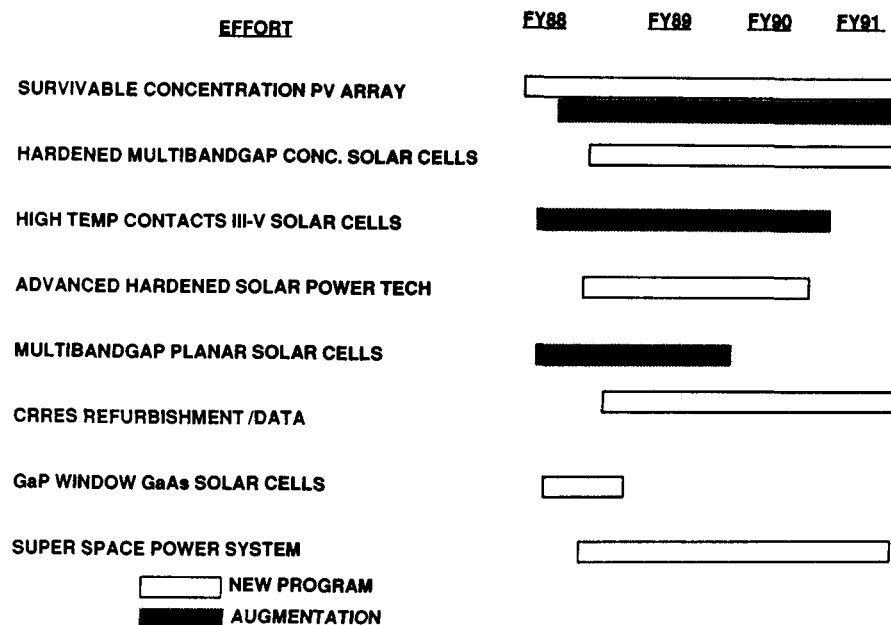


PHOTOVOLTAIC LIGHTWEIGHT ARRAYS



LIGHTWEIGHT
FIG 3

FIG 4
SDI SUPPORTED PV PROGRAMS



Session 1
InP Technology

PRECEDING PAGE BLANK NOT FILMED

Progress in Indium Phosphide Solar Cell Research

I. Weinberg, C. K. Swartz and R. E. Hart, Jr.
NASA Lewis Research Center
Cleveland, OH 44135

Abstract

Progress, dating from the start of the Lewis program, is reviewed emphasizing processing techniques which have achieved the highest efficiencies in a given year. To date, the most significant achievement has been attainment of AM0 total area efficiencies approaching 19%. Although closed tube diffusion is not considered to be an optimum process, reasonably efficient 2cm \times 2cm and 1cm \times 2cm InP cells have been produced in quantity by this method with a satellite to be launched in 1990 using these cells. Proton irradiation of these relatively large area cells indicates radiation resistance comparable to that previously reported for smaller InP cells. A similar result is found for the initial proton irradiations of ITO/InP cells processed by D. C. sputtering. With respect to computer modelling, a comparison of n/p homojunction InP and GaAs cells of identical geometries and dopant concentrations has confirmed the superior radiation resistance of InP cells under 1 MeV electron irradiations.

Introduction

Indium Phosphide solar cells are excellent candidates for use in the space radiation environment. This follows from their significantly increased radiation resistance when compared to gallium arsenide and silicon [ref. 1]. In addition, InP cells have been observed to anneal at room temperature under dark conditions and under the influence of incident light [refs. 2,3]. Furthermore, AM0 total area efficiencies of over 20% have been predicted using a conservative model [ref. 4]. For these reasons, the NASA Lewis Research Center has been conducting a program aimed at developing high efficiency, radiation resistant InP solar cells. The current paper reviews progress, during the past year, in both the U. S. and Japan. It is noted that a summary of the results presented at this conference would, in itself, constitute a progress review. However, to avoid unnecessary duplication, the present review deals mainly with results which are in addition to the remaining InP papers presented at this conference.

Cell Performance

Interest in InP solar cells was stimulated by the demonstration, in 1984, that relatively high efficiency n/p InP solar cells with excellent radiation resistance could be processed by a relatively simple closed tube diffusion process [refs. 5,6]. Progress in achieving high efficiencies, dating from that time, is shown in figure 1. All data shown are air mass zero, total area measurements obtained at NASA Lewis. The highest AM0 efficiency shown (18.8%) was obtained by a combination of

OMCVD and ion-implantation [ref. 7]. Additional details regarding this highest efficiency cell can be found in reference 7 and in the paper by Keavney and Spitzer presented at this conference.

For reasons of economy, all of the cells shown in figure 1 are of small area (0.25 cm^2). Recently, however, larger (4 cm^2) cells have been produced using a closed tube diffusion process [refs. 8,9]. For these latter cells In_2S_3 was used as a diffusion source to produce the sulphur doped n-region into a zinc doped p-type substrate doped to $2 \times 10^{16}/\text{cm}^3$. These cells were produced on a production basis to yield $1\text{cm} \times 2\text{cm}$ cells in addition to the 4 cm^2 cells (figure 2). A small sample of these cells was received and measured at NASA Lewis, the results being shown in table I. Also shown for comparison are measurements performed on the small area, highest efficiency cell of figure 1. It is noted that the cells produced by OMCVD have much higher open circuit voltages than the cells produced by closed tube diffusion. This is believed to be due, mainly, to the absence of back surface field in the large area cells [ref. 8]. This deficiency is inherent in the methodology used to produce these cells, i.e. diffusion into a thick Czochralski grown InP wafer [ref. 8]. The larger area cells, which presently are of moderately high efficiencies, are intended for use on a small piggyback lunar orbiter, attached to the Muses-a spacecraft, to be launched in February, 1990. A cutaway view of the spacecraft is shown in figure 3. The larger spacecraft will perform periodic lunar swingbys. At the first swingby, the small lunar orbiter will be injected into an orbit around the moon. Power for the lunar orbiter will be generated by approximately $1000 \text{ } 2 \text{ cm}^2$ InP cells with 50 micrometer thick cover glass. The orbiter is spin-stabilized with the InP cells generating about 10 watts of power [ref. 10]. Since the moon lacks a measureable magnetic field, the lunar orbiter will not be subjected to a severe ambient radiation environment. In fact, radiation due to solar flares will present the severest radiation hazard to the small lunar orbiter. Thus, rather than being a severe test of the behavior of InP cells in a strong radiation environment, the forthcoming lunar orbiter will serve mainly as a vehicle for space qualification of these cells.

Radiation Effects

The results of 10 MeV irradiations are shown in figure 4 where the 2 cm^2 cells, typical of those to be used on the lunar orbiter, are compared to n/p GaAs and small area, diffused junction, n/p InP cells. Pre-irradiation parameters for these cells are shown in table II together with pre-irradiation parameters for ITO/InP cells to be discussed in a subsequent section of the present paper. It is seen from figure 4, that the 2 cm^2 InP cells outperform the smaller area InP cells at the lower fluences but fall off at the higher fluences. Both InP cells exhibit radiation resistance superior to the GaAs cell. With regard to the behavior at high fluence, it is noted that the larger area InP cell has a junction depth between 0.2 and 0.3 micrometers [ref. 8], while the junction depth for the small area cell is well under 0.1 micrometer [ref. 11]. Dependence of radiation resistance on junction depth has been previously observed for GaAs where a decrease in junction depth was observed to accompany increased radiation resistance [ref. 12]. In the absence of similar data for InP, it is speculated that the fall off at higher fluences may be due to the cell's relatively large junction depth. On the other hand, the increased radiation resistance observed at lower fluence may possibly be due to better substrate quality in the larger area cells.

ITO/InP solar cells present a lower cost processing alternative to the more common n/p homojunction cells. Previous experience with silicon solar cells, in which an oxide was an active cell component, led to the strong possibility that radiation induced degradation in the oxide was a significant factor in cell degradation [ref. 13]. Thus it is relevant to assess the performance of ITO/InP cells in a radiation environment rather than taking it for granted that their radiation resistance will

be similar to that observed for the n/p homojunction cells. The results of such irradiations are shown in figure 5 while pre-irradiation cell parameters are listed in table II. This indicates that the present ITO/InP cells have radiation resistance, under 10 MeV proton irradiation, which is comparable to that of the n/p homojunction cells [ref. 14]. The present ITO/InP cells, supplied by Dr. T. J. Coutts of the Solar Energy Research Institute, were processed by D. C. magnetron sputtering of ITO onto zinc doped p-type InP whose dopant concentration was $3 \times 10^{16}/\text{cm}^3$. Examination of the ITO/InP interface by Raman spectroscopy and ellipsometry indicates that the cell configuration is most probably that of a semiconductor-insulator-semiconductor, the insulator being a-InP.

Theory

Comparisons of InP and GaAs cells, under laboratory irradiations, have employed cells with widely different pre-irradiation parameters. For example; the n/p GaAs cell of figure 4 has a base dopant concentration which is an order of magnitude greater than that of the n/p InP cells. Previous comparisons, under 1 MeV electron irradiation, have used p/n GaAs cells with an AlGaAs window for comparison with n/p InP cells [ref. 1]. In this latter case, the base dopant concentration of the GaAs cell was again an order of magnitude greater than that of the InP cell. In addition, the geometry of the two cell types was markedly different. In order to compare these cells on an equal basis, a computer calculation was performed using a previously published computer model [refs. 4, 16]. The parameters chosen for comparing both n/p cells are shown in table III. Using these parameters, an AM0 efficiency of 20.4% is predicted for InP while 21.5% is predicted for GaAs [ref. 16]. However, by reducing the emitter width to 250-300 Angstroms, front contact grid shadowing to 4% and by use of an optimized two layer AR coating, the optimum efficiency is 21.5% for InP and 22.5% for GaAs [ref. 16].

Because of carrier removal effects, it was necessary to use lifetime damage coefficients K_T to compute the degradation. The plot used to obtain K_T for InP is shown in figure 6, a similar plot being used for GaAs [ref. 16]. From these data it is found that $K_T = 1.3 \times 10^{-6} \text{ cm}^2/\text{s}$ for InP while for GaAs $K_T = 3.1 \times 10^{-5} \text{ cm}^2/\text{s}$. The computed results for identical cell configurations and doping densities show that the calculated performance of InP is superior to that of GaAs under 1 MeV electron irradiation (figure 7) [ref. 16]. It was also concluded that the superior radiation resistance in this case was not due to the higher absorption coefficient of InP, but was due to the intrinsic nature of the defects in these two cell types [ref. 16]. In this connection, Yamaguchi has tentatively concluded that "the radiation properties of the InP cells was attributable to room temperature and light enhanced annealing phenomena of the major defect centers in InP. The radiation resistance of InP was associated with the lower migration energy of indium and phosphorus displaced atoms in InP compared with those of the Ga or As displaced atoms in GaAs." [ref. 17]

Conclusion

Achievement of AM0 efficiencies approaching 19% makes the ultimate goal (20%) appear attainable. Although the present highest efficiency cells are relatively small, it should be recalled that, for GaAs, efficiencies over 18% were reported, in 1972, for cells whose area was considerably smaller than the present small area cells [ref. 18]. The latter cells are of adequate size for concentrator applications such as in the miniature cassegrainian concentrator [ref. 19]. However, much larger areas are required for planar arrays. The present larger area InP cells, with moderately high efficiencies, are

a first step in this direction. However, as previously noted, the method used to produce these larger area cells apparently has inherent limitations. In addition to its flexibility, the use of an epitaxial growth method usually results in a cell base which has less defects than a base consisting solely of a Czochralski grown wafer. Thus it is anticipated that the highest efficiency large area InP cells would ultimately be produced by an epitaxial technique. Aside from this there remains the question of cost and the capability of producing large, useable quantities of these cells. The present substrate costs are high but should be reduced when the cells are produced in large quantities. However, a more attractive cost reduction alternative lies in the use of heteroepitaxial growth on cheaper, sturdier substrates. Another alternative for cost reduction lies in the use of techniques, such as the CLEFT process, in which the substrate is reuseable [ref. 20]. With respect to production in quantity, the example of the cells intended for the small lunar satellite indicates that, if a demand exists, cells of moderately high efficiencies can be produced in relatively large amounts. However, for quantity production of large area higher efficiency cells, epitaxial growth appears to be the method having the greater possibility of success.

References

- [1] I. Weinberg, C. K. Swartz, R. E. Hart, Jr., and R. L. Statler, *Proceedings 19th IEEE Photovoltaic Specialists Conference*, p. 548 (1987).
- [2] M. Yamaguchi, Y. Itoh and K. Ando, *Appl. Phys. Lett.* **45**, 1206 (1984).
- [3] K. Ando and M. Yamaguchi, *Appl. Phys. Lett.* **47**, 846 (1985).
- [4] C. Goradia, J. Geier and I. Weinberg, *Proceedings 19th IEEE Photovoltaic Specialists Conference*, p. 937 (1987).
- [5] M. Yamaguchi, C. Uemura, A. Yamamoto and A. Shibukawa, *Japanese Journal of Applied Physics* **23**, 302 (1984).
- [6] A. Yamamoto, M. Yamaguchi and C. Uemura, *Appl. Phys. Lett.* **44**, 611 (1984).
- [7] C. J. Keavney and M. B. Spitzer, *Appl. Phys. Lett.* **52**, 1439 (1988).
- [8] H. Okazaki, T. Takamoto, H. Takamura, T. Kamei, M. Ura, A. Yamamoto and M. Yamaguchi, *Tech. Digest, 3rd Int'l Photovoltaic Science and Engineering Conf.*, Tokyo, p. 791 (1987).
- [9] I. Weinberg, C. K. Swartz, R. E. Hart, Jr., S. K. Ghandhi, J. M. Borrego, K. K. Parat and M. Yamaguchi, *Solar Cells* **22**, 113 (1987).
- [10] M. Nagatomo, Institute of Space and Astronautical Science, Tokyo, Private Communication.
- [11] K. K. Parat, S. Bothra, J. M. Borrego and S. K. Ghandhi, *Solid State Electronics* **30**, 283 (1987).
- [12] R. Loo, G. S. Kamath and R. C. Knechtli, *Proceedings 14th IEEE Photovoltaic Specialists Conference*, p. 1090 (1980).
- [13] I. Weinberg, H. W. Brandhorst, Jr., C. K. Swartz and V. G. Weizer, *Proceedings 2nd European Symposium on Photovoltaic Generators in Space*, p. 129 (1980).
- [14] I. Weinberg, C. K. Swartz, R. E. Hart, Jr. and T. J. Coutts, to be published in *Proceedings 20th IEEE Photovoltaic Specialists Conference*, (1988).
- [15] T. J. Coutts, Solar Energy Research Institute, Private Communication.
- [16] C. Goradia, J. V. Geier and I. Weinberg, *Tech. Digest, 3rd Int'l Photovoltaic Science and Engineering Conf.*, Tokyo, p. 207 (1987).
- [17] M. Yamaguchi, *Tech. Digest, 3rd Int'l Photovoltaic Science and Engineering Conf.*, Tokyo, p. 471 (1987).
- [18] J. M. Woodall and H. J. Hovel, *Appl. Phys. Lett.* **21**, 379 (1972).
- [19] R. E. Patterson, H. S. Rauschenbach and M. D. Cannady, *Proceedings 16th IEEE Photovoltaic Specialists Conference*, p. 39 (1982).
- [20] R. W. Mclelland, C. O. Bozler and J. C. C. Fan, *Appl. Phys. Lett.* **37**, 560 (1980).

TABLE I. - AMO PARAMETERS-INP SOLAR CELLS

C E L L		NO OF CELLS	Jsc MA/CM ²	Voc MV	FF PERCENT	EFFICIENCY PERCENT
JAPAN 2 CM ²	BEST		32.9	825	83	16.4
	AVERAGE	6	31.6±1	824±1	82.4±1	15.6±.6
JAPAN 4 CM ²	BEST		33.7	828	81.6	16.6
	AVERAGE	5	33.5±.2	826±1	81.5±.5	16.4±.1
U.S.A. 0.25 CM ²	BEST		35.7	873	82.9	18.8
	AVERAGE	8	35.7±.2	868±6	80.8±2	18.2±.5

TABLE II. PREIRRADIATION AMO PARAMETERS OF CELLS IN FIGS. 4&5

CELL	AREA CM ²	EFFICIENCY %	Jsc MA/CM ²	Voc MV	FF %
N/P INP	2	16.4	32.9	825	83
N/P INP	0.25	13.6	27.6	826	81.8
N/P GaAs	4	16.6	29	960	81.8
ITO/INP	0.72	13.2	32.6	761	78

TABLE III. - PREIRRADIATION CELL PARAMETERS USED IN THEORETICAL COMPARISON OF InP AND GaAs

	InP	GaAs
Junction Area, cm ²	1.00	1.00
Total Illuminated Area, cm ²	0.94	0.94
Grid Coverage, %	6.00	6.00
Specific Contact Resistance, ohm-cm ²	1.0E-3	1.0E-3
Front SRV, cm/sec	1.0E5	3.0E5
N ⁺ Emitter Width, angstroms	400	400
N ⁺ Emitter Doping, cm ⁻³	6.0E17	6.0E17
P Base Width, micrometers	1.50	1.0
P Base Doping, cm ⁻³	5.0E16	5.0E16
P ⁺ BSF/Buffer Width, micrometers	250	250
P ⁺ BSF/Buffer Doping, cm ⁻³	5.0E18	5.0E18

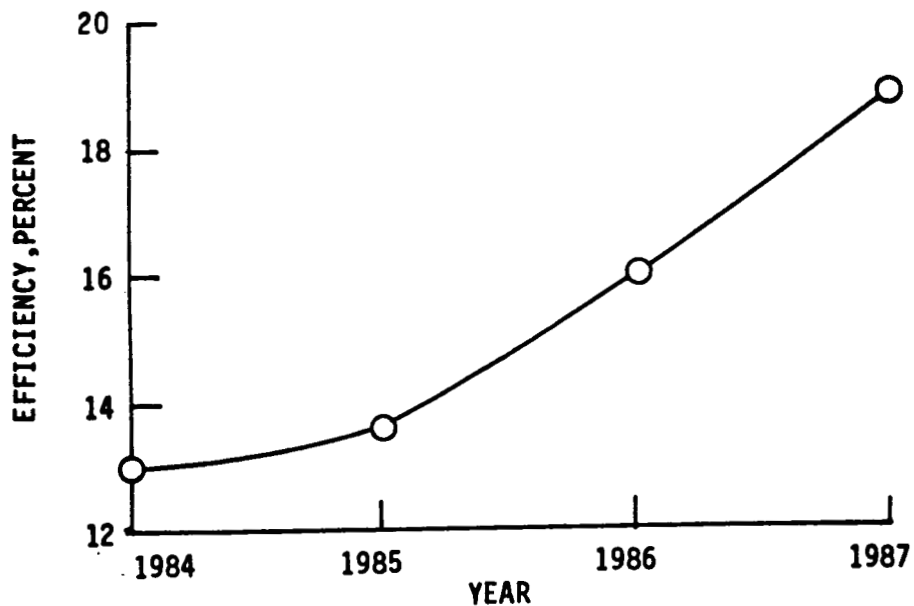
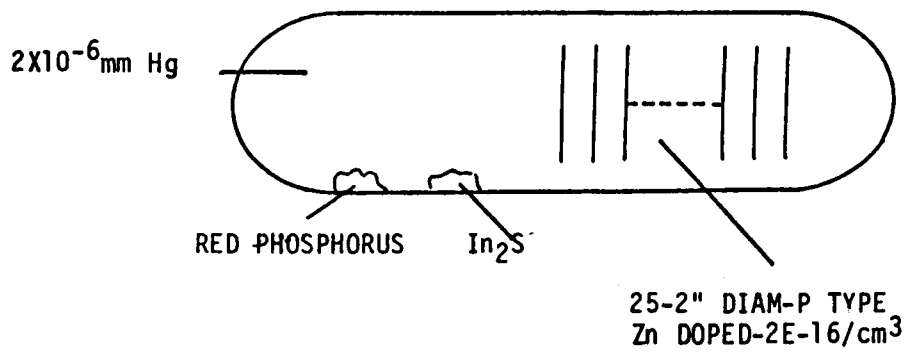


FIGURE 1. - PROGRESS IN ACHIEVING HIGH EFFICIENCY InP SOLAR CELLS.



AMO-TOTAL AREA PERFORMANCE PARAMETERS

$\frac{\text{AREA}}{\text{cm}^2}$	$\frac{J_{sc}}{\text{mA/cm}^2}$	$\frac{V_{oc}}{\text{mV}}$	$\frac{FF}{\%}$	$\frac{EFF.}{\%}$
4	33.8	821	83	16.7

H. OKAZAKI, ET. AL. PVSEC 3, PG. 793, TOKYO, NOV.1987

FIGURE 2. PRODUCTION OF LARGE AREA InP CELLS

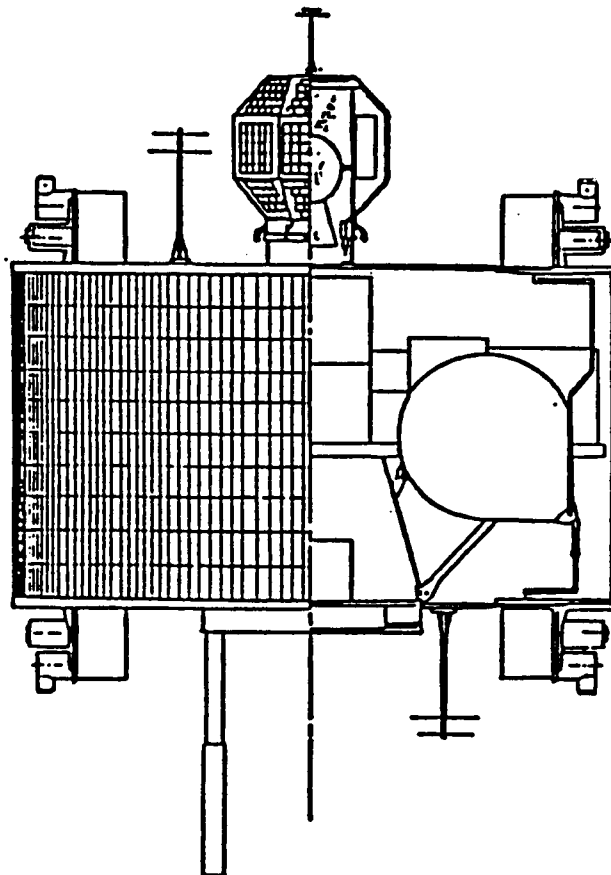


FIGURE 3 MUSES-A SPACECRAFT

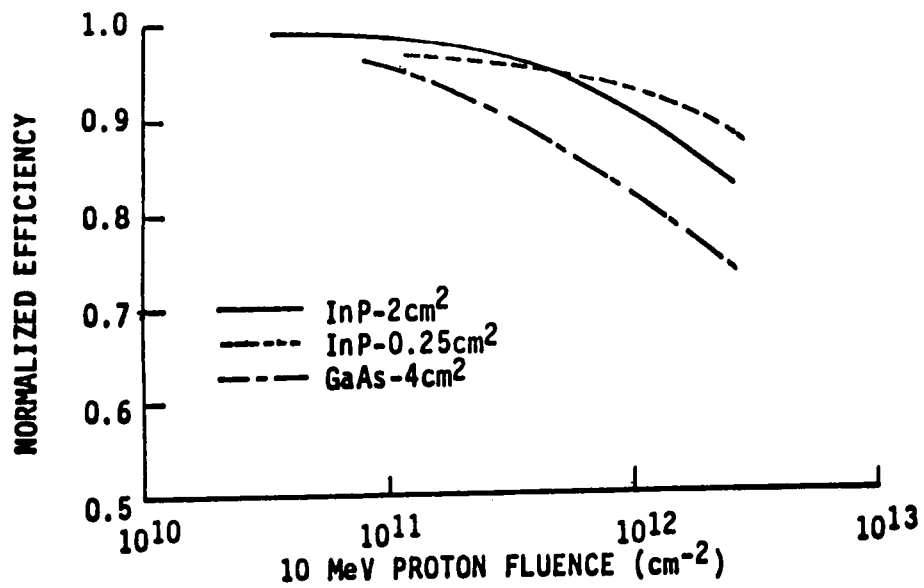


FIGURE 4. - NORMALIZED EFFICIENCIES UNDER 10 MeV PROTON IRRADIATION-InP AND GaAs.

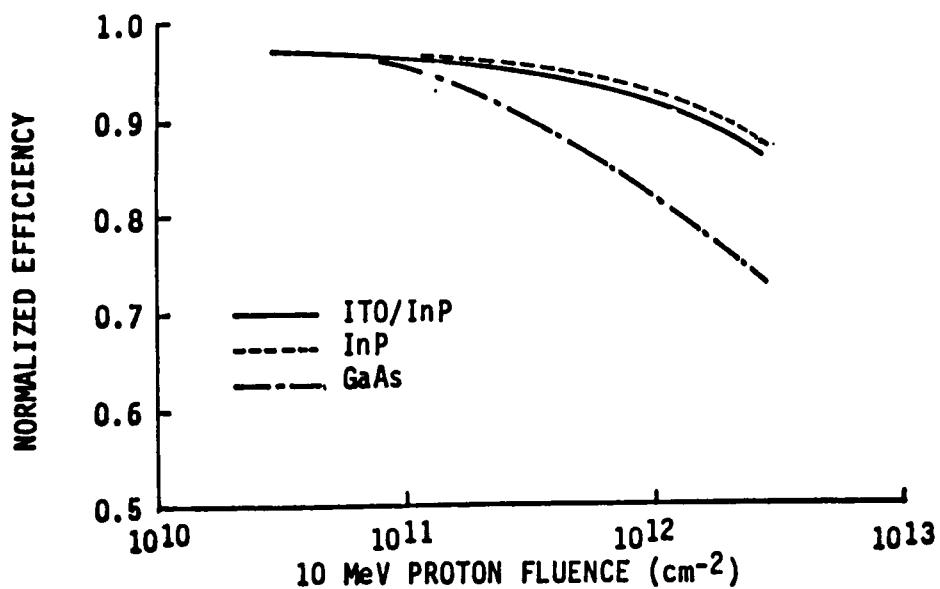


FIGURE 5. - NORMALIZED EFFICIENCIES UNDER 10 MeV PROTON IRRADIATION-ITO/InP, InP and GaAs.

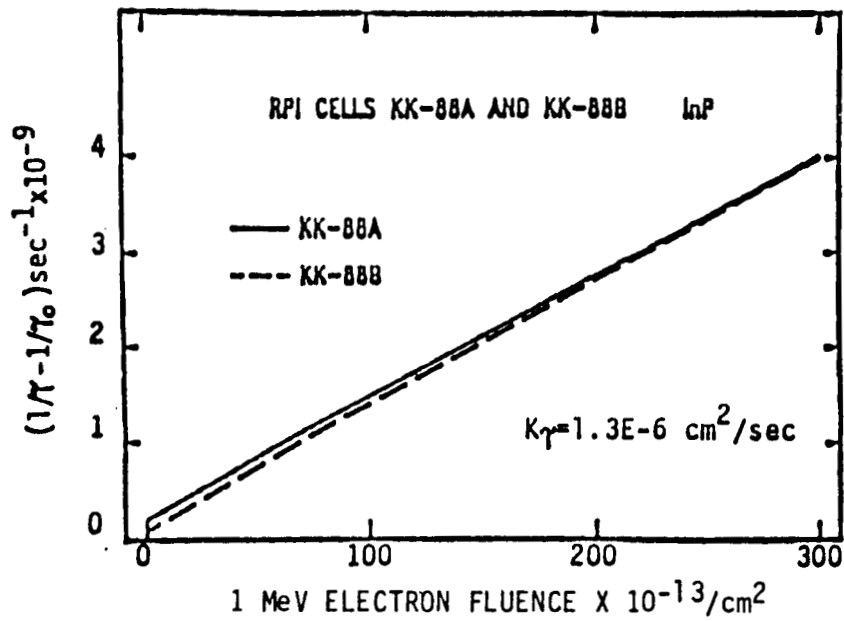


FIGURE 6. - GRAPHICAL PLOTS USED TO OBTAIN LIFE-TIME DAMAGE COEFFICIENTS OF InP.

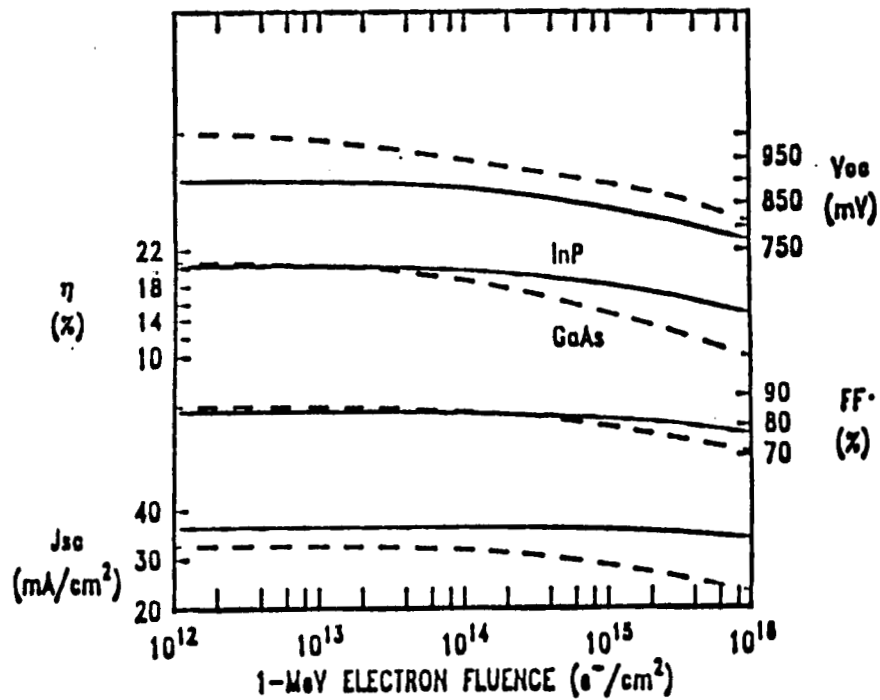


FIGURE 7. - CALCULATED PERFORMANCE OF InP AND GaAs UNDER 1 MeV ELECTRON IRRADIATION.

InP Shallow-Homojunction Solar Cells*

Christopher Keavney, Mark B. Spitzer, Stanley M. Vernon, Victor E. Haven
Spire Corporation

Godfrey Augustine
Georgia Institute of Technology

Summary

Indium phosphide solar cells with very thin n-type emitters have been made by both ion implantation and metalorganic chemical vapor deposition. Air mass zero efficiencies as high as 18.8% (NASA measurement) have been achieved. Although calculations show that, as is the case with GaAs, a heterostructure is expected to be required for the highest efficiencies attainable, the material properties of InP give the shallow-homojunction structure a greater potential than in the case of GaAs.

The best cells, which were those made by ion implantation, show open-circuit voltage (V_{oc}) of 873 mV, short-circuit current of 357 A/m² (35.7 mA/cm²), and fill factor of 0.829. Improvements are anticipated in all three of these parameters. Internal quantum efficiency peaks at over 90% in the red end of the spectrum, but drops to 54% in the blue end. Other cells have achieved 74% in the blue end. Detailed modeling of the data indicates that a high front surface recombination velocity is responsible for the low blue response, that the carrier lifetime is high enough to allow good carrier collection from both the base and the emitter, and that the voltage is base-limited.

Introduction

Recently, much effort has been devoted to the study of InP solar cells for space applications. This work was sparked by the discovery that exposure to radiation, as in earth orbit, causes less damage to the photovoltaic performance of these cells than to that of GaAs or Si cells. Furthermore, the damage which is done can be annealed at a relatively low temperature [refs. 1 to 5].

The development of high-efficiency InP-based solar cell structures has proceeded quickly. Yamamoto [ref. 1] reported high-efficiency cells by a diffusion process and by liquid-phase epitaxy [ref. 6], while Coutts and Naseem [ref. 7] achieved remarkable results with a simple sputtered indium tin oxide heterojunction. Bothra [ref. 8] used another diffusion technique. Most recently, the highest-efficiency cells have been formed by metalorganic chemical vapor deposition [refs. 9 to 11]; these include p on n structures of 15.6% (AM0) efficiency [ref. 9] and the n on p structures described here of 18.8% [refs. 10 and 12]. Theory predicts an attainable beginning-of-life efficiency for this material nearly the same as that for GaAs. Because of the superior radiation resistance, this would correspond to a considerably higher end-of-life efficiency in typical space applications than any other known material.

*This work was performed under contract with the NASA Lewis Research Center.

Experimental

High-efficiency cells were made by metalorganic chemical vapor deposition (MOCVD), by ion implantation, and by a combination of the two techniques.

MOCVD cells were grown on heavily-doped p-type substrates ($4 \times 10^{24} \text{m}^{-3}$ [$4 \times 10^{18} \text{cm}^{-3}$], 2° off 100 orientation) and consisted of three layers: a buffer layer $0.5 \mu\text{m}$ thick, doped p-type to $4 \times 10^{24} \text{m}^{-3}$, a p-type base layer $3 \mu\text{m}$ thick doped to approximately $2 \times 10^{22} \text{m}^{-3}$ ($2 \times 10^{16} \text{cm}^{-3}$), and an n-type emitter layer, doped to 10^{24}m^{-3} (10^{18}cm^{-3}) or higher, which varied in thickness. Growth was carried out in a SPI-MO CVDTM 450 reactor from tri-methylindium and phosphine. The growth conditions were as follows: 10 KPa (0.1 atm) pressure, 873–923 K temperature (600–650°C), P/In molar ratio of 80–400, and growth rate of 0.28–0.42 nm/s (1–1.5 $\mu\text{m}/\text{hour}$). SiH_4 and dimethylzinc were used as dopant sources.

For emitter thicknesses less than 100 nm, anodic oxidation was used to adjust the emitter thickness after epitaxy, as was done for GaAs cells by Fan, Bozler and Chapman [ref. 13]. The procedure of Robach et al. [ref. 14], using a dilute solution of phosphoric acid, was followed. An oxide of very uniform and controllable thickness could be formed in this manner, and cells with emitter thicknesses as small as 20 nm were successfully made.

Ion-implanted cells were formed from lightly doped ($2 \times 10^{22} \text{m}^{-3}$ [$2 \times 10^{16} \text{cm}^{-3}$]) p-type wafers. The wafers were implanted with an n-type dopant (Si, Se, or S) and then annealed at 1023 K (750°C) in a hydrogen atmosphere containing 2% PH_3 . The substrate, in this structure, forms an active part of the cell.

The effects of implantation dose and energy were observed. Surface preparation was also found to be important; wafers chemically polished before implantation gave much better results than wafers implanted as received from the vendor; the latter showed some pitting during the anneal and gave low open-circuit voltages.

Hybrid cells were made by growing the buffer and base layers by MOCVD as described above, and then forming the emitter by ion implantation. This combination has yielded the highest efficiencies to date, because it combines the advantages of both techniques.

Both implanted and CVD cells were metallized as follows: 50 nm each of Zn and Au–10% Zn alloy were evaporated onto the back, then annealed at 723 K (450°C) for 60 s in a strip heater. 50 nm Pd and 500 nm Ag were evaporated after the anneal. The front contacts were Au:Ge–Ag or Cr–Au–Ag, with 2 μm of Ag, patterned by liftoff. The cells were mesa etched to 0.25 cm^2 final area, and a ZnS/MgF_2 antireflection coating was applied. Cells were tested under simulated AM0 conditions (1372 W/m^2) at 298 K (25°C), both at Spire and at NASA Lewis Research Center.

Results

Ion Implantation

Figure 1 shows the spectral response of three cells made by silicon implantation at three ion beam accelerating potentials. The dramatic increase in blue response with decreasing energy demonstrates the importance of thin junctions, a subject which is discussed at greater length in the modeling

section below. Table 1 gives the corresponding cell performance. The short-circuit currents reported for the 5 KV silicon implants are higher than those of any of the epitaxial cells below; the 5 KV implant was incorporated into the hybrid cells which achieved 18.8%.

Anodic oxidation was used to examine the doping profile of three cells by differential Hall effect measurements; the results are seen in figure 2. The cells were repeatedly anodized to 10 V in the solution described above and the doping density in the removed layer was calculated from the change in the Hall coefficient and sheet conductivity with each anodization step. Since we were not able to measure the exact amount of material removed by an anodization step, these measurements must be taken as approximate, but they serve to indicate the general shape of the profile.

We conjecture that the high short-circuit current seen on wafer #57-1 is due to the shallow junction and the steep decrease in doping from a very high value at the front surface. The low voltage is apparently due to a back contact problem; the results from the hybrid cells below show that low saturation current and high V_{oc} are not incompatible with this doping profile.

MOCVD

Likewise, in the case of epitaxial cells, the factor to which the cell performance is most sensitive was found to be the emitter thickness. Figure 3 compares the spectral response of epitaxial cells of three different emitter thicknesses and table 2 gives the corresponding cell performance. The dramatic improvement in current is apparent.

Attempts to make emitters thinner than 50 nm by straightforward MOCVD were not successful, but we were able to produce shallower junctions by beginning with a 100 nm emitter and thinning it by anodization. Figure 4 shows the increase in current we observed from this thinning.

The MOCVD process allows the doping levels to be controlled continuously, so we were able to investigate step- and graded-emitter structures, and to attempt to match the doping profiles of the successful implanted cells. Table 3 describes these cell structures briefly. The graded structures were processed into cells without thinning. Table 4 presents the results.

The spectral response curves of the step- and graded-emitter cells (figure 5) contain some interesting data. The two 100 nm graded emitters show relatively low blue response, indicating that they were not successful in providing improved collection of carriers generated at the surface, but the 30 nm graded emitter shows blue response surpassing that of the 18.8% implanted cell.

These results are very encouraging as they show that the necessary structures for a high-performance emitter can be grown in one step. After antireflection coating, the cells on wafer 241 achieved an open-circuit voltage of 882/mV, which is the highest yet achieved.

Hybrid Cells

As noted above, the implanted cells showed the highest short-circuit currents, and the epitaxial cells the highest open-circuit voltages. Accordingly, we undertook to combine the advantages of both structures by making cells with an epitaxial base and an implanted emitter.

MOCVD was used to grow a base layer without an emitter. The structure was the same as that used for the cells described in section 3, except that the final n-type layer was omitted. A piece of this wafer was then implanted with $3 \times 10^{18} \text{m}^{-2}$ ($3 \times 10^{14} \text{cm}^{-2}$) of silicon and annealed as

described above. Table 5 gives the Spire and NASA measurement results from this wafer, along with those from the 17.9% all-epitaxial wafer and those from a polished implanted wafer for comparison. It was this hybrid cell which achieved 18.8% efficiency in NASA measurements. Spectral response and I-V characteristics are shown in figures 6 and 7, respectively.

As can be seen from figures 6 and 7, the implanted emitter has better collection efficiency in the blue end of the spectrum than the thinned epitaxial emitter, and its saturation current is almost as low. We have found, as expected, that combining the epitaxial base with the implanted emitter yields a cell with the advantages of both: the high red response and high voltage of the epitaxial cells and the high blue response of the implanted cells.

Modeling

Theoretical modeling of the blue response was carried out in an attempt to estimate the emitter lifetime and the front surface recombination velocity.

A closed-form equation which describes the collection efficiency of a homogeneous emitter as a function of thickness, carrier lifetime and mobility, surface recombination velocity, and optical absorption length was derived. Cells of identical doping concentrations and different emitter thicknesses, ranging from 10 nm to 300 nm, were compared using the same equation.

Figure 8 compares the results with the theoretical model. The best fit resulted from a high surface recombination velocity of 1.5 to 1.8×10^5 m/s, a hole mobility in the emitter of 70 to 100 $\text{cm}^2/\text{V s}$, and a high carrier lifetime in the emitter (0.1 ns). This value for surface recombination velocity is very close to the electron thermal velocity, which provides an upper limit on the SRV.

Although the agreement is not perfect, its persistence over more than a factor of ten in emitter thickness gives us confidence that surface recombination velocity is the limiting factor in the current collection. Models with lower recombination velocity required a shorter lifetime to fit the data from the thinner cells, and consequently they predicted a lower response than was observed for the thicker cells.

Finally, we attempted to use these modeling results to project the maximum efficiency for InP cells. The highest short-circuit current measured (from the hybrid implanted cells) was 360 A/m^2 (36.0 mA/cm^2) (NASA measurement). Although epitaxial cells have yielded lower currents (339 A/m^2 [33.9 mA/cm^2] was the highest), presumably the epitaxial cells could reach the same current, or slightly higher, with improved tailoring of the dopant profile. If this can be done while preserving the high V_{oc} (882 mV) and fill factor (84%) which we have seen in epitaxial cells, we would have an efficiency of 19.5% AM0. Although not yet achieved, this may be considered a realistic short-term goal.

Taking this as a baseline, there are two areas of improvement which we may consider. First, despite the considerable theoretical interest generated by InP, the parameters of the material are not well enough known to allow a definitive determination of the maximum achievable open-circuit voltage. V_{oc} of 1021 mV has been achieved with GaAs, [ref. 15] which has a very similar band structure, and so, in the absence of theoretical indications to the contrary, we may suppose that the achievable limit to the V_{oc} for InP is the same relative to the band-gap, or in the neighborhood of

950 mV. Our results indicate that the V_{oc} of the current cells is largely base-limited, and so efforts to increase V_{oc} must focus on improving the material quality toward the level achieved with GaAs.

The theoretical maximum AM0 current for indium phosphide is calculated to be 420 to 440 A/m² (42 to 44 mA/cm²). It is clear that the largest part of the uncollected current in the current cells is in the blue end of the spectrum, and our results suggest that the surface recombination velocity is the cause. If this is true, then finding a way to passivate the front surface of these cells could be very important.

Table 6 shows our estimates of the efficiencies realizable under various conditions. By making certain assumptions about the surface recombination velocity, we can project that efficiencies over 20% will be possible with a lattice-matched window layer.

Radiation Effects

The radiation resistance of these cells was evaluated as well. Cells were irradiated with $5 \times 10^{19} \text{m}^{-2}$ ($5 \times 10^{15} \text{cm}^{-2}$) electrons at 1 MV, and then annealed, both thermally and by forward-bias current injection. The effects of the radiation and annealing were assessed by both cell performance measurements and deep level transient spectroscopy (DLTS). Table 7 gives the anneal conditions and results. Figure 9 shows that the most important mechanism of efficiency degradation is the loss of red response, which presumably is the result of a decrease in base carrier lifetime. The anneal seems to have recovered some of the radiation damage, but it is difficult to quantify since control cells which were not irradiated also improved during the anneal.

References

- [1] A. Yamamoto, M. Yamaguchi, and C. Uemura, "High Conversion Efficiency and High Radiation Resistance InP Homojunction Solar Cells," *Appl. Phys. Lett.* **44**, 611 (1984).
- [2] M. Yamaguchi, K. Ando, A. Yamamoto and C. Uemura, "Minority-Carrier Injection Annealing of Electron Irradiation-Induced Defects in InP Solar Cells," *Appl. Phys. Lett.* **44**, 432 (1984).
- [3] M. Yamaguchi, Y. Ito, and K. Ando, "Room-Temperature Annealing of Radiation-Induced Defects in InP Solar Cells," *Appl. Phys. Lett.* **45**, 1206 (1984).
- [4] A. Yamamoto, M. Yamaguchi, C. Uemura, "High Efficiency Homojunction InP Solar Cells," *Appl. Phys. Lett.* **47**, 975 (1985).
- [5] I. Weinberg, C.K. Swartz, R.E. Hart and R.L. Statler, "Radiation and Temperature Effects in Gallium Arsenide, Indium Phosphide, and Silicon Solar Cells," *Rec. of the 19th IEEE Photovoltaic Specialists Conference*, New Orleans, May 1987, p. 548.
- [6] M. Yamaguchi, Y. Ito, and C. Uemura, "22% Efficient and High Radiation-Resistant InP Solar Cells," *Proc. of the Second International Photovoltaic Science and Engineering Conf.* (Beijing) Aug. 1986.
- [7] T. J. Coutts and S. Naseem, "High Efficiency Indium Tin Oxide/Indium Phosphide Solar Cells," *Appl. Phys. Lett.* **46**, 164 (1985).
- [8] S. Bothra et al., "Characterization and Modeling of Open Tube Diffused N⁺-P Bulk InP Solar Cells," *19th IEEE Photovoltaic Specialists Conference*, May 1987.

- [9] K. Y. Choi, C. C. Shen, and B. I. Miller, "P/N InP Homojunction Solar Cells by LPE and MOCVD Techniques," *19th IEEE Photovoltaic Specialists Conference*, May 1987.
- [10] M. B. Spitzer, C. J. Keavney, S. M. Vernon and V. E. Haven, "Indium Phosphide Shallow Homojunction Solar Cells Made by MOCVD," *Appl. Phys. Lett.* **51**, 364 (1987).
- [11] M. Sugo, A. Yamamoto and M. Yamaguchi, "n+-p-p+ Structure InP Solar Cells Grown by Organometallic Vapor-Phase Epitaxy," *IEEE Trans. ED-34*, 772 (1987).
- [12] C. J. Keavney and M. B. Spitzer, "Indium Phosphide Solar Cells Made by Ion Implantation," *Appl. Phys. Lett.* **52**, 1439 (1988).
- [13] J. C. C. Fan, C. O. Bozler and R. L. Chapman, "Simplified Fabrication of GaAs Homojunction Solar Cells with Increased Conversion Efficiencies," *Appl. Phys. Lett.* **32**(6), 390 (1978).
- [14] Y. Robach et al., "New Native Oxide of InP with Improved Electrical Interface Properties," *Appl. Phys. Lett.* **49**(19), 1281 (1986).
- [15] S. P. Tobin et al., "A 23.7% Efficient One-sun GaAs Solar Cell," *Rec. of the 19th IEEE Photovoltaic Specialists Conference*, New Orleans, May 1987, p. 1492.

Table 1. Effect of Implant Energy on Cell Performance

Wafer Ion #	Implant Voltage (kV)	Avg. V_{oc} (mV)	Avg. J_{sc} (A/m ²)	Avg. FF	Avg. Eff. (%)	Highest Eff. (%)
57-1 ^{a,c} Si (4 cells)	5	614 (+11)	331.6 (+ 1.7)	0.723 (+0.038)	10.7 (+0.5)	11.2
42-2f Si (2 cells)	10	806 (+ 1)	298.2 (+ 1.3)	0.718 (+0.061)	12.6 (+1.0)	13.3
42-3a ^{a,b} Si (1 cell)	50	777	182.1	0.757	7.8	7.8

Measurements at Spire, Air mass 0 (1372 W/m²), 298 K, silicon reference cell, with antireflection coating.

- Notes: ^a Results estimated from measurements without antireflection coating.
- ^b Results calculated from AM1.5 measurement.
- ^c The low voltage is attributed to an incomplete back contact anneal.

Table 2. Performance of Epitaxial Cells.

Run #	Emitter Thickness (nm)	Avg. V_{oc} (mV)	Avg. J_{sc} (A/m ²)	Avg. FF	Avg. Eff. (%)	Highest Efficiency (%)
72 (6 cells)	20	855 (+3)	223.3 (+1.0)	0.828 (+0.013)	11.5 (+0.2)	11.8
67 (3 cells)	100	850 (+16)	172.7 (+2.6)	0.807 (+0.016)	8.8 (+0.2)	9.0
68 (3 cells)	300	850 (+4)	103.1 (+0.5)	0.814 (+0.016)	5.3 (+0.1)	5.4

Measurements at Spire, Air mass 0 (1372 W/m²), 298 K, silicon reference cell, no antireflection coating.

Table 3. Cell Structures Investigated by MOCVD

Run #	Thickness (nm)	Doping (m ⁻³)	Purpose
233	50	1.5×10^{25}	Control
240	100	Two Step: 1.5×10^{23} - 1.5×10^{25}	High-low emitter structure to shield the lightly-doped layer from the surface
241	100	Graded 1.5×10^{23} - 1.5×10^{25}	To test the graded emitter structure
242	30	Graded 1.5×10^{23} - 3×10^{25}	To duplicate the implanted emitter

Table 4. Performance of Graded Epitaxial Cells.

Run #	Emitter Thickness (nm)	Avg. V_{oc} (mV)	Avg. J_{sc} (A/m ²)	Avg. FF	Avg. Eff. (%)	Highest Efficiency (%)
233b (4 cells)*	35 nm	814 (+15)	211.5 (+0.2)	0.777 (+0.032)	9.8 (+0.6)	10.2
240 (8 cells)	100 nm	789 (+22)	206.0 (+1.3)	0.707 (+0.017)	8.4 (+0.4)	9.0
241 (7 cells)*	100 nm	869 (+1)	208.0 (+1.0)	0.837 (+0.003)	11.0 (+0.1)	11.1
242 (8 cells)	30 nm	768 (+50)	218.2 (+3.9)	0.645 (+0.068)	7.9 (+1.1)	9.8

Measurements at Spire, Air mass 0 (1372 W/m²), 298 K, silicon reference cell, no antireflection coating.

*On each of these two wafers, one cell, located near the edge of the wafer, had much lower efficiency. These cells have been omitted from the averages.

Table 5. Comparison of Best Cells.

Run #	Process	Measured at	Avg. V_{oc} (mV)	Avg. J_{sc} (A/m ²)	Avg. FF	Avg. Eff. (%)	Highest Efficiency (%)
4970 (6 cells)*	All-Epitaxial	Spire	865 (+2)	318.9 (+0.5)	0.830 (+0.011)	16.7 (+0.3)	17.0
		NASA	864 (+2)	336.7 (+1.9)	0.826 (+0.013)	17.5 (+0.4)	17.9
5021-2 (9 cells)*	Implanted	Spire	833 (+5)	340.8 (+0.5)	0.797 (+0.014)	16.5 (+0.4)	17.0
5021-3 (8 cells)*	Hybrid	Spire	870 (+6)	349.5 (+1.4)	0.806 (+0.015)	17.9 (+0.4)	18.2
		NASA	868 (+6)	356.7 (+1.7)	0.808 (+0.016)	18.2 (+0.5)	18.8

Measurements at Spire, Air mass 0 (1372 W/m²), 298 K, silicon reference cell, with antireflection coating.

*On each of these two wafers, one cell, located near the edge of the wafer, had much lower efficiency. These cells have been omitted from the averages.

Table 6. Projected InP Cell Efficiencies.

	V_{oc} (mV)	J_{sc} (A/m ²)	FF	Efficiency (%)
Present best cell (5021-3)	873	357	0.829	18.8
Non-ideal recombination reduced	882	357	0.850	19.5
Shadow loss reduced to 3% (larger cell)	882	364	0.850	19.9
Window layer added (surface recombination reduced to 10 ³ m/s)	886	377	0.850	20.7
Bulk diffusion length increased to 15 μ m	933	379	0.855	22.0
Theoretical upper limit (no shadow, reflection, or series resistance)	950	427	0.878	26.0

Table 7. Effects of Irradiation and Annealing.
(Cell 248-8)

	H ₄ Trap Density (m ⁻³)	V _{oc} (mV)	J _{sc} (A/m ²)	FF	Eff. (%)
Initial	0	768	311.1	0.745	13.0
After irradiation (5 x 10 ¹⁹ m ⁻² Electrons @ 1 MV)	8.4 x 10 ¹⁸	712	259.5	0.727	9.8
After thermal anneal 348K, 1800 s (75°C, 30 min)	1.7 x 10 ¹⁸				
After thermal anneal 373 K, 1800 s (100°C, 30 min)	5.8 x 10 ¹⁷				
After current anneal 270 KA/m ² , 90 s	9.2 x 10 ¹⁶				
After thermal anneal 523K, 1800 s (250°C, 30 min)		730	283.6	0.732	11.0

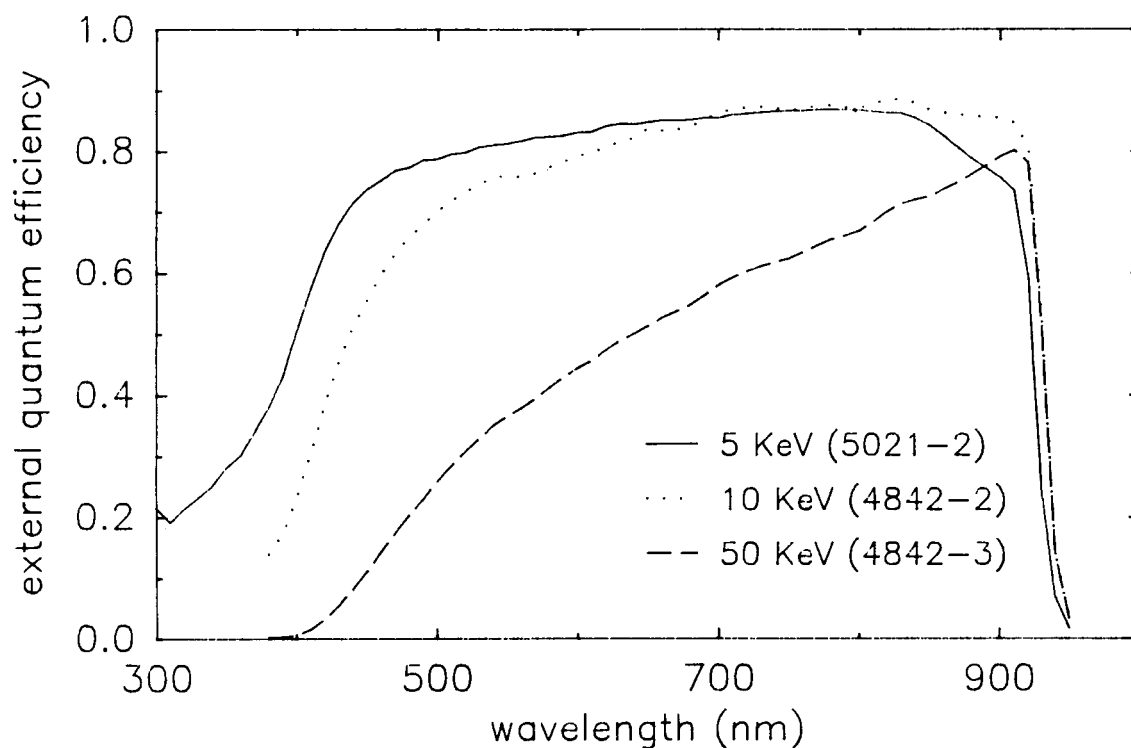


Figure 1. EFFECT OF IMPLANT ENERGY ON IMPLANTED InP CELLS. The lower voltages, which yield the shallower junctions, give improved blue response.

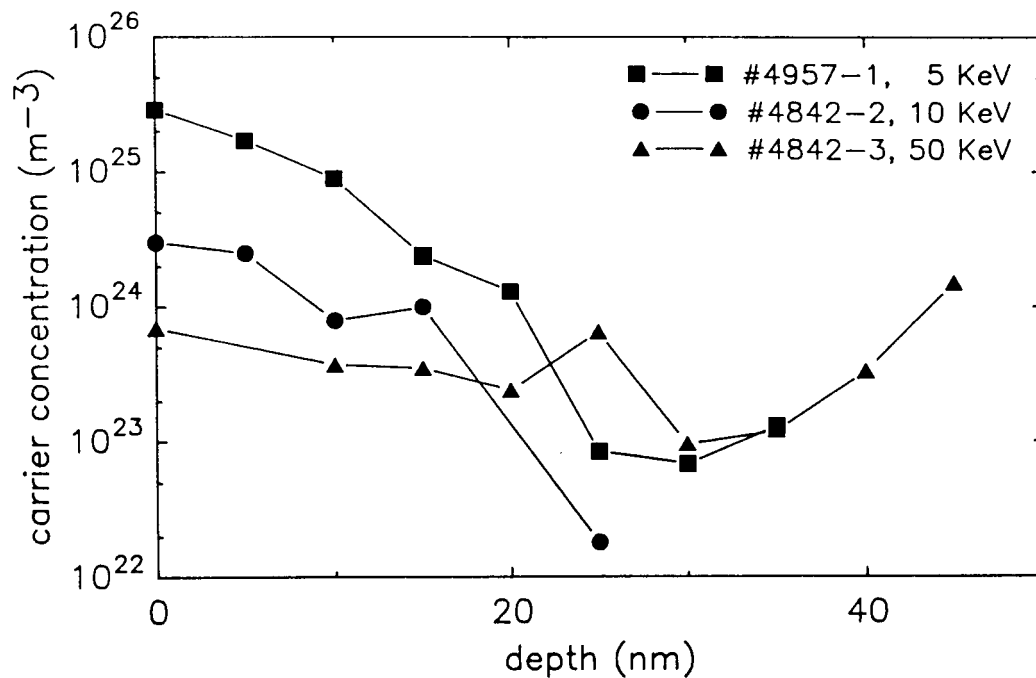


Figure 2. DOPING PROFILES OF JUNCTIONS FORMED IN InP BY ION IMPLANTATION OF SILICON. Differences in the processing apparently cause large differences in the overall doping levels, but the shallow, graded junction which results from the low-energy implant is apparent.

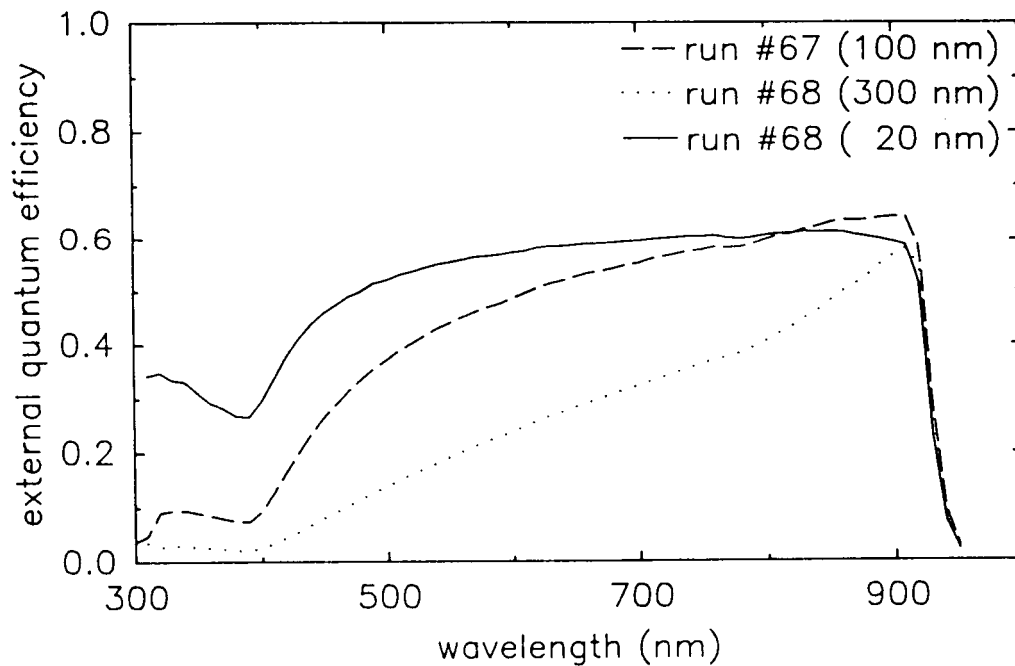


Figure 3. EFFECT OF EMITTER THICKNESS ON EPITAXIAL CELLS. (External quantum efficiency before antireflection coating is shown.) The cell with the 20 nm emitter was made by anodization.

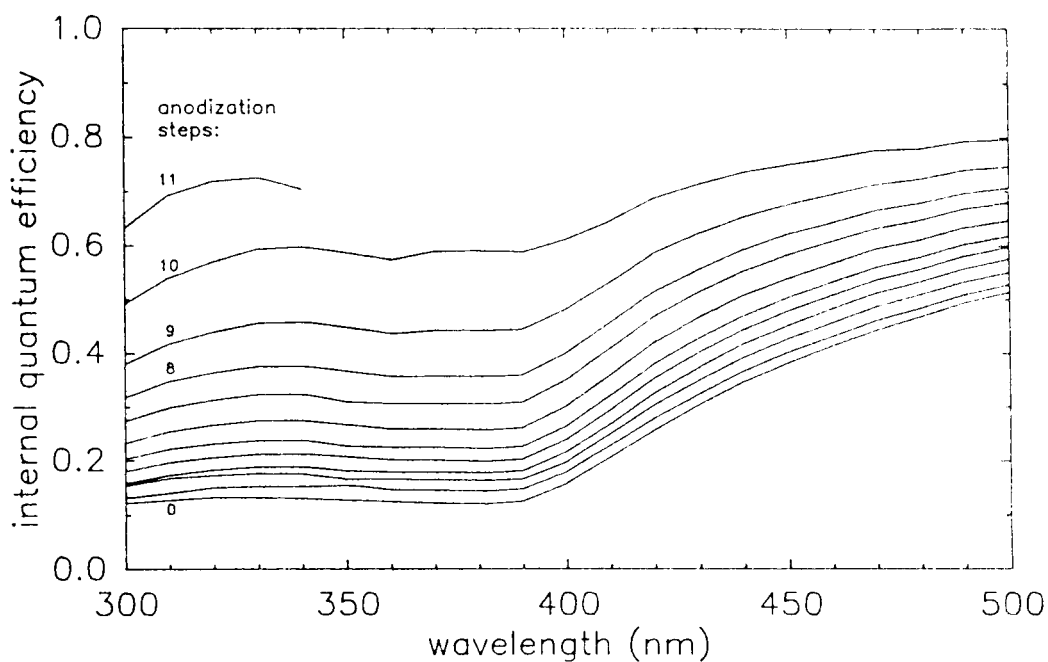


Figure 4. CHANGE IN THE QUANTUM EFFICIENCY WITH ANODIZATION OF AN EPITAXIAL CELL. Each anodization step removes approximately 10 nm from the front of the cell; since the cell failed after the eleventh step, the initial emitter thickness was apparently close to 110 nm.

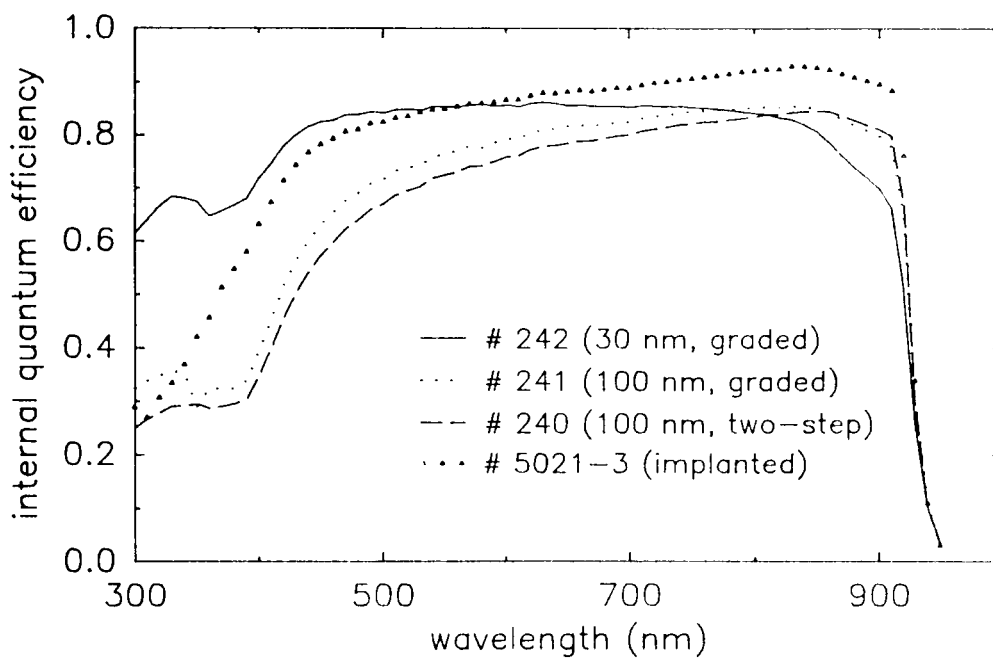


Figure 5. GRADED-DOPING EMITTERS, COMPARED TO THE IMPLANTED EMITTER OF THE 18.8% CELL. The thin graded structure has resulted in remarkable blue response.

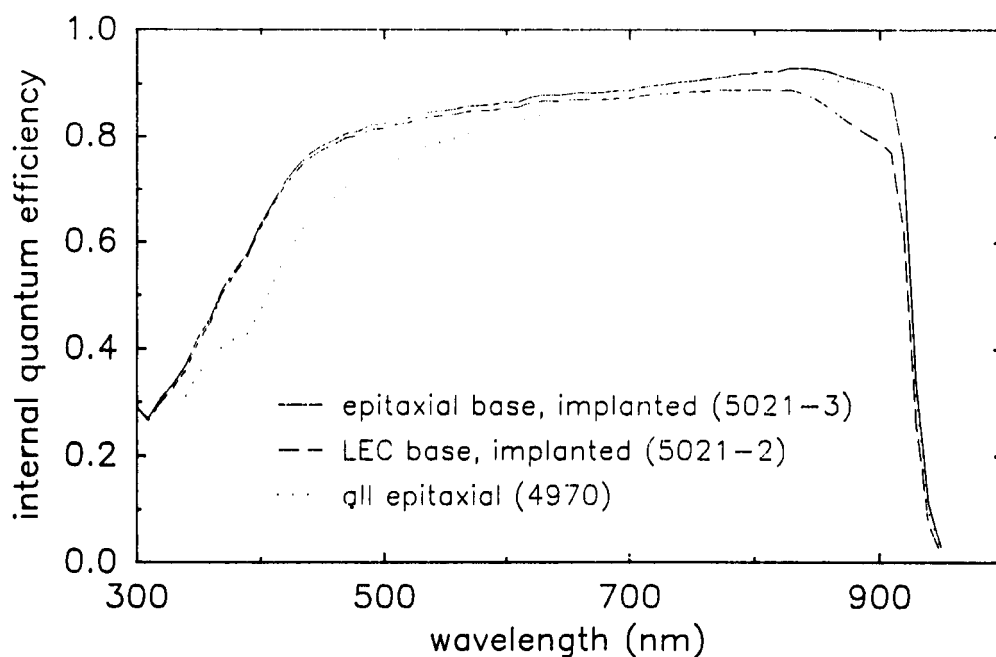


Figure 6. SPECTRAL RESPONSE CURVES OF THE IMPLANTED-EMITTER SOLAR CELLS, WITH AN EPITAXIAL CELL CURVE FOR COMPARISON. The curves show that the epitaxial base yields higher red response and the ion-implanted emitter yields higher blue response.

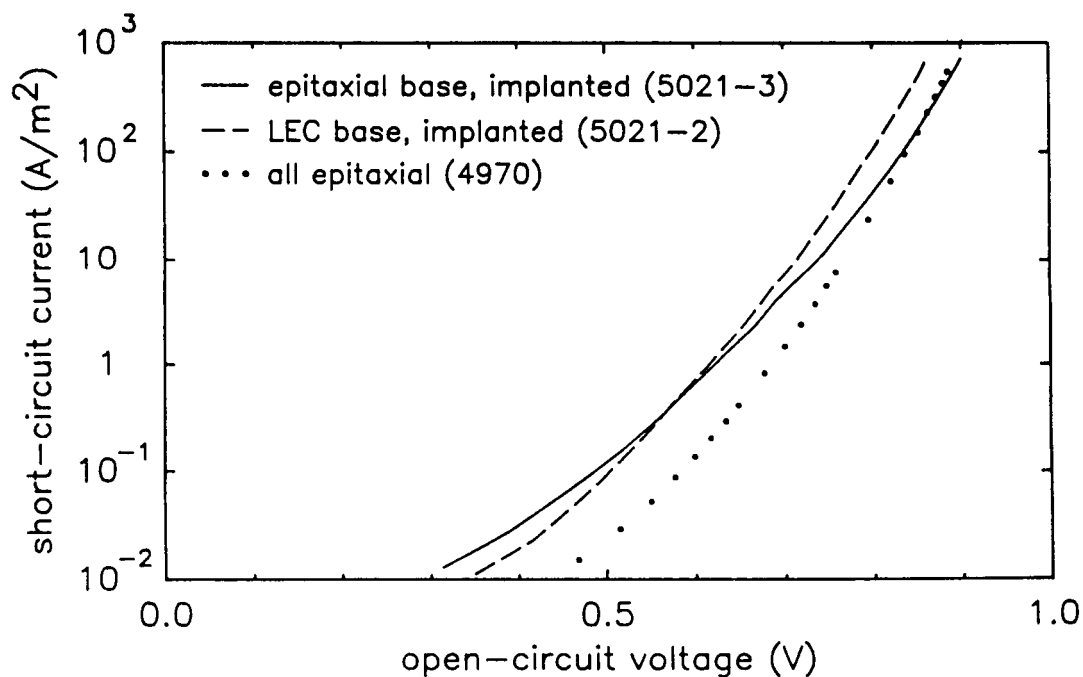


Figure 7. CURRENT-VOLTAGE CHARACTERISTICS OF THE IMPLANTED-EMITTER SOLAR CELLS, WITH AN EPITAXIAL CELL CURVE FOR COMPARISON.

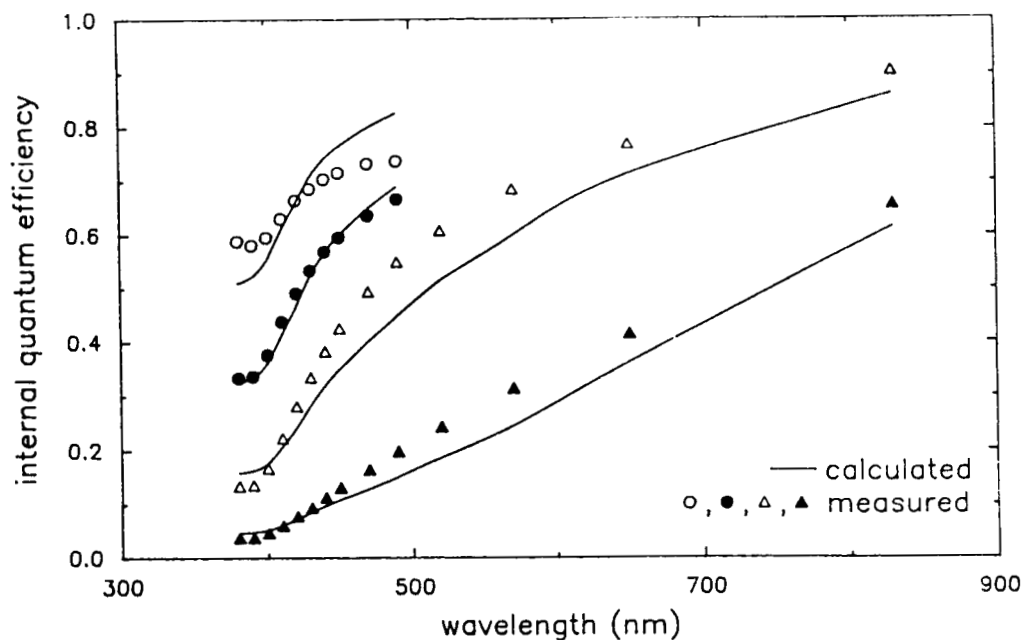


Figure 8. MODELING OF SPECTRAL RESPONSE OF THE THINNED EPITAXIAL CELLS. The estimated emitter thicknesses of these four cells (from top to bottom) were 11, 34, 110, and 300 nm. The thicknesses derived from the modeling are respectively 23, 42, 93, and 300 nm. As before, the modeling indicates that the low blue response is due to a high surface recombination velocity, rather than a low carrier lifetime.

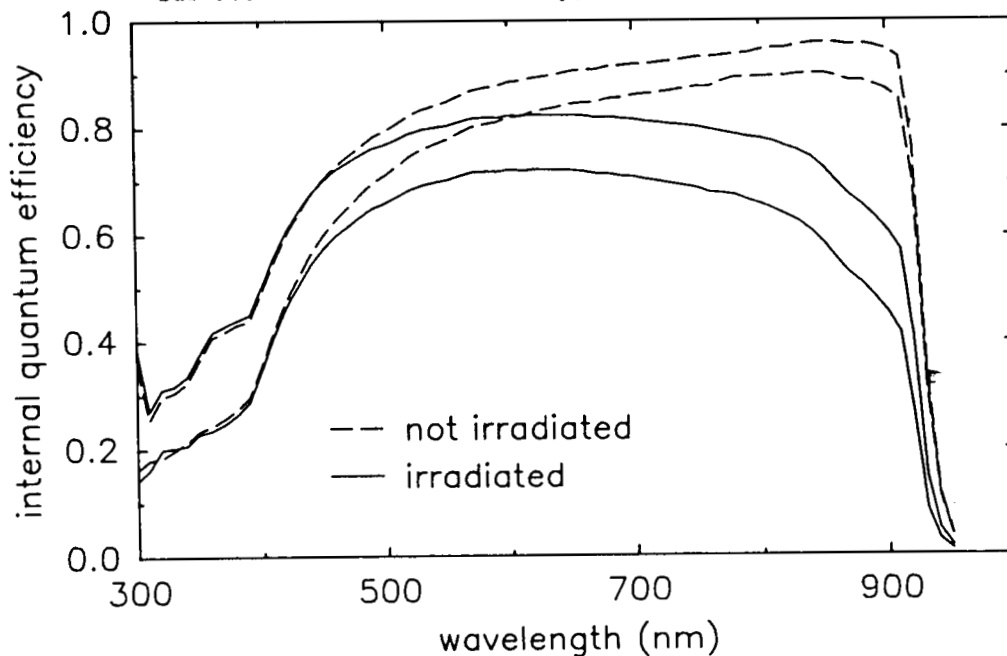


Figure 9. EFFECT OF ELECTRON IRRADIATION AND ANNEALING ON SPECTRAL RESPONSE OF AN EPITAXIAL SOLAR CELL. The primary mechanism of efficiency degradation is the loss of red response, which presumably is the result of a decrease in base carrier lifetime. The electron dose was $5 \times 10^{19} \text{ m}^{-2}$ ($5 \times 10^{15} \text{ cm}^{-2}$) at 1 MV. Two anneals were used: 348 K (75°C) and 373 K (100°C) for 1800 s (30 min) each. (The upper curve in each pair was measured after annealing.)

An Empirical Study of the Performance of APMOVPE AM0 InP Homojunction Solar Cells as a Function of Emitter Thickness and Doping, and Base Doping

M. W. Wanlass, T. A. Gessert, K. A. Emery and T. J. Coutts
Solar Energy Research Institute
1617 Cole Blvd.
Golden, CO 80401

Introduction

Their excellent radiation resistance [ref. 1] and conversion efficiencies $> 20\%$, measured under global conditions [ref. 2], make InP shallow-homojunction solar cells very attractive for space or terrestrial application. In addition, modeling studies [ref. 3] show that, for optimized design, efficiencies of these devices should exceed 20% even under AM0 conditions. However, a systematic experimental investigation of the influence of the various cell design parameters on cell performance has not as yet been made. For the $n^+/p/p^+$ structures investigated in the previous modeling study, the design parameters include the impurity concentrations and thicknesses of the emitter and base layers. In the work reported here, we discuss an experimental investigation of the effects on cell performance of varying the impurity concentrations of the emitter and base and thickness of the emitter.

Shallow-Homojunction Solar Cell Structure

A schematic cross-section of the InP shallow homojunction structure under investigation is shown in Figure 1. The structure consists of a single-crystal p^+ -InP substrate upon which are deposited three successive homoepitaxial layers of InP. These include a $0.5\ \mu\text{m}$ p^+ buffer layer with an impurity concentration of $5 \times 10^{18}\text{cm}^{-3}$, a $3\ \mu\text{m}$ p -type base layer with a variable impurity concentration and an emitter layer with variable thickness and impurity concentration. A study of photovoltaic performance vs cell design was carried out by systematically varying each of the emitter thickness, base doping and emitter doping while holding the other two parameters at constant values. Thus, the emitter thickness was varied from 100\AA to 700\AA while holding the base doping at $4 \times 10^{16}\text{cm}^{-3}$ and the emitter doping at $4 \times 10^{18}\text{cm}^{-3}$, the base doping was varied from $3 \times 10^{15}\text{cm}^{-3}$ to $3 \times 10^{17}\text{cm}^{-3}$ while holding the emitter doping at $4 \times 10^{18}\text{cm}^{-3}$ and the emitter thickness at 400\AA and the emitter doping was varied from $6 \times 10^{17}\text{cm}^{-3}$ to $4 \times 10^{18}\text{cm}^{-3}$ while holding the base doping constant at $4 \times 10^{16}\text{cm}^{-3}$ and the emitter thickness at 700\AA . For the emitter doping variation, the doping was spiked to $4 \times 10^{18}\text{cm}^{-3}$ over the last 150\AA of the emitter (i.e., near the surface) to facilitate formation of an ohmic grid contact. The variations in each of the parameters was achieved entirely through control of the epitaxial growth procedure. Over 100 individual cells were fabricated and analyzed for this study.

Epitaxial Layer Growth and Evaluation

The device layers investigated in the study were formed via the atmospheric pressure metalorganic vapor phase epitaxy (APMOVPE) process utilizing the chemical reactants, substrates, and growth conditions listed in Table I. A specially designed crystal growth system was constructed for this purpose with several important features. The gas handling system was composed of interior-electropolished 316 stainless steel tubing connected by a combination of leak-tight welded, VCR and O-ring fittings with electronic mass flow controllers for metering and controlling the source gas flow rates. The system is a run/vent type utilizing a split main mixing manifold composed of a series/parallel combination of air-operated 3-port and 4-port bellows valves. The term "split" refers to a separation of the organometallic source vapors from the others until just prior to introduction into the reactor vessel. Such a manifold arrangement allows for fast gas switching times and also reduces the possibility of homogeneous or heterogeneous reactions in the vapor phase preceding InP growth. Palladium-diffused hydrogen is used as the carrier gas throughout the system. A high-performance quartz reactor vessel capable of producing highly uniform epilayers was used, the design details of which are described elsewhere [ref. 4]. Water cooling of the reactor vessel walls served to condense excess phosphorus from the growth process and confined it to the upper portions of the reactor. This, combined with a helium purging sequence, essentially eliminated the problems of spontaneous ignition of the phosphorus when the reactor was opened to air for loading or unloading wafers. Experience has shown that water-cooled and air-cooled reactor vessels yield epilayers with similar properties. A susceptor, composed of uncoated high-purity graphite and heated by radio frequency induction, was used. The substrate temperature was measured using a thermocouple inserted within the susceptor with temperature stability achieved via a feedback power controller for the RF generator.

The substrates used in this process were single-crystal, liquid encapsulated Czochralski (LEC) InP and were delivered polished on one side and etched on the other from each of the vendors listed in Table I. Wafers were loaded into the reactor as received without any further preparation. Prior to growth, the substrates were heated to 700°C for five minutes with phosphine flowing to the reactor from a cold start. The temperature was then lowered and stabilized at 650°C and the desired mole fractions of $(\text{CH}_3)_3\text{In}$ and $(\text{C}_2\text{H}_5)_2\text{Zn}$ were then introduced to the run stream to commence the growth of p-type InP. The thickness of the individual epilayers was assumed to be equal to the growth time multiplied by the calibrated growth rate determined from measurements on thicker layers. In the case of p-type layers, the desired impurity concentration was achieved in two different ways depending upon the desired level. For $(N_A - N_D) > 1 \times 10^{17} \text{cm}^{-3}$ the doping was obtained through the usual manner of bubbling through the source, while for $(N_A - N_D) < 1 \times 10^{17} \text{cm}^{-3}$ a special controlled source evaporation technique was employed. Impurity concentrations for the n- and p-type layers were verified using capacitance-voltage measurements on finished cells with one-sided n^+/p junctions or with similar measurements using a mercury probe on single layers. Formation of the n^+/p homojunction was achieved by simultaneously stopping the $(\text{C}_2\text{H}_5)_2\text{Zn}$ flow and introducing H_2S , with the emitter thickness being equal to the time from the introduction of the H_2S to the termination of growth, multiplied by the calibrated growth rate. Generally, the surface morphology and overall epilayer quality was ostensibly the same for substrates obtained from each of the vendors.

Solar Cell Fabrication

Following growth, the device wafers were processed into arrays of electrically isolated solar cells with the cell areas and grid contacts defined using standard photolithographic and chemical etching techniques. Mesa cells 0.10 cm^2 in area with a nominal grid coverage of 10% were formed by etching orthogonal isolation troughs with $9\text{ H}_3\text{PO}_4:1\text{ HCl}$ at room temperature. The top grid contacts were formed by electroplating pure Au to the n^+ layer while the back contact was formed by sintering a 1500\AA thick layer of evaporated Au/Be in flowing forming gas at 400°C for 1 minute and then overplating with $\sim 2\text{ }\mu\text{m}$ of pure Au. This process yielded seven to twelve finished solar cells on each device wafer. For the purposes of the study, antireflection coatings (ARC) were not applied to the cells in order to keep the analysis of the results as simple as possible. However, after analyzing the results, a few cells with near-optimum design parameters had a two-layer ARC of ZnS/MgF_2 applied. The individual thicknesses of these were determined using a recently developed two-layer coating optimization technique.

Results and Discussion

Performance of the shallow-homojunction cells was characterized using dark J-V, light J-V and spectral response techniques. For comparison purposes, the light J-V data were obtained under standard global conditions at 25°C with total irradiance of 1000 Wm^{-2} and using total cell area [ref. 5]. The quantum efficiency was calculated using active area. For the better cells which had a two-layer ARC applied a light J-V measurement under AM0 conditions was also performed using total cell area, a junction temperature of 25°C and a total irradiance of 1367 Wm^{-2} . The measurement uncertainty for each of the global and AM0 conversion efficiency measurements is $\pm 2\%$.

The variation of cell performance parameters with nominal emitter thickness is given in Figure 2 for cells with emitter and base doping concentrations held constant at $N_D = 4 \times 10^{18}\text{ cm}^{-3}$ and $N_A = 4 \times 10^{16}\text{ cm}^{-3}$, respectively. The data indicate a strong steady increase in J_{sc} as the emitter thickness is reduced from 700\AA to 200\AA . Figure 3 shows a composite of internal quantum efficiency curves for the same devices indicating a decrease in overall response as the emitter thickness increases, particularly in the blue. Returning to Figure 2, V_{oc} and FF remain roughly constant with emitter thickness down to 200\AA showing only slight fluctuations which are thought to be due to minor, unintentional variations in the growth and processing procedures from run to run. Thus, for emitter thicknesses $> 200\text{\AA}$, the conversion efficiency dependence on the emitter thickness is dominated by the behavior of the quantum efficiency. The decrease in photocurrent results from increasing recombination losses at the surface, and within the bulk, of the heavily doped emitter layer as the thickness is increased. For emitter thicknesses $< 200\text{\AA}$, however, the performance parameters, particularly V_{oc} and FF, decrease dramatically resulting in a significant drop in the conversion efficiency. A similar behavior has been observed in our laboratory for shallow-homojunction cells fabricated in other III-V materials such as GaAs [ref. 6] and $\text{GaAs}_{0.74}\text{P}_{0.26}$. In all cases, the catastrophic failure of the cells correlates well with a dramatic increase in the dark reverse saturation current for junctions with emitters thinner than the critical value. However, the physical mechanism(s) responsible for the increase have not been identified as yet. Surface recombination effects and “narrow” diode behavior are possible causes. In any case, the peak efficiency occurring for an emitter thickness in the $200\text{--}300\text{\AA}$ range is a direct consequence of these effects and represents an intrinsic limiting factor for the shallow-homojunction cell performance.

The effects of varying the base doping concentration are summarized in Figure 4. In this case, the emitter thickness and doping concentration were held constant at 400Å and $N_D = 4 \times 10^{18} \text{cm}^{-3}$, respectively. V_{oc} and FF each tend to improve as the base doping concentration is increased and this trend is consistent with an increasing value of the product $N_A N_D$ and a decreasing recombination component of the dark current due to a decreasing depletion width. J_{sc} , however, remains relatively constant as the base doping concentrations increased up to a value of $6 \times 10^{16} \text{cm}^{-3}$, and decreases thereafter. Internal quantum efficiency curves for the same cells are compared in Figure 5 and show that the red response decreases for the higher values of base doping concentration indicating that the minority carrier diffusion length and lifetime are insufficient for the higher values. The combined effects of the variations in V_{oc} , J_{sc} and FF result in the conversion efficiency reaching a maximum for a base doping concentration of about $5 \times 10^{16} \text{cm}^{-3}$. Thus, the optimum values for the emitter thickness (200-300Å) and base doping concentration ($\sim 5 \times 10^{16} \text{cm}^{-3}$) are in agreement with those predicted by Goradia et al. in a recent modeling study [ref. 3].

The cell performance dependence on emitter doping concentration is illustrated in Figures 6 and 7. The emitter thickness was held constant at a higher-than-optimum value (700Å) to see more clearly the doping effect whereas the base doping concentration was held at $4 \times 10^{16} \text{cm}^{-3}$. V_{oc} and FF show a monotonic increase with increasing emitter doping which is due presumably to a lower emitter sheet resistance, an increasing value of $N_A N_D$ and a decreasing recombination current component from the emitter. A monotonic decrease in both J_{sc} and the internal quantum efficiency red response is observed as the emitter doping increases indicating that the minority carrier diffusion length and lifetime are insufficient at higher emitter doping levels. The opposing trends in V_{oc} , FF versus J_{sc} tend to compensate one another and result in the conversion efficiency showing little variation with emitter doping, at least for the emitter thickness of 700Å used here. For thinner emitters, the overall effect on conversion efficiency may be quite different and further work should be performed in this regard.

The better junctions in this work, had ideality factors (n) and reverse saturation current densities (J_0) of $1.03 < n < 1.08$ and $1 - 2 \times 10^{-13} \text{mA cm}^{-2}$, respectively. Cells with emitters $< 200\text{Å}$ thick or bases with $< 2 \times 10^{16} \text{cm}^{-3}$ impurity concentration had larger values of both n and J_0 . Although a detailed analysis of the latter variations has not been performed, it seems likely that excessively thin emitters cause enhanced surface recombination while lightly doped bases cause enhanced recombination in the space charge region. In addition, a larger diffusion current would be expected due to the lower built-in potential of the cells with lightly doped bases.

Using the information derived from this work, a few cells with near-optimum design parameters were fabricated to test our conclusions. The cells had a total area of 0.108cm^2 , 5% grid coverage, a 2-layer ARC of ZnS/MgF₂ with a structure consisting of a $0.5 \mu\text{m}$ buffer layer doped to $5 \times 10^{18} \text{cm}^{-3}$, a $3 \mu\text{m}$ base layer doped to $5 \times 10^{16} \text{cm}^{-3}$, and a 250Å emitter layer doped to $4 \times 10^{18} \text{cm}^{-3}$. Performance data for one of the better cells are given in Figures 8 and 9. The achievement of global and AM0 conversion efficiencies of 20.3% and 17.6%, respectively, demonstrate the success of the study, however further improvements in cell performance should be possible. The internal quantum efficiency data indicate that substantial gains in J_{sc} can be made, particularly in the blue, and we feel that improved grid designs and emitter layer properties will lead to values of J_{sc} under global conditions in the $29\text{-}30 \text{mA cm}^{-2}$ range. Furthermore, a degradation of the junction dark J-V characteristics, illustrated in Figure 10, was observed after deposition of the ZnS component of the

two-layer ARC. J_0 increased by an order of magnitude and n by $\sim 10\%$ which we estimate lowered V_{oc} by about 4 mV. The degradation is believed to be due to either a shunting path formed by the ZnS deposition along the edge of the cell mesa or to cell damage occurring during the electron-beam evaporation coating process. Revised processing procedures are being developed to address this problem. Finally, improved values for FF are possible since we have already observed values as high as 86% for similar cells fabricated in our laboratory. Therefore, a realistic upper limit for the conversion efficiency using the present structure appears to lie in the 21-22% range. The results obtained so far are particularly encouraging considering that the epilayers were formed using a simple growth procedure at atmospheric pressure with a relatively low V/III ratio.

Conclusions and Future Directions

The emphasis in this work to-date has been on an empirical investigation of the effect of the cell design parameters on performance. Devices with efficiencies $> 20\%$, measured under standard global conditions, have been achieved and the trends in device behavior with emitter and base doping and emitter thickness are in general accordance with expectations from elementary theory. The key conclusions which can be drawn from the work are:

1. Of the three variables investigated, the dominant influence is the emitter thickness. The cell efficiency increases monotonically with decreasing emitter thickness but decreases catastrophically at a thickness of $< 200\text{\AA}$. This effect is unlikely to be due to morphological shortcomings and its origins remain to be determined. It should be pointed out that elementary theory does not incorporate this effect.
2. Further improvements in device efficiency are likely to result from a thorough investigation of the factors influencing V_{oc} and from an improvement in the blue response. These will result from improved materials properties and cell design.

Improvements in efficiency towards the goal of a device with an AM0 efficiency of $> 20\%$ are likely to result from both fundamental and technological developments. Under the classification of fundamental aspects, the following can be included.

1. More attention must be paid to the level of emitter doping and the possibility of establishing an emitter doping profile. Equally, the optimum thickness of the base is not yet established although preliminary data on this are now available.
2. It is essential to establish the variation of epilayer quality as a function of that of the substrate. Therefore an assessment of wafer quality from a range of different vendors using a variety of optical and structural characterization techniques should be performed.
3. Little work has yet been undertaken on optimizing the growth parameters (e.g., temperature and V/III ratio) of the epilayers to achieve improved materials properties. Although the materials properties seem excellent, significant improvements may result from this. Preliminary investigations of dark current mechanisms imply a significant contribution from space charge recombination through near mid-gap states. Attempts are presently being made to correlate these data with DLTS measurements and, together, this information may influence the selected growth conditions.

4. Preliminary device modeling has been performed but reveals a shortage of accurate values for input parameters. Hence, it is essential to perform independent measurements of lifetimes, diffusion lengths and surface recombination velocity. None of these is presently well established for these devices.

Under the category of technological aspects can be included:

1. Since device efficiencies are now within 2% of the theoretical maximum, it is suggested that significant improvements may result from a scale up in the size and number of devices produced. It is believed that this will lead to refinements in and better understanding of the growth procedure and device processing.
2. It is also essential to produce larger area devices including standard space cell size for realistic measurements of radiation resistance and the modification of design aspects such as the grids. Larger area devices will also reduce the effects of leakage at the perimeter of the devices through a reduction in the ratio of perimeter to surface area. In addition, the growth of large area devices is sure to introduce new problems which should be investigated sooner rather than later.
3. Studies of grid adhesion and back-contact stability are also an imperative and should be initiated as soon as possible.

References

- [1] M. Yamaguchi, K. Ando, A. Yamamoto and C. Uemure, *Appl. Phys. Lett.*, **44**, 432 (1984).
- [2] M. B. Spitzer, C. J. Keaveney, S. M. Vernon and V. E. Haven, *Appl. Phys. Lett.*, **51**, 364 (1987).
- [3] C. Goradia, J. V. Geier and I. Weinberg, *Proc. 19th IEEE Photovoltaic Specialists Conference*, New Orleans, Louisiana, (1987), p. 937.
- [4] M. W. Wanlass, U.S. Patent No. 4,649,859.
- [5] "Standard Test Methods for Electrical Performance of Non- Concentrator Terrestrial Photovoltaic Cells Using Reference Cells," ASTM Standard E948.
- [6] A. E. Blakeslee, H. Aharoni, M. W. Wanlass, A. Kibbler, K. Emery and C. R. Osterwald, *Proc. 18th IEEE Photovoltaic Specialists Conference*, Las Vegas, Nevada, (1985), p. 146.

TABLE I. A summary of the chemical reactants, substrates, and growth conditions used in the APMOVPE process

Chemical Reactants			
Reactant	Application	Vendor	
Trimethylindium [(CH ₃) ₃ In]	In Source	Alfa Products	
Phosphine [PH ₃]	P Source	Phoenix Research	
Diethylzinc (C ₂ H ₅) ₂ Zn	Zn Source (p-doping)	Alfa Products	
500 ppm Hydrogen Sulfide in Hydrogen [500 ppm H ₂ S/H ₂]	S Source (n-doping)	Scientific Gas	
Substrates			
Vendor	Orientation	Dopant	Carrier Concentration
ICI Americas Inc.	(100)	Cd	1.7 × 10 ¹⁸ cm ⁻³
Sumitomo Electric Industries, Ltd.	(100) ± 0.5°	Zn	4.1 × 10 ¹⁸ cm ⁻³
Nippon Mining Co., Ltd.	(100)2°→(110)±0.09°	Zn	4.3 × 10 ¹⁸ cm ⁻³
Growth Conditions			
Parameter		Value	
Reactor Pressure		640 mm Hg	
Growth Temperature		650°C	
Growth Rate		6 μm hr ⁻¹	
H ₂ Carrier Flow Rate		3000 sccm	
Group V/Group III in Vapor		33.9	
(CH ₃) ₃ In Mole Fraction		2.2 × 10 ⁻⁴	

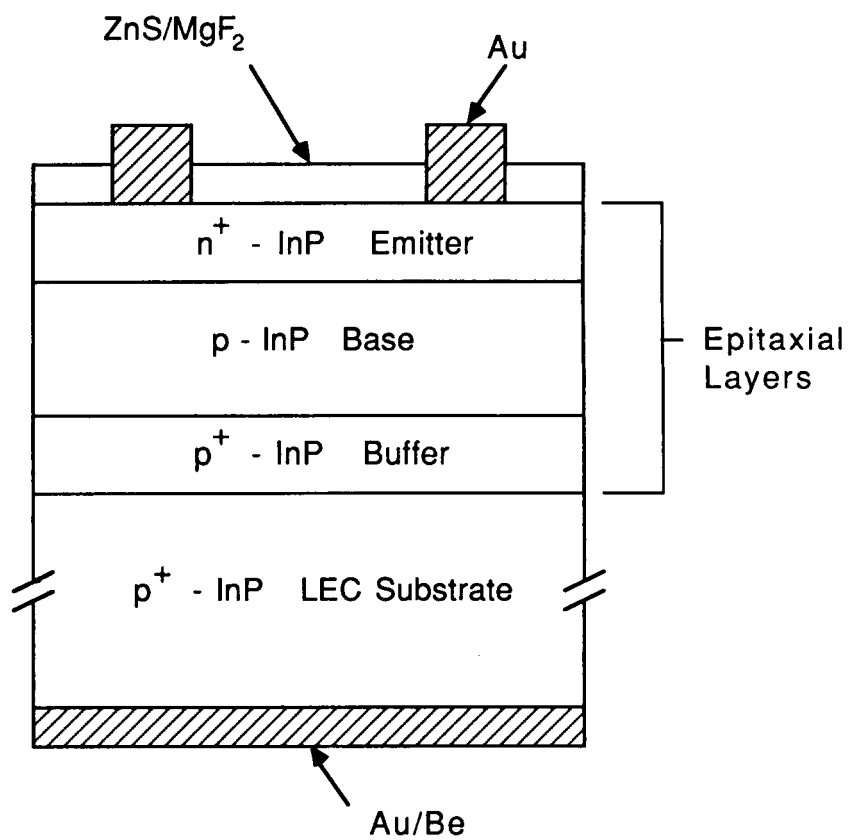


Figure 1. Schematic cross section of the $n^+/p/p^+$ InP shallow-homojunction cell structure under investigation.

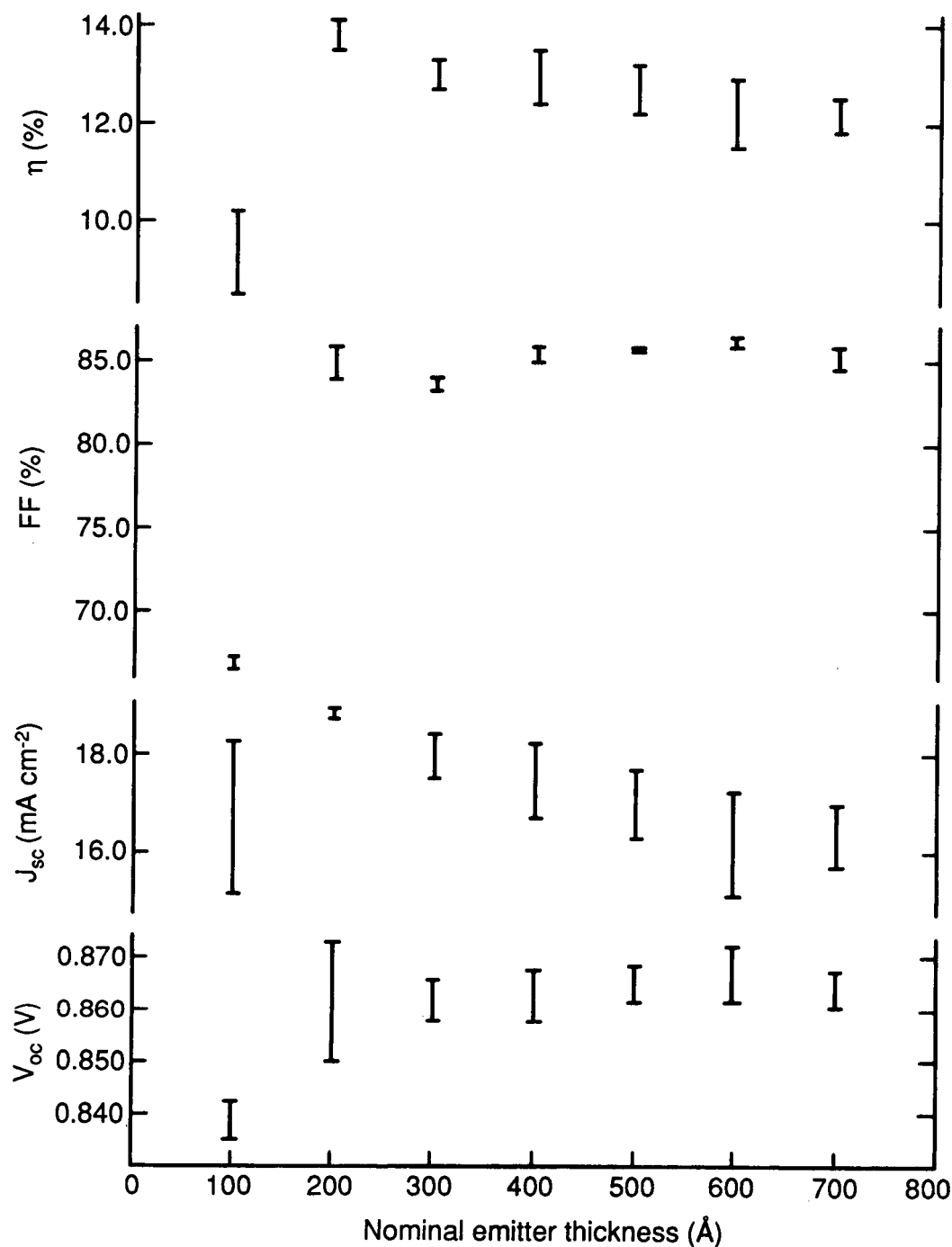


Figure 2. Variation of cell performance parameters V_{oc} , J_{sc} , FF , and η with nominal emitter thickness. The emitter and base doping concentrations were held constant at $N_D = 4 \times 10^{18} \text{ cm}^{-3}$, and $N_A = 4 \times 10^{16} \text{ cm}^{-3}$, respectively. The bars indicate the range of values observed on each device wafer.

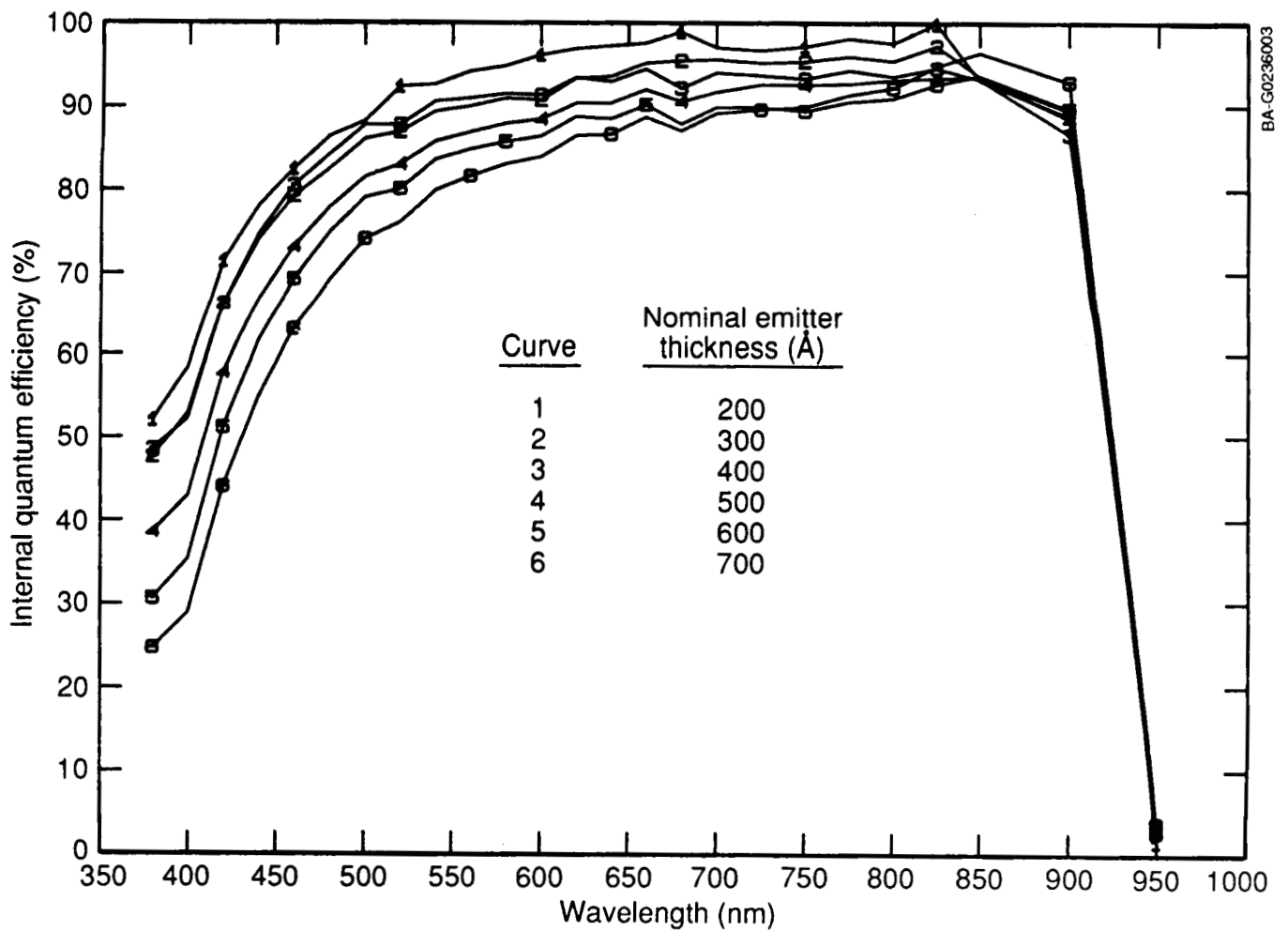


Figure 3. Internal quantum efficiency versus wavelength for different nominal emitter thicknesses showing a decrease in overall response as the thickness increases, particularly in the blue. These curves correspond to devices with parameters shown in Figure 2.

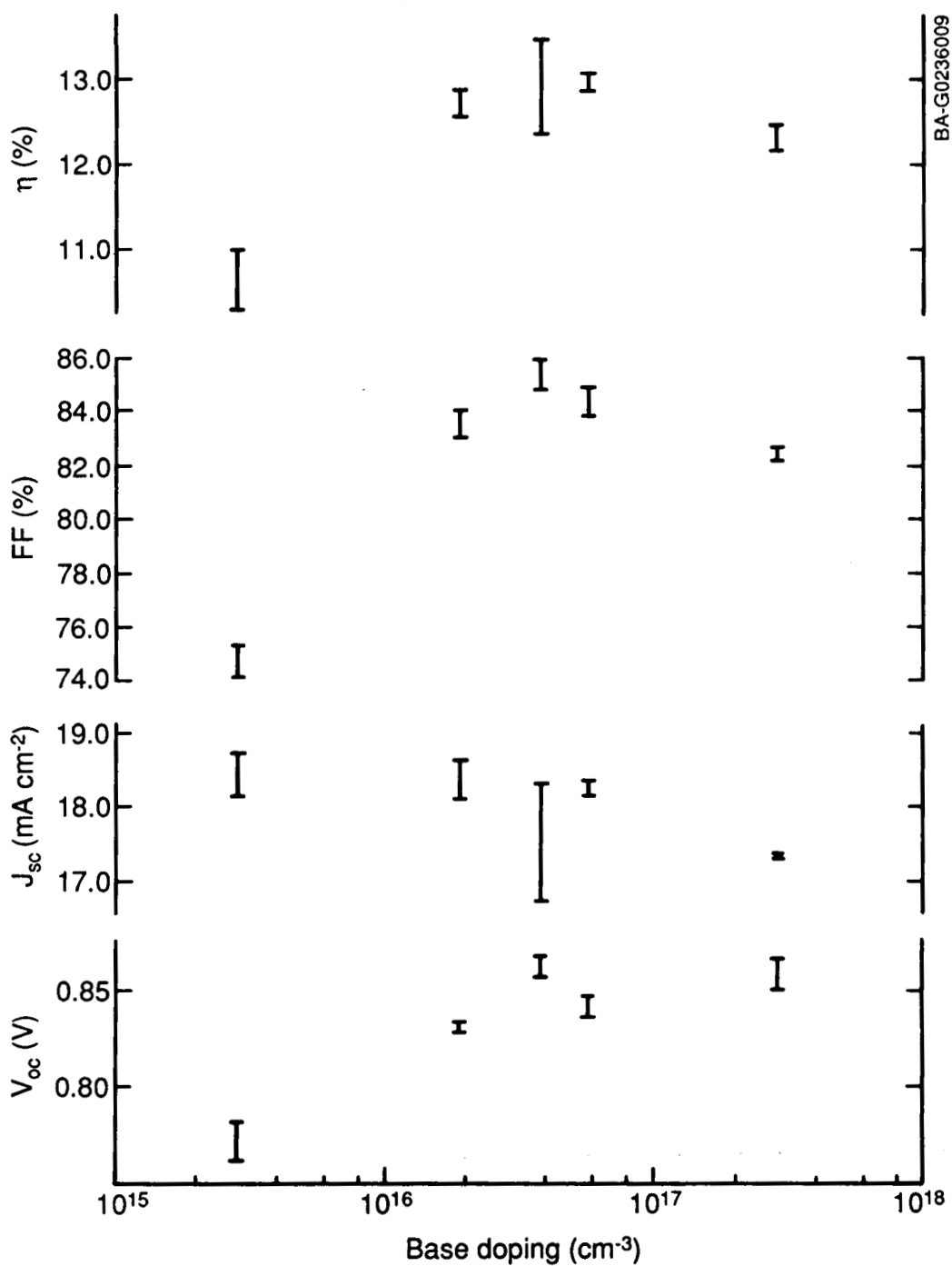


Figure 4. Variation of cell performance parameters V_{oc} , J_{sc} , FF, and η with base doping concentration. The emitter thickness and doping concentration were held constant at 400 \AA and $N_D = 4 \times 10^{18} \text{ cm}^{-3}$, respectively. The bars indicate the range of values observed on each device wafer.

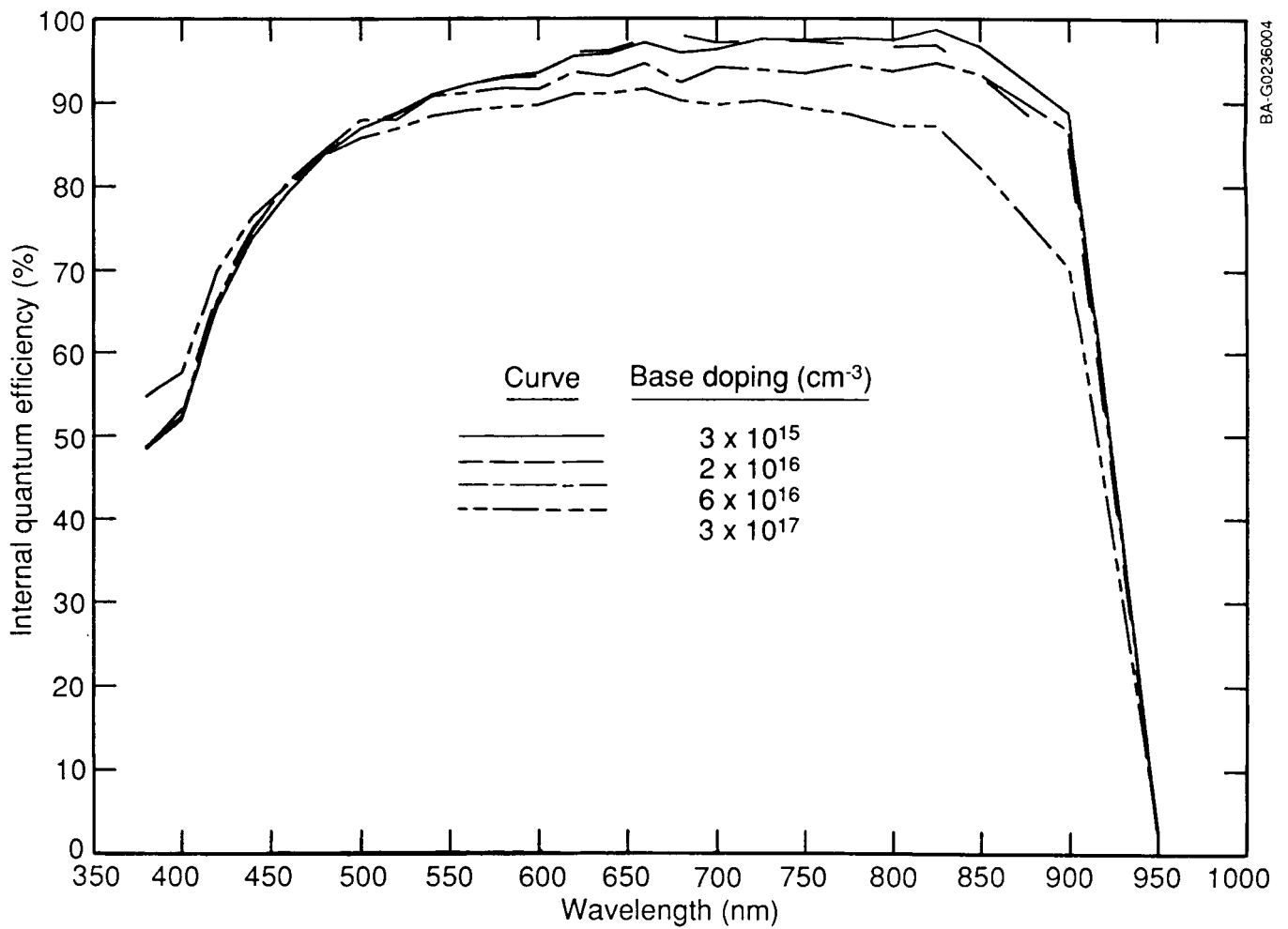


Figure 5. Internal quantum efficiency versus wavelength for different base doping concentrations showing a strong decrease in the red response as the doping concentration is increased beyond $6 \times 10^{16} \text{ cm}^{-3}$. These curves correspond to devices with parameters shown in Figure 4.

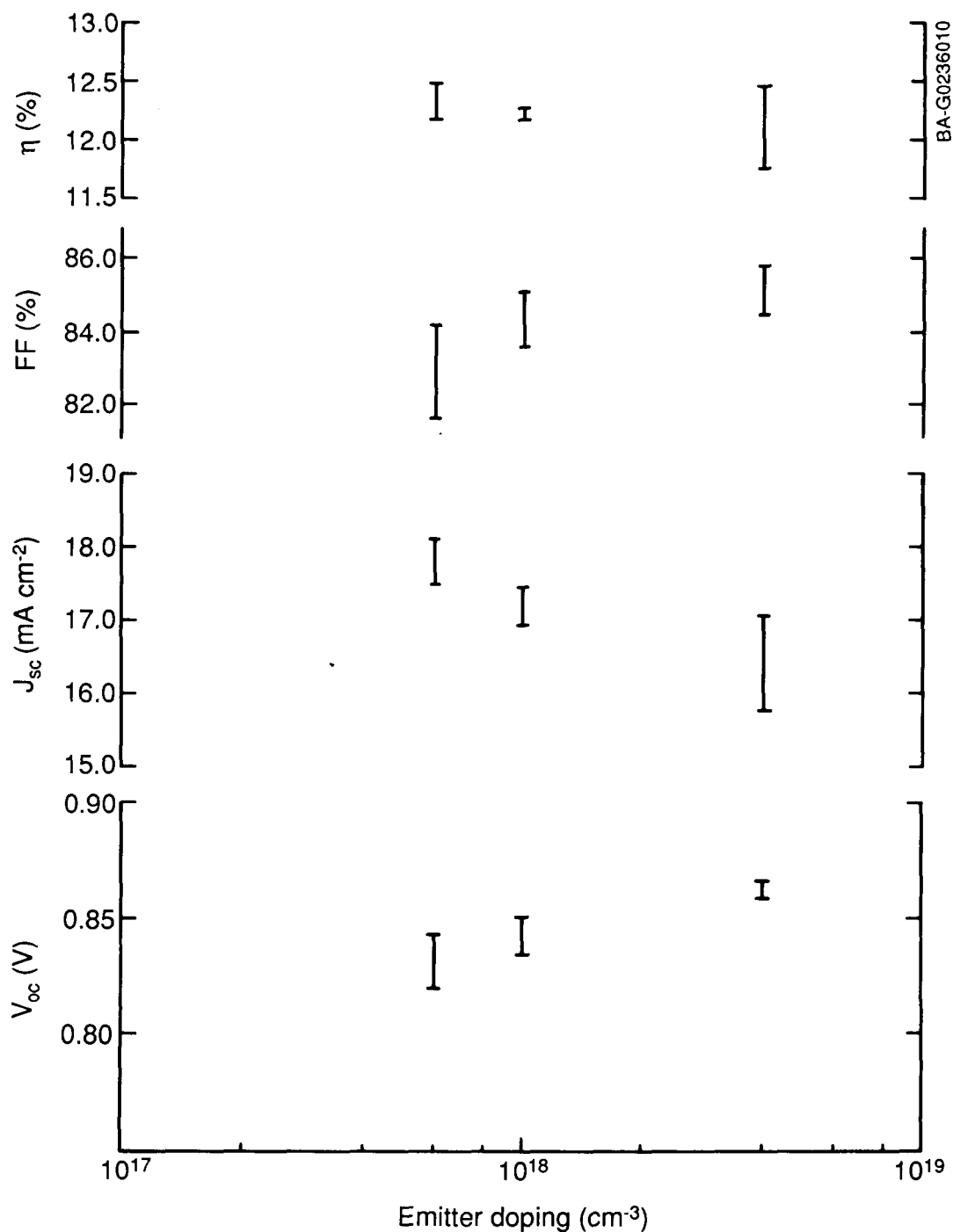


Figure 6. Variation of cell performance parameters V_{oc} , J_{sc} , FF, and η with emitter doping concentration. The emitter thickness and base doping concentration were held constant at 700 Å and $N_A = 4 \times 10^{16} \text{ cm}^{-3}$, respectively. The bars indicate the range of values observed on each device wafer.

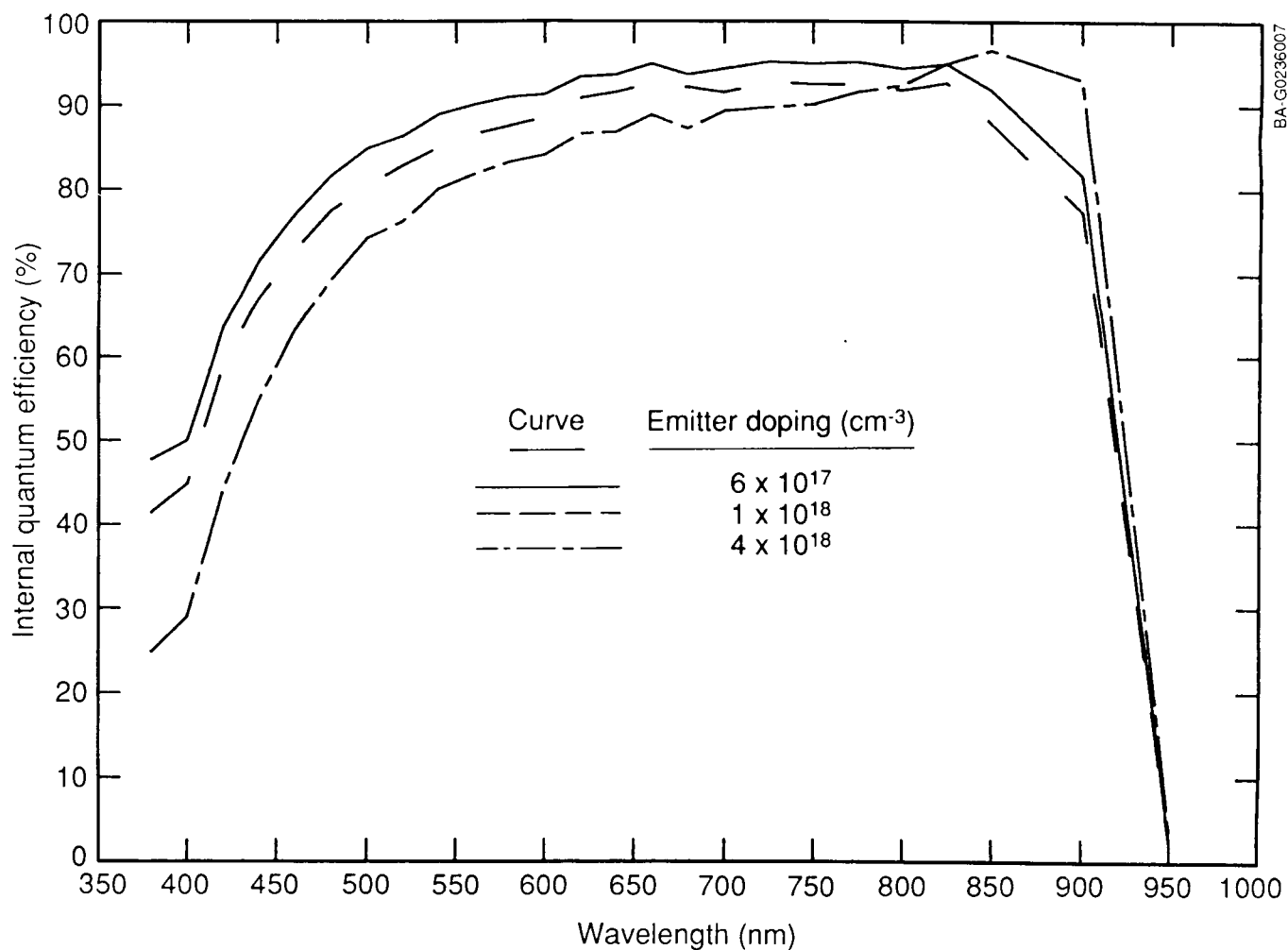


Figure 7. Internal quantum efficiency versus wavelength for different emitter doping concentrations showing a substantial decrease in blue response as the doping concentration is increased. These curves correspond to devices with parameters shown in Figure 6.

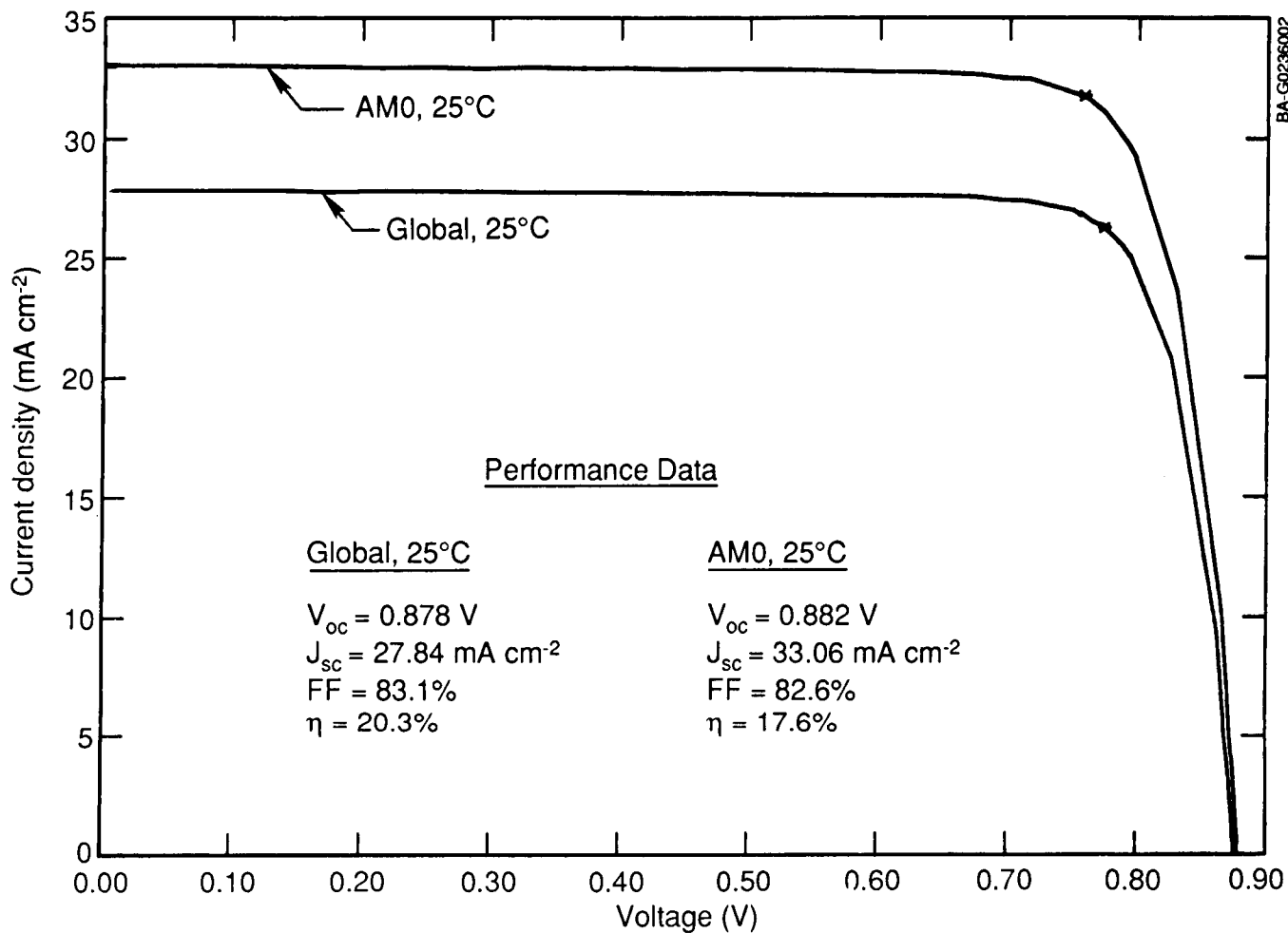


Figure 8. Light J-V characteristics for a near-optimum $n^+/p/p^+$ InP shallow homojunction under global and AM0 illumination at 25°C. The cell performance data for each case are also shown. The cell has a 2-layer antireflection coating of ZnS/MgF_2 .

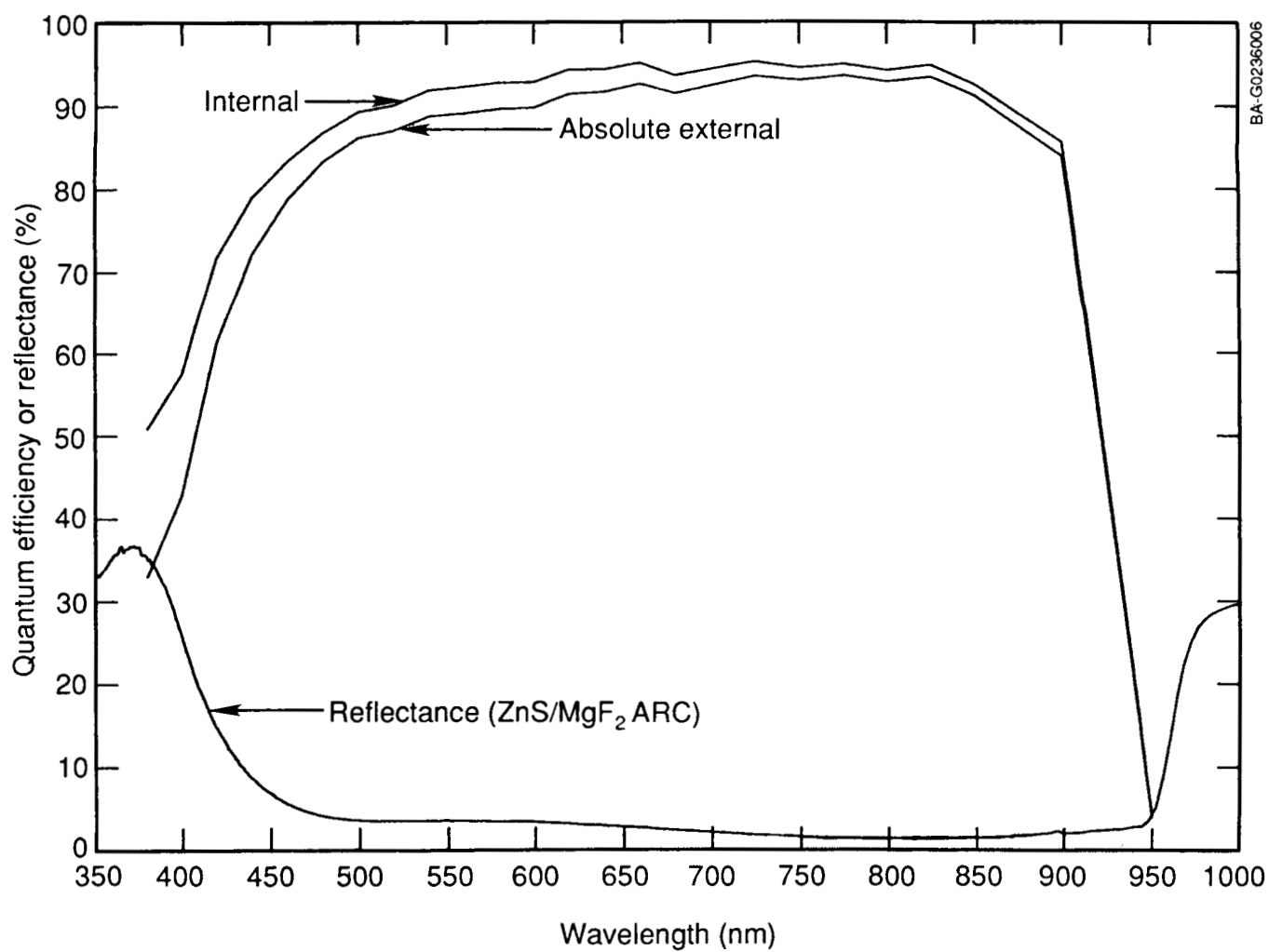


Figure 9. Internal quantum efficiency, absolute external quantum efficiency and reflectance data for the cell of Figure 8.

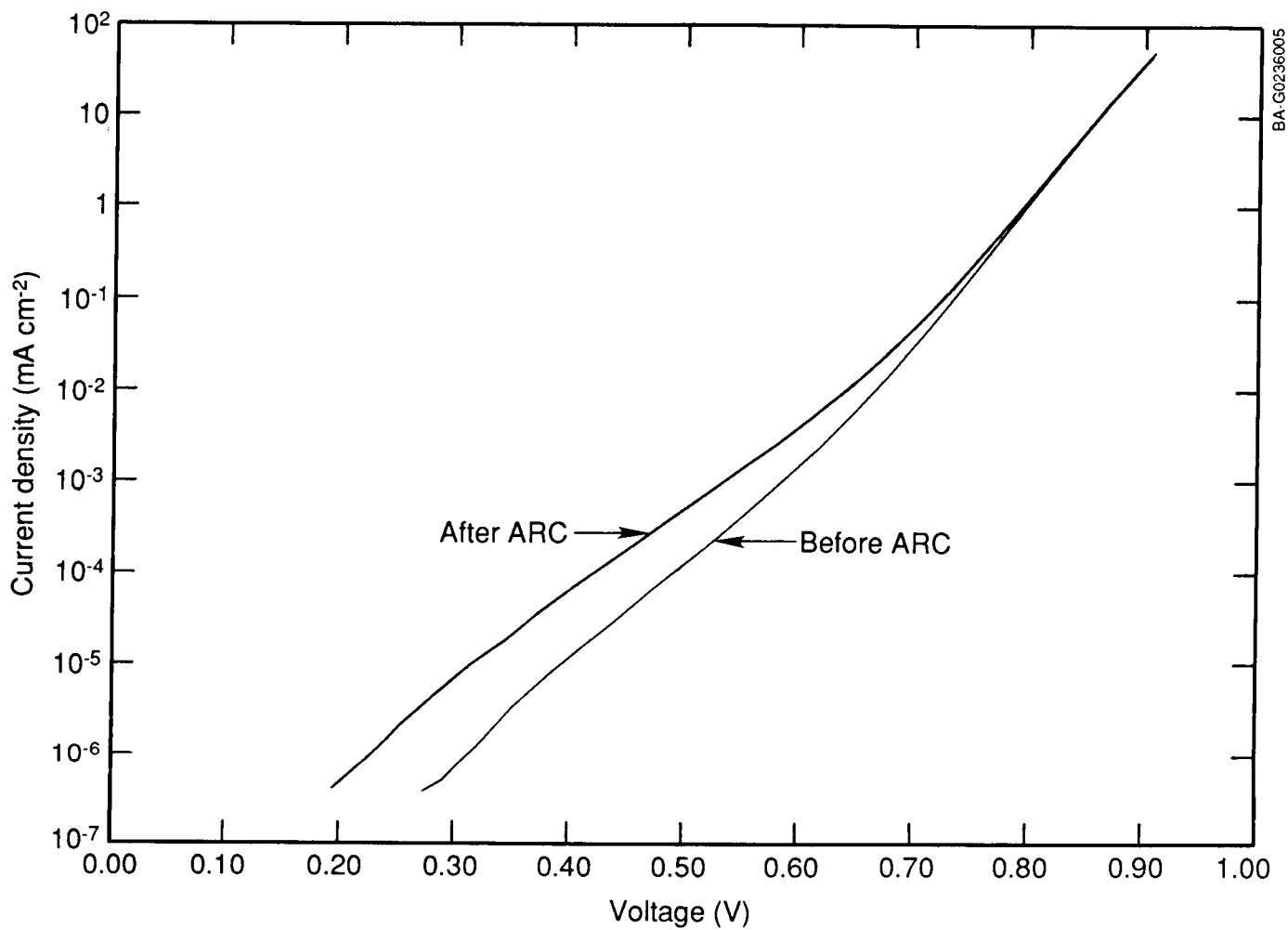


Figure 10. Forward-bias dark J-V data for a high-performance InP cell before and after deposition of the ZnS component of the 2-layer antireflection coating. Note the slight degradation of the characteristic after the ZnS deposition.

N/P InP Homojunction Solar Cells with an $\text{In}_{0.53}\text{Ga}_{0.47}\text{As}$ Contacting Layer Grown by Liquid Phase Epitaxy*

C. C. Shen and K. Y. Choi
Center for Solid State Electronics Research
Arizona State University
Tempe, Arizona 85287

N/P InP homojunction solar cells with an $\text{In}_{0.53}\text{Ga}_{0.47}\text{As}$ contacting layer were fabricated by liquid phase epitaxy (LPE). Electron-Beam-Induced-Current (EBIC) measurements were performed on several selected samples. It was found that the background doping level in the base region sometimes results in a deep junction, which greatly affects the cell performance.

Introduction

In the past few years we have developed a special contacting scheme in order to facilitate the front grid contact to P/N InP homojunction solar cells [ref. 1, 2]. This contacting scheme utilizes a heavily doped $\text{In}_{0.53}\text{Ga}_{0.47}\text{As}$ layer, which is deposited on the emitter layer during the epitaxial growth cycle. With the aid of the InGaAs contacting layer, very heavy doping at the emitter surface is no more required for obtaining low resistance front contact. The possibility of the formation of "dead layer" at the front surface is therefore eliminated. In this work, we extended this contacting scheme to N/P InP homojunction solar cells grown by LPE. The LPE growth procedures, cell fabrication and experimental results are presented in the following sections.

Cell Fabrication

The schematic diagram of the N/P homojunction InP solar cells developed in this work is shown in Fig. 1. The LPE growth was performed in a conventional horizontal LPE system, which employs a multiple-bin sliding graphite boat for multiple-layer growth.

The starting material was a (100) oriented $\text{p}^+\text{-InP}$ single crystal substrate which had been polished previously into a mirror-like surface by chemical-mechanical method. Three epitaxial layers were grown successively onto the substrate. A p-InP base layer of several microns thick was first grown on the substrate, which was followed by a thin n-InP emitter layer and a thin $\text{n}^+\text{-InGaAs}$ contacting layer. Zinc was used as p-type dopant and tellurium was used as n-type dopant. The typical growth temperature was between 622°C and 638°C , with a cooling rate of $0.5^\circ\text{C}/\text{min}$.

Selected grown wafers were processed into mesa-type solar cells. The processing sequence used in this work is similar to what we used for P/N InP homojunction solar cell [ref. 1]. The total area of the cells processed in this work are of two different sizes; they are 0.04 cm^2 and 0.25 cm^2 . The

* This work is supported by the NASA Lewis Research Center.

front grid contact covers 6% and 12.5% of the total surface area for 0.25 cm² size cells and 0.04 cm² size cells, respectively. ZnS/MgF₂ double-layer AR coating was deposited on the front surface by thermal evaporation.

Electron-Beam-Induced-Current (EBIC) Measurements

EBIC measurements were performed routinely on broad-area diodes processed from grown wafers. It is a useful technique for determining the exact location of the p-n junction in a junction device such as a solar cell. During the course of this study, we had some interesting observations from the EBIC data on several grown wafers which were prepared under slightly different growth conditions. Our findings are described below.

Several LPE samples were grown under similar growth conditions. Doping level in the p-InP base region was adjusted by varying the Zn content in the melt used for growing the base layer. For this particular series of growth experiments, the melt was not intentionally baked for any prolonged period of time prior to the growth to minimize the background doping.

In Table I, we list the LPE growth recipes we used for the preparation of two samples (sample A and sample B), both contain a N/P InP homojunction and a n⁺-InGaAs layer. The targeted doping levels in the base region for these two samples are $5 \times 10^{16} \text{ cm}^{-3}$ for sample A and $1 \times 10^{17} \text{ cm}^{-3}$ for sample B.

Both samples were made into broad-area devices. Devices with rectifying I-V characteristics and smooth cleaved-facets were selected for EBIC studies. To delineate the InGaAs/InP interface, the diodes to be tested were first etched in a solution of 3H₂SO₄: 1H₂O₂: 1H₂O at room temperature for 20 sec. The SEM photomicrographs of the cleaved and etched section of two diodes are shown in Fig. 2(a) and 2(b). The photomicrograph shown in Fig. 2(a) was taken from a diode processed from sample A while the one in Fig. 2(b) was from a diode processed from sample B. The heterojunction interface between the InGaAs contacting layer and the InP emitter layer is revealed in the secondary emission image. The location of the p-n junction is identified by the peak of the superimposed beam-induced current trace. For sample B, the p-n junction is about one micron from the InGaAs/InP interface as expected. However, the p-n junction in sample A, as revealed in the EBIC photomicrograph, is four microns from the InGaAs/InP interface. Our explanation for this striking result is that in sample A, the n-type background doping in the base region was higher than the targeted p-doping; as a result, the amount of Zn incorporated in the melt for the growth of the p-base layer was not enough to overcome the background doping and the base layer turned out to be n-type instead of p-type, resulting in a p-n junction between the first epitaxial layer and the p⁺-InP substrate. Such a deep junction is not desirable because it will result in low short-circuit current. The background doping in the base region for sample A was estimated to be in the high 10^{16} cm^{-3} range, as measured by a Polaron profile plotter. Since no pre-bakeout of the melts were employed in this particular growth experiment, high level of background doping was obtained. In order to avoid this problem, proper pre-bakeout of the melts prior to growth is definitely necessary.

Cell Performance

The spectral response of two representative cells, one processed from sample A (cell A) and the other from sample B (cell B), are shown in Fig. 3(a) and 3(b). The external quantum efficiency of cell A in the short wavelength region is relatively low in comparison to that of cell B. This result is not surprising, since cell A has a deeper junction and optically generated carriers near the cell surface are not collected efficiently. It is worthwhile to point out that for the two cells discussed here, their cell structures are far from optimized. The peak value of the quantum efficiency for both cells are therefore quite low.

Figure 4 shows the dark I-V characteristics for these two cells. Cell A exhibits very poor dark I-V characteristics, which might be caused by the poor quality of the junction formed between the epitaxial layer and the substrate. The cells were tested under simulated AM1 illumination and their light I-V characteristics are shown in Fig. 5. The conversion efficiencies for cell A and cell B are 2.0% and 9.8%, respectively. The photovoltaic properties of cell A and cell B under AM1 illumination are summarized in Table II. These two cells have a total surface area of 0.25 cm^2 . Total-area conversion efficiencies up to 13.5% at AM1 was obtained from a small cell with a total surface area of 0.04 cm^2 . The smaller cell also exhibits higher V_{oc} and larger fill factor.

A comparison between N/P and P/N homojunction InP cells grown by LPE growth techniques at our laboratory indicates that the short-circuit current for N/P InP cells seem to be more sensitive to the emitter thickness. In order to achieve high conversion efficiency for N/P InP cell, the emitter layer needs to be very thin, probably in the order of 500\AA .

Conclusion

We have prepared N/P InP homojunction solar cells with an $n^+-\text{In}_{0.53}\text{Ga}_{0.47}\text{As}$ contacting layer by LPE growth techniques. EBIC studies showed that the high background doping in the base region can create a deep p/n junction, which greatly affects the cell performance. Pre-bakeout of the growth melts is required if low doping concentration in the p-base region is desired for the preparation of N/P InP homojunction solar cells by LPE growth techniques. N/P InP homojunction solar cells grown by MOCVD growth techniques may encounter similar problems if the background doping level in the epitaxial InP layer is high due to impure sources or system contamination. EBIC measurements can therefore serve as a useful diagnostic tool for investigating this particular problem.

For the N/P InP homojunction solar cells described here, both the LPE growth procedures and the cell parameters need to be improved and optimized in order to obtain higher conversion efficiencies. Adding a buffer layer may improve the quality of the epitaxial layers and the p/n junction quality.

References

- [1] K. Y. Choi, C. C. Shen and B. I. Miller, "P/N InP Homojunction Solar Cells by LPE and MOCVD Techniques", *19th IEEE Photovoltaic Specialists Conference*, New Orleans, LA, 1987, Conf. Rec., pp. 255-260.
- [2] K. Y. Choi and C. C. Shen, "P/N InP Homojunction Solar Cells with a Modified Contacting Scheme by Liquid Phase Epitaxy", *J. Appl. Phys.* **63**, no. 6, Feb. 1988, pp. 1198-1202.

Table 1. LPE growth recipes for sample A & B.

Growth recipe for sample A

Layer	In (gm)	InP (mg)	GaAs (mg)	InAs (mg)	Zn (ug)	Te (mg)	Growth Temp.	Growth Period	Expected Carrier Concentration (cm ⁻³)
p-InP	1.0	9.0	----	----	1.5	---	638.0°C	30 min	5 x 10 ¹⁶
n-InP	1.0	7.0	----	----	---	2.2	623.0°C	10 sec	5 x 10 ¹⁸
n ⁺ -In _{0.53} Ga _{0.47} As	1.0	---	30.9	50.9	---	4.0	622.8°C	3 sec	1 x 10 ¹⁹

Growth recipe for sample B

Layer	In (gm)	InP (mg)	GaAs (mg)	InAs (mg)	Zn (ug)	Te (mg)	Growth Temp.	Growth Period	Expected Carrier Concentration (cm ⁻³)
p-InP	1.0	9.0	----	----	1.7	---	638.0°C	30 min	1 x 10 ¹⁷
n-InP	1.0	7.0	----	----	---	2.0	623.0°C	10 sec	4 x 10 ¹⁸
n ⁺ -In _{0.53} Ga _{0.47} As	1.0	---	30.9	51.6	---	4.0	622.8°C	3 sec	1 x 10 ¹⁹

Table 2. Photovoltaic and electrical characteristics of N/P homojunction InP solar cells under AM1 illumination.

ELH lamp, 100 mW/cm^2 , 27°C

Cell area: 0.25 cm^2

Sample	V_{oc} (V)	J_{sc} (mA/cm^2)	FF (%)	Eff. (%)	n factor	J_o (A/cm^2)
A	0.72	6.0	46.8	2.0	10.2	1.5×10^{-4}
B	0.82	20.8	57.6	9.8	2.8	1.8×10^{-7}

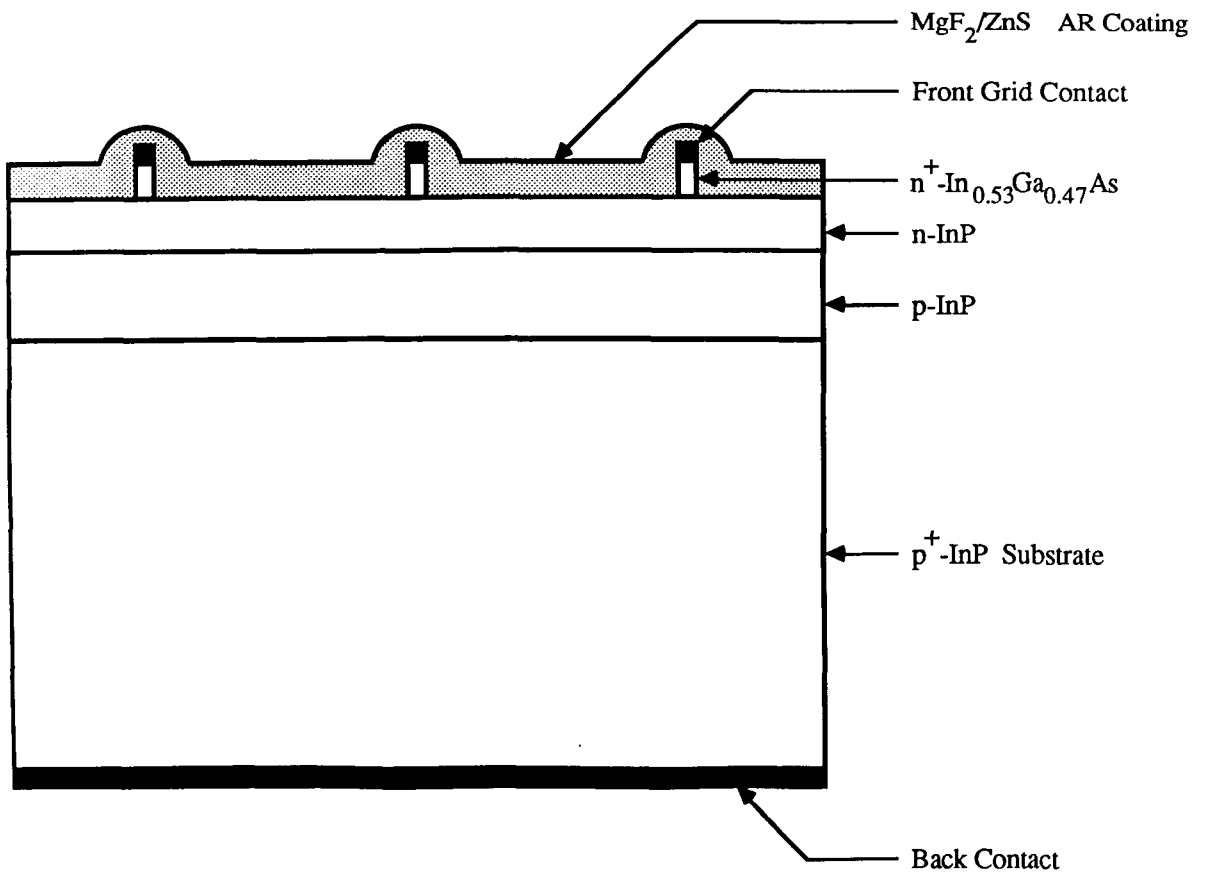
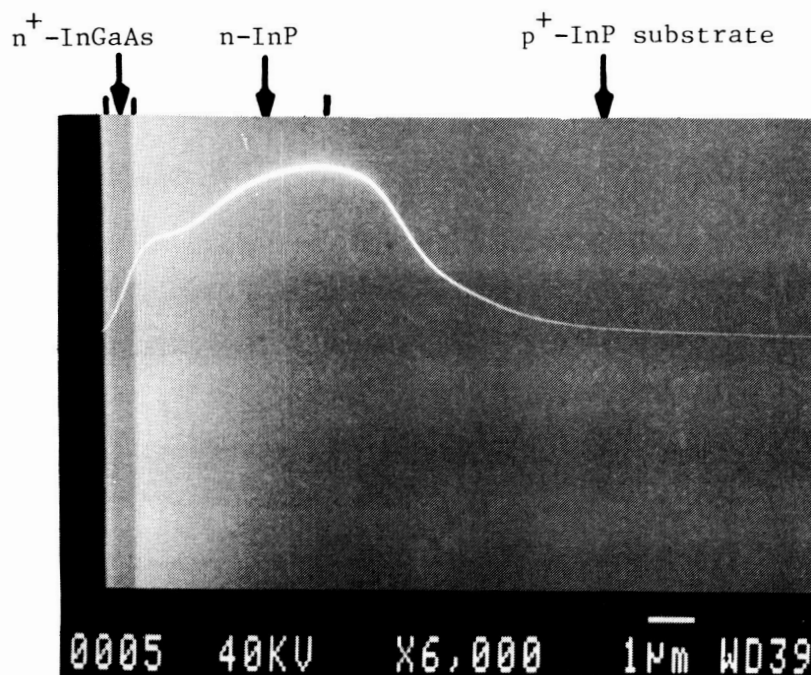
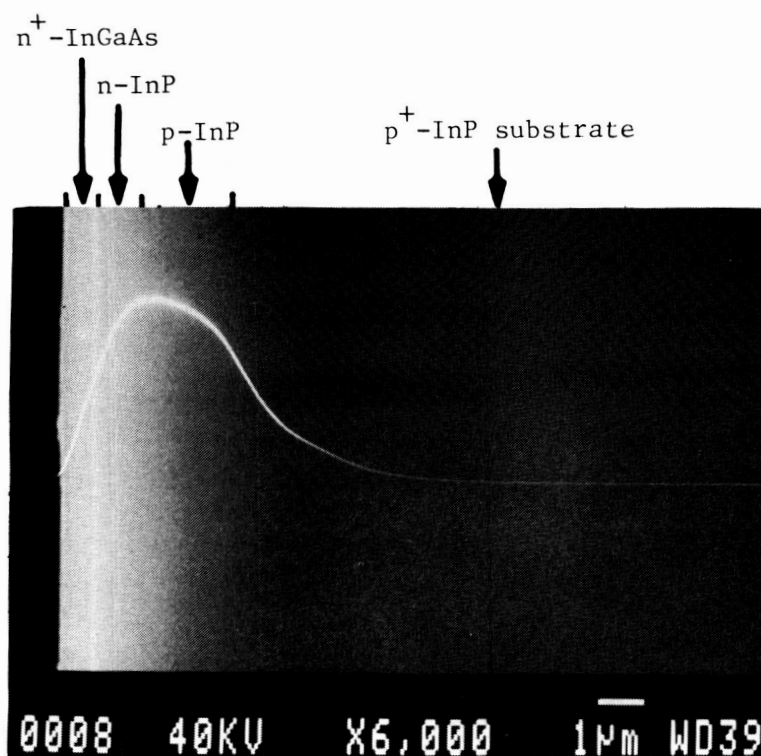


Figure 1. Schematic diagram of the cross section of an N/P InP homojunction solar cell.

ORIGINAL PAGE
BLACK AND WHITE PHOTOGRAPH



(A)



(B)

Figure 2. Secondary emission and EBIC images of the cross section of
(A) Cell A and (B) Cell B.

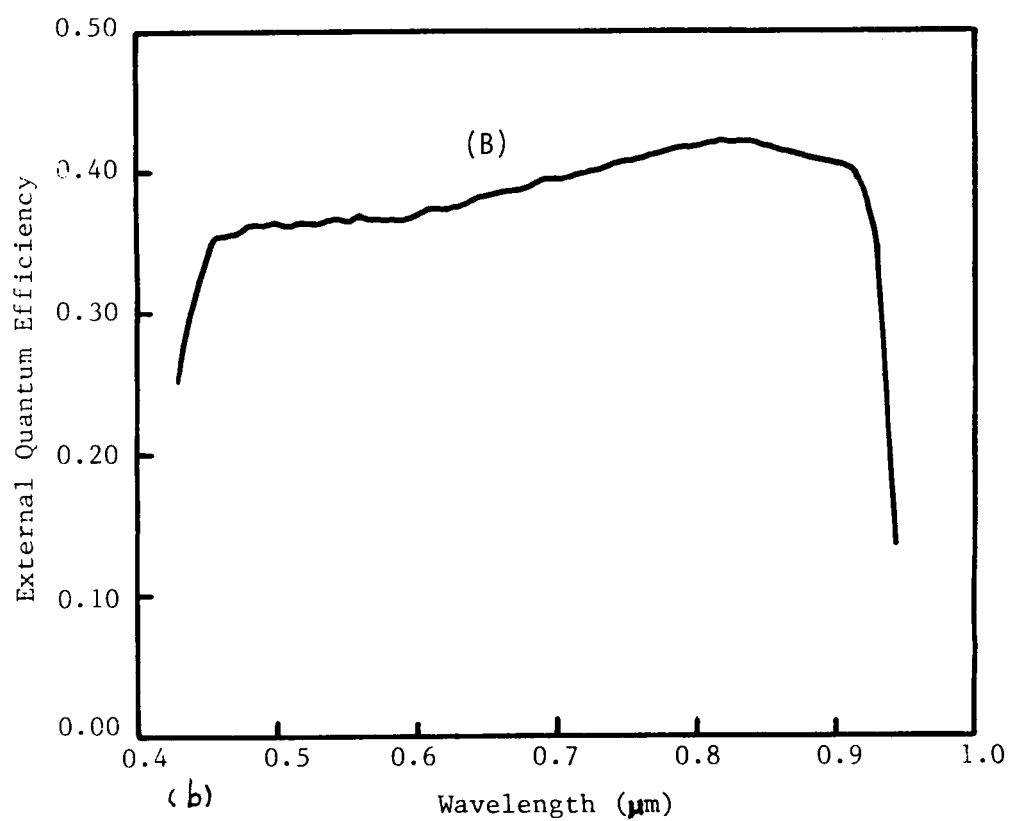
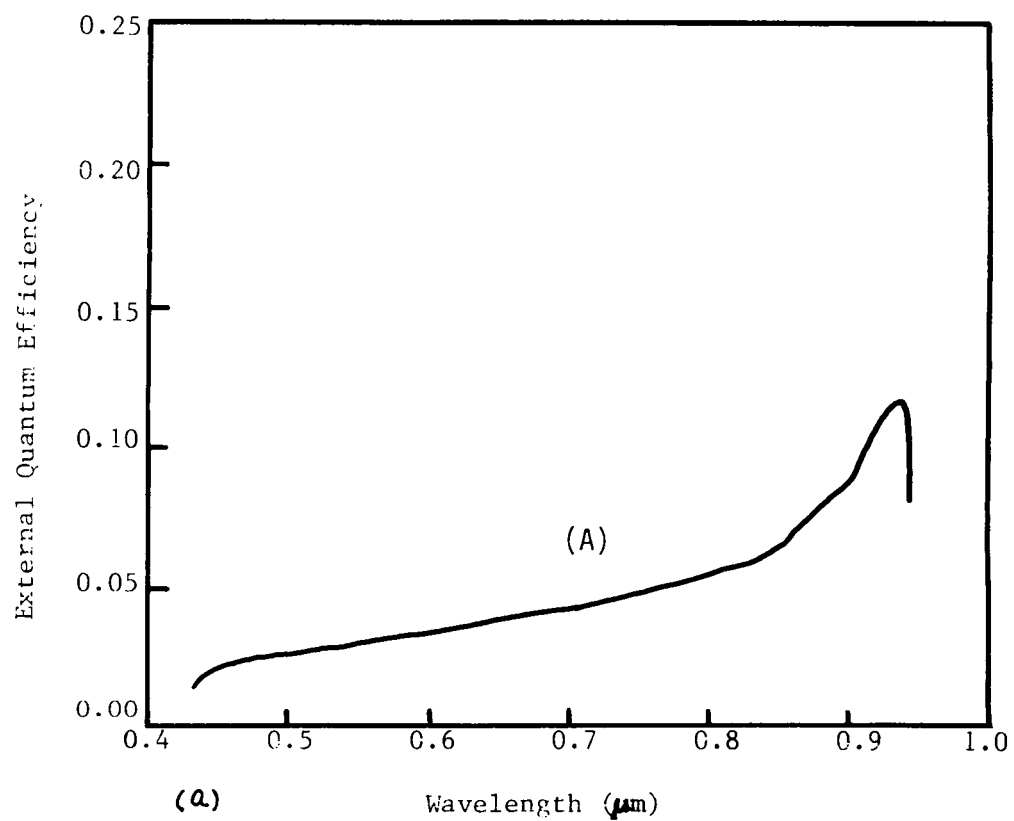


Figure 3. Spectral response of (A) Cell A and (B) Cell B.

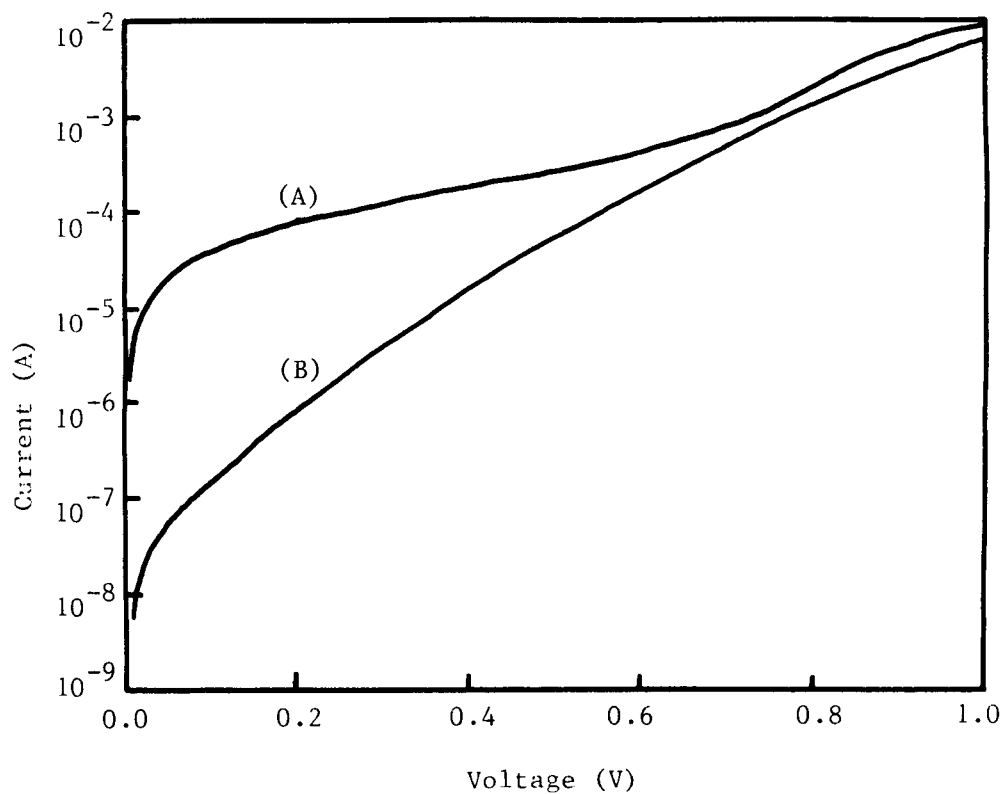


Figure 4. Dark I-V characteristics of (A) Cell A and (B) Cell B.

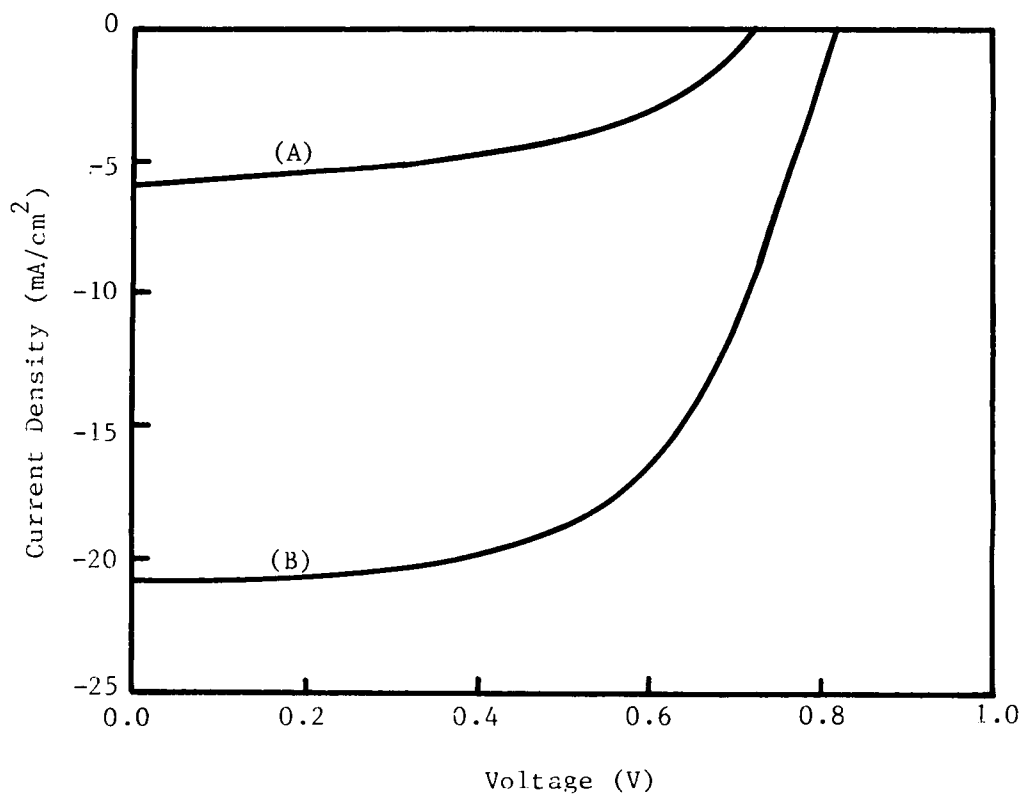


Figure 5. Light I-V characteristics of (A) Cell A and (B) Cell B under AM1 illumination.

**Predicted Performance of InP Solar Cells
in Cassegrainian and Slats Space Concentrator
Arrays at 20 to 100 AM0, 80° to 100°C**

Chandra Goradia, William Thesling and Manju Ghalla Goradia
*Electrical Engineering Department
Cleveland State University
Cleveland, Ohio 44115*

Irving Weinberg, Clifford K. Swartz
*NASA Lewis Research Center
Cleveland, Ohio 44135*

Summary

We have calculated the expected performance dependence of near-optimally designed shallow homojunction n^+pp^+ InP solar cells on incident intensities up to 200 AM0 and temperatures up to 100°C (373K). Both circular and rectangular cells have been considered, the former for use in a Cassegrainian concentrator array at 100 AM0, 80°-100°C and the latter for use in a Slats type concentrator array at 20 AM0, 80°-100°C. Calculation of the temperature dependence of the performance parameters I_{sc} , V_{oc} , FF and η was done by first verifying that the use of the measured temperature variation of I_{sc} , of the best published value of the temperature dependence of the bandgap of InP, and of the temperature dependences of the lifetimes and mobilities of electrons and holes the same as in equivalently doped GaAs, gave calculated results that closely matched measured data on the temperature variation of I_{sc} , V_{oc} and FF of four existing InP cells at 1 AM0. It was then assumed that the same temperature dependences of I_{sc} , the bandgap and lifetimes and mobilities would hold in the near-optimally designed cells at the higher concentrations.

Introduction

Designs already exist for Cassegrainian [ref. 1] and Slats [ref. 2] lightweight space concentrator arrays for use with high efficiency GaAs solar cells [ref. 3] of geometries and dimensions shown in Fig. 1. Also indicated in this figure are the design operating points of 100 AM0, 80°C, with total illuminated area (also cell area) of a 4 mm diameter circle for the Cassegrainian concentrator and 20 AM0, 80°C, with total illuminated and cell area of a 2.5 mm \times 1 cm rectangle for the Slats or Venetian Blind concentrator. Note that practical considerations of minimizing payload weight in space require that the cells be operated at the somewhat higher temperatures of 80°C to 100°C.

In an earlier paper [ref. 3], we had predicted the performance of near-optimum GaAs solar cells at 100 and 20 AM0, 80°C when used in these concentrator arrays. Because of the superior radiation tolerance behavior of InP solar cells in comparison to GaAs cells, there is now interest in predicting the performance of near-optimally designed InP space solar cells at 100 and 20 AM0, 80°C to 100°C for use in these same concentrator arrays.

The problem with predicting the performance of near-optimally designed InP solar cells at 100 AM0 and 20 AM0, 80°C to 100°C is that there are no reliable data in the published literature on the temperature variations of such fundamental parameters as the bandgap, optical absorption coefficient, and electron and hole mobilities and lifetimes in both n-type and p-type InP with various doping concentrations. Thus, while our rather comprehensive computer simulation model is capable of predicting the performance and thereby generating a near-optimum design of the InP cell at 100 AM0 and 20 AM0, 27°C (300K), it cannot predict the performance at 80° C to 100°C. We therefore went around this problem using the following multistep approach.

To begin with, we generated near-optimum designs for both the circular and rectangular cells for operation at 100 AM0 and 20 AM0, respectively, at 27°C (300K). This was done with the help of our simulation model, the details about which have been published earlier [ref. 4]. Next, we measured the temperature dependences of the performance parameters I_{sc} , V_{oc} and FF at 1 AM0 for four InP shallow homojunction solar cells. Figure 2 shows these temperature dependences for one typical cell. Then, using a two-diode model,

$$I = I_{ph} - I_{01}[\exp((V + IR_s)/V_T) - 1] - I_{02}[\exp((V + IR_s)/2V_T) - 1] - (V + IR_s)/R_{sh},$$

we obtained, for each of the four cells, all the unknowns of this model at 300K, namely, I_{ph} , I_{01} , I_{02} , R_s and R_{sh} by curve-fitting the above equation to the measured illuminated I-V curve at 300K for each cell. Next, for the temperature variation of I_{ph} , we used the measured temperature variation of I_{sc} . We also used the temperature variation of the bandgap of InP from the published literature and for the temperature dependences of the mobilities and lifetimes, we used those of equivalently doped GaAs. We then calculated I_{sc} , V_{oc} and FF at various temperatures for each of the four cells, using the above-described temperature dependences of the various parameters and found nearly perfect fits to the measured data in the temperature range of 300K to 373K. This indicated to us that the temperature dependences we used for the various parameters must be close to the true temperature dependences of those parameters for InP. As a final step, we then assumed that these same temperature dependences would hold in the near-optimally designed cells not just at 1 AM0 but at the higher intensities of 20 AM0 and 100 AM0. This allowed us to calculate the predicted performance of the near-optimum rectangular and circular cells at 20 AM0, 80°C -100°C and 100 AM0, 80°-100°C respectively. The results of these calculations are presented and discussed in the following section.

Calculated Results and Discussion

Tables 1A and 1B give the general design parameters and the geometrical and material parameters of the near-optimum designs of the rectangular and circular cells. The key points to be noted in these tables are as follows: 1) While we have used a single layer antireflection (AR) coating of 750Å of SiO₂, we are in the process of incorporating into our model a two-layer ZnS/MgF₂ AR coating which will somewhat boost the short circuit current I_{sc} . 2) A significant portion, nearly 40%, of the total series resistance R_s , which is relatively high, comes from the contact resistance of the front grid fingers; hence, for these concentrator cells, it is imperative that research be done to bring the specific contact resistivity of the front metallization down to about 5E-6 ohm-cm². This would raise the fill factor FF slightly. 3) There is some uncertainty in the value of the intrinsic

carrier concentration n_i at 300K; if its value is closer to $1E7 \text{ cm}^{-3}$ as some researchers claim, that would boost the expected open circuit voltage V_{oc} by more than 25mV at 300K. 4) The effective front surface recombination velocity (SRV) S_f is an area-weighted average between half the thermal velocity over the area of actual contact of the front grid fingers, which we took as 35% of the grid finger area, and a passivated surface SRV value of $2E4 \text{ cm/s}$ over the rest of the area. While this area-weighted average of S_f is believed to be correct for the calculation of the dark or loss current contribution from the emitter, we strongly suspect that it is not correct for the photocurrent contribution from the emitter, for which S_f should be closer to the lower passivated value of $2E4 \text{ cm/s}$. We are in the process of doing calculations with separate values of S_f for the dark and photocurrent contributions from the emitter and these should again boost I_{sc} somewhat. 5) Present experimental results indicate that at 1 AM0, a thinner emitter ($\sim 200\text{\AA}$) and a thicker base ($\sim 3\mu\text{m}$) than our values in Table 1B would most probably yield a somewhat higher efficiency [refs. 5,6]. However, we feel that for a concentrator cell, a thinner emitter would require heavier emitter doping to keep the series resistance low and that would add to the uncertainties of any detrimental heavy doping effects. Thus, we have chosen to stay with an emitter thickness of $\sim 400\text{\AA}$. As to the base thickness, radiation damage considerations would favor our thinner base. 6) The effective lifetime values for each region in Table 1B take into account both radiative and Hall-Shockley-Reed recombinations. Auger recombination is insignificant at the low carrier densities and the relatively low temperatures considered.

Table 2 gives the temperature dependence of I_{sc} for the circular cell for various AM0 concentrations. This was based on the average measured temperature dependence of $J_{sc}(T) = 0.030475 + 21.91E-6 \cdot T \text{ A/cm}^2/\text{AM0 sun}$ obtained from the four measured cells, and the assumption that J_{sc} is a linear function of incident intensity. For the rectangular cell, the I_{sc} values will be proportionally larger in the ratio of the areas of the two cells. It is expected that a two-layer AR coating and a reduced value of S_f for photocurrent in the emitter will boost the 300K value of J_{sc} from its present $36.45 \text{ mA/cm}^2/\text{AM0 sun}$ to about $40 \text{ mA/cm}^2/\text{AM0 sun}$.

Tables 3A and 3B give the V_{oc} , FF and efficiency η as functions of AM0 intensity and temperature for the circular and rectangular cell respectively. Here, the two columns labeled 'Expected' and 'Worst Case' refer to calculations made two different ways. The numbers in the 'Expected' columns were obtained by taking into account the temperature variations of I_{sc} , the bandgap, and mobilities and lifetimes, that is, all parameters that vary with temperature. The numbers in the 'Worst Case' columns were obtained by ignoring the temperature variations of mobilities and lifetimes but taking into account only the temperature variations of I_{sc} and the bandgap. Since 27°C (300K) is the reference temperature, the 'Expected' and 'Worst Case' values coincide at 300K. Figures 3, 4 and 5 give 'expected' and 'worst case' curves of V_{oc} , FF and η as functions of temperature at various AM0 concentrations for both the circular (C) and rectangular (R) cells. It is seen from both the Tables 3A, 3B and Figures 3, 4 and 5, that since the 'worst case' values are so close to the 'expected' values, the primary temperature variation of the performance parameters comes from the variations of I_{sc} and the bandgap with temperature. Actually, since most of the temperature variation of I_{sc} is also due to the temperature variation of the bandgap (and thence of the optical absorption coefficient), the reduction of the bandgap with temperature is the single most important factor contributing to the temperature variation of the performance of the cell.

From Figure 3, it is seen that over the temperature range of interest, 27°C (300K) to 100°C (373K), V_{oc} degrades linearly with increasing temperature. Since fill factor FF is directly dependent on V_{oc} , FF also degrades with increasing temperature, but not quite linearly, as seen in Figure 4. Finally, Figure 5 shows the somewhat nonlinear degradation of the efficiency η with increasing temperature. Note that for both the circular and rectangular cells, the fill factor appears to degrade

monotonically for concentrations above 20 AM0. This is due to the relatively high series resistance for both geometries. If the specific contact resistivity of the front grid fingers can be brought down to about $5\text{E-}6\text{ ohm-cm}^2$ or lower, it may then be possible for the FF to reach its maximum at 100 AM0 or higher instead of at ~ 20 AM0 as is presently the case. Table 4 gives the rate of degradation with temperature of V_{oc} and η , that is dV_{oc}/dT in $\text{mV}/^\circ\text{C}$ and $d\eta/dT$ in $\%/^\circ\text{C}$, around the nominal operating temperature of 80°C for the circular cell. Note that the magnitudes of dV_{oc}/dT and $d\eta/dT$ decrease with increasing sunlight concentration, as expected. The dV_{oc}/dT is less than $1.75\text{ mV}/^\circ\text{C}$ in magnitude for concentrations above 20 AM0. This is between the value for Si ($\sim 2.0\text{ mV}/^\circ\text{C}$) and for GaAs ($\sim 1.5\text{ mV}/^\circ\text{C}$) at 20 AM0 [ref. 3].

Finally, the most important thing to note from Tables 3A, 3B and Figure 5 is that at the nominal operating point of 100 AM0, 80°C , the circular cell is expected to have an efficiency of 21.1%. However, with a two-layer AR coating and a lower S_F for photocurrent from the emitter, a 10% increase in I_{sc} should increase the efficiency to 23.2%, which we think is a realistically achievable efficiency of the circular cell at 100 AM0, 80°C . Similarly, we feel that a realistically achievable efficiency for the rectangular cell at 20 AM0, 80°C is 22.6% instead of the presently predicted 20.57% in Table 3B. These compare very favorably with similar efficiencies predicted for GaAs solar cells [ref. 3].

Concluding Remarks

We may make the following final comments:

1. When reliable data on the temperature dependences of key material parameters such as bandgap, and lifetimes and mobilities of electrons and holes are not available, as is the case with InP, extracting these from a comparison between calculated and measured illuminated I-V curves at several temperatures is a very useful technique. In the case of InP, it turns out that excellent results are obtained by using the published temperature dependence of the bandgap, the measured temperature variation of I_{sc} and the temperature variations of lifetimes and mobilities the same as those in equivalently doped GaAs.

2. The primary temperature dependence of the performance parameters of a solar cell comes from the temperature variation of the bandgap, which causes a temperature variation of I_{sc} through the variation of the optical absorption coefficient and of V_{oc} and FF through the strong temperature dependence of the intrinsic carrier concentration n_i . Thus, as a first approximation, one may even ignore the temperature dependences of lifetimes and mobilities, as we have done to calculate the 'worst case' values.

3. At the design temperature of 80°C, the expected performance of a near-optimum shallow homojunction InP cell is:

	100 AM0 (Circular)	20 AM0 (Rectangular)
J_{sc} A/cm ²	3.821	0.764
V_{oc} mV	946.2	896.8
FF %	81.40	83.72
η %	21.10	20.57

As stated earlier, efficiencies of 23.2% and 22.6%, should be realistically achievable for the circular and rectangular cell respectively, at their design operating points.

4. With efficiencies exceeding 22% at 80° C, 20 AM0 and 100 AM0, both the rectangular and circular InP shallow homojunction solar cells compare very favorably to GaAs cells of the same design and may be preferred in space over the GaAs cells because of the superior radiation tolerance of the InP cells.

References

- [1] R. E. Patterson, H. S. Rauschenbach and M. D. Cannady, *Conf. Rec. 16th IEEE PVSC, IEEE Publ. No. 82CH1821-8*, 1982, pp. 39-44.
- [2] M. Cornwall et al, Interim Reports from General Dynamics to Air Force Wright Aeronautical Labs. Under Contract No. F-33615-83-C-2319.
- [3] C. Goradia, M. Ghalla-Goradia and H. Curtis, *Conf. Rec. 17th IEEE PVSC, IEEE Publ. No. 84CH2019-8*, 1984, pp. 56-62.
- [4] C. Goradia, J. Geier, I. Weinberg, *Conf. Rec. 19th IEEE PVSC, IEEE Publ. No. 87CH2400-0*, 1987, pp. 937-943.
- [5] C. Keavney, "InP Shallow Homojunction Solar Cells", these Proceedings.
- [6] M. Wanlass, T. Gessert, K. Emery, T. Coutts, "Emperical and Theoretical Studies of the Performance of OMCVD InP Homo-junction Solar Cells as a Function of Emitter Thickness and Doping, and Base Doping", these Proceedings.

TABLE 1A

General Cell Parameters of
Near-Optimum Cell Design

	Rectangular	Circular
Total Area A, cm ²	0.25	0.1257
Grid Shadowing	4%	4%
AR Coating	750 Å SiO ₂	750 Å SiO ₂
Specific Contact		
Resistance R _{ms} , ohm-cm ²	2E-5	2E-5
To n ⁺ emitter	1E-3	1E-3
To p ⁺ BSF layer		
Series Resistance R _s , milliohms	59.7	92
Shunt Resistance R _{sh} , ohms	1E7	1E7
Bandgap of InP at 300K, E _g , eV	1.35	1.35
Intrinsic Carrier Concentration n _i at 300K, cm ⁻³	1.65E7	1.65E7
Effective Front SRV S _f , cm/s	1.1E5	1.1E5

TABLE 1B

Geometrical and Material Parameters of Near-Optimum Cell Design

Note: The following parameters are identical
for both rectangular and circular cells.

Emitter	
Width W _E	0.04 μm(400 Å)
Doping N _{DE}	2E18 cm ⁻³
Effective Lifetime τ _{pE}	1.26 ns
Diffusion Length L _{pE}	0.42 μm
Base	
Width W _B	1.5 μm
Doping N _{AB}	5E16 cm ⁻³
Effective Lifetime τ _n	17.8 ns
Diffusion Length L _{nB}	12.75 μm
BSF Region	
Width W _{BSF}	250 μm
Doping N _{B,BSF}	5E18 cm ⁻³
Effective Lifetime τ _{n,BSF}	0.18 ns
Diffusion Length L _{n,BSF}	1.06 μm

TABLE 2
Temperature Dependence of I_{sc}

$$J_{sc}(T) = 0.030475 + 21.91E-6 \cdot T \quad A/cm^2/AMO \text{ sun}$$

T is in kelvins

At 300K, this gives $J_{sc} = 36.45 \text{ mA/cm}^2/AMO \text{ sun}$

AMO Concentration	Short Circuit Current I_{sc} , mA		
	@ 27°C (300K)	@ 80°C (353K)	@ 100°C (373K)
1	4.581	4.8029	4.858
20	91.62	96.058	97.16
100	458.1	480.29	485.8
200	916.2	960.58	971.6

TABLE 3A

Predicted Parameters of Near-Optimum Circular Cell
at 27°C, 80°C and 100°C at 1, 20, 100 and 200 AMO

AMO Concentration	@ 27°C (300K)		@ 80°C(353K)		@ 100°C(373K)	
	Expected	Worst Case	Expected	Worst Case	Expected	Worst Case
	V _{oc} mV					
1	906.4	906.4	802.3	796.6	762.6	754.5
20	987.0	987.0	896.8	891.8	862.4	855.2
100	1029.0	1029.0	946.2	941.2	914.5	907.5
200	1047.0	1047.0	967.4	962.4	936.9	929.9
	FF %					
1	85.14	85.14	82.01	81.76	80.80	80.33
20	86.52	86.52	83.97	83.86	82.90	82.74
100	84.11	84.11	81.40	81.30	80.29	80.15
200	80.65	80.65	77.65	77.54	76.44	76.28
	η %					
1	20.49	20.49	18.04	17.84	17.08	16.80
20	22.67	22.67	20.63	20.49	19.82	19.61
100	22.98	22.98	21.10	20.96	20.35	20.15
200	22.41	22.41	20.57	20.44	19.84	19.66

TABLE 3B

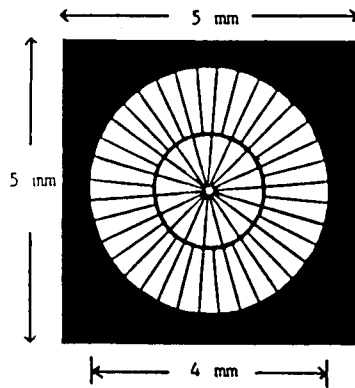
Predicted Parameters of Near-Optimum Rectangular Cell
at 27°C, 80°C and 100°C at 1, 20, 100 and 200 AMO

AMO Concentration	@ 27°C (300K)		@ 80°C(353K)		@ 100°C(373K)	
	Expected	Worst Case	Expected	Worst Case	Expected	Worst Case
	V _{oc} mV					
1	906.4	906.4	802.3	796.6	762.6	754.5
20	987.0	987.0	896.8	891.8	862.4	855.2
100	1029.0	1029.0	946.2	941.2	914.5	907.5
200	1047.0	1047.0	967.4	962.4	936.9	929.9
	FF %					
1	85.14	85.14	82.01	81.76	80.80	80.33
20	86.29	86.29	83.72	83.61	82.64	82.47
100	83.01	83.01	80.18	80.08	79.03	78.88
200	78.48	78.48	75.28	75.17	73.99	73.82
	η %					
1	20.49	20.49	18.04	17.84	17.08	16.80
20	22.61	22.61	20.57	20.43	19.75	19.55
100	22.67	22.67	20.78	20.65	20.03	19.84
200	21.81	21.81	19.94	19.81	19.21	19.02

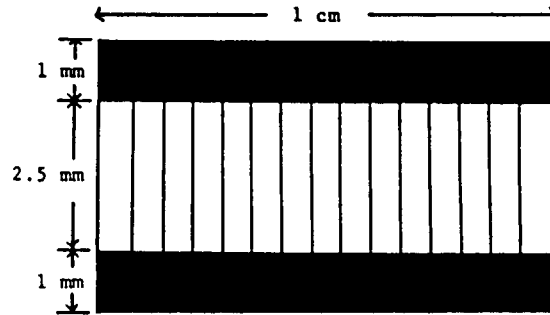
TABLE 4
Temperature Dependence of V_{OC} and n

AMO Concentration	dV_{OC}/dT mV/°C		dn/dT %/°C	
	Expected	Worst Case	Expected	Worst Case
20	-1.72	-1.82	-0.04	-0.0435
100	-1.575	-1.68	-0.037	-0.0395
200	-1.515	-1.615	-0.036	-0.0390

ORIGINAL PAGE
BLACK AND WHITE PHOTOGRAPH



Circular Cell for
Cassegrainian Concentrator
100 AMO, 80°C



Rectangular Cell for
Slats Concentrator
20 AMO, 80°C

Figure 1. Geometries and Dimensions of the Concentrator Cells Modelled

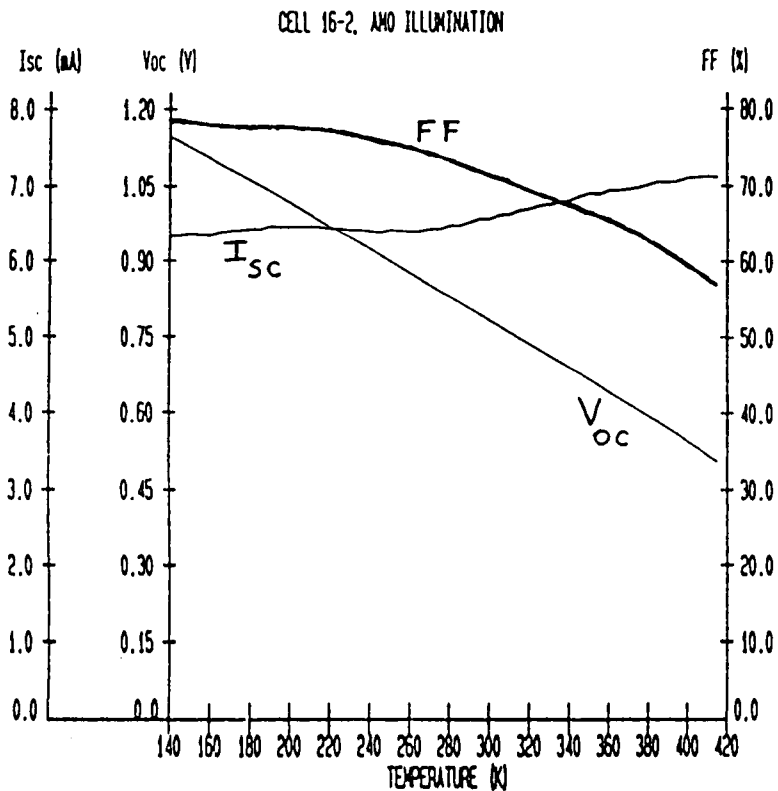


Figure 2.

Measured Variation of
Performance Parameters with
Temperature for One of Four
InP Solar Cells

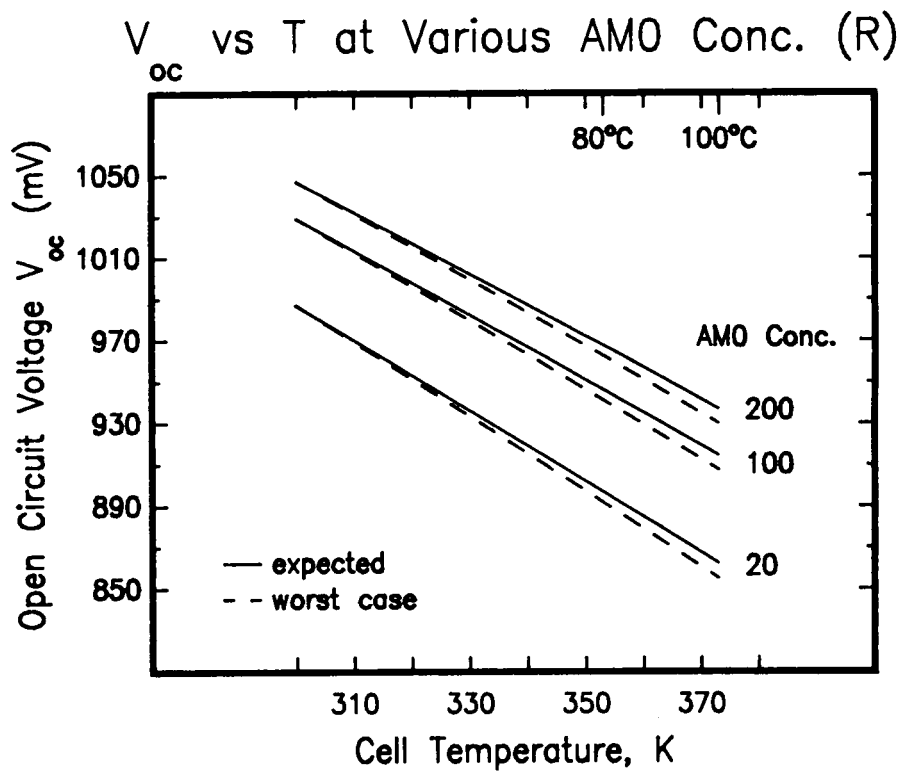
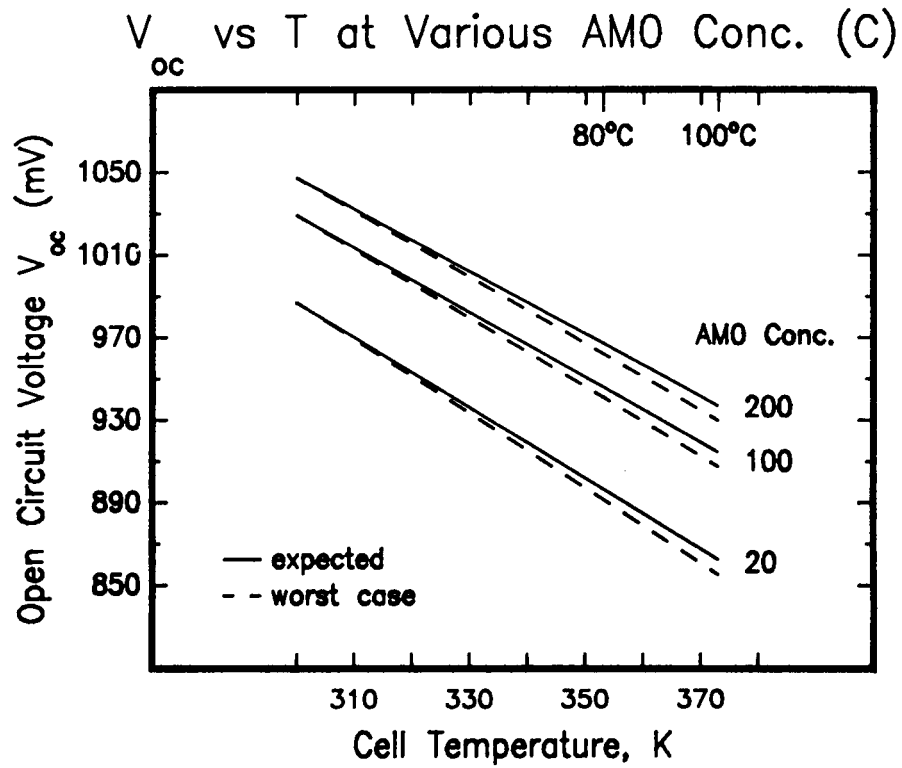
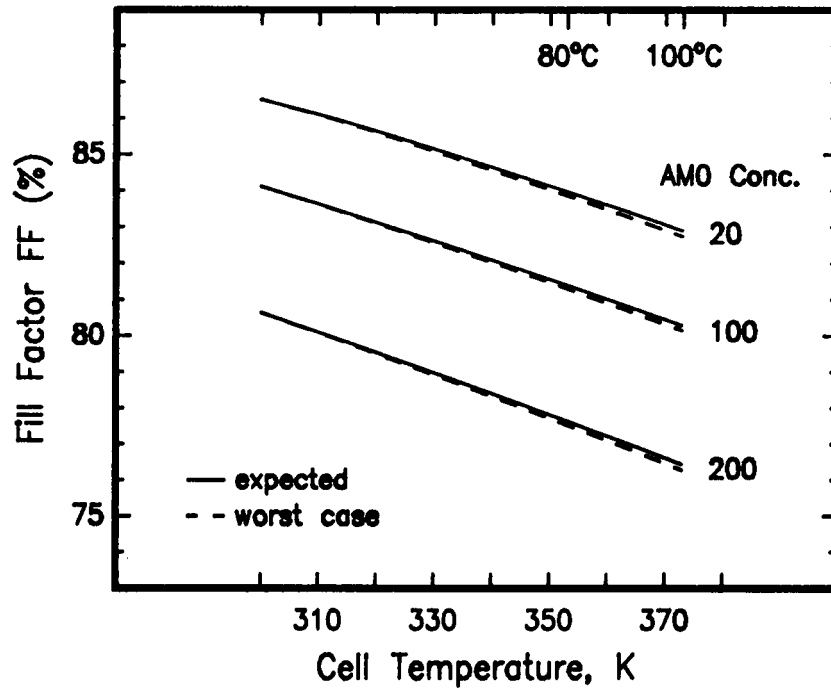


Figure 3. V_{oc} versus Temperature and AMO Concentrations for Circular (C) and Rectangular (R) Near-Optimum Cells

FF vs T at Various AMO Conc. (C)



FF vs T at Various AMO Conc. (R)

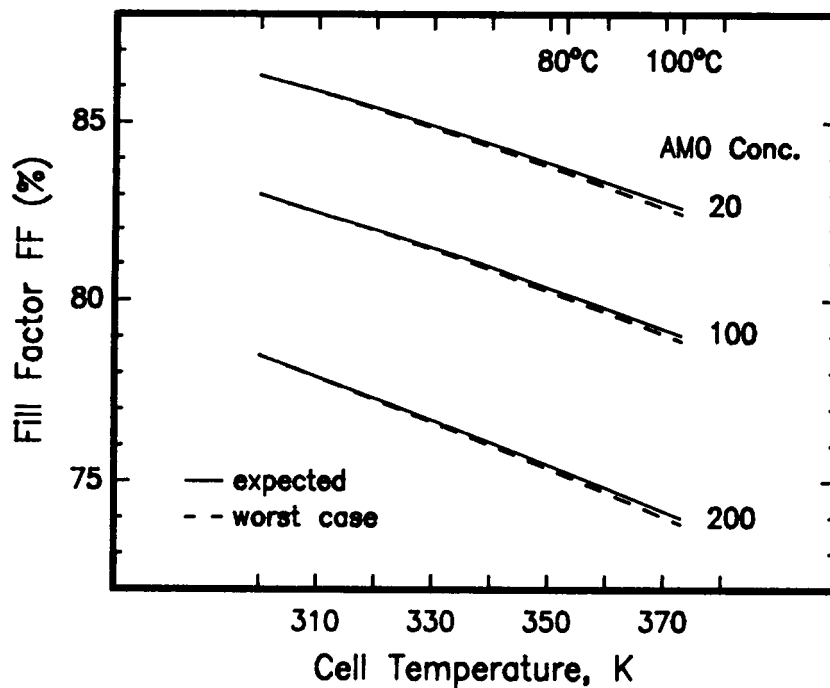
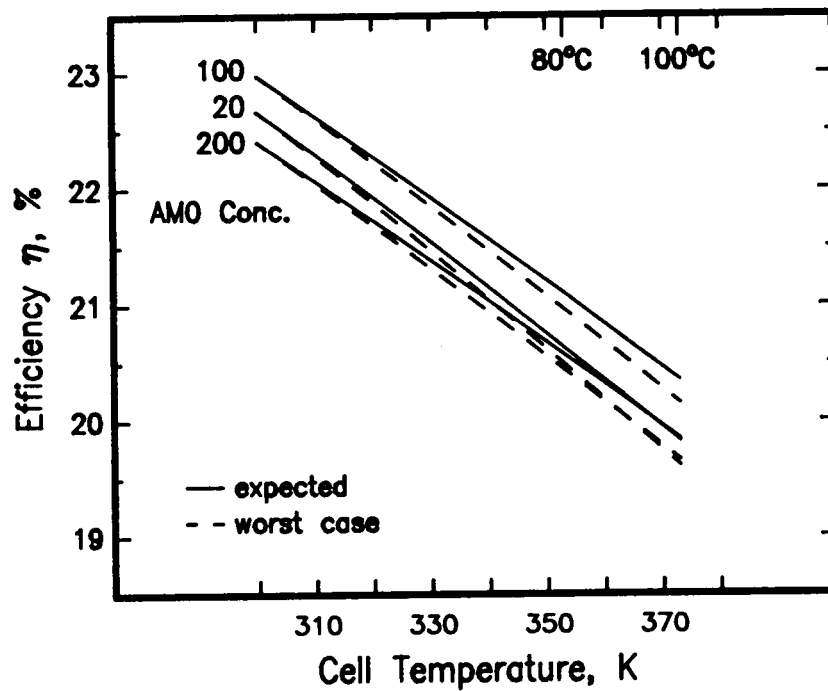


Figure 4. FF versus Temperature and AMO Concentrations for Circular (C) and Rectangular (R) Near-Optimum Cells

Eff. vs T at Various AMO Conc. (C)



Eff. vs T at Various AMO Conc. (R)

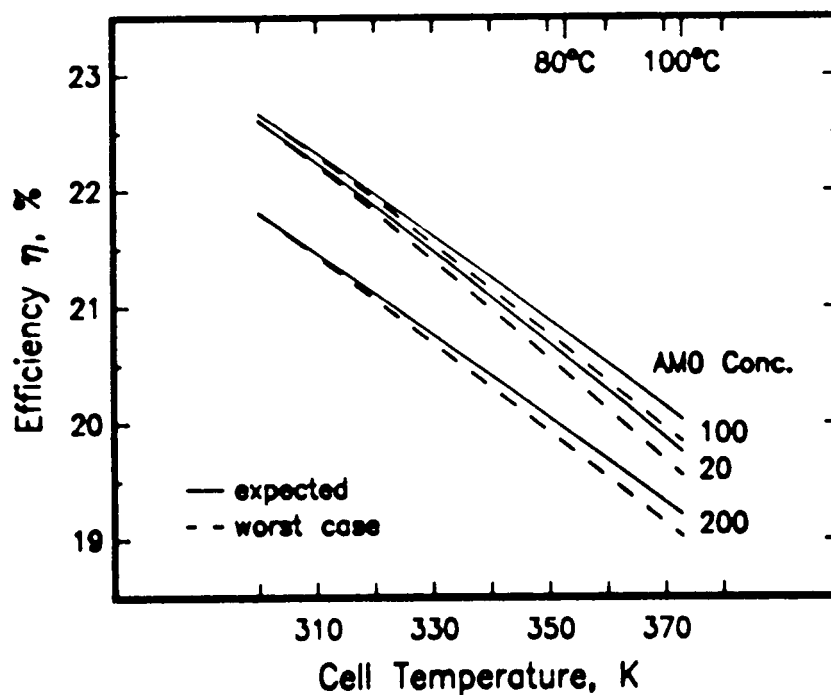


Figure 5. Efficiency versus Temperature and AMO Concentrations for Circular (C) and Rectangular (R) Near-Optimum Cells

Modelling and Design of High Performance Indium Phosphide Solar Cells

Sandra L. Rhoads
AstroPower Division/Astrosystems, Inc.

Allen M. Barnett
University of Delaware

Abstract

A first principles pn junction device model has predicted new designs for high voltage, high efficiency InP solar cells. Measured InP material properties were applied and device parameters (thicknesses and doping) were adjusted to obtain optimal performance designs. Results indicate that p/n InP designs will provide higher voltages and higher energy conversion efficiencies than n/p structures. Improvements to n/p structures for increased efficiency are predicted. These new designs exploit the high absorption capabilities, relatively long diffusion lengths, and modest surface recombination velocities characteristic of InP.

Predictions of performance indicate achievable open-circuit voltage values as high as 943 mV for InP and a practical maximum AM0 efficiency of 22.5% at 1 sun and 27°C. The details of the model, the optimal InP structure and the effect of individual parameter variations on device performance will be presented.

Introduction

The goal of this study was to derive InP solar cell designs yielding high open-circuit voltage without significantly sacrificing short-circuit current. It is appropriate to begin such a study with a look at today's InP solar cell designs. The widely accepted optimum design for InP solar cells is an n+/p/p+ structure offering a maximum open-circuit voltage of 902 mV for epitaxial structures [ref. 1]. However, from first principles, open-circuit voltages well above 900 mV should be achievable for a bandgap of 1.35 eV. The design requirements yielding maximum voltage and maximum energy conversion efficiency for InP solar cells are described.

The highest efficiency InP solar cells were reported by Keavney and Spitzer [ref. 2]. The device structure was an n+/p/p+ design formed by silicon ion implantation of epitaxial material. Wanlass et. al. [ref. 3] has also reported high efficiency InP solar cells fabricated using MOCVD. The device parameters and experimental results are shown in Table 1 and Table 2. These tables also include the device parameters and predicted performance of the near-optimum structure predicted by Goradia

[ref. 1]. It is important to note that all three designs are very similar. All have an ultrathin emitter layer, an emitter with a high carrier concentration and a base with a low carrier concentration.

Theoretical Model

The model used in this study is based on the diode equation. Reverse saturation current and short-circuit current are expressed as basic solutions to transport equations derived by many different authors [refs. 4,5] for the pn junction. This study uses standard modelling assumptions of one-dimensional carrier movement, low-level injection and uniform doping. It calculates the reverse saturation current contributed by the emitter and the base, and the short circuit current contributed by the emitter, base, and depletion region. These current equations describe the minority carrier behavior in each region of a solar cell structure.

The expression for open-circuit voltage is of standard form -- proportional to the natural log of the ratio of short-circuit current and reverse saturation current. The expression used for fill factor is based on the ideal definition which expresses fill factor as a function of open-circuit voltage only [ref. 6].

The reverse saturation current and short-circuit current values predicted by the equations described above include loss mechanisms inherent to InP according to its material properties. These current values are sensitive to surface recombination velocities, diffusion lengths, and minority carrier lifetimes which reflect material purity and quality.

Additional corrections were made to short-circuit current and fill factor values to account for device losses. Short-circuit current values were reduced by 6.6% for grid shading and reflection losses. Fill factor values were reduced by 2% to account for series resistance losses. These specific percentages were determined for GaAs [ref. 7], however, electrical losses for InP solar cells are expected to be the same.

For calculation of light generated current, detailed knowledge of the solar spectrum is required. The solar spectrum was divided into narrow bands such that photon flux and absorption coefficient could be considered constant within each band. The current generated within each band was calculated and then all band currents were summed together to yield the current generated over the entire usable solar spectrum.

Flux, as a function of wavelength, was obtained from the solar spectral-irradiance standard curve (AM0) [ref. 8] generated by measurements from aircraft. The total amount of power incident from the sun at unit area in the orbit was determined to be 135.3 mW/cm². Optical constants for determination of absorption coefficient as a function of wavelength were obtained from the Handbook of Optical Constants [ref. 9].

Values for minority carrier diffusion length as a function of carrier concentration were taken from experimental results published by Yamaguchi et al [ref. 10]. The data were determined from the relationship between photoluminescence intensity and carrier concentration in InP and that between solar cell photoresponse and carrier concentration in InP. Values for mobility as a function of carrier concentration were taken from experimental results published by Kuphal [ref. 11] for liquid phase epitaxial InP. Characterization was performed mainly by Van der Pauw and capacitance-voltage (C-V) measurements.

The results predicted by the device modelling studies are sensitive to the material parameters (intrinsic carrier concentration, mobilities, diffusion lengths, lifetimes) assumed by the model. Great care was taken in this study to use conservative values; the material parameter data used in this study are more conservative than estimates used by others. The material parameters assumed for the optimum device designs predicted by this model are listed in Table 3.

Baseline Study

As a baseline test of this model, the device parameters used for the experimental devices by Wanlass et al were introduced to our model using the material parameter data (such as mobility and diffusion length as a function of carrier concentration) discussed above.

Figure 1 is a plot of the resulting open-circuit voltage and conversion efficiency values predicted for a wide range of emitter carrier concentrations. The conversion efficiencies predicted by Goradia and achieved by Spire [ref. 2] and SERI [ref. 3] have been added for comparison. Note that Goradia's model and this model are in complete agreement for the given n+/p/p+ design. The experimental results indicate that the n+/p/p+ design described by Goradia is being successfully fabricated.

Table 1 indicates that a major difference exists between Goradia's model and this model in the material parameters of the p-type base. Mobility values are similar, however diffusion length and minority carriers lifetime values are extremely different for the same carrier concentration. Differences in performance are reflected in the predicted open-circuit voltage values shown in Table 2. Goradia predicts lower reverse saturation currents are achievable -- open-circuit voltage is higher.

InP Design Optimization Results

Figure 1 indicates an upward trend in efficiency as emitter doping is lowered. By lowering the emitter doping and raising the base doping, the conversion efficiency predicted for the n/p design can be increased as shown in Figure 2.

A further increase in efficiency can be realized if the emitter layer is expanded to 0.29 microns. In fact, as shown in Figure 3, efficiency actually increases with increasing emitter thickness up to 0.29 microns. Figure 3 also illustrates that for the n/p+ design, efficiency is not extremely sensitive to wide variations in emitter thickness. The maximum efficiency for this design is 21.5%, corresponding to a 7% gain in efficiency over the traditional n+/p/p+ structure. This design maximizes current gain in the emitter while open-circuit voltage remains relatively constant. Table 3 provides device parameters for this optimized design.

The maximum attainable voltage and efficiency for an InP solar cell is predicted for a p/n design. A 943 mV maximum is predicted for a 2×10^{18} base and emitter, however this is not a maximum efficiency design. A design with a more traditional emitter to base doping ratio offers the maximum efficiency of 22.5%. This design is sensitive to emitter thickness and requires an emitter less than or equal to 0.07 microns. The details of the optimized p/n structure are given in Table 3.

A careful comparison of n/p and p/n InP designs suggests a physical dependence of the InP solar cell on the properties of its p-type layer which determines the optimum device parameters. Table

3 reveals that the optimal p-type carrier concentration in both designs is identical -- 6×10^{16} . The p-type material, whether it forms the emitter or the base, is the main contributor to reverse saturation current. For n/p designs, the only way to significantly reduce (by an order of magnitude) reverse saturation current is to increase base doping; this explains the n/p+ design being optimum rather than an n+/p design. As shown in Figure 5, variations in emitter doping have no effect on total J_0 for n/p designs.

For p/n designs, J_0 is still dominated by the p-type component. However, by increasing emitter doping (Figure 6) and decreasing base doping, saturation current can be brought to an absolute minimum. This explains why the p+/n is the absolute optimum device design for a high voltage, high efficiency InP solar cell.

Another comparison of n/p and p/n designs is presented in Figures 7 and 8. Short-circuit current and open-circuit voltage values remain relatively unchanged within a certain range of surface recombination velocity values. For the n/p structure, the surface recombination limit is about 1×10^3 . For the p/n structure, the limit is about 1×10^5 . These values are in agreement with the physical constants listed for InP by Coutts [ref. 12].

Figures 7 and 8 also uncover another difference between n/p and p/n InP designs. The reduction in short-circuit current is less drastic for the p/n design as surface recombination exceeds its acceptable limit. Absorption in the n/p design occurs primarily in the emitter; an increase in surface recombination velocity drastically reduces the number of collectable carriers. The short-circuit current of the p/n design is less emitter-dependent. Significant absorption takes place within the depletion region and base layer where minority carrier diffusion lengths are longer; a larger number of carriers are collected beyond the emitter layer.

Conclusions

The significance of this model is three fold. This model:

- (1) provides nontraditional designs for high voltage, high efficiency InP solar cells.
- (2) reveals that the p-type material (through reverse saturation current) is the key to high voltage, high efficiency InP solar cell performance.
- (3) supports the conversion efficiency predicted for the traditional n+/p/p+ InP solar cell.

Acknowledgement

Special thanks is extended to Dr. Timothy J. Coutts for helpful discussions and for a copy of his InP review paper [ref. 12].

References

- [1] C. Goradia, J. V. Geier, and I. Weinberg, "Modelling and Design of High Efficiency Radiation Tolerant Indium Phosphide Space Solar Cells", *Proceedings of the 19th IEEE PVSC*, New Orleans, Louisiana, (1987), p. 937.
- [2] C.J. Keavney and M.B. Spitzer, "Indium Phosphide Solar Cells Made by Ion Implantation", *Appl. Phys. Lett.* **52** (17), (1988), p. 1439.
- [3] M.W. Wanlass, T.A. Gessert, K.A. Emery, and T.J. Coutts, "Empirical and Theoretical Studies of the Performance of OMCVD InP Homojunction Solar Cells as a Function of Emitter Thickness and Doping, and Base Doping", presented at this conference.
- [4] C. Hu and R.M. White, "Solar Cells: From Basic to Advanced Systems", McGraw-Hill, Inc., (1983), p. 5155.
- [5] H.J. Hovel, *Semiconductors and Semimetals, vol. 2 (Solar Cells)*, ed. Willardson and Beer, Academic Press, Inc., (1975), p.18.
- [6] M.A. Green, *Solar Cells*, Prentice-Hall, Inc., (1986), p. 80.
- [7] J. B. McNeely, G. H. Negley, M. E. Nell, S. F. Brennan, A. M. Barnett, "Design and Fabrication of GaAsP Top Solar Cells", *Proc. 18th IEEE PVSC*, (1985), p. 151.
- [8] M.P. Thekaekara, "Extraterrestrial Solar Spectrum, 3000-6100 Å at 1-Å Intervals", *Applied Optics* **13**, No. 3, (1974), p.518.
- [9] O.J. Glembocki and H. Pillar, in *Handbook of Optical Constants of Solids*, ed. E.D. Palik, Academic Press, Inc., New York (1985), p. 503.
- [10] M. Yamaguchi, A. Yamamoto, N. Uchida and C. Uemura, "A New Approach for Thin Film InP Solar Cells", *Solar Cells*, **19** (1986-1987) p. 85.
- [11] E. Kuphal, "Preparation and Characterization of LPE InP", *Journal of Crystal Growth*, **54**, 117 (1981).
- [12] T.J. Coutts and M. Yamaguchi, "InP Based Solar Cells: A Critical Review of Their Fabrication, Performance and Operation", *Current Topics in Photovoltaics*, **3**, Academic Press, London, to be published, 1988.

TABLE 1: Device parameters of the accepted n+/p/p+ optimum design.

	Goradia's Model	SPIRE Device	SERI Device	This * Model
emitter:				
thickness (μm)	.04	.03	.025	.025
doping ($1/\text{cm}^3$)	6×10^{17}	3×10^{19}	4×10^{18}	4×10^{18}
diffusion length (μm)	1.00	-----	-----	0.36
mobility ($\text{cm}^2/\text{V}\cdot\text{s}$)	93.4	-----	-----	66.0
lifetime (ns)	4.19	-----	-----	0.76
base:				
thickness (μm)	1.5	3.0	3.0	3.0
doping ($1/\text{cm}^3$)	5×10^{16}	2×10^{16}	5×10^{16}	5×10^{16}
diffusion length (μm)	12.8	-----	-----	2.3
mobility ($\text{cm}^2/\text{V}\cdot\text{s}$)	3550	-----	-----	3566
lifetime (ns)	17.9	-----	-----	.57

*Intrinsic carrier concentration (n_i^2) = 1.5×10^{14}

TABLE 2: Performance parameters for the accepted n+/p/p+ optimum design.

	Goradia's Model	SPIRE Device	SERI Device	This Model
Voc (mV)	901.6	873	882	883
JSC (mA/cm^2)	36.53	35.7	33.06	36.2
FF (%)	84.79	82.9	82.6	85.3
AM0 Eff. (%)	20.34	18.8	17.6	20.1

Table 3: New high voltage, high efficiency designs predicted by this model.

	N/P	P/N
emitter:		
thickness (μm)	.22 to .56	.02 to .07
doping ($1/\text{cm}^3$)	2×10^{16}	6×10^{17}
diffusion length (μm)	3.0	.80
mobility ($\text{cm}^2/\text{V}\cdot\text{s}$)	145.0	2292.0
lifetime (ns)	24.0	.11
base:		
thickness (μm)	5.0	5.0
doping ($1/\text{cm}^3$)	6×10^{17}	6×10^{16}
diffusion length (μm)	.80	2.7
mobility ($\text{cm}^2/\text{V}\cdot\text{s}$)	2292.0	130.0
lifetime (ns)	.11	22.0
front surface rec. (cm/s)	1×10^3	1×10^5
back surface rec. (cm/s)	1×10^7	1×10^7

Table 4: Predicted performance for the new designs described in Table 3.

	N/P	P/N
Voc (mV)	901	928
Jsc (mA/cm^2)	37.7	38.2
FF (%)	85.5	85.8
Efficiency (AM0)	21.5%	22.5%

Figure 1: Open-circuit voltage and efficiency predictions of this model assuming SERI's emitter thickness, base doping, and base thickness.

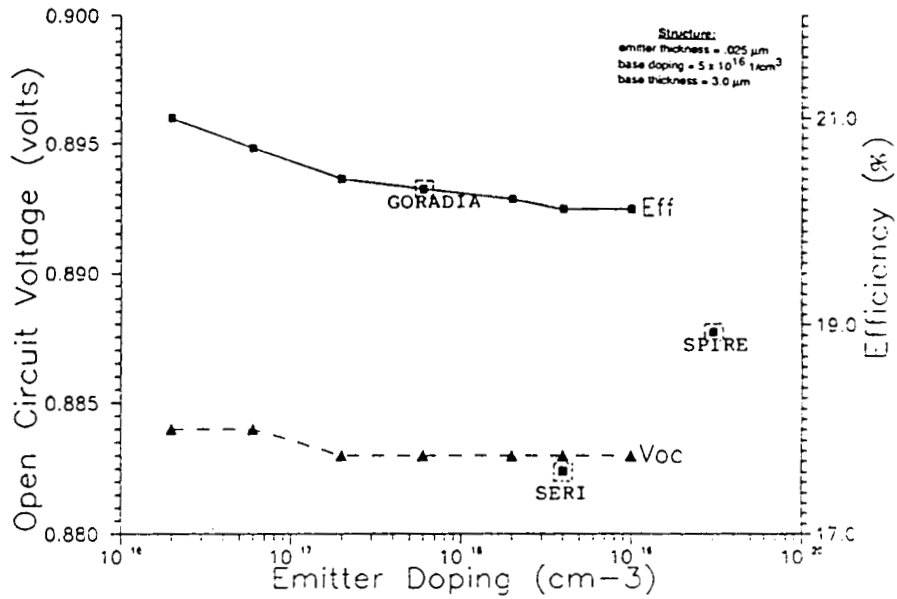


Figure 2: Higher efficiency is predicted for the N/P structure if the emitter concentration is reduced and the base concentration is increased.

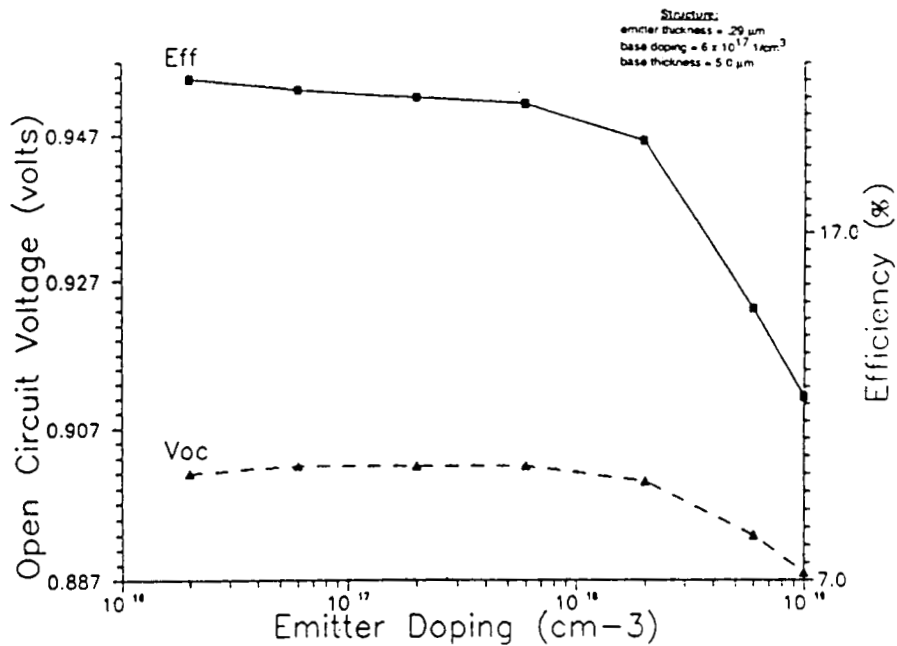


Figure 3: The N/P+ design offers a wide range of acceptable emitter thicknesses yielding high efficiencies.

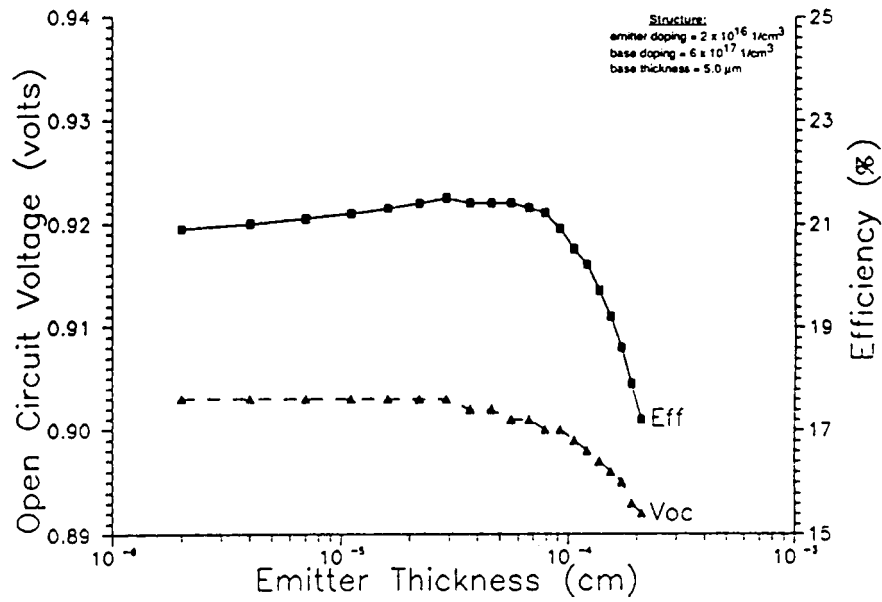


Figure 5: J_0 of the optimum N/P+ design (Figure 2) is dominated by its base (P-type) component.

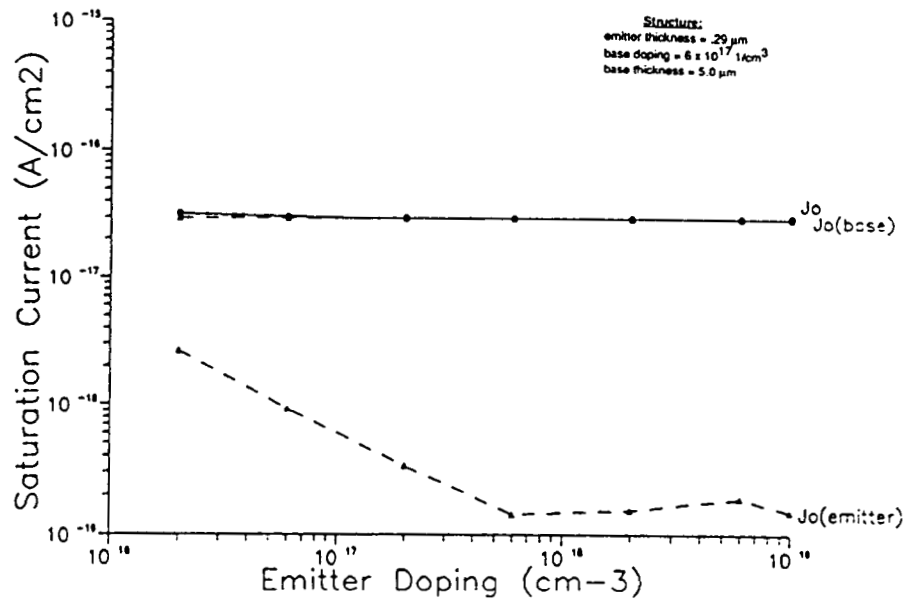


Figure 6: J_0 of the optimum P/N design (Figure 4) is dominated by its emitter (P-type) component.

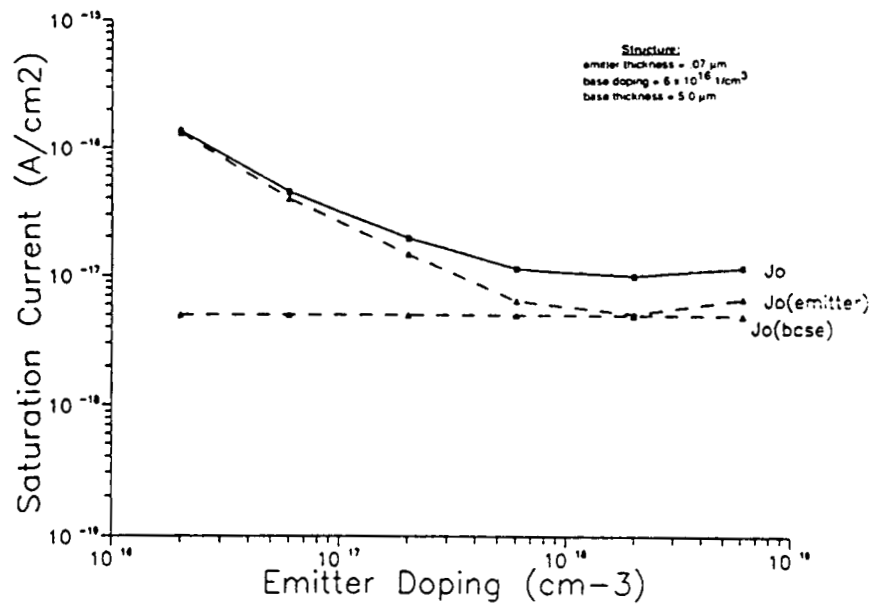


Figure 7: Acceptable bounds for front surface recombination velocity for the optimum N/P+ design.

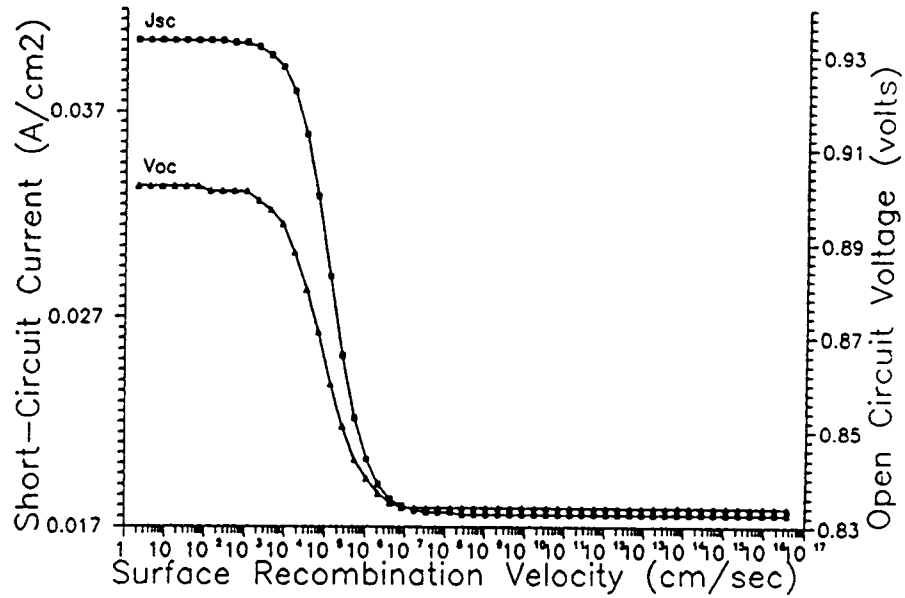
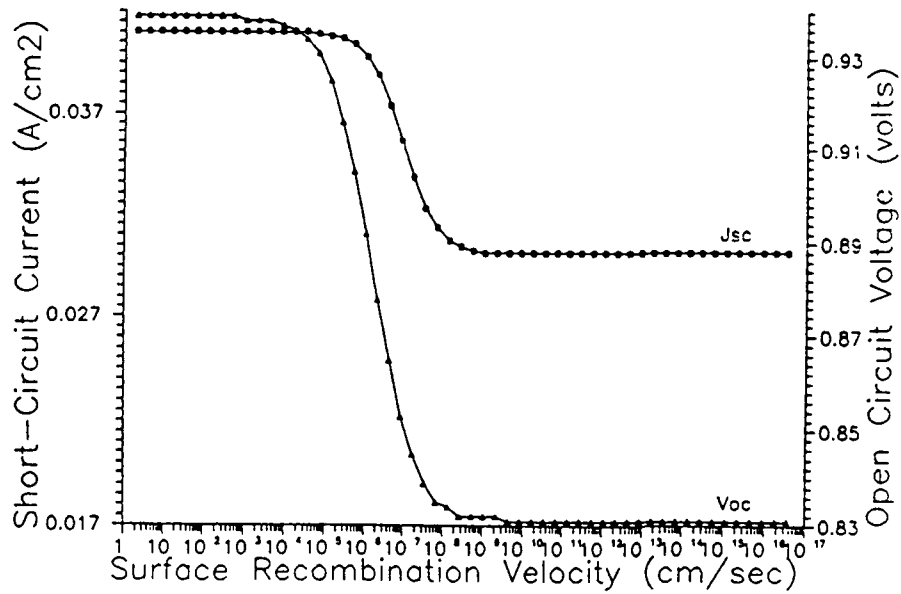


Figure 8: Acceptable bounds for front surface recombination velocity for the optimum P/N design.



Deep Levels and Radiation Effects in p-InP

W.A. Anderson, A. Singh, K. Jiao and B. Lee
Center for Electronic and Electro-optic Materials
State University of New York at Buffalo
Electrical and Computer Engineering
Room 217C Bonner Hall
Amherst, NY 14260

Summary

A survey was conducted on past studies of hole traps in InP. An experiment was designed to evaluate hole traps in Zn-doped InP after fabrication, after electron irradiation and after annealing using deep level transient spectroscopy. Data similar to that of Yamaguchi was seen with observation of both radiation-induced hole and electron traps at $E_A = 0.45$ eV and 0.03 eV, respectively. Both traps are altered by annealing. It is also shown that trap parameters for surface-barrier devices are influenced by many factors such as bias voltage, which probes traps at different depths below the surface. These devices require great care in data evaluation.

Introduction

InP is an important material for the fabrication of solar cells for space applications [refs. 1-4] because of the high conversion efficiency and radiation resistance. Applications as detectors, high-speed transistors and quantum well structures also benefit from radiation hardness and high carrier mobility. Deep levels in the material can play an important role in limiting the minority carrier lifetime and therefore controlling the performance in electro-optic applications. A search of the literature reveals very few reports on the study of deep level traps in p-InP.

Bremond [ref. 5] studied bulk p-type InP using DLTS to reveal hole traps with $E_A=0.36$ and 0.70 eV. Sibille [ref. 6] examined Ti-Au Schottky diodes on (100) Zn-doped LPE layers to reveal a hole trap with $E_A=0.14$ eV. More recently, Yamaguchi [ref. 7] has studied effects of 1.0 MeV electron irradiation of n^+-p (Zn-doped) InP to reveal radiation-induced traps with $E_A=0.37$ and 0.52 eV, in agreement with Sibille [ref. 6]. It is the purpose of this paper to present a thorough study of both hole and electron traps in the same p-InP substrate, using a very high Schottky barrier to the p-InP provided by Yb metal. We have used the standard boxcar based DLTS technique [ref. 8] to determine the activation energy, capture cross section and concentration of the deep level traps. In addition, surface effects are separated from bulk effects in surface-barrier devices. These data may be useful to those using Zn-doped InP in device fabrication.

Experimental Method

Fabrication

Zn-doped p-InP, (100) orientation, one side polished, single crystal substrates used in this work were obtained from Crysta Comm. Inc. Before ohmic contact deposition, the substrates were ultrasonically rinsed in electronic grade trichloroethylene, acetone, methanol and deionized (DI) water. The samples were then etched for 30 s in $\text{H}_2\text{SO}_4 : \text{H}_2\text{O}_2 : \text{H}_2\text{O}$ (3:1:1) and $\text{HF} : \text{H}_2\text{O}$ (1:1) followed by DI water rinse and drying with gaseous N_2 . Au/Zn ohmic contacts were deposited at a pressure of 10^{-6} Torr and annealed in forming gas for 7 min. at 400°C . The polished surface was then etched in the above acid- H_2O rinse combination, protecting the back ohmic contact by a photoresist technique. Thermal oxide was grown for 45 min. at 350°C in 3 LPM gaseous O_2 . The resulting oxide thickness, measured with a Gaertner L117 ellipsometer was 20–35 Å. High barrier Schottky diodes were prepared by evaporating Yb dots of area $2.0 \times 10^{-2} \text{ cm}^2$ onto the polished surface of p-InP. An illustration is given in Figure 1.

Measurements

DLTS measurements were performed by a computer controlled Bio-Rad Polaron S4600 DLTS system. The Yb/p-InP diodes were placed in a continuous flow liquid nitrogen cryostat which was typically cycled between 80 K and 450 K. A three terminal temperature controller, with microprocessor, controlled the temperature ramp programmer. A 1-MHz Boonton 72B capacitance meter with fast response time and a boxcar system with three sampling gates permitted the simultaneous measurement of DLTS spectra at two rate windows. Only the absolute value of the DLTS signal was plotted and the contributions due to the majority and the minority carriers represented as solid and dotted curves, respectively. The timing events were programmed so that for all the rate windows, the DLTS peak height, ΔC is one third of the true transient amplitude, ΔC_{TOT} . However, a gain of three is included so that ΔC_{TOT} equals the amplitude of the S4600 output at the DLTS peak. This feature facilitates the determination of trap concentrations.

The quiescent reverse bias applied to the Schottky diodes ranged between 0 V and 3 V. The forward filling pulse voltage was between 0 V and 0.6 V in the forward direction, with pulse widths between 1 μs and 50 ms. The temperature was swept at a rate of 0.2 K/s and the measurements performed for various rate windows between 20 s^{-1} and 10^3 s^{-1} . In order to investigate the interfacial traps, the quiescent voltage was set at a small forward bias (0.2 V) followed by a fill pulse of 0.6 V in the forward direction. The data acquisition system was controlled by an HP 9000 series computer. The capacitance transients were digitized, stored and analyzed by software to obtain trap parameters.

Irradiation and Annealing

After an initial DLTS study, samples were removed from the DLTS system and irradiated with the Au-leads intact. A 1.0 MeV van de Graaff generator was utilized with the samples resting on a water-cooled metal block. Samples were simultaneously irradiated to a fluence of $1 \times 10^{15} \text{ e}^-/\text{cm}^2$ with great care to avoid heating during irradiation.

Samples were replaced in the DLTS system and re-tested prior to in situ annealing. Annealing was conducted in several stages with testing between each stage. The stages consisted of 200 mA/cm² for 15 min. at 300°K , 200 mA/cm² for 15 min. at 400°K , 100 mW/cm² illumination for 10 min.

at 300° K and 100 mW/cm² illumination for 10 min. at 400°K. These levels of injection and illumination are similar to those used by Yamaguchi et al [ref. 7].

Experimental Data

A typical DLTS scan for a Yb-MS device 44, given in Figure 2, reveals a majority (hole) trap and minority (electron) trap with activation energies (E_A) of 0.48 eV and 0.13 eV, respectively. After each preliminary scan, a C-V plot was conducted at the temperature of a particular DLTS peak. A more complete DLTS scan was then conducted to separately analyze each peak with six rate windows as illustrated in Figure 3 for the main peak before irradiation. The computer software then calculated trap parameters and gave an activation energy plot illustrated in Figure 4. Subsequent irradiation added a new hole with $E_A=0.45$ eV while slightly shifting the two original traps. This is illustrated by the DLTS scan of Figure 5.

Annealing procedures, outlined in the previous section, did not dramatically change the DLTS profile but did alter trap parameters as illustrated in Table 1. Radiation caused a slight shift and increased density of h1, the addition of a new hole trap (h2) and an energy shift plus change in capture cross-section of e1. Completion of annealing resulted in little change in h1, a significant decrease in σ for h2 with a downward shift in E_A , and little change in e1.

Discussion

A DLTS study was conducted for a Yb-MS device with data taken as fabricated, after irradiation and after annealing. Irradiation caused a new trap at $E_A=0.45$ eV which shifted to 0.35 eV after annealing. Annealing caused a significant decrease in capture cross-section as well. Yamaguchi [ref. 7] observed radiation-induced traps H4 at $E_v+0.37$ eV and E_2 at $E_c-0.19$ eV which quite likely correspond to our h2 and e1 after irradiation. We did not observe the large annealing effect which he observed which may be related to irradiations at $1 \times 10^{16} \text{e}^-/\text{cm}^2$ compared to our $1 \times 10^{15} \text{e}^-/\text{cm}^2$.

A similar study performed on a Yb-MIS structure gave similar results although more noticeable changes were observed with annealing. Irradiation reduced the trap density and shifted E_A for the main hole trap and introduced a new electron trap at $E_A=117$ meV. The altered hole trap is a combination of the original and a new one which could not be resolved. Annealing at 200 mA/cm² reduced the hole trap density but not the electron trap density. Optical annealing shifted electron traps and hole traps to a lower E_A , caused a shrinkage in the radiation-induced hole trap density and a growth of the original hole trap. These observations are similar to those of Yamaguchi [ref. 7] and are illustrated by Figure 6.

The difference in trap location between this work and that of Yamaguchi may be explained by a very thorough study by Singh [ref. 9]. It is evident that surface barrier devices provide different trap parameters with distance beneath the surface until the "true" bulk is reached. Thus, DLTS data on surface-barriers are influenced by surface preparation, type of metal, presence of an oxide, and bias levels used during measurement. This is illustrated by data of Table 2 which shows variation of parameters of a single trap with changes in reverse bias. The picture would be further complicated by effects of radiation and annealing which may contribute to variation in depletion width.

A further illustration is given in Table 3 as a report of hole traps in InP by other workers. Some differences are evident depending on type of device and method of semiconductor growth. These

differences are not nearly as severe as for electron traps in InP where almost every activation energy has been observed.

Conclusions

Data reported herein reveal trap introduction in p-InP due to e^- irradiation with subsequent changes upon annealing with forward bias and illumination. Annealing by current injection or photo-injection gives a different annealing behavior. Trap parameters are very sensitive to many conditions for surface barrier devices which requires great care in design of experiments and interpretation of data.

References

- [1] G.W. Turner, J.C.C. Fan and J.J. Hsich, Appl. Phys. Lett., **37**, 400 (1980).
- [2] A. Yamamoto, M. Yamaguchi and C. Vemura, Appl. Phys. Lett., **44**, 611 (1984).
- [3] A. Yamamoto, M. Yamaguchi and C. Vemura, Appl. Phys. Lett., **47**, 975 (1985).
- [4] T.J. Coutts and S. Naseem, Appl. Phys. Lett., **46**, 164 (1985).
- [5] D. Bremond, A. Nouailhat and G. Guillot, *Int. Symp. GaAs & Related Compounds*, Japan, 1981.
- [6] A. Sibille and J.C. Bourgoin, Appl. Phys. Lett., **41**, 956 (1982).
- [7] M. Yamaguchi, K. Ando, A. Yamamoto and C. Vemura, J. Appl. Phys., **58**, 568 (1985). ALSO Appl. Phys. Lett., **47**, 846 (1985).
- [8] D.V. Lang, J. Appl. Phys., **45**, 3023 (1974).
- [9] A. Singh and W.A. Anderson, submitted for publication.

TABLE 1.- TRAP DATA WITH IRRADIATION AND ANNEALING AS PARAMETERS

Sample	Activation Energy E_A (eV)	Capture Cross-Section σ (cm ²)	Trap Density N_T (#/cm ³)
44-h1	0.48	1.3×10^{-18}	3.5×10^{14}
44R-h1	0.50	2.6×10^{-18}	2.0×10^{15}
44RA-h1	0.50	3.5×10^{-18}	1.8×10^{15}
44R-h2	0.45	1.0×10^{-16}	2.0×10^{14}
44RA-h2	0.35	2.7×10^{-18}	3.5×10^{14}
44-e1	0.13	9.0×10^{-20}	4.0×10^{14}
44R-e1	0.031	1.1×10^{-21}	3.5×10^{14}
44RA-e1	0.038	8.0×10^{-22}	3.5×10^{14}

* R - irradiated

RA - annealed after irradiation

TABLE 2.- VARIATION OF THE PARAMETERS OF DOMINANT HOLE TRAP WITH QUIESCENT REVERSE BIAS IN Zn-DOPED p-InP BY DLTS USING SCHOTTKY DIODES [9]

Reverse Bias (V)	$E_{Tp} - E_V$ (eV)	σ_p (10^{-21} cm ²)	N_{Tp}^a (10^{14} cm ⁻³)	W^a (μ m)
3.0	0.56	4000	1.5	1.02
2.0	0.48	400	2.1	0.85
1.0	0.38	30	2.4	0.67
0.3	0.34	9	2.7	0.53
0.0	0.36	40	2.3	0.45
0.2 ^b	0.25	4	0.9	0.33

a. Space charge layer width.

b. Quiescent forward bias value.

TABLE 3.- PREVIOUS WORK ON HOLE TRAPS IN InP

<u>Identity</u>	<u>E_A</u>	<u>σ_2 (cm²)</u>	<u>N_T cm⁻³</u>	<u>REF*</u>	<u>Reason</u>
IH1	0.70			Bremond (81)	bulk p:Fe
H5	0.535	6E-15		Sibille (82)	LPE, Zn-doped, rad
H5	0.52			Yamaguchi (85)	<u>Zn-doped, rad.</u> point defect- impurity complex
IH2	0.48	1E-13		Bremond (81)	bulk p-undoped
H4	0.37	1.7E-15		Sibille (82)	LPE, Zn-doped, rad
H4	0.37	5E-15		Yamaguchi (85)	<u>Zn-doped, rad.</u> a recomb. center point defect
IH3	0.36			Bremond (81)	bulk p-undoped
H3	0.33	2.4E-15		Sibille (82)	LPE, Zn-doped, rad
H0	\approx 0.14			Sibille (82)	LPE,

* Bremond (81): LEC or VPE (n&p), Au-Schottky

Sibille (82): LPE on p⁺, <100> Zn-doped, 2E16, Ti-Au Schottky

Yamaguchi (84): n⁺/p(Zn) and p⁺/n(Si) [also seen as a minority trap in n-InP after irradiation]

Yamaguchi (85): n⁺/p diffused, Zn-doped (4.5E15-1E18)

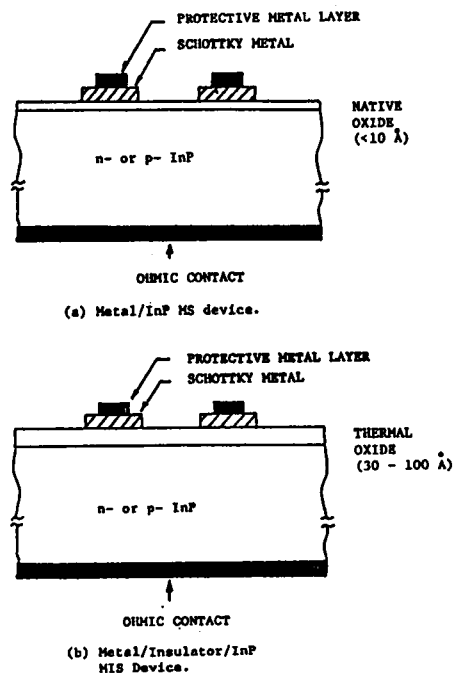


Figure 1 Diagram of samples studied by DLTS.

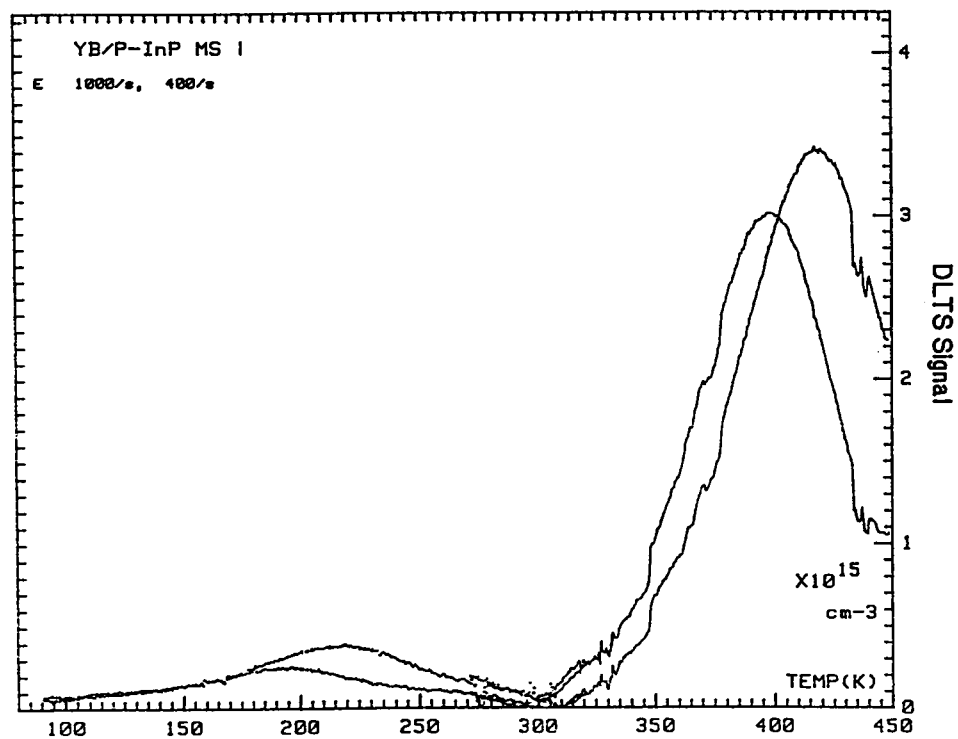


Figure 2 DLTS scan showing peak location prior to irradiation.

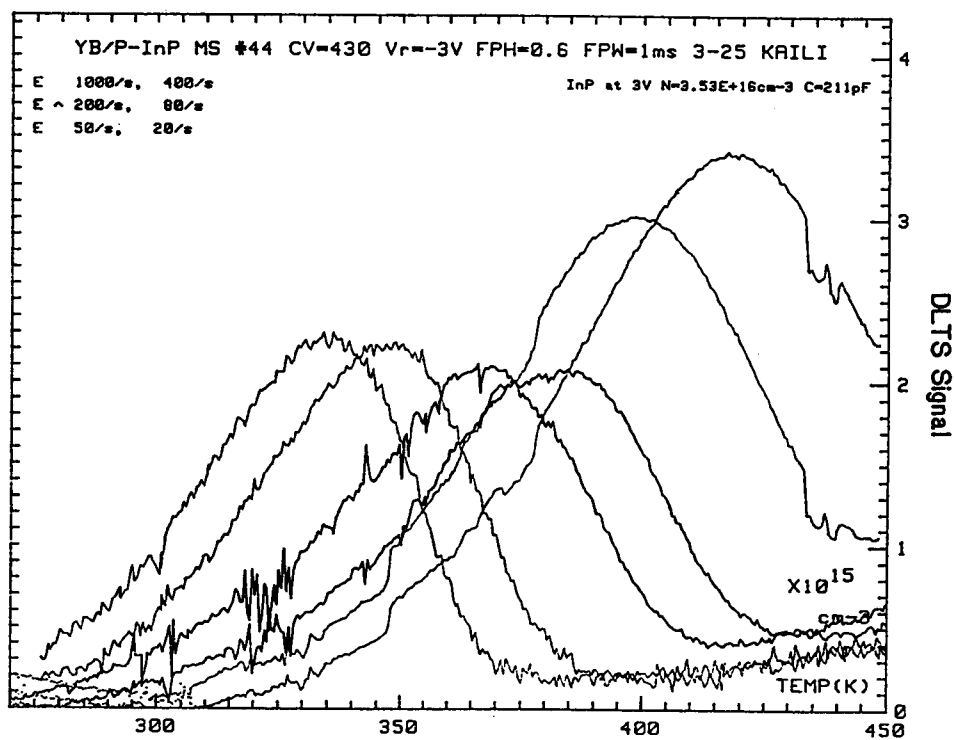


Figure 3 A complete DLTS analysis of the main hole trap prior to irradiation.

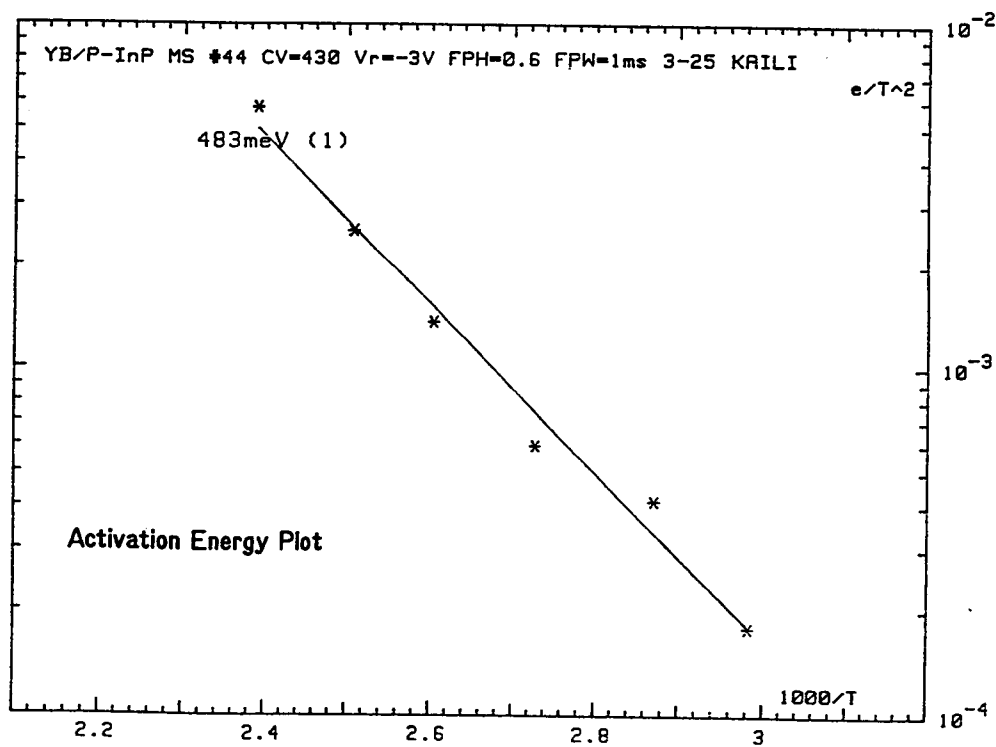


Figure 4 An activation energy plot prior to irradiation.

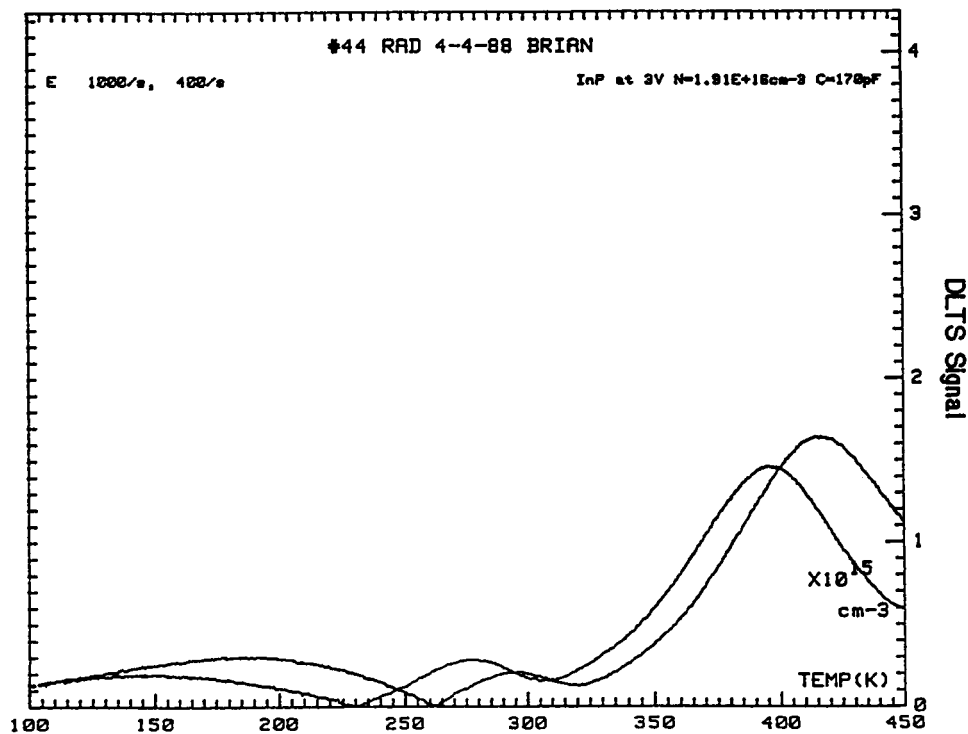


Figure 5 DLTS scan showing an added hole trap due to 1.0 MeV electron irradiation to a fluence of $1.0 \times 10^{15} \text{cm}^{-2}$.

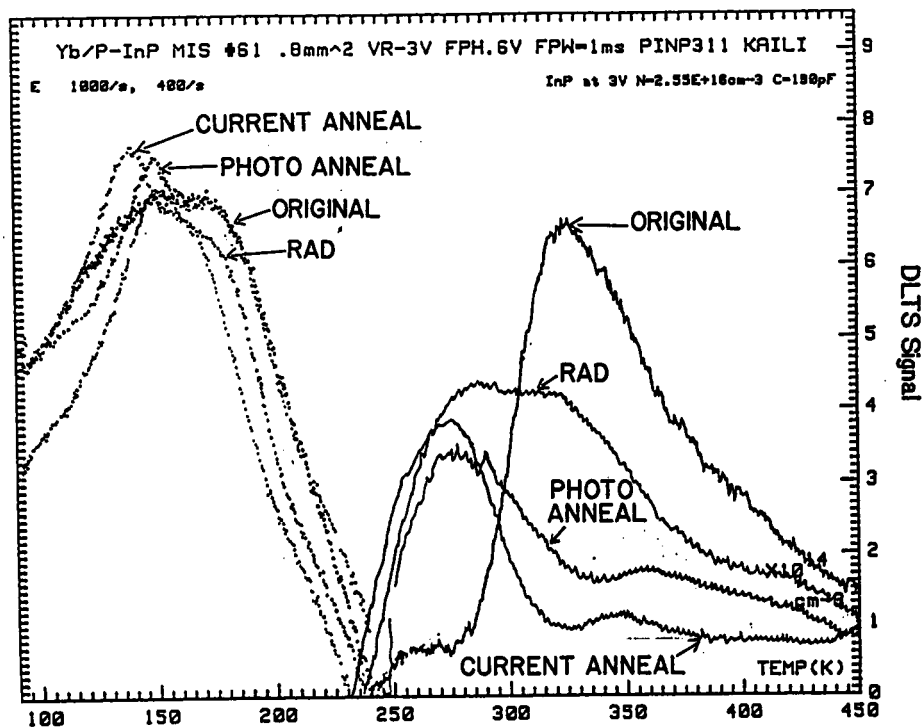


Figure 6 Series of DLTS scans showing different stages of irradiation and annealing for a Yb-MIS diode.

Encapsulated Diffusion of Sulphur into InP

K.K. Parat, J.M. Borrego, S.K. Ghandhi
*Electrical, Computer and Systems Engineering Department
 Rensselaer Polytechnic Institute
 Troy, New York 12180*

Abstract

This talk outlines a simple process for the fabrication of n^+p solar cells in indium phosphide. Large area cells ($>0.25 \text{ cm}^2$) have been made by this process, with a photovoltaic conversion efficiency of 15.21% under AM0 conditions of illumination. An ideality factor of 1.1 and a saturation current density of $8 \times 10^{-15} \text{ A/cm}^2$ have been observed for these cells.

The technique for cell fabrication involves the diffusion of sulphur into InP by an open tube process, and gives highly reproducible results from run to run. A vacuum-deposited layer of gallium sulphide (Ga_2S_3) was used as the source for sulphur diffusion, with a chemically vapor deposited SiO_2 cap layer to prevent decomposition of the InP surface during heat treatment. Diffusions were carried out in a flowing nitrogen ambient at 585°C to 708°C , and characterized by their surface carrier concentration and the diffusion constant. The diffusion profile for sulphur in InP is estimated to be of the complementary error function type. The activation energy of the diffusion was estimated to be 1.94 eV.

The technique described here is ideally suited for the fabrication of shallow n^+p junctions in InP, and has been used for space-borne solar cells.

Introduction

At the present time, there is considerable interest in indium phosphide as an active material for solar cells. InP is a direct bandgap semiconductor with an energy gap of 1.34 eV, which is close to that required for maximum conversion efficiency at AM 1.5 [ref. 1]. An important property of this material is its ability to be surface passivated. Typically, the surface recombination velocity of n -type InP is about 10^3 cm/sec as compared to $1 \times 10^7 \text{ cm/sec}$ for GaAs [ref. 2]. It has been reported that InP solar cells have a higher resistance to gamma ray radiation degradation than Si or GaAs solar cells of comparable junction depths [ref. 3]. Thus, these solar cells are of particular interest for space applications.

Conventionally, diffusion of n -type impurities in III-V compounds has been carried out [refs. 4-6] in sealed tubes, in order to prevent evaporation of the more volatile group V element, which leads to massive deterioration of the surface. These diffusions require both high temperature as well as long duration, due to the low diffusion coefficient of donor impurities, with some vapor phase etching of the substrate.

There are two other problems associated with the sealed tube diffusion technique. First, the diffusion constants of impurities in III-V compounds are critically dependent upon the vacancy concentrations, and thus on the partial pressures of the host lattice elements. The inability to

maintain identical partial pressure conditions from run to run makes results hard to reproduce, so that there is a large disagreement between different workers because of the different diffusion conditions involved. The second problem is the necessity of handling the highly toxic substances such as arsenic, or hygroscopic materials such as phosphorus, which have to be carefully weighed and sealed in tubes.

The possibility of an open tube technique [ref. 7], where the diffusion can take place in a flowing inert ambient gas, is thus very attractive. Ease of implementation, adaptability to large scale batch processing, and potential low cost are its main advantages.

This paper describes the technical details and the results obtained with the open tube diffusion of sulphur into InP.

We have used a vacuum evaporated layer of gallium sulphide as the source for sulphur doping, capped by a chemical vapor deposited film of SiO_2 to prevent the loss of phosphorus from the surface of InP. This results in excellent morphology even after high temperature processing. The equilibrium vapor pressure of phosphorus during diffusion does not depend upon extrinsic parameters as in the case of sealed tube diffusion, where the phosphorus vapor pressure is set by the amount of phosphorus in the tube. As a result, this technique is simple to implement, and is highly reproducible from run to run. Solar cells made by this method have demonstrated equal (or slightly superior) performance than those made by the sealed tube process [refs. 8, 9].

Experimental

The p-type substrates used for the fabrication of n^+p InP solar cells were pre-polished LEC grown 50 mm diameter slices, obtained from Crystacom, Inc., Mountain View, CA 94043. These were (100) misoriented 2° towards (110), and doped with Zn to a concentration of $5 \times 10^{16}/\text{cc}$. The as-received material was cut into suitable pieces and degreased in successive hot baths of trichloroethylene, acetone and methanol. Next, they were etched in a 1% Br-methanol solution for 5 minutes to remove the residual polishing damage. This was followed by etching in $\text{HF}:\text{HCl}:\text{H}_2\text{O}_2:\text{H}_2\text{O}$ in a ratio of 2:2:1:8 by volume, and by a rinse in 10% H_3PO_4 solution to remove the oxide present on top. Finally gallium sulphide (99.99% purity) was evaporated onto the frontside of the wafer using an alumina coated tantalum boat.

After the deposition of the Ga_2S_3 film, the slices were transferred to a cold wall resistance heated chemical vapor deposition system operated at atmospheric pressure. The transfer time was kept short (under 10 min.) to avoid any possible contamination from the atmosphere. The samples were first encapsulated on the frontside with $0.5 \mu\text{m}$ of SiO_2 , which was grown by the oxidation of SiH_4 in an argon ambient. The partial pressures of oxygen and silane used for this purpose were 6.46×10^{-3} and 7.5×10^{-4} atm. respectively. The growth temperature was 325°C with an approximate growth rate of $100\text{\AA}/\text{min}$. Next, the samples were turned over and the backside was also capped with $0.5 \mu\text{m}$ of SiO_2 . This is necessary to prevent phosphorus evaporation from the back of the slices during the diffusion step. Moreover, it provides a balancing of stress in the InP during heat treatment, and thus avoids dislocation formation, as well as damage to the cap layers.

Diffusions were carried out at temperatures ranging between 585°C and 708°C in an open tube diffusion system with a flowing nitrogen ambient, for times varying from 5 minutes to 24 hours. After diffusion, the SiO_2 cap was removed in dilute HF. The Ga_2S_3 layer was then removed in the

etch formulation described earlier ($\text{HF}:\text{HCl}:\text{H}_2\text{O}_2:\text{H}_2\text{O}=2:2:1:8$ by vol.). No visual damage of the InP surface was observed after the entire diffusion process.

In order to make solar cells on these diffused structures, back contacts to the p-substrates were made by evaporating Au/5% Zn and alloying at 420°C in forming gas (80% H_2 , 20% N_2) for 20 seconds. Next, the front contact grids were defined photolithographically. Electroplated gold was used to make contacts to the top n^+ -layer. These top contacts were well adhering, and ohmic (as plated) without any heat treatment. This is because the top n^+ -layer is very heavily doped. A total cell area of 0.31 cm^2 was delineated by photolithography and mesa etching in an iodic acid (10% by wt.) bath, with the aid of a second photomask.

Diffused junctions were characterized using the van der Pauw technique. A clover leaf pattern was delineated on the InP slices for this purpose by etching in 1% Br-methanol. Ohmic contacts to the n^+ layers were formed by alloying tin dots at 260°C for 1 minute in a flowing forming gas ambient. The sheet conductance and the effective Hall mobilities on these samples were measured at room temperature and at 77K. Following this, samples were etched in a 3% iodic acid etch with an approximate etch rate of $200\text{ \AA}/\text{min}$ for short durations of time. After each successive etch (i.e., the removal of a thin n^+ layer), Hall measurements were made until the sheet conductance of the remaining layer was less than 1% of the initial value. The etch rate of the individual samples was determined by simultaneously etching part of an identically diffused sample and then measuring its etched depth by a multiple beam interferometer. An etch rate of approximately $200\text{ \AA}/\text{min}$ was measured in this manner.

Results and Discussion

Figure 1 shows the sheet conductance of the diffused layers, plotted as a function of the square root of the diffusion time for three different thicknesses of the Ga_2S_3 layer. All the diffusions were carried out at a fixed temperature of 625°C . The straight line nature of the graphs shows that, for the diffusion durations considered here, the Ga_2S_3 layer always served as an infinite source of sulphur [ref. 10]. The effective mobilities of the diffused layers were found to be independent of the Ga_2S_3 thickness. If we assume that the general nature of the sulphur diffusion profile into InP is the same for all these diffusion cases, and that the mobility of these diffused layers is limited by impurity scattering, and hence doping dependent, it follows that the surface concentration is independent of the Ga_2S_3 source layer thickness. For a given doping profile (e.g., a complementary error function type) with a fixed surface concentration, the sheet conductance changes in proportion to the change in $(Dt)^{1/2}$. The parallel nature of the three sheet conductance vs. $(\text{time})^{1/2}$ graphs leads to the conclusion that the diffusion constant of sulphur into InP is the same for all three cases, and hence is independent of the Ga_2S_3 thickness.

The reason for the initial delay could be due to strain enhanced diffusion, as has been observed [ref. 11] during Zn diffusion into GaAs. However, this explanation does not seem to hold here. Note the absence of a slow diffusion regime in the beginning; rather, the sheet conductance rises abruptly after a finite time delay. Moreover, mobility values measured on these samples are sufficiently high so as to rule out the possibility of significant stress in the diffused layer. This has been reaffirmed by the fact that $\text{n}^+\text{-p}$ diodes formed by this diffusion technique have ideality factors close to unity, as seen in Fig. 2.

Figure 2 shows the delay as a function of the $(\text{Ga}_2\text{S}_3 \text{ thickness})^2$. The character of this curve is indicative of the fact that S diffusion into InP is taking place through a barrier. We propose that atomic sulphur required for the sulphur diffusion is primarily generated at the $\text{Ga}_2\text{S}_3/\text{SiO}_2$ interface, and then diffuses through the Ga_2S_3 layer to reach the InP. This would introduce a specific time delay before any substantial diffusion is observed. In addition, this delay should be proportional to the square of the Ga_2S_3 thickness, as seen in Fig. 3.

Figure 4 shows the sheet conductance and room temperature Hall mobility, measured after successive etching and removal of thin layers of the n^+ region. The sample shown here had 200Å of Ga_2S_3 as the dopant source and was diffused for 4 hours at 625°C. The mobility values shown here are the effective values for the remaining n^+ layer. Local mobility values were determined from these by a technique described elsewhere [ref. 12]. Here, we assumed that the drift mobility of electrons in these n^+ layers is the same as the measured Hall mobility, since the layers were degenerately doped [ref. 13].

The carrier concentration can be determined by differentiating the sheet conductance curve; however, unless the data is smoothed out, the error introduced by this process will be very large. Because of this, we preferred to assume a profile and specific values of the surface concentration and $(Dt)^{1/2}$, and have iteratively fit the sheet conductance data points using the mobility values obtained by the technique outlined above. The best fit (as denoted by the dark continuous line in Fig. 4) was obtained for a complementary error function (erfc) type of profile, with a surface concentration of $3.4 \times 10^{18}/\text{cm}^3$ and a $(Dt)^{1/2}$ of 633Å. Similar graphs were obtained for samples diffused at different temperatures and different times. In all cases, erfc doping profiles were obtained, independent of the time and temperature of the diffusion. Similar results have been obtained for sulphur diffusion profiles in GaAs [ref. 14], which are also of the complementary error function type.

Figure 5 shows the sheet conductance versus $(\text{diffusion time})^{1/2}$ for diffusions carried out at 585°C, 625°C, and 708°C. The thickness of the Ga_2S_3 layer was kept constant at 200Å for all these diffusions. The conventional practice here is to plot junction depth vs. $(\text{diffusion time})^{1/2}$, which necessitates diffusion into a substrate of opposite polarity, in this case, p-type. However, diffusion into p-type InP introduces the problem that heat treatment of Zn doped InP alters the carrier concentration in the substrate [ref. 15], thus seriously affecting the interpretation of junction depth data. Consequently, we have made our diffusions into semi-insulating InP. Here if we assume (as shown above) that the doping profile is of the erfc type irrespective of the diffusion time and temperature, and that the surface carrier concentration is a function only of the diffusion temperature, then the rate of change of sheet conductance should be directly proportional to the change in $(Dt)^{1/2}$. This is indeed the case, as seen in this figure.

Doping profiles were measured on several samples diffused at these temperatures, for different durations of time. The surface concentration and diffusion constants were determined by the method outlined before. Table 1 presents the data on sulphur diffusion into InP at these temperatures. These include the surface concentration, D and the effective Hall mobility of the diffused layer as a function of the diffusion temperature. Finally, Fig. 6 shows the log of the diffusion constant as a function of $1/T$. The activation energy of sulphur diffusion into InP was calculated to be 1.94 eV. The pre-exponential term was calculated to be $3.6 \times 10^{-4} \text{ cm}^2/\text{sec}$.

Conclusion

Open tube diffusion of sulphur into InP was studied in the temperature range of 585°C to 708°C. The diffusion profile was found to be of the complementary error function nature. Diffusion was dependent on the thickness of the Ga₂S₃ layer, which was used as the source sulphur diffusion. It was proposed that diffusion occurs through a barrier, which in this case is the Ga₂S₃ layer itself.

A capped diffusion, of the nature described here, results in a constant overpressure of phosphorus and sulphur at any given temperature. This is a distinct advantage over conventional diffusion methods, from the point of obtaining reproducible diffusions as required in device applications.

Acknowledgement

The authors would like to thank J. Barthel for technical assistance and P. Magilligan for manuscript preparation. This work was performed on Grant No. NAG 3-604 from the National Aeronautics and Space Administration, Cleveland, Ohio. This support, as well as discussions with Dr. I. Weinberg, have been of much profit and hereby acknowledged.

References

- [1] S.M. Sze, *Physics of Semiconductor Devices*, 2nd Ed., New York: Wiley, 1981, p. 798.
- [2] H.C. Casey, Jr. and E. Buehler, *Appl. Phys. Lett.*, **30**, 247 (1977).
- [3] A. Yamamoto, M. Yamaguchi and C. Uemura, *Appl. Phys. Lett.*, **44**, 611 (1984).
- [4] A. Yamamoto, M. Yamaguchi and C. Uemura, *IEEE Trans. Electron Dev.*, Ed-32, 2780 (1985).
- [5] H.C. Casey, Jr., "Diffusion in Compound Semiconductors", *Atomic Diffusion in Semiconductors*, Ed. D. Shaw, Plenum Press, New York (1973).
- [6] J.J. Coleman, *Appl. Phys. Lett.*, **31**, 283 (1977).
- [7] S.K. Ghandhi and K.K. Parat, *Appl. Phys. Lett.*, **26**, 209 (1987).
- [8] K.K. Parat, S. Bothra, J.M. Borrego and S.K. Ghandhi, *Solid State Electron.*, **30**, 383 (1987).
- [9] I. Weinberg, C.K. Swartz, R.E. Hart, Jr., S.K. Ghandhi, J.M. Borrego, K.K. Parat, M. Yamaguchi, *Solar Cells*, **22**, 123 (1987).
- [10] Ref. to basic straight line differential theory.
- [11] C.H. Ting and G.L. Pearson, *J. Electrochem. Soc.*, **118**, 1454 (1971).
- [12] H. Weider, *Thin Solid Films*, **31**, 123 (1976).
- [13] W. Walukiewicz, L. Lagowski, L. Jastrzebski, P. Rava, M. Lichtensteiger, C.H. Gatos, and H.C. Gatos, *J. Appl. Phys.*, **51**, 2659 (1980).
- [14] A.B.Y. Young and G.L. Pearson, *J. Phys. Chem. Solids*, **31**, 517 (1970).
- [15] K. Tsubaki and K. Sugiyama, *Jpn. J. Appl. Phys.*, **19**, 1789 (1980).

TABLE 1

Temperature °C	N_{SURF} (/cm ³)	EFFECTIVE MOBILITY (cm ² /V-sec)	$D_{\text{S, InP}}$ (cm ² /sec)
485	1.9×10^{18}	2050	1.6×10^{-15}
625	3.4×10^{18}	1800	5.0×10^{-15}
670	5.6×10^{18}	1600	1.1×10^{-14}
708	7.7×10^{18}	1350	5.2×10^{-14}

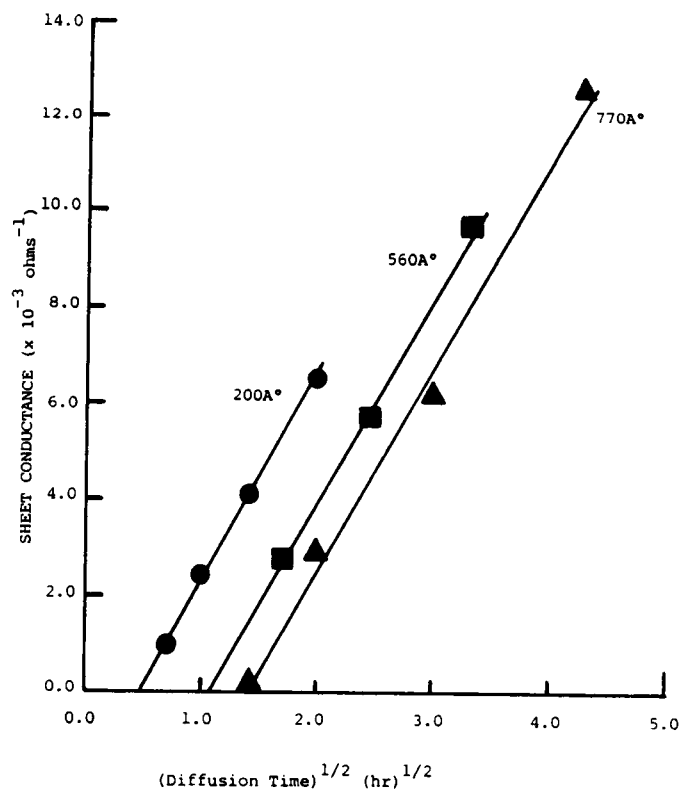


Fig. 1. Sheet conductance of the diffused n^+ layer as a function of $(\text{diffusion time})^{1/2}$. Different curves are for different Ga_2S_3 layer thicknesses.

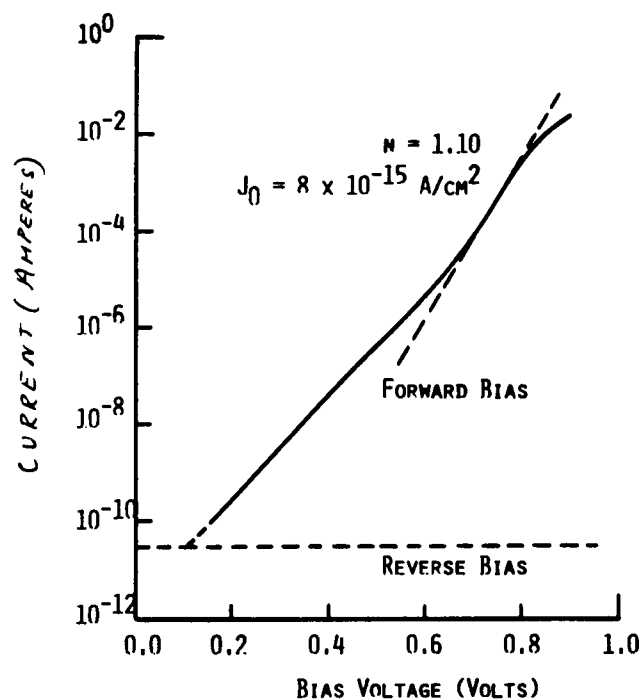


Fig. 2. Forward and reverse log I vs. V characteristics of an n^+p cell made by this technique. (Taken without illumination.)

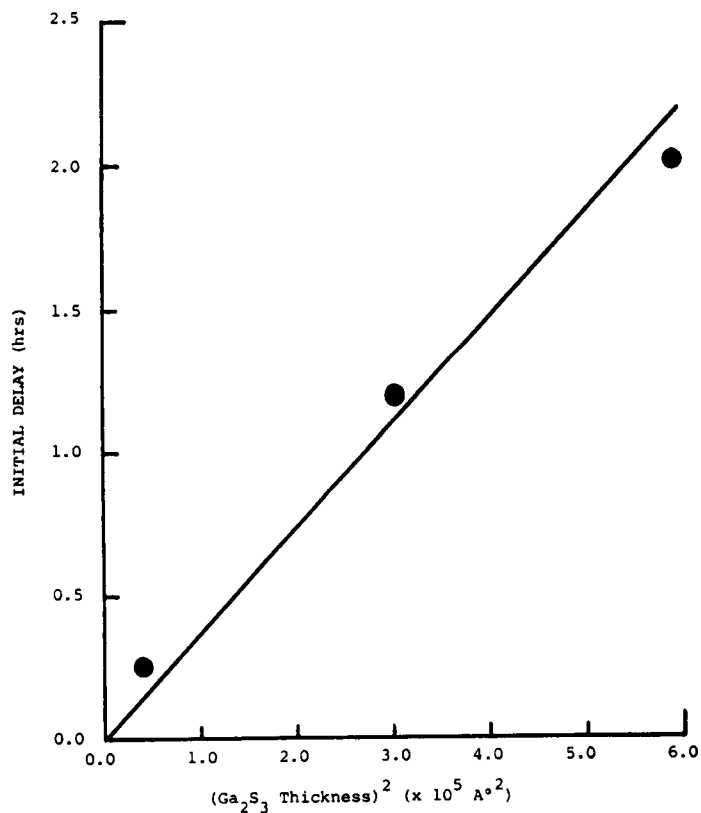


Fig. 3. Initial delay vs. square of the Ga_2S_3 layer thickness. Diffusions at 625° .

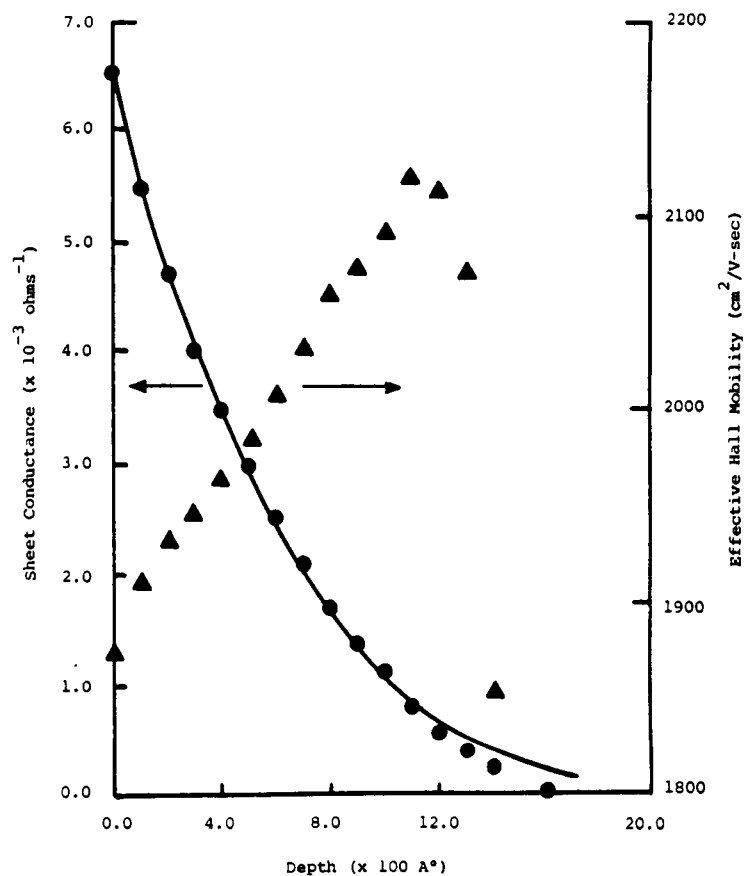


Fig. 4. Sheet conductance and effective mobility of the diffused layer after successive etching.

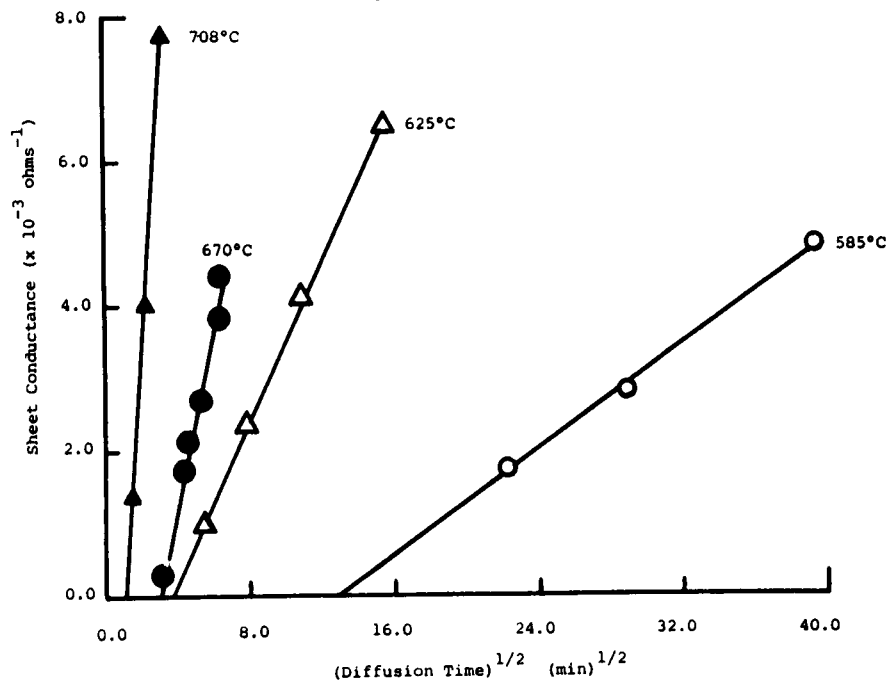


Fig. 5. Sheet conductance vs. (time)^{1/2} for samples diffused at different temperatures.

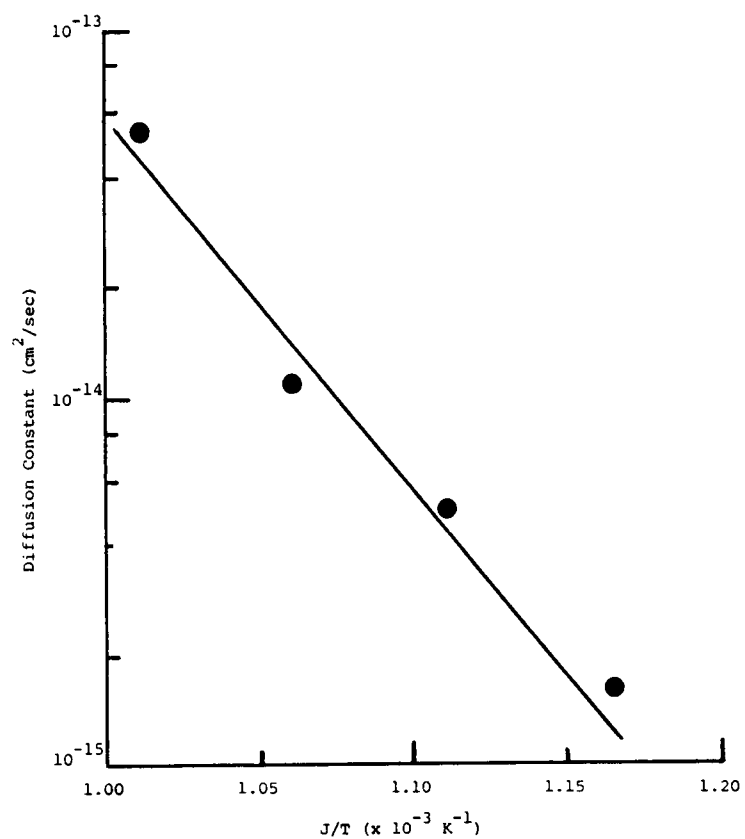


Fig. 6. Diffusion constant of sulphur in InP vs. $1/T$.

Session 2
Lightweight and Ultralightweight PV Technology

PRECEDING PAGE BLANK NOT FILMED

The Impact of Solar Cell Technology on Planar Solar Array Performance

Michael W. Mills and Richard M. Kurland
TRW Space & Technology Group

Introduction

This paper presents the results of a study into the potential impact of advanced solar cell technologies on the characteristics (weight, cost, area) of typical planar solar arrays designed for low, medium and geosynchronous altitude earth orbits. The study considered planar solar array substrate designs of lightweight, rigid-panel graphite epoxy and ultra-lightweight Kapton. The study proposed to answer the following questions:

Do improved cell characteristics translate into array-level weight, size and cost improvements?

What is the relative importance of cell efficiency, weight and cost with respect to array-level performance?

How does mission orbital environment affect array-level performance?

Important features of the study were: comparisons were made at the array level including all mechanisms, hinges, booms, harnesses. Array designs were sized to provide 5kW of array power (not spacecraft bus power, which is system dependent but can be scaled from given values). The study used important "grass roots" issues such as use of the GaAs radiation damage coefficients as determined by Anspaugh [ref. 1]. Detailed costing was prepared, including cell and cover costs, and manufacturing attrition rates for the various cell types.

The Solar Cell Technologies

Five solar cell types were studied (see table 1). The low cost, 200 μm (8-mil) thick, back surface reflector (BSR), nontexturized cell, at 12.3% efficiency represents the industry standard against which the other designs were compared. This "generic" silicon cell technology is reasonably well understood so that it was used as a control and a benchmark case study. Thin silicon cells were also included. These devices were assumed to be 66 μm (2.6 mils) thick with a boron back surface field and a back surface reflector.

Three GaAs cell technologies were studied, as follows: standard GaAs cells grown on 300 μm (12-mil) GaAs substrates, GaAs cells grown on 200 μm (8-mil) Germanium (Ge) substrates, and GaAs cells grown on 75 μm (3-mil) Ge substrates. The existence of technologies to grow GaAs cells on thinner, yet rugged substrates is the key which prompted this trade study. The effect of variable GaAs cell substrate thickness on radiation fluence at the junction was included in this study.

It was assumed, and recent data supports this, that cell substrate type has no effect on cell conversion efficiency. It was further assumed that the radiation response of these three GaAs cell types were identical after backside shielding effects are incorporated.

The Orbital Environments and Their Impacts

The study considered three orbits which, taken as a set, encompass most earth orbit missions. A mission life of 10 years was assumed.

The low earth orbit (LEO) mission selected for study was 520 km (280 n.mi) altitude, 28.5° inclined. This is typical of Shuttle/Space Station related missions and the Advanced X-Ray Astronomy Facility (AXAF). This orbit has a relatively benign radiation environment, but has high aerodynamic drag. EOL cell efficiency (low array area) will be a key design driver for this orbit. The LEO atomic oxygen environment is a driver in the selection of array materials and components but does not significantly effect the characteristics at the array level.

The mid-altitude earth orbit (MEO) selected was 6500 km (3500 n.mi) altitude, 60° inclined to demonstrate the effects of flying in a high radiation (trapped protons) environment. This type of orbit is geo-magnetically shielded from solar flare protons. In this type of orbit, a strong trade exists between coverglass thickness and array characteristics (weight, area and cost). The array characteristics are very sensitive to orbital altitude in this regime, as EOL radiation dose (but not species) changes by orders of magnitude with varying altitude.

The geosynchronous (GEO) altitude orbit, 35760 km/0° inclined (19300 n.mi/0° inclined), was considered due to the large number of missions flying this orbit. The orbital environment is rich in high energy trapped electrons, and high energy solar flare protons. The rigid particle spectra as well as the launch cost premiums make array weight a significant driver and preclude thick coverglasses.

The Array Technologies

Two planar array types were studied: flat rigid panel substrate and flat flexible blanket substrate. The rigid substrate characteristics are based upon 125 μm (5 mil) graphite/epoxy facesheets. The flexible substrate design is based upon the JPL/TRW Advanced Photovoltaic Solar Array (APSA) design [ref. 2]. Both technologies were being produced by TRW for flight or protoflight applications.

The rigid panel array configuration is shown in figure 1. The design assumed two wings were used for the rigid-panel, flat, accordion-fold array. The study did not include the solar array drive assembly (SADA) characteristics, and the simplifying assumption was made that the array would be sun-pointed about two axes for normal incidence. No provision was made for retraction or orbital change-out mechanisms.

Radiation Degradation

The method used to estimate the damage equivalent normal incidence 1 MeV electron fluence is given in detail in reference 1, chapter 6 and will not be further described. Fluences were calculated over a wide range of front side shield densities (coverglass thicknesses) for weight optimization. Silicon solar cell conversion efficiency vs. fluence was taken from reference 1. Similar GaAs properties were taken from reference 3.

The radiation models used for the three orbits are given in table 2, as are some of the assumptions used in the analyses. Most important among these is that, for the region of interest, a value of 1500 was used for the conversion from DENI 10 MeV protons to DENI 1 MeV electrons for the GaAs devices, whereas a value of 3000 was used for the Si devices. A comparison of observed relative damage coefficients observed by three different experimenters is shown in figure 2. This comparison lent credibility to the data from reference 3, as used in this study, as the measured data is repeatable by other experimenters [refs. 4 and 5].

The rigid panel substrate had an areal mass density of 1.5 kg/m^2 (0.3 lb/ft^2) which, when added to the cell adhesive mass, represented an equivalent fused silica shield thickness of $736 \mu\text{m}$ (29 mils). The flexible substrate and the cell adhesives represented a fused silica equivalence of $75 \mu\text{m}$ (3 mils).

On-Orbit Operating Temperature

Operating temperatures were calculated using steady state energy balance considerations. Albedo and earth emission heating were considered only for the LEO cases. The temperatures were calculated based upon their end of life cell conversion efficiencies and the solar cell absorptance values given in table 1. Geometry, temperature coefficients and method are shown in figure 3.

Cost Estimates

The array costs were based upon the unit prices given in table 3. The substrate cost, as well as the cost of the balance of the hardware, was per recent TRW hardware experience. This data is presented as relative values only to protect the underlying proprietary information.

Array Weight

Array weight was the sum of the weights for: cells, covers, cover adhesive, cell adhesive, substrates, hinges, tie down/release/deployment mechanisms, harnesses, booms.

A cover thickness was selected for each condition that would optimize the array performance in terms of area and weight. For LEO and GEO, the optimum cover turned out to be the thinnest cover possible - $75 \mu\text{m}$ (3 mil) ceria-doped glass. For MEO, the cover thickness optimized at 500 to $750 \mu\text{m}$ (20 to 30 mil) fused silica cover (cell type dependent).

The weight for the rigid panel array included all wing components outboard of the solar array drive and power transfer assembly. Boom and mechanisms were taken as 30% of the cell-covered substrate weight. Panel wiring and boom harnesses were taken as 0.3 kg/m^2 (0.0615 lb/ft^2). Substrate area and weight were based upon cell area requirements, and the packing factor ($\text{pf}=0.85$) was taken at $\sim 1100 \text{ } 2 \times 4 \text{ cm cells/m}^2$ (100 cells/ft^2).

Summary

Tables 4, 5 and 6 compare the characteristics of the array types of a graphite/epoxy structure rigid panel planar solar array as a function of cell type for three types of 10 year, 5kW end-of-life (EOL) missions.

Relative cost figures are included in the last two columns to provide an initial indication of the cost effectiveness of the cell type. Cost is included because it will always be a key factor for both NASA and military missions. In many instances cost will be equal in importance to weight, with array size considerations being of secondary importance. Only for high radiation belt orbit missions or for existing designs where array size is limited does array size begin to have an equivalent importance with weight and cost.

One key conclusion that should be drawn is that there is never one "typical" value for specific power or power density that can be used. For a given cell type it is highly dependent on the orbit because of the order-of-magnitude variation in natural space radiation and cell degradation that will occur. Except for the very high natural radiation missions (MEO), the currently available $50 \text{ }\mu\text{m}$ (2-mil) thick silicon cell provides superior EOL specific power performance relative to the currently available $300 \text{ }\mu\text{m}$ (12-mil) thick GaAs/GaAs cell at a reduced cost, even though the GaAs cell array is $1/3$ smaller in area. For LEO and GEO missions, the advanced GaAs/Ge cell must be substantially less than $200 \text{ }\mu\text{m}$ (8-mil) thick or have efficiency characteristics above 18% in order to provide better specific power performance. Even then there will be a cost penalty when using the GaAs cells. In high radiation belt orbits (MEO), GaAs cell arrays show superior specific power performance primarily because the radiation resistance of those cells relative to silicon, in conjunction with their higher BOL efficiency characteristics, permits the array size to be also half that for silicon cell arrays. Also the cost differentials are smaller.

Figures 4 and 5 plot the GEO specific power results, respectively, for rigid panel and flexible blanket arrays as a function of AM0 cell efficiency to better illustrate some key points. Included on Figure 4 are zones for the advanced technology multi-bandgap (MBG) cells that are still in the early development stages. The $200 \text{ }\mu\text{m}$ (8-mil) GaAs/Ge cell at 18% efficiency is equivalent to the $50 \text{ }\mu\text{m}$ (2-mil) silicon cell and the cost differentials are small. The $200 \text{ }\mu\text{m}$ (8-mil) GaAs/Ge cell is assumed to be the immediate successor to the $300 \text{ }\mu\text{m}$ (12-mil) GaAs/GaAs cell because of performance, cost and ruggedness. The results show that the $75 \text{ }\mu\text{m}$ (3 mil) GaAs/Ge cell is a very attractive alternative to thin silicon cells for most orbit conditions if weight is a key issue, especially if the BOL efficiency is in the 18 to 21 percent range. Because of the expected high cost for MBG cells they must be made very thin 150 to $200 \text{ }\mu\text{m}$ (6 to 8 mils), if they are going to be competitive with the thin GaAs/Ge cell.

References

- [1] Anspaugh, Downing, et al, *Solar Cell Radiation Handbook*, third edition, JPL publication 82-69, November 1, 1982
- [2] R.M. Kurland et. al., "Advanced Photovoltaic Solar Array Development," *9th Space Photovoltaic Research and Technology Conference Proceedings*, 19-21 April 1988 at NASA/LeRC, Cleveland, Ohio.
- [3] Anspaugh and Downing, *Radiation Effects in Silicon and Gallium-Arsenide Solar Cells*, JPL publication 84-61, September 1, 1984
- [4] G. Moreno et al, "Analysis of Low Energy Proton GaAs Solar Cell Degradation", *Photovoltaic Generators in Space, Proceedings of the Fifth European Symposium (ESA SP-267)*, November 1986, pp 313-316
- [5] Takata, et al, "Energy Dependence of Proton Irradiation Damage in GaAs Solar Cells and Combined Radiation on Them," *Photovoltaic Generators in Space, Proceedings of the Fifth European Symposium (ESA SP-267)*, November 1986, pp 425-432

Table 1. Cover and Cell Characteristics

Covers <ul style="list-style-type: none"> • Fused silica or CMX (thickness dependent) • Thickness orbit optimized <ul style="list-style-type: none"> — Front shielding from 3 to 60 mils — Highest EOL W/kg determined thickness • Efficiency optimized shielding not practical (too heavy) 				
Cell Types	Thickness (mil)	Efficiency at 28°C AMO (%)	Solar Absorptance	Type
Silicon*	8.0	12.3	0.75	BSR
Thin Silicon	2.6	13.5	0.72	BSR/B-BSF
Gallium-arsenide	12.0	18.0	0.78	—
GaAs/Germanium	8.0	18.0	0.78	—
Thin GaAs/Ge	3.0	18.0	0.78	—

*Cell type selected showed highest EOL efficiency at operating temperature of all production thick silicon cells available

Table 2. Space Radiation Data

Free field environments <ul style="list-style-type: none"> • GEO: AE8MAX, Pruett flare • MEO: AP8MAX, flares not significant • LEO: AP8MIN, geomagnetically shielded <p>Equivalent fluence approach and Si degradation per Reference 1</p> <p>GaAs damage coefficients and degradation per Reference 2 agree with Reference 3 and 4</p> <p>10 MeV proton in GaAs equals 1500 1 MeV electrons (Si = 3000)</p> <p>Cell substrate included in backside shielding for GaAs cells</p>
References <ol style="list-style-type: none"> 1. Solar Cell Radiation Handbook, Third edition, JPL Publications 82-69, November 1, 1982, By Anspaugh, Downing, et al. 2. Radiation Effects in Silicon and Gallium Arsenide Solar Cells, JPL publication 84-61, September 1, 1984, by Anspaugh, Downing 3. Analysis of Low Energy Proton GaAs Solar Cell Degradation, by Moreno, et al. 4. Energy Dependence of Proton Irradiation Damage in GaAs Solar Cells, by Takata, et al.

Table 3. Unit Cost Data

2 x 4 cm cells
• Silicon — \$12; thin silicon — \$36
• GaAs/GaAs — \$125
• GaAs/Ge — \$100; thin GaAs/Ge — \$100
Covers
• 2 mil CMX — \$5; 20 mil fused silica — \$10; 30 mil FS — \$15
Coverage
• 100 cells/ft ²
Attrition rates
• Varies with cell type (based on TRW production line experience)
Manufacturing, integration, and test costs based on TRW experience

Table 4. Comparative Performance, Rigid Panel Deployable Solar Array (LEO Mission, 5 kW EOL Power)

10 Year Orbit	Cell Type	Optimum Cover Thickness (mils)	EOL Specific Power (W/Kg)	EOL Power Density (W/m ²)	Array* Weight (kg)	Array** Area (m ²)	Cell Stack Material Relative Cost	Array Relative Recurring Cost
LEO 280 nmi 28.5° i	8 mil silicon	2	30	101	167	49.3	0.97	0.98
	2 mil silicon	2	38	112	133	44.7	2.31	1.30
	12 mil GaAs	2	34	170	146	29.5	5.02	1.73
	8 mil GaAs/Ge	2	40	170	124	29.5	3.73	1.42
	3 mil GaAs/Ge	2	49	170	103	29.5	3.73	1.42
η_0 = 12.3% at 28°C for 8 mil silicon cell (10 Ω -cm BSR, DAR; α_s = 0.75) η_0 = 13.5% at 28°C for 2 mil silicon cell (10 Ω -cm BSR/B-BSF; DAR; α_s = 0.72) η_0 = 18% at 28°C for all GaAs or GaAs/Ge cells (α_s = 0.78) Substrate = 10 mil graphite/epoxy facesheets and 0.75-in aluminum honeycomb core (\approx 29 mil equivalent fused silica shielding)								

*Weight includes all wing components exclusive of SADA

**Array area is total panel area for two multi-panel wings

Table 5. Comparative Performance, Rigid Panel Deployable Solar Array (MEO Mission, 5 kW EOL Power)

10 Year Orbit	Cell Type	Optimum Cover Thickness (mils)	EOL Specific Power (W/Kg)	EOL Power Density (W/m ²)	Array* Weight (kg)	Array** Area (m ²)	Cell Stack Material Relative Cost	Array Relative Recurring Cost
MEO 3500 nmi 60° i	8 mil silicon	20	11	52	440	95.3	2.42	1.76
	2 mil silicon	20	13	55	385	91.6	5.31	2.26
	12 mil GaAs	30	15	105	330	47.7	8.75	2.86
	8 mil GaAs/Ge	30	16	100	310	50.2	6.96	2.42
	3 mil GaAs/Ge	20	17	82	290	61.2	8.11	2.76
η_0 - 12.3% at 28°C for 8 mil silicon cell (10 Ω -cm BSR, DAR; α_s - 0.75) η_0 - 13.5% at 28°C for 2 mil silicon cell (10 Ω -cm BSR/B-BSF; DAR; α_s - 0.72) η_0 - 18% at 28°C for all GaAs or GaAs/Ge cells (α_s - 0.78) Substrate - 10 mil graphite/epoxy facesheets and 0.75-in aluminum honeycomb core (\approx 29 mil equivalent fused silica shielding)								

*Weight includes all wing components exclusive of SADA

**Array area is total panel area for two multi-panel wings

Table 6. Comparative Performance, Rigid Panel Deployable Solar Array (GEO Mission, 5 kW EOL Power)

10 Year Orbit	Cell Type	Optimum Cover Thickness (mils)	EOL Specific Power (W/Kg)	EOL Power Density (W/m ²)	Array* Weight (kg)	Array** Area (m ²)	Cell Stack Material Relative Cost	Array Relative Recurring Cost
GEO	8 mil silicon	2	29	98	173	51.0	1.00	1.00
	2 mil silicon	2	37	110	135	45.4	2.40	1.33
	12 mil GaAs	2	32	159	156	31.5	5.37	1.83
	8 mil GaAs/Ge	2	37	158	134	31.6	4.00	1.50
	3 mil GaAs/Ge	2	45	158	112	31.6	4.00	1.50
η_0 - 12.3% at 28°C for 8 mil silicon cell (10 Ω -cm BSR, DAR; α_s - 0.78) η_0 - 13.5% at 28°C for 2 mil silicon cell (10 Ω -cm BSR/B-BSF; DAR; α_s - 0.72) η_0 - 18% at 28°C for all GaAs or GaAs/Ge cells (α_s - 0.78) Substrate - 10 mil graphite/epoxy facesheets and 0.75-in aluminum honeycomb core (\approx 29 mil equivalent fused silica shielding)								

*Weight includes all wing components exclusive of SADA

**Array area is total panel area for two multi-panel wings

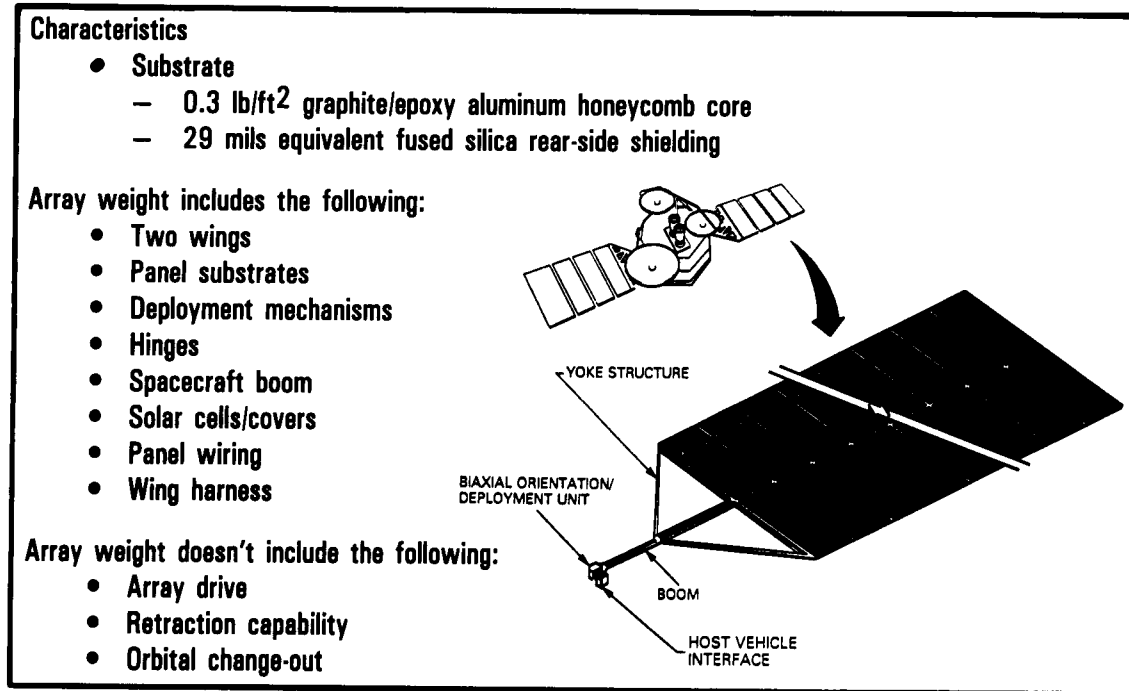


Figure 1. Solar Array Configuration

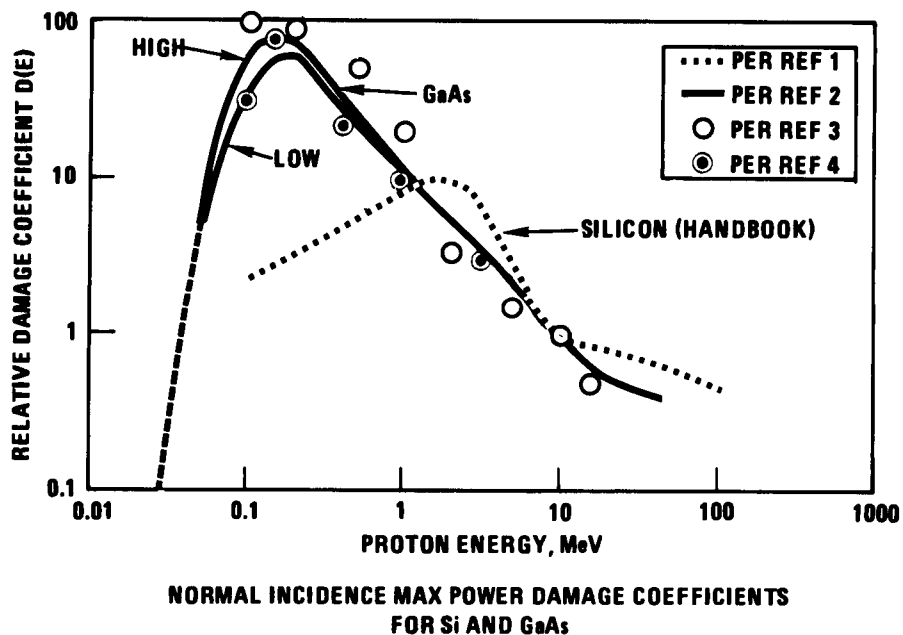


Figure 2. Solar Cell Damage Coefficients

Steady state energy balance model

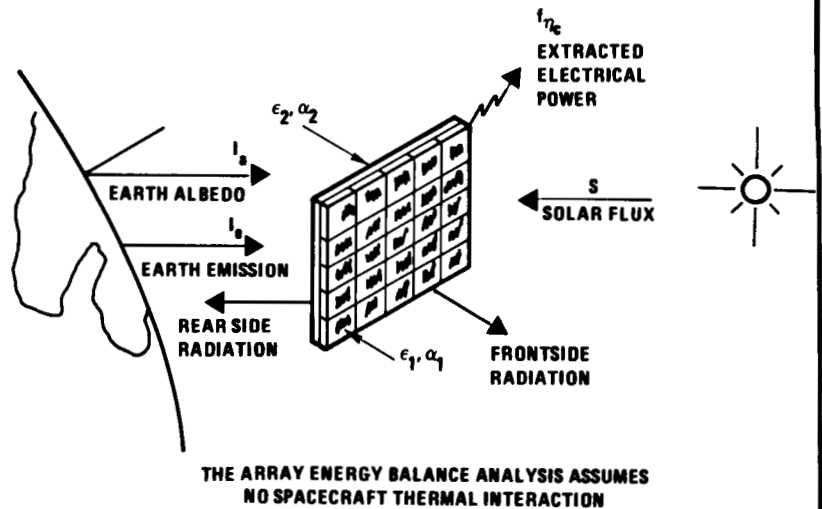
Albedo and earth emission for LEO only

End-of-life cell efficiency used

Cell absorptance varies with cell type

Temperature coefficients

- Si = -0.0045%/°C
- GaAs = -0.002%/°C



$$T_c = \frac{S(\alpha_1 - f\eta_c) + (I_a\epsilon_2 + I_e\alpha_2)^{1/4}}{\sigma(F_1\epsilon_1 + F_2\epsilon_2)}$$

Figure 3. Solar Array On-Orbit Operating Temperature Model

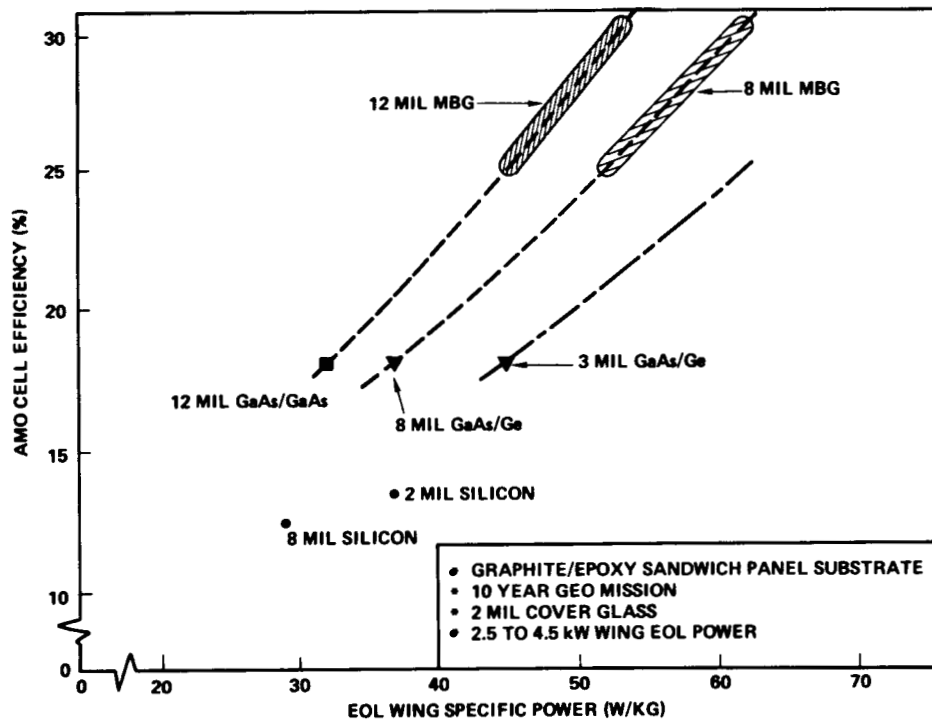


Figure 4. Cell Type Versus Wing Specific Power, Rigid Panel Deployable Solar Array

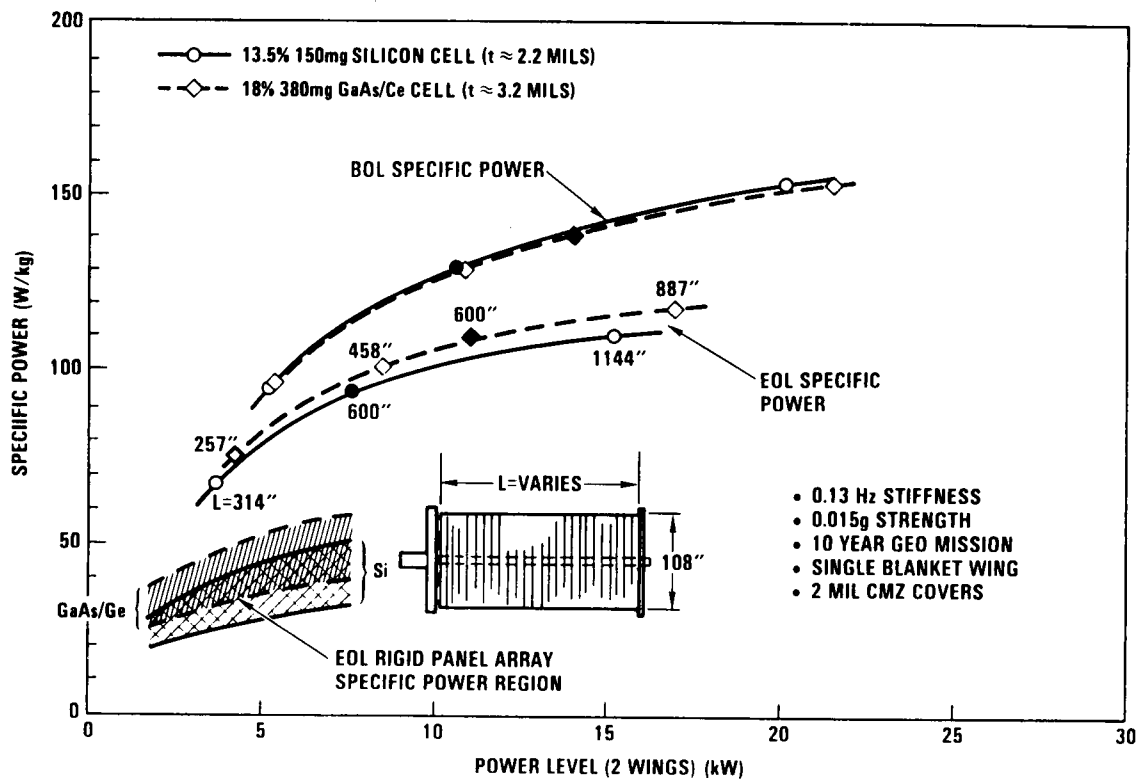


Figure 5. Effect of Power Level on Specific Power Performance for APSA Flexible Blanket Array (Thin Silicon Versus Thin GaAs/Ge Cells)

Advanced Photovoltaic Solar Array Development*

Richard M. Kurland
TRW Space & Technology Group
Redondo Beach, California 90278

Paul Stella
Jet Propulsion Laboratory
California Institute of Technology
Pasadena, California 91109

Summary

The Jet Propulsion Laboratory (JPL), under sponsorship from the NASA Office of Aeronautics and Space Technology (OAST), has pursued the development of high performance solar array component technology for more than a decade in anticipation of the eventual need by the year 2000 for an array with a specific power of 300 W/kg at beginning-of-life (BOL) at a power level of 25 kW (BOL). In 1985, the Advanced Photovoltaic Solar Array (APSA) program was initiated to combine the separate advanced array component efforts and demonstrate a producible array system by the end of this decade. JPL selected >130 W/kg (BOL) at a 10 kW (BOL) array power level as an intermediate near-term milestone specific power goal, which would provide a cost- and weight-effective alternative to radioisotope thermoelectric generators for interplanetary missions and also meet the needs of a wide range of near-earth military, scientific, and commercial missions. Phase I of the APSA program was completed in 1986 with preliminary design of an ultralightweight, flatpack fold-out flexible blanket wing that met all the critical electrical and mechanical performance goals using existing and near-term technology. The design represents a factor-of-two improvement in the 66 W/kg (BOL) SAFE I flexible-blanket wing developed by NASA-OAST and flight-demonstrated in 1984 on STS-41D. It also represents a three-fold improvement in the specific power performance of current rigid-panel planar arrays. Phase II of the APSA program, started in mid-1987, is currently in progress to fabricate prototype wing hardware that will lead to wing integration and testing in 1989. This paper reviews the design configuration and key details, provides a status of prototype hardware fabricated to date, discusses results from key component-level tests, and shows revised estimates of array-level performance as a function of solar cell device technology for geosynchronous missions.

Program Definition

Figure 1 presents the overall development schedule for the current APSA program, whose goal is to demonstrate a prototype wing with a projected specific power performance of >130 W/kg (BOL). Phase I, completed in 1986, led to the selection of a preferred design concept and a contractor to

*This paper presents the results of one phase of the Advanced Photovoltaic Solar Array program carried out by TRW Space & Technology Group for the Jet Propulsion Laboratory (JPL), California Institute of Technology, under JPL Contract 957990, sponsored by NASA/OAST (NAS7-918). Primary units for measurements and calculations are in the English System.

design, fabricate, and test a prototype wing. During Phase II, the prototype wing is being designed and fabricated. Because of fiscal constraints, this phase was broken into two parts. The first part, ending in August 1988, includes the detail design for the complete prototype wing and fabrication of two of the three major subassemblies: 1) an 8-panel flexible blanket assembly covered with live and mass-simulated solar cells; and 2) the blanket deployment system. The second part of Phase II will result in fabrication of the blanket housing assembly and integration and functional checkout testing of the prototype wing. This latter part of Phase II has yet to be funded, but is anticipated to start August 1988. An option being considered after initial functional checkout of the 8-panel wing system is to modify the blanket assembly by adding more panels to increase the wing's length by 50 percent. Phase III of the program will include ground verification testing of the prototype wing after exposure to launch and orbital environmental conditions.

Design Description

Configuration

Figure 2 illustrates the generic wing design that resulted from the Phase I trade study [ref. 1]. The overall wing geometry is similar to the NASA Solar Array Flight Experiment (SAFE I) wing [ref. 2] and the European Olympus Wing [ref. 3] designs. The wing consists of a flatfold, multiple panel, flexible-blanket assembly on which solar cell modules are installed and connected to electrical harnesses that run along the outside longitudinal edges of the blanket assembly. When stowed, the accordion-folded blanket assembly is sandwiched between two graphite/epoxy facesheet sandwich plate structures (lid and pallet structures) with a polyimide foam layer on the inner surfaces to cushion the folded blanket during launch. There is no interleaving cushioning material between the folded panels. Solar cells are in direct contact when the blanket is folded and stowed under a preload pressure of 7000 Pa (~ 1 psi) from a torque tube, motor-actuated, multiple latch/release mechanism that is integrated to the lid/pallet structures. The blanket housing assembly is rigidly attached to the blanket deployment mast system through a series of struts and interface fittings with no secondary articulation between the blanket housing structure and the mast system.

The blanket assembly is deployed (unfolded) by extension of a motor-actuated, fiberglass, continuous trilateron lattice mast that uncoils from an aluminum cylindrical canister structure. During blanket unfolding and deployment, the blanket assembly is supported by two tensioned guidewire systems attached to the rear foldlines of the blanket to prevent any large out-of-plane excursions. When fully deployed, the blanket assembly is tensioned in the longitudinal direction by a series of constant-force springs at the inboard end of the blanket attached to the pallet structure. The design goals for APSA did not require the array to be self-retractable. Therefore, the presently designed wing is only self-deployable. Self-retraction could be achieved by redesign of the blanket assembly hingelines.

Figures 3 and 4 illustrate the deployed and stowed size for the baseline 5.3 kW (BOL) wing as the result of the Phase IIA prototype detail design study. Two wings of this configuration integrated to opposite sides of a spacecraft provide 10.6 kW (BOL) and 7.6 kW (EOL) power after 10 years in geosynchronous orbit (GEO). Overall deployed wing dimensions are 16.3-m (642-in.) long (measured

from the inboard end of the mast canister at the spacecraft interface to the lid) by 2.8-m (110-in.) wide with a blanket size of 15.3 by 2.7 m (600 by 108-in.).

Blanket Assembly

The basic blanket substrate material is carbon-loaded Kapton polyimide film 50- μm (2-mils) thick (commercially available from DuPont under the name XC10¹⁰, which refers to the surface resistivity of the material). The resistivity of the material is sufficiently low to permit grounding of the blanket substrate to prevent electrostatic charge buildup from GEO substorm environments, but sufficiently high to prevent shorting of the solar cell strings.

The 5.3-kW (BOL) blanket is accordion folded into 42 panels, 39 of which are covered with solar cell modules. The blanket consists of 13 three-panel solar panel assemblies (SPA) and two blank leader assemblies (one leader consists of one panel; the other has two panels). Figure 5 illustrates details of the SPA. Nominal panel size is 2.5 \times 0.36 m (99.4 \times 14.3 in.), exclusive of 0.12-m (4.6-in.) wide extensions bonded along each longitudinal edge where the electrical harness runs are installed. The inter-SPA hingelines are unreinforced heat-set crease folds in the Kapton material. Each SPA is linked to the next SPA through a piano hinge constructed along each outer lateral edge of the SPA. The hinge pin is a pultruded graphite/epoxy rod 1.3 mm (50 mils) in diameter.

Blanket Housing Assembly

Except for localized details, the blanket housing lid pallet structures are identical in size and construction. Nominal panel size is 0.44 \times 2.8 m (17.3 \times 110.4 in.). The panels are constructed from 250 μm (10-mil) high-modulus P100 graphite/epoxy facesheets bonded to an aluminum honeycomb core 13-mm (0.50-in.) thick. In local areas to react concentrated loads, the facesheets are reinforced with additional plies of material and the core is filled with low-density syntactic foam. Attached to the inside surface of the lid and pallet panels is a flexible polyimide foam layer, 13-mm (0.5-in.) thick, encased in a thin polyvinylfluoride sheet.

Figures 6 and 7 illustrate the motor-actuated torque tube mechanism used to simultaneously release the latches that secure the lid to the pallet structure before deployment of the blanket assembly. The lid is clamped to the pallet structure with braided steel cables at four locations along the length of the housing structure. Each cable is attached to the lid structure and has small end-loops that engage hook latches located on the edges of the pallet structure. The hook latches are locked in place by small graphite/epoxy pushrod struts that are connected to an overcenter crank on a central graphite/epoxy torque tube.

The guidewire systems attached to the rear foldlines of the blanket assembly are each tensioned to 5 N (1 lb). Deployed wing dynamics and strength analyses indicate that a total blanket tension force of 68 N (14 lb), in conjunction with the stiffness of the mast and the 0.15-m (6-in.) clearance between the mast surface and the blanket plane, ensures acceptable deployed wing dynamic characteristics and prevents the blanket from "slapping" the mast structure when subjected to 0.01-g inertial loads.

Blanket Deployment System

Figure 8 illustrates the mast system. It is a canister-deployed continuous longeron lattice mast similar in configuration to that used on the SAFE I and Olympus solar array wings. A major development under the APSA program was to weight-optimize the design of the mast system, especially the canister structure and deployment mechanism. The mast system was sized to meet 0.10 Hz and 0.01 g wing stiffness/strength requirements. The 0.21-m (8.2-in.) diameter mast is constructed from fiberglass (longerons and battens) except for the stainless steel braided cable diagonals. The stowage canister is aluminum.

Solar Cell Module

Each cell-covered panel contains eight rows of 2×4 cm cells with each row containing 120 cells (fig. 9). There are 37,440 cells per blanket assembly. The solar cell stack consists of: (a) 50- μ m (2-mils) thick ceria-doped coverglass coated on the front surface with a UV-rejection filter and an enhanced emittance filter to reduce the operating temperature of the cell; (b) 55- μ m (2.2-mil) thick 10 Ω -cm boron-doped back surface field, aluminum back surface reflector, polished silicon solar cell ($\eta_0 = 13.5$ percent at 28°C AM0); (c) two inplane stress relief loop silver plated Invar interconnectors soldered to the solar cell in a front/back fashion; and (d) DC93500 silicone adhesive bondlines to attach the coverglass to the solar cell and the solar cell stack to the carbon-loaded Kapton substrate. Operating temperature of the solar cell ranges from 27°C (BOL) to 32°C (EOL). Panel packing factor for cell installation is 0.84 (~ 1100 cells per m^2) exclusive of the electrical harness regions.

The three-panel SPA circuit configuration is illustrated in figure 10 and its features are summarized in table 1. Cells and electrical circuits are arranged on the SPA to create mirror-imaged geometry with respect to the longitudinal centerline of the SPA to minimize current-induced magnetic field effects. Cell rows are arranged in a serpentine manner so string turnaround occurs at the center and the string returns to the outer edge of the panel. An electrical circuit module consists of a single parallel cell by 360 cells in series to obtain a nominal voltage of 150V (EOL). An SPA contains eight circuits, four each on the left- and right-hand sides of the SPA. A 5.3-kW (BOL) blanket assembly contains 104 circuits (13 SPAs). All positive and negative terminations for each circuit occur along the outside edge of the SPA adjacent to the printed circuit harness segment that is bonded to the 0.12-m (4.6-in.) extensions of the basic blanket substrate. All electrical connections in the series circuit as well as between the circuit and harness are soldered.

Electrical Harness

Electrical power is collected via flexible printed-circuit Kapton-insulated copper harnesses. The harness runs from the outboard leader panel to a diode box on the underside of the pallet structure. The harness is bonded to the cell side of the blanket to permit direct access to the solar cell circuit terminations located along the outer edge of the main substrate. Because the blanket is assembled from a number of discrete SPAs and leader panels, the harness is segmented to conform to the individual SPAs. At each piano hingeline, the adjacent end of each harness segment is brought together to form a "cusp"-shaped fold and is soldered together. In between these locations where the blanket panels are crease-folded to form a hingeline, the harness segment is designed with sufficient length to permit a "cusp" fold in the segment.

The series orientation of adjacent cell circuits on the panels are alternated (clockwise, counter-clockwise, etc.) such that the positive terminations for adjacent circuits are located next to one another, as are the negative terminations. There are individual positive copper traces in the harness for each circuit; however, each adjacent pair of circuit negative terminations are bused together on a common trace. A grounding turnout for each panel is connected to a convenient available negative trace.

The copper traces are sized to carry at least 0.3 A (positive traces) and 0.6 A (negative traces) with a net harness voltage drop of about 2 percent (~ 3.2 V). The copper traces are 2-oz copper 0.64-mm (25-mils) wide by 68- μ m (2.7-mils) thick with 0.5-mm (20-mils) spacing between the traces. In order to minimize the number of unique harness trace patterns for each harness segment, one trace pattern is used for every cell-covered SPA segment (thereby reducing cost and potential confusion). Also, the negative traces are tied together to help reduce the net harness drop. Figure 11 illustrates the trace and end details of a typical SPA harness segment.

Circuit Protection

The adopted approach is to use single, nonredundant isolation diodes between each string and the spacecraft common bus. The diodes are colocated in a small box that is attached to the underside of the pallet structure at the inboard end of each harness run. The box serves as the transition point between the flexible printed circuit blanket harness and a stranded round wire transition harness leading to the spacecraft.

The use of bypass diodes was not evaluated since: (a) there were no shadowing requirements; (b) the selection of single-cell parallel circuits alleviated the need to protect the circuits against "hot spot" failure propagation when a single-cell module fails, and (c) vibration tests on a stowed blanket segment suggest that circuit integrity can be maintained with single-cell parallel circuits. Should the need arise to design for shadowing, or subsequent reliability analyses or test results indicate that circuits with multiple parallel cells are warranted, then flat packaged diodes can be easily added to the panel in the 19-mm (0.75-in.) wide zone adjacent to the hingelines. An example of this paralleling would be to change the layout of a single panel to four rows of cells in parallel running side-by-side with cross-straps across each 10 cells in series to create a circuit module. The four-row circuit would turn around at the centerline of the panel and return to the same panel edge for a total of $4p \times 120s$. Connecting three panels in series would create an SPA with two circuits per three panels with each 150-V (EOL) circuit having $4p \times 360s$ cells.

Array Performance Estimates

Table 2 presents a weight summary for the APSA wing. The weights shown for the blanket assembly and blanket deployment assembly are derived from weights of prototype hardware elements and subassemblies; weight of the blanket housing assembly is derived from mass properties analysis of detail prototype hardware drawings. Since the Phase I Conceptual Design Study, the weight has increased about 5 percent, primarily in the blanket housing assembly components and from using 150-mg cells instead of 130-mg cells. The weight for the blanket assembly accounts for about 50 percent of the total. The electrical components (cell stack, wiring, electrical harness, diode box) represent about 45 percent of the total. Trade studies during Phase I showed that wing aspect ratio (blanket length divided by blanket width) is not a major factor on overall wing weight and specific

power performance. The flatness of the curves for wing weight versus aspect ratio (over an aspect ratio range from 2 to 10) suggests that the wing width should be as wide as possible consistent with stowage constraints, interference issues relative to other deployed appendages or sensor fields-of-view, and manufacturing/handling limitations.

Table 3 summarizes the predicted performance in comparison to the original program goals. The changes in performance are indicated between the Phase I conceptual design and the present estimates based on updated design drawings, revised analyses, and actual hardware fabrication. Essentially, all design goals have been met. The 10.6 kW (BOL) array has a 10-year GEO EOL power output of 7.6 kW. Including a 10 percent contingency for weight and power output uncertainties, the BOL specific power and power density (based on total panel area) are 132 W/kg and 136 W/m², respectively. Corresponding EOL values are 95 W/kg and 97 W/m².

Figure 12 shows the impact of power level on specific power performance for two cell types: (a) the thin silicon cell, and (b) the thin gallium arsenide on germanium cell (GaAs/Ge). Power growth (or reduction) is achieved by adding (or moving) SPAs from the blanket assembly, with appropriate redesign of the electrical harness and resizing of the mast system. The blanket housing assembly would remain virtually unchanged. At higher power levels with comparable deployed stiffness and strength, the specific power performance improves. Even at low power levels, the specific performance is two-to-three times higher than for rigid panel arrays. The figure also shows that advanced planar cells such as GaAs/Ge must be thin ($\sim 0.80\text{ }\mu\text{m}$ or 3 mils) and have conversion efficiencies above 18 percent to provide specific power performance comparative to that using thin silicon cells, even though the wing length is reduced about 25 percent. This is because advanced cells such as GaAs/Ge (or InP) are made from substantially denser materials than silicon.

Figure 13 depicts the impact of cell efficiency and cell technology on array specific power, both for thin discrete cells and for "thin-film" devices. Trend lines are shown for the "thin-film" devices with and without the need for a 50- μm (2-mil) coverglass. The upper lefthand corner of the figure illustrates that thin advanced discrete cells such as GaAs/Ge will only provide a 25-to-35 percent improvement in specific power performance. The lower righthand region of the figure shows the potential impact for the "thin-film" devices assuming they can be shown to have good stability against the natural radiation environment. EOL specific power of 200 to 250 W/kg may be achievable with the prospect of significant array cost reduction and the potential for even lighter-weight deployment concepts and greater packaging efficiency. Although not envisioned as a near-term item, these thin-film devices exhibit the potential for dramatically opening up new photovoltaic solar power space applications at performance levels approaching the far-term APSA goal of 300 W/kg (BOL)

Current Program Status

Prototype Wing Development

Figure 14 shows the configuration of the prototype wing that is now under construction. Its design is based on the 5.3 kW (BOL) wing described in the previous sections. The prototype is identical to the full-power wing except in four respects: (a) it is truncated in length, consisting of a blanket assembly with two 3-panel SPAs and two 1-panel leader panels; (b) the live solar cell modules are mechanical representations of flight-quality cells/covers (the covers are uncoated ceria-doped glass rather than being coated and the cells are electrically active, but do not possess high

electrical performance characteristics); (c) construction is being done to standards consistent with the prototype nature of the hardware rather than to flight-quality standards; and (d) the electromechanical actuators to activate the blanket housing preload/release mechanism and for deploying the mast are not flight-qualified.

The SPAs are covered with 1440 2×4 cm live thin silicon solar cell modules interconnected together to obtain a series of high voltage circuits ranging from 50 V (120 cells in series) to 150 V (360 cells in series), with the rest of the SPA area covered with mass-simulated aluminum chips. Along both edges of the 8-panel blanket assembly are installed flexible printed circuit harnesses running from the outboard leader panel to diode boxes on the pallet structure. The solar cell circuits tie into the electrical harness on one edge of the blanket. The mast system is full scale in terms of the canister system, but with a truncated length of mast (4.5m or 15 ft instead of 15.3 m or 50 ft). The blanket housing assembly is full scale with representative mechanisms for preload and release of the stowed blanket.

The design of prototype wing hardware is completed with the release of engineering drawings to manufacturing for construction of the blanket assembly and deployment mast system. Fabrication of the blanket housing assembly and wing integration are deferred to Phase IIB of the program. Fabrication of the blanket assembly substrate is completed as well as the electrical harness segments. The electrical harness segments have been installed and the live and mass-simulated cell modules are presently being installed. The harness segments were fabricated by MINCO of Minneapolis, MN. Thin silicon cells were obtained from all three major domestic suppliers (Solarex, Spectrolab, ASEC). The cells are divided into three weight groups (130, 150, and 170 mg) to evaluate which will be the minimum weight cell that is mechanically compatible with installation on a flexible blanket substrate when subjected to handling and launch loadings and deployment movements. This weight range can have a 4 percent swing on wing weight and specific power. Coverglass (CMZ and CMZDG) was obtained from Pilkington in England. The measured weight of the blanket assembly was very close to that predicted from mass properties analysis of engineering drawings and weighing of constituent elements.

Work is nearing completion on the fabrication and assembly of the mast structure and canister system. The hardware was designed and built by AEC-Able Engineering, Goleta, CA. The as-manufactured weight is very close to that estimated from analysis of engineering drawings. Strengths and stiffness tests on the mast are planned in the near future as are functional deployment/retraction and system-level strength/ stiffness tests when the mast-canister hardware is fully integrated.

Component Tests

To support the prototype design development, two component-level tests were conducted to obtain data on the performance of key aspects of the design: (a) load-relaxation tests on the polyimide foam material used to cushion the stowed blanket assembly; and (b) vibration tests on stowed cell-covered SPA sections to evaluate the effectiveness of the stowed blanket protection scheme to prevent unacceptable damage to the solar cell modules.

The results from the load-relaxation tests indicate that after long-term storage (6 months to 1 year under 7000 to 14000 Pa [~ 1 to 2 psi] of initial preload stowage pressure), at least 70 to 75 percent of the initial preload pressure would remain. This fact, coupled with the stowed vibration component test results, indicates that the TA301 polyimide foam would be acceptable for use as launch protection for the stowed folded blanket assembly.

A series of 21 stowed vibration tests were completed on an 8-panel, 0.3-m (12-in.) wide section of the prototype blanket assembly containing 348 glassed, interconnected thin silicon solar cells (from Solarex) and 228 mass-simulated aluminum chips. One panel was filled with "light" (~130 mg) cells glassed with 50- μ m (2-mil) thick CMX and CMZ ceria-doped glass covers. On the opposing panel, "heavy" (~170 mg) cells were placed with CMX and CMZ covers. The other two central panels were covered with "medium" weight (~150 mg) cells with CMX and CMZ covers. The remaining SPA panels were covered with mass-simulated aluminum chips. Prior to the first series of stowed vibration tests, visual and infrared camera inspection revealed about 10 percent of the total covers were cracked and about 5 percent of the total cells were cracked, with the predominance of damage to the CMX covers and 130- to 150-mg cells. After a series of 15 one-minute duration vibration tests in multiple axes ranging from 10 to 30 gs (rms) (representative of simulated shuttle vibroacoustic launch environments) at a nominal stowage pressure of 7000 Pa (~ 1 psi), an additional 14 percent of the covers had cracked and an additional 3 percent of the cells had cracked. Under a subsequent series of 6 stowed one-minute duration vibration tests in multiple axes ranging from 20 to 30 gs (rms) at a nominal stowage pressure of 3500 Pa (~0.5 psi), an additional 3 percent of the covers cracked with no additional cell damage. Cover damage was primarily in the CMX material, implying that the CMZ material is more crack resistant and should be the baseline coverglass material. More damage occurred to the 130 mg cells than to the 150 or 170 mg cells. The difference in percentage damage between the 150 and 170 mg cells was small; hence, 150 mg cells were selected as the baseline cell for the prototype wing. In no instance did any damage to the cells result in open circuits. Examination of the cell/cover damage also revealed: (a) once a cell cracked, no new cracks developed or existing cracks propagated in the cell; (b) in only a few instances did the cover and cell crack in the same cell stack; and (c) in only a few instances did a crack occur both in the cover and cell of a cell stack during the same test.

References

- [1] R. M. Kurland et al, "Advanced Photovoltaic Solar Array Design," *22nd IECEC Conference Proceedings*, vol I, Aug. 1987, pp. 103-114.
- [2] *Solar Array Flight Experiment (SAFE I) Final Report*, LMSC Document F087173, Apr. 1986.
- [3] L. Gerlach et al, "The Design of the L-Sat (Olympus) Solar Array," *3rd European Symposium on Photovoltaic Generators in Space Proceedings*, May, 1982, p. 241.

Table 1. Electrical Circuit Design Features

DESIGN FEATURES	DESIGN RATIONALE
8 x 120 CELLS PER PANEL = 960 CELLS	MAXIMIZE PACKING FACTOR INTEGER NUMBER FOR CIRCUITS
2 x 4 cm, 55 μ m (2.2-mil) CELLS; 50 μ m (2-mil) COVERS	MINIMIZE CELL STACK WEIGHT MAXIMIZE SIZE FOR THIN CELLS
360 CELLS IN SERIES	PROVIDE 176 V (BOL) AND 147 V (EOL)
8 ELECTRICAL CIRCUIT MODULES FOR EVERY 3 PANELS	DRIVEN BY NUMBER OF CELLS PER CIRCUIT
104 ELECTRICAL CIRCUIT MODULES PER BLANKET	DRIVEN BY WING NOMINAL POWER REQUIREMENT
LAYOUT CANCELS CURRENT-INDUCED MAGNETIC FIELDS	MINIMIZE EFFECTS ON EXPERIMENT PACKAGES AND ATTITUDE CONTROL

Table 2. 5.3 kW (BOL) Wing Weight Summary (BOL/EOL Power = 5.3/3.8 kW, $F_n = 0.12$ Hz, $N = 0.015$ g)

ITEM	WEIGHT, kg (lb)
BLANKET ASSEMBLY	18.23 (40.23)
SUBSTRATE COMPONENTS	3.43 (7.56)
SOLAR CELLS (150 mg/CELL) (37,440 CELLS)	5.61 (12.37)
COVERS (106 mg/COVER) (37,440 COVERS)	3.96 (8.74)
CELL STACK ADHESIVE	2.76 (6.09)
INTERCONNECTORS (TWO PER CELL)	0.41 (0.92)
ELECTRICAL HARNESS (TWO RUNS)	2.06 (4.55)
BLANKET HOUSING ASSEMBLY	11.65 (25.73)
LID AND PALLET STRUCTURE (GRAPHITE/EPOXY)	5.46 (12.05)
BLANKET PROTECTION FOAM	0.54 (1.19)
PRELOAD/RELEASE MECHANISM	2.41 (5.32)
BLANKET TENSION SYSTEM (SEVEN UNITS)	0.09 (0.20)
GUIDEWIRE SYSTEM (TWO UNITS)	0.88 (1.94)
DIODE BOX ASSEMBLY (TWO UNITS)	1.44 (3.18)
INTEGRATION HARDWARE	0.83 (1.85)
BLANKET DEPLOYMENT ASSEMBLY	6.64 (14.64)
LATTICE MAST (FIBERGLASS)	3.23 (7.12)
CANISTER (ALUMINUM)	2.29 (5.06)
ACTUATOR (ELECTRICALLY REDUNDANT)	1.12 (2.46)
	36.52 (80.60)
CONTINGENCY (10%)	3.65 (8.06)
	40.17* (88.66)

*WAS 38.2 kg AT PHASE I

Table 3. Solar Array Performance Summary, 10-Year Geosynchronous Mission

Parameter	1986 Goal (C/N 957358)	Phase I 1986 Estimate (C/N 957358)	Phase IIA 1988 Estimate (C/N 957990)
BOL power (GEO)	10 kW (2 wings)	10.4 kW	10.6 kW
EOL power (GEO)	Not specified; 8 kW implied by EOL specific power goal	7.4 kW	7.6 kW
BOL specific power at equinox	>130 W/Kg	136.1 W/Kg*	131.5 W/Kg*
EOL specific power at equinox	>105 W/Kg	96.7 W/Kg*	94.5 W/Kg*
EOL power density at equinox	>110 W/M ² ; reference area not specified	94.6 W/M ² **	97.4 W/M ² **
BOL D.C. voltage	<200 volts	210 volts	214 volts
Wing weight	Not specified	38.2 Kg*	40.2 Kg*
Deployed frequency	>0.01 Hz; 0.1 Hz preferred	0.10 Hz	0.14 Hz (bending) 0.12 Hz (torsion)
Deployed stiffness	>0.001 g; 0.01 g preferred	0.015 g	0.015 g

*Includes 10 percent weight contingency

**Based on total panel area with harness

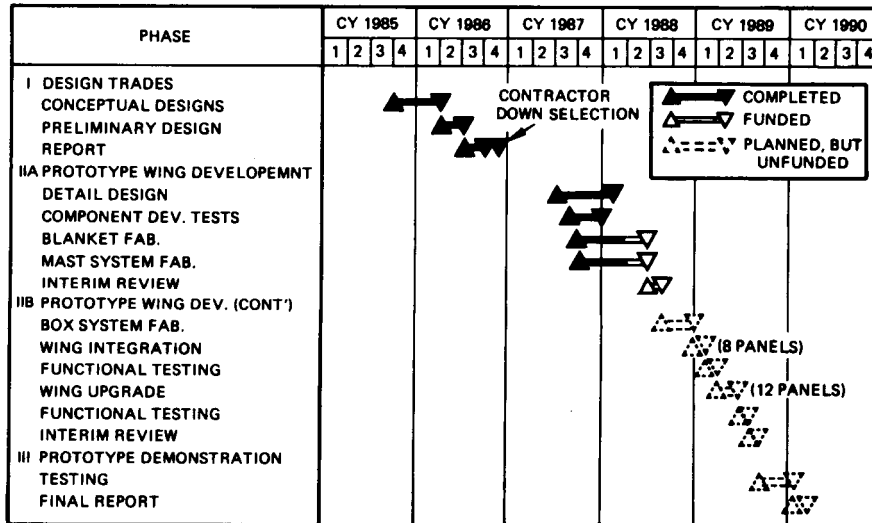


Figure 1. Development Schedule

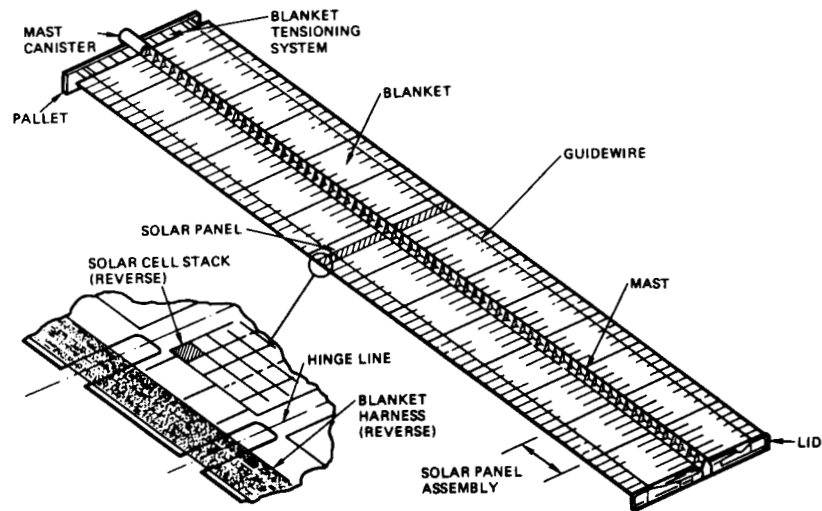


Figure 2. Generic Wing Configuration (Rear Side Shown)

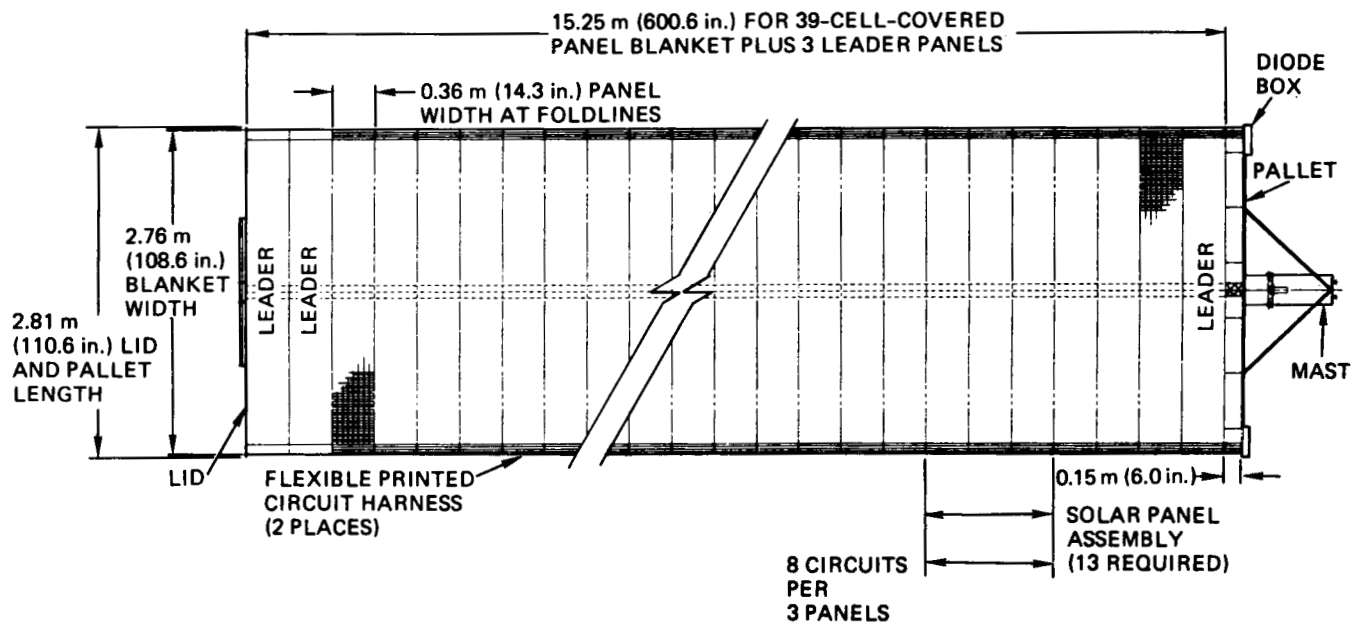


Figure 3. 5.3 kW (BOL) GEO Deployed Wing Configuration

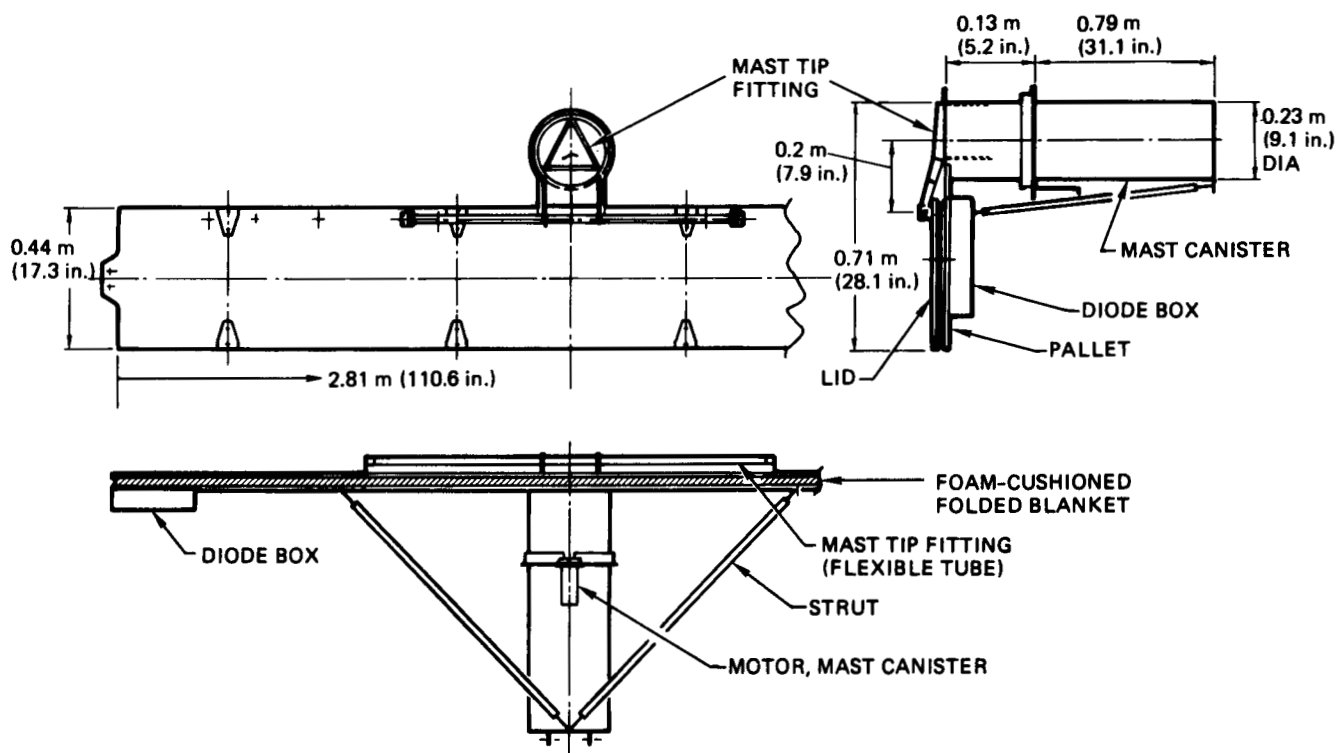


Figure 4. 5.3 kW (BOL) GEO Stowed Wing Configuration

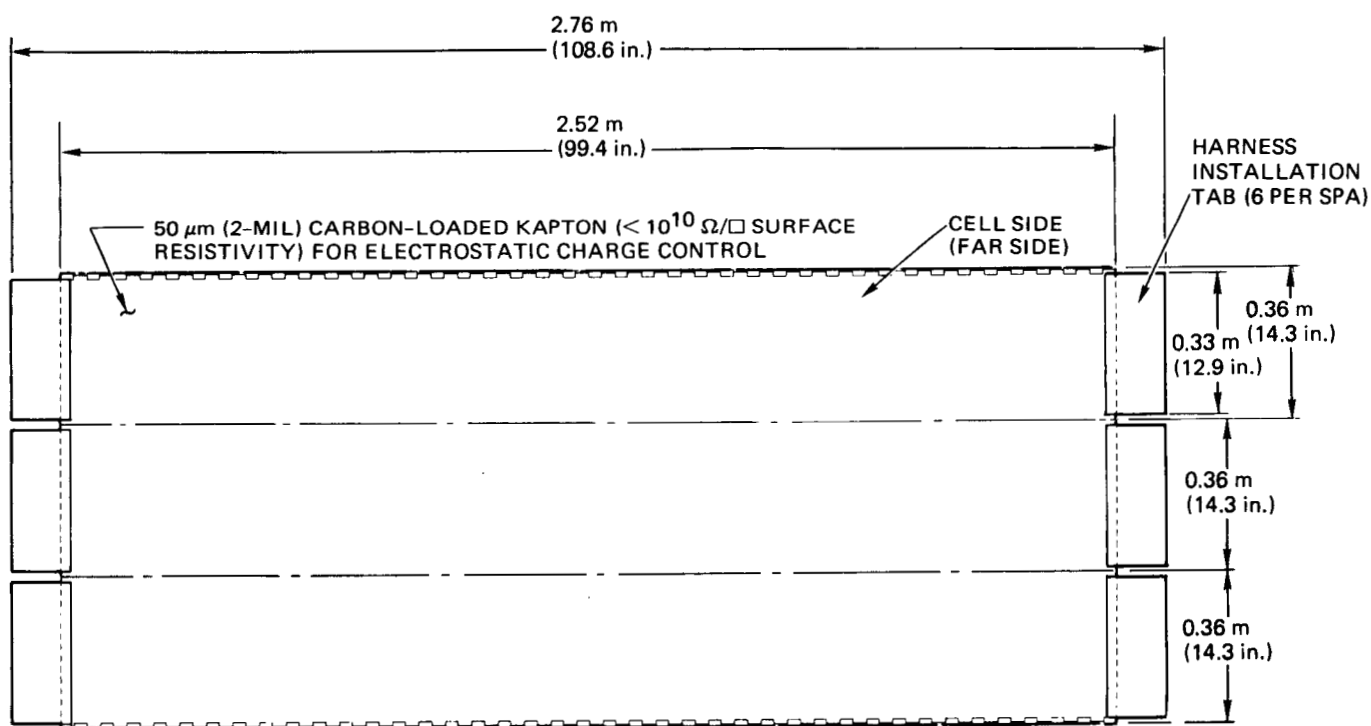


Figure 5. Solar Panel Assembly (SPA) Substrate

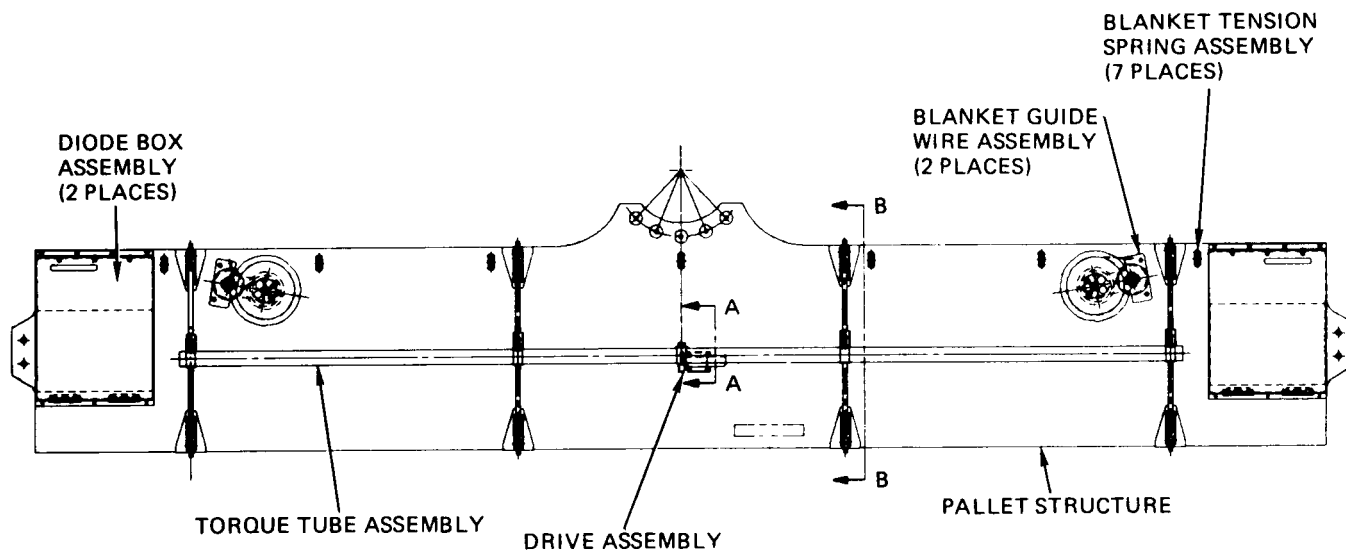


Figure 6. Stowed Blanket Preload/Release Mechanism

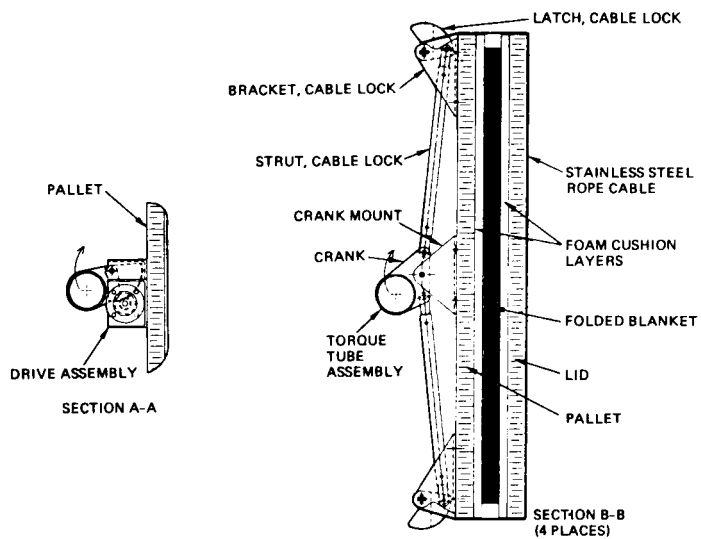


Figure 7. Stowed Blanket Preload/Release Mechanism (Cross-Sectional View)

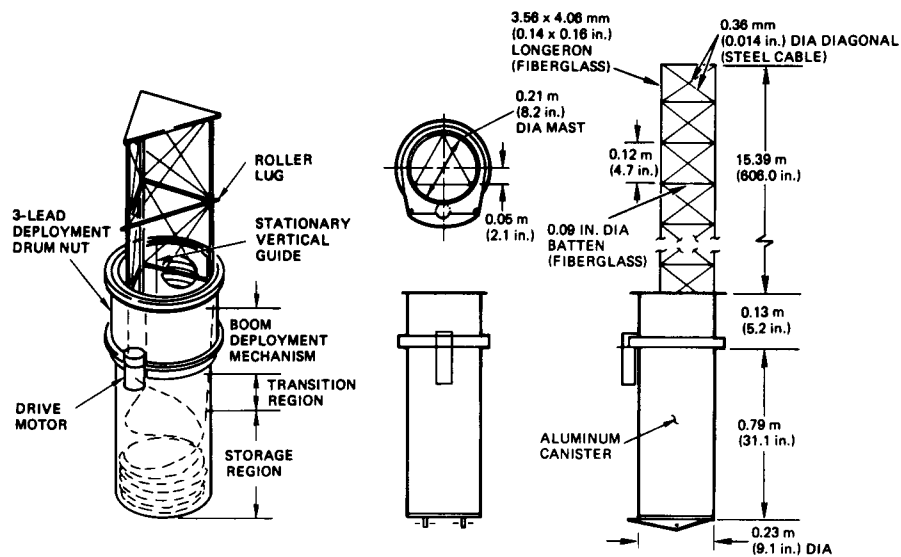


Figure 8. Wing Deployment Mast System (Canister Deployed Continuous Longeron Lattice Mast)

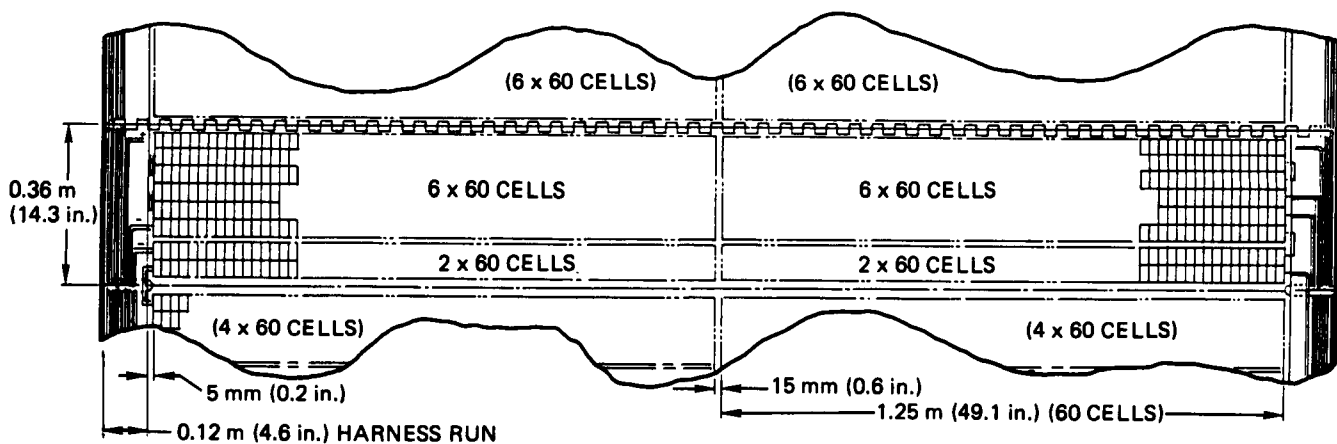


Figure 9. Typical Solar Panel Showing Layout of Solar Cell Modules and Electrical Harness

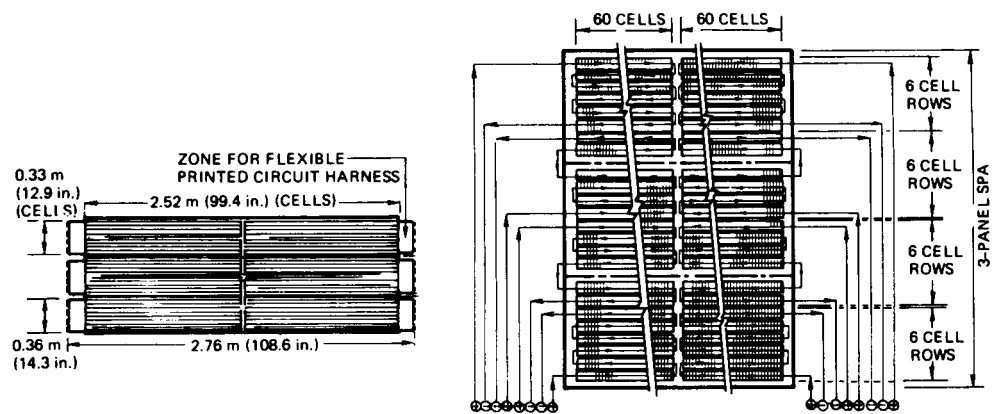


Figure 10. Schematic of Solar Cell Panel Assembly (SPA) Circuitry

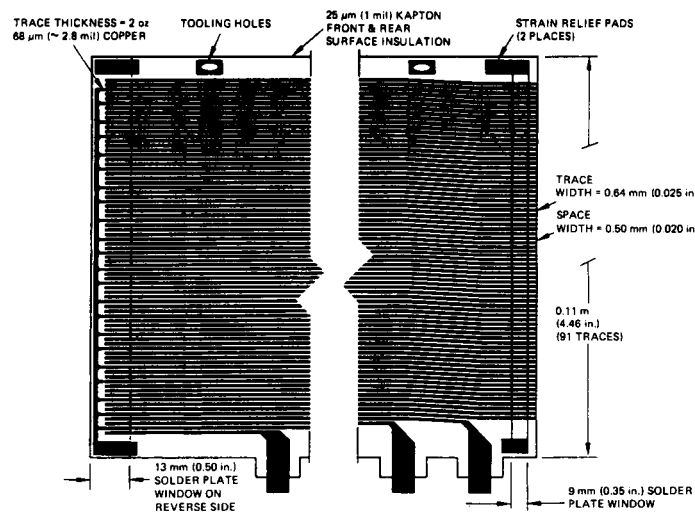


Figure 11. SPA Electrical Harness Segment End Detail

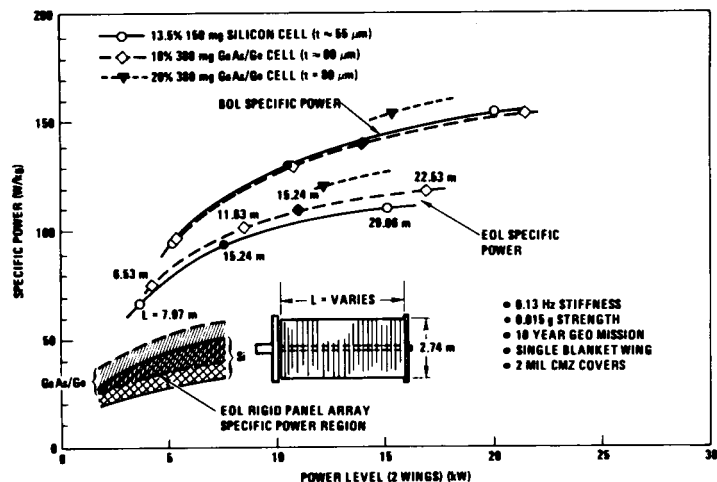


Figure 12. Effect of Power Level on Specific Power Performance (Thin Silicon Versus Thin GaAs/Ge Cells)

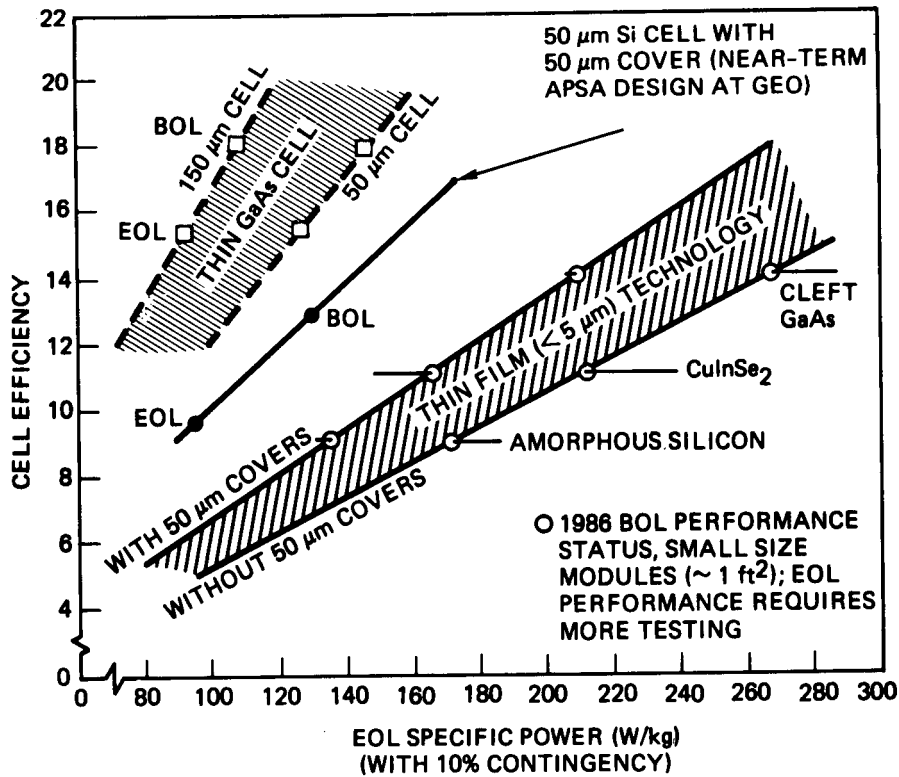


Figure 13. Impact of Advanced Cell Technology on Solar Array Specific Power, 10-Year Geosynchronous Mission

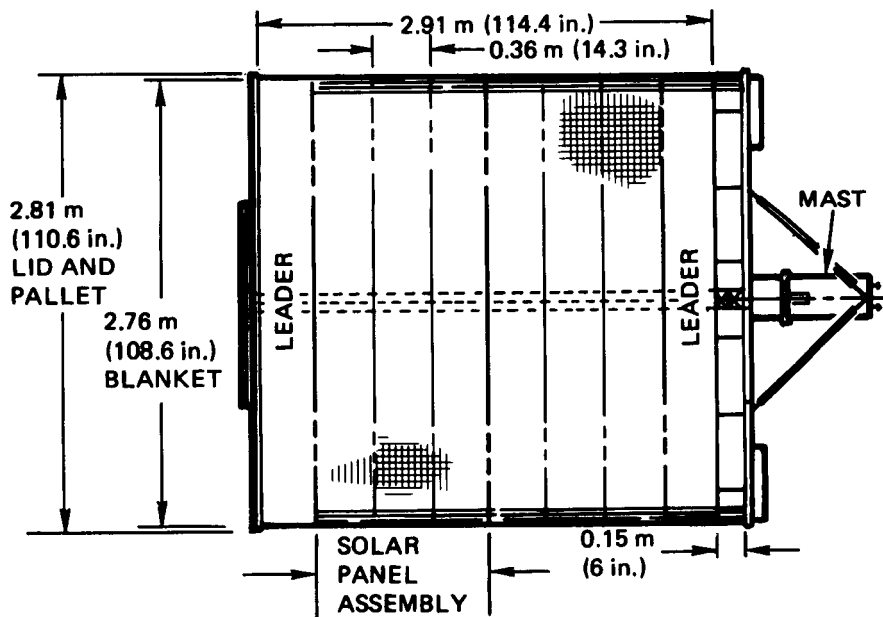


Figure 14. Baseline Prototype Wing Configuration

Development of Tandem Cells Consisting of GaAs Single Crystal and CuInSe₂/CdZnS Polycrystalline Thin Films

Namsoo P. Kim and Billy J. Stanbery
Boeing Electronics Co.

Ronald P. Gale and Robert W. McClelland
Kopin Corp.

Summary

The tandem cells consisting of GaAs single crystal and CuInSe₂ polycrystalline thin films are being developed under the joint program of the Boeing Co. and Kopin Corp. to meet the increasing power needs for future spacecraft. The updated status of this program is presented along with experimental results such as cell performance, and radiation resistance. Other cell characteristics including the specific power of and the interconnect options for this tandem cell approach are also discussed.

Introduction

Energy demands for future spacecraft are expected to increase significantly. The development of high-efficiency, light weight, and radiation resistant photovoltaic arrays is required to meet these demands. The Boeing Co. and Kopin Corp. have been jointly developing mechanically stacked tandem cells based on GaAs(AlGaAs) top cells and CuInSe₂(CIS) lower cells to address these requirements.

The thin film GaAs(AlGaAs) has been chosen as top cell due to its high efficiency and good radiation resistance. The CIS cell has been chosen as bottom cell due to its excellent radiation hardness, high optical absorption coefficient, and optimal bandgap value in combination with an AlGaAs top cell. Since both cells are incorporated as thin films, the specific power of this tandem is expected to be extremely high. In addition, this tandem cell approach provides interconnect flexibility to permit more efficient arrays since each cell is fabricated and tested independently and can be selectively matched. In this paper, we discuss the characteristics of these cells and present the current status of this program.

Tandem Cell Fabrication

The structure of the tandem cell under development is shown schematically in Figure 1. It consists of a double heterostructure GaAs/AlGaAs CLEFT top cell mechanically stacked on a CdZnS/CuInSe₂ thin film bottom cell. Fabrication of the cell is accomplished in a similar manner to the one described elsewhere [ref.1].

The very thin GaAs single crystal film (10 μm thick) is fabricated by the CLEFT technique [ref.2] and the layers of p⁺ AlGaAs, p GaAs base, n GaAs emitter, n⁺ AlGaAs window, and n⁺ GaAs cap are grown by OMCVD [ref.3] to form a double-heterostructure. After the front face of

the cell is processed, a support is mounted to the cell and the thin film is separated from the bulk GaAs. Grid deposition and anti-reflection coating, and etch removal of inactive GaAs film complete the top cell fabrication.

The CIS lower cell is fabricated by sequential deposition directly onto a glass substrate of a Mo electrode, CuInSe₂ absorber, and CdZnS window and metallic contact grid. The CuInSe₂ film is deposited by a simultaneous elemental coevaporation process and the CdZnS film is deposited by coevaporation of the CdS and ZnS binary compounds [refs. 4 and 5].

Mechanical stacking of the top cell and the bottom cell is accomplished using a space qualified optical adhesive to form the final structure consisting of a coverglass and the subcells. Interconnecting the top cell grids to contact pads on the CIS cell substrate completes fabrication of the tandem cell.

Tandem Cell Characteristics

Efficiency

The best performance of this tandem approach that we have achieved so far is 20.3%* (20.5%) AM0 for a four terminal 1 cm² cell design. The results of this cell are shown in Figure 2. The subcell efficiencies were 18.1% and 2.2%* (2.4%) for the GaAs top cell and the CIS bottom cell respectively. Measurements were conducted at 28°C, with a Xenon solar simulator intensity setting of 137.2 mW/cm². The external quantum efficiency measured with the same cell is shown in Figure 3. Exact optical loss mechanisms for the bottom cell are being investigated and the tandem stack is being further optimized. Details of this work will be published at a later date.

Earlier projections using the combination of bandgap values of AlGaAs(1.75 eV) and CIS(1.0 eV) predicted the maximum efficiency of 32.9% [ref.6]. Using a realistic tandem cell model, we expect to achieve 22.7% AM0 cells with our current cell structure(GaAs/CIS) in the very near future. When combined with a high quality AlGaAs top cell, further improvement of efficiency up to 26% AM0 is anticipated.

Radiation Hardness

Radiation resistance of this tandem cell is expected to be superb. In order to assess the radiation effects on these cells, bare CIS and bare GaAs solar cells were fabricated, and submitted for radiation experiments using facilities at Boeing Radiation Effects Laboratory(BREL).

*Adjusted for white light response of the lower cell (suspected to be due to light trapping in the layers between cells)

The experimental results on the normalized power degradation for CLEFT GaAs and CIS cells as a function of irradiation fluence are shown respectively in Figure 4 and Figure 5. These results reaffirmed our previous report [refs.1 and 7] that the CIS cells have superior radiation hardness when compared to Si and GaAs solar cells. The illuminated I-V curves measured on the 1.0 and 2.0 MeV electron radiation samples of CIS exhibited a negligible degradation at all fluences. The CIS cells showed much more resistance to proton radiation than GaAs or Si cells as shown in Figure 6. We also observed a recovery of the CIS performance to near pre-irradiation values with samples stored at room temperature and ambient pressure. The results of radiation experiments on the GaAs cells showed comparable values to the ones that have been reported with bulk. We expect, however, somewhat better performance with CLEFT GaAs film on radiation hardness due to its n-on-p structure, the shallowness of junction in these CLEFT cells, and to the thinness of the film. Radiation results on GaAs cells from various reports are plotted for relative comparison in Figure 7. Since radiation effects depend on parameters such as cell structure, operating temperature, initial performance or device parameters and many others, direct comparison is not easily possible. Thus, we have to consider the present comparison of GaAs radiation hardness results as being more relative than absolute.

Based on these results combined with our enhanced solar cell modeling program, however, further improvement is expected with GaAs cell structure optimization. Even further improvement of radiation hardness is expected when an AlGaAs top cell currently being evaluated, is included in the tandem stack.

Weight

One distinct advantage of this approach is found in weight consideration. Compared to conventional approaches involving cell growth on a bulk substrate, this tandem utilizes the CLEFT technique to fabricate a very thin GaAs film. Combined with the thin-film CIS cell directly deposited onto thin glass, we expect the weight of a 4 cm² tandem cell including coverglass to be 190 mg, as shown in the Table 1. With the efficiency of 20.5% already achieved, this provides specific power of 590 W/kg. When a projected efficiency of 26% is used, we expect specific powers upto 750 W/kg in these cells.

Interconnect Options

Since this tandem cell is mechanically stacked, it provides considerable interconnection flexibility. Using the four terminal approach, each cell can be fabricated with high processing yields, optimized independently and then selected for array level optimization. Since it is not series-interconnected, degradation of each cell due to radiation and/or operating temperature would have less impact on the other, especially when the array is configured in voltage matching condition. It is known [ref. 8] that voltage matching offers advantages such as less sensitivity to radiation damage, and spectral variation and wider selection of bandgaps for optimal performance. It was found that a configuration of three series connected CIS cells in parallel with a GaAs cell is suitable for voltage

matching and this configuration can be realized at either the module (tandem cell) level or array level.

Tandem Cell Optimization

In addition to our current effort toward improving the GaAs/CIS tandem cell efficiency by minimizing optical transmission losses, evaluation of AlGaAs/CIS tandem has been undertaken for the purpose of achieving higher EOL efficiency. Also being developed is a larger area(4 cm²) tandem cell. Masks for both top and bottom cell have been fabricated and initial device fabrication has shown promising results.

Conclusion

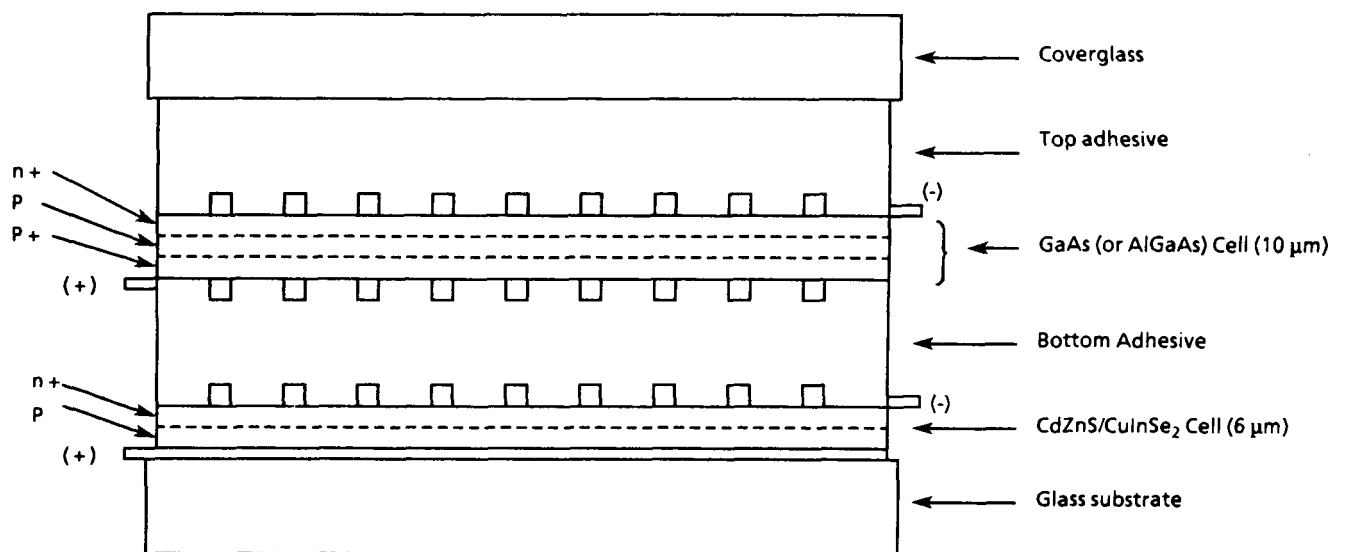
The updated status of our GaAs/CIS tandem cell program has been summarized, and the characteristics of cells have been discussed. This tandem cell approach utilizing thin film GaAs single crystal and polycrystalline CIS thin film cells is viable, mature and nearing readiness for implementation in high-performance space power systems.

References

- [1] B.J. Stanbery, J.E. Avery, R.M. Burgess, W.S. Chen, W.E. Devaney, D.H. Doyle, R.A. Mickelsen, R.W. McClelland, B.D. King, R.P. Gale and John C.C. Fan, *Conference Record 19th IEEE Photovoltaic Specialists Conference* (IEEE, New York, 1987), p. 280.
- [2] John C.C. Fan, C.O. Bozler, and R.W. McClelland, *Conference Record 15th IEEE Photovoltaic Specialists Conference* (IEEE, New York, 1981), p. 666.
- [3] R.P. Gale, John C.C. Fan, G.W. Turner, and R.L. Chapman, *Conference Record 18th IEEE Photovoltaic Specialists Conference* (IEEE, New York, 1985), p. 296.
- [4] R.A. Mickelsen, and W.S. Chen, *Conference Record 16th IEEE Photovoltaic Specialists Conference* (IEEE, New York, 1982), p.781.
- [5] R.A. Mickelsen, W.S. Chen, B.J. Stanbery, H. Dursch, J.M. Stewart, Y.R. Hsiao, and W. Devaney, *Conference Record 18th IEEE Photovoltaic Specialists Conference* (IEEE, New York, 1985), p. 1069.
- [6] John C.C. Fan, B-Y. Tsaur and B.J. Palm, *Conference Record 16th IEEE Photovoltaic Specialists Conference* (IEEE, New York, 1982), p.692.
- [7] H. Dursch, W.S.Chen and D. Russell, *Proceedings of Space Photovoltaic Research and Technology 1985*, NASA Conf. Pub. 2408, p.165.
- [8] J.M. Gee, *Conference Record 19th IEEE Photovoltaic Specialists Conference* (IEEE, New York, 1987), p.536.

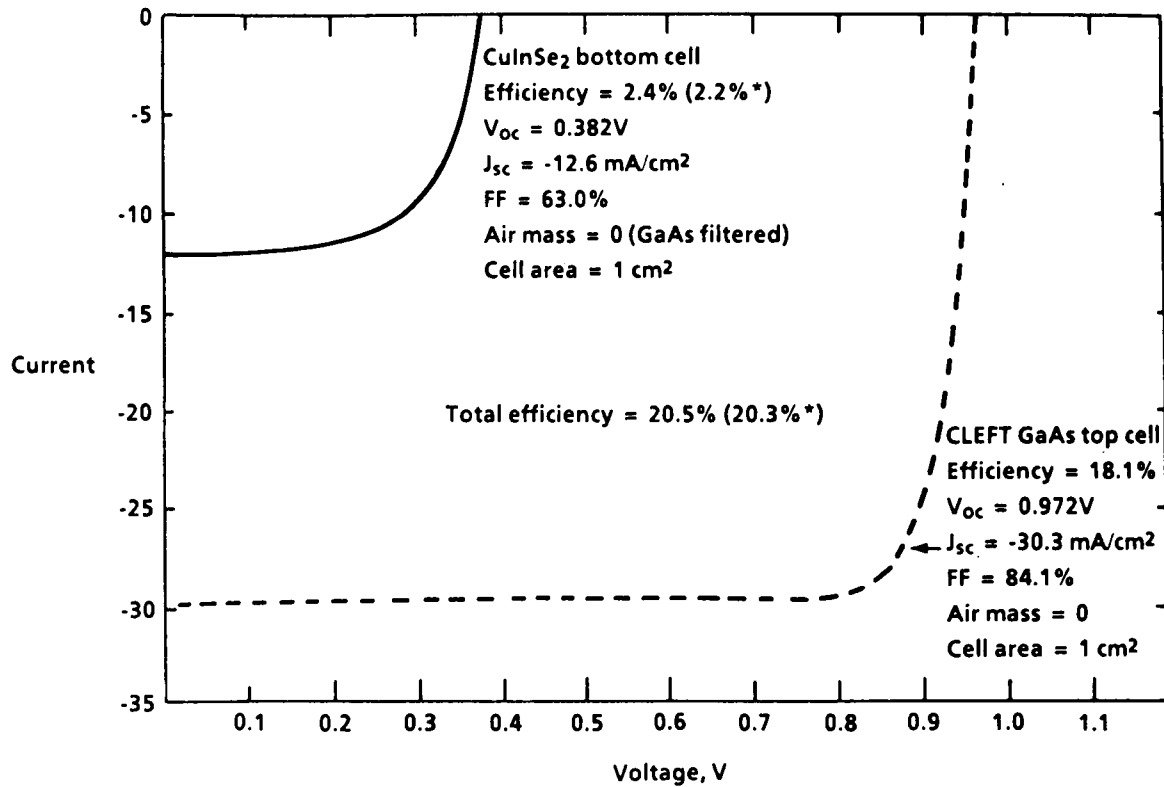
Table 1. Weight of Tandem Cell (4 cm²)

Component	Thickness	Weight
Coverglass	2 mil	53.1 mg
Top adhesive	2 mil	21.6 mg
GaAs CLEFT	10 μ m	21.2 mg
Bottom adhesive	2 mil	21.6 mg
CuInSe ₂	6 μ m	13.0 mg
Glass substrate	2 mil	53.1 mg
Others		3.0 mg
Total		188.0 mg



Vertical dimensions not to scale
(see Table 1 for details)

Figure 1. Schematic of Tandem Cell Structure



*Corrected for white light response of lower cell

Figure 2. I-V Measurements of Tandem Cell (*corrected for white light response of lower cell)

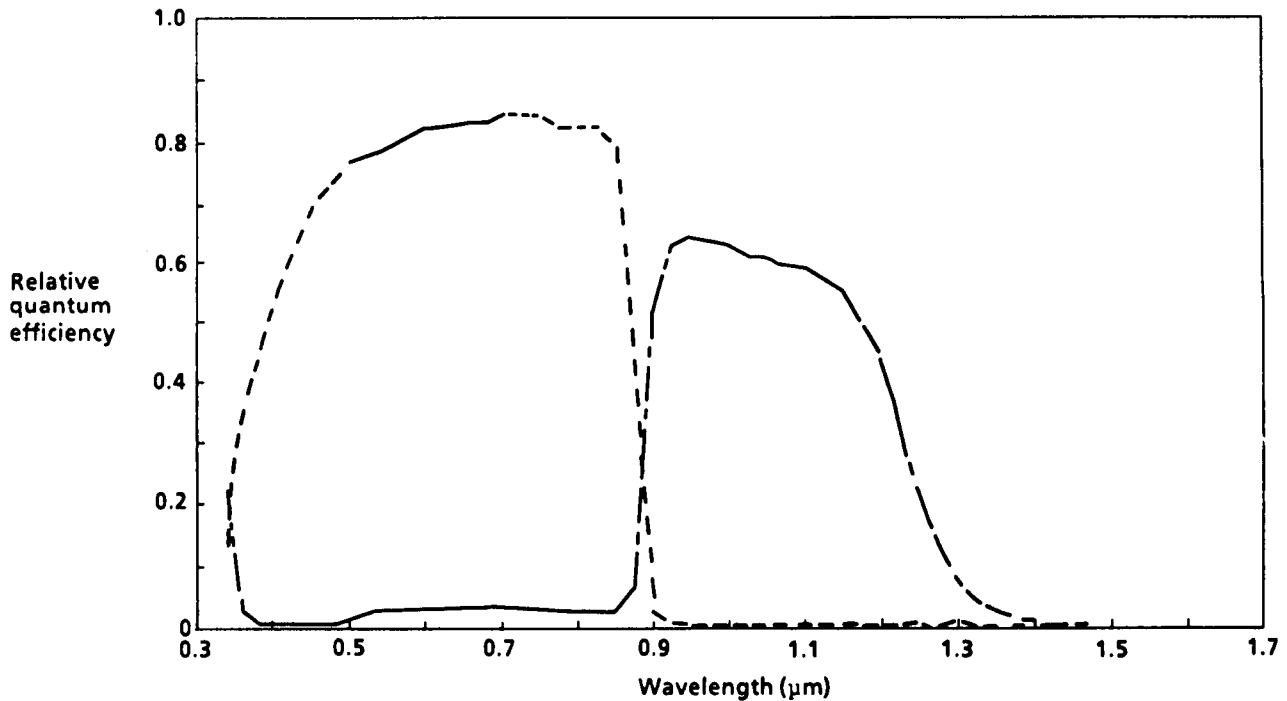


Figure 3. Spectral Response of Tandem Cell

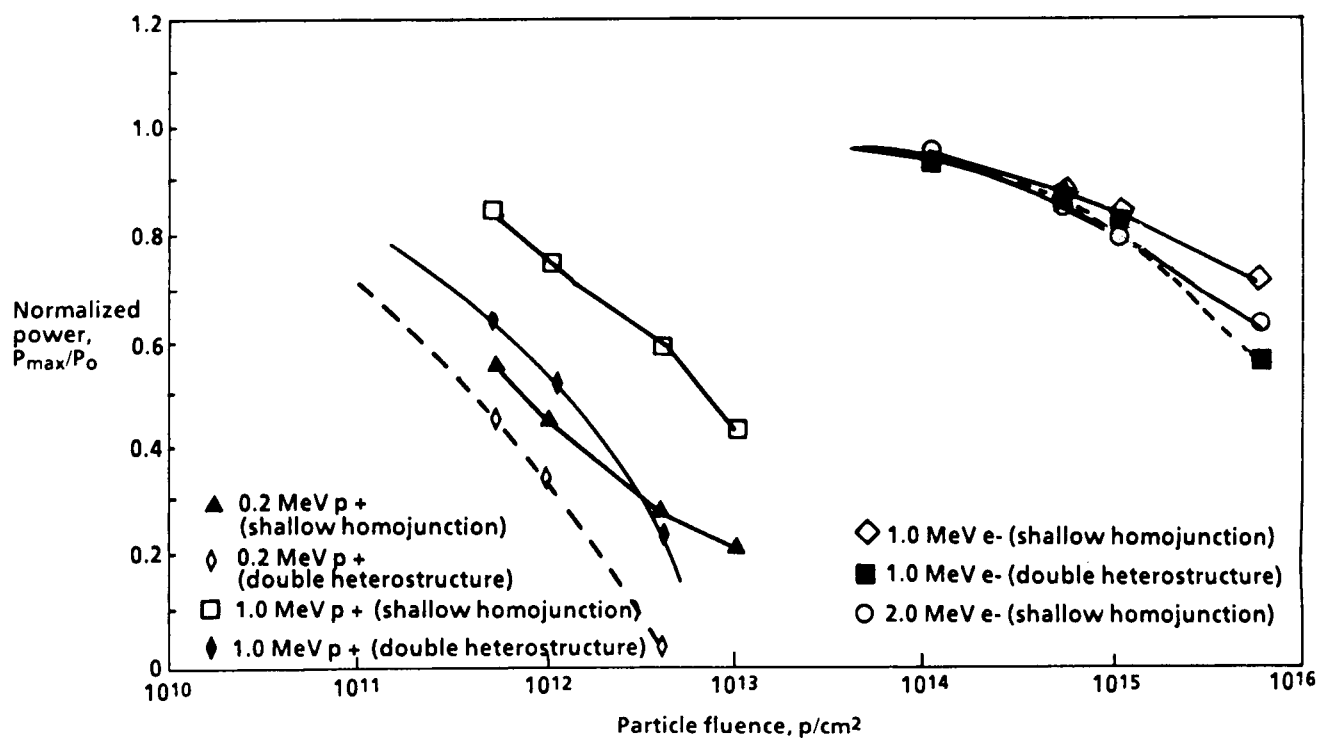


Figure 4. Normalized Power Versus Particle Fluence Results of Irradiations of CLEFT GaAs Solar Cells by Protons and Electrons

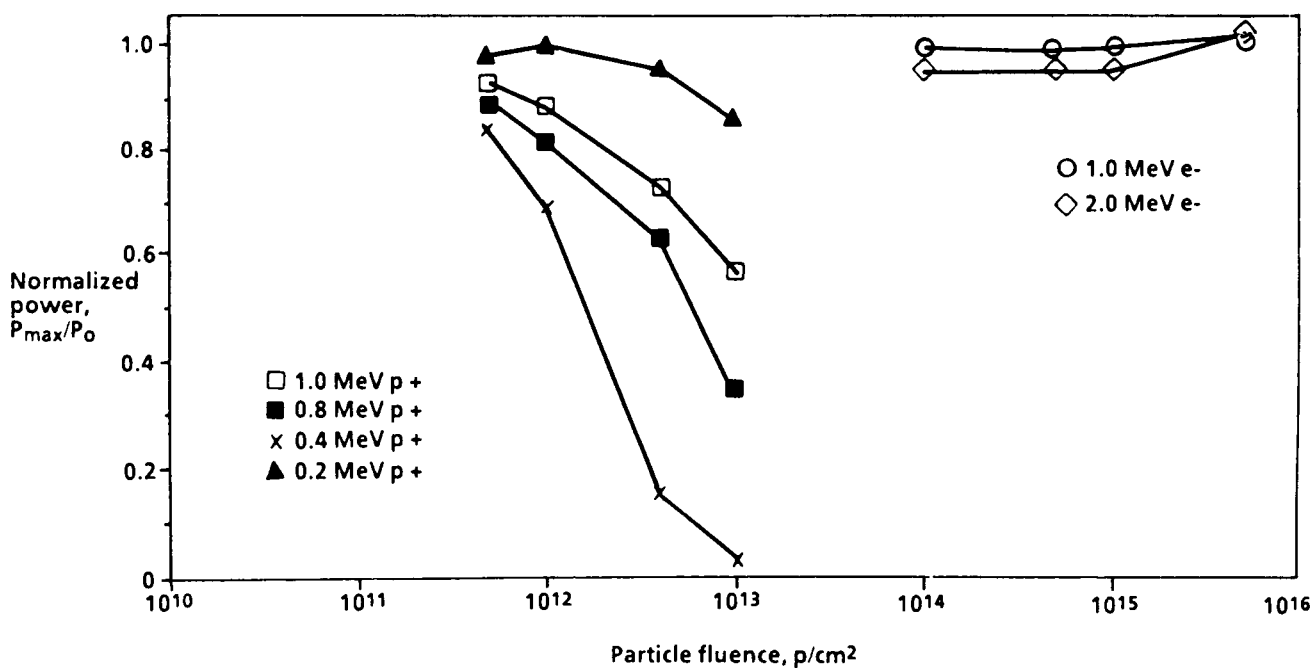


Figure 5. Normalized Power Versus Particle Fluence Results of Irradiations of CuInSe_2 Cells by Protons and Electrons

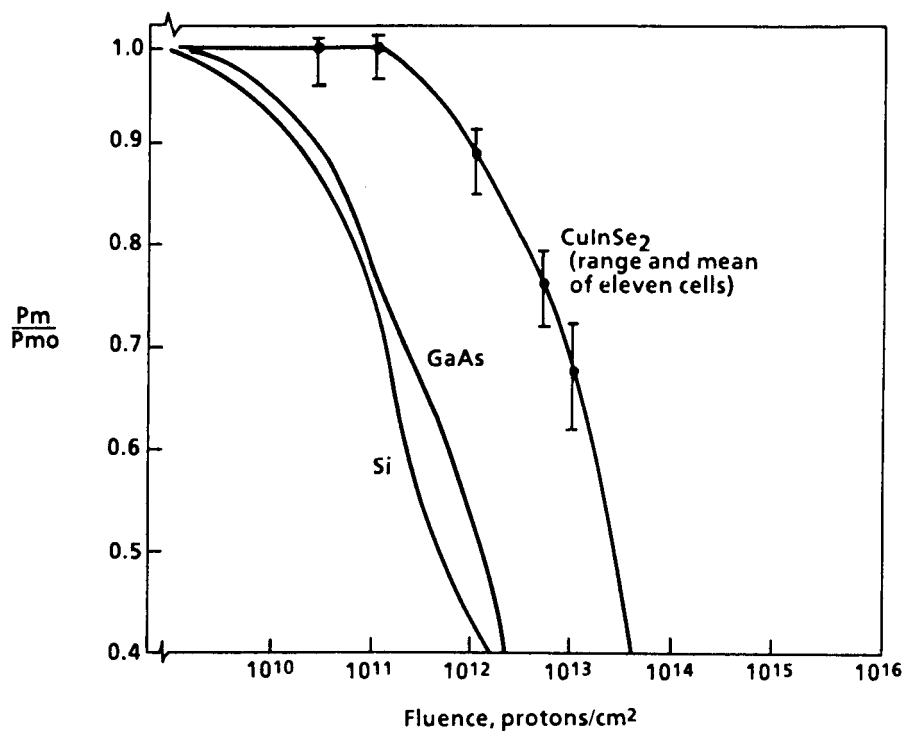


Figure 6. Degradation of Thin-Film CdS/CuInSe₂ Solar Cells as Function of 1 MeV Proton Fluence (ref. 7)

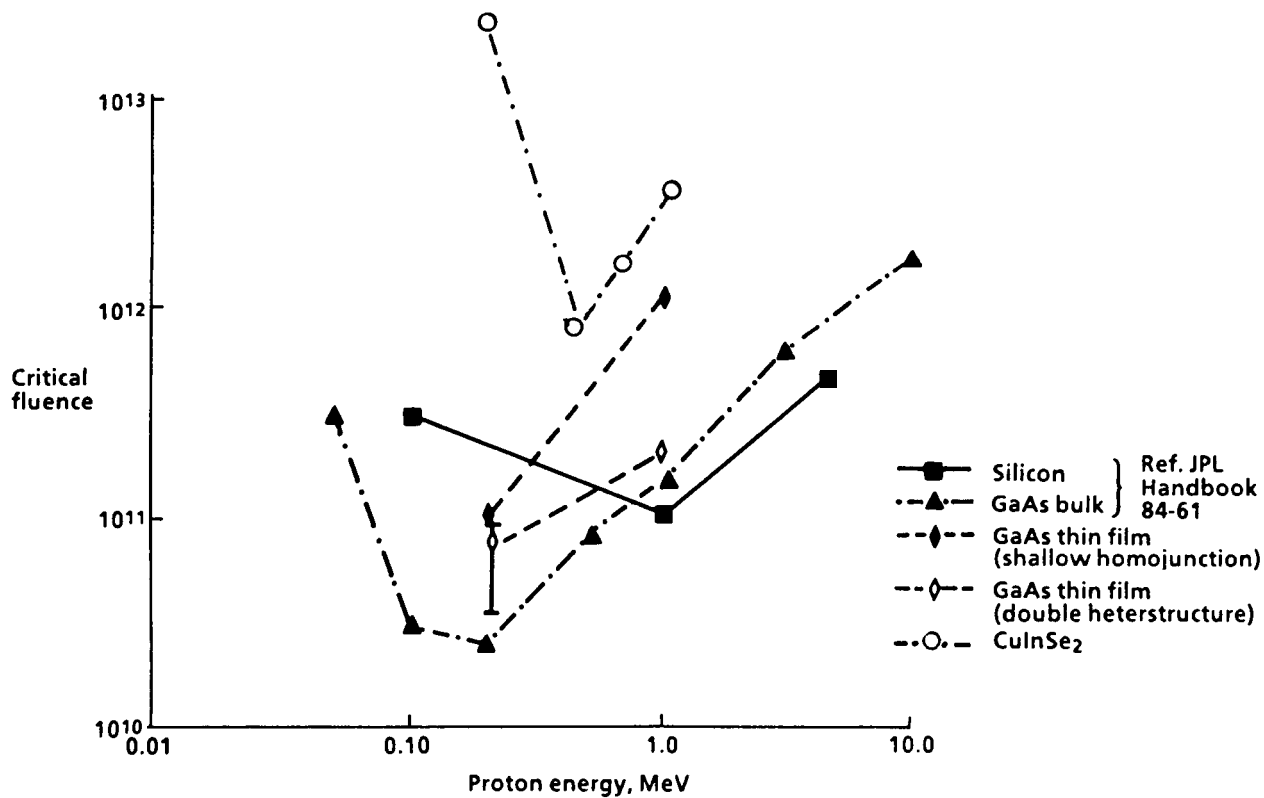


Figure 7. Critical Fluence vs. Proton Energy for Various Semiconductors

Directions for Further Development of GaAs/CuInSe₂ Thin Film Tandem Cells

B.J. Stanbery
Boeing Electronics

Summary

Multijunction thin film solar cells utilizing GaAs and CuInSe₂ as semiconductor absorbers are rapidly developing, becoming a viable technology for space power systems with an unparalleled combination of high efficiency, low mass, and high radiation tolerance. The prospect for evolutionary improvement of this type of cell towards efficiency of $\approx 30\%$ and specific power greater than 1 kW/kg while retaining the attribute of high radiation tolerance are good. Limitations of the present configuration and possible avenues for circumventing these problems are presented.

Introduction

In the nine years since the first demonstration of both thin film CuInSe₂ cells and the CLEFT process for fabricating thin film single crystals of GaAs, tremendous strides have been made in the maturation of both technologies. Each has been shown capable of fabricating large-area films [refs. 1 & 2] of high quality as attested to by the recent achievement of tandem efficiency greater than 20% AM0. Bereft of excess high density semiconductor bulk, the practical lower mass limit for these cells is determined by their support structures, shifting the focus of mass reduction efforts to the module, panel, and array level designs. It is the conjunction of this inherently low mass with both high efficiency and high radiation tolerance, however, which enables the array designer to capitalize on this asset, since the array size may be smaller relative to other options and still guarantee adequate End-Of-Life (EOL) system power.

Although there is little benefit at the systems level of further reducing the *direct* cell mass, improvements in EOL specific power may still be achievable by reducing mass contributions of associated components, increasing Beginning-Of-Life (BOL) efficiency, and increasing radiation tolerance. The remainder of this paper will comprise a discussion of means by which this may be achieved.

Bandgap Engineering of AlGaAs/CuInSe₂ Tandem Cells

CuInSe₂ is a ternary chalcopyrite semiconductor, which unlike the ternary alloy of AlAs and GaAs, Al_xGa_{1-x}As, has a fixed bandgap (to first order). Its attributes that commend its use in space photovoltaics include one of the highest known absorption coefficients of any semiconductor [ref. 3], an optimum bandgap for the lower cell in two-junction tandems [ref. 4], and an exceptional tolerance to high-energy particulate radiation [ref. 5]. In a heterojunction with CdZnS it has shown excellent minority carrier collection, achieving internal quantum efficiencies nearing unity [ref. 6]. Its greatest liability is the low voltage of the cell compared to its bandgap. Conventional diffusion-current dominated ideal photodiodes with this bandgap would be predicted to exhibit open-circuit

voltages as high as ≈ 560 mV [ref. 7] at comparable current levels to those of $\text{CuInSe}_2/\text{CdZnS}$ in tandem with GaAs, compared to an observed $V_{oc} \approx 380$ mV. The reasons for this low voltage are an active area of research and debate in the literature, but it is most likely due to interface states acting as a recombination pathway for minority carriers [ref. 8 and 9], with deep level defects in the bulk possibly playing a role [ref. 10]. Improvements in CuInSe_2 cell voltage are most likely to result from refinement of the component materials and their fabrication processes. Certainly *any* success in improving the voltage performance of CuInSe_2 cells will contribute to the overall performance of the tandem. In practice this plays a crucial role, however, in selection of the optimum bandgap for the $\text{Al}_x\text{Ga}_{1-x}\text{As}$ upper cell.

Hybrid Tandem Cells

The present state-of-the-art thin film solar cells are hybrid or mechanically stacked, each component cell fabricated independently before being incorporated into the tandem. There are numerous advantages to this approach, foremost being *flexibility*. A range of bandgaps for upper and lower cell are possible, permitting their design to be tailored to the requirements of the mission and properties of the available materials. Other advantages include series/parallel buss interconnect flexibility and less sensitivity to temperature effects on orbit. The principal disadvantage of hybrid tandems is the increased complexity of fabrication and interconnection concomitant with its increased flexibility.

Previously published calculations [Table 1 in ref. 11] for $\text{Al}_x\text{Ga}_{1-x}\text{As}$ *shallow homojunction* cells in four-terminal tandem configuration with CuInSe_2 cells showed minor ($\leq 0.7\%$) losses in BOL efficiency for increasing $x \leq 0.3$ though it still remained over 22% in all cases. This was due in part to assumptions regarding minority carrier lifetimes in $\text{Al}_x\text{Ga}_{1-x}\text{As}$ subsequently shown to be overly pessimistic [ref. 12]. This was also a consequence, however, of the upper cell with increased bandgap losing current to the lower cell operating at less than ideal voltage. These considerations indicate that the aluminum content (x -value) that maximizes BOL efficiency for $\text{Al}_x\text{Ga}_{1-x}\text{As}/\text{CuInSe}_2$ tandems is less than the theoretical optimum of $x \approx 0.3$ calculated for ideal cells in reference 4. Radiation degradation effects, however, provide a countervailing influence on the optimum choice of aluminum content in the upper $\text{Al}_x\text{Ga}_{1-x}\text{As}$ cell for four-terminal tandem operation. Since both CuInSe_2 and $\text{Al}_x\text{Ga}_{1-x}\text{As}$ cells are more radiation resistant than GaAs cells [refs. 5, 13, and 14], and available data suggest that the radiation effects in $\text{Al}_x\text{Ga}_{1-x}\text{As}$ are less severe for higher aluminum content [refs. 15 and 12] in the range $x \leq 0.37$, EOL efficiency maximization *for many missions* will increase the optimum value of x over the optimum for BOL efficiency.

Another available path for improved efficiency in the hybrid tandem configuration is the use of a monolithic $\text{Al}_x\text{Ga}_{1-x}\text{As}/\text{GaAs}$ tandem cell mechanically stacked on a CuInSe_2 cell. The choice of bandgaps is near optimum in this case for $x \approx 0.4$ [ref. 4], and practical efficiencies near 30% should be achievable.

Monolithic Thin Film Tandem Cells

Certain components to the successful fabrication of high efficiency monolithic tandems appear important. Current matching (at some optimum point in the mission lifetime) is necessary. The calculations reported in reference 11 predict BOL current matching at an upper cell absorber layer composition near $\text{Al}_{0.2}\text{Ga}_{0.8}\text{As}$, a modest aluminum content for which high quality films should be

readily achievable. Fabrication of an Intercell Ohmic Contact (IOC) is one of the persistently vexing difficulties in the fabrication of monolithic tandem cells. One solution used successfully in references 16 and 17 has been fabrication of a tunnel junction between upper and lower cells, but steps must be taken to avoid interdiffusion at the highly-doped, abrupt interface which can result in a resistive, highly compensated transition region which destroys the tunnel junction.

The lattice mismatch between CuInSe_2 and GaAs is less than 2% and the chalcopyrite symmetry of CuInSe_2 is a ternary equivalent of two GaAs zincblende crystal unit cells distorted slightly along the connecting c-axis. Heteroepitaxial single-crystal cell structures in material systems with comparable or greater amounts of lattice mismatch have been widely pursued, utilizing the techniques of advanced epitaxial growth technology such as graded composition lattice-matching transition layers and superlattice dislocation propagation filters. Given the nearly perfect carrier collection efficiency in *polycrystalline* CuInSe_2 cells, it appears that the minority-carrier electron transport in the material is tolerant of the native defects in the material. This may relax the requirement for crystalline perfection compared to III-V based materials. Study of the epitaxial growth of CuInSe_2 on GaAs has been reported in reference 18 and references therein.

I propose a novel solution [ref. 19] to these problems which capitalizes on the unique abilities of the CLEFT process and properties of the constituent materials. Figure 1 shows a cross-sectional schematic of the proposed structure. Fabrication is begun by the overgrowth of a GaAs CLEFT buffer on a GaAs wafer. Next, the $\text{Al}_x\text{Ga}_{1-x}\text{As}$ cell is fabricated in an 'inverted' configuration with the emitter nearest the buffer. Since this is the first device structure deposited, it can be deposited at high temperature to improve the quality of the $\text{Al}_x\text{Ga}_{1-x}\text{As}$ without degrading the tunnel junction. The proposed tunnel junction is formed between a $p^+-\text{Al}_x\text{Ga}_{1-x}\text{As}$ and subsequently deposited $n^+-\text{ZnSe}$ layer. This ZnSe layer is compositionally and dopant graded to form an $n\text{-CdZnSSe}$ contact to the final semiconductor $p\text{-CuInSe}_2$ absorber layer. Back contacts are deposited, the film is cleaved from the bulk GaAs wafer, front contacts formed and the excess buffer layer removed before AR coating completes the device.

The technology for fabrication of the tunnel junction has only recently been demonstrated, although to the author's knowledge it has not yet been done. High-quality single-crystal ZnSe and GaAs lattice-matched $\text{Zn}_{0.05}\text{Se}_{0.95}$ can be deposited on GaAs or $\text{Al}_x\text{Ga}_{1-x}\text{As}$ by numerous processes including MBE [ref. 20] and MOCVD [ref. 21]. Recently, effective doping of ZnSe, long an elusive goal of research, has been demonstrated [ref. 22]. In fact, degenerate doping of ZnSe to levels of $2.8 \times 10^{19} \text{ cm}^{-3}$ with Hall mobilities of $140 \text{ cm}^2/\text{V}\cdot\text{s}$ and resultant resistivity of $10^{-3} \Omega\cdot\text{cm}$ have been reported at a temperature of 318°C [ref. 23], quite adequate for tunnel junction fabrication without significant interdiffusion. Though a reliable direct measurement of the ZnSe/GaAs conduction band offset is unavailable, application of the theory of Tersoff in reference 24 predicts a valence band offset of 0.04 volts, essentially zero within the accuracy of the theory, though this calculation is only thought to be accurate to within ≈ 0.15 volts. Certainly recent evidence suggests that the density of interfacial surface states between ZnSe and GaAs can be very low [ref. 25].

Perhaps the greatest challenge in fabricating the monolithic $\text{Al}_x\text{Ga}_{1-x}\text{As}/\text{CuInSe}_2$ tandem is the formation of a high-quality heterojunction between the CdZnSSe interconnect region and the subsequently deposited CuInSe_2 absorber. The results reported in reference 18 for deposition of epitaxial single crystal CuInSe_2 on GaAs suggest that careful control of composition can produce p-type films without a Cu-rich second phase which appears to minimize Cu out-diffusion. This is important since Cu forms a deep level trap in the ZnSe, ZnS, and CdS binary constituents of the interconnect alloy. It would appear from this previous work that the key to successful fabrication of this device is the development of a lower temperature process for the fabrication of high quality CuInSe_2 than

the elemental codeposition process presently employed. Given the widespread technological effort to develop lower temperature processes for the deposition of other important semiconductor materials, usually for the same reason of minimizing interdiffusion in multilayered structures, I believe the solution of this problem to be feasible.

References

- [1] R.A. Mickelsen, B.J. Stanbery, J.E. Avery, Wen S. Chen and W.E. Devaney, "Large Area CuInSe₂ Thin Film Solar Cells", *Conference Record 19th IEEE Photovoltaic Specialists Conference*, IEEE, 1987, pp.744-748.
- [2] R.P. Gale, B.D. King and J.C.C. Fan, "Large-Area GaAs CLEFT Layers for Solar Cell Applications", *Conference Record 19th IEEE Photovoltaic Specialists Conference*, IEEE, 1987, pp.293-295.
- [3] A.M. Hermann, L. Fabick, K. Zweibel and R. Hardy, "Progress in Polycrystalline Thin-film Photovoltaic Device Research", *Conference Record 16th IEEE Photovoltaic Specialists Conference*, IEEE, 1982, pp.840-845.
- [4] John C.C. Fan, B-Y. Tsaur and B.J. Palm, "Optimal Design of High-efficiency Tandem Cells", *Conference Record 16th IEEE Photovoltaic Specialists Conference*, IEEE, 1982, pp.692-701.
- [5] R.A. Mickelsen, Wen S. Chen, B.J. Stanbery, H. Dursch, J.M. Stewart, Y.R. Hsiao and W. Devaney, "Development of CuInSe₂ Cells for Space Applications", *Conference Record 18th IEEE Photovoltaic Specialists Conference*, IEEE, 1985, pp.1069-1073.
- [6] W.E. Devaney, R.A. Mickelsen and W.S. Chen, "Recent Improvements in CuInSe₂/ZnCdS Thin Film Solar Cell Efficiency", *Conference Record 18th IEEE Photovoltaic Specialists Conference*, IEEE, 1985, pp.1733-1734.
- [7] A.M. Barnett, S.L. Rhoads and G.H. Negley, "A Three Solar Cell Mechanical Stack with an AM0 Efficiency Greater than 30%", *Conference Record 19th IEEE Photovoltaic Specialists Conference*, IEEE, 1987, pp.1526-1527.
- [8] W.A. Miller and L.C. Olsen, *IEEE Trans. Electron Devices* **31**, 654 (1984).
- [9] C. Goradia, M. Goradia and R. Lopez, "On the Possible Enhancement of Open Circuit Voltage in n-(Cd,Zn)S/p-CuInSe₂ Polycrystalline Thin Film Solar Cells", *Conference Record 18th IEEE Photovoltaic Specialists Conference*, IEEE, 1985, pp.1399-1404.
- [10] Evangelos C. Demetriou and Allen Rothwarf, "An Admittance Study of the CuInSe₂/CdS Solar Cell", *Conference Record 19th IEEE Photovoltaic Specialists Conference*, IEEE, 1987, pp.764- 769.
- [11] B.J. Stanbery, J.E. Avery, R.M. Burgess, W.S. Chen, W.E. Devaney, D.J. Doyle, R.A. Mickelsen, R.W. McClelland, B.D. King, R.P. Gale and John C.C. Fan, "Thin Film Tandem GaAs/CuInSe₂ Solar Cells for Space Power Applications", *Conference Record 19th IEEE Photovoltaic Specialists Conference*, IEEE, 1987, pp.280-284.
- [12] R.K.Ahrenkiel, D. Greenberg, D.J. Dunlavy, T. Hanak, J. Schlupmann, H.C. Hamaker and C.R. Lewis, "Minority-Carrier Properties of 1.93-eV Al_xGa_{1-x}As Grown by MOCVD", *Conference Record 19th IEEE Photovoltaic Specialists Conference* IEEE, 1987, pp.1180-1186.
- [13] H.B. Curtis, C.K. Swartz, and R.E. Hart, Jr., "Radiation Performance of AlGaAs and InGaAs Concentrator Cells and Expected Performance of Cascade Structures. *Conference Record 19th IEEE Photovoltaic Specialists Conference*, IEEE, 1987, pp.727-732.

- [14] H.C. Hamaker, J.G. Werthen, C.R. Lewis, H.F. MacMillan, C.W. Ford, G.F. Virshup, R.K. Ahrenkiel, D.L. Greenberg and J. Schlupmann, "Radiation Damage of 1.93-eV $\text{Al}_x\text{Ga}_{1-x}\text{As}$ and GaAs Solar Cells Grown By Metalorganic Chemical Vapor Deposition", *Conference Record 19th IEEE Photovoltaic Specialists Conference*, IEEE, 1987, pp.733-736.
- [15] Sheng S. Li, C.G. Choi and R.Y. Loo, "Studies of Radiation-Induced Defects in One-MeV and Low Energy Proton Irradiated Germanium and $\text{Al}_x\text{Ga}_{1-x}\text{As}$ P-N Junction Solar Cells", *Conference Record 18th IEEE Photovoltaic Specialists Conference*, IEEE, 1985, pp.640-645.
- [16] Masafumi Yamaguchi, Chikara Amano, Hideo Sugiura and Akio Yamamoto, "High Efficiency AlGaAs -GaAs Tandem Solar Cells with Tunnel Junction", *Conference Record 19th IEEE Photovoltaic Specialists Conference*, IEEE, 1987, pp.1484-1485.
- [17] Chikara Amano, Hideo Sugiura, Koshi Ando and Masafumi Yamaguchi, "High-efficiency $\text{Al}_{0.3}\text{Ga}_{0.7}\text{As}$ Solar Cells Grown by Molecular Beam Epitaxy", *Appl. Phys. Lett.* **51** (14), 5 October 1987, pp. 1075-1077.
- [18] E.R. Don, G.J. Russell and R. Hill, "RHEED Studies of CuInSe_2 Epitaxial Films", *Conference Record 18th IEEE Photovoltaic Specialists Conference*, IEEE, 1985, pp.1060-1064.
- [19] B.J. Stanbery, "Single Crystal, Heteroepitaxial, GaAlAs / CuInSe_2 Tandem Solar Cell and Method of Manufacture", U.S.S.N. 072,316 (1987).
- [20] B.J. Skromme, M.C. Tamargo, J.L. de Miguel and R.E. Nahory, "Photoluminescence Characterization of Heteroepitaxial ZnSe/GaAs and ZnSe/AlAs Grown by MBE Epitaxy of Semiconductor Layered Structures", *Materials Research Society Symposium Proceedings of the 1987 Fall Meeting* (in press).
- [21] A. Kamata, K. Hirahara, M. Kawachi and T. Beppu, "Lattice Matched Epitaxial Growth of ZnSSe on GaAs by MOCVD", *Extended Abstracts of the 17th Conference on Solid State Devices and Materials*, Tokyo, 1985, pp. 233-236.
- [22] T. Yao, *J. Crystal Growth*, **72**, 1985, p. 31.
- [23] T. Hariu, S. Yamaguchi, S. Goto, K. Shida and K. Matsushita, "Highly Conductive ZnSe Layers by Plasma-Assisted Epitaxy", *Extended Abstracts of the 18th (1986 International) Conference on Solid State Devices and Materials*, Tokyo, 1986, pp. 639-642.
- [24] J. Tersoff, "Summary Abstract: Failure of the common anion rule for lattice-matched heterojunctions", *J. Vac. Sci Technol. B* **4** (4), Jul/Aug 1986, pp. 1066-1067.
- [25] D.J. Olego, "Effects of ZnSe Epitaxial Growth on the Surface Properties of GaAs", *Appl. Phys. Lett.* **51** (18), 2 November 1987, pp. 1422-1424.

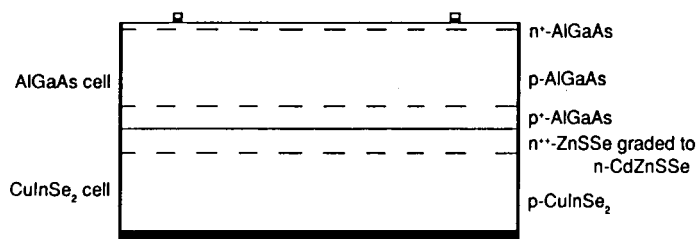


Figure 1.- Schematic of monolithic $\text{AlGaAs}/\text{CuInSe}_2$ cell.

Ultra-Thin, Light-Trapping Silicon Solar Cells

Geoffrey A. Landis*
NASA Lewis Research Center, 302-1
Cleveland, OH 44135

Summary

Design concepts for ultra-thin ($2\text{-}10\ \mu$) high efficiency single-crystal silicon cells are discussed. Light trapping allows more light to be absorbed at a given thickness, or allows thinner cells of a given J_{sc} . Extremely thin cells require low surface recombination velocity at both surfaces, including the ohmic contacts. Reduction of surface recombination by growth of heterojunctions of ZnS and GaP on Si has been demonstrated. The effects of these improvements on AM0 efficiency is shown. The peak efficiency increases, and the optimum thickness decreases. Cells under $10\ \mu$ thickness can retain almost optimum power.

The increase of absorptance due to light trapping is considered. This is not a problem if the light-trapping cells are sufficiently thin.

Ultra-thin cells have high radiation tolerance. A $2\ \mu$ thick light-trapping cell remains over 18% efficient after the equivalent of 20 years in geosynchronous orbit. Including a $50\ \mu$ thick coverglass, the thin cells had specific power after irradiation over ten times higher than the baseline design.

Introduction

Recent advances in silicon solar cell technology has resulted in cell efficiencies [ref. 1,2] as good or better than those obtained by competing technologies. Advances in efficiency, power/weight, and radiation tolerance for next-generation silicon space cells space use will require reducing the thickness. As thickness is decreased, the effect of surface recombination at both front and back surfaces becomes increasingly important; ultra-thin silicon cells will require both surfaces to be passivated, including the ohmic contacts. To avoid loss of short circuit current, an optical confinement structure will be required [ref. 2].

We have thinned silicon wafers to under $10\ \mu$ without breakage. Thinner cells may require special handling, or will have to be bonded to a substrate (or superstrate) for processing.

Light Trapping

Light trapping techniques increase the pathlength of light within the cell, allowing more of the light to be absorbed at a given thickness, or allowing thinner cells of a given J_{sc} . Several light trapping geometries have been proposed [ref. 3,4,5]. One effective light trapping geometry is the cross-grooved structure proposed by the author [ref. 6] and recently analyzed by Campbell and Green [ref. 7]. This is shown in figure 1. The grooved geometry has the low reflectivity typical of textured cells.

Figure 2 shows a ray-tracing of the path travelled by a typical light ray. A figure of merit for optical confinement is the average path length for weakly absorbed light. For random (Lambertian) confinement, this pathlength is $4n^2$ times the thickness [ref. 4], where n is the refractive index. $4n^2$ equals about 50 for silicon in the wavelengths of interest. For the cross-grooved geometry, the effective light trapping is slightly better, since all of the light is confined for the first two round-trip passages, a pathlength of about 8 times the thickness. After this the light is nearly randomized in direction. The average pathlength is thus about $4n^2 + 8$ times the cell thickness. This is similar to the results of Campbell and Green's ray-tracing analysis [ref. 7], who show an optical path length of 52-72 times the thickness, depending on groove spacing to width ratio.

This difference is more important at shorter wavelengths, since the first four round-trip passages are more important.

Modelling Light Trapping

The increases in optical pathlength are due to three effects: back surface reflection (BSR), oblique passage of light through the cell, and geometry-related trapping reducing the probability of a ray exiting.

The BSR is modelled simply as an additional light source illuminating the cell from the back with intensity $I = I_0 \exp(-\alpha_{eff} T)$. This effectively doubles the pathlength for weakly absorbed light.

Oblique light passage is modelled as an increase in the absorption constant; $\alpha_{eff} = \alpha / \cos\theta$. For fully randomized light, θ_{ave} is 60° , and the effective absorption constant is doubled.

Confinement geometry is modelled as an effective increase in light intensity inside the cell. If the escape probability of a ray incident on the interior surface is B , then the average pathlength increase factor is $1/B$, and the (wavelength-dependent) effective intensity increase is:

$$I' = \frac{1}{1 - (1 - B^{-1})e^{-2\alpha_{eff}T}} \quad (1)$$

For Lambertian confinement, $B=n^{-2}$. Figure 3 shows this geometrical enhancement factor versus αT , cell thickness T measured as a multiple of the absorption depth α^{-1} . The factor approaches the asymptotic limit $n^2 \approx 12.5$ at very low thicknesses (or long absorption depths). Oblique light passage and back surface reflection (BSR) together contribute a further enhancement, a factor of 4 in the weakly-absorbed limit. (For the cross-grooved geometry, the effect of the first two fully-trapped passes must also be included.) The enhancement factor is low for higher absorption constants because most of the light is already absorbed in the first few passages. Clearly, the effective enhancement is only important for very short cell thicknesses, or for very low absorption (long wavelength) light.

Absorptivity

Thermal alpha is an important consideration for space solar cells, since the higher the absorption, the higher the cell operating temperature will be. Unless the cells are covered with an IR-rejection filter, this will vary greatly with the absorption of sub-bandgap IR light. A light trapping structure very effectively increases the pathlength for weakly absorbed light, thus increasing alpha.

Calculated absorptivity will depend greatly on the absorption length of IR light in the silicon, which is dependant on silicon quality, oxygen and carbon content, doping level, etc. Figure 4 shows an idealized result, calculated assuming that the sub-bandgap light had an absorption depth α^{-1} for sub-bandgap light of 5000μ . The figure compares a structure with light trapping effectiveness of 50 times the thickness with an ideal gridded-back contact cell, modelled here as a once-through design. (An actual gridded-back cell will have slightly higher absorption, since the back will not actually be fully transparent.) Cell temperatures shown on the right side are calculated using data from Garlich and Lillington [ref. 8]. The result of the light-trapping is to shift the absorption to lower thicknesses. The 5μ light-trapping cell shown has the same absorption as the 250μ gridded-back cell.

Grid Shadowing

An additional gain can be realized when the contact metallization is highly reflective, and applied to only one of the groove sides, as shown in figure 1 (proposed by Borden and Walsh, [ref. 9]). Incident light striking the metallized portion reflects onto the opposite side and enters the cell. A variant geometry is to run the contact lines at an angle across the groove [ref. 10]. All of these techniques can result in elimination of the effective grid shadowing.

Surface Passivation

Extremely thin cells also require the surface recombination velocity S to be low at both front and back surfaces. As noted by Lindholm *et al.* [ref. 11], a small area of surface with high recombination velocity will degrade the efficiency of the cell much more than proportionately to the area. While oxide passivation has been shown to result in surfaces of extremely low S [ref. 12], SiO_2 is non-conductive and thus the technique must leave the surface unpassivated at the ohmic contacts. We have proposed [ref. 13] reduction of the surface recombination velocity of Si by use of a heterojunction window layer such as is used on GaAlAs/GaAs cells. The theoretical band diagram of an ideal heterojunction-passivated cell is shown in figure 5. ZnS (lattice constant 5.41\AA , bandgap 3.6 eV) and GaP (lattice constant 5.41\AA , bandgap 2.3 eV) are the available wide-bandgap semiconductors which are lattice matched to silicon. Of the two, ZnS is a preferable choice for the front window layer, since the bandgap of 3.6 eV results in nearly complete transparency to the solar spectrum. The slightly narrower bandgap of GaP could result in as much as 10% reduction in I_{sc} unless the layer is extremely thin.

ZnS is an excellent AR coating material, with a measured refractive index of 2.2 to 2.3 for the films we deposited. It can only be doped n-type. We have grown ZnS heterojunctions onto solar cells by vacuum evaporation [ref. 4]. Figure 6 shows a typical cell quantum efficiency. An elevated substrate temperature is required for growth; this result was done with the substrate temperature of 450° C. The growth rate was about 100Å/min. This was done on a textured surface; similar results were also obtained on planar (100) surfaces. Three quantum efficiency curves are shown, that of the cell with an oxide passivation, that of the same cell with the oxide stripped, and that of the same cell again, after ZnS was deposited. The lowered surface recombination can be seen in the increased response at short wavelengths and in an increased open circuit voltage compared to the bare cell. S does not appear to be quite as low as the value obtained by thermal oxidation, although it is considerably better than that obtained on the bare surface. No decrease is seen in long wavelength response, indicating no degradation in bulk minority carrier lifetime.

Similar reductions of surface recombination velocity have been shown for films of ZnS and GaP on Si grown at Spire Corporation by MO-CVD [ref. 15,16]. Figure 7 shows the spectral response of a GaP coated cell compared to a control cell. Growth temperature here was 675° C. The absorption cut-on of the GaP is quite clear. When the curves are corrected for absorption in the GaP, the increase in short-wavelength quantum efficiency is quite clear. Again, no decrease is seen in the bulk lifetime

We expect that lower surface recombination velocity can be achieved with improvements in ZnS deposition methods. If this is not achieved, however, an alternate structure is proposed where a thermal oxide is grown on the surface and holes etched at small-area spots for ZnS growth where the contacts are to be made.

Cell Performance Modelling

Solar cell performance was modelled using a computer program that calculated a four-layer solution to the transport equations, based on the analyses of Wolf [ref. 17], Godlewski [ref. 18], and others. Sample calculations were also run with a finite element simulation [ref. 19] to check the model validity. Figure 8 shows results of computer modelling of advanced cell performance at AM0. The cell modelled was a n on p configuration, with $x_j = 1\mu$, emitter doping $10^{19}/cm^3$, and base doping $10^{17}/cm^3$. Representative doping levels were chosen to avoid extremes of heavy-doping and bandgap narrowing; the junction depth and doping was not optimized for the thin cell. In all of the cases shown the front and back surfaces were assumed to be passivated with $S=10$ cm/sec. The model neglects external losses such as grid coverage, reflection, etc., which in any case will presumably be small, due the use of textured front surface and zero grid-shadow geometry. The effect of light trapping is to increase the peak efficiency of the cell and to decrease the optimum cell thickness.

Radiation damage was modelled by assuming diffusion length degradation according to the formula [ref. 20]:

$$L^{-2} = L_o^{-2} + K_L \Phi \quad (2)$$

where Φ is the radiation fluence. For 1 MeV electrons, the value for K_L assumed was $5 \cdot 10^{-9}$, a value typical of the highly doped substrates modelled. Figure 9 shows the cell power after a

radiation dose of 10^{15} electrons/cm². After radiation damage the thin cells have considerably higher power than the thick ones. The 2μ cell retains 77% of its initial power after 10^{15} electrons/cm², corresponding to roughly 20 years in geosynchronous orbit. Greater radiation fluences result in even greater advantage to the thin cells.

An important figure of merit for space solar cells is the power to weight ratio, or specific power. Figure 10 shows the comparative specific power of these cells after irradiation, assuming a 50μ thick coverglass. Using thin cells and covers, it should be possible to achieve EOL cell specific power targets of well over 1000W/Kg.

Conclusions

Ultra-thin cells with light trapping and surface passivation can increase the efficiency and radiation tolerance of silicon cells markedly. A 2μ thick light-trapping cell remains over 18% efficient after the equivalent of 20 years in geosynchronous orbit. Including a 50μ thick coverglass, the thin cells had specific power after irradiation over ten times higher than the baseline design.

Acknowledgements

I would like to thank some of the people who contributed to the results presented here, in particular Stan Vernon, Patricia Sekula, Chris Keavney and Mark Spitzer at Spire, and Roland Beaulieu and Joseph Loferski at Brown.

**Portions of this work were done while the author held a National Research Council Research Associateship at NASA Lewis Research Center. Other portions were done at Brown University in collaboration with Spire Corporation, supported in part by DOE.*

References

- [1] R.A. Sinton et al., *18th IEEE Photovoltaic Specialists Conference*, p. 61-65 (1985)
- [2] M.A. Green, S.R. Wentham and A.W. Blakers, *19th IEEE Photovoltaic Specialists Conference*, 6-12 (1987).
- [3] M.B. Spitzer, Ph.D. Thesis, Brown University; M.B. Spitzer et al., *14th IEEE Photovoltaic Specialists Conference*, 375-380 (1980).
- [4] E. Yablonovitch and G.D. Cody, *IEEE Trans. Electron Dev.*, ED-29:2, 300 (1982).
- [5] D. Redfield, *Appl. Phys. Lett.*, **35** 11, 647-648 (1974).
- [6] G.A. Landis, Cross-grooved Solar Cell, U.S. Patent No. 6,608,451 (1986).
- [7] P. Campbell and M.A. Green, *J. Appl. Phys.*, **62** 1, 243-249 (1987).
- [8] G.F. Garlich and D.R. Lillington, *Space Photovoltaic Research and Technology 1986*, NASA CP 2475, 87-97, (1986).
- [9] P.G. Borden and R.V. Walsh, *Appl. Phys. Lett.*, **41** 1, 649-651 (1982).

- [10] M.A. Green et al., *19th IEEE Photovoltaic Specialists Conference*, 49-52 (1987).
- [11] F.A. Lindholm et al., *Solid State Electronics* **23**, 967-971 (1980).
- [12] M.B. Spitzer et al., *17th IEEE Photovoltaic Specialists Conference*, 398-402 (1984); L.C. Olsen et al., *17th IEEE Photovoltaic Specialists Conference*, 403-408 (1984); A. Rohatgi et al., *17th IEEE Photovoltaic Specialists Conference*, 409-414 (1984).
- [13] G.A. Landis, Ph.D. Thesis, Physics Department, Brown University (1988);
- [14] C. Case et al., *19th IEEE Photovoltaic Specialists Conference*, 398 (1987).
- [15] P. Sekula et al., "Reducing the Surface Recombination Velocity of Silicon Solar Cells", *Spire Corporation, Final Report for U.S. Department of Energy*, July 1987.
- [16] M.B. Spitzer, S. M. Vernon, and C.J. Keavney, "Development of Gallium Phosphide Heteroface Back Surface Field Structures", *Spire Corporation, Final Report for NASA Lewis Research Center Contract NAS3-24642*, October 1986.
- [17] M. Wolf, *14th IEEE Photovoltaic Specialists Conference*, 563-568 (1980).
- [18] M.P. Godlewski, C.R. Baraona, and H.W. Brandhorst, Jr., *10th IEEE Photovoltaic Specialists Conference*, 40-49 (1973).
- [19] PC-1D Computer Program, Available from Iowa Microelectronics Center. See D.T. Rover, P.A. Basore and G.M. Thorson, *18th IEEE Photovoltaic Specialists Conference*, p. 703 (1985).
- [20] *Solar Cell Radiation Handbook*, Third edition, JPL Publication 82-69 (1982).

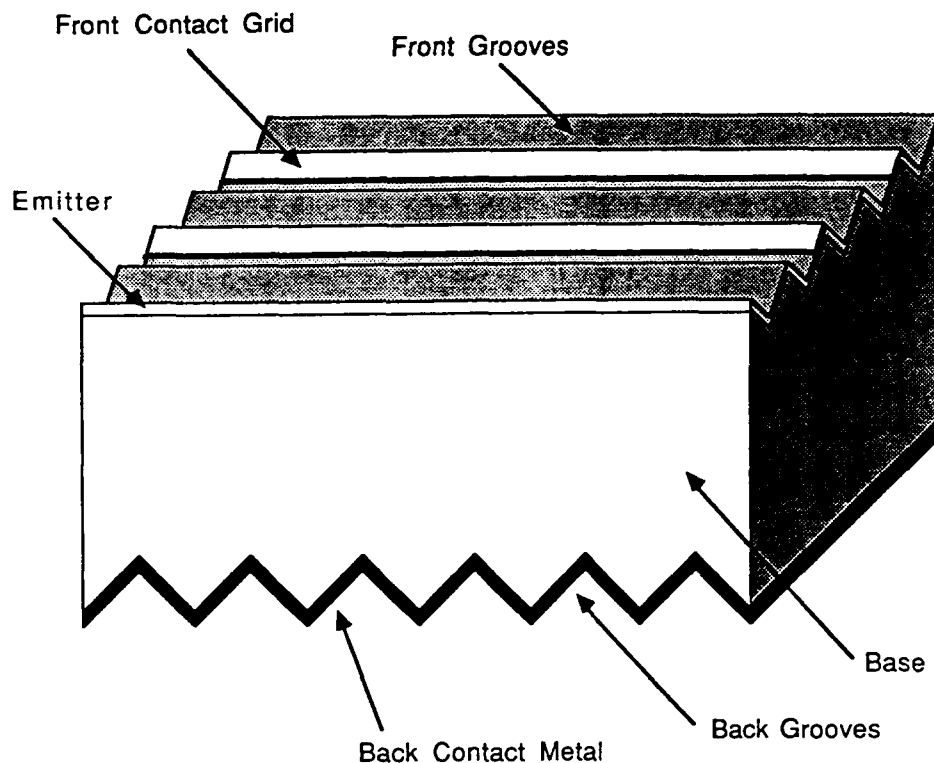


Figure 1. Schematic of solar cell incorporating cross-grooved light-trapping geometry.

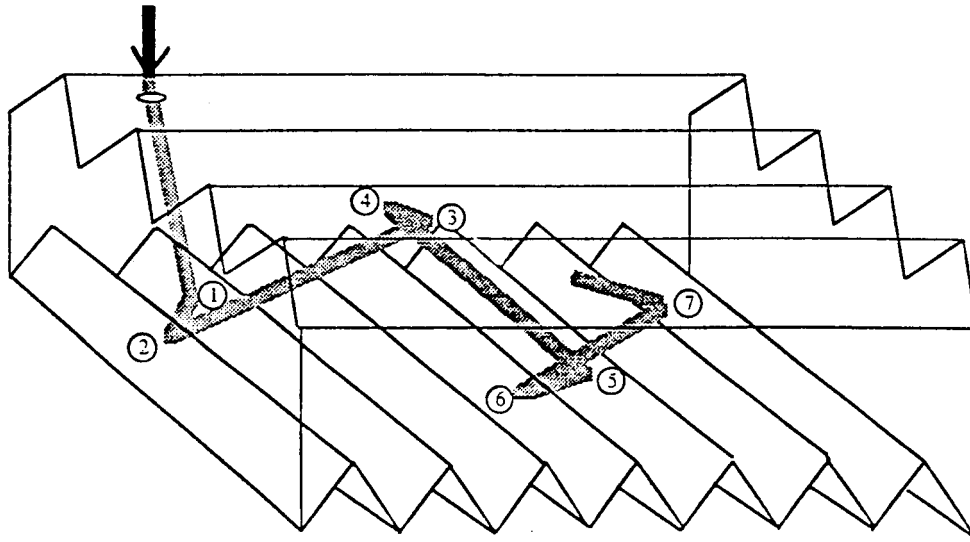


Figure 2. Typical ray passage in cross-grooved geometry, showing typical light path for first two passages through cell.

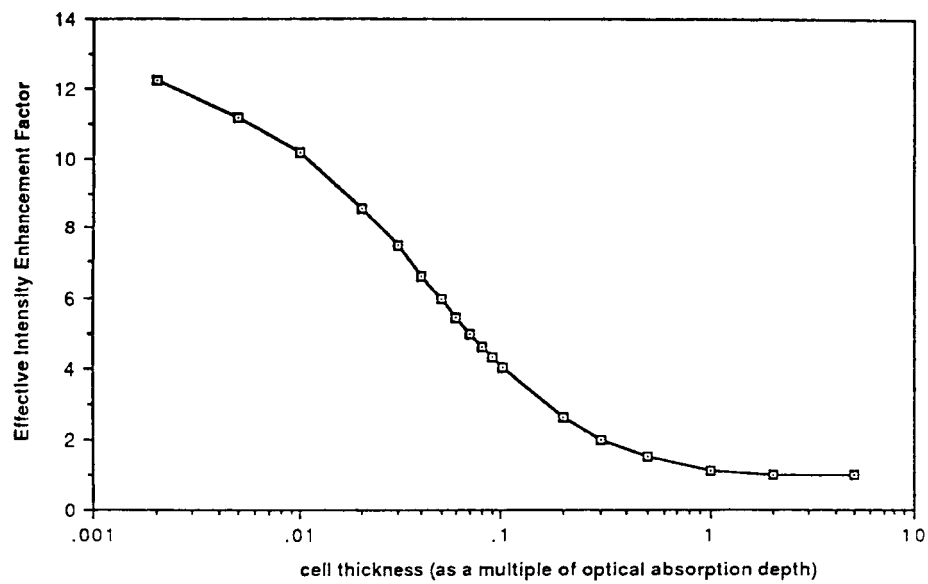


Figure 3. Effective intensity enhancement due to geometrical light trapping (not including effects of oblique passage or BSR) as a function of αT .

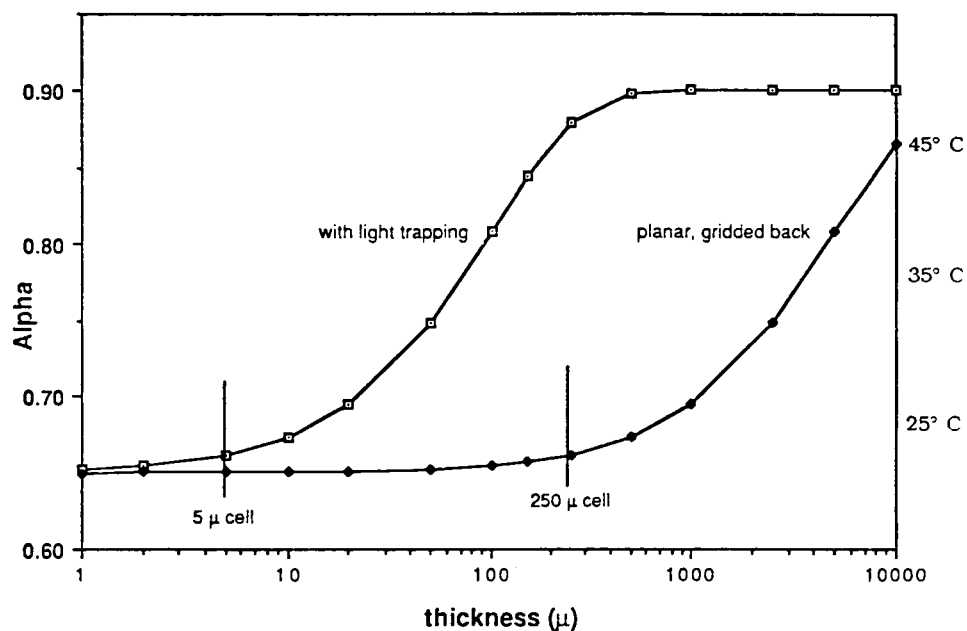


Figure 4. Idealized thermal α versus cell thickness for light trapping cell and gridded back contact cell.

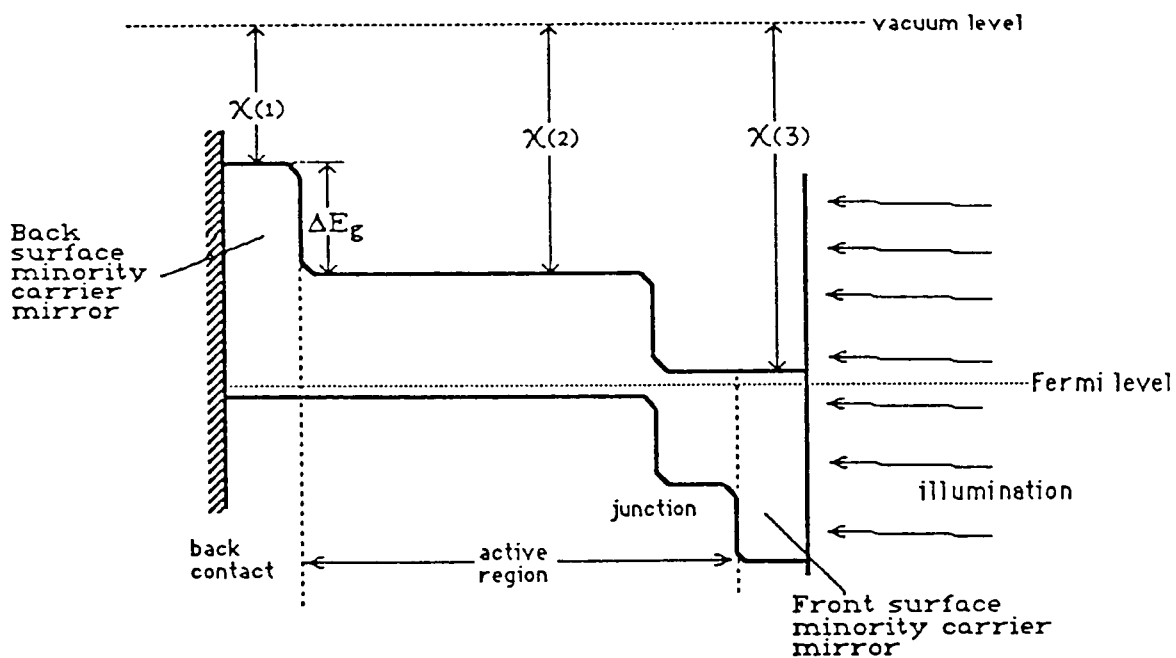


Figure 5. Idealized band diagram for heterojunction passivated solar cell.

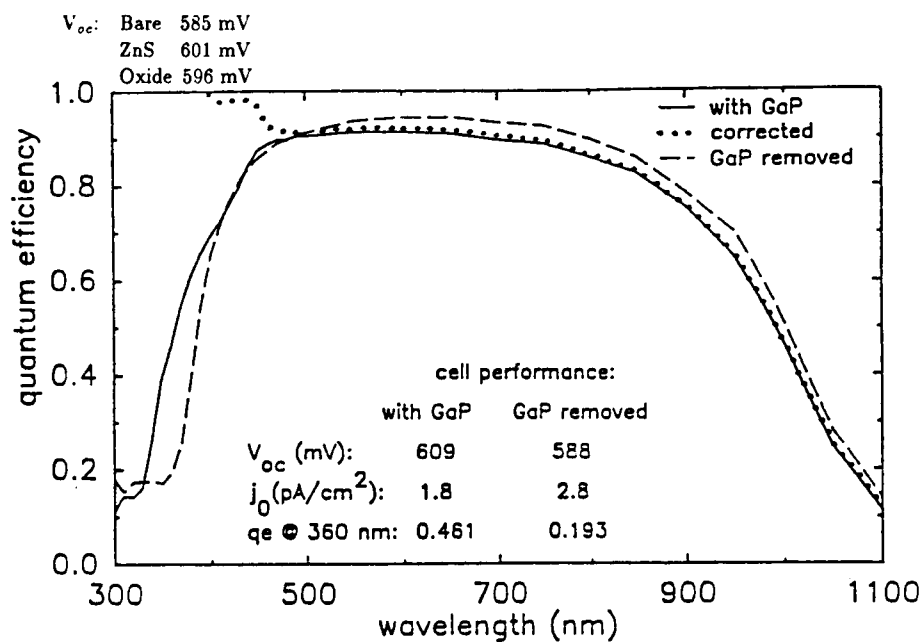


Figure 6 (External) Quantum Efficiency of Si cell with zinc sulfide heterojunction window grown by vacuum deposition, showing response of bare cell, cell with thermal SiO_2 , and cell with ZnS window (measurement courtesy Spire Co.)

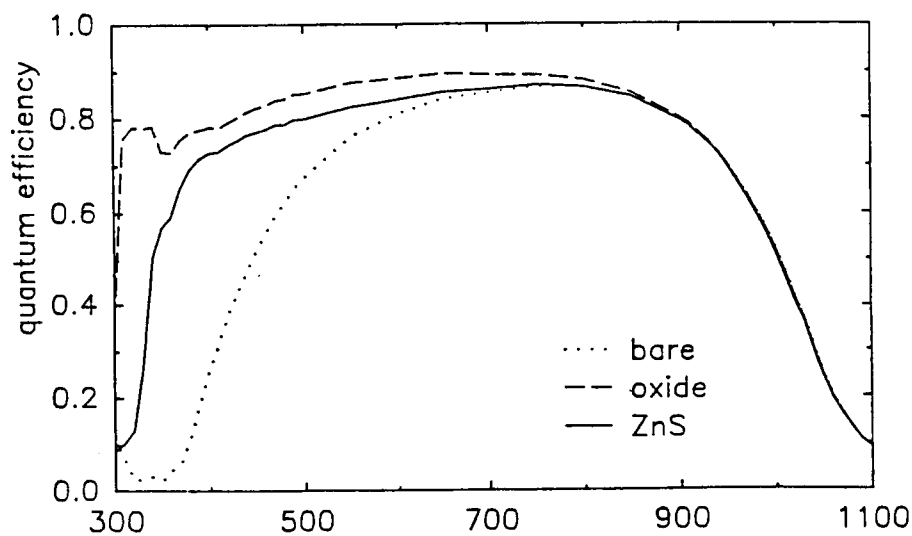


Figure 7. (External) Quantum Efficiency of Si cell with MO-CVD deposited gallium phosphide heterojunction window, showing response of bare cell, cell with GaP, and cell with GaP after correction for absorption in window layer (figure courtesy Spire Co.).

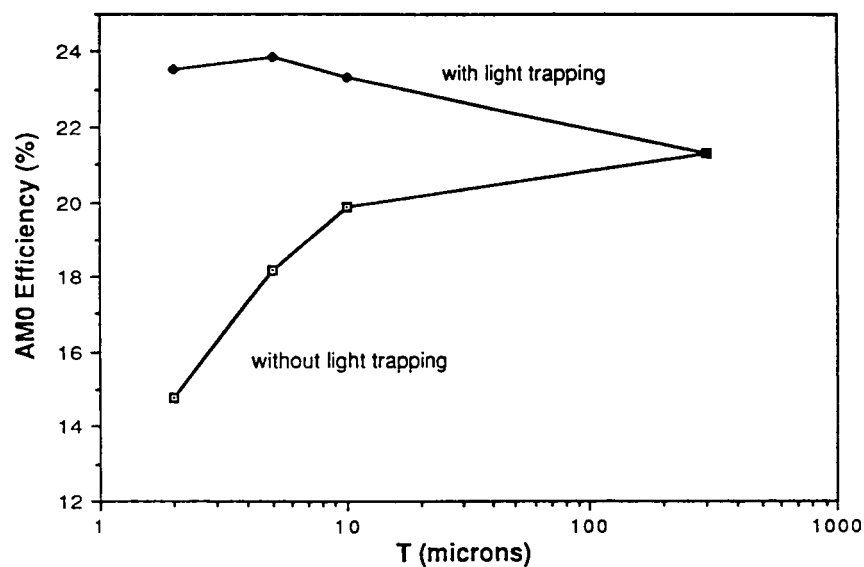


Figure 8. Calculated AMO Efficiency versus thickness for Si cells with and without light trapping.

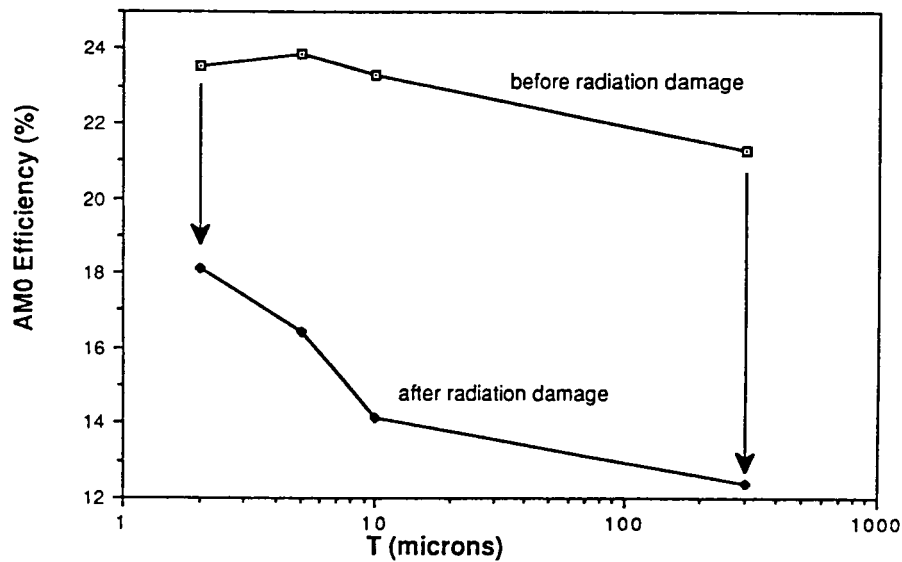


Figure 9. Calculated AMO Efficiency versus thickness for Si cells with light trapping, before and after 10^{15} 1-MeV electron/cm² irradiation.

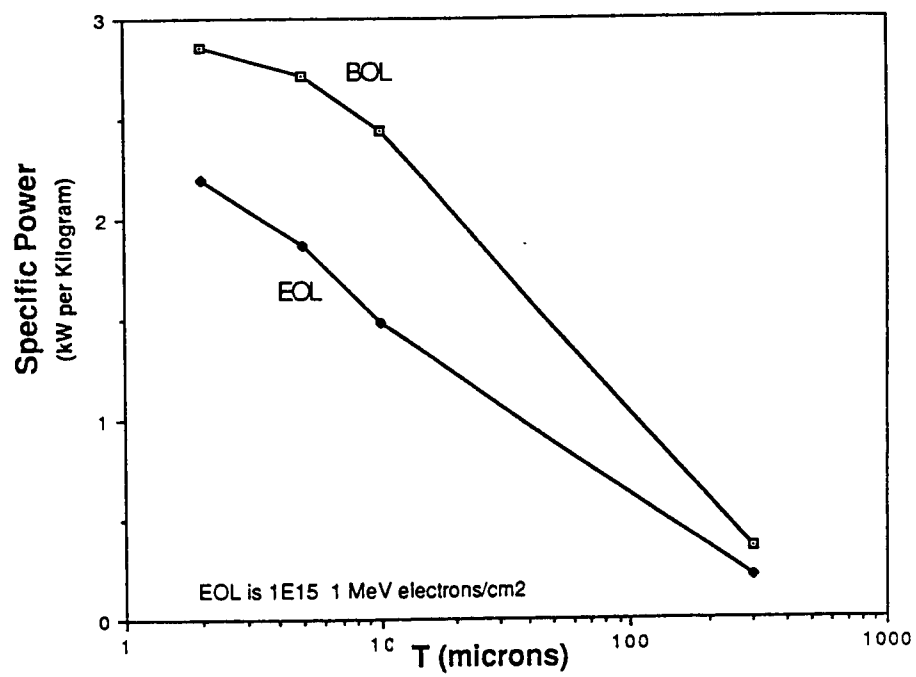


Figure 10. Cell specific power as a function of thickness, at beginning of life and after 10^{15} 1-MeV e^-/cm^2 (includes $50\ \mu$ glass cover).

Deployable Aerospace PV Array Based on Amorphous Silicon Alloys

Joseph J. Hanak, Lee Walter, David Dobias and Harvey Flaisher

Sovonics Solar Systems, Inc.

a Subsidiary of Energy Conversion Devices, Inc.

1100 West Maple Road

Troy, MI 48064

Summary

We report the development of the first commercial, ultralight, flexible, deployable, PV array for aerospace applications. It is based on thin-film, amorphous silicon alloy, multijunction, solar cells deposited on a thin metal or polymer by a proprietary, roll-to-roll process. The array generates over 200 W at AM0 and is made of 20 giant cells, each 54 cm x 29 cm (1566 cm² in area). Each cell is protected with bypass diodes. Fully encapsulated array blanket and the deployment mechanism weigh about 800 g and 500 g, respectively. These data yield power per area ratio of over 60 W/m², specific power of over 250 W/kg (4kg/kW) for the blanket and 154 W/kg (6.5 kg/kW) for the power system. When stowed, the array is rolled up to a diameter of 7 cm and a length of 1.11 m. It is deployed quickly to its full area of 2.92 m x 1.11 m, for instant power. Potential applications include power for lightweight space vehicles, high altitude balloons, remotely piloted and tethered vehicles. These developments signal the dawning of a new age of lightweight, deployable, low-cost space arrays in the range from tens to tens of thousands of watts for near-term applications and the feasibility of multi-100 kW to MW arrays for future needs.

Extended Abstract

This report describes the development of an ultralight, deployable, photovoltaic (PV) array for aerospace applications, having performance capabilities one order of magnitude beyond the state of the art. Sovonics' approach in the design of this commercially available array is to use proprietary UltralightTM monolithic modules which are extremely lightweight, flexible, stowable and damage tolerant [ref.1]. They are based on thin-film, amorphous silicon alloy, tandem-junction solar cells deposited on a thin metal or polymer by a roll-to-roll process. The array structure is formed by patterning of continuous sheets of the solar cell material into a matrix of cells interconnected in series and parallel.

The specific objective was to design and fabricate a commercial PV array generating 200 W at AM0 for applications in lightweight space vehicles and high altitude balloons. The array design which was used in successful fabrication consisted of 20 giant solar cells, each measuring 54 cm x 29 cm (1566 cm² in area). Each cell is fully protected with bypass diodes to prevent damage upon partial shading or cell mismatch. The array is stowable, deployable and self-supporting upon deployment. Fully encapsulated array blanket and the deployment mechanism weigh 800 g and 500 g, respectively. These performance characteristics include a power per area ratio of 60 W/m², specific power of 250 W/kg (4kg/kW) for the blanket and 154 W/kg (6.5 kg/kW) for the power system, including the array and the deployment and support mechanism. This system performance is at least one order of magnitude higher than any known aerospace PV power system. The use

of the giant cells has been made possible by the recent Sovonics development of a novel means of eliminating all shorting defects between the top and bottom electrodes, which makes possible the fabrication of single cells of virtually unlimited area.

When stowed, the array is rolled up to a diameter of less than 7 cm and a length of 1.11 m. It can be deployed quickly to its full area of 2.92 m x 1.11 m. The array is suitable for applications such as lightweight space vehicles, high altitude balloons, remotely piloted vehicles and tethered vehicles. Extension to higher power arrays is readily achievable.

Higher array power density can be anticipated for future arrays by utilizing other technological achievements which have been reported by Sovonics. These include active area conversion efficiency of 13% at AM1.5 and 10% at AM0 for triple-junction, dual-gap test cells, and a specific power of 2.4 kW/kg and power-to-volume ratio of 6.4 MW/m³ for 10-watt unencapsulated modules. These devices are well suited to a space environment since it has also been shown that they have a 50 to 100 times higher resistance to MeV proton radiation for a-Si alloy cells than for silicon and GaAs crystalline cells.

The development of this first commercial amorphous silicon alloy aerospace PV array signals the arrival of a new generation of very lightweight, deployable, low-cost arrays in the range from tens to tens of thousands of watts for near-term applications and the feasibility of PV arrays in the multi-100 kW to MW range for future space needs.

One such array had the following AM0 performance data calculated from results measured at AM1.5 and temperature of ca. 35°C: Power = 207 watt

$$V_{mp} = 25 \text{ V}$$

$$I_{mp} = 8.3 \text{ A}$$

$$\text{Fill factor} = 0.57$$

where mp denotes the maximum power point.

* This work was sponsored in part by the Defense Nuclear Agency under RDT&E RMSS Code B 4693 C RL RB 00046 RAEV 3230 A B 7660 D SF SB 00043 RAEV 3230 A.

References

- [1] J. J. Hanak, Englade Chen, C. Fulton A. Myatt, and James R. Woodyard, "Ultralight Amorphous Silicon Alloy Photovoltaic Modules for Space Applications", NASA Conference Publication 2475, *Space Photovoltaic Research and Technology (SPRAT)*, (1986).

Session 3
Heteroepitaxial Cells

PRECEDING PAGE BLANK NOT FILMED

High Efficiency GaAs-Ge Tandem Solar Cells Grown by MOCVD

S.M. Vernon, S.P. Tobin, C. Bajgar, V.E. Haven, and L.M. Geoffroy

Spire Corporation

Bedford, MA 01790

D.R. Lillington

Spectrolab, Inc.

Sylmar, CA 91342

R.E. Hart, Jr.

NASA Lewis Research Center

Cleveland, OH 44135

Introduction

High conversion efficiency and low weight are obviously desirable for solar cells intended for space applications. One promising structure is GaAs on Ge. The advantages of using Ge wafers as substrates include the following:

- high efficiency: by forming a two-junction tandem cell
- low weight: superior strength allows usage of thin (3 mil) wafers
- good substrate for GaAs: is lattice matched, thermal expansion matched, and available as large-area wafers.

Experimental

The cell structure studied in this work is shown schematically in figure 1. The GaAs and GaAlAs layers are grown by metalorganic chemical vapor deposition (MOCVD) in a SPI-MO CVDTM 450 system. This reactor deposits onto five two-inch diameter or three three-inch diameter wafers per run, with a typical thickness uniformity of $\pm 4\%$ over the entire batch. The substrates used in this work are two-inch Ge wafers, 0.008-inch thick, n-type, with a resistivity of 0.014 ohm-cm. The surface preparation before GaAs growth consists of scrubbing the surface with a modified commercial cleanser, etching the wafer in a $\text{NH}_4\text{OH}-\text{H}_2\text{O}_2-\text{H}_2\text{O}$ mixture, rinsing in deionized water and a final blow dry in filtered N_2 . The bottom cell (Ge p-n junction) is formed by in-diffusion of Ga and As from the GaAs layer growth. The As diffuses faster than the Ga, but since Ga has a higher solid solubility at the growth temperature, a p-type Ge top layer is formed. Measured and calculated Ga and As profiles in the Ge are shown in figure 2. The Ge junction profile is controlled by the time-temperature schedule used during growth of the top cell. The basic MOCVD growth parameters used are listed in table 1. The Ge wafers, before being subjected to growth of the GaAs top cell, are

PRECEDING PAGE BLANK NOT FILMED

first coated on the backside with MOCVD-grown GaAs to minimize autodoping effects. The device fabrication tests are listed in table 2, and the cell size used in this work is 2 cm \times 2 cm.

Ge Autodoping

The high vapor pressure of Ge causes the vapor transport of Ge atoms from hot, exposed Ge surfaces (typically the back of the wafer) to the growing film. In the MOCVD growth of GaAs on Ge these atoms are incorporated into the GaAs as donors, which can cause major problems by compensating the acceptors in the p-type regions of the cell (emitter, window, and cap layers). A straight-forward solution to this problem is to coat the back of the Ge wafers before growing the cell structure. We have found that a few microns of MOCVD-grown GaAs is an effective coating for this purpose. The results of one of our early studies of this problem are displayed in figure 3. The inset shows a typical Polaron doping profile of autodoped GaAs grown on Ge. The doping level at the GaAs surface is not a function of how thick the grown layer is. This figure shows that the autodoping level for GaAs on Ge is a strong function of growth temperature, but can be reduced dramatically by the GaAs back-side coating.

Solar Cell Results

The efficiency-measurement I-V curve for our best GaAs-Ge cell is shown in figure 4. This measurement was performed at NASA Lewis Research Center through the courtesy of R.E. Hart, Jr. The 1-sun AM0 efficiency value of 21.7% is the highest reported to date for a GaAs-Ge cell and for a two-terminal monolithic tandem cell. The AM1.5 1-sun measurement of this cell at Spire yields an efficiency of 24.3%, and at SERI yields a value of either 24.4% or 20.2% depending on the solar simulator used. These data point out the extreme sensitivity of tandem cell efficiency to the exact spectrum of the incident radiation, and improved methods of testing tandem cells are currently being developed at the national laboratories.

Discussion

To understand the operation of these cells, we first examine the quantum-efficiency curve, figure 5. The data were measured without light or voltage biases. The spectral response is identical to that of a good GaAs cell, with negligible response indicated from the Ge. The Ge cell does not contribute because at wavelengths beyond 870 nm the high-quality GaAs junction is turned off, blocking current generated in the Ge cell. (In cases where the GaAs junction is short-circuited, we do see a long-wavelength response characteristic of Ge). The Ge junction, in contrast, is leaky, as indicated by its low V_{oc} (about 0.2 V), and does not interfere with measurement of the GaAs response. Efforts to measure the Ge response by light-biasing the GaAs cell have not been successful yet, but are continuing. We believe that the Ge cell is in fact generating a large photocurrent, and this accounts for the relatively high measured fill factor. If the GaAs and Ge cells were seriously current-mismatched, then we could not measure both high short circuit current and high fill factor.

We have obtained several types of data showing the existence of a p/n junction in the Ge wafer, supporting our tandem cell hypothesis. These include spreading resistance doping profiles of the Ge, cross-sectional EBIC line scans, and temperature coefficient measurements.

Figures 6 and 7 show doping profiles in the Ge substrate determined by spreading resistance after growth of the GaAs cell. A highly-doped n-type region extends about 6 microns into the Ge substrate, which has a background doping of about $5 \times 10^{17} \text{cm}^{-3}$. The n-type doping profile is caused by rapid in-diffusion of arsenic during growth of the GaAs cell. A more detailed look at the profile near the GaAs interface (figure 7) reveals a very shallow but clear p-n junction in the Ge. As explained earlier, the p-type doping is from diffusion of Ga, which over-dopes the n-type As profile. This is the most direct evidence possible of a Ge p-n junction.

We have also detected the positions of the GaAs and Ge junctions by Electron Beam Induced Current (EBIC) line scans of cross-sectioned cells. Figure 8 shows such a line scan superimposed on a simple diagram of the sample. The two peaks in the EBIC scan correspond to the GaAs and Ge junctions. From the scale on the original micrograph, these occur at depths below the surface of about 0.7 and 6.2 microns respectively. (Note that the junction depth is about 0.2 microns shallower in the finished cell of figure 8 compared to the as-grown material of figures 6 and 7, due to removal of the GaAs contact layer and addition of the antireflection coating). This data would indicate a junction depth within the Ge of about 1 micron, larger than what was obtained from spreading resistance. At this time we do not understand the discrepancy. However, the important point is that we do see a second junction within the Ge wafer by both techniques. As a point of interest, it was necessary to forward bias the cell to 775 mV in order to detect the Ge response. This is the same problem encountered in the quantum efficiency measurement: unless the GaAs junction is turned on, its high resistance blocks current generated in the Ge.

Temperature coefficient measurements made at SERI also imply a GaAs/Ge tandem. Table 3 summarizes the temperature coefficients of efficiency, V_{oc} , I_{sc} , and FF from 10 to 80°C. Data are shown for the GaAs/Ge cell of figure 1 and for a GaAs/GaAs control cell. The temperature coefficient of the GaAs/Ge cell is more than twice that of the GaAs cell, because Ge, with its small band gap, is much more temperature sensitive than GaAs. The V_{oc} values extrapolated to zero Kelvin are 1.519 V for the GaAs cell and 2.299 V for the GaAs/Ge cell. The difference is roughly the band gap of Ge, again as expected for a series tandem.

Given that we have a series-connected monolithic tandem cell of GaAs and Ge, it is somewhat surprising that the tandem does not appear to be seriously current-limited by the Ge subcell. An earlier report of a mechanically-stacked tandem achieved only 7.86 mA/cm² from the Ge cell at AM1.5 [ref.1]. However, our calculations show that if all light absorbed in a single pass were collected in the Ge, a maximum one-sun AM0 photocurrent of 38.7 mA/cm² (at 25°C and 39.7 mA/cm² at 75°C) is possible under a GaAs filter. The fact that our best cells are not current limited implies very good collection in the Ge subcell (or a very red-rich simulator).

We have seen indications of Ge current-limiting in some cells, particularly under AM1.5 measurement conditions. The reason is the infrared absorption bands in the AM1.5 spectrum, which do not affect the GaAs cell but reduce the current of the Ge cell. Figure 9 shows the efficiency curves of the same cell measured on two different simulators at SERI. The V_{oc} and J_{sc} are nearly identical, but the fill factors are very different. The curve with the dent in the knee is for the simulator with less infrared light, giving a lower Ge photocurrent. The reason that I_{sc} is not affected is that the Ge cell is leaky, and breaks down at very low reverse voltages. Even though the Ge cell is driven into reverse bias by the current mismatch, it causes little voltage loss.

To summarize our understanding of the high-efficiency GaAs/Ge cell, a p-n junction is created in the Ge substrate as part of the GaAs cell growth process. This junction is in series with the GaAs junction, creating a monolithic tandem structure. The Ge junction is leaky enough in the reverse direction that it does not limit the short-circuit current of the series-connected tandem. However, it can limit the fill factor if the short-circuit current of the Ge subcell is too low. Finally, since the polarities of the GaAs and Ge junctions are the same, their open circuit voltages add.

Summary

A 4 cm² GaAs-Ge two-terminal monolithic tandem cell grown by MOCVD has demonstrated 21.7% efficiency measured at NASA (1-sun, AM0) and 24.3% measured at Spire (1-sun, AM1.5). The existence of a p-n junction in the Ge has been confirmed by spreading resistance probe, EBIC, and temperature coefficient data, and is explained by the diffusion properties of Ga and As in Ge. The top cell-bottom cell interconnect is accomplished by the GaAs-Ge tunnel junction which appears to be adequate for one-sun operation. The testing methodology for determining the absolute efficiency of two-terminal tandem cells needs improvement. Finally, the use of Ge substrates has been shown to be a viable route to achieving high-efficiency solar cells for space applications.

Reference

- [1] L.D. Partain, M.S. Kuryla, R.E. Weiss, R.A. Ransom, P.S. McLeod, L.M. Fraas and J.A. Cape, "26.1% Solar Cell Efficiency for Ge Mechanically Stacked Under GaAs," J. Appl. Phys., **62**, pp. 3010-3015, 1987.

Table 1. Growth Parameters

Sources:	TMGa, TMA1, AsH ₃
Dopants:	SiH ₄ (N) DMZn (P)
Pressure:	1 atm.
Main Flow:	5 slpm H ₂
Growth Rate:	4 μm/hr
Temperature:	700°C
V-III Ratio:	15:1

Table 2. Process Sequence for GaAs-Ge Solar Cell

1. Remove GaAs Back Coating
2. Evaporate Back Contact (AuAg)
3. Alloy Back Contact
4. Image-reversal Photolithography for Front Grid
5. Evaporate Front Grid (CrAuAg)
6. Liftoff
7. Sinter Contacts
8. Plate Metal (Au)
9. Photolithography for Mesa Etch
10. Mesa Etch
11. Selective Etch to Remove GaAs Cap
12. Evaporate AR coating ($\text{ZnS} + \text{MgF}_2$)

Table 3. Temperature Coefficients (ppm/deg C) of Efficiency, V_{oc} , I_{sc} , and FF Measured for GaAs/Ge and GaAs/GaAs solar Cells

Parameter	GaAs/Ge	GaAs/GaAs
V_{oc}	-3702	-1669
I_{sc}	+ 445	+ 246
FF	- 175	- 29
Eff	-3067	-1466

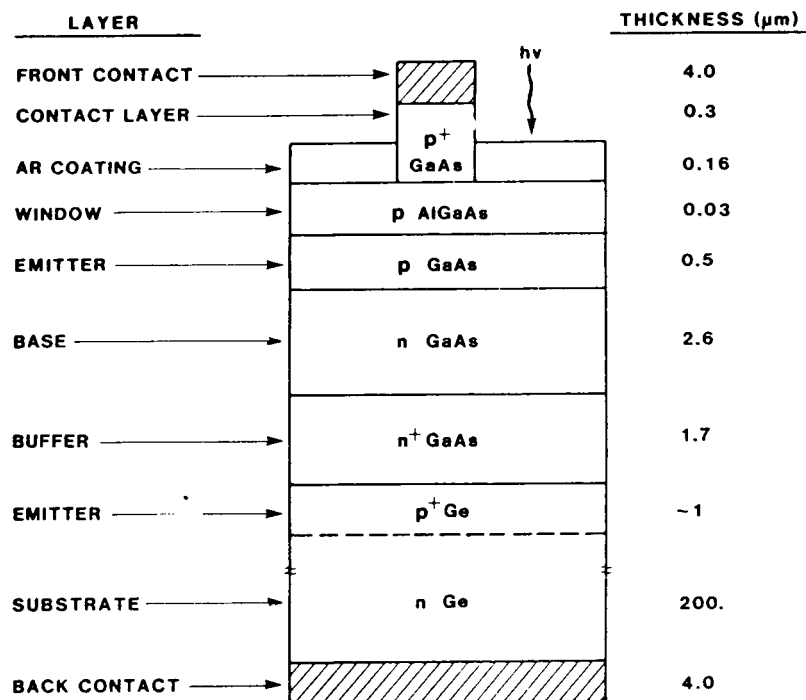


Figure 1. Structure of GaAs-Ge Tandem Solar Cell

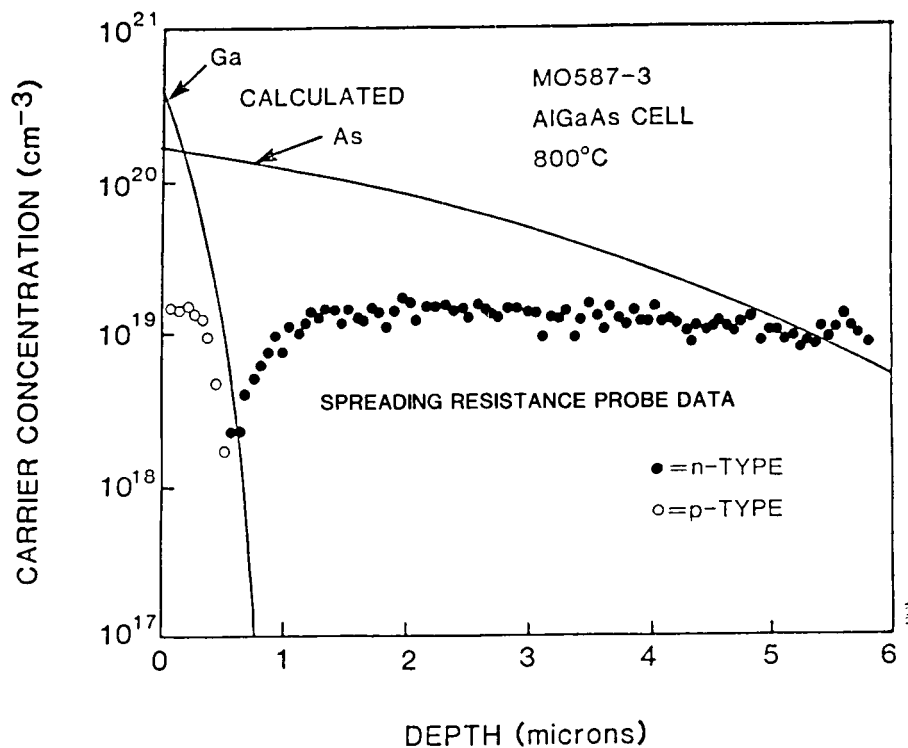


Figure 2. Doping Profile in a Ge Substrate after Growth of an AlGaAs Solar Cell at 800°C.

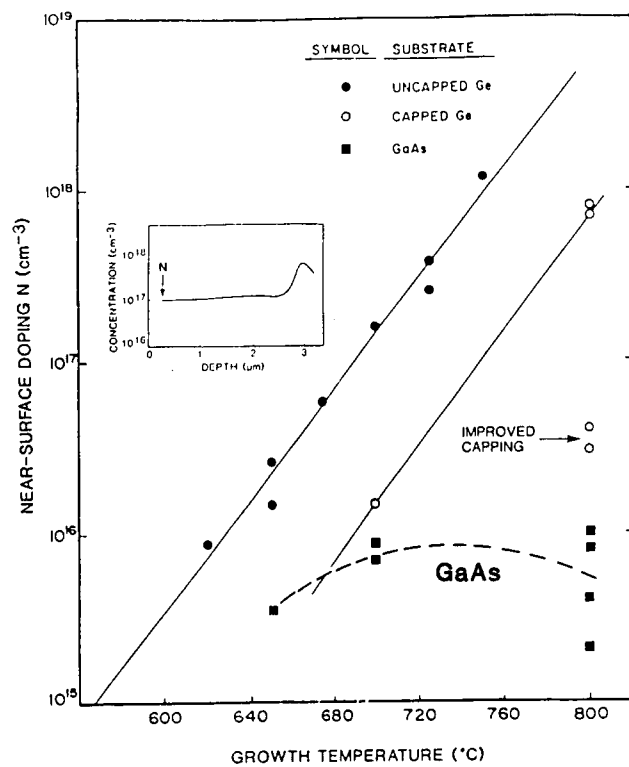


Figure 3. Autodoping of GaAs from Ge Substrate.

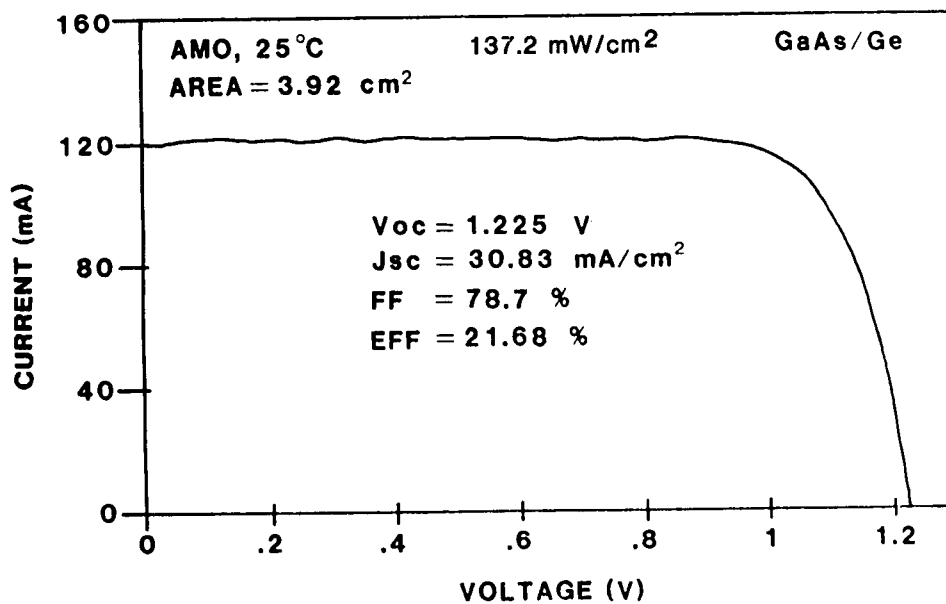


Figure 4. GaAs-Ge Tandem Cell Efficiency Measurement at NASA-Lewis.

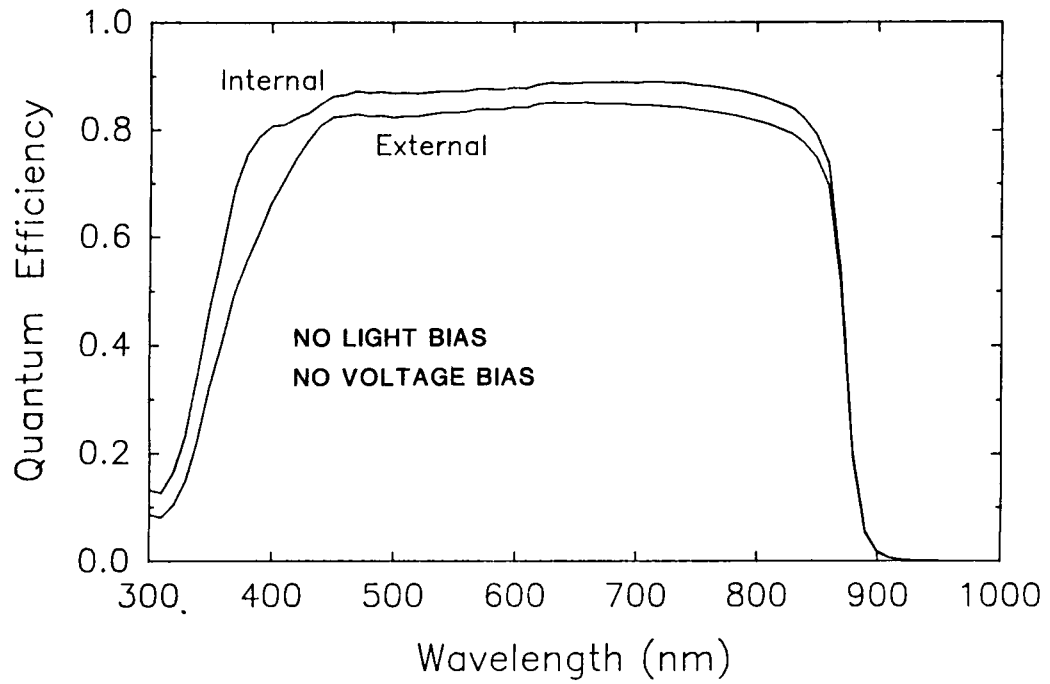


Figure 5. Measured Spectral Response of GaAs-Ge Tandem Cell.

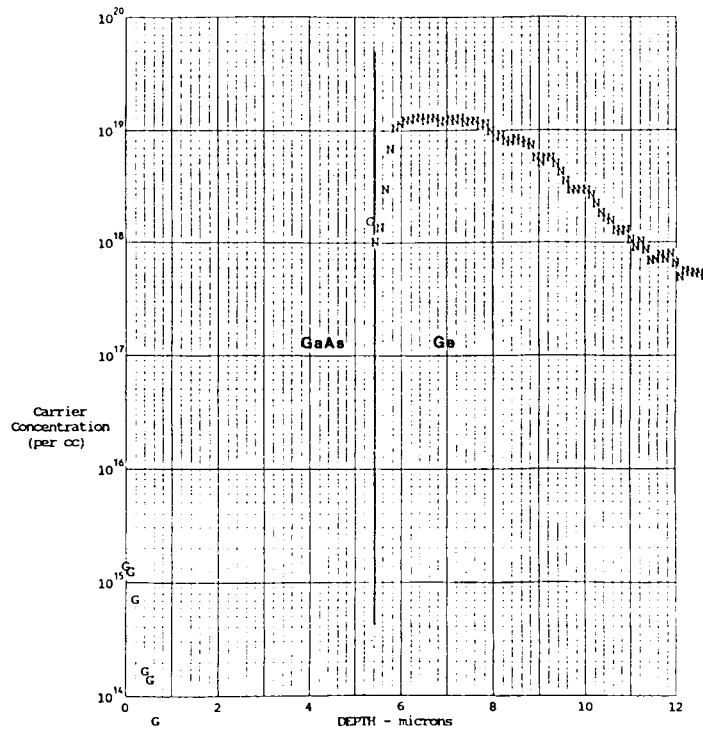


Figure 6. Doping Profile of the Ge Substrate after Growth of a GaAs solar Cell, Obtained by Spreading Resistance. The heavy n-type doping is caused by in-diffusion of arsenic from the GaAs.

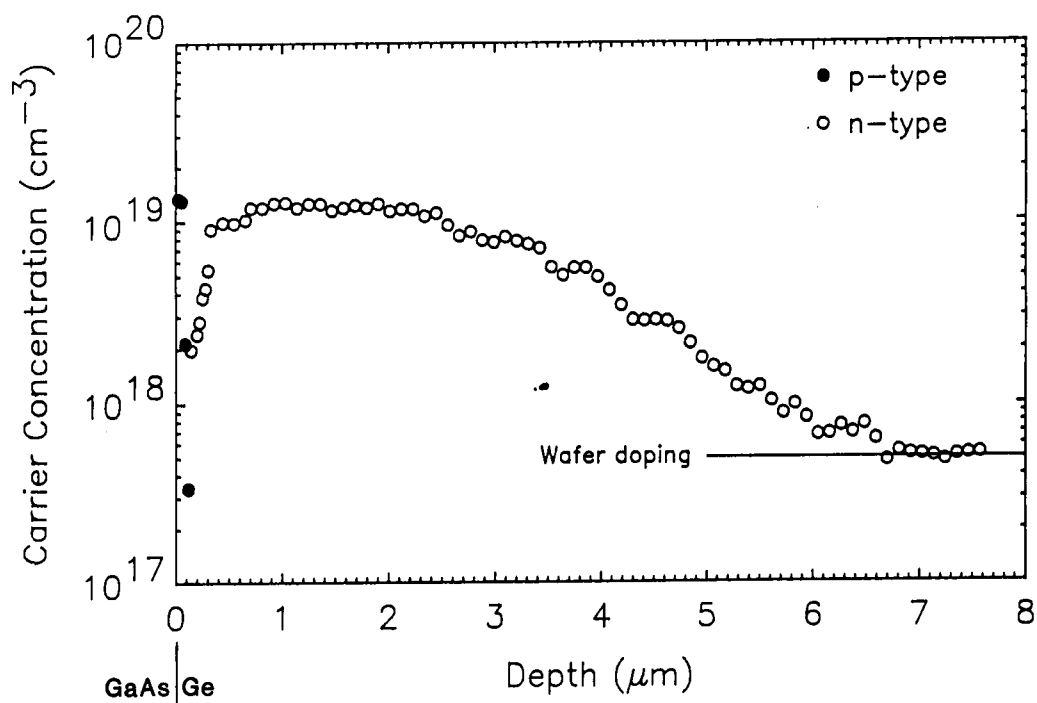
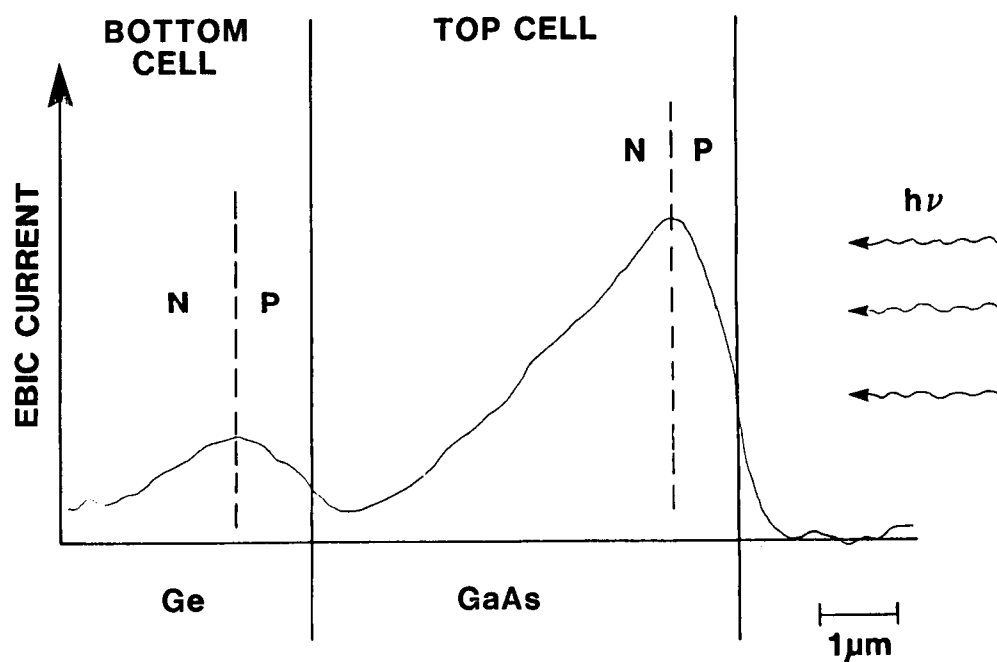


Figure 7. Spreading Resistance Probe Profile of Ge Bottom Cell.



MEASUREMENT COURTESY OF R. MATSON, SERI

Figure 8. EBIC Line Scan on Cross-Section of GaAs-Ge Tandem Cell.

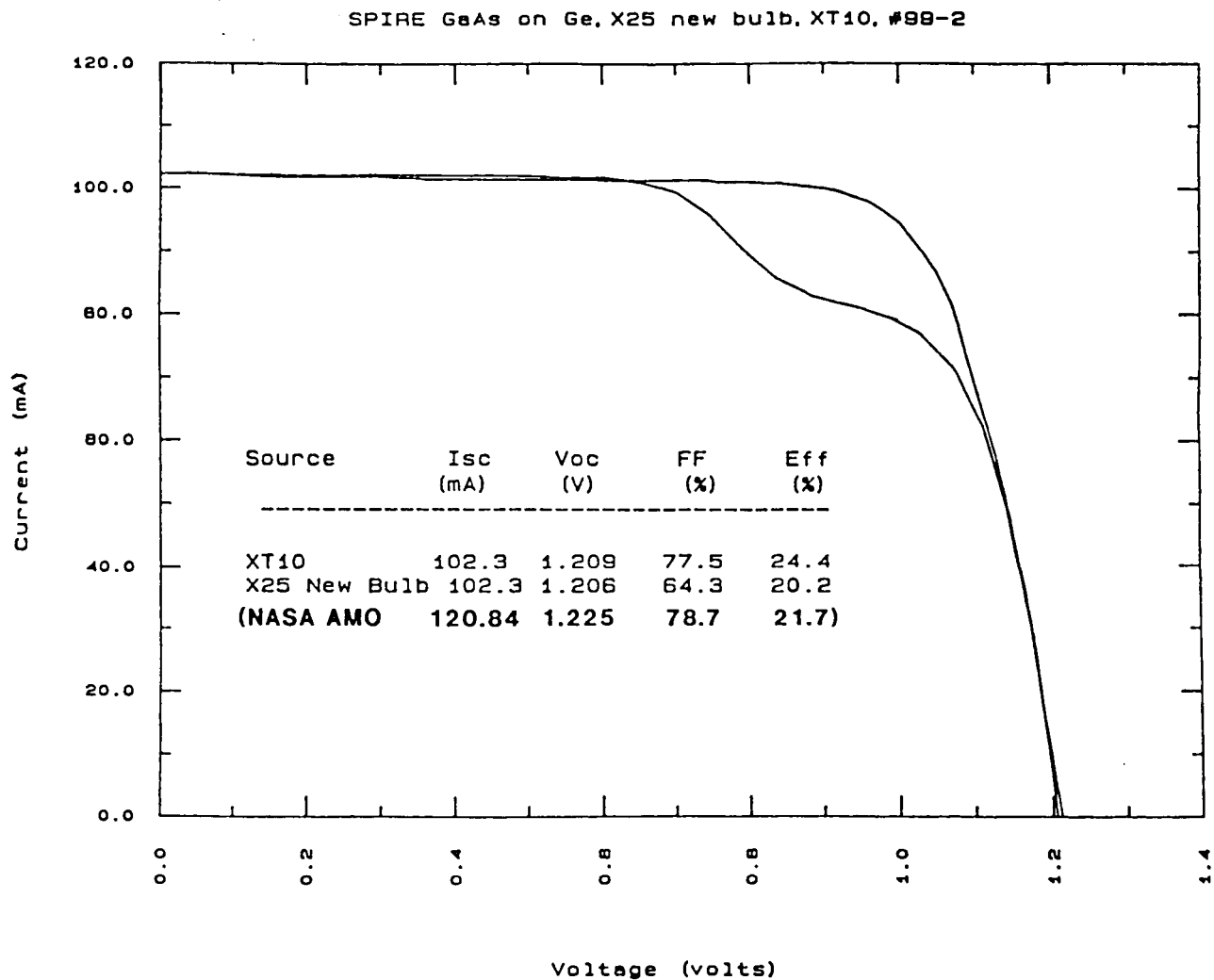


Figure 9. AM1.5 Efficiency Curves of a GaAs/Ge Solar Cell Measured on Two Different Simulators at SERI.

Response of Single Junction GaAs/GaAs and GaAs/Ge Solar Cells to Multiple Doses of 1 MeV Electrons

D. L. Meier, J. R. Szedon, and J. Bartko
Westinghouse R&D Center
Pittsburgh, PA 15235

M. A. Chung
Air Force Wright Aeronautical Laboratories
Wright-Patterson Air Force Base, OH 45433

Summary

A comparison of the radiation tolerance of MOCVD-grown GaAs/GaAs cells and GaAs/Ge cells was undertaken using 1 MeV electrons. Both types of cells were fabricated by the Applied Solar Energy Corporation under contract to the Air Force. The electron radiation was delivered in doses of $1 \times 10^{16} \text{ cm}^{-2}$ up to a total dose of $1 \times 10^{17} \text{ cm}^{-2}$ for GaAs/GaAs and a total dose of $7 \times 10^{16} \text{ cm}^{-2}$ for GaAs/Ge. Following each dose of $1 \times 10^{16} \text{ cm}^{-2}$, the cells were annealed at either 250°C or 300°C for one hour in nitrogen. It was found that the radiation tolerance of the GaAs/Ge cells was superior to that of the GaAs/GaAs cells. Because the primary effect of radiation is to decrease the diffusion length of the minority carriers in the emitter and the base of the cell, the short-circuit current density (J_{sc}) is the parameter affected most directly.

For GaAs/Ge cells annealed at 250°C, the value of J_{sc} measured under AM0 conditions decreased from $29.1 \pm 1.0 \text{ mA/cm}^2$ as-received to $19.6 \pm 1.2 \text{ mA/cm}^2$ after a total dose of $7 \times 10^{16} \text{ cm}^{-2}$. Thus, 67% of the initial value of J_{sc} was retained. For GaAs/GaAs cells annealed at 250°C, 56% of the initial value of J_{sc} was retained after the same dose, as the measured J_{sc} decreased from the initial value of $28.8 \pm 0.8 \text{ mA/cm}^2$ to $16.0 \pm 1.0 \text{ mA/cm}^2$. The results were similar for cells annealed at 300°C. After accumulating a total electron dose of $7 \times 10^{16} \text{ cm}^{-2}$, the GaAs/Ge cells retained 75% of their as-received value of J_{sc} ($29.3 \pm 1.0 \text{ mA/cm}^2$ to $21.9 \pm 1.0 \text{ mA/cm}^2$), while the GaAs/GaAs cells retained just 60% of their as-received value ($28.8 \pm 0.3 \text{ mA/cm}^2$ to $17.4 \pm 0.3 \text{ mA/cm}^2$).

Similar results were obtained for the efficiency of the two types of cells, although the initial efficiency of the GaAs/Ge cells ($13.4 \pm 1.4\%$) was less than that of the GaAs/GaAs cells ($16.5 \pm 0.8\%$). This difference in initial efficiency exists because the GaAs/Ge cells had a low fill factor (0.617 ± 0.038) associated with the interface between the GaAs layer and the Ge substrate while the GaAs/GaAs cells had a normal value of fill factor (0.774 ± 0.030).

In an attempt to examine in greater detail the causes for the observed radiation behavior, preliminary DLTS and EBIC measurements were made. Two deep levels were found to result from the electron radiation, and the concentration of these levels was reduced significantly by the annealing. The EBIC measurements, along with cross-sectional SEM views, enabled the determination of epi-layer thickness, junction depth, and hole diffusion length in the n-type base of the cells.

Introduction

GaAs solar cells offer the highest efficiency demonstrated to date for space applications, with measured values exceeding 20% (AM0, 137.2 mW/cm², 25°C) for cells having an area of 4 cm² [ref. 1]. Because GaAs substrates are somewhat fragile, the cell thickness must be appreciable (300 μm) in order for the cell to be durable. Cell weight is a concern because of the rather high density (5.32 g/cm³) for GaAs.

GaAs cells fabricated on Ge substrates are of interest because the Ge is a rugged material which can be thinned to 75 μm in order to reduce cell weight. In addition, the combination of GaAs on Ge offers the possibility of a tandem cell structure which could make more efficient use of the photons in the AM0 spectrum. GaAs and Ge are well matched both in lattice constant at 300 K (5.653 Å for GaAs and 5.646 Å for Ge) and in thermal expansion coefficient ($5.8 \times 10^{-6}/^{\circ}\text{C}$ for GaAs and $5.7 \times 10^{-6}/^{\circ}\text{C}$ for Ge). This means that high quality GaAs material can be expected in the epitaxial growth of GaAs on Ge substrates. Because GaAs is a direct bandgap semiconductor, only a thin layer (10 μm or less) is required for absorption of the AM0 photons.

The response of GaAs cells fabricated on Ge substrates (GaAs/Ge) to radiation has yet to be explored and compared to the response of GaAs cells fabricated on GaAs substrates (GaAs/GaAs). The purpose of this paper is to report on such a comparative study in which 1 MeV electrons were used to simulate the radiation in a space environment. The cells examined were fabricated by the Applied Solar Energy Corporation under contract to the Air Force. The electron irradiation, annealing, and cell parameter measurements were done at the Westinghouse R&D Center, along with DLTS and EBIC measurements on selected samples. A unique feature of this work is that the electron radiation was administered in doses of $1 \times 10^{16}\text{cm}^{-2}$ to a substantial total of $1 \times 10^{17}\text{cm}^{-2}$ for the GaAs/GaAs cells and to $7 \times 10^{16}\text{cm}^{-2}$ for the GaAs/Ge cells. After each dose, the cells were annealed at either 250°C or 300°C. Such an approach simulates a situation in which the cells are exposed to a heavy dose of radiation (perhaps by passing through the Van Allen belts) and the radiation damage incurred is partially annealed upon return to a base station.

Cell Structure

Both the GaAs/GaAs and the GaAs/Ge cell layers were grown by metal-organic chemical vapor deposition (MOCVD) at the Applied Solar Energy Corporation to form a p on n GaAs active region with an AlGaAs window layer for surface passivation. Layer thicknesses and doping densities for the GaAs/GaAs cell are given in Figure 1. The structure for the GaAs/Ge cell is similar, except that the substrate is Ge which is doped n-type with Sb. The cell is completed with the addition of an antireflective (AR) coating ($\text{TiO}_x\text{Al}_2\text{O}_3$) and contacts to the p-type GaAs emitter (Au Zn Au Ag) and to the n-type GaAs or Ge substrate (Au Ge Ni Au Ag). Further details concerning cell fabrication and structure can be found in references 2 and 3.

Radiation and Annealing Results

In a set of preliminary experiments, two GaAs/GaAs cells were irradiated with 1 MeV electrons and then annealed for 1 hour in nitrogen. It was found that below 200°C no significant increase in cell parameters was obtained and that above 300°C (up to 375°C) only marginal improvement was realized. It was decided, therefore, to carry out the annealing studies at 250°C and at 300°C.

An electron Van de Graaff accelerator at the Westinghouse R&D Center was used for the irradiation which took approximately six hours for a dose of $1 \times 10^{16} \text{cm}^{-2}$ (dose rate of $2.8 \times 10^{13} \text{cm}^{-2} \text{min}^{-1}$). During the irradiation, the cells were moved beneath the electron beam on a conveyor belt so that the temperature of the cells was kept below 40°C . Rapid and accurate dosimetry was accomplished by integrating the charge collected by a Faraday cup which was permanently affixed to the conveyor belt. The charge was directed to a capacitor for integration.

Four groups of cells were selected with six or seven cells in each group. There were two groups of GaAs/GaAs cells (one for the 250°C anneal and one for the 300°C anneal) and two corresponding groups of GaAs/Ge cells. Because the GaAs/Ge cells were not available at the beginning of the experiment, the first three doses of radiation were administered only to the GaAs/GaAs cells. Thus, the GaAs/GaAs cells accumulated a total dose of $1 \times 10^{17} \text{cm}^{-2}$ during the course of the study, while the GaAs/Ge cells accumulated only $7 \times 10^{16} \text{cm}^{-2}$. All available groups of cells were irradiated together, so that the GaAs/GaAs cells received their fourth increment of radiation at the same time that the GaAs/Ge cells received their first increment. All annealing was done for one hour in a nitrogen ambient.

The effect of each increment of radiation and of each annealing step on short-circuit current density and AM0 efficiency (135 mW/cm^2 , 27°C) for the four groups of cells are given in Figures 2, 3, 4, and 5. The data are plotted as averages for each group of six or seven cells, with error bars representing the standard deviation from the average value. A comparison of the GaAs/GaAs cell data with the GaAs/Ge cell data over the full range of radiation dose can be made from these Figures. In addition, key results are given in Table 1 for the four groups of cells as-received, after the first increment of radiation ($1 \times 10^{16} \text{cm}^{-2}$), after the first increment and anneal, and after the seventh increment ($7 \times 10^{16} \text{cm}^{-2}$) and anneal.

From Table 1 it can be seen that the as-received average values for J_{sc} and V_{oc} are quite similar for the GaAs/Ge cells and the GaAs/GaAs cells. However, the fill factor (FF) is considerably lower for the GaAs/Ge cells than it is for the GaAs/GaAs cells. This low FF is thought to be associated with the interface between the Ge substrate and the GaAs epi-layer [ref. 3]. The data of Table 1 show that the GaAs/Ge cells retain a greater fraction of their values of J_{sc} , V_{oc} , and efficiency through all phases of the radiation and anneal than do the GaAs/GaAs cells. In fact, the absolute efficiency of the GaAs/Ge cells exceeds that of the GaAs/GaAs cells after the seventh irradiation ($7 \times 10^{16} \text{cm}^{-2}$) and anneal. At this point (Table 1d), the GaAs/Ge cells annealed at 250°C retained 60% of their initial efficiency while their GaAs/GaAs counterparts retained only 42%. Similarly, for cells annealed at 300°C , the GaAs/Ge cells retained 68% of their initial efficiency while the GaAs/GaAs cells retained 48%.

After the first increment of radiation ($1 \times 10^{16} \text{cm}^{-2}$, Table 1b), the efficiency of the GaAs/GaAs cells dropped from 16.5% to 4.3%. Thus, only 26% of the as-received efficiency was retained. This is a greater degradation than has been reported in the past. In reference 4, 59% of the average initial efficiency (19.9% to 11.8%) of four MOCVD GaAs/GaAs p on n cells was retained after an exposure to 1 MeV electrons at $1 \times 10^{16} \text{cm}^{-2}$. The cells described in reference 4 had a p-type emitter thickness of $0.5 \mu\text{m}$. For the GaAs/Ge cells of Table 1b, 39% of the initial efficiency was retained after the first increment of radiation. In an attempt to understand in greater detail the differences between the GaAs/GaAs and the GaAs/Ge cells in this study, and also to understand the rather severe degradation experienced by the GaAs/GaAs cells, some preliminary deep level transient spectroscopy (DLTS) and electron beam induced current (EBIC) measurements were undertaken.

It might be mentioned in passing that a small additional group of four GaAs/GaAs cells was irradiated and annealed at 350°C . The average as-received efficiency of these cells was 17.0%. After the first increment of 1 MeV electron irradiation ($1 \times 10^{16} \text{cm}^{-2}$), the efficiency dropped to 29% of

its initial value. Annealing at 350°C for one hour in nitrogen raised the efficiency back to 83% of the initial value. After six increments of radiation and 350°C anneal (total dose of $6 \times 10^{16} \text{ cm}^{-2}$), the cells retained 67% of their initial efficiency with an average efficiency of 11.4%. This is to be compared with a retention of 51% of the initial efficiency for GaAs/GaAs cells annealed at 300°C, and with a retention of 42% for cells annealed at 250°C and subjected to the same total dose. This suggests that an anneal temperature of 350°C may be desirable.

DLTS Measurements

Capacitance DLTS samples were prepared by etching the AR coating from the cells and evaporating 50 nm of Ti and 500 nm of Au on the front surface of the cells using a planetary adapter. Contact between the evaporated metals and the cell emitter was made by way of the grid lines on the cell. Square pieces, 30 mils on a side, were cut from the back of the cell by a laser. These were mounted on T0-5 headers for the DLTS measurement, so the test devices were small p-n junction diodes rather than Schottky diodes. Such diodes had a soft breakdown at approximately 6 V reverse bias. At 4 V reverse bias, however, the leakage current was less than 10 μA , so these samples were suitable for DLTS measurements. The traps in the depletion region were filled with majority carriers when the reverse bias was pulsed from 4 V to 1 V.

Three GaAs/GaAs cells were examined by DLTS. Cell OP-27 had an efficiency of 17.4% (29.0 mA/cm², 1.002 V, 0.812 fill factor) when measured as-received. Cell OP-21, with an as-received efficiency of 17.3%, was measured after being irradiated by 1 MeV electrons with a dose of $1 \times 10^{16} \text{ cm}^{-2}$ (no anneal) to reduce the efficiency to 4.5% (9.8 mA/cm², 0.804 V, 0.780 fill factor). Cell OP-22, with an as-received efficiency of 16.9%, was irradiated with the same dose and annealed at 300°C for 1 hour in nitrogen to bring its efficiency to 11.8% (23.6 mA/cm², 0.909 V, 0.743 fill factor). The measured DLTS data for these three cells are given in Figure 6.

No deep levels were detected in as-received sample OP-27A, indicating a concentration of such levels below the detection limit of $2 \times 10^{13} \text{ cm}^{-3}$. One increment ($1 \times 10^{16} \text{ cm}^{-2}$) of radiation produced two deep levels in sample OP-21B, as shown. Assuming these are majority carrier traps associated with electrons in the n-type base, the positions of the energy levels in the bandgap are at $E_c - 0.15 \text{ eV}$ and at $E_c - 0.62 \text{ eV}$, where E_c is the edge of conduction band. Assuming the base doping is $2 \times 10^{17} \text{ cm}^{-3}$ [ref. 2], the concentration of these levels is $2.7 \times 10^{14} \text{ cm}^{-3}$ and $7.8 \times 10^{14} \text{ cm}^{-3}$ respectively. Annealing of irradiated sample OP-22A reduces the concentration of the $E_c - 0.15 \text{ eV}$ level to below the detection limit and also reduces the concentration of the $E_c - 0.62 \text{ eV}$ level to $1.2 \times 10^{14} \text{ cm}^{-3}$, as shown in Figure 6. Increasing the bias pulse in order to forward bias the p-n junction diode by 1.5 V, thereby injecting minority carriers into the base and emitter, resulted in no additional DLTS peaks beyond those given in Figure 6. Thus, only the two majority carrier electron traps are present in these samples. It appears that the level at $E_c - 0.62 \text{ eV}$ is responsible for limiting the recovery of cell OP-22 to only 11.4% in efficiency.

Similar results were obtained with a corresponding set of three GaAs/Ge DLTS samples. Cell 135-7 was examined by DLTS as-received, with an efficiency of 16.1%, and no deep levels were detected. Cell 135-R1, which was irradiated with 1 MeV electrons (no anneal) at a dose of $1 \times 10^{16} \text{ cm}^{-2}$, had an efficiency of 6.3%, and deep levels very similar to those seen in GaAs/GaAs sample OP-21B were observed. A level at $E_c - 0.09 \text{ eV}$ having a concentration of $1.3 \times 10^{14} \text{ cm}^{-3}$ was detected, along with a level at $E_c - 0.62 \text{ eV}$ having a concentration of $5.1 \times 10^{14} \text{ cm}^{-3}$. The concentration of these levels (again assuming a base doping of $2 \times 10^{17} \text{ cm}^{-3}$) is less than those measured for GaAs/GaAs sample OP-21B. Finally, GaAs/Ge cell 135-R2, which was irradiated at

$1 \times 10^{16} \text{cm}^{-2}$ and annealed at 300°C for 1 hour in nitrogen to give an efficiency of 13.6%, behaved similarly to GaAs/GaAs cell OP-22A in Figure 6c. The concentration of both levels was significantly reduced, with the $E_c - 0.09 \text{ eV}$ level sinking below the detection limit ($2 \times 10^{13} \text{cm}^{-3}$) and the $E_c - 0.62 \text{ eV}$ level reduced to $1.4 \times 10^{14} \text{cm}^{-3}$. There does not appear to be a significant difference in the DLTS spectra of the GaAs/GaAs cells and the GaAs/Ge cells.

Radiation damage caused by 1 MeV electrons is one of displacement, where Ga and As atoms are displaced from their equilibrium positions by the energetic electrons. This means that the defects created are likely to be vacancies (Ga or As), interstitials (Ga or As), antisite defects (Ga on As site or As on Ga site), or perhaps complexes of point defects including impurity atoms. Unfortunately, the association of a DLTS level with a particular crystalline defect cannot yet be made with certainty. The level observed at $E_c - 0.62 \text{ eV}$ (Figure 6b) is close in energy to the EL2 level in GaAs, which is a deep donor at $E_c - 0.67 \text{ eV}$ [ref. 5]. This level is often intentionally introduced during GaAs crystal growth to make the crystal semi-insulating. It is thought to be associated with a Ga vacancy or an antisite defect caused by an As atom occupying a Ga site. The level observed at $E_c - 0.15 \text{ eV}$ may be associated with the displacement of an As atom. In any event, only two deep levels were observed in this work. Earlier DLTS studies of GaAs irradiated by 1 MeV electrons have shown as many as 5 electron traps and 2 hole traps [ref. 5]. The situation may be simpler in the present study because of higher purity GaAs material, with fewer impurity atoms present to join in forming electrically active complexes.

EBIC Measurements

The EBIC measurements were made using an AMRAY Model 1635 scanning electron microscope and associated electronics. The energy of the electron beam was 30 keV. GaAs/GaAs cell OP-50 was examined as received. This cell had an efficiency of 17.0% (29.0 mA/cm^2 , 0.996 V, and 0.805 fill factor) and was cleaved to expose a clean cross-section. The epi thickness was found to be $10.5 \mu\text{m}$ for this sample. A cross-sectional EBIC scan is shown in Figure 7a. Three distinct regions of the cell can be discerned from the scan. From the external surface, the linear region is the p-emitter, the relatively flat peak is the depletion region, and the exponential fall-off is the n-base.

The junction depth is $0.80 \mu\text{m}$ from the external surface. Assuming the AlGaAs window layer is $0.1 \mu\text{m}$ thick [ref. 2], the GaAs emitter is $0.70 \mu\text{m}$ in depth. This may explain the relatively poor radiation tolerance of these cells. According to reference 6, an emitter thickness of $0.70 \mu\text{m}$ is expected to lead to a reduction in efficiency to approximately 25% of the initial efficiency following a 1 MeV electron dose of $1 \times 10^{16} \text{cm}^{-2}$. This is in good agreement with the values observed (Table 1). The hole diffusion length in the n-base can be estimated from the exponential profile of Figure 7a as $3.7 \mu\text{m}$.

For comparison, a cleaved cross-section of GaAs/Ge cell 6 was also examined by EBIC and is shown in Figure 7b. This cell had undergone one increment of electron irradiation ($1 \times 10^{16} \text{cm}^{-2}$) and an anneal at 250°C for one hour in nitrogen prior to the EBIC measurement. After the irradiation and anneal the efficiency was 11.3% (25.6 mA/cm^2 , 0.960 V, 0.618 fill factor), which was 83% of the initial efficiency of 13.5%. In this case the GaAs epi thickness was only $3.8 \mu\text{m}$, significantly less than the $10.5 \mu\text{m}$ thickness for cell OP-50 in Figure 7a. The diffusion length of holes in the n-base of GaAs/Ge cell 6 appears to be limited by the epi thickness of $3.8 \mu\text{m}$, since the fall-off of the EBIC signal in the base is nearly linear.

The depth of the junction from the surface for cell 6 is $0.71\text{ }\mu\text{m}$ from Figure 7b. Again assuming an AlGaAs window thickness of $0.1\text{ }\mu\text{m}$, the GaAs emitter is then $0.61\text{ }\mu\text{m}$ in depth. This is somewhat better than the $0.70\text{ }\mu\text{m}$ found for GaAs/GaAs cell OP-50, and may be partially responsible for the improved radiation tolerance of the GaAs/Ge cells relative to the GaAs/GaAs cells. This assumes that the junction depths estimated for the cells of Figure 7 are representative for the cells of Figures 2 to 5. According to reference 6, the junction depth must be less than $0.5\text{ }\mu\text{m}$ (preferably $0.3\text{ }\mu\text{m}$ or less) in order to obtain a high degree of radiation tolerance.

Conclusions

The GaAs/Ge cells are somewhat more tolerant of 1 MeV electron irradiation and more responsive to annealing than are the GaAs/GaAs cells examined in this study. However, both types of cells suffer a greater degradation in efficiency than has been observed in other recent studies. The reason for this is not certain, but it may be associated with an emitter thickness which appears to be greater than desired. DLTS spectra following irradiation are not significantly different for the GaAs/Ge and the GaAs/GaAs cells, with each having just two peaks. The annealing behavior of these peaks is also similar in the two samples examined. It appears that no penalty in radiation tolerance, and perhaps some benefit, is associated with fabricating MOCVD GaAs cells on Ge substrates rather than GaAs substrates.

References

- [1] R. E. Hart, Jr., NASA-Lewis Research Center, private communication.
- [2] P. A. Iles, K. I. Chang, and W. Pope, "Review of MANTECH Program for GaAs Solar Cells," *Conf. Rec. 19th IEEE Photovoltaic Specialists Conf.* (87CH2400-0) (New Orleans, LA), p. 331, 1987.
- [3] K. I. Chang, Y. C. M. Yeh, P. A. Iles, J. M. Tracy, and R. K. Morris, "Heterostructure GaAs/Ge Solar Cells", *Conf. Rec. 19th IEEE Photovoltaic Specialists Conf.* (87CH2400-0) (New Orleans, LA), p. 273, 1987.
- [4] H. C. Hamaker, J. G. Werthen, C. R. Lewis, H. F. MacMillan, C. W. Ford, G. F. Virshup, R. K. Ahrenkiel, D. L. Greenberg, and J. Schlupmann, "Radiation Damage of 1.93-eV $\text{Al}_{0.37}\text{Ga}_{0.63}\text{As}$ and GaAs Solar Cells Grown by Metalorganic Chemical Vapor Deposition", *Conf. Rec. 19th IEEE Photovoltaic Specialists Conf.* (87CH2400-0) (New Orleans, LA), p. 733, 1987.
- [5] A. G. Milnes, "Impurity and Defect Levels (Experimental) in Gallium Arsenide", in *Advances in Electronics and Electron Physics, Volume 61*, edited by P. W. Hawkes, Academic Press, New York, 1983 (pp. 64-160)
- [6] R. Loo, G. S. Kamath and R. C. Knechtli, "Radiation Damage in GaAs Solar Cells", *Conf. Rec. 14th IEEE Photovoltaic Specialists Conf.* (80CH1508-1) (San Diego, CA), p. 1090, 1980.

Table 1. Average GaAs Cell Parameters for Each of the Four Groups at Key Points in the Irradiation/Anneal Sequence

Substrate	Temperature (°C)	J_{sc} (mA/cm ²)	V_{oc} (V)	FF	η (%)
a) As-received					
GaAs	250	28.8	0.997	0.776	16.5
Ge	250	29.1	1.007	0.631	13.6
GaAs	300	28.8	1.004	0.772	16.5
Ge	300	29.3	0.996	0.606	13.1
b) Immediately after first irradiation of 1×10^{16} cm ⁻²					
GaAs	250	9.7	0.802	0.773	4.4
Ge	250	11.7	0.924	0.657	5.3
GaAs	300	9.5	0.800	0.754	4.2
Ge	300	11.9	0.914	0.624	5.0
c) After first irradiation (1×10^{16} cm ⁻²) and anneal (1 hour in N ₂)					
GaAs	250	21.4	0.856	0.775	10.6
Ge	250	25.7	0.975	0.609	11.3
GaAs	300	24.0	0.911	0.748	12.1
Ge	300	26.4	0.989	0.567	11.0
d) After seventh irradiation (7×10^{16} cm ⁻²) and anneal (1 hour in N ₂)					
GaAs	250	16.0	0.802	0.726	6.9
Ge	250	19.6	0.938	0.600	8.3
GaAs	300	17.4	0.840	0.734	8.0
Ge	300	21.9	0.973	0.559	8.9

Measurement Conditions: AM0, 135 mW/cm², 27°C

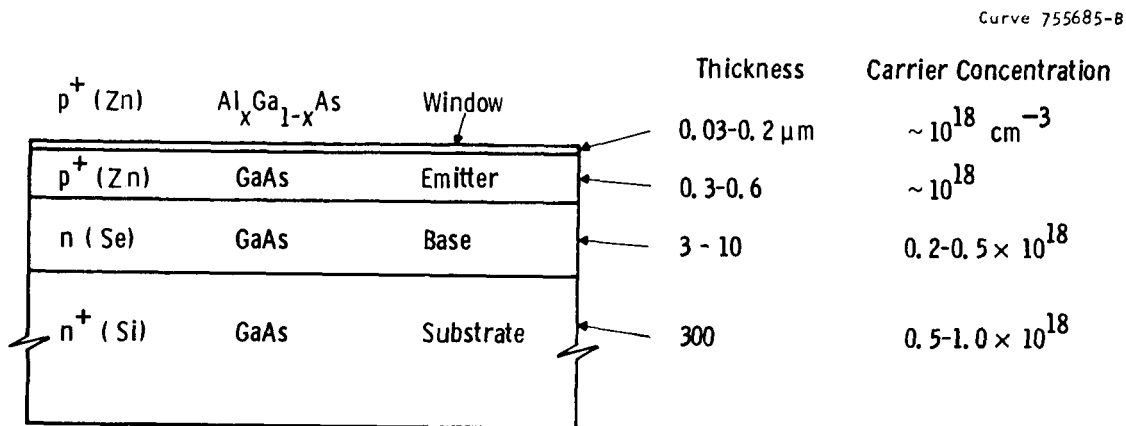


Fig. 1—GaAs/GaAs structure following MOCVD layer growth

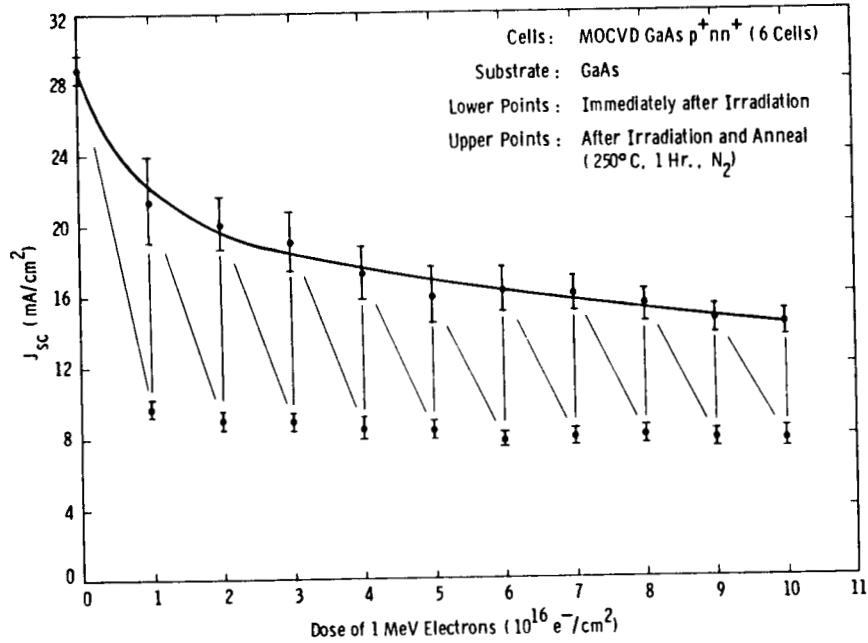


Fig. 2a—Effect of electron irradiation and 250°C anneal on short-circuit current density of GaAs/GaAs cells. (Cells OP-1, OP-2, OP-4, OP-5, OP-7, OP-8)

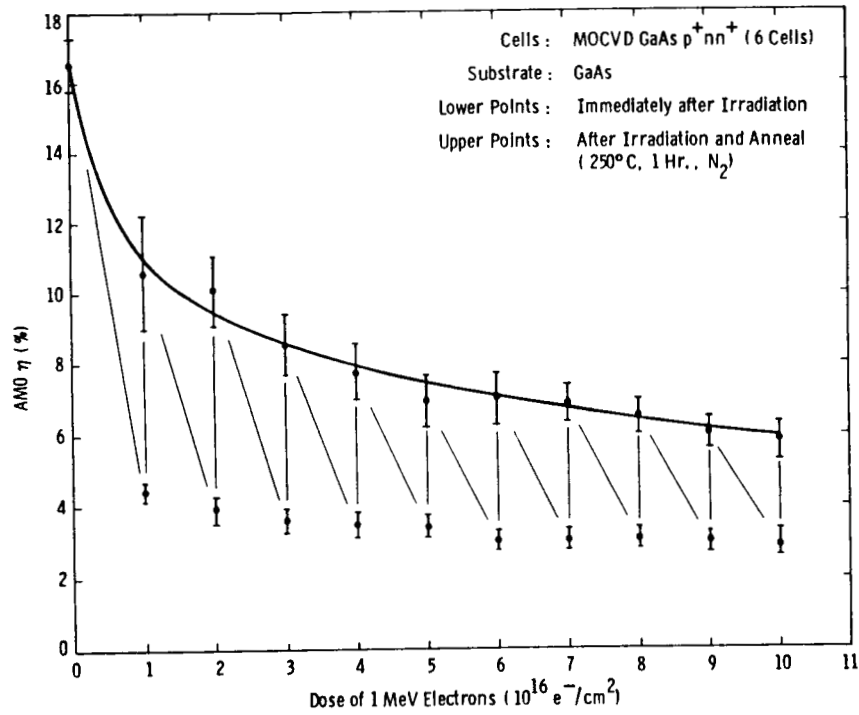


Fig. 2b—Effect of electron irradiation and 250°C anneal on AMO efficiency of GaAs/GaAs cells. (Cells OP-1, OP-2, OP-4, OP-5, OP-7, OP-8)

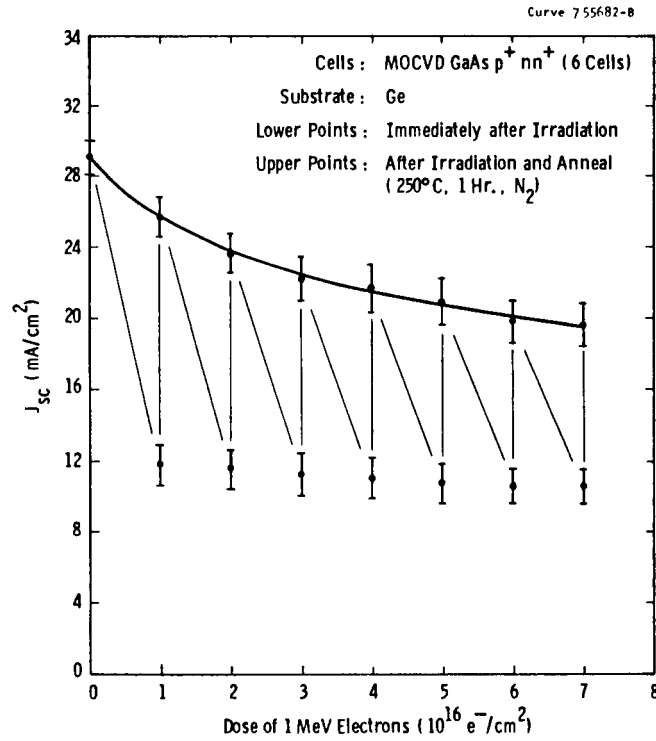


Fig. 3a—Effect of electron Irradiation and 250°C anneal on short-circuit current density of GaAs/Ge cells. (Cells 2, 3, 4, 7, 135-8, 135-9)

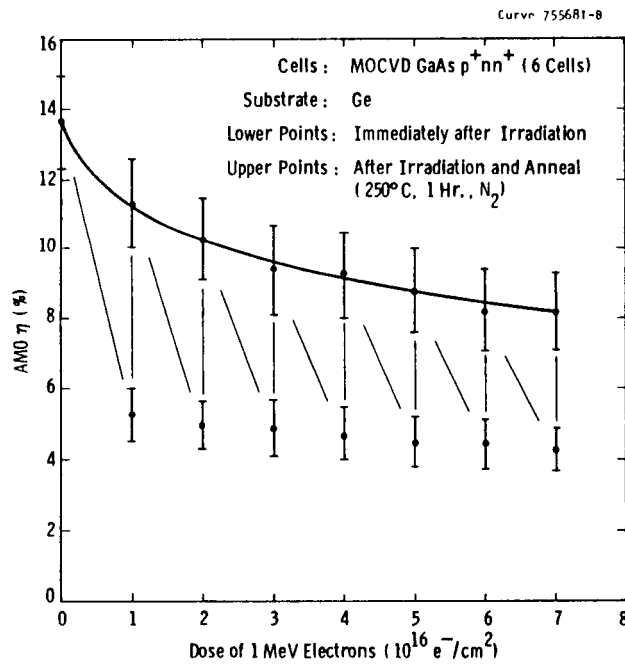


Fig. 3b—Effect of electron Irradiation and 250°C anneal on AMO efficiency of GaAs/Ge cells. (Cells 2, 3, 4, 7, 135-8, 135-9)

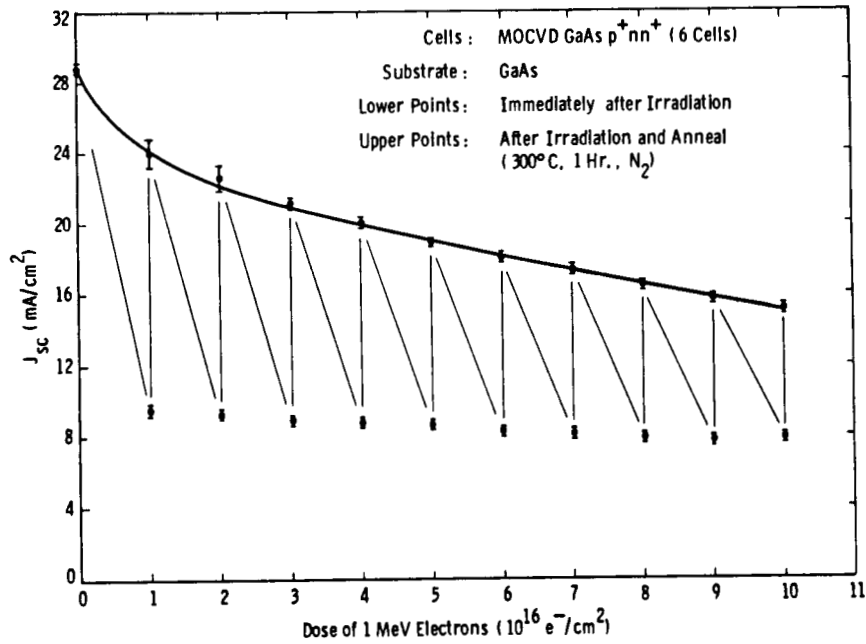


Fig. 4a—Effect of electron Irradiation and 300°C anneal on short-circuit current density of GaAs/GaAs cells. (Cells OP-11, OP-12, OP-13, OP-16, OP-17, OP-19)

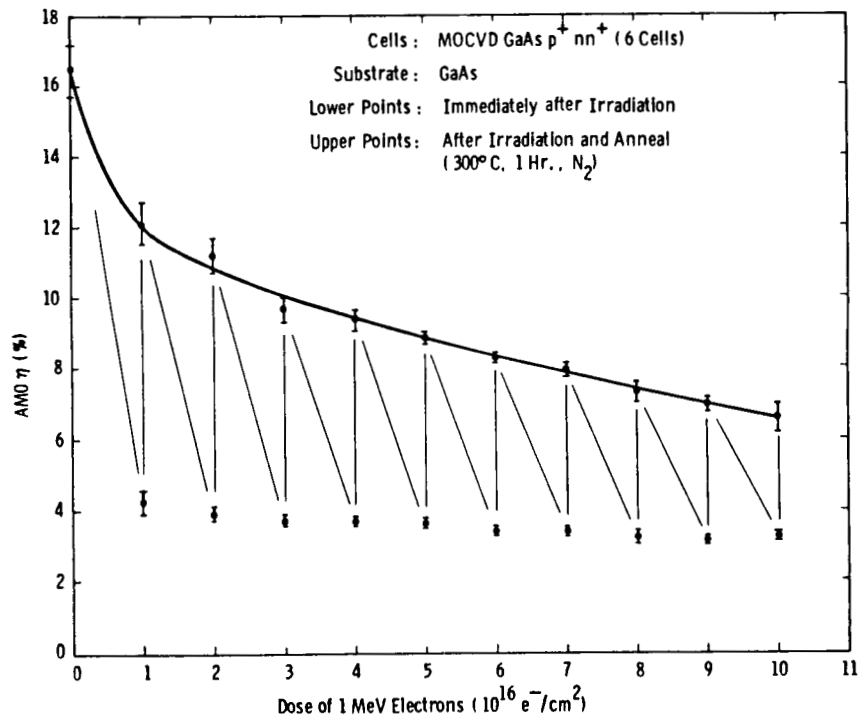


Fig. 4b—Effect of electron Irradiation and 300°C anneal on AMO efficiency of GaAs/GaAs cells. (Cells OP-11, OP-12, OP-13, OP-16, OP-17, OP-19)

Curve 755678-B

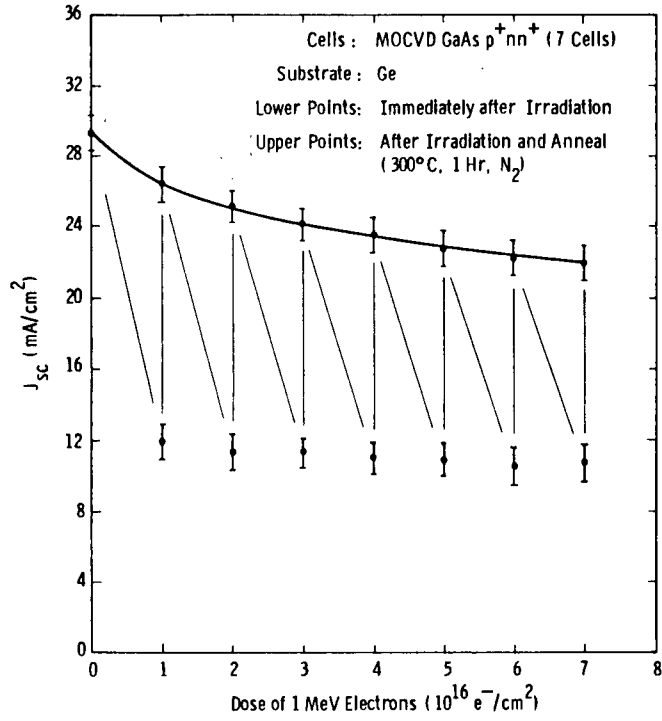


Fig. 5a—Effect of electron irradiation and 300°C anneal on short-circuit current density of GaAs/Ge cells. (Cells 10, 11, 12, 14, 15, 135-10, 135-12)

Curve 755677-B

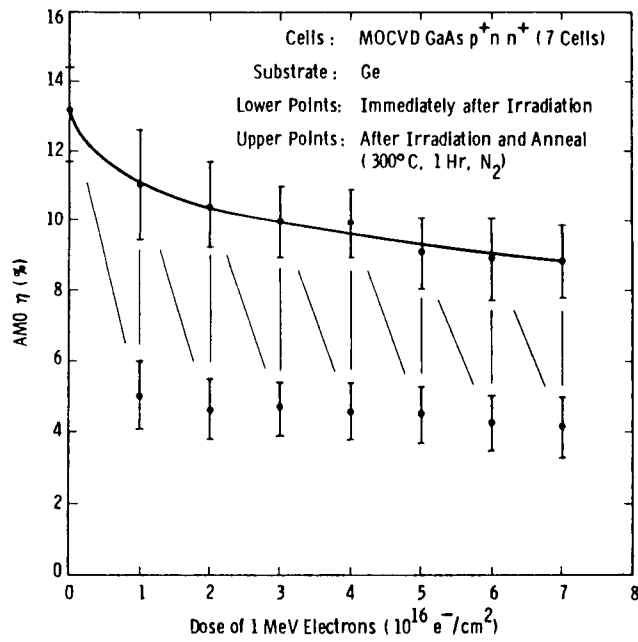
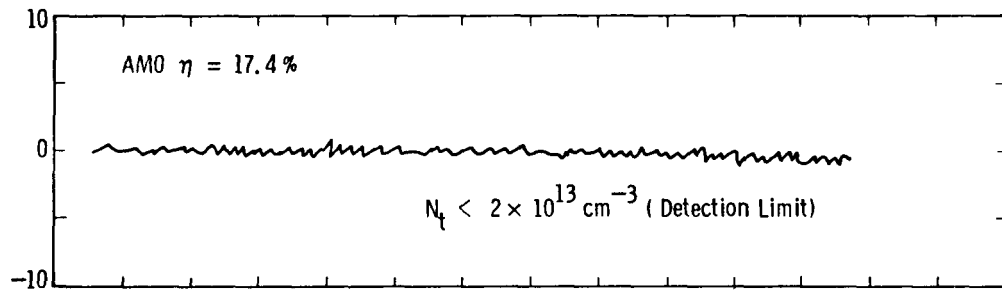


Fig. 5b—Effect of electron irradiation and 300°C anneal on AMO efficiency of GaAs/Ge cells. (Cells 10, 11, 12, 14, 15, 135-10, 135-12)



a) Cell OP-27A As-Received (No Irradiation or Annealing)

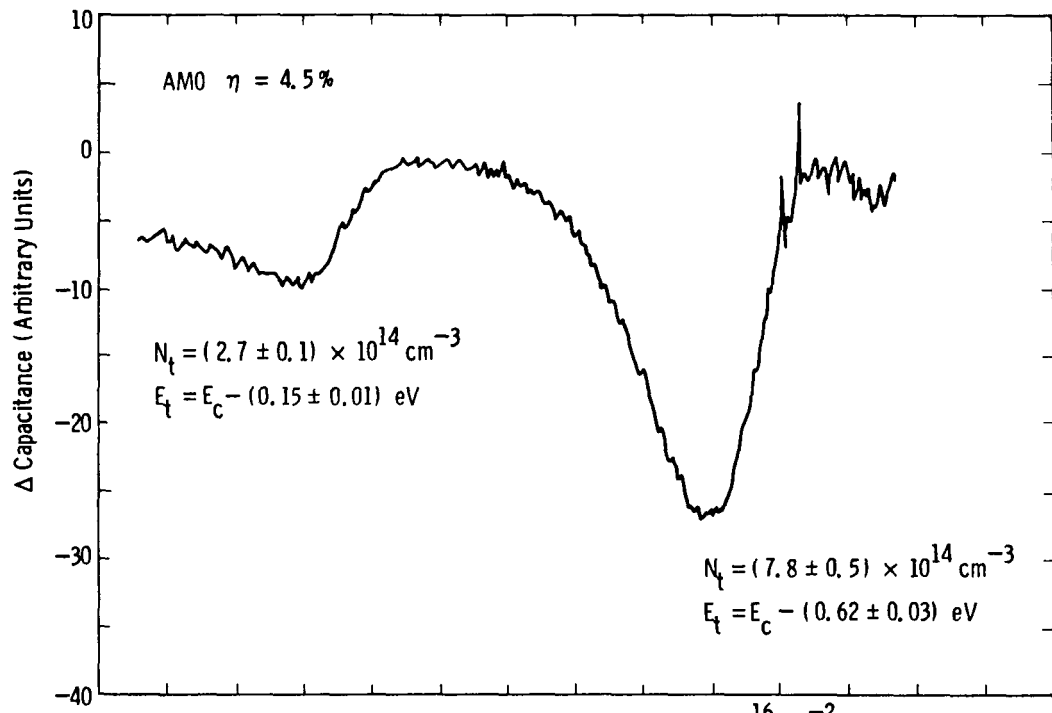
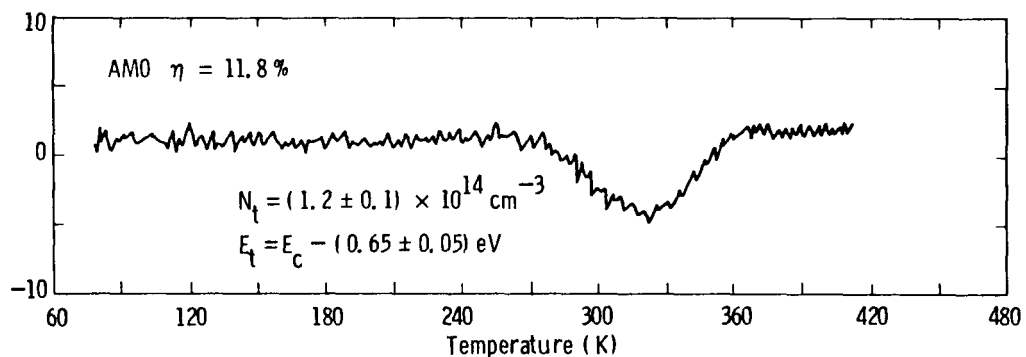
b) Cell OP-21B after Irradiation by 1 MeV Electrons ($1 \times 10^{16} \text{ cm}^{-2}$) (No Annealing)c) Cell OP-22A after Irradiation ($1 \times 10^{16} \text{ cm}^{-2}$) and Annealing (300°C, 1 Hr., N_2)

Fig. 6—DLTS scans for GaAs/GaAs cells showing the creation and subsequent annealing of deep levels from 1 MeV electron irradiation

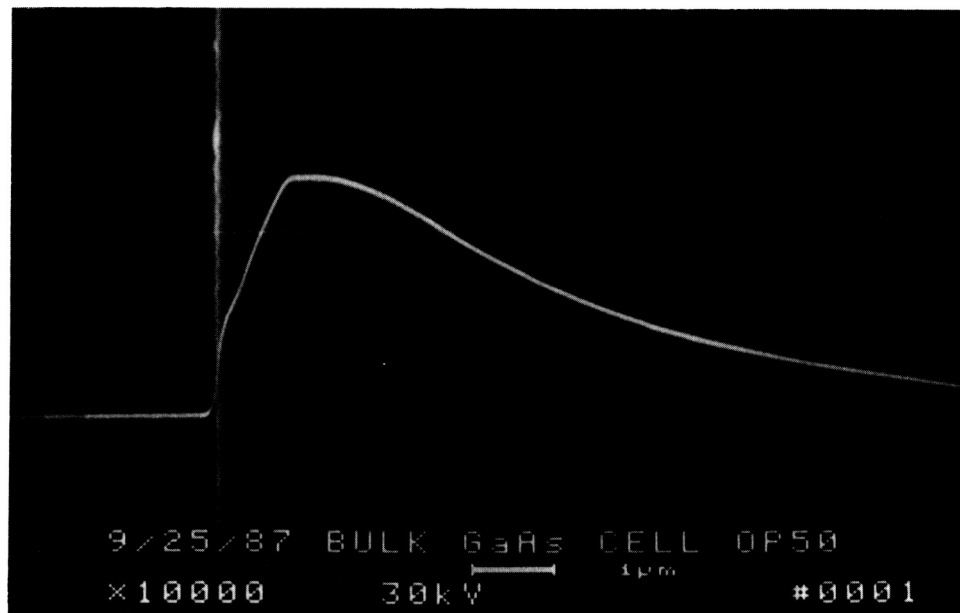


Figure 7a — EBIC scan of GaAs/GaAs cell with 10.5 μm epi thickness showing 0.80 μm junction depth and 3.7 μm base diffusion length.

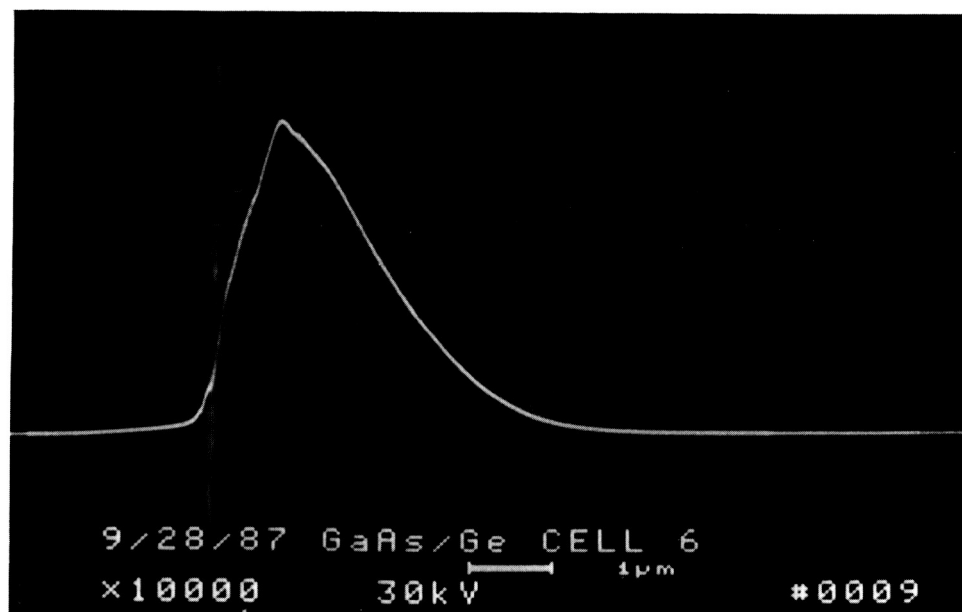


Figure 7b — EBIC scan of GaAs/Ge cell with 3.8 μm epi thickness showing 0.71 μm junction depth and base diffusion length apparently limited by epi thickness.

A Three Solar Cell System Based on a Self-Supporting, Transparent AlGaAs Top Solar Cell*

Gerald H. Negley, Sandra L. Rhoads,
Nancy E. Terranova, and James B. McNeely
AstroPower Division/Astrosystems, Inc.

Allen M. Barnett
University of Delaware

Abstract

Development of a three solar cell stack can lead to practical efficiencies greater than 30% ($1\times$, AM0). A theoretical efficiency limitation of 43.7% at AM0 and one sun is predicted by our model. Including expected losses, a practical system efficiency of 36.8% is anticipated. These calculations are based on a 1.93eV/1.43eV/0.89eV energy band gap combination. AlGaAs/GaAs/GaInAsP materials can be used with a six-terminal wiring configuration. A current-matched, two-terminal wiring configuration yields a practical system efficiency of 34.2% ($1\times$, AM0). This is based upon an optimum bandgap combination of 1.93eV/1.35eV/0.95eV, and corresponds to the same top and bottom materials and the substitution of InP for GaAs.

The key issues for multijunction solar cells are the top and middle solar cell performance and the sub-bandgap transparency. AstroPower has developed a technique to fabricate AlGaAs solar cells on rugged, self-supporting, transparent AlGaAs substrates. Top solar cell efficiencies greater than 11% AM0 have been achieved.

State-of-the-art GaAs or InP devices will be used for the middle solar cell.

GaInAsP will be used to fabricate the bottom solar cell. This material is lattice-matched to InP and offers a wide range of bandgaps for optimization of the three solar cell stack. LPE is being used to grow the quaternary material. Initial solar cells have shown open-circuit voltages of 462 mV for a bandgap of 0.92eV.

This paper will discuss design rules for the multijunction three solar cell stack and will present the progress in the development of the self-supporting AlGaAs top solar cell and the GaInAsP bottom solar cell.

Introduction

Multijunction solar cells, mechanically-stacked or monolithic, present a major improvement in power density in space. For a practical system, a mechanically-stacked tandem solar cell efficiency of over 30% is possible in the long term and greater than 25% for the short term [ref. 1]. One tandem approach uses the top solar cell to boost the performance of the lower bandgap solar cell. An

* The GaInAsP bottom solar cell work was supported in part by the Air Force Aero Propulsion Laboratory under contact No. F33615-88-C-2807.

alternative approach is based upon scavenging low energy photons from a good, relatively wide bandgap top solar cell [ref. 2]. Combining both tandem solar cell approaches naturally leads to a three solar cell stack with efficiencies of over 40% at AM0 and one sun insolation.

A six-terminal wiring configuration is being proposed for the three solar cell stack. A two terminal wiring configuration requires the stacked solar cells to be current matched. In a radiation orbit, where the radiation damage to the three solar cells will cause different degrees of damage, current-matched multibandgap solar cells are current limited by the solar cell generating the least current. This current mismatch will result in more power loss over the lifetime of the array when compared to the six-terminal wiring configuration.

The key to high efficiency mechanically-stacked multijunction solar cells is the top solar cell. This top solar cell must: i) be highly efficient since one-half of the stack efficiency is the result of the top solar cell, and ii) be highly transparent to sub-bandgap photons. In this paper, the design rules for the multijunction will be discussed, and the progress in the development of the top and bottom solar cell will be discussed.

Design

Originally, the theoretical limits for the three solar cell stack (TSCS) were determined using a solar cell model by Nell [ref. 3] based upon tabulated standard spectra and the fit of experimentally achieved open-circuit voltages assuming unit quantum efficiency. Nell's model predicts an efficiency limit of 41.5% at AM0 and one-sun insolation with a bandgap combination of 2.28eV, 1.55eV, and 0.99eV. However, these specific bandgap choices do not utilize existing, well-developed technologies. In addition, more recent work by Terranova and Barnett [ref. 4] indicate that Nell's model underestimates the open-circuit voltages.

The model being used to predict the solar cell performance is that of Nell, but modified by Terranova and Barnett. The model was modified by using fundamental parameters to estimate the open-circuit voltages of well known materials in accord with the diode equation. Using this approach, the open-circuit voltages predicted by the model agree very well with experimental results of well developed solar cells.

Due to material limitations, AstroPower proposes bandgap choices of 1.93eV, 1.43eV and 0.89eV for the TSCS wired in a six-terminal configuration. Our model predicts an efficiency limit of 43.7% AM0, 1x. At a concentration ratio of 100x, this bandgap combination yields a limit of 48.9%. The 100x values are obtained by assuming a 100x increase in short-circuit current values and scaling other values in accordance with the diode equation.

For a two-terminal wiring configuration, the requirement of current-matching changes the bandgaps of the middle and bottom solar cell. Using a 1.93eV, 1.35eV and a 0.95eV bandgap combination, the model predicts an efficiency limit of 40.7% at 1x, AM0. At 100x AM0, an efficiency limit of 45.1% exists. By manipulating the energy bandgaps in the TSCS, only a small penalty in efficiency exists when the requirement for current matching is imposed.

Table I illustrates the theoretical maximum efficiency predicted by the model.

The proposed bandgap combination for the six-terminal wiring configuration corresponds to an $\text{Al}_{0.37}\text{Ga}_{0.63}\text{As}$ top solar cell, a GaAs middle solar cell, and a GaInAsP bottom solar cell. For the two-terminal case, the top and bottom materials remain the same, and the GaAs middle solar cell is replaced with InP.

AlGaAs solar cells have demonstrated high efficiencies, and AlGaAs is the most developed material for a top solar cell [ref. 5]. AstroPower has developed a technique to fabricate AlGaAs solar cells on a transparent AlGaAs substrate. This approach utilizes the most developed wide bandgap material on a transparent substrate.

The middle solar cell in the TSCS is GaAs or InP depending on the wiring configuration. GaAs solar cells are approaching their practical efficiency limit; hence, they represent a mature technology in the TSCS. InP solar cells represent a newer technology; however, recent technological breakthroughs indicate an advanced stage for this material. Using either material for the middle solar cell will not limit the TSCS performance.

GaInAsP is the material of choice for the bottom solar cell. This quaternary material offers lattice-matched alloys to InP with a tunable bandgap range of 0.75eV to 1.35eV. This material has been successfully developed for device applications in the fiber-optic and semiconductor-laser fields. This wide technology base is directly applicable to material development for bottom solar cell designs.

Practical System Performance

The potential performance of a photovoltaic material can be predicted through the comparison of the modelled theoretical maximum performance versus the achieved performance of well developed solar cells. A survey of the literature indicates that, in general, well-developed solar cells achieve 96%, 91% and 96% of their theoretical limits for open-circuit voltage, short-circuit current and fill factor, respectively [ref. 2]. Using these "scale factors", one may predict the "best case" performance of a photovoltaic material including optical and electrical losses. Table II illustrates the "best case" performance of a GaAs solar cell compared to the best reported device in literature.

This approach of scaling theoretical limits to predict the "best case" performance has been demonstrated to be valid for all well-behaved solar cells. This is particularly true of the III-V compounds. Using this approach, we can predict the performance of the TSCS by scaling each solar cell from the model's theoretical limit to the "best case" performance.

Assuming 100% transmission of the photons less energetic than the bandgap, we may predict the performance of each individual solar cell. By reducing the current in the middle (bottom) solar cell by the current generated in the top (top two) solar cells, an evaluation of the stack can be done. This approach is valid since the model assumes unit quantum efficiency. When using existing devices in a stack, one should convolute the spectrum with the external quantum efficiency to determine the current generated in the middle and/or bottom solar cell(s). Using the "scale factors", and reducing the current to simulate the TSCS, the best case prediction is given in Table III.

In our preliminary study, our 4mm diameter devices (on 5mm × 5mm die) were limited by a shunt diode, hence the devices suffered from lower than expected fill factors as shown in Figure 3. The origin of the shunt diode has been determined, and future devices will reflect this improvement. Under concentrated light, this problem was eliminated. Using the concentration fill factor, an analysis of our device was done. This is illustrated in Table IV.

The use of the “concentration” fill factor is reasonable. Mayet [ref. 7] have fabricated 1.89eV solar cells from AlGaAs with fill factors of 0.874. The most needed improvement for our preliminary AlGaAs devices (other than FF) is in the open-circuit voltage. This will be accomplished by optimizing the junction fabrication technique and the precise control of the base layer doping.

The AlGaAs devices show good current collections. An external quantum efficiency curve is shown in Figure 4. The external quantum efficiency measurement indicates good blue response and good bandedge response. The good blue response indicates that the window layer is reducing surface recombination. The good bandedge response indicates that the diffusion length is not limiting device performance.

GaInAsP Bottom Solar Cell Development

GaInAsP is the material system of choice for the bottom solar cell. This system offers a tunable bandgap range (0.35 to 2.26eV) low enough for bottom cell requirements with compositions lattice-matched to InP for bandgaps between 0.75 and 1.35eV. GaInAsP material technology has been successfully developed for device applications in the fiber-optic and semiconductor-laser field. This wide technology base is directly applicable to material development for bottom solar cell designs.

AstroPower is using liquid phase epitaxy (LPE) to develop GaInAsP devices down to 0.89eV. Smooth surface morphology has been obtained for bandgaps down to 0.92eV using modified meltback and two-phase solution techniques. Figure 5 is a photograph of this smooth morphology. Figure 6 is a EDS quantitative profile, showing layer composition and thickness.

Homojunction 0.92eV GaInAsP solar cells have been fabricated in our laboratory. Undoped 0.92eV GaInAsP material was diffused with zinc; device areas were chemically isolated; and Au alloy contacts were applied. Emitter thickness and grid design have not yet been optimized. Open-circuit voltage values up to 462mV at AM0 (1×) were recorded. This corresponds to 78% of the theoretical maximum open circuit voltage value calculated for 0.92eV material.

These results are particularly encouraging considering that open-circuit voltage values are a good indicator of the performance potential of solar cell materials, like silicon and GaAs [ref. 2]. In addition, the open circuit voltage exceeds that of well-developed germanium bottom solar cells by 44%. Recently reported values for germanium bottom solar cells are 306mV at AM1.5 (238×) or 320mV at AM0 (1×) [ref. 8].

Figure 7 shows a quantum efficiency versus wavelength plot for the 0.92eV bottom solar cell covered by an InP filter.

The “peaked” response in the quantum efficiency is the result of an unoptimized junction. The junction on this device was too deep and surface recombination dominated the high energy

Device Fabrication

The AlGaAs top solar cell and the GaInAsP bottom solar cell are being developed in our laboratories. The material is being grown by liquid phase epitaxy (LPE). LPE is the technique of choice given the stoichiometry control, the tendency of the impurities to segregate away from the solid, and the longer diffusion lengths. LPE is known to produce devices that are superior in performance to those grown by other methods. The majority of the commercial III-V semiconductor devices being produced in Japan are grown by LPE.

AlGaAs Top Solar Cell Development

AlGaAs solar cells have demonstrated high efficiencies, and AlGaAs is the most developed material for a top solar cell [ref. 5]. However, all AlGaAs solar cells reported in the literature are fabricated on GaAs substrates. This opaque substrate must be removed before application to a mechanical stack. Integrating a highly transparent, self-supporting AlGaAs top solar cell coupled with existing, well-developed solar cells will achieve increases in solar cell efficiency with multijunction structures. A technique to fabricate AlGaAs solar cells on transparent AlGaAs substrates has been developed. AstroPowers' approach utilizes the most developed wide bandgap material on a transparent substrate.

The rugged, self-supporting, transparent AlGaAs top solar cell can be mechanically stacked on any well developed, existing solar cell. The key issue for multijunction solar cells - - mechanically stacked or monolithic - - is the top solar cell. This solar cell must be transparent to the sub-bandgap photons, and must be approaching its theoretical efficiency limit. It is our practice to first investigate the material transparency since this is the most critical parameter. Figure 1 shows quantum efficiency curves for a silicon solar cell with and without an AlGaAs filter. This AlGaAs filter was transparent to 91% of the photons less energetic than the bandgap of the active device layer.

To improve the transparency, one must determine where the losses have occurred. Two possible loss mechanisms exist: i) reflection, and ii) free carrier absorption. Each loss mechanism can be reduced through optical optimization. More detailed measurements on our AlGaAs filter, reflection + transmission (R+T), indicate that the effect of free-carrier absorption is less than 2%. Sub-bandgap transparency is not a problem with this material.

AstroPower's preliminary work on this system has yielded a 11.2% (AM0, 1 \times) AlGaAs top solar cell. The detailed characteristics were V_{oc} =1.285 volts, J_{sc} =15.7 mA/cm², and FF=0.75. In addition, we have demonstrated transparency greater than 90%. Our preliminary investigation indicates the lattice-matched AlGaAs system is easier to work with and, hence, will yield faster results.

AstroPower recently investigated 1.93eV AlGaAs solar cells. We have demonstrated the capability of growing transparent AlGaAs substrates, and the capability of fabricating AlGaAs solar cells. Our best one sun (AM0) device is 11.2% efficient. These devices are shown in Figure 2. response. Nonetheless, the sub-bandgap transparency of the filter is encouraging as is the response of the GaInAsP in the "stacked" situation.

Conclusion

Solar cell efficiencies greater than 30% AM0 are realizable in the near future with a three solar cell stack (TSCS). With expected losses, a practical system efficiency of 36.8% is anticipated. These calculations are based on the 1.93eV/1.43eV/0.89eV energy bandgap combination. AlGaAs/GaAs/GaInAsP materials can be used with a six-terminal wiring configuration. A current-matched, two-terminal wiring configuration yields a practical system efficiency of 34.2% (1x,AM0). This is based upon an optimum bandgap combination of 1.93eV/1.35eV/0.95eV, and corresponds to the same top and bottom materials and the substitution of InP for GaAs.

The self-supporting AlGaAs structure eliminates the low yield problem that others encountered when trying to remove the fragile AlGaAs from the GaAs substrate. Technological risk is minimized for all materials by drawing upon available technology. The key to high efficiency triple stacks is in the top and middle solar cell. Both must be approaching their efficiency limit and must be highly transparent to photons less energetic than their bandgaps.

Continued progress for the AlGaAs top solar cell and the GaInAsP bottom solar cell will result in practical system efficiencies greater than 30% AM0.

References

- [1] G.H. Negley, J.B. McNeely, P.G. Lasswell, E.A. Gartley, A.M. Barnett, and T.M. Trumble, "Design and Development of GaAsP on GaP/Silicon Mechanically Stacked, Multijunction Solar Cells", *19th IEEE Photovoltaic Specialist Conference*, 119, New Orleans, (1987)
- [2] A.M. Barnett and J.S. Culik, "New Solar Cell Design Options", *19th IEEE Photovoltaic Specialists Conference*, New Orleans, p. 931, 1987.
- [3] M.E. Nell and A.M. Barnett, "The Spectral p-n Junction Model for Tandem Solar Cell Design", *IEEE Trans. Electron Devices*, ED-34, 257-266, (1987).
- [4] Terranova and Barnett, to be published.
- [5] S.M. Vernon, S.P. Tobin, R.G. Wolfson, "Gallium Arsenide and Multibandgap Solar Cell Research", Final Subcontract Report, April 1984-April 1986, SERI/STR-211-3188.
- [6] J.G. Werthen, G.F. Virshup, H. F. MacMillan, C.W. Ford, H.C. Hamaker, "High-Efficiency GaAs Concentrator Space Cells", *Space Photovoltaic Research and Technology 1986*, NASA CR-2475, p.25.
- [7] M. Gavand, L. Mayet, B. Montegu, R. Zerdoum, A. Laugier, "High Efficiency $\text{Al}_{0.35}\text{Ga}_{0.65}\text{As}$ Liquid Phase Epitaxy Grown Solar Cells For Bicolor Applications", *19th IEEE Photovoltaic Specialists Conference*, p. 1528, New Orleans (1987).
- [8] L.D. Partain, M.S. Kuryla, R.E. Weiss, R.A. Ransom, P.S. McLeod, L.M. Frass, and J.A. Cape, "26.1% Solar Cell Efficiency for Ge Mechanically Stacked Under GaAs", *Journal of Applied Physics*, 62(7), 3010-3015 (1987).

TABLE I

Predicted Theoretical Maximum Efficiency
for the Six-Terminal and Two-terminal
Three Solar Cell Stack, AM0

6-TERMINAL CONFIGURATION

Bandgap (eV)	Voc (volts)	Jsc (mA/cm ²)	FF	Eff [1x] (%)	Eff [100x] (%)
1.93	1.58	21.8	0.91	23.2	25.0
1.43	1.07	16.7	0.88	11.6	13.0
0.89	0.54	27.9	0.80	<u>8.9</u>	<u>10.9</u>
Stack Efficiency				43.7	48.9

2-TERMINAL CONFIGURATION

1.93	1.58	19.7	0.91	20.9	22.5
1.35	0.99	19.7	0.87	12.7	14.1
0.95	0.60	19.7	0.81	<u>7.1</u>	<u>8.5</u>
Stack Efficiency				40.7	45.1

TABLE II

Expectation of "Best Case" GaAs Solar (AMO)

	Voc (volts)	Jsc (mA/cm ²)	FF	Eff (%)
Theoretical	1.09	38.5	.88	27.3
%Theoretical	96%	91%	96%	
Best Case	1.05	35.0	.84	22.9
Best Achieved [6]	1.06	32.4	.85	21.5

TABLE III

Best Case Prediction at AM0
For The Three Solar Cell Stack

6-TERMINAL CONFIGURATION

<u>Material</u>	<u>Voc</u> (volts)	<u>Jsc</u> (mA/cm ²)	<u>FF</u>	<u>Eff(1x)</u> (%)	<u>Eff(100x)</u> (%)
AlGaAs	1.52	19.8	0.88	19.5	21.0
GaAs	1.03	15.2	0.85	9.8	10.9
GaInAsP	0.52	25.4	0.77	<u>7.5</u>	<u>9.1</u>
Stack Efficiency				36.8	41.0

2-TERMINAL CONFIGURATION

AlGaAs	1.52	17.9	0.88	17.7	19.0
InP	0.96	17.9	0.84	10.6	5.9
GaInAsP	0.57	17.9	0.78	<u>5.9</u>	<u>7.1</u>
Stack Efficiency				34.2	38.0

TABLE IV

Potential of 1.93eV AlGaAs Solar
Cells Using "Best Case" Fill Factor

<u>Concentration</u>	<u>Voc</u> (volts)	<u>Jsc</u> (mA/cm ²)	<u>FF</u>	<u>Eff</u> (%)
1x	1.285	15.4	.88	12.9
25x	1.38	385.0	.88	13.8
100x	1.42	1540.0	.88	14.2

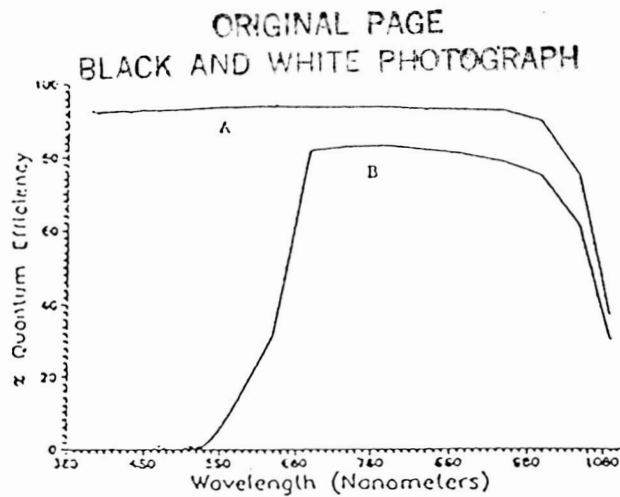


Figure 1. A) Q.E. of Silicon Solar Cell without AlGaAs filter.
B) Q.E. of Silicon Solar Cell with AlGaAs filter.

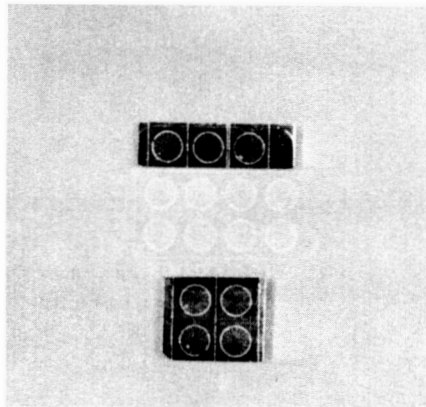


Figure 2. AlGaAs Devices with Concentrator Mask.

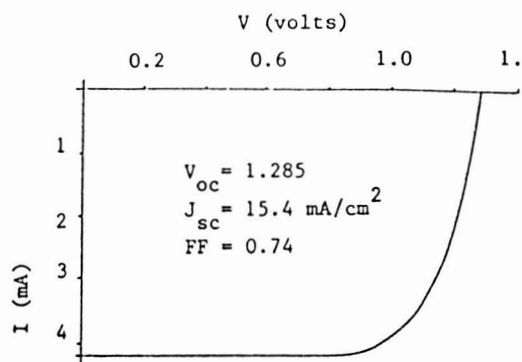


Figure 3. Representative I-V Curve for an AlGaAs top solar cell at 1X, AM0.

ORIGINAL PAGE
BLACK AND WHITE PHOTOGRAPH

AlGaAs#31-11
AlGaAs/GaAs p/n w/AR

2-16-88

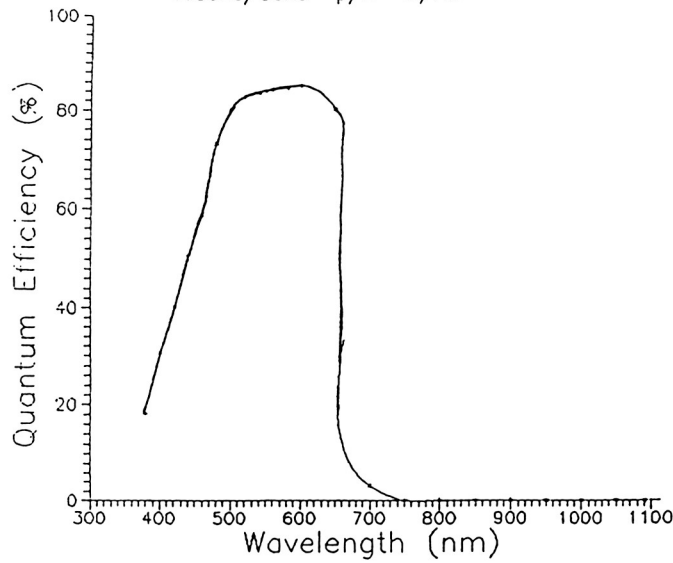


Figure 4. Representative External Quantum Efficiency Plot of an AlGaAs Top Solar Cell.

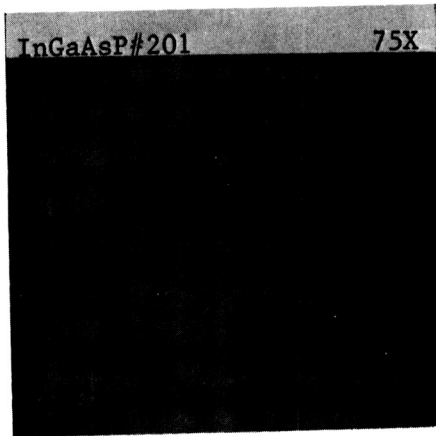


Figure 5. Smooth, unfeatured surface morphology of 0.92eV GaInAsP grown by LPE.

ASTROPOWER

TUE 02-FEB-88 15:45

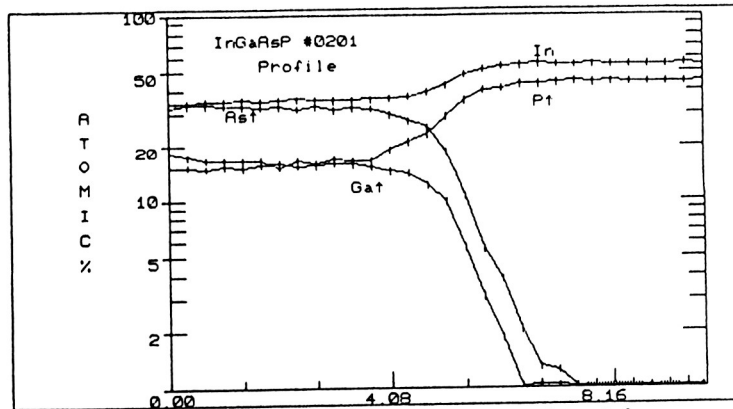


Figure 6. EDS quantitative profile of 0.92eV GaInAsP composition.

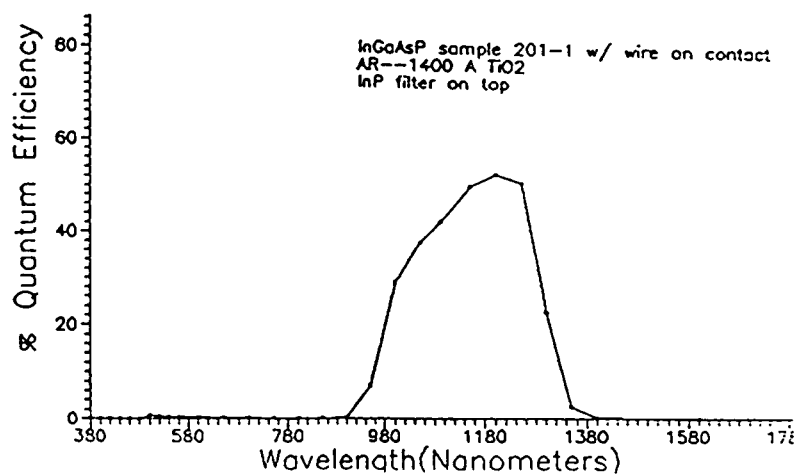


Figure 7. Quantum efficiency of 0.92eV GaInAsP solar cell under an InP filter.

Session 4
GaAs Cells

Investigation of High Efficiency GaAs Solar Cells

Larry C. Olsen, Glen Dunham, F.W. Addis, and Dan Huber
Tri-Cities University Center
Richland, WA

Kurt Linden
Spire Corporation
Bedford, MA

This paper concerns investigations of basic mechanisms which limit the performance of high efficiency GaAs solar cells. P/N heteroface structures have been fabricated from MOCVD epi-wafers. Typical AM1 efficiencies are in the 21-22% range, with a SERI measurement for one cell being 21.5%. The cells are nominally 1.5×1.5 cm in size. Studies have involved photoresponse, T-I-V analyses, and interpretation of data in terms of appropriate models to determine key cell parameters. Results of these studies are utilized to determine future approaches for increasing GaAs solar cell efficiencies.

Introduction

Electro-optical characteristics of high efficiency GaAs solar cells have been investigated in an effort to identify approaches to further improvement of cell performance. This work is part of an effort to optimize the GaAs cell structure for maximum efficiency. In the following sections, cell fabrication, performance, photoresponse analyses and current-voltage analyses are discussed.

Cell Fabrication and Performance

GaAs solar cell structures studied in this work were fabricated from epi-wafers purchased from Spire Corporation. Layered structures were grown by MOCVD according to our specifications. All other steps in cell fabrication were carried out at the Tri-Cities University Center (TUC).

The basic cell structure is described by Figure 1. An outline of cell fabrication procedures is given in Table 1. The features which distinguish the TUC approach are the use of electroplated Au and Au(Sn) contacts, $\text{Al}_x\text{Ga}_{1-x}\text{As}$ back reflector with $x = 0.45$, and a 1.5×1.5 cm die size. The use of a P^+ GaAs cap layer, the emitter and base layer thicknesses are similar to those used by other groups.

Illuminated current-voltage characteristics measured by SERI are given in Figure 2. Numerous cells have been fabricated which exhibit an efficiency between 21% and 22%.

PRECEDING PAGE BLANK NOT FILMED

Photocurrent Analyses

A photon economy analysis has been carried out to identify approaches to increase the photocurrent of GaAs cells discussed in this paper. External photoresponse of cells was measured versus wavelength before AR coatings were deposited. Internal photoresponse was then determined by measuring the reflected photon flux and accounting for collector grid shadowing.

The internal photoresponse data were interpreted in terms of the electron band structure described by Figure 3. We have found that a single region emitter model is inadequate to fit the internal photoresponse data, even if the aluminum concentration of the AlGaAs window layer is allowed to vary. Photoresponse data are fit exceptionally well if two assumptions are made, namely: the window layer is assumed to have a x -value on the order of 0.65; and the emitter is assumed to have a dead region adjacent to the AlGaAs window layer. Referring to Figure 3, layer 3A is the dead layer, that is, the minority carrier lifetime is assumed to be zero in layer 3A. The two region emitter model used here is a limiting case. In particular, we assume that minority carrier transport in the emitter only takes place in layer 3B, with the interface between 3A and 3B being characterized by a surface recombination velocity S_F .

Assumed values for the optical absorption coefficient versus wavelength for $\text{Al}_x\text{Ga}_{1-x}\text{As}$ are given in Figure 4. Presently, a complete set of experimental optical constants for all values of x does not exist. Semiempirical expressions for the absorption coefficient of $\text{Al}_x\text{Ga}_{1-x}\text{As}$ were used which contained parameters used to fit data at the compositional ends of GaAs and AlAs. This approach, with a few variations, was first employed by Hutchby and Fudurich in a theoretical modeling of graded-bandgap solar cells [ref. 1]. Our approach, which closely follows Maziar's, considers the contribution of all three band edges, $E_{\Gamma 1}$, E_L and E_{x1} , to the absorption process [ref. 2]. Equations for the value of the different bandgaps as a function of aluminum concentration were taken from Casey and Panish [ref. 3].

For direct transitions, the expressions for the absorption coefficients divide the absorption spectrum into three distinct regions: $h\nu \leq E_g$, $E_g \leq h\nu \leq E_g + \Delta_{so}$, and $h\nu \geq E_g + \Delta_{so}$ where Δ_{so} is the split-off band separation and taken as 0.33 eV. The first region follows an exponential equation and is known as the Urbach tail. We used an empirical relation with a two parameter fit as given in Maziar as

$$\alpha_{\Gamma} = B \exp[\gamma(h\nu - E_g^{\Gamma})], \quad h\nu \leq E_g$$

with $B = 3000$ and $\gamma = 100$ as fit to GaAs data by Casey and Sells [ref. 4]. In the region $E_g \leq h\nu \leq E_g + \Delta_{so}$ the equation follows the form

$$\alpha_{\Gamma} = (A^{\Gamma}/h\nu)(h\nu - E_g^{\Gamma})^{1/2}, \quad A^{\Gamma} = 7.5 \times 10^4$$

Above the split-off band the absorption data is fit by the equation

$$\alpha_{\Gamma} = 3885(10^{0.543h\nu})(1 - x)$$

Again these equations are fit to data by Casey and Sells [ref. 5] which is also contained in Casey and Panish [ref. 3].

The indirect bandgap transitions give absorption data modeled by the following

$$\alpha = (B/h\nu)(h\nu - E_g)^2$$

for both the L and X bands with $B = 5.5 \times 10^4$ as given in Maziar [ref. 2].

Figure 5 shows the effect of the dead layer on calculated values of internal photoresponse. Note that as one increases the dead layer thickness, the curve essentially pivots about a center located on the "shoulder" of the curve ($\lambda \simeq 830$ nm). Values assumed for other parameters are:

$$x = 0.65$$

$$L(F) = 5 \text{ microns}$$

$$S(F) = 3 \times 10^4 \text{ cm/sec}$$

$$L(B) = 5 \text{ microns}$$

$$S(B) = 5 \times 10^3 \text{ cm/sec}$$

The most important assumption we had to make in order to fit the data was that $x = 0.65$, instead of 0.90. Figure 6 illustrates the sensitivity of the calculated photoresponse curves to the value of x .

Figure 7 depicts the effect of varying $L(F)$ on the calculated curve. Note that the photoresponse curve between $\lambda = 350$ nm and $\lambda = 850$ nm shifts as $L(F)$ is varied. Figure 8 shows the effect of varying $S(F)$. The effects of $L(F)$ and $S(F)$ are very similar. As a result, we can only assign a range of values for these parameters. We estimate that $L(F)$ is in the range of 2.0 to 5.0 microns, and $S(F)$ is in the range of 10^4 to 3×10^4 cm/sec.

Figures 9 and 10 describe calculated internal response for ranges of $L(B)$ and $S(B)$, respectively. Like the parameters in the emitter region, the effects of $L(B)$ and $S(B)$ on calculated photoresponse curves are similar. We estimate the values for $L(B)$ and $S(B)$ to be 4.0 to 6.0 microns and 10^3 to 5×10^3 cm/sec., respectively. Results of the photoresponse analyses are summarized in Table 2.

Results of the photoresponse analyses have been used to determine potential increases in photocurrent. Table 3 summarizes key results of the photon economy analysis. Values of photocurrent were calculated by integrating internal photoresponse data (or calculated curves) over the solar spectrum. In particular, J_{PH} is calculated by

$$J_{PH} = \int_{\text{Solar Spectrum}} q N_{\lambda} S_{\lambda} d\lambda$$

where N_{λ} is the photon flux with wavelengths in the interval λ to $\lambda + d\lambda$. We find that the maximum possible value for J_{sc} is 31.6 mA/cm². The measured active current was 25.7 mA/cm². If we assume the AlGaAs window layer has an aluminum concentration of $x = 0.9$, then the active area current should increase to 26.9 mA/cm². If the dead layer were eliminated, then an increase of 0.8 mA/cm² would be obtained. A double AR coating would subsequently increase $(J_{sc})_{ACTIVE}$ to 29.0 mA/cm². Such a value for $(J_{sc})_{ACTIVE}$ is approximately the same as that reported by Spire Corporation. If we assume the collector grid shadowing to be 3%, $V_{oc} = 1.016$ Volts, $FF = 85.1\%$, then an efficiency of 24.3% would be achieved.

T-I-V Analyses

Current-voltage data have been taken for various temperatures from -30 C to 60 C, and then analyzed in terms of accepted theoretical models. I-V data at a particular temperature can usually be interpreted in terms of two current mechanisms acting in parallel. One mechanism is dominant at low voltages (0.4 to 0.8 Volts), and another is dominant at higher voltages (0.8 to 1.1 Volts). The upper mechanism is usually characterized by an n -value of 1.0 and $J_0 = 3 \times 10^{-19}$ A/cm², and can be interpreted as being due to minority carrier injection. The lower mechanism of the 21% to 22% cells is characterized by an n -value of approximately 2.0. Thus, we can interpret these characteristics as being due to depletion region recombination.

J_0 -T analyses have also been carried out. We assume J_0 can be written as

$$J_0 = J_{00} \exp(-\phi/kT)$$

$$\phi = E_{g0}, \text{ Minority Carrier Injection}$$

$$\phi = E_{g0}/2, \text{ Depletion Region Recombination}$$

where $E_g = E_{g0} - \alpha T$.

J_0 -T analyses involve plotting $\log(J_0)$ versus T^{-1} so that J_{00} and ϕ can be determined. Figure 12 shows $\log(J_0)$ versus T^{-1} for the large voltage mechanism (A), and the low voltage mechanism (B). The activation energies, $\phi = 1.50$ eV and 0.68 eV are consistent with minority carrier injection and depletion region recombination, respectively.

Conclusions

Photocurrent analyses of 21 to 22% GaAs cells indicate that an improved AlGaAs/GaAs interface in the emitter region, and a double AR coating will lead to an active area, AM1 value for J_{sc} of 29 mA/cm². This result combined with properties of cells reported in this paper would yield cells with total area, AM1 efficiencies greater than 24%. Further reduction of the magnitude of the depletion-layer-recombination current mechanism will allow efficiencies to exceed 25%. A new MOCVD reactor will be operational at TUC July, 1988. We plan to concentrate on improving the front surface AlGaAs/GaAs interface to obtain larger values of J_{sc} ; and continue to improve edge passivation procedures in order to reduce the depletion layer recombination mechanism, which will lead to larger values of FF and V_{oc} .

References

- [1] James A. Hutchby and Richard L. Furdurich, "Theoretical Optimization and Parametric Study of n-on p-Al_xGa_{1-x}GaAs Graded Band-Gap Solar Cells" *Journal of Applied Physics* **47**, 3152-3158 (1976).
- [2] Maziar MS Thesis, Purdue University, 1984.
- [3] H.C. Casey, Panish, *Heterojunction Lasers, Part A*, Academic Press, 1978.

- [4] H.C. Casey, D.D. Sell and K.W. Wecht, "Concentration Dependence of the Absorption Coefficient for n- and p-type GaAs Between 1.3 and 1.6 eV," Journal of Applied Physics **46**, 250-257 (1975).
- [5] D.D. Sell, H.C. Casey and K.W. Wecht, "Concentration Dependence of the Absorption Coefficient for n- and p-type GaAs Between 1.3 and 1.8 eV," Journal of Applied Physics **45** 2650-2657 (1974).

Table 1. Cell Fabrication Procedure

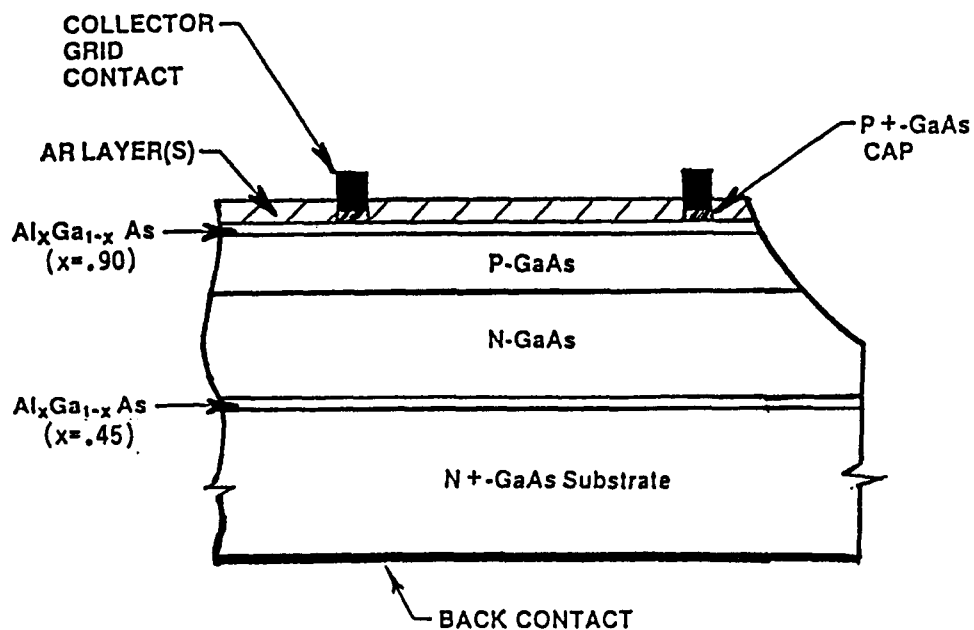
1. Grow Layered Structure by MOCVD (by Spire Corporation).
2. Dice Wafer into 1.5 X 1.5 cm Die.
3. Clean Die.
4. Apply and Pattern Photoresist.
5. Electroplate Au Collector Grid on P-Type Emitter.
6. Electroplate Au(Sn) on N-Type Substrate for Back Contact.
7. Heat Treat Contacts.
8. Form Mesa Junction.
9. Etch GaAs Cap.
10. Apply SiN_x AR Film.

Table 2. Results of Photoresponse Analyses

Apparent Al _x Ga _{1-x} As Composition:	$x = 0.65$
Dead Layer in GaAs:	40Å to 60Å
Emitter Parameters:	
	$S(E) = 1E4 - 3E4 \text{ cm/sec}$
	$L(E) = 2.0 - 5.0 \text{ microns}$
Base Parameters:	
	$S(B) = 1E3 - 5E3 \text{ cm/sec}$
	$L(B) = 4.0 - 6.0 \text{ microns}$

Table 3. AM1 Photocurrent of GaAs Cells

	Active Area Current (mA/cm ²)
Maximum J_{sc}	31.6
Measured Active Area J_{sc}	25.7
TUC Cell with Al _x Ga _{1-x} As Window Layer, x = 0.90	26.9
TUC Cell with No Dead Layer	27.7
TUC Cell with No Dead Layer and DBL AR	29.0



LAYER	ALUMINUM CONCENTRATION (%)	DOPANT CONCENTRATION (cm^{-3})	THICKNESS (μm)
P ⁺ GaAs CAP	-	Zn: $>3\text{E}18$	0.1
P-AlGaAs WINDOW	90%	Zn: $1\text{E}18$.05
P-GaAs EMITTER	-	Zn: $1\text{E}18$	0.5
N-GaAs BASE	-	Si: $3\text{E}17$	3.0
N-AlGaAs REFLECTOR	45%	Si: $1\text{E}18$	0.1
N-GaAs BUFFER	-	Si: $1\text{E}18$	0.5
N-GaAs SUBSTRATE	-	Si: $>1\text{E}18$	-

Figure 1. GaAs Cell Structure.

GaAs		global, 1000W/m ²
Sample: 87GaAs43D		Voc = 1.016 volts
Aug 24, 1987 12:54 pm		Jsc = 24.91 mA/cm ²
Temp = 25.0 C		Fill factor = 85.08 %
Area = 2.307 cm ²		Efficiency = 21.5 %

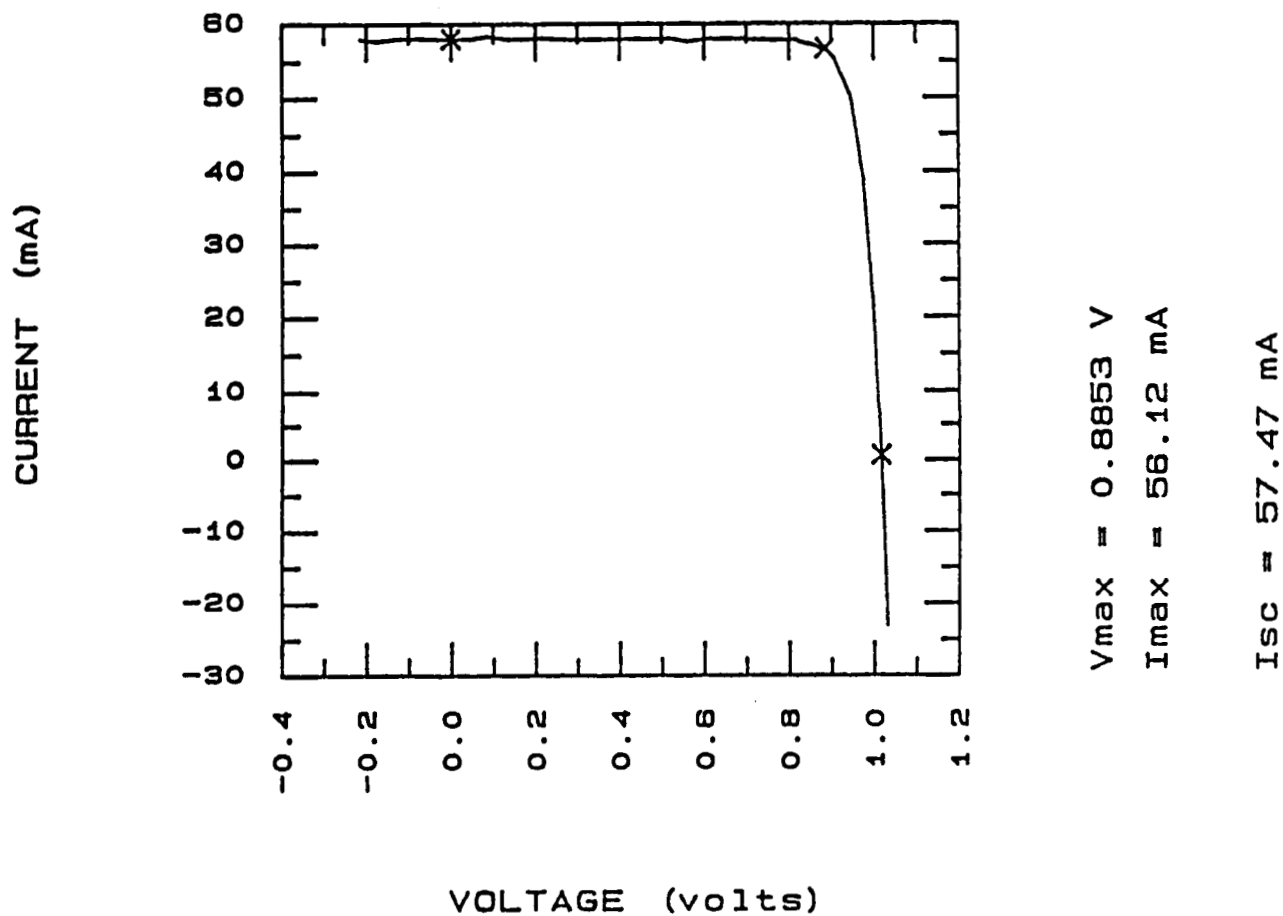


Figure 2. Illuminated I-V Characteristics for a GaAs Cell Measured by SERI.

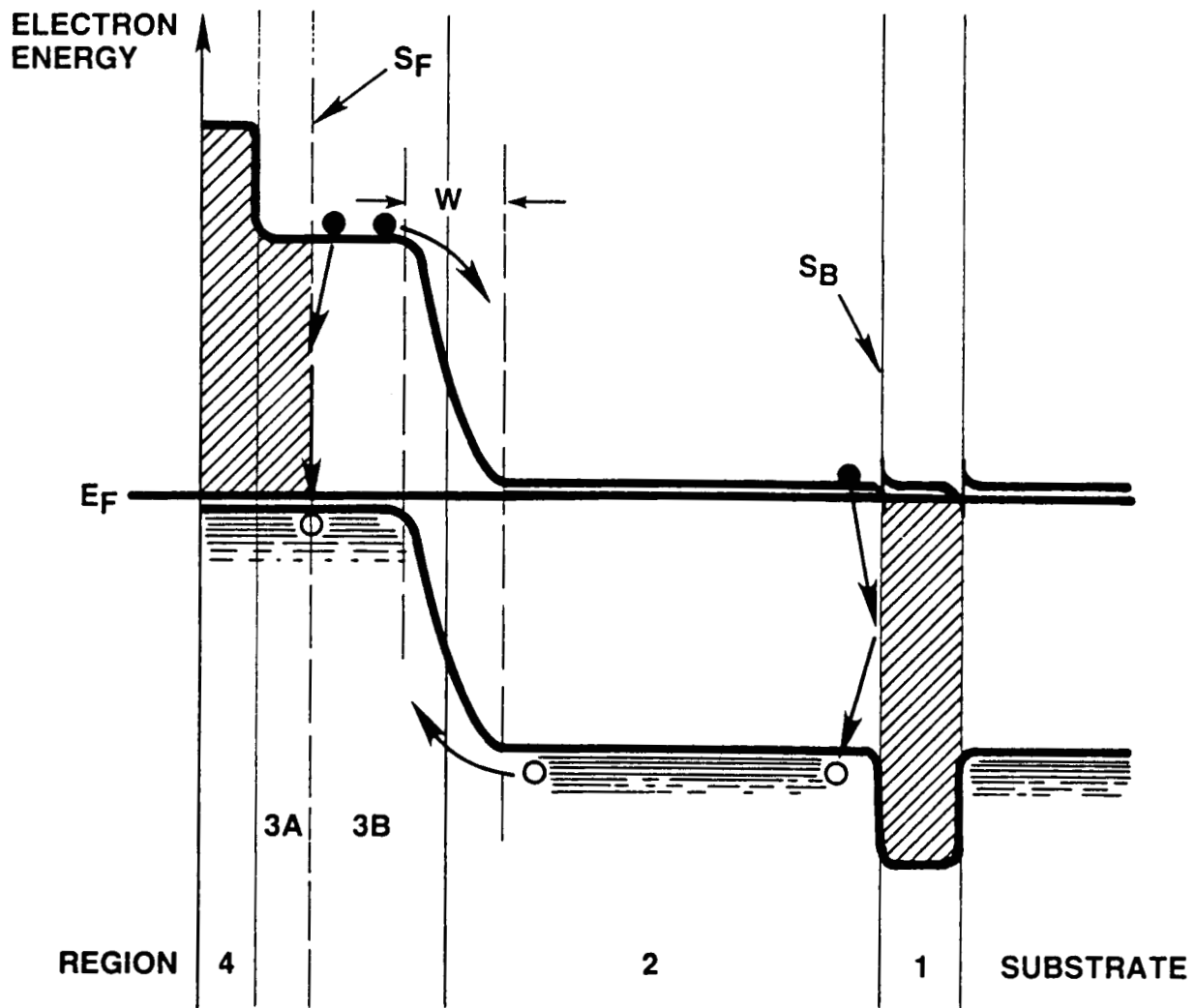


Figure 3. Assumed Electron Band Structure for GaAs Cells.

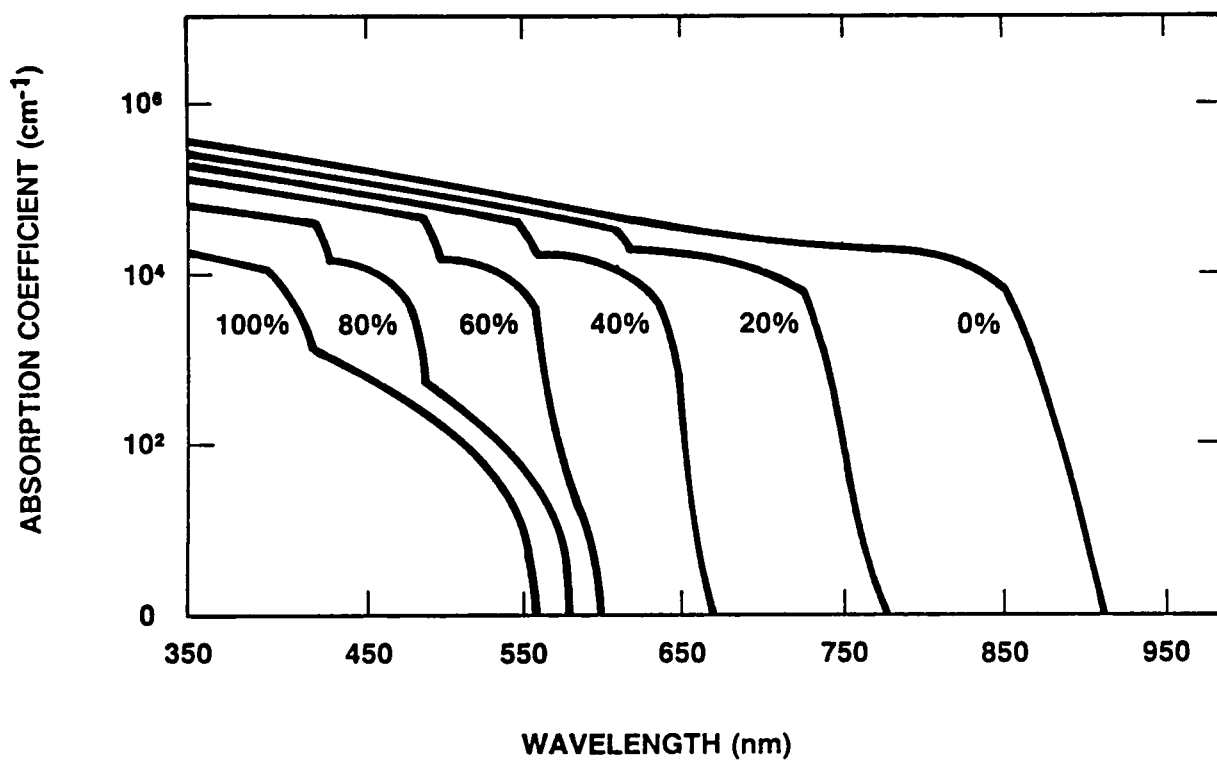


Figure 4. $\text{Al}_x\text{Ga}_{1-x}\text{As}$ Optical Absorption Coefficient for Various Values of x .

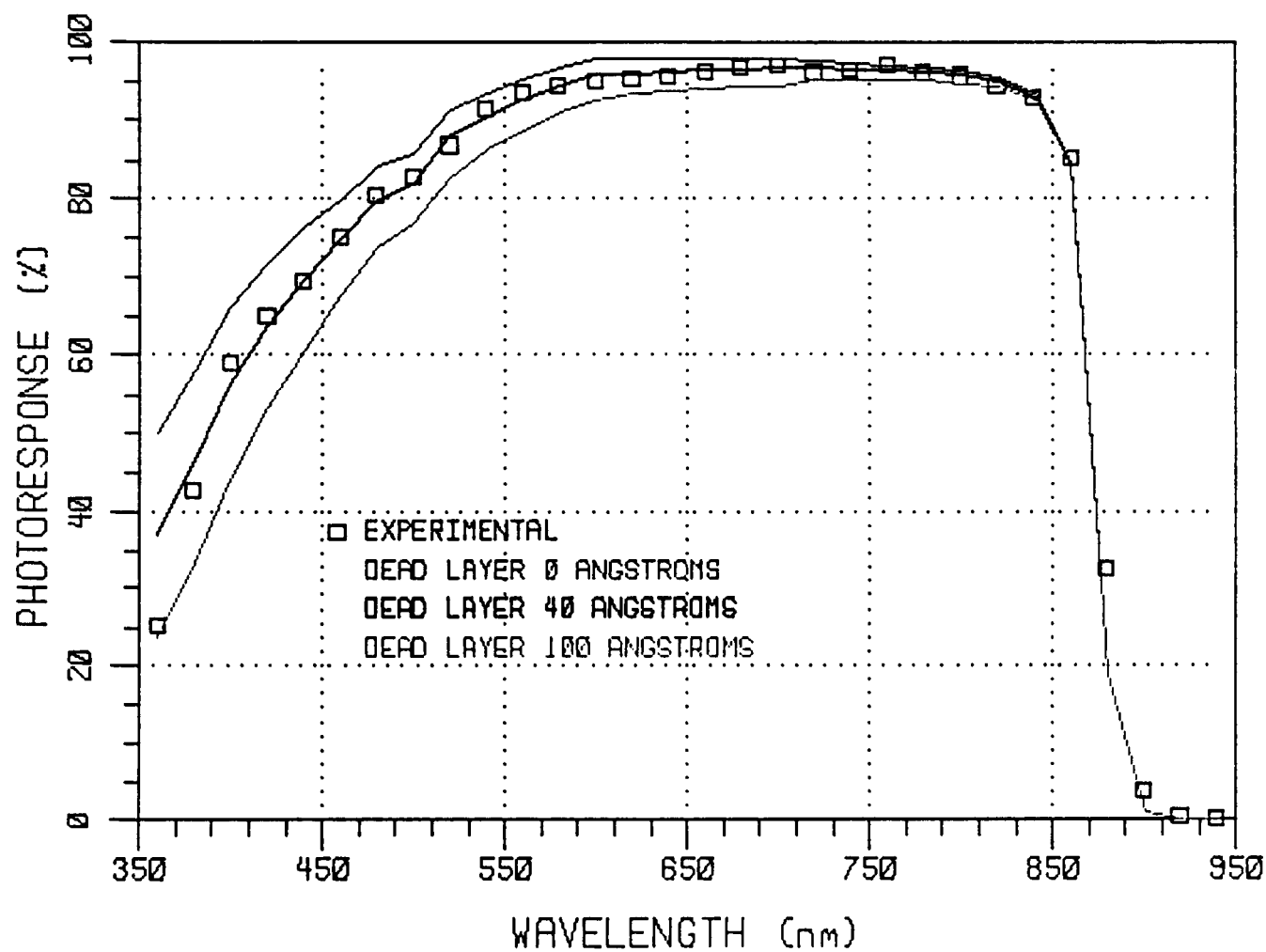


Figure 5. Experimental Data and Calculated Values for Internal Photoresponse versus Wavelength for Three Dead Layer Thicknesses.

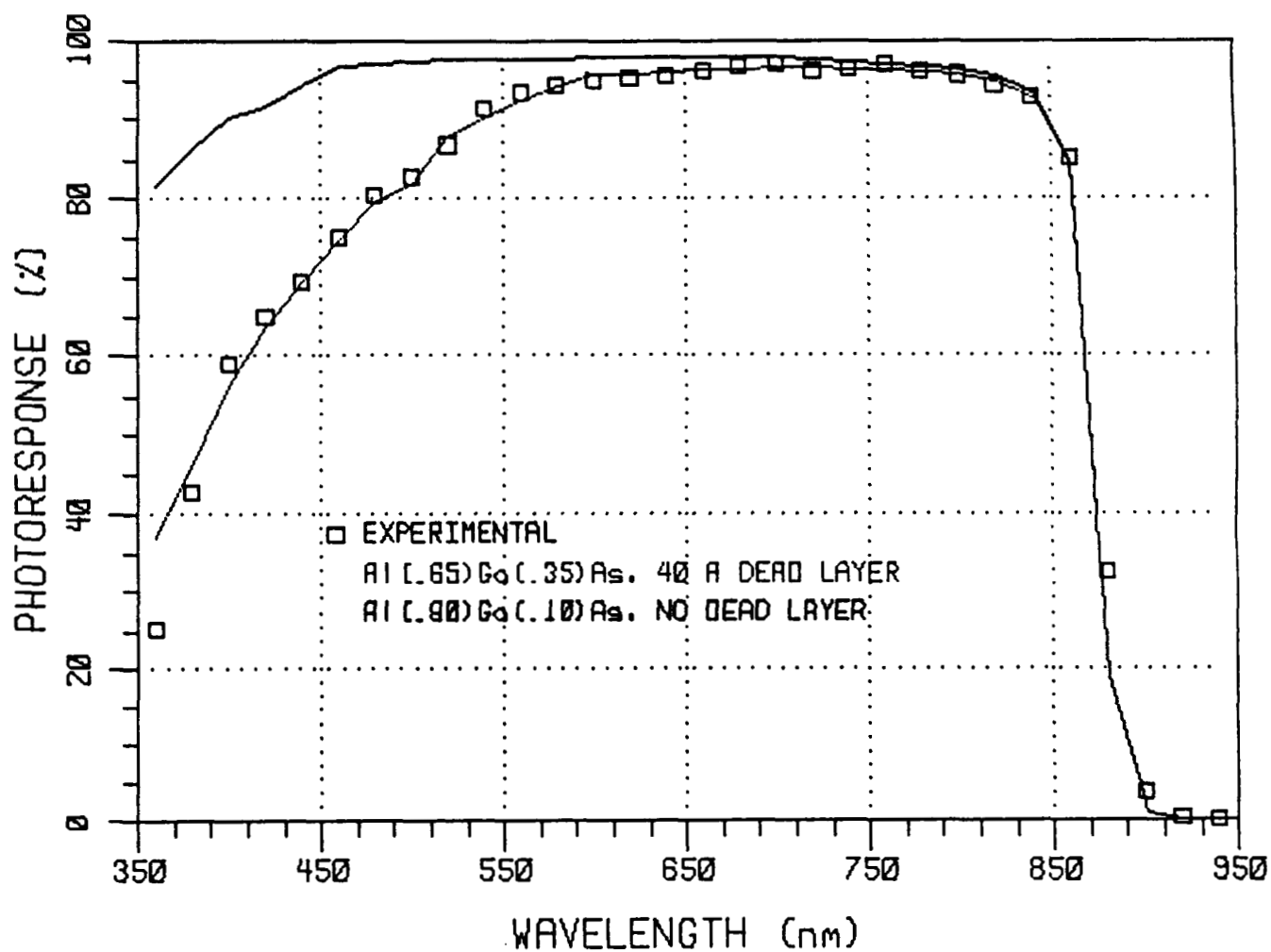


Figure 6. Experimental Data and Calculated Values for Internal Photoresponse Assuming $x = 0.9$ and No Dead Layer, and $x = 0.65$ and a Dead Layer Thickness of 40 Å.

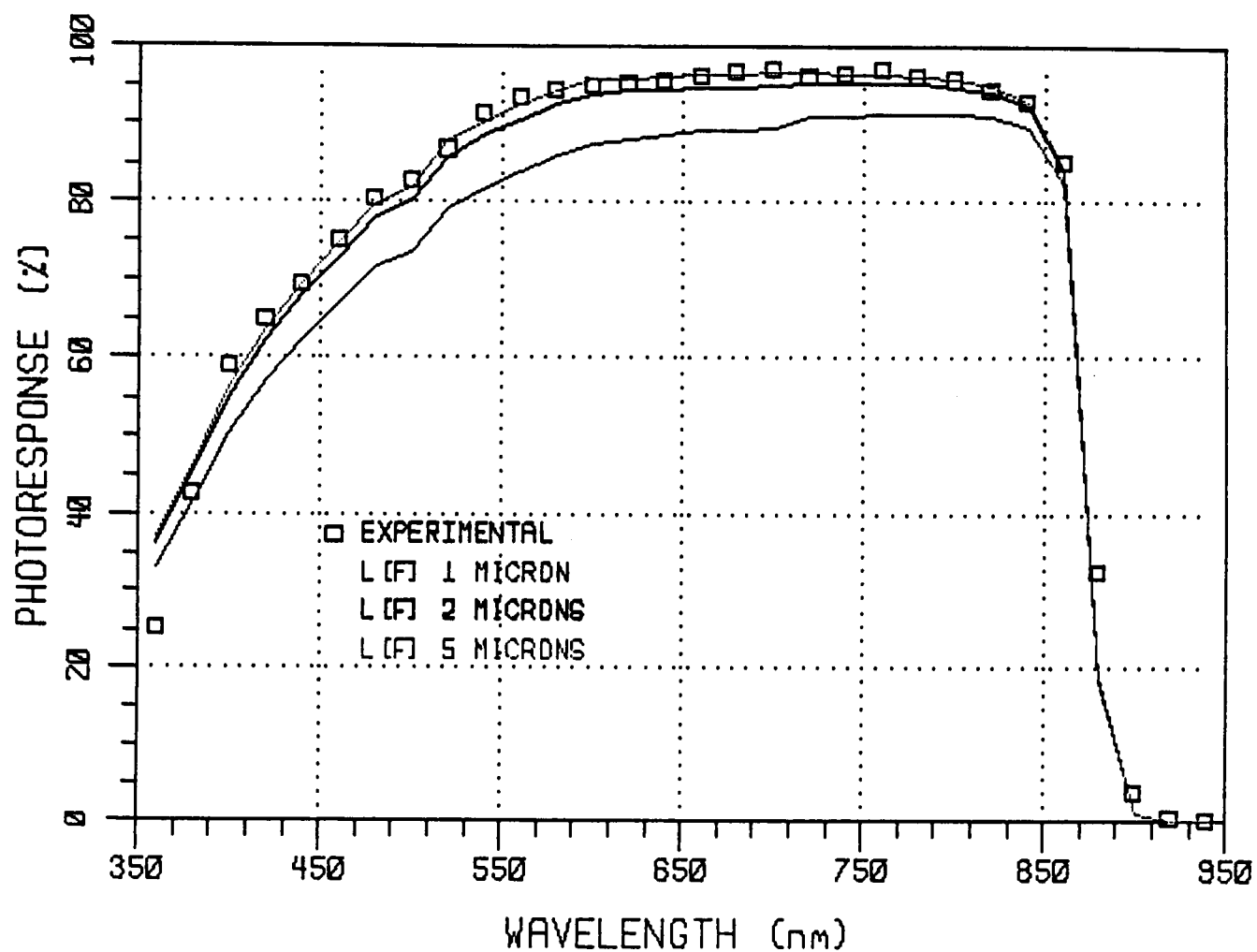


Figure 7. Calculated Values of Internal Photoresponse for a Range of Values for the Emitter Diffusion Length, $L(F)$.

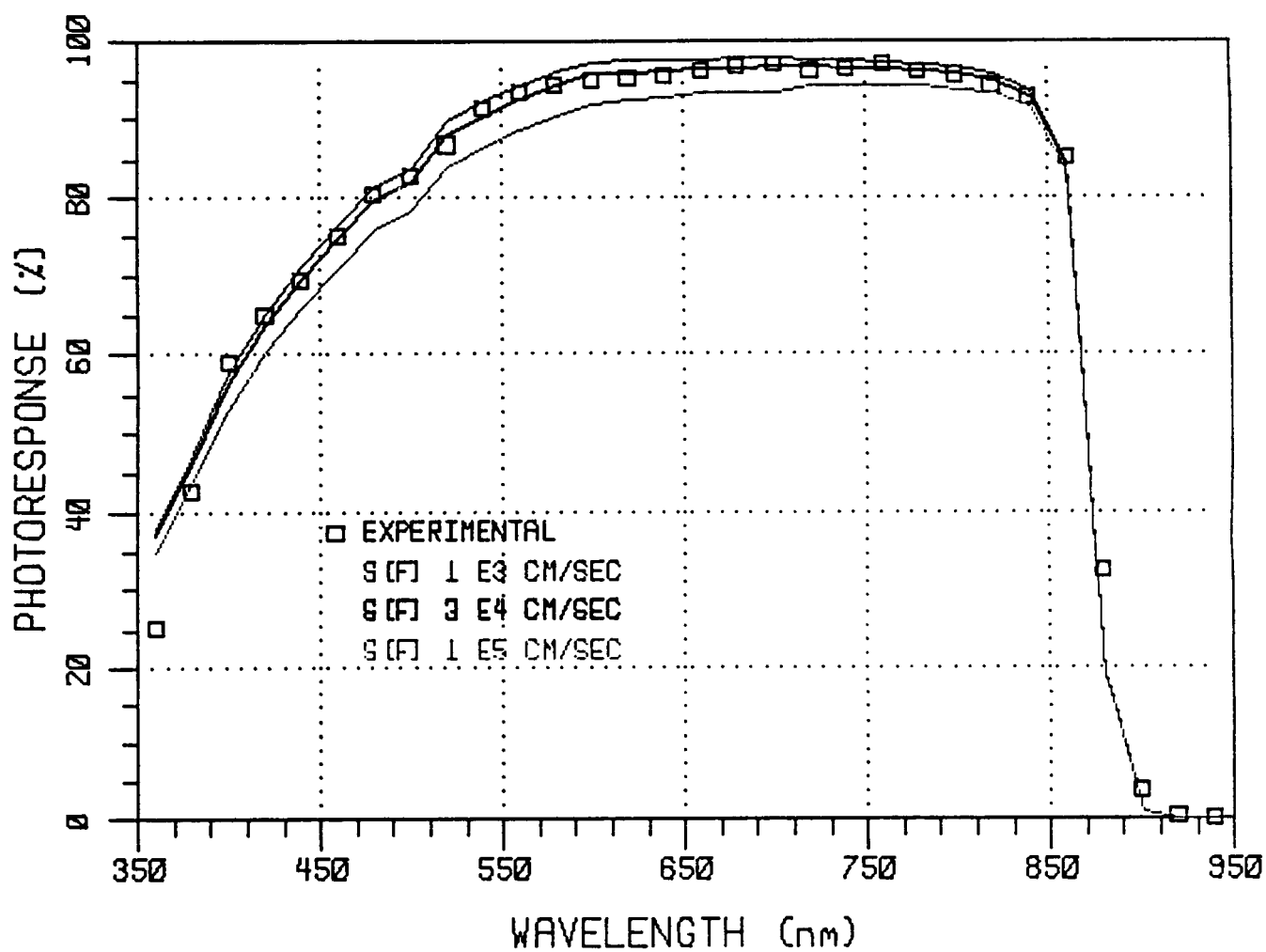


Figure 8. Calculated Values of Internal Photoresponse for a Range of Values for the Emitter Surface Recombination Velocity, $S(F)$.

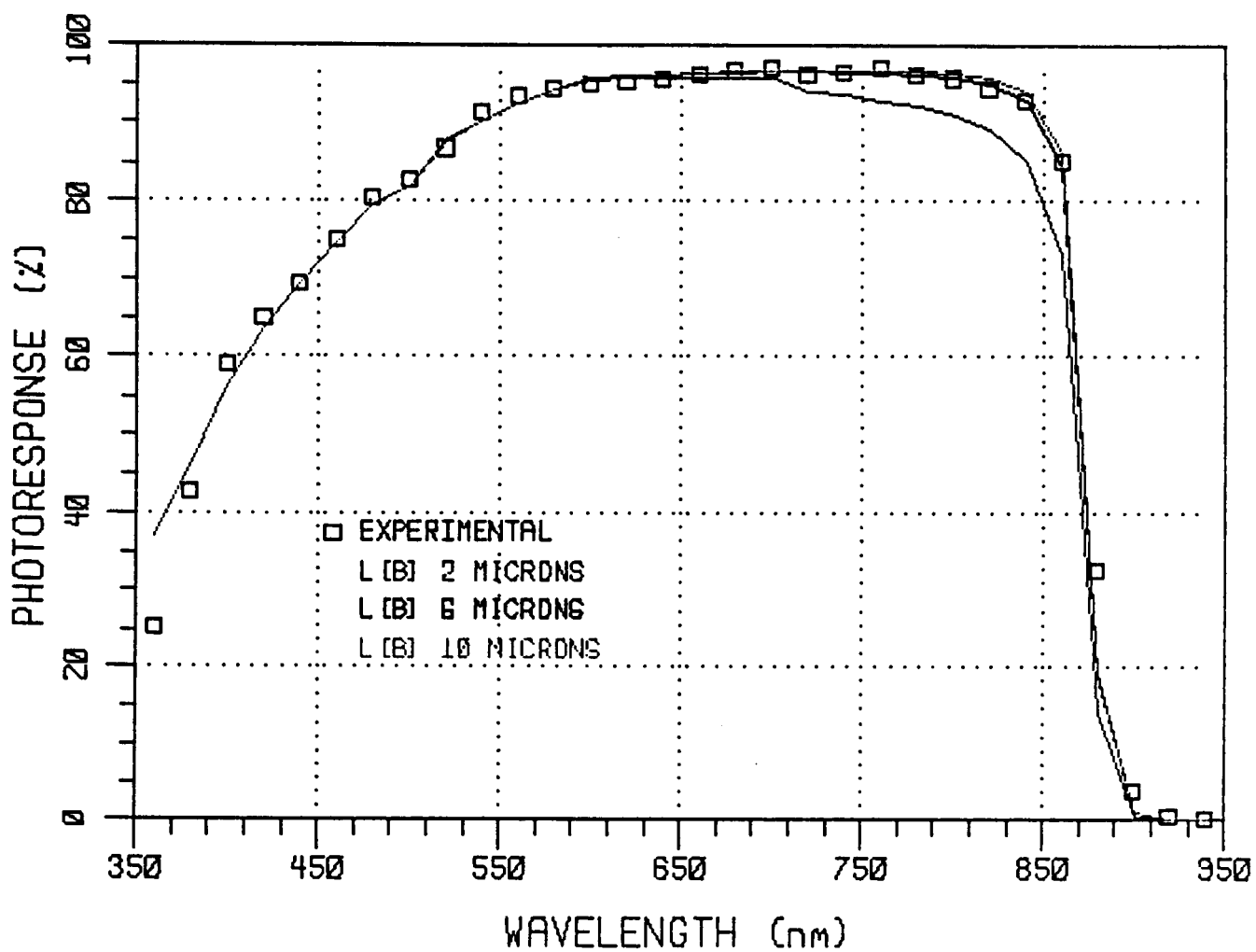


Figure 9. Calculated Values of Internal Photoresponse for a Range of Values for the Base Diffusion Length, $L(B)$.

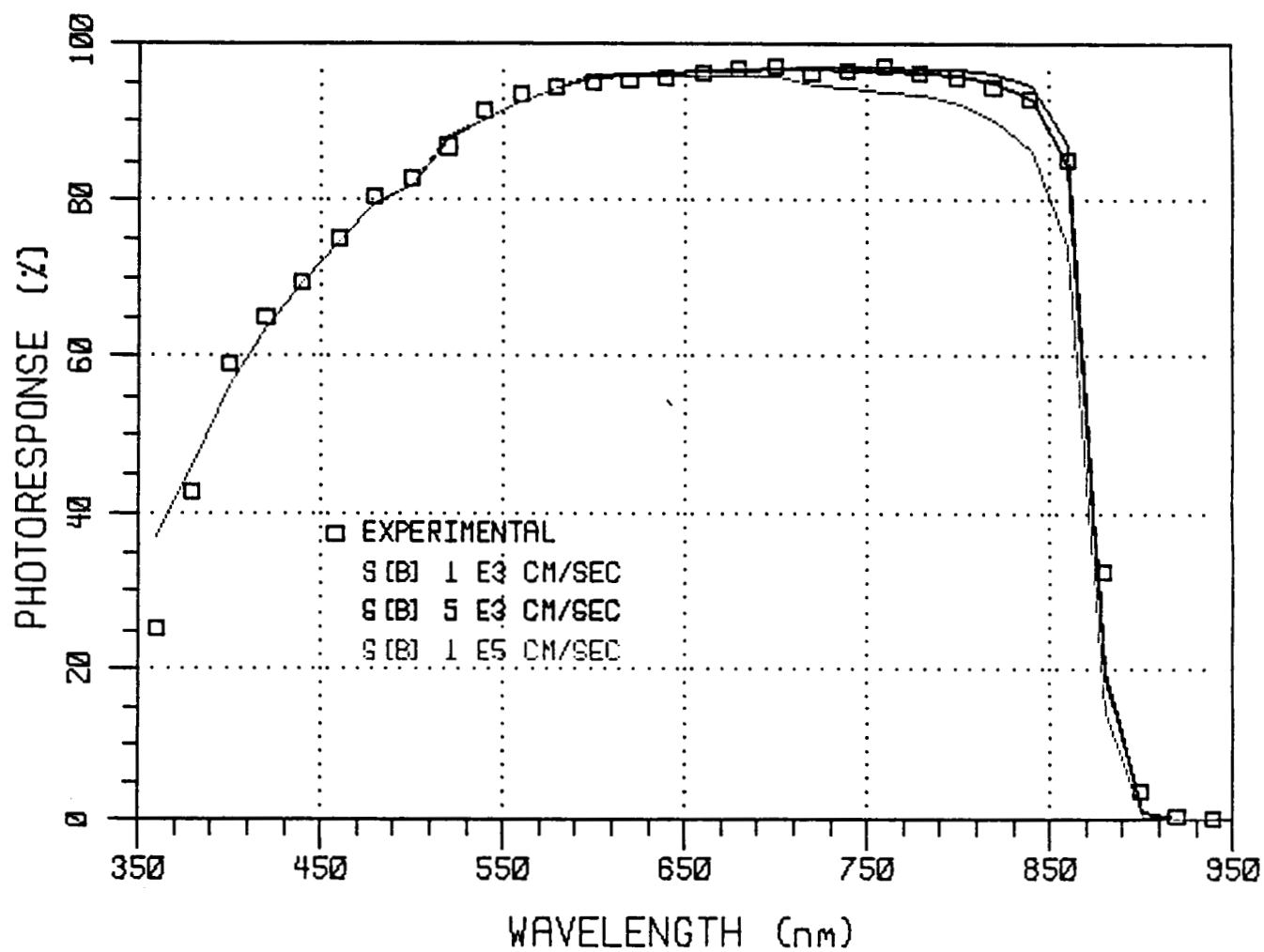


Figure 10. Calculated Values of Internal Photoresponse for a Range of Values for the Surface Recombination Velocity at the Back Surface, $S(B)$.

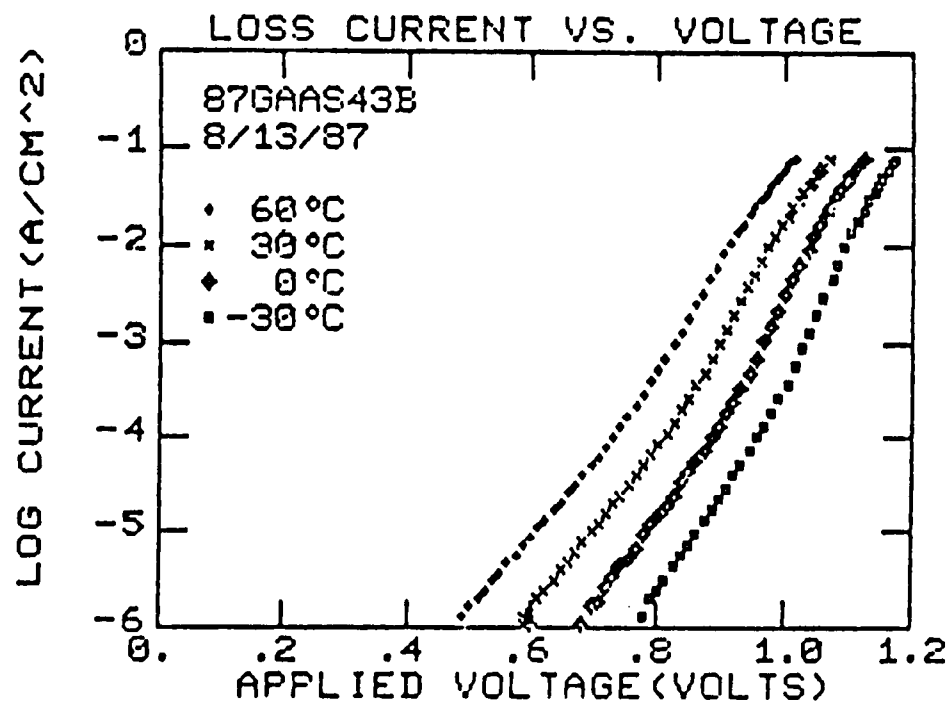


Figure 11. I-V Data Measured for Various Temperatures.

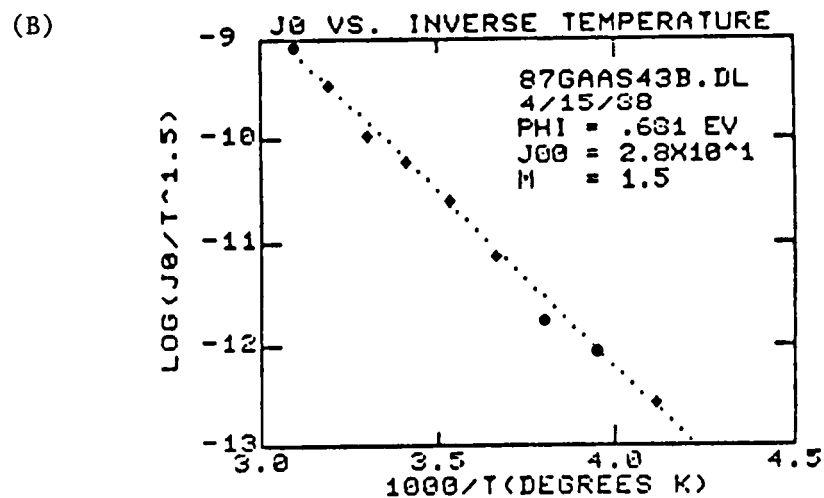
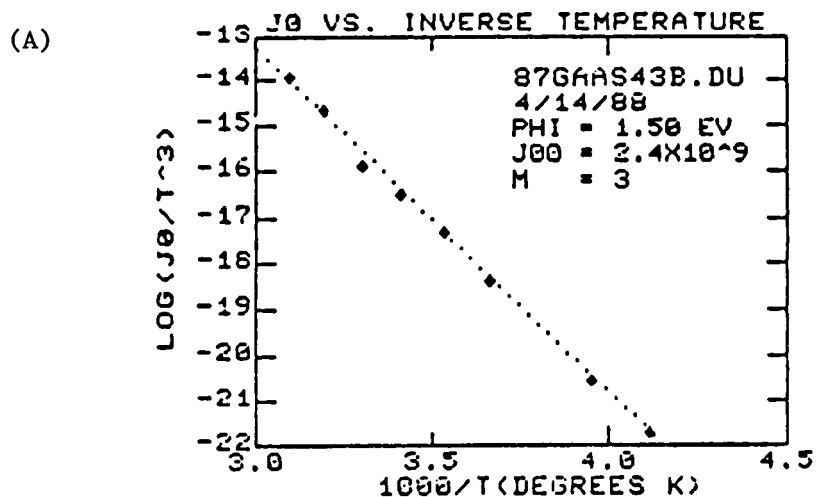


Figure 12. J_0 - T Analysis for GaAs Cell 87-43. (A) $\log J_0$ versus T^{-1} for the Large Voltage Mechanism. (B) $\log J_0$ versus T^{-1} for the Low Voltage Mechanism.

A New Structure for Comparing Surface Passivation Materials of GaAs Solar Cells *

Gregory C. DeSalvo and Allen M. Barnett
University of Delaware
Department of Electrical Engineering
Newark, DE 19716 302-451-2405

New Structure Design

The surface recombination velocity (S_{rec}) for bare GaAs is typically as high as 10^6 to 10^7 cm/sec, which dramatically lowers the efficiency of GaAs solar cells. Early attempts to circumvent this problem by making an ultra thin junction ($x_j < .1 \mu\text{m}$) proved unsuccessful when compared to lowering S_{rec} by surface passivation [ref. 1,2,3]. Present day GaAs solar cells use an GaAlAs window layer to passivate the top surface [ref. 4,5]. The advantages of GaAlAs in surface passivation are its high bandgap energy and lattice matching to GaAs. Although GaAlAs is successful in reducing the surface recombination velocity, it has other inherent problems of chemical instability (Al readily oxidizes) and ohmic contact formation.

The search for new, more stable window layer materials requires a means to compare their surface passivation ability. Therefore, a device structure is needed to easily test the performance of different passivating candidates. Such a test device is shown in Figure 1.

This design has three important features:

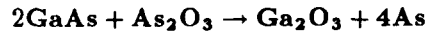
1. The device allows direct comparison of identical GaAs solar cells with and without passivation. This is accomplished by growing the window layer on only half of the light active region and by employing a parallel metallization scheme. The solar cell can be cleaved in half, permitting any measurable improvements due to surface passivation to be related to the same GaAs solar cell without a window layer [Figure 2].
2. The structure avoids ohmic contact problems to the window layer. A separate thick p-GaAs region is grown to provide the necessary top contact [cf. Figure 1]. This thicker p-region prevents contact punch through of the thin p-GaAs collector, as well as blocking any shunt defects from forming due to incomplete window/collector layer growth. Since the objective is to compare the surface passivation ability of various materials, problems associated with making contacts to the window are eliminated.
3. The multilevel device provides for testing of all semiconductor layers of the solar cell (i.e., the absorber, collector, and window). Absorber contacts are formed on the exposed top portion of the n-GaAs layer, allowing measurement of the absorber layer's doping concentration and resistivity. The parallel contact pattern provides the same measurements of the p-GaAs collector. Further tests of the p/n junction solar cell supply numerous other useful parameters, as listed in Table 1.

* This work was supported by NASA Lewis Research Center under contract # NAG3-422.

The multilevel design is fabricated by utilizing the special masking abilities of the growth method used. The GaAs solar cell is grown by the liquid phase epitaxy (LPE) process using a horizontal sliding graphite boat. The LPE growth process is used because of its superior device performance [ref. 7]. Normal LPE grown layers have melt wells approximately equal in size to the seed and positioned linearly over the movable GaAs substrate. Pulling the seed wafer under each successive melt produces a multiple layer device, with each new layer completely covering the last one. This sliding boat technique allows for easy modification of melt sizes by opening wells of different areas at various locations over the seed position. Proper positioning of the GaAs substrate provides localized LPE (L²PE) growth to occur only in designated regions on the seed wafer [Figure 3]. That is, the device is made by sequentially moving the substrate under each growth melt, forming localized layers on top of each other. This L²PE process provides the freedom to design a multilevel structure to test surface passivation of GaAs solar cells.

Surface Recombination

Surface recombination in GaAs is due to excess anion charges at the crystal surface, which deforms the lattice. When GaAs is exposed to air (O₂), its surface forms a native oxide layer of about 20–50Å in thickness. This oxide is predominantly Ga₂O₃, although several forms of arsenic oxide can also form, namely As₂O₃ [ref. 8]. However, any As₂O₃ formed is unstable and reacts with GaAs at the GaAs–oxide interface to form elemental As through the chemical reaction [ref. 9]:



Thus, with much of the Ga on the surface bound together with oxygen, a large amount of elemental As is present at the interface. It is this free excess As anion concentration which causes a slight crystal deformation of GaAs at the surface [Figure 4a][ref. 10,11]. This rearrangement moves the empty energy states associated with the As atom from the conduction band into the bandgap region. These As acceptor states are located about .7 eV below the conduction band minimum ($\approx E_{gap}/2$), and are ideal recombination centers due to their mid bandgap energy level [Figure 4b][ref. 11].

Surface recombination in GaAs solar cells deteriorates the light generated current (J_{light}), as minority carriers are trapped by the recombination centers of the surface As atoms, instead of being collected at the junction. However, surface recombination also detrimentally affects (i.e., increases) the reverse saturation current (J_o). The combined effect of these two increased losses are shown in the open circuit voltage (V_{oc}) of the solar cell. That is, a reduction in surface recombination (S_{rec}) will result in higher open circuit voltages. Thus, a change in V_{oc} as measured by this new structure indicates the level of surface passivation by any material.

Solar Cell Equation:

$$J = J_o(e^{qV/kT} - 1) - J_{light}$$

$$V_{oc} = \frac{kT}{q} \ln \left(\frac{J_{light}}{J_o} \right)$$

Surface Passivation

The window layer passivates the surface of the GaAs solar cells by eliminating dangling bonds and reducing the surface recombination velocity (S_{rec}). Theoretical calculations predict passivated, high efficiency GaAs solar cells when S_{rec} is reduced from its normally high $10^6 - 10^7$ cm/sec to only 10^4 cm/sec [Figure 6]. In essence, the window material does not need to achieve perfect surface passivation ($S_{rec} \rightarrow 0$) in order to obtain optimum performance from GaAs, only a lowering of S_{rec} to 10^4 cm/sec is required.

Numerous materials are available for trial application to GaAs, but choice of the best window layer should meet most of the criteria described below:

Surface Passivation Material Design Rules for GaAs

1. Passivate the top surface of GaAs by reducing S_{rec} to $10^3 - 10^4$ cm/sec.
2. Be transparent to the useful sunlight of GaAs (i.e., $E_{gap}^{window} > E_{gap}^{GaAs}$).
3. Chemically stable in space and earth atmosphere for the duration of the solar cell's life.
4. Minimize lattice mismatch to GaAs.
5. Form stable, low resistance ohmic contacts.

Some promising window candidates are given in Table 2. New semiconductor compounds incorporating Al are still applicable (i.e., $Al_{.48}In_{.52}P$), since Al_x mole fractions of $x \leq .50$ may be stable and form ohmic contacts [ref. 12].

New window layer materials must reduce S_{rec} by tying up the excess As anions at the surface, or by preventing atomic As from forming. The first procedure involves a chemical reaction which bonds the As with the passivating material (e.g., $Na_2S \cdot 9H_2O$ [ref. 13]), while the latter procedure requires the application of a window layer on the freshly grown GaAs before oxidation occurs (e.g., GaAlAs or GaP). Finally, a combination of these procedures could be used to allow a broader range of window layer materials. An example of this might be the application of $Na_2S \cdot 9H_2O$ on the GaAs surface, followed immediately by the application of a layer preventing surface oxidation. Using the new device structure will provide accurate comparisons of various experimental window materials now under investigation.

References

- [1] H.J. Hovel and J.M. Woodall, "Improved GaAs Solar Cells with Very Thin Junctions", *Proc. 12th IEEE Photovoltaic Specialists Conference*, 945 (1976).
- [2] A.E. Blakeslee, H. Aharoni, M.W. Wanlass, A. Kibbler, K. Emery and C.R. Osterwald, "Effect of Junction Depth on the Parameters of GaAs Shallow Junction Homojunction Solar Cells", *Proc. 18th IEEE Photovoltaics Specialists Conference*, 146 (1985).
- [3] C.O. Bozler and J.C.C. Fan, "High efficiency GaAs shallow homojunction solar cells", *Appl. Phys. Lett.*, **31**, 629 (1977).
- [4] M. Gillander, B. Cavicchi, D. Lillington, and N. Mardesich, "Pilot Production Experience of LPE GaAs Solar Cells", *Proc. 19th IEEE Photovoltaic Specialists Conference*, 289 (1987).
- [5] P.A. Iles and Kou-I Chang, "Review of Mantech Program for GaAs Solar Cells", *Proc. 19th IEEE Photovoltaic Specialists Conference*, 331 (1987).
- [6] H.H. Berger, "Models for Contacts to Planar Devices", *Solid State Electron.*, **15**, 145 (1972).
- [7] R.L. Moon, "Liquid Phase Epitaxy", *Crystal Growth*, 2nd ed., Pergamon Press (1980), p. 421.
- [8] B. Schwartz, "GaAs Surface Chemistry — A Review", *CRC Critical Reviews in Solid State Sciences*, 609 (Nov. 1975).
- [9] F. Capasso and G.F. Williams, "A Proposed Hydrogenation/Nitridization Passivation Mechanism for GaAs and Other III-V Semiconductor Devices, Including InGaAs Long Wavelength Photodetectors", *J. Electrochem. Soc.*, **129**, 821 (1982).
- [10] W.E. Spicer, P.W. Chye, P.R. Skeath, C.Y. Su, and I. Lindau, "New and unified model for Schottky barrier and III-V insulator interface states formation", *J. Vac. Sci. Technol.*, **16**, 1422 (1979).
- [11] T.E. Kazior, J. Lagowski, and H.C. Gatos, "The electrical behavior of GaAs — insulator interfaces: A discrete energy interface state model", *J. Appl. Phys.*, **54**, 2533 (1983).
- [12] S. Tiwari, J. Hintzman, and A. Callegari, "Rapid thermal diffusion and ohmic contacts using zinc in GaAs and GaAlAs", *Appl. Phys. Lett.*, **51**, 2118 (1987).
- [13] E. Yablonovitch, C.J. Sandroff, R. Bhat, and T. Gmitter, "Nearly ideal electronic properties of sulfide coated GaAs surfaces", *Appl. Phys. Lett.*, **51**, 439 (1987).

Table 1

Available Non-Destructive Tests for the Multilevel Structure	
Test Station	Calculated Parameters
Current – Voltage (IV)	$I_{sc}, V_{oc}, P_{max}, \eta, FF$ $I_0, A, R_{shunt}, R_{series}$
Four Point Probe	$\rho_{collector}, \rho_{absorber}$ N_A, N_D, μ_n $R_{contacts}$ [6]
Capacitance – Voltage (CV)	N_D
Spectral Response	η_q, L_n, S_{rec}

Table 2

Prospective Window Layer Materials for GaAs Solar Cells				
Semiconductor Material	E_{gap} (eV)	Bandgap Type	Lattice Constant (Å)	Lattice Mismatch (%)
GaAs	1.424	direct	5.653	—
Ga _{0.15} Al _{0.85} As	2.103	indirect	5.659	0.106
GaP	2.260	indirect	5.451	3.573
GaAs _{0.50} P _{0.50}	2.043	indirect	5.552	1.787
Ga _{0.51} In _{0.49} P	1.883	direct	5.653	—
Al _{0.48} In _{0.52} P	2.350	indirect	5.653	—
ZnSe	2.670	direct	5.667	0.248

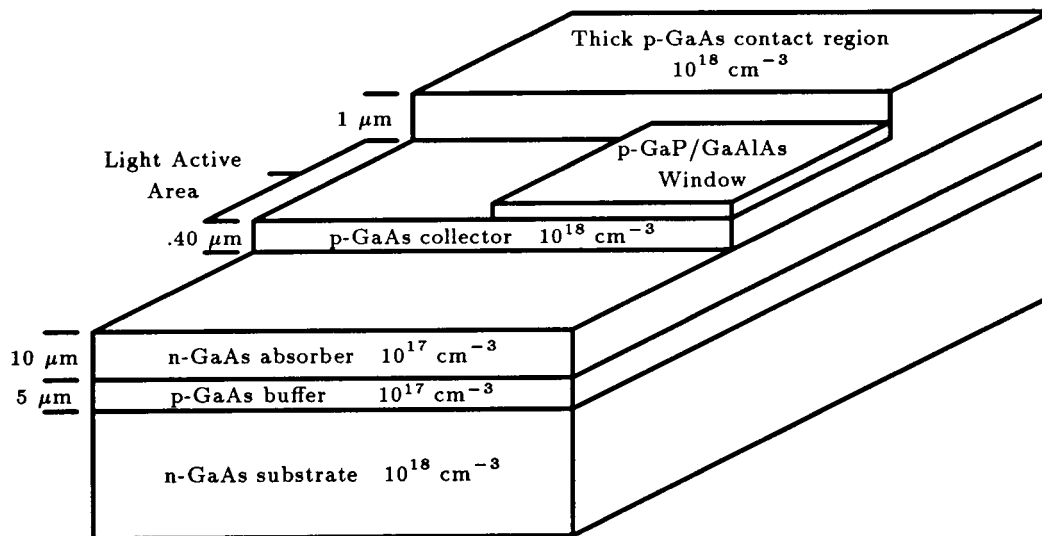


Figure 1. Multilevel structure side view showing the grown layers.

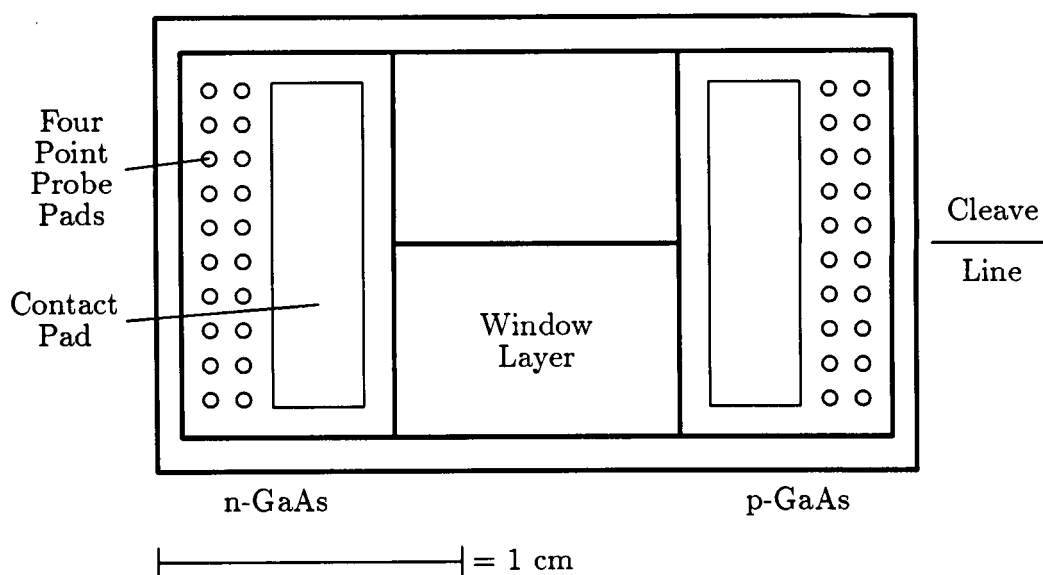


Figure 2. Top view of test structure showing metallization pattern.

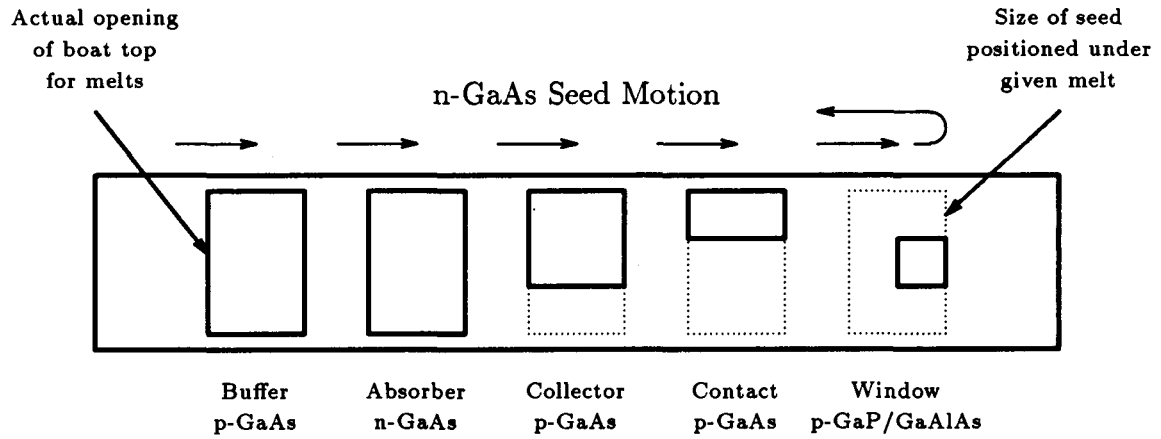


Figure 3. General schematic of LPE melt positions to grow the test device structure.

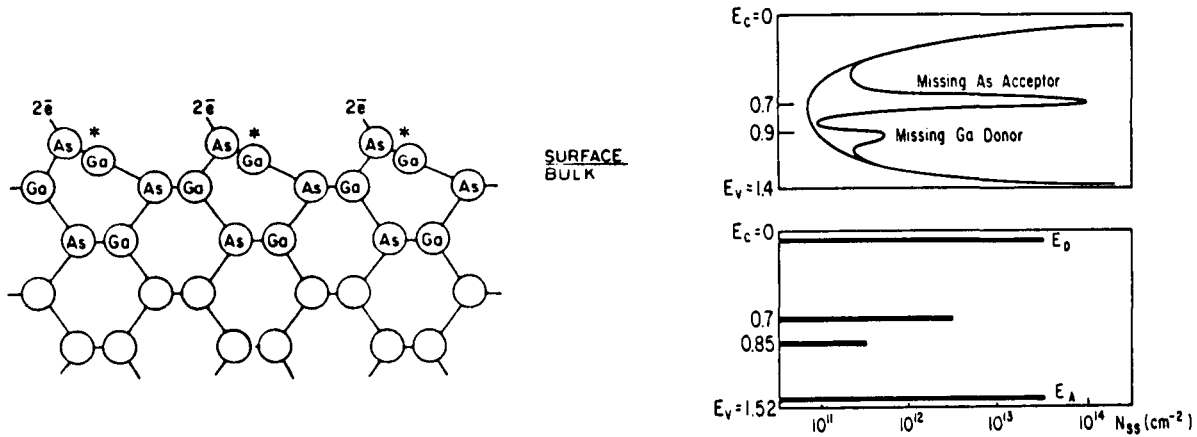


Figure 4. (a) Schematic of GaAs lattice structure at the surface due to presence of excess As atoms [10], and (b) the corresponding shift of interface state density distributions inside the energy bandgap region [11].

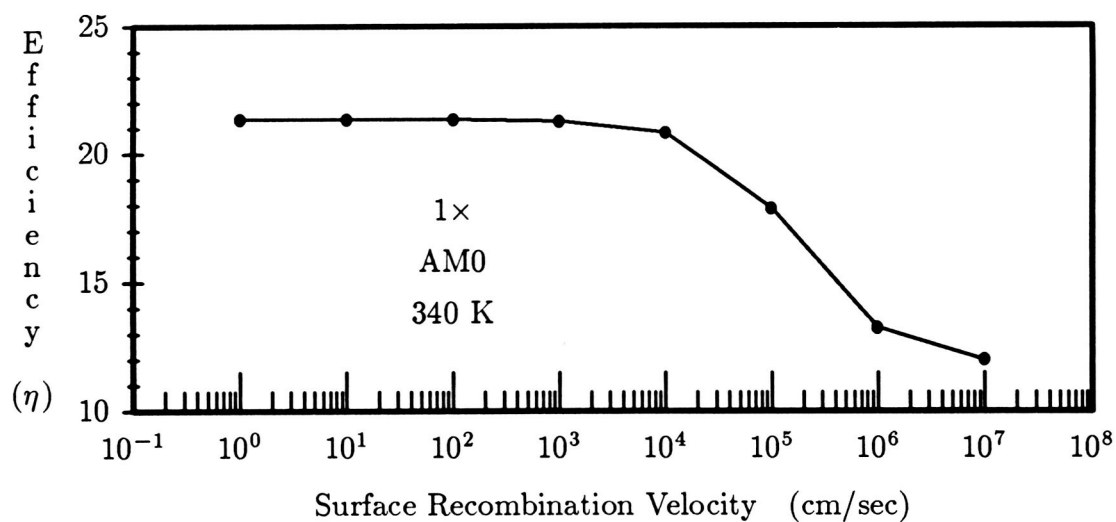


Figure 5. Theoretical calculation of output power efficiency vs. surface recombination velocity for an N/P GaAs solar cell (with losses).



Figure 6. Top view photograph showing preliminary LPE growth process of multilevel GaAs solar cell with GaAlAs window layer.

Improved Defect Analysis of Gallium Arsenide Solar Cells Using Image Enhancement*

Louis C. Kilmer, Christiana Honsberg, Allen M. Barnett
Electrical Engineering Department
University of Delaware

James E. Phillips
Institute of Energy Conversion
University of Delaware

Summary

A new technique has been developed to capture, digitize, and enhance the image of light emission from a forward biased direct bandgap solar cell. Since the forward biased light emission from a direct bandgap solar cell has been shown to display both qualitative and quantitative information about the solar cell's performance and its defects, signal processing techniques can be applied to the light emission images to identify and analyze shunt diodes. Shunt diodes are of particular importance because they have been found to be the type of defect which is likely to cause failure in a GaAs solar cell. The presence of a shunt diode can be detected from the light emission by using a photodetector to measure the quantity of light emitted at various current densities [ref. 1]. However, to analyze how the shunt diodes affect the quality of the solar cell the pattern of the light emission must be studied. With the use of image enhancement routines, the light emission can be studied at low light emission levels where shunt diode effects are dominant.

Introduction

Shunt defects are imperfections which lower the current through the junction of a solar cell by providing an alternate path for the light generated current to flow. As the solar cell model shows (figure 1), shunt defects may be modeled as resistors or as diodes. Shunt defects are most commonly thought of as light independent conductances caused by depressions, impurities, voids, or dirt on the top layer or surface of the solar cell. However, a shunt defect may also be modeled as a diode having exponential characteristics. The shunt diodes are in parallel with the junction diode which will affect the overall value of the saturation current. Shunt diodes can be caused by various means in the space charge regions including deep level traps, dislocations, variations in doping, and Schottky barriers at the junction. Because shunt diodes follow the exponential diode equation, a variable light intensity plot of the open circuit voltage versus the natural log of the short circuit current ($V_{oc} - \ln(I_{sc})$) is used to identify the presence of such diodes. Ideally, the solar cell would not contain any shunt diodes and the slope of the $V_{oc} - \ln(I_{sc})$ curve would be constant. The presence of a shunt diode produces regions on the curve with different slopes because the shunt diode has different parameters than the junction diode. The relationship between V_{oc} and I_{sc} can be seen in the solar cell current and voltage equations (eqs. 1 and 2).

* This work is partially supported by the U.S. Air Force Wright Aeronautical Laboratories under contract # F33615-86-C-2723 Task 1.

$$I = I_0(e^{\frac{qV}{nkT}} - 1) - I_L \quad (1)$$

$$V_{oc} = \frac{nkT}{q} \ln\left(\frac{I_{sc}}{I_0} + 1\right) \quad (2)$$

The slope of the $V_{oc} - \ln(I_{sc})$ curve is proportional to the n parameter of the diode. A shunt diode has a larger effect of the solar cell's response at low output light intensities (low currents). At high light intensities, the junction diode dominates and the shunt diode is not noticeable. The transition of the shunt diode's effect on the solar cell's response as the current and light intensity increase is reflected by the changing slope of the $V_{oc} - \ln(I_{sc})$ curve. At low currents, the shunt diode has a lower resistance than the junction diode. Because the diodes are in parallel, more current will flow through the shunt diode than the junction diode. The decrease in current through the junction diode causes the open circuit voltage to decrease. However, the amount that V_{oc} decreases is small because, from equation (2), V_{oc} is proportional to the natural log of I_{sc} . The small change in the current causes an even smaller change in the voltage. Therefore, the presence of a shunt diode is difficult to detect by standard I-V analysis.

Light Emission From GaAs Solar Cells

A solar cell is a p-n junction designed to absorb light, generate minority carriers, and collect them efficiently. A light emitting diode (LED) is also a p-n junction device which, under a forward bias, produces light. The main difference between an LED and a solar cell is the thin top layer of the solar cell. The top layer, the collector, is made thin so the light will not be absorbed but pass through to the active region. A solar cell made from a direct bandgap material (GaAs for example) will emit light under a forward bias. The thin top layer allows the generated light to pass through to the surface.

It has already been shown that the forward biased light emission of a direct bandgap solar cell provides a quick and simple method of testing for the presence of shunt defects [ref. 2]. Because the light emission is caused by the injected minority carrier current, it is very sensitive to any defects which affect the current through the junction. The pattern of light emission shows the overall quality of the solar cell by displaying those areas which do not emit light. The light emission may also be quantized by using a detector solar cell to measure the amount of light emitted. By using a Si detector solar cell, the transition point of the shunt diode's effects on the performance of the solar cell was found to be around $J_{sc} = 0.25 \text{ ma/cm}^2$. Therefore, to view the effects of the shunt defects, the solar cell must be biased with a very low forward current so the shunt diode will dominate over the junction diode [ref. 3].

Image Enhancement of Light Emission

The amount of light generated with a forward current of less than 1 milliampere (equivalent to $J_{sc} = 0.25 \text{ ma/cm}^2$ for the 4 cm^2 GaAs solar cells used) is very small. The light may be quantized in order to detect its presence, but this does not provide any localized or qualitative information

about the shunt defects. By observing the light emission from several GaAs solar cells, it was found that the light became visible at a forward current of around 4 milliamperes. At this level of current, the junction diode is dominating and the shunt diode's effect may not be noticeable. Therefore, to view the effects of the shunt diode, the solar cell should be biased below the visible threshold and the light emission must be enhanced to be able to view it.

Our new technique involves the use of precise optics with a short focal length to image the light emission on a CCD detector array. Enhancement of the image is done using signal processing techniques. The light emission is digitized by an IBM PC computer which produces a processable image. The image can then be enhanced with several processing routines such as noise reduction, enlargement, histogram equalization for image contrast, and color mapping. The images can be printed on a laser printer for hardcopies or viewed on a display monitor for faster, interactive processing. Figure 2 is the medium-level light emission from a GaAs solar cell biased at the visible threshold without any image enhancement. (The terms low-level, medium-level, and high-level light emission refer to the light emission below, at, and above the visible threshold respectively.) The image is mostly black because the amount of light at the threshold is very small. The light emission shows the grid lines (dark horizontal lines) but does not show any discernible defects. Figure 3 is the medium-level light emission at the visible threshold after the image was processed. The enhanced image shows several defects which were not apparent without the enhancement. This demonstrates the usefulness of the image enhancement routines for defect analysis.

Figure 4 is the high-level light emission. Comparison of the light emission at the high-level and the medium-level reveals similar defects (locations of dark areas). Figure 5 is the high-level light emission after image enhancement. Again, the enhanced image reveals more defects than were apparent before the enhancement. Now comparing the enhanced high-level light emission with the enhanced medium-level light emission, the high-level light emission shows more defects. This exemplifies the difference between the levels of light emission and how the defects vary depending on the current density through the solar cell.

Figure 6 is the low-level light emission after image enhancement. The low-level light emission before enhancement was not included because the image was entirely black. The light emission was not perceivable because it was below the visible threshold. After the enhancement, the appearance of horizontal grid lines became visible. This again demonstrates the advantage of the image enhancement programs. The ability to analyze the light emission will not be limited by visual perception, but can be increased by the enhancement programs.

Conclusions

Shunt diodes have been found to be the type of defect which is likely to degrade and cause failure in solar cells. Because the shunt diodes affect the solar cell's response at very low levels of current, standard I-V analysis is ineffective in determining their presence. Additionally, standard I-V analysis does not provide any localized information about the defects. Light emission has been demonstrated to be an effective method for determining the presence and location of shunt defects. However, at the low levels of current needed to allow the shunt diode to dominate over the junction diode, the light emission is too low to study qualitatively. The image enhancement allows for a better study of the low-level light emission by making the light visible. Therefore, it is now possible to study the shunt diode's effects on the light emission and, more importantly, use the low-level light

emission to analyze the shunt diode's effect on the solar cell. Since the shunt diodes are the likely cause of failure in GaAs solar cells, these techniques can be used to predict durability.

References

- [1] C. Honsberg and A. M. Barnett, "Light Emission As A Stability Predictor for GaAs Solar Cells" *Proc. 19th IEEE Photovoltaic Specialist Conf.*, New York, IEEE Press, 1987, p. 1150-1155.
- [2] C. Honsberg and A. M. Barnett, "Light Emission As A Solar Cell Analysis Technique", *Solar Cells* 20 (1987) 59-63.
- [3] L. Kilmer, "Image Enhancement For Defect Analysis Of Gallium Arsenide Solar Cells", (University of Delaware Senior Thesis), 1987.

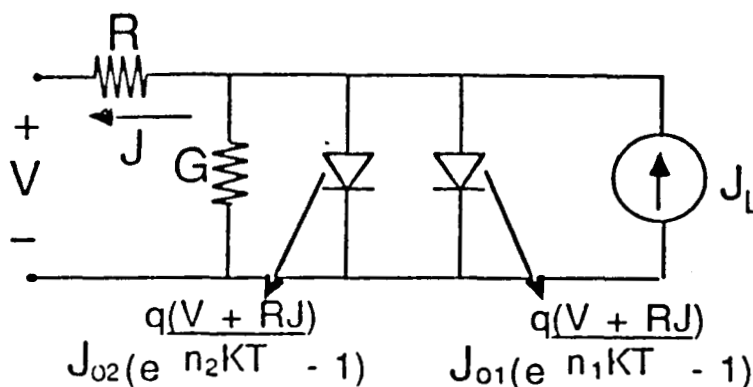


Figure 1. Equivalent circuit model of a solar cell.

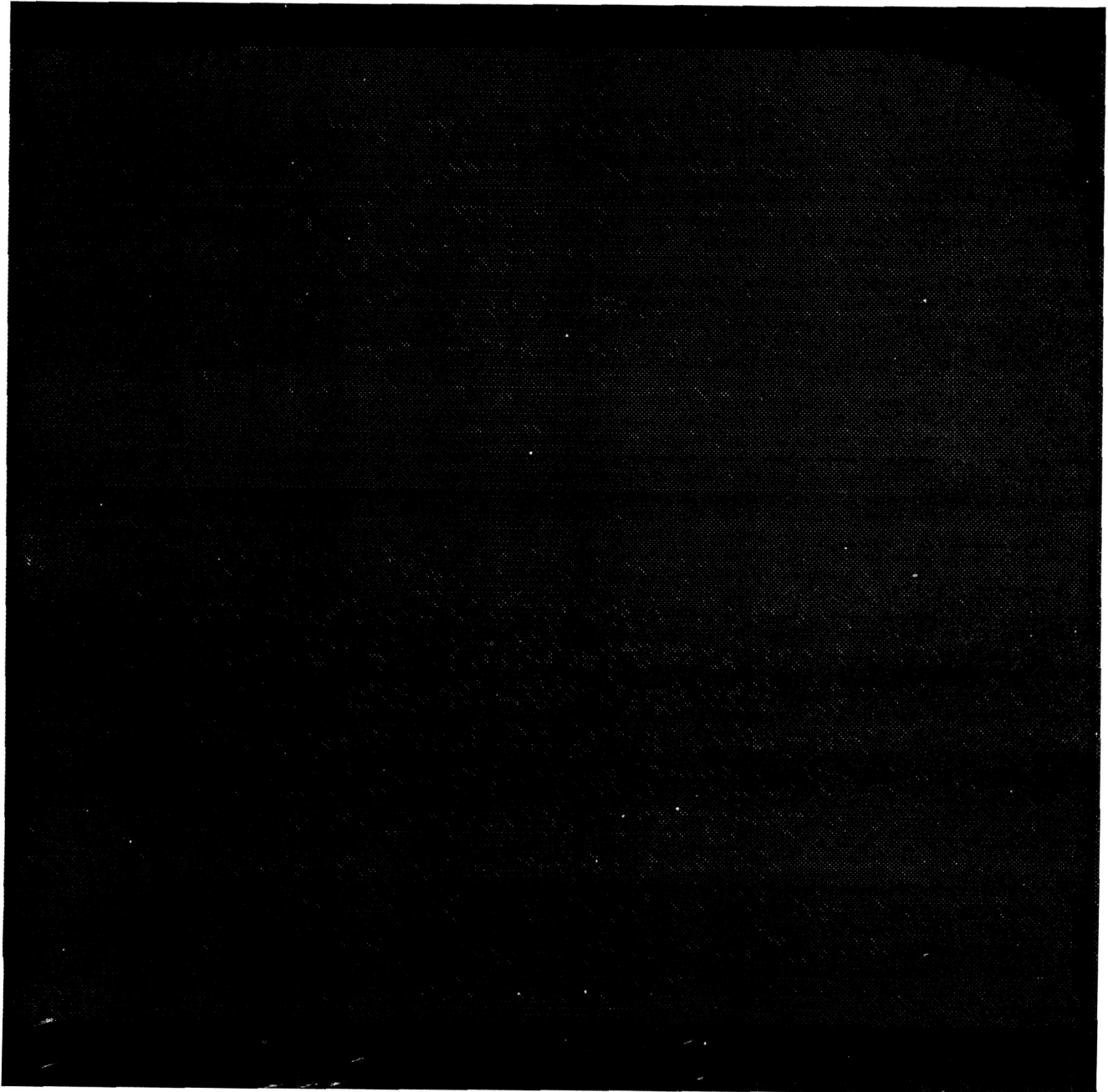


Figure 2. Medium-level light emission before image enhancement.

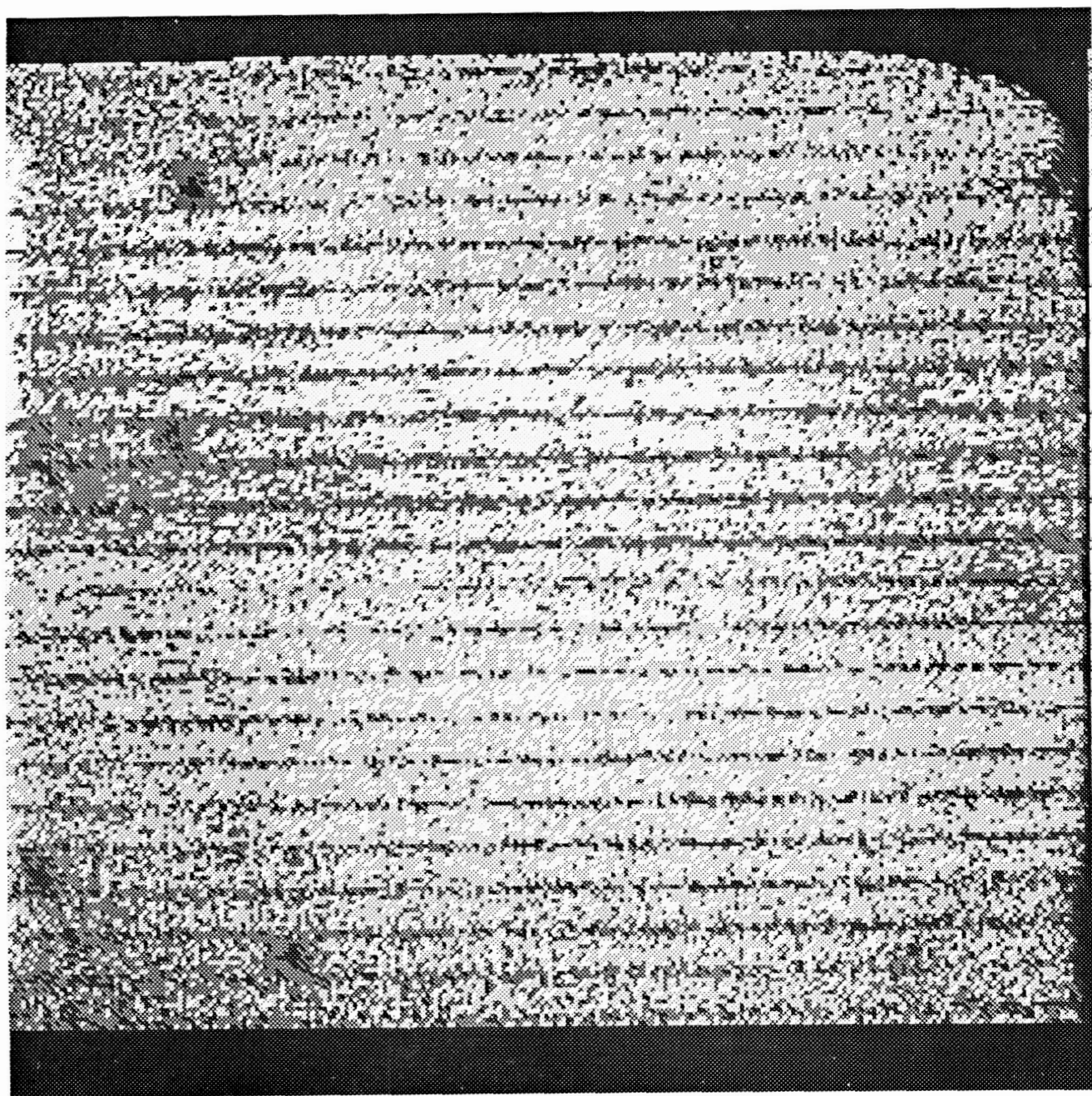


Figure 3. Medium-level light emission after image enhancement.

ORIGINAL PAGE
BLACK AND WHITE PHOTOGRAPH

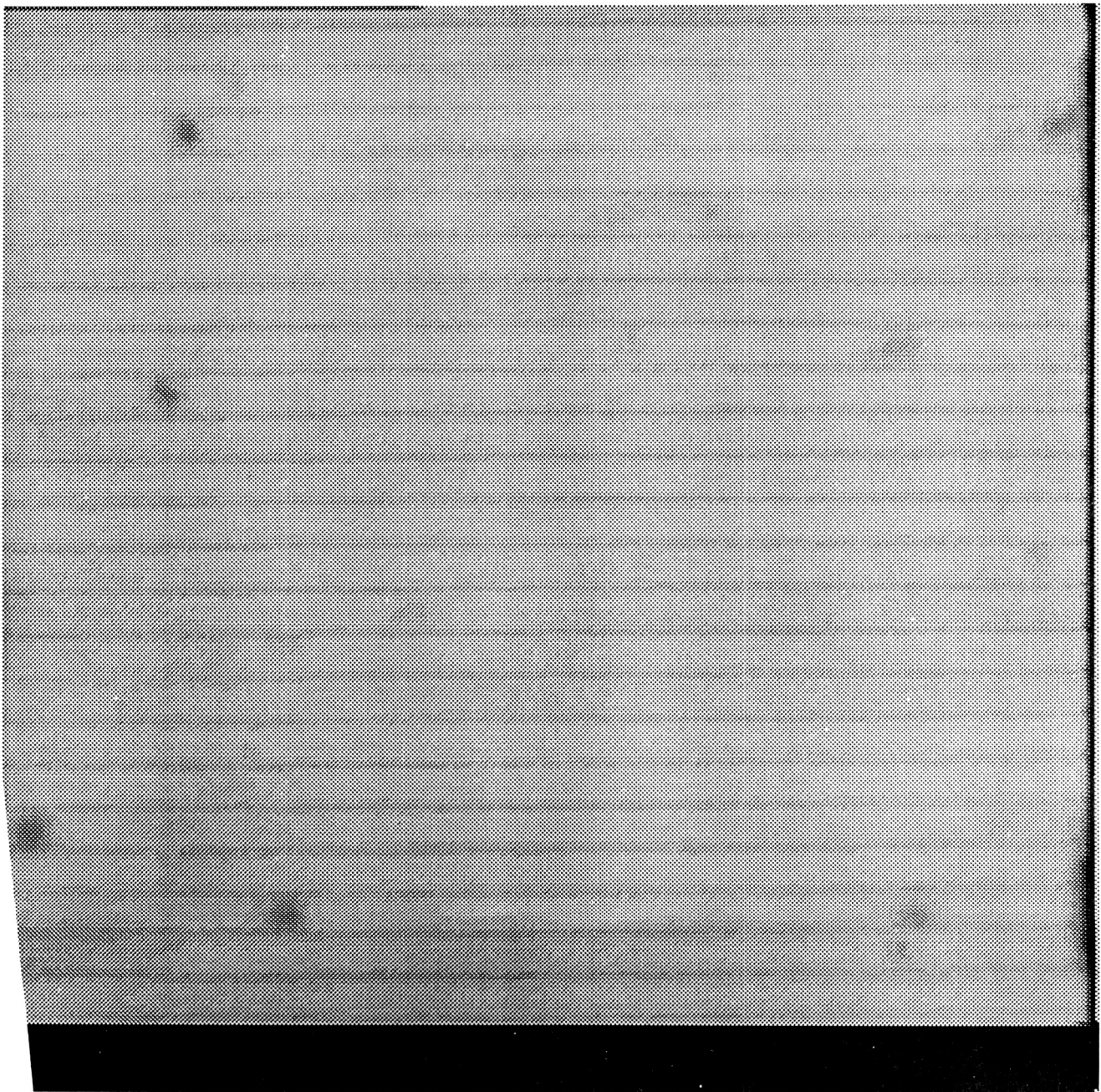


Figure 4. High-level light emission before image enhancement.

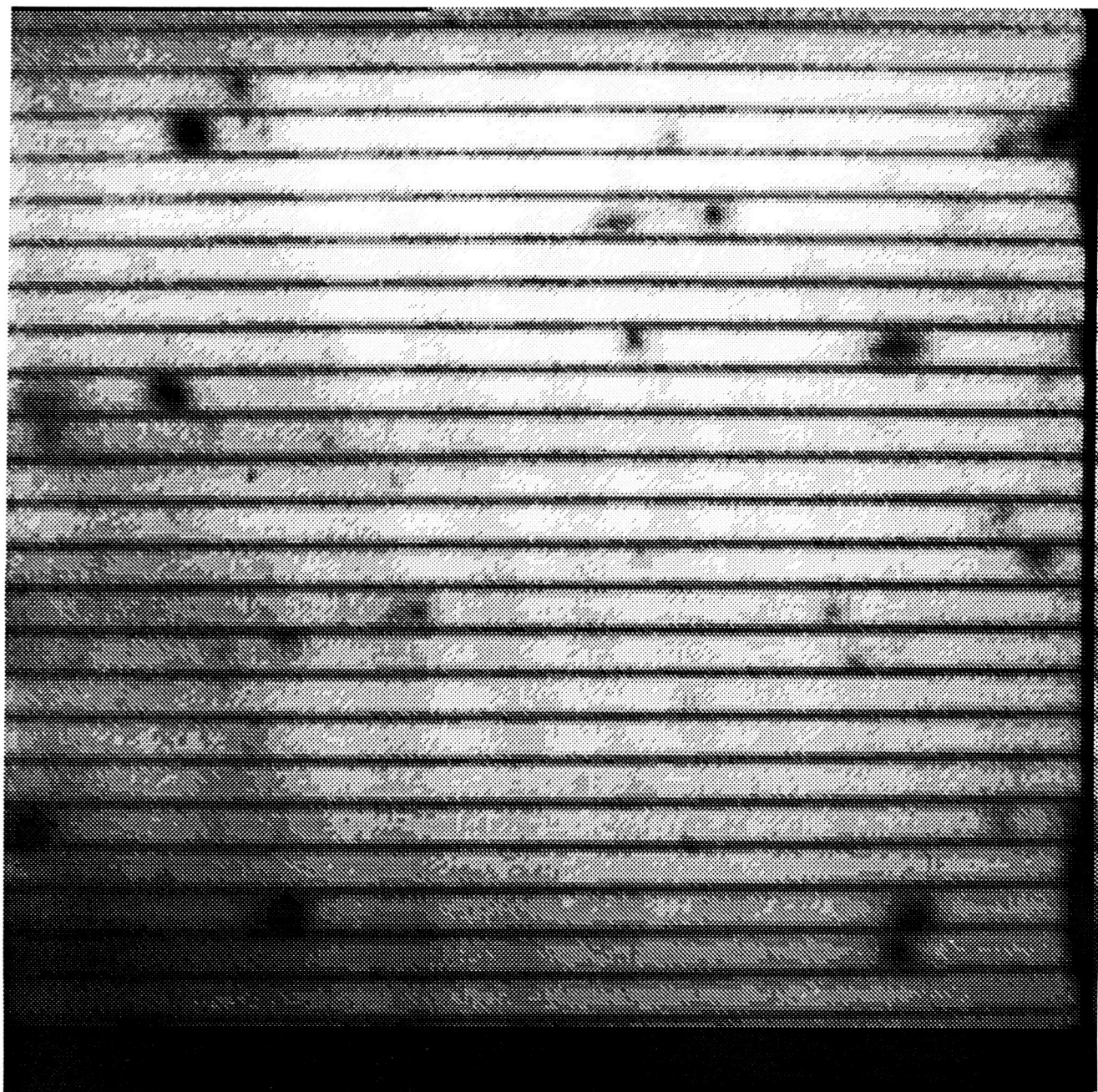


Figure 5. High-level light emission after image enhancement.

ORIGINAL PAGE
BLACK AND WHITE PHOTOGRAPH

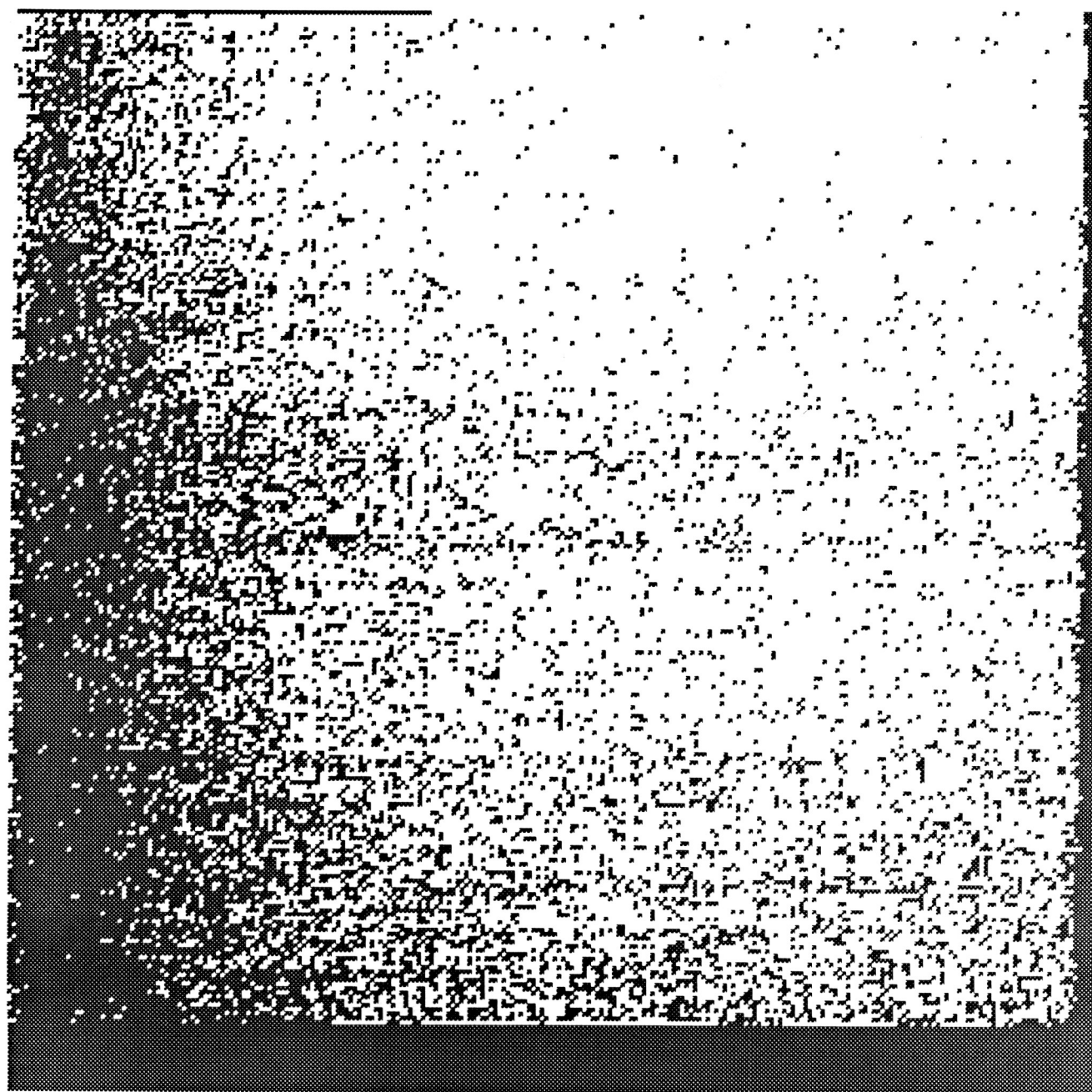


Figure 6. Low-level light emission with image enhancement.

ORIGINAL PAGE
BLACK AND WHITE PHOTOGRAPH

Aging Behavior of Au-based Ohmic Contacts to GaAs

Navid S. Fatemi
Sverdrup Technology Inc.
NASA Lewis Research Center Group
Cleveland, Ohio

Summary

Gold based alloys, commonly used as ohmic contacts for solar cells, are known to react readily with GaAs. It is shown that the contact interaction with the underlying GaAs can continue even at room temperature upon aging, altering both the electrical characteristics of the contacts and the nearby pn junction. Au-Ge-Ni as-deposited (no heat-treatment) contacts made to thin emitter ($0.15\mu\text{m}$) GaAs diodes have shown severe shunting of the pn junction upon aging for several months at room temperature. The heat-treated contacts, despite showing degradation in contact resistance, did not affect the underlying pn junction. Au-Zn-Au contacts to p-GaAs emitter ($0.2\mu\text{m}$) diodes, however, showed slight improvement in contact resistance upon 200°C isothermal annealing for several months, without degrading the pn junction. The effect of aging on electrical characteristics of the as-deposited and heat-treated contacts and the nearby pn junction, as well as on the surface morphology of the contacts are presented.

Introduction

Gold-based alloys are the most commonly used metallization materials for both the front grid and the back ohmic contacts of GaAs solar cells. Au-Zn and Au-Ge-Ni have been the most popular systems for making ohmic contacts to p- and n-GaAs respectively, mainly due to very low values of specific contact resistivity (ρ_c) achievable with these systems upon a post deposition heat-treatment. ρ_c values in the low $10^{-6} \Omega\text{-cm}^2$ range have been reported by many workers for these contact systems to variously doped GaAs substrates [refs. 1,2,3]. These low values are necessary to keep the contact resistance contribution to the series resistance of a solar cell negligible if these cells are to be operated under $>100\times$ sunlight concentrations [ref. 4].

It is highly desirable that the ohmic contacts remain stable during the life of the solar cell regardless of its operating temperature. Space concentrator solar cells e.g., are expected to operate in the $80\text{-}100^\circ\text{C}$ range. They may also be annealed periodically at 200 to 400°C for a few hours at a time in order to reverse the radiation damage effects caused by electron and proton bombardment in the space environment [refs. 5,6]. Several months of cumulative periodic high-temperature annealing may therefore be necessary during the life of the solar cell. High temperature aging studies of Au-Ge-Ni contacts at 330 to 390°C for several days, for example, have revealed increased interactions between GaAs and the contacts and also a general increase in contact resistance [refs. 7,8], pointing to possible instability of these contacts with high temperature aging.

In this work, the high temperature (200 and 400°C) aging stability of Au-Zn contacts to p-GaAs, as well as the room temperature aging stability of Au-Ge-Ni contacts to n-GaAs for several months

were investigated. The effects of aging on specific contact resistivity, metal-GaAs interaction, and surface morphology of the contacts are presented.

Au-Zn Contacts

Au-Zn contacts were made to highly doped ($2 \times 10^{18} \text{cm}^{-3}$) thin emitter ($0.2 \mu\text{m}$ quasi-neutral region thickness) p-type epi-layer GaAs (obtained from Spire), whose structure is shown in figure 1b. The 200-300Å thin Au layer interposed between GaAs and Zn helps the uniformity and adhesion of the contact at the interface. Six samples were heat-treated immediately after E-Beam deposition of the contacts to a maximum temperature of 434°C for 90 seconds. The ρ_c values for these contacts varied from 4.7×10^{-6} to $3.4 \times 10^{-5} \Omega - \text{cm}^2$. The samples were then annealed at 200°C in flowing N_2 for a period of slightly more than 3 months. Subsequently, they were also subjected to a 400°C anneal for a period of 64 hr in air. Contact resistance values, measured via the Transmission Line Method [ref. 9], and current-voltage characteristics of the p/n diodes underneath the contacts were monitored periodically for all samples. The effect of 200 and 400°C isothermal annealing of these contacts, as well as 13 months of subsequent aging of the contacts at room temperature on ρ_c is given in Table 1. Figure 2 compares a typical p/n diode I-V curve with a Au-Zn emitter contact at various stages of aging.

As shown in Table 1, the 200°C isothermal annealing actually slightly improved ρ_c for all samples, indicating the stability of these contacts with high temperature aging, although the Au-Zn/GaAs interaction must have continued to some degree as to bring about the change in ρ_c . However, this continued interaction between the contact and GaAs does not appear to have a significant effect on the nearby p/n junction as evident from figures 2a and 2b. At 400°C however Au-Zn/GaAs interactions were more severe, as shown in figure 2c, resulting in much degradation in the I-V characteristics of the underlying junction. The contact resistance, on the other hand, showed little degradation for most samples and a slight improvement for one sample. Also, the subsequent room temperature aging of the contacts for 13 months did not appear to affect ρ_c or p/n diode I-V characteristics of these samples significantly (fig. 2d).

Despite the minimal changes occurring in ρ_c for Au-Zn contacts after 13 months, the interaction in the Au-Zn/GaAs system continues at room temperature. This room temperature aging is portrayed in figure 3, where the surface morphologies of the contacts for both as-deposited and heat-treated contacts are compared for new and aged contacts. As shown in figures 3a and 3c, the 450°C heat-treatment for 1 min did not appear to change the surface morphology of the contact, whereas the 13 months room temperature aging of both as-deposited (fig. 3b) and heat-treated (fig. 3d) contacts altered the surface morphology dramatically.

Au-Ge-Ni Contacts

Au-Ge-Ni contacts were made to variously doped n-GaAs epi-layers (MOCVD grown, in-house). The n/p current-voltage characteristic measurements however, were done on moderately doped ($6 \times 10^{17} \text{cm}^{-3}$) thin emitter ($0.15 \mu\text{m}$) n-GaAs samples (obtained from Spire Co.), as shown in fig. 1a. For these samples, the as-deposited contacts showed rectifying characteristics. Upon heat-treatment in the 353 to 490°C temperature range for short periods (15 to 60 sec.), however, most samples exhibited $10^{-6} \Omega - \text{cm}^2$ ρ_c values. In Table 2 the ρ_c values for many samples heat-treated at

different temperatures and aged at room temperature for 9 to 31 months are given. As shown, the change in ρ_c upon aging for most samples was slight regardless of the heat-treatment temperature or the period of aging. In some cases, ρ_c values for identically treated samples took different directions upon aging for the same time period. This points to the complex mechanism involved in the low resistance contact formation at the metal-GaAs interface. The relative stability of the heat-treated contacts, however, is attributed to the formation of the low resistance ternary Ni_2GaAs phase at the interface [ref. 10]. It is apparent, therefore that the room temperature aging of these contacts should not cause any dramatic increases in the contact resistance in solar cells.

The main concern for using Au-Ge-Ni as the front grid metallization in shallow junction solar cells is that penetration of the contact species into GaAs can damage the nearby n/p junction. As shown in figures 5a and 5b, heat-treating the contacts at 360 and 395°C for 20 sec can severely short out the junction. One solution to this problem is not to heat-treat the contacts. In case of low to moderately doped emitters, the contacts will be rectifying, but in case of highly doped ($> 1 \times 10^{18} \text{cm}^{-3}$) emitters, ρ_c will be in the high $10^{-4} \Omega\text{-cm}^2$ range which is acceptable for one sun operation of solar cells. However, if the contacts are not heat-treated, the Au-Ge-Ni/GaAs interactions can continue at room temperature to a greater degree than for the heat-treated contacts. This can be due to the absence of stable binary and ternary phases which are created at the metal-semiconductor interface upon heat-treatment. Figure 4 shows typical n/p diode I-V characteristics for several diodes with as-deposited Au-Ge-Ni contacts aged at room temperature for 14 months. As shown in figure 4a, the newly deposited contact to $6 \times 10^{17} \text{cm}^{-3}$ doped emitter is rectifying. Upon aging, most contacts became non-rectifying (i.e. showing linear metal-semiconductor I-V behavior over a given current range), but most of them also severely degrade the nearby (0.15 μm) n/p junction (figs. 4c and 4d). In rare cases, the contacts can become non-rectifying and at the same time do not shunt the junction (fig. 4b).

Consequently, contacts must be heat-treated to remain stable with room temperature aging. But as mentioned earlier, heat-treatment of the contacts can severely shunt the n/p junction under a thin emitter. One method to circumvent this problem is by encapsulating the contacts with SiO_2 or Ta_2O_5 , and/or by the use of a diffusion barrier such as TiN incorporated into the contact system prior to heat-treatment (ref. 12). The diffusion barrier in the case of Au-Ge-Ni contacts can be interposed between the top Au(1550Å) layer and the underlying Ni-Ge-Au thin active layer, replacing the 100Å Ni layer. The ρ_c values for the contacts made with and without TiN barriers were measured to be comparable.

Figures 5c and 5d show the I-V characteristics of two n/p diodes with Au-Ge-Ni contacts heat-treated to 396 and 400°C for 20 sec, respectively. The contacts of the diodes in fig. 5c contained TiN (600Å) layers and those in figure 5d were encapsulated with Ta_2O_5 (600Å), and they were aged for 8 and 21 months at room temperature, respectively. As shown, no sign of shunting can be detected in these I-V curves even after long periods of room temperature aging. Therefore, the use of diffusion barriers and/or dielectric encapsulants with Au-Ge-Ni contacts made to thin emitter diodes seems to be a necessity.

Additional evidence for the continued interactions between Au-Ge-Ni and GaAs is the change that occurs in the surface morphology of the contacts upon room temperature aging. Figure 6 compares the surface morphology of the as-deposited new (fig. 6a), as-deposited and aged for 11 months (fig. 6b), heat-treated new (400°C) (fig. 6c), and heat-treated and aged for 9 months (fig. 6d) contacts. Upon aging, both the as-deposited and heat-treated contacts seem to approach an end form with a more definite grain structure not evident prior to the aging process. High temperature aging of these contacts indicates the continued out diffusion of Ga through the metallization and

Ga₂O₃ oxide formation at the surface of the contact [ref. 7]. Again, an effective diffusion barrier incorporated into the contact system should limit the dissolution of Ga into the metallization system greatly.

It is known that GaAs reacts readily with pure Au at room temperature [ref. 11]. The effect of this room temperature interaction of Au with GaAs upon aging on ρ_c was also studied. Au contacts were made to highly doped ($5 \times 10^{18} \text{cm}^{-3}$) thick (1 to 1.2 μm) n-type GaAs epi-layers. As shown in Table 3, hardly any degradation in ρ_c is observed for any of the contacts after room temperature aging of the contacts for 32 months. This indicates that the Au-GaAs interaction does not appear to affect the resistance at the metal-semiconductor interface.

Conclusions

Isothermal annealing of Au-Zn contacts on p-GaAs at 200 and 400°C for 3 months and 64 hrs, respectively have shown that the specific contact resistivity of these contacts are relatively stable with high temperature aging. No p/n junction degradation was observed in the 200°C aging study, but for the case of annealing at 400°C, the p/n diodes underneath the contacts degraded severely. The emitter thickness in both cases was 0.2 μm .

Room temperature aging of Au-Ge-Ni contacts on n-GaAs for several months indicates that ρ_c values for these contacts do not increase significantly compared to their as-fabricated values, and for many cases they remain very stable. It was also shown that the as-deposited contacts continue to interact with the underlying GaAs at room temperature, usually resulting in n/p junction degradation underneath the 0.15 μm emitter. The heat-treated contacts on the other hand can severely short out the n/p junction underneath after 360°C heat-treatment for a few seconds. The use of a TiN diffusion barrier and a SiO₂ or Ta₂O₅ dielectric encapsulant can prevent degradation, even with these shallow emitters (0.15 μm), even after heat-treating the contacts to 400°C. Their use will also inhibit the metal-GaAs interactions that would otherwise occur during room-temperature aging.

In addition, the contact resistances for pure Au contacts were found to be very stable after 32 months of room temperature aging. It was also shown that the surface morphology of Au-Zn and Au-Ge-Ni contacts alter after several months of room temperature aging for both as-deposited and heat-treated contacts, which is another indication that the interaction between GaAs and its metallization continues at room temperature, whether or not the contact is heat-treated. The I-V characteristics of the junction underneath the contacts, however, indicate that this interaction is negligible for the heat-treated contacts compared to the as-deposited contacts.

Acknowledgement

I would like to thank the following people for their contributions to this work: Manju Ghalla-Goradia and Victor Weizer for their help in formulating some of the concepts in this work, George Mazaris and David Wilt for the MOCVD growth of some of the epi-layers, Ralph Thomas for providing the Polaron measurements of most of the GaAs samples, and David Brinker for his help in initiating this effort.

References

- [1] T. Sanada and O. Wada, Jpn. J. Appl. Phys., **19**, L491 (1980).
- [2] M. I. Nathan and M. Heiblum, Solid-State Elect. **25**, 1063 (1982).
- [3] H. G. Henry et al, IEEE Trans. Electron. Dev. **ED-31**, 1100 (1984).
- [4] D. K. Schroeder, *Fundamentals of Metal-Semiconductor Contacts. Proceedings of the Flat Plate Solar Array Project Research Forum on Photovoltaic Metallization Systems*, DOE/JPL-1012-92, NASA CR-173477 (1983), pp. 69-93.
- [5] G. H. Walker and E. J. Conway, J. Electrochem. Soc. **125**, 1726 (1979).
- [6] R. Loo, G. S. Kamath and R. C. Knechtli, *Fourteenth IEEE Photovoltaic Specialists Conference*, 1980, pp. 1090-1097.
- [7] G. S. Marlow, M. B. Das and L. Tongson, Solid-State Elect. **26**, 259 (1983).
- [8] R. A. Bruce and G. R. Piercy, Solid-State Elect. **30**, 729 (1987).
- [9] W. Kellner, Siemens Forsch. Entwicklungsber **4**,137 (1975).
- [10] T. S. Kuan et al, J. Appl. Phys. **54**, 6952 (1983).
- [11] A. Hiraki et al, Surf. Sci. **86**, 706 (1979).
- [12] N. S. Fatemi, *Study of Ohmic Contacts to GaAs for Solar Cell Applications*, M.S. Thesis, Cleveland State University, 1987.

Table 1. Effect of Isothermal Annealing at 200°C for 3 Months, at 400°C for 64 Hours, and Room Temperature Aging for 13 Months on the Specific Contact Resistivity of Au-Zn Ohmic Contacts to p-GaAs

Sample	$\rho_c(\text{ohm-cm}^2)$	$\rho_c, 200^\circ\text{C}$	$\rho_c, 400^\circ\text{C}$	$\rho_c, \text{Room Temp.}$
SR004-1	4.7E-6	3.8E-6	5.3E-6	5.1E-6
SRO05-2	3.4E-5	2.5E-5	1.7E-5	1.6E-5
SR008-1	9.6E-6	8.8E-6	2.9E-5	2.8E-5
SR008-2	5.9E-6	5.3E-6	9.0E-6	7.7E-6
SR010-1	8.8E-6	7.7E-6	*	*
SROIO-2	1.3E-5	1.1E-5	3.6E-5	3.2E-5

* TLM data line fit not good enough for meaningful extraction of ρ_c due to unequal contact resistance of TLM contact electrodes

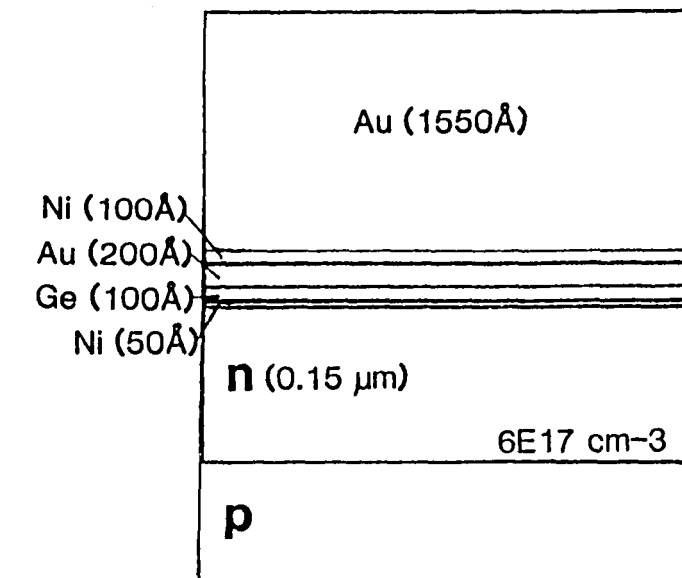
**Table 2 Effect of Aging on Specific Contact Resistivity of Au-Ge-Ni
Ohmic Contacts to n-GaAs**

Sample	$\rho_c(\text{ohm-cm}^2)$	$\rho_c(\text{ohm-cm}^2)/\text{aged (months)}$	Heat-treatment (sec., °C)
050-2A	7.8E-6	6.8E-6 / 31	30, 353
050-2B	7.2E-6	1.6E-5 / 31	30, 353
053-2	1.1E-4	1.9E-4 / 31	240,600
058-4	1.1E-6	8.5E-7 / 30	60, 371
057-1	3.1E-5	4.7E-5 / 26	60, 490
057-2	1.1E-5	1.1E-5 / 26	60, 490
058-5	9.2E-6	6.2E-6 / 23	600,450
128-4A	4.0E-6	3.9E-6 / 12	20, 490
SPO14-F	1.5E-6	9.7E-6 / 12	35, 385
2SP025-1	7.2E-6	8.5E-6 / 10	20, 370
2SP026-1	1.0E-5	* / 10	20, 503
2SP027-1	3.4E-6	* / 9	15, 400
2SP031-A	1.0E-5	1.0E-5 / 9	15, 400
2SP033-A	5.0E-6	3.4E-5 / 9	15, 400

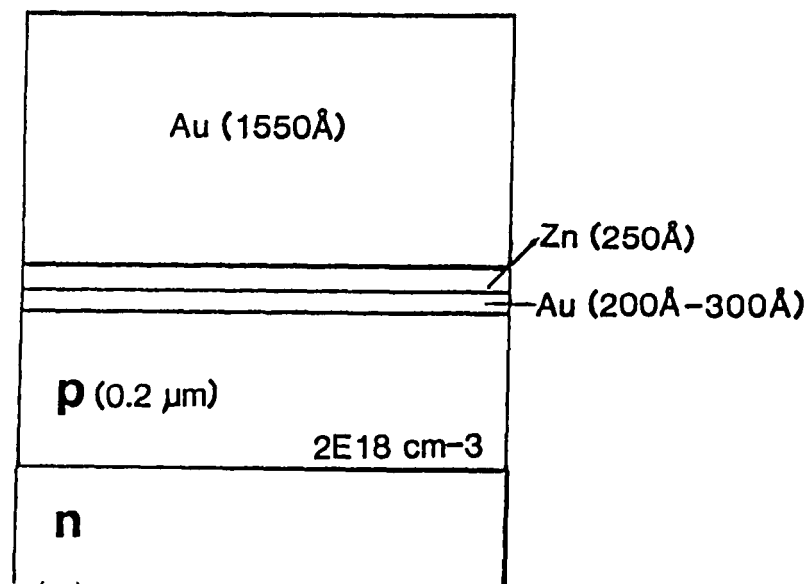
* TLM data line fit not good enough for meaningful extraction of ρ_c due to unequal contact resistance of TLM contact electrodes

**Table 3 Effect of 32 Months of Aging on Specific Contact Resistivity
of Au Ohmic Contacts to n-GaAs**

Sample	$\rho_c(\text{ohm-cm}^2)$	$\rho_c(\text{ohm-cm}^2)$	Heat-treatment (min., °C)
058-1	1.6E-5	1.5E-5	2.0, 371
058-2	1.9E-5	2.1E-5	4.0, 409
059-1	7.7E-5	8.6E-5	1.0, 350
059-2L	7.9E-5	7.7E-5	1.0, 350
059-2R	5.3E-5	5.3E-5	1.0, 350
059-3L	6.0E-5	6.2E-5	1.0, 350
059-3R	7.1E-5	7.4E-5	1.0, 350



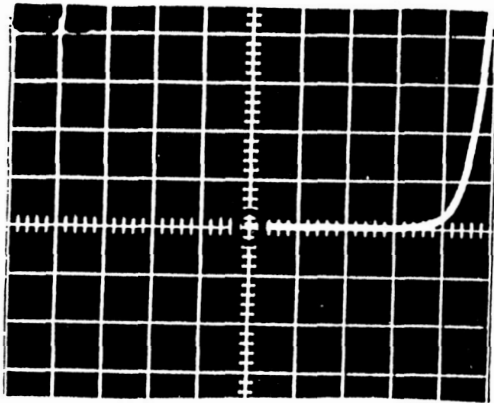
(a)



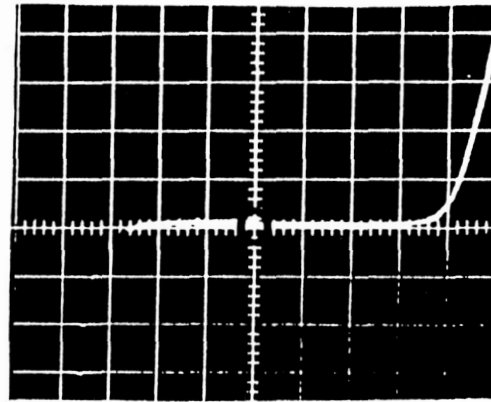
(b)

Figure 1.
 (a) Au-Ge-Ni contact structure,
 (b) Au-Zn contact structure.

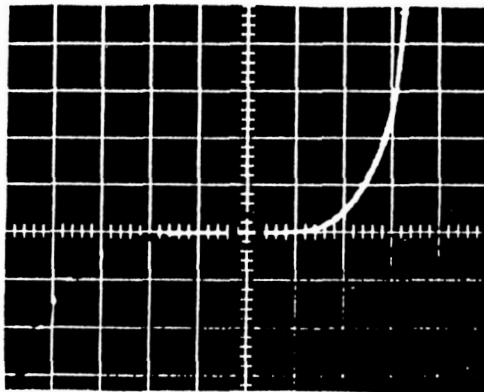
ORIGINAL PAGE
BLACK AND WHITE PHOTOGRAPH



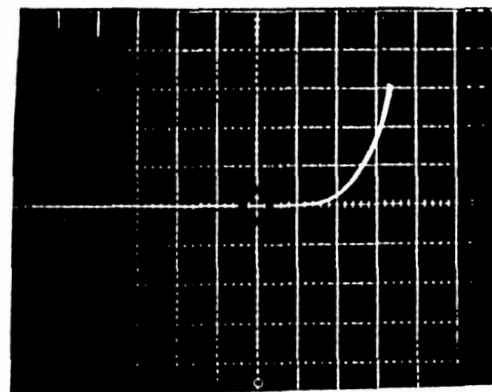
(a)



(b)



(c)



(d)

Figure 2. p/n diode I-V curves (0.2V, 1mA/div.) with Au-Zn contacts aged for,
(a) 432 hours at 200 °C,
(b) 3 months at 200°C,
(c) 64 hours at 400 °C,
(d) 13 months at room temperature.

ORIGINAL PAGE
BLACK AND WHITE PHOTOGRAPH

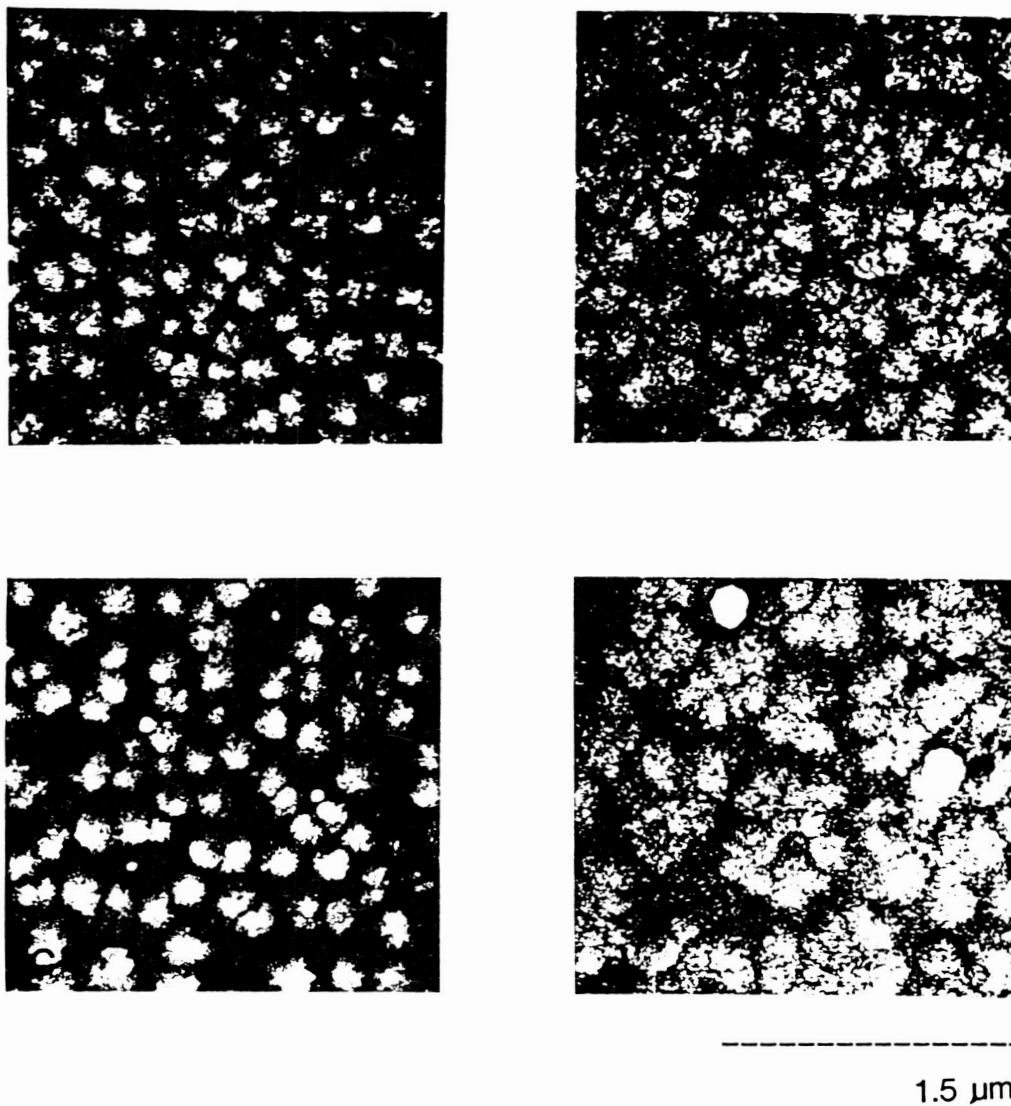
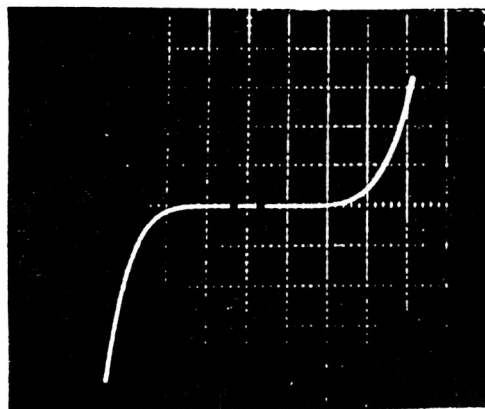
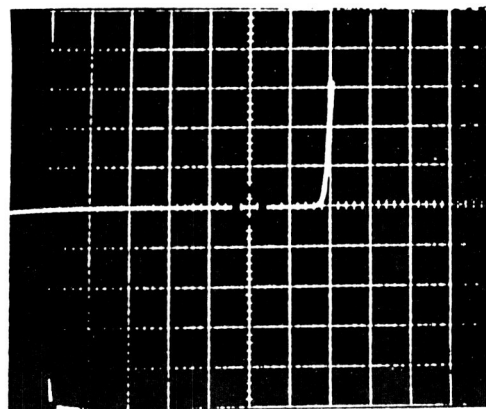


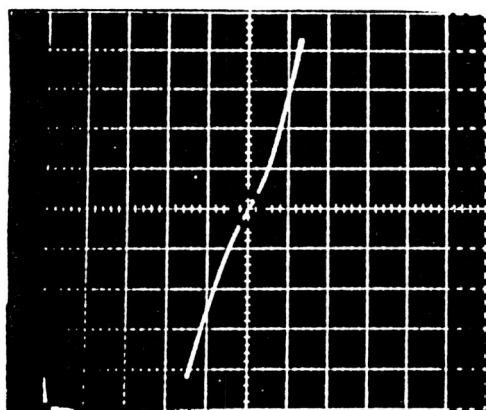
Figure 3. Surface morphology of Au-Zn contacts,
(a) as-deposited new,
(b) as-deposited aged for 13 months,
(c) heat-treated at 450 °C new,
(d) heat-treated at 450 °C aged for 13 months.



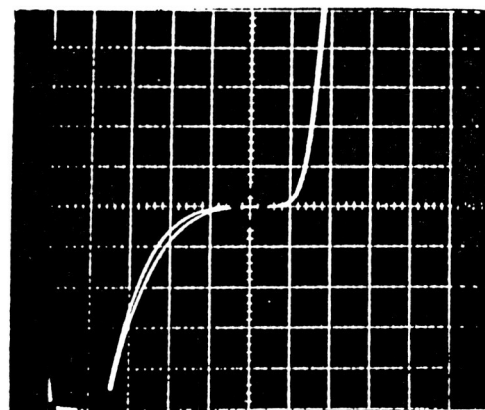
(a)



(b)



(c)

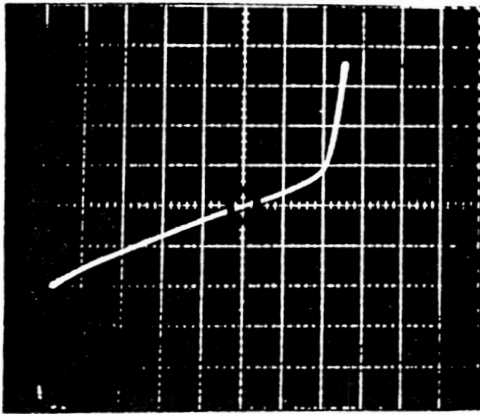


(d)

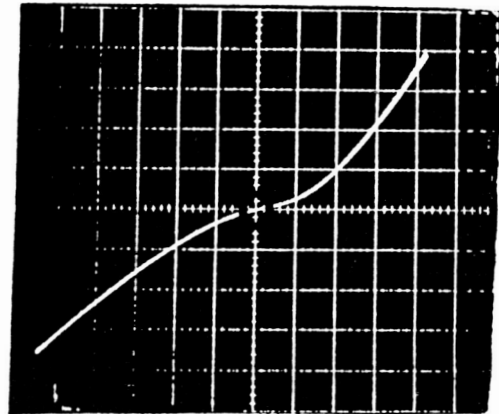
Figure 4. n/p diode I-V curves with as-deposited Au-Ge-Ni contacts aged for 14 months,

- (a) new contacts are rectifying (1.0V, 1mA/div.),
- (b) non-rectifying and non-shunting (0.5V, 1mA/div.),
- (c) severely shorted (0.5V, 1mA/div.),
- (d) most typical with as-deposited aged contacts 0.5V, 1mA/div.).

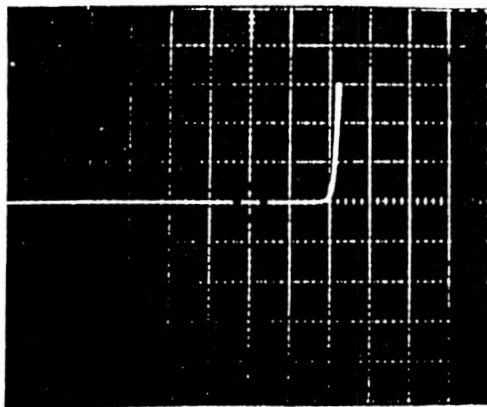
ORIGINAL PAGE
BLACK AND WHITE PHOTOGRAPH



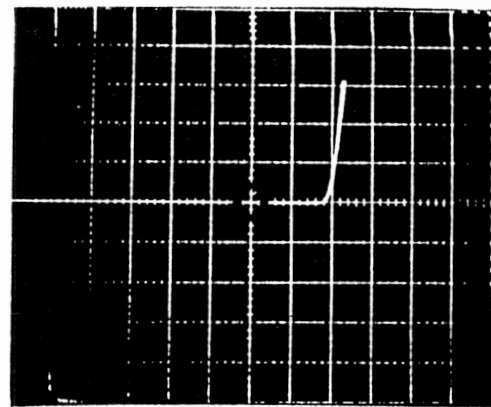
(a)



(b)



(c)



(d)

Figure 5. n/p diode I-V curves with heat-treated Au-Ge-Ni contacts (0.5V, 1mA/div.),
(a) 360 °C for 20 sec. new,
(b) 395 °C for 20 sec. new,
(c) 396 °C for 20 sec. with TiN aged for 8 months,
(d) 400 °C for 20 sec. with Ta₂O₅ encapsulation aged for 21 months.

ORIGINAL PAGE
BLACK AND WHITE PHOTOGRAPH

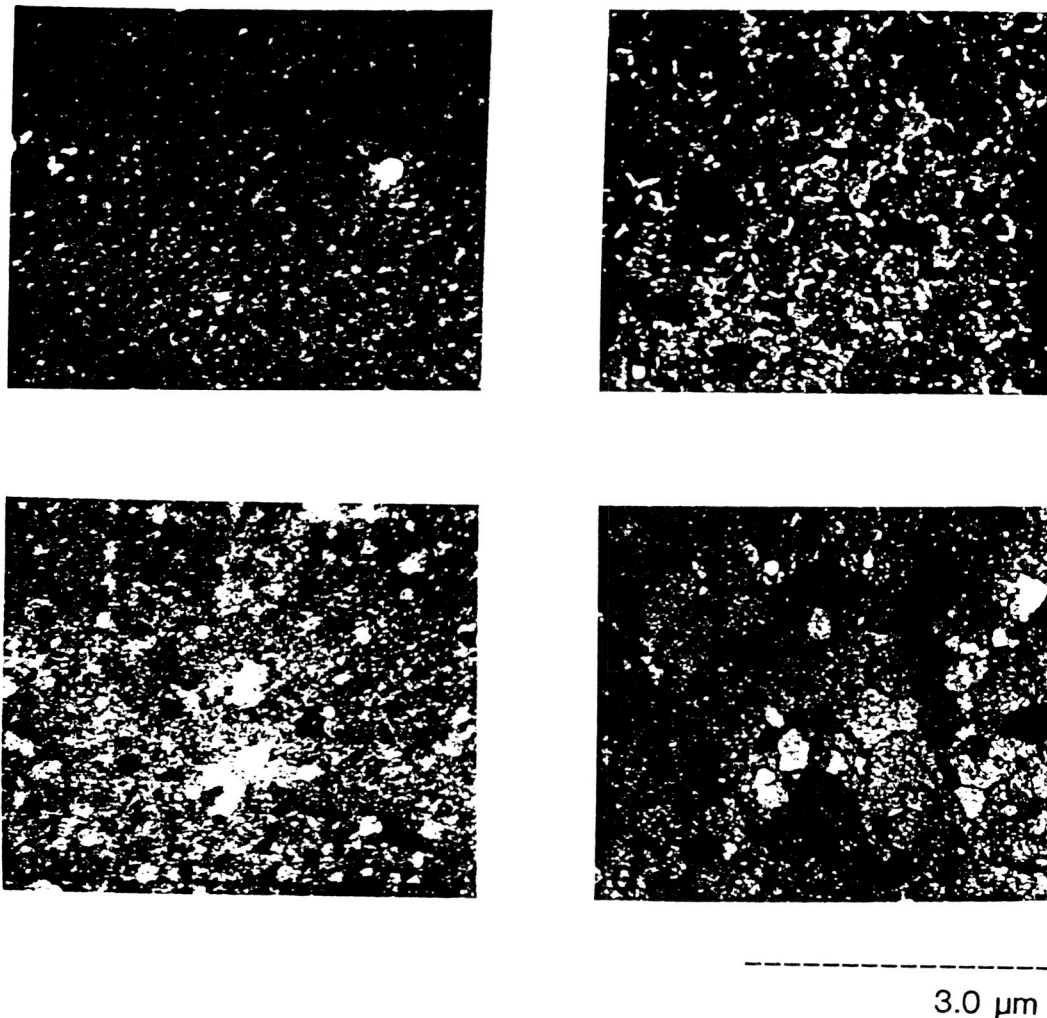


Figure 6. Surface morphology of Au-Ge-Ni contacts,
(a) as-deposited new,
(b) as-deposited aged for 11 months,
(c) heat-treated at 400 °C new,
(d) heat-treated at 400 °C aged for 9 months.

Chemical Etching and Organometallic Chemical Vapor Deposition on Varied Geometries of GaAs

Sheila G. Bailey, Geoffrey A. Landis, and David M. Wilt

NASA Lewis Research Center,

Cleveland, OH 44135

Summary

Results of micron-spaced geometries produced by wet chemical etching and subsequent OM-CVD growth on various GaAs surfaces are presented. The polar lattice increases the complexity of the process. The slow-etch planes defined by anisotropic etching are not always the same as the growth facets produced during MOCVD deposition, especially for deposition on higher-order planes produced by the hex groove etching.

Introduction

The technology of anisotropic etching to produce a geometrically structured surface [ref. 1] has become increasingly important in raising the efficiency of silicon solar cells [ref. 2]. Benefits of surface structure produced by anisotropic etching include reduced reflectance, oblique passage of light through the cell, and light trapping. These lead to the possibilities of increased efficiencies and reduced radiation damage. To date, however, little work has been done on the use of anisotropic etching for III-V solar cells. Implementation of these geometrical improvements in GaAs solar cells will require an understanding of etch characteristics and the growth process of metal-organic chemical vapor deposition (MOCVD) on multiple crystallographic planes with micron-scale periodicity. Wet chemical etching has been shown [ref. 3] to be capable of providing a simple, inexpensive method for fabricating structures with less than two micron spacings. In previous work [3,4] we have demonstrated MOCVD growth on V-grooved surfaces.

Anisotropic etching in GaAs is more complicated than on silicon due to the polar nature of the lattice [ref. 5]. The (111) plane is chemically different from the $(\bar{1}\bar{1}\bar{1})$ plane, and both etching and deposition will behave differently on the different surfaces.

Figure 1 shows a representative solar cell structure using a structured surface. The surface structure we chose here utilizes V-grooves, rather than the pyramidally etched surfaces typically used in silicon cells, because of the difference in etch characteristics of (111) Gallium and the (111) Arsenic faces.

We refer to a plane as (111)Ga because the atomic nature of the surface consists of gallium atoms bonded to arsenic atoms slightly below the surface by three bonds; likewise, (111)As surface consists of surface As atoms bonded to Ga atoms slightly below the surface.

Figure 2 shows the orientation of (111)Ga and (111)As faces on a (100) wafer. Since the (111) plane is a Ga plane, $[111]$ planes with an even number of barred indices, such as (111) or $(\bar{1}\bar{1}\bar{1})$, will be gallium planes, while planes with an odd number of barred indices, such as $(1\bar{1}\bar{1})$ or $(\bar{1}\bar{1}1)$, are Arsenic planes. The (111)Ga planes are the least reactive (slowest etching) planes, and are the

planes preferentially revealed in the anisotropic etch. Note that V-grooves running perpendicular to one another on the same side are *not* equivalent; if the V-groove running in the $(01\bar{1})$ direction shows a $(111)\text{Ga}$ planes, one perpendicular to it (*i.e.*, in the (011) direction) would show a $(111)\text{As}$ plane. In general $(111)\text{As}$ grooves cannot be formed by anisotropic etching. The $(111)\text{Ga}$ V-groove on the back side is perpendicular to one on the front side.

Anisotropic Etching

The process of etching V-grooves consists of

- (1) masking the surface with photoresist stripes, aligned in the $(01\bar{1})$ direction;
- (2) etching in an anisotropic etch.

Figure 3 shows a Scanning Electron Microscope (SEM) photograph of a surface after the photoresist step. The photoresist used was AZ 4110. The photomask we used produces fine groove spacings, either 4.2μ photoresist stripes separated by 1.3μ openings ("5.5 micron pattern"), or separated by 2.8μ openings ("7 micron pattern").

Several anisotropic etches for GaAs exist [ref. 5]. In this work, the etch used was the Caros etch, consisting of 5:1:1 proportions of H_2SO_4 , H_2O_2 , and H_2O respectively. Etch temperature was 24°C . This etch does not attack photoresist, so that the photoresist was sufficient to serve as a mask. We also looked at etches with different proportions [ref. 6], such as "vertical" etch (1:8:1 $\text{H}_2\text{SO}_4\text{:H}_2\text{O}_2\text{:H}_2\text{O}$) and "horizontal" etch (1:1:50), which produced faster and slower etch rates respectively.

Figure 4 shows the etch process when the photomask is aligned in the "correct" direction, *i.e.*, stripes running in the $(01\bar{1})$ direction. The Caros etch proceeds much faster in the (100) direction than in the (111) direction; the $(111)\text{Ga}$ is a slow-etch face. The V-grooves are nearly flat-bottomed during the etch process; the width of the flat decreases as the etch proceeds. As the etch nears completion, the photoresist is slowly undercut. To make sharp-topped grooves, we terminate the etch just before the photoresist is undercut at the groove tops, typically about two minutes into the etch for the groove spacings (7μ periodicity) used here. For flat-topped grooves the etch is terminated earlier. The photoresist is then removed with acetone and the surface given a solvent clean before growth.

Quite different results are shown when the photoresist stripes are oriented in the opposite (011) direction, as shown in figure 5. In this case the V-groove walls would be $(111)\text{As}$ planes, however, the $(111)\text{As}$ face is not a slow-etch plane, and V-grooves are not formed. Instead a "hex" groove is formed. The photoresist is undercut much more rapidly than in the V-groove etch. In this case, however, the GaAs is cut through even more rapidly, and the photoresist peels from the surface when the GaAs cuts through, leaving a narrow wedge of GaAs attached to the photoresist as shown in figure 5C.

The bottoms of the hex-groove is slightly rounded, rather than nearly flat as in the case of the V-groove etch, a result of the divergent etch front, rather than convergent.

The upward facing walls are $(111)\text{As}$ and the downward facing walls are $(441)\text{Ga}$ faces.

Note that in this orientation the striations on the etched surface are much more pronounced than in the case of V-groove formation. This is due to the fact that the (111)As plane revealed here is more easily attacked than the (111)Ga plane revealed by the V-groove etching.

Some researchers [ref. 7] have seen "dovetail" grooves, as in figure 6, for stripes oriented in this direction, where the downward-facing walls are the slow-etch (111)Ga faces. We have not observed this groove shape in etches done on GaAs.

Identification of Crystal Planes

When specific crystal planes are identified here, identification is based on comparing angles measured on SEM photographs of a cleaved surface with theoretical angles of the crystal planes. Causes for error in the measured angle include residual distortions in the SEM photograph, misalignment of the grooves, cleavage at a slight angle from the theoretical cleavage plane, observations taken with the sample not perpendicular to the beam, and inaccuracies in the angle measurement.

In samples with a MO-CVD overgrowth, the epitaxial layer can be seen in the SEM photograph as a brightness difference between the p and n type material. This voltage contrast results from the Fermi level changing from p to n which changes the probability of secondary electron emission, and thus the apparent brightness.

Epitaxial Growth on V-Grooves

Table 1 shows the conditions used for the epitaxial deposition. The growth rate is a strong function of crystal orientation [ref. 8,9], which can result in preferential formation of certain crystal planes, or "faceting".

Table One: MOCVD Growth Conditions

Reactor: Horizontal geometry cold-wall reactor; RF Induction heated substrate

Sample clean: Solvent degrease followed by DI H₂O rinse and N₂ blow dry

Source: TMGa and AsH₃ (10% in H₂)

Dopant: Diethyl Zinc

Growth Temperature: 620°C

Growth Pressure: 190 Torr

Ga Mole Fraction: $1.5 \cdot 10^{-4}$

V/III Ratio: 20

Growth Rate: About 0.1μ/min.

In general, a crystal plane which is slow to etch will also be a plane which is slow to grow, since an etch process can be viewed conceptually as the reverse of a deposition process. However, since the kinetics of epitaxial growth are not identical to those of etching, it is not always true that the growth facets will necessarily be the same as those revealed by etching.

Figure 7 shows a typical epitaxial growth on a fully etched normal V-groove. The interface between the n-type buffer layer and the n substrate shows as a narrow white line; the p surface layer

as a lighter color. The gas flow for this growth was parallel to the grooves. The growth is slightly thicker toward the groove bottom.

In this growth we found the (100) surface at the groove tops to grow at a rate about equal to that on the (111)Ga surface of the groove walls. In other work (using slightly different growth conditions, [ref. 4]) we have found growth on the (100) surface to be up to 2.2 times faster than that on the (111)Ga face.

Figure 8 shows a slightly more complex growth, on partially etched V-groove (1-minute Caros etch) with flat tops to the grooves. In this case, two crystal planes are revealed. The angle between planes on the groove walls is about 10 degrees. (Note also that the tops of the grooves are slightly tilted. The epitaxial growth follows the true (100) face, and the wafer is cut 4 degrees off (100)).

Angle measurements show that neither of these planes is the true (111); the planes are tilted 5 degrees off (111) respectively toward and away from (110). This is reasonable if the (100) faces on the tops and bottoms of the grooves grow slightly faster than the (111)Ga face on the sides of the grooves. The (divergent) faster growth at the (100) groove tops tends to stabilize planes tilted slightly more than (111), while the (convergent) faster growth at the (100) groove bottoms tends to stabilize planes tilted slightly less than (111).

Epitaxial Growth on "Hex" Grooves

Figure 9 shows MOCVD growth on the hex orientation groove. In this sample the grooves were etched about 30 seconds. The deposition forms facets of high-order planes. The original (100) surface has been faceted with (111)As faces. The bottoms of the grooves are beginning to develop (411) facets.

Figure 10 shows the results when growth is done on a hex-groove which has been etched to completion (*i.e.*, until the groove walls cut through and the photoresist spontaneously peels, as seen in figure 5C). In this case, quite clear (411) facets form on the bottoms of the grooves.

The (411) plane is, like the (111), a polar plane. As seen in figure 11, the (411) plane can be cleaved in such a way that the exposed surface atoms are predominantly Ga atoms bonded to the surface with two bonds, with some As atoms bonded to the surface with three bonds.

Figure 12 shows the groove walls and the edges of the (411) planes in more detail. The groove walls, nominally (111)As faces, are seen to be ridged. The actual surface consists of (211) facets.

Conclusions

The polar nature of the lattice makes etching and chemical vapor deposition on GaAs a considerably more complex process than on non-polar material such as silicon. The slow-etch planes defined by anisotropic etching are not always the same as the growth facets produced during MOCVD deposition, especially for deposition on higher-order planes produced by the hex groove etching.

References

- [1.] C.R. Baraona and H.W. Brandhorst, Jr., *Eleventh IEEE Photovoltaic Specialists Conference*, 44-48 (1975).
- [2.] M.A. Green, S.R. Wenham and A.W. Blakers, *Nineteenth IEEE Photovoltaic Specialists Conference*, 6-12 (1987).
- [3.] R.P. Leon, S.G. Bailey, G.A. Mazeris and W.D. Williams, *Appl. Phys. Lett*, **49**, 945-947 (1986).
- [4.] S.G. Bailey, R.P. Leon and A. Arrison, *Nineteenth IEEE Photovoltaic Specialists Conference*, 421-426 (1987).
- [5.] S. Adachi and K. Oe, *J. Electrochem. Soc.*, **130**, 2427-2435 (1983).
- [6.] S. Lida and K. Ito, *J. Electrochemical Soc.*, **118:5**, 768-771 (1971).
- [7.] P.M. Holm and R.J. Roedel, *17th IEEE Photovoltaic Specialists Conference*, 921-926 (1984).
- [8.] T. Nakanisi, *J. Crystal Growth* **68**, 282-194 (1984).
- [19.] R.P. Gale, R.W. McClelland, J.C. Fan and C.O. Bozler, *Inst. Phys. Conf. Ser. No. 65*, 101-108 (1982).

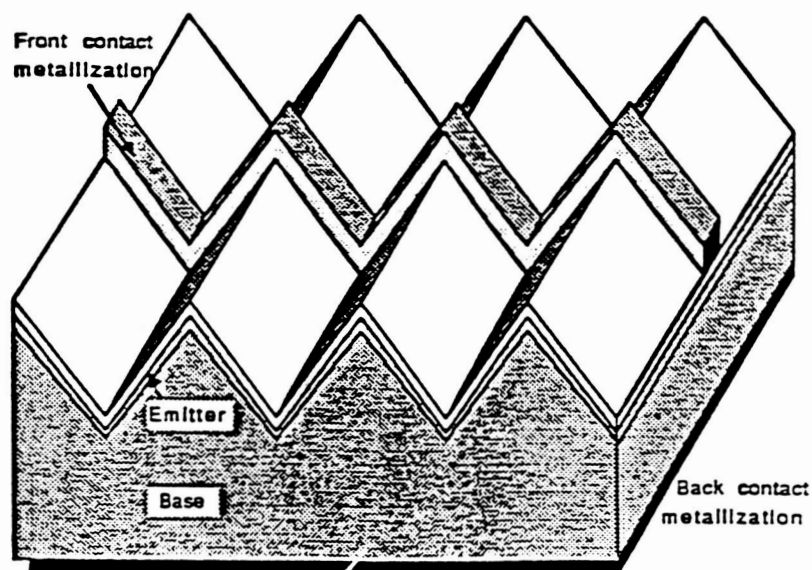


Figure One: Schematic of V-groove Gallium Arsenide Solar Cell (not to scale).

(111) planes on (100) GaAs wafer

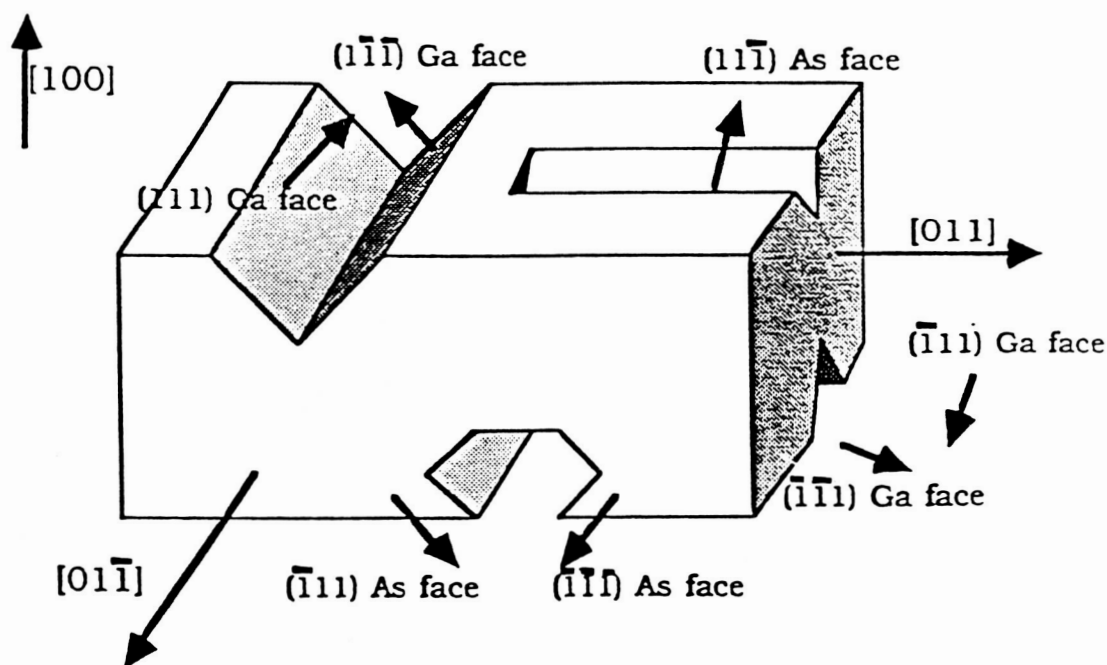


Figure Two: (111) Planes on (100) GaAs Wafer. There are two non-equivalent types of (111) plane; the (111)Ga and the (111)As planes. Anisotropic etching preferentially defines the (111)Ga face.

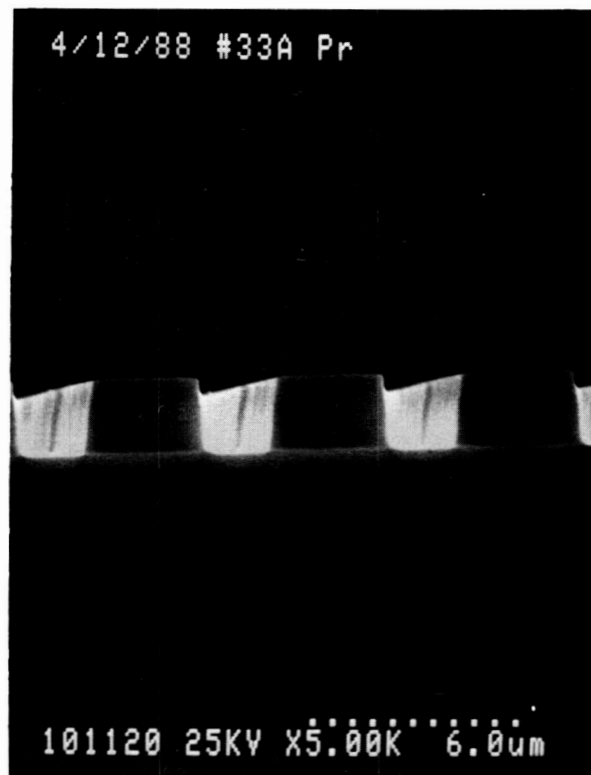
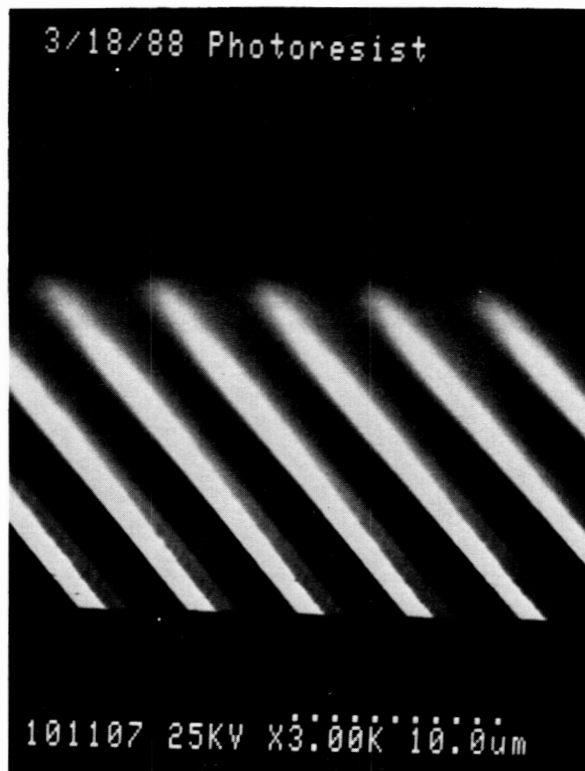
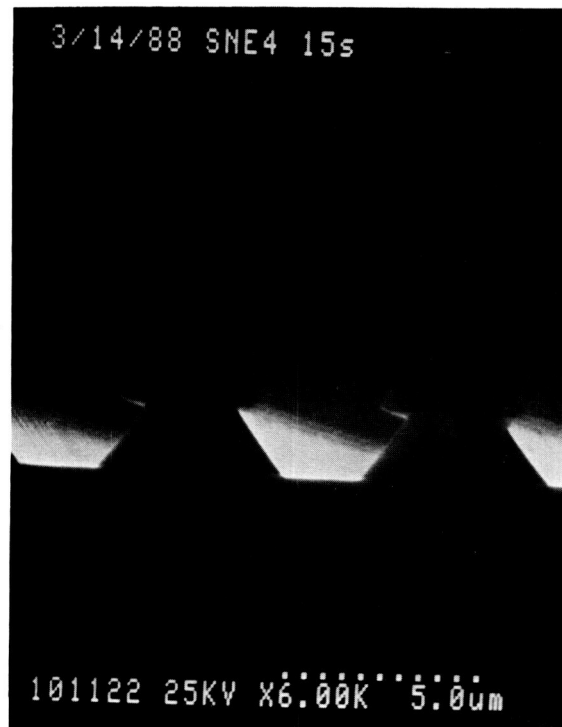
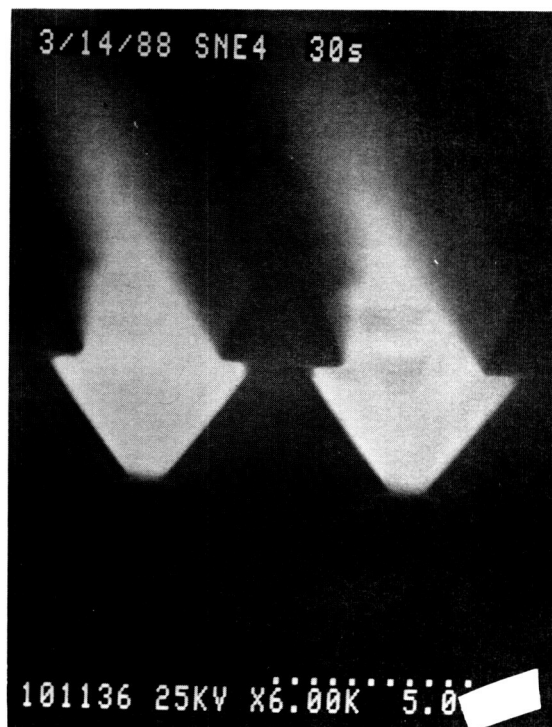


Figure Three: SEM Photograph of Photoresist Stripes on GaAs Wafer.

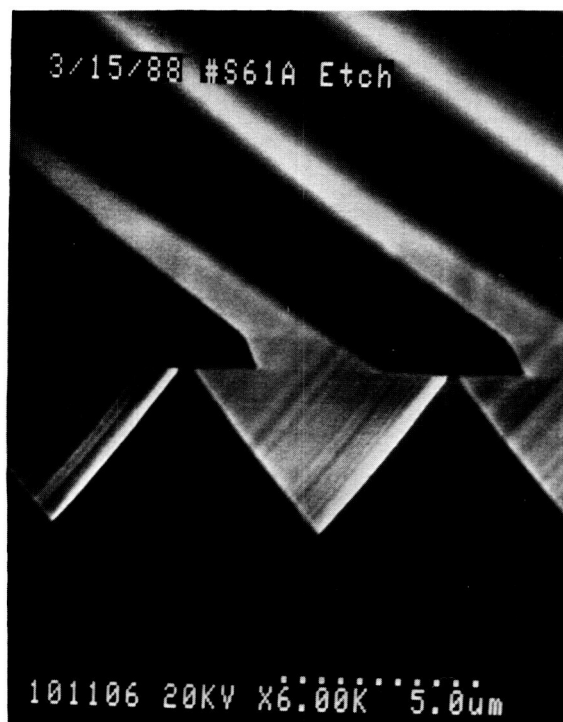
ORIGINAL PAGE
BLACK AND WHITE PHOTOGRAPH



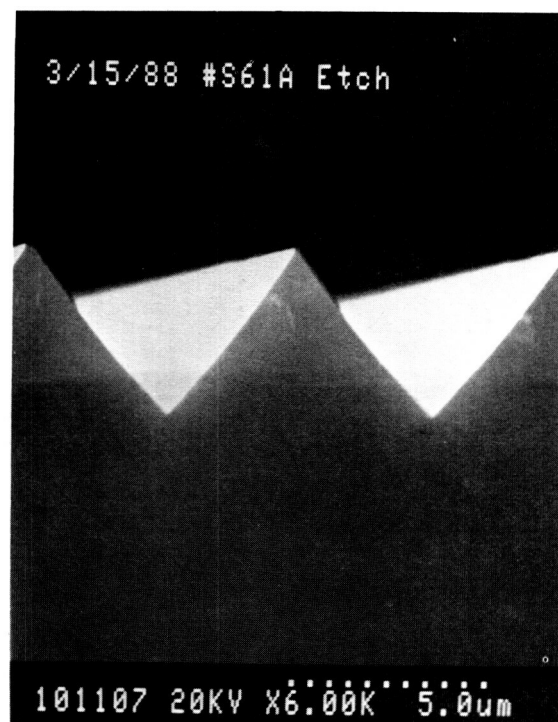
4A: after 15 seconds of etch



4B: after 30 seconds

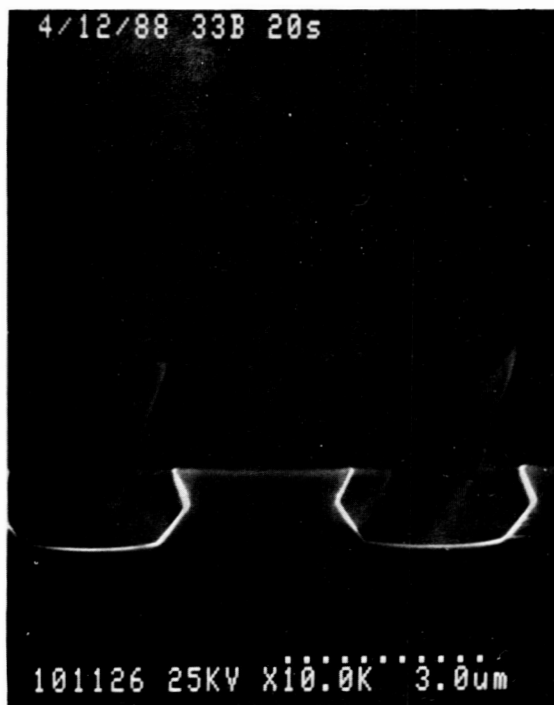


4C: after two minutes

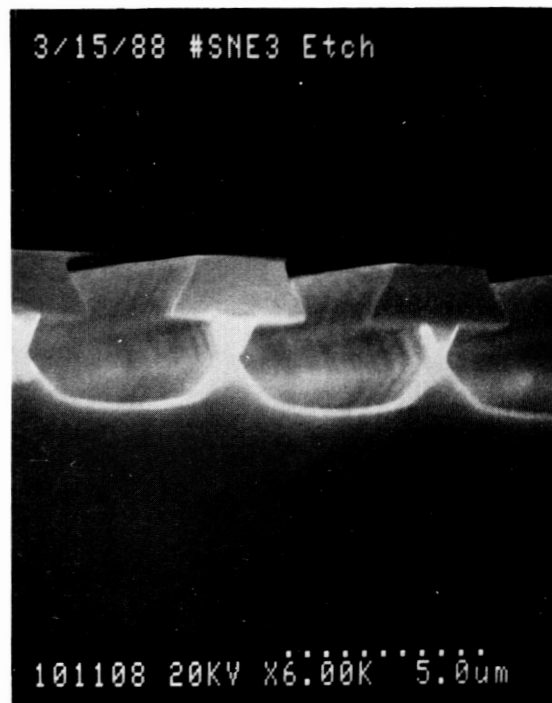


4D: after removal of photoresist.

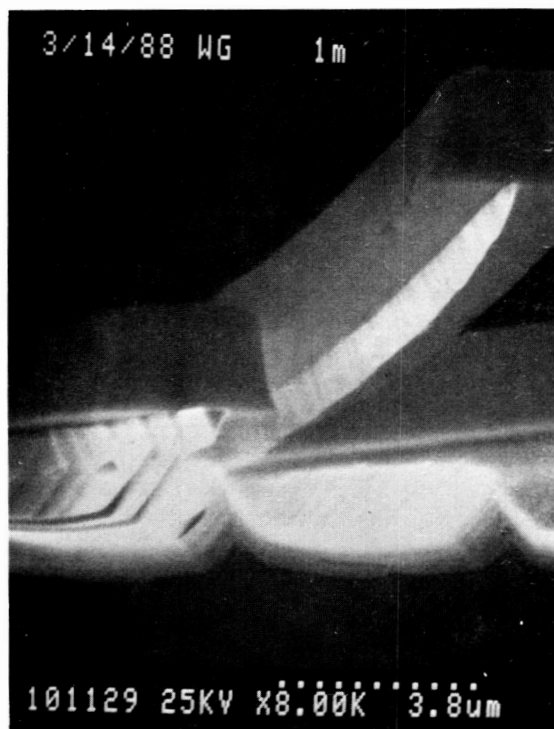
Figure Four: SEM Photographs of V-Groove Etch Process:



5A: after 20 seconds of etch



5B: after one minute of etch



5C: after one minute, showing etch-through and resist stripping

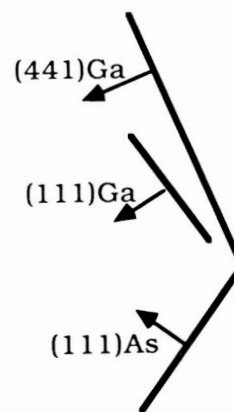


Figure Five: SEM Photographs of "Hex" Groove Etch Process:

ORIGINAL PAGE
BLACK AND WHITE PHOTOGRAPH

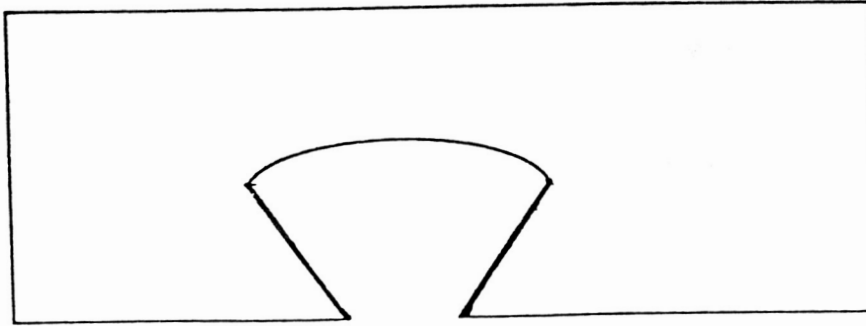


Figure Six: Some experimenters have seen "Dovetail" cross-section grooves as shown above. None of our experiments produced this pattern.

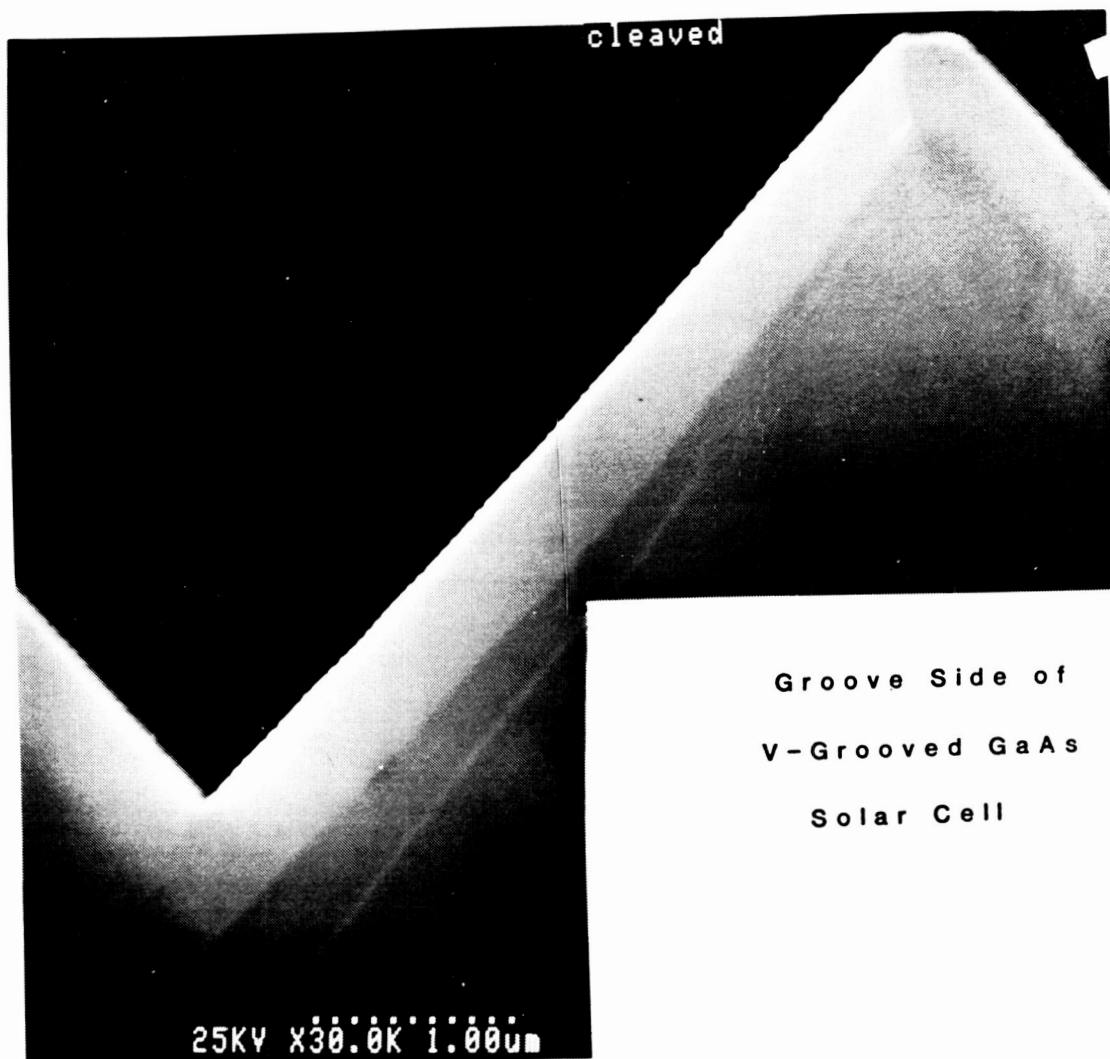


Figure Seven: SEM Photograph of Cleaved Cross-section of Epitaxial p-n junction on Fully V-Grooved Etched GaAs surface.

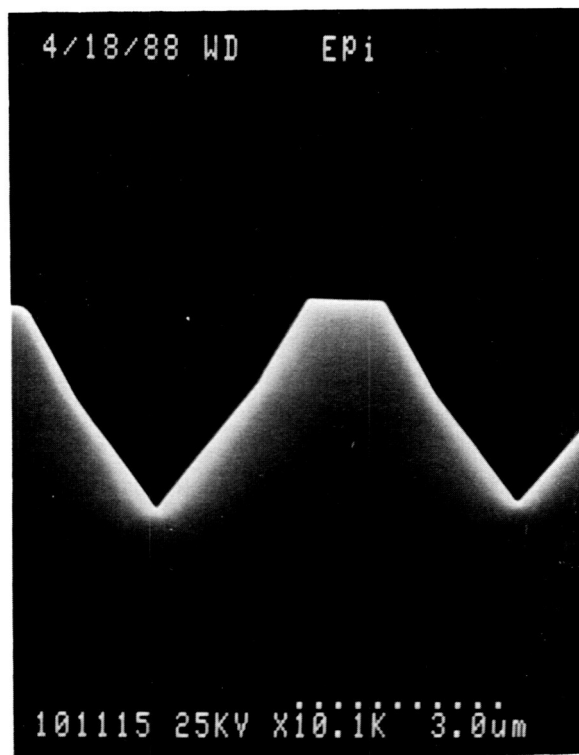
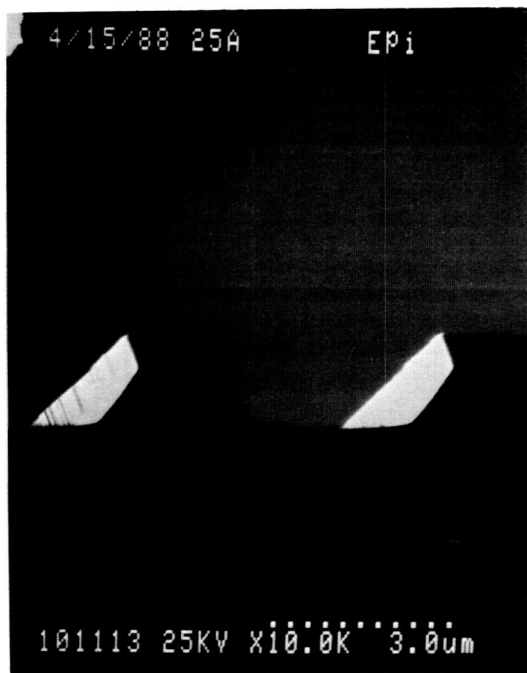
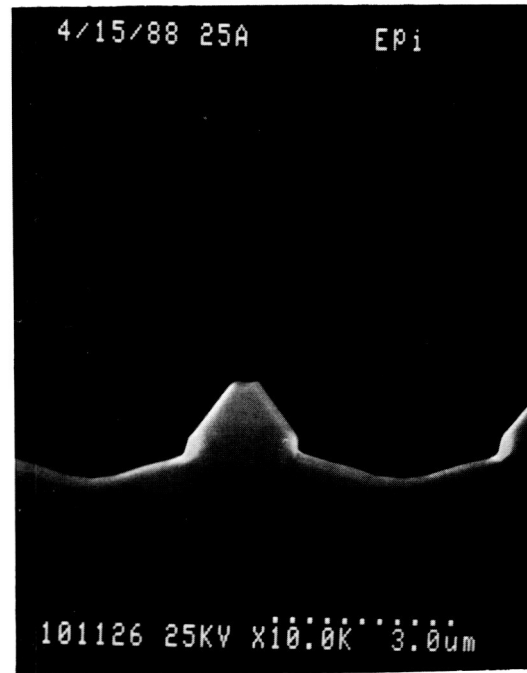


Figure Eight: SEM Photograph of Epitaxial Growth on Partially V-Groove Etched Surface.



8A: Before growth.



8B: After growth.

Figure Nine: Epitaxial Growth on "Hex" Groove:

ORIGINAL PAGE
BLACK AND WHITE PHOTOGRAPH

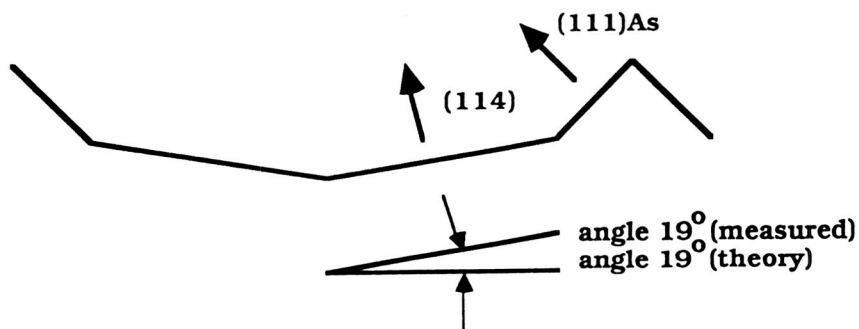
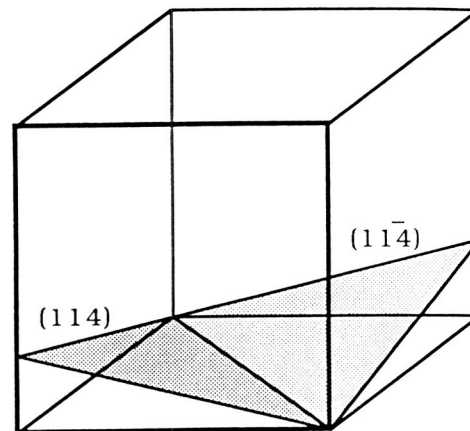
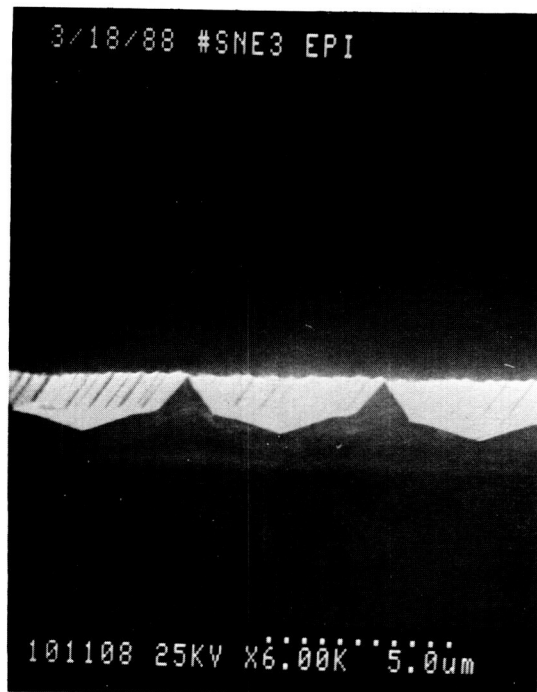


Figure Ten: Epitaxial Growth on "Hex" Groove etched to Completion, showing orientation of major planes.

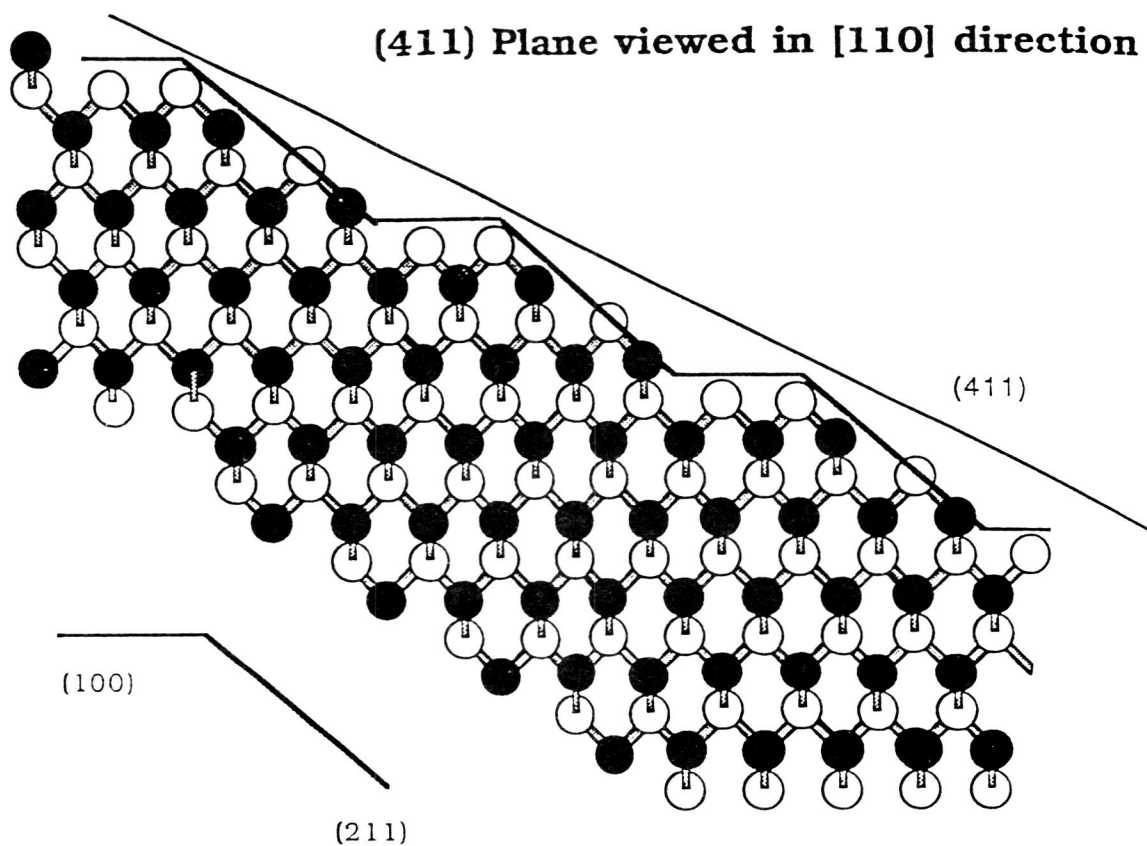


Figure Eleven: GaAs Lattice, showing (411) Plane. Ga atoms (white) are held to the surface with two bonds, while As atoms (black) are held to the surface with three bonds. For the $(\bar{4}11)$ surface, the situation is reversed.

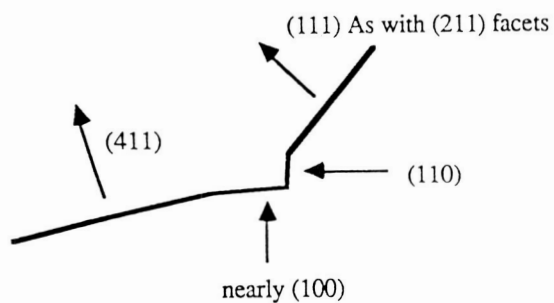
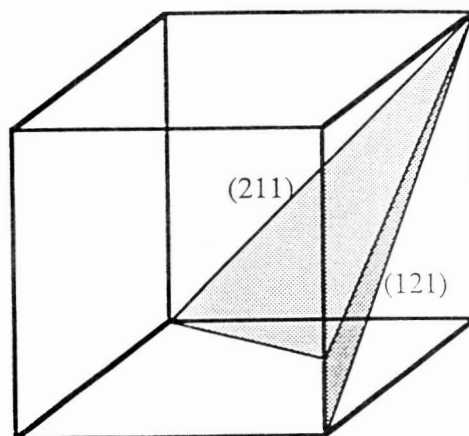
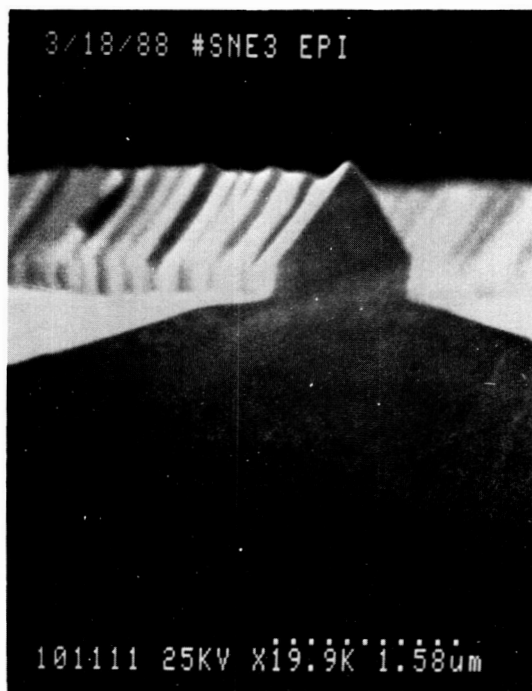


Figure Twelve: Detail of Epitaxial Growth on "Hex" Groove Etched to Completion, showing (211) facets on the (111)As face.

ORIGINAL PAGE
BLACK AND WHITE PHOTOGRAPH

Session 5
Arrays, Cell Production

PRECEDING PAGE BLANK NOT FILMED

Status of GaAs Solar Cell Production

Milton Yeh, Frank Ho, Peter Iles
Applied Solar Energy Corporation

Summary

This paper reviews recent experience in producing GaAs solar cells, to meet the full requirements of space-array manufacturers. The main problems have been in extending MOCVD technology to provide high throughput of high quality epitaxial layers, and to integrate the other important factors needed to meet the full range of user requirements. Some discussion of evolutionary changes is also given.

Introduction

GaAs cells were intensively studied in the laboratory and later in a AF MANTECH Program. The latter program was extended (before the program was completed to meet the needs of a space-array application).

Although the basic technology steps had been identified, considerable adjustment was needed to provide continuous throughput with consistent quality, also meeting all the detailed requirements of the user.

This paper surveys some of the production areas which have been resolved in the past few years.

User Needs

For spacecraft use, several criteria have been developed to define solar cell performance.

The first area of interest is to ensure that the cells have the specified power output, especially after exposure to the radiation fluences expected in orbit. This involves selecting a cell design and processing sequence which provide consistent electrical performance and reasonable resistance to degradation from charged particle radiation.

For GaAs cells, these features are mostly determined by controlling the MOCVD growth conditions, with some influence from the quality of the substrate and of its surface properties. The most important factors lie in the tradeoffs needed to achieve the correct layer quality and uniformity in a reactor which can provide sufficient throughput under continuous use. Demonstration that these factors could be well controlled was achieved by processing consistently larger areas of GaAs substrates (about 1000 cm² per reactor) than was considered practicable a few years ago.

The second area of attention involves the post-growth cell processing. This is mostly application of suitable contacts but also involves deposition of the coatings along with several other steps included to meet specific concerns of the users.

The contacts must provide consistently low contact resistance to the active layers and must also fulfill user requirements—good bondability, and good stability under specified environmental stressing. The front contact system must also be combined with effective grid formation methods. The contact adhesion must be high to adapt to array-laydown techniques.

The third area of interest involves special concerns of the users. These concerns vary for different missions, but may include additional attention to cell ruggedness to allow ready combination into the array laydown methods, precautions to reduce cell degradation from solder-leakage (if soldered contacts are required), checking that the cells can withstand periodic shading without degradation. Also this area includes conforming to all the mechanical and visual specifications.

Last, the cells must qualify under the specified set of environmental stresses (temperature cycling, UV exposure, moisture exposure).

The following section demonstrates that most of these user needs have been filled by the present GaAs production processes.

Production Cell Performance

Present throughput is in excess of 350W/week which provides more than 18 KW per year. Median efficiency levels have risen steadily, and now range from 17.5% towards 18.5%. Figure 1 shows wafers of GaAs and Ge, and solar cells of different configurations made on those wafers.

Individual process step yields have also been increased and are monitored by a computer system. Contact pull strengths have also been increased. All contact pulling strength (for both front and back contacts) exceeds stringent space solar cell requirements.

Product Development

The GaAs space solar cell line has been expanded into other product variations.

The first of these involved a limited production run, under tight deadlines to deliver about 40% of the high efficiency GaAs cells used on the GM/Hughes Sunrayer Car. These cells were specified as space-like components. The average AM0 efficiency was 17.7%, corresponding to AM1 efficiencies over 20%. The histogram of AM0 efficiency of these production 2 x 4 cm GaAs solar cells is shown in Figure 2.

Also, the grown layers used for space cells have been combined with carefully designed grid contacts to give cells with high efficiency under high concentration (up to 500x, AM1 efficiencies about 24%, AM0 efficiency 20%). Figure 3 shows an enlargement of the Cassegranian cell produced by ASEC.

ASEC has also begun partial switchover to use of Ge substrates following four years of development work on these structures with the Ge wafer thinned to around 3 mils. Physically these cells look similar to regular GaAs/GaAs cells. However, they have slightly different I-V curves, based on photoactive junction between the GaAs and Ge. Hence, higher open-circuit-voltage values for

GaAs/Ge solar cells are typically observed. The light I-V curve of a 2×4 cm GaAs/Ge solar cell is shown in Figure 4. A very impressive AM0 efficiency of 20.5% was obtained from this GaAs/Ge solar cell. The other photovoltaic parameters are as follows:

1. V_{oc} -1.187V
2. I_{sc} -240.8mA
3. CFF-77.7%

Several minor changes in the established GaAs production sequence are needed to provide efficient GaAs/Ge cells.

First, suitable Ge substrates must be specified and obtained.

Next the MOCVD growth conditions must be slightly modified to ensure good quality GaAs layers are grown (reduce interface imperfections such as antiphase formation), and also to provide the best interfacial junction conditions.

The AR coating is also similar with fine-tuning to provide best current matching for the GaAs and Ge regions.

Conclusions

GaAs solar cells have been produced at high throughput with well controlled properties. Efficiencies and stability have been demonstrated for users. Present work is aimed at diversifying to include Ge substrates and at the same time, to reduce costs. High costs arise from expensive material costs, and particularly from the high costs needed to purchase and maintain the MOCVD reactors. Nevertheless, the feasibility of high throughput production of reliable, high efficiency GaAs cells on either GaAs or Ge substrates has been well proven.

GaAs and Ge wafers, and a Range of Cells

ORIGINAL PAGE
BLACK AND WHITE PHOTOGRAPH

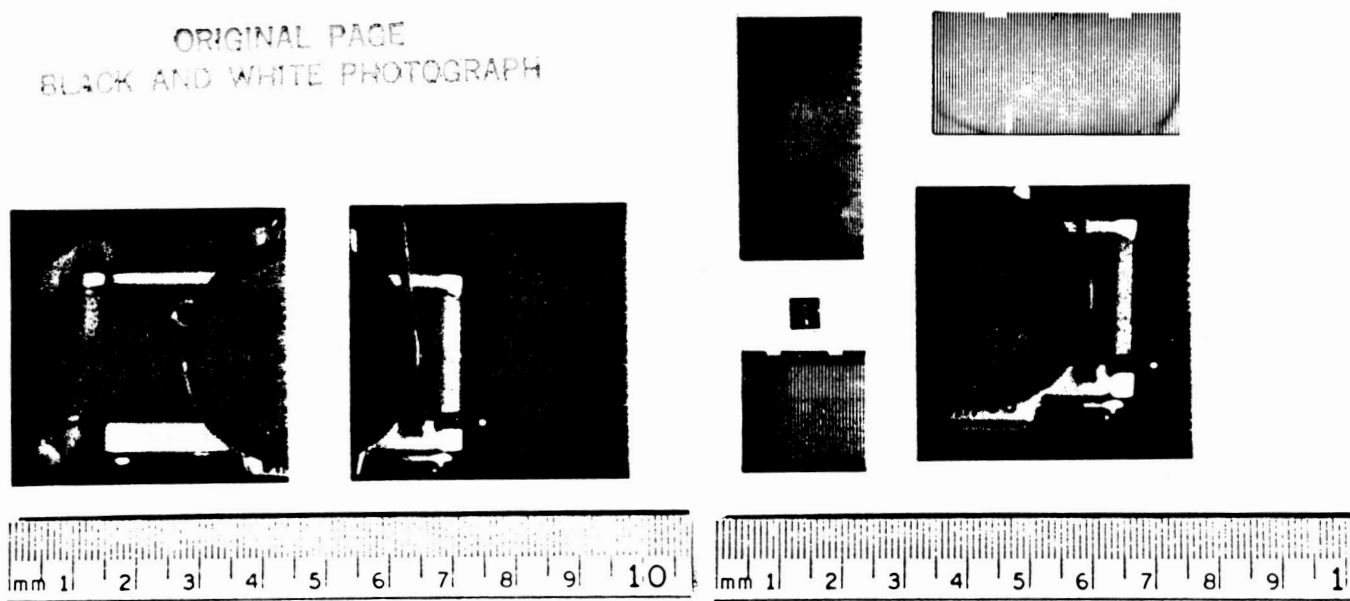
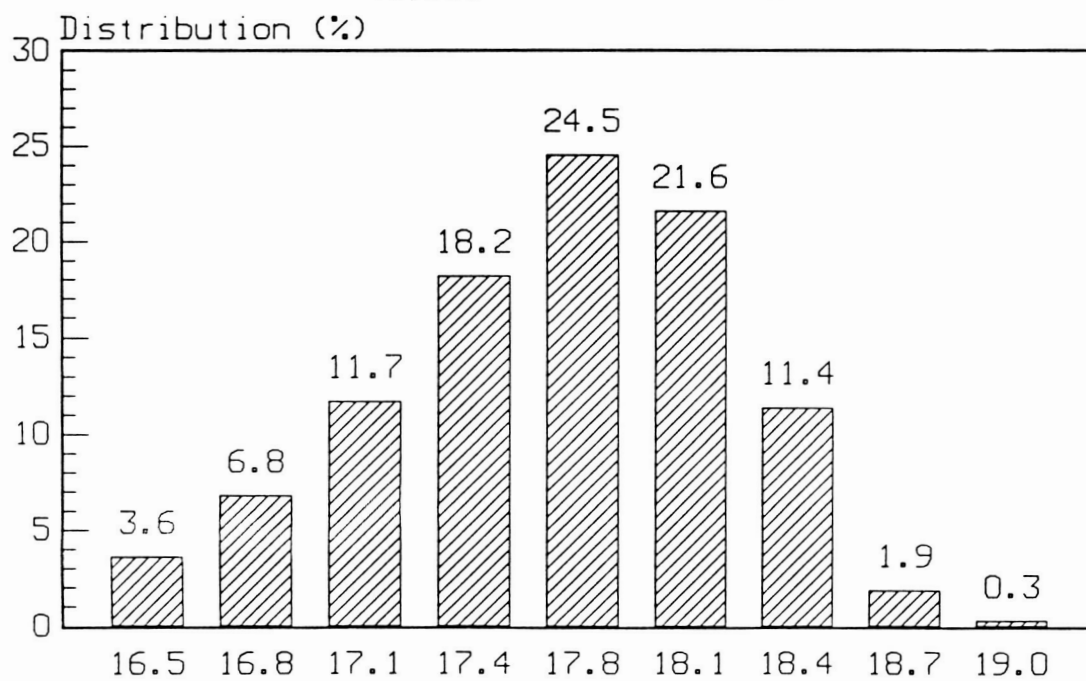


Figure 1

Histogram of AMO Efficiency
of 2x4 GaAs Solar Cell
(5,300 CIC Assemblies)



Efficiency (%)
Figure 2

C-41

An enlargement of the Cassigranian GaAs Solar Cell

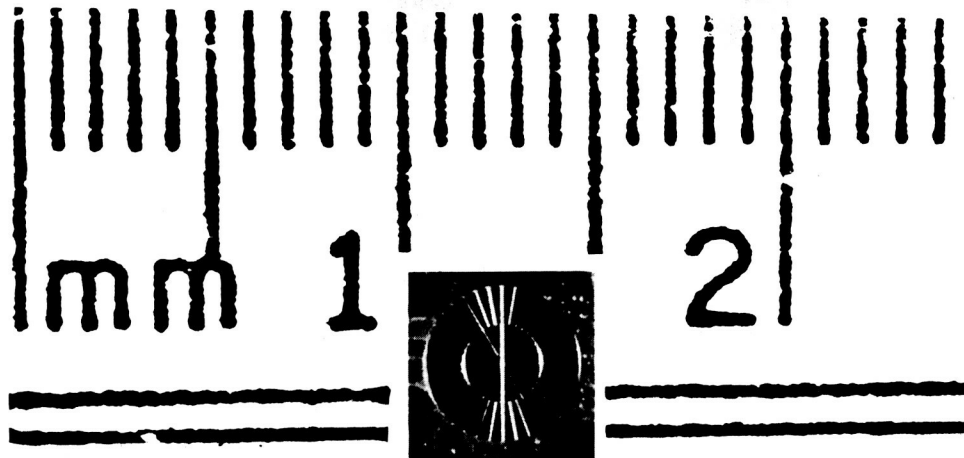


Figure 3

The Light I-V Curve of a 2x4cm GaAs/Ge Solar Cell.

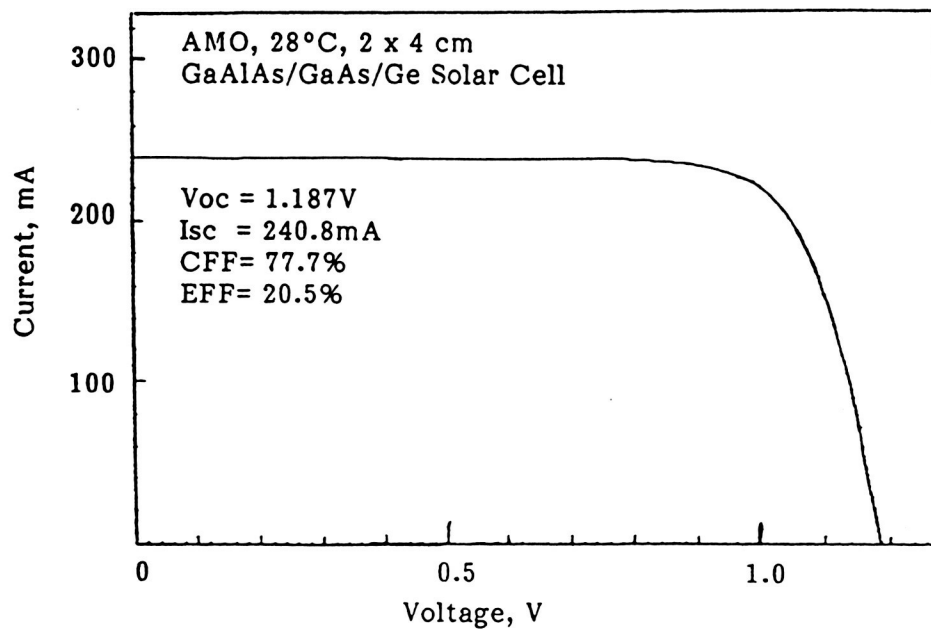


Figure 4

Flexibility in Space Solar Cell Production

Scott Khemthong and Peter A. Iles
Applied Solar Energy Corporation

Summary

This paper describes the wide range of cells that must be available from present-day production lines for space solar cells.

Introduction

After over thirty years of space-cell use, there is very little standardization in solar cell design. It is not generally recognized what a wide range of designs that must remain available on cell production lines. This paper surveys this range of designs.

Cell Design Variations

There are obvious variations, namely whether the cells are made from Silicon or GaAs. There are also differences in size. Concentrator cells are specifically designed for particular collectors, and range from 0.5 cm square to 2×6 cm (or sometimes even larger). Mostly for space use, the range is from 0.5 cm square to 1.5 cm square.

For flat plate cells, the sizes used nowadays extend from 2×2 cm to 8×8 cm. Even for discrete sizes (say 2×4 cm), there are several minor variations dictated by the user's preference in matching cell size to the planned array layout. This means that "2×4" cells often include 6 to 8 different variations; in some cases, this also complicates the efficiency claims for "nominal" size cells. The specified contacts also cover a wide range. The external contacts may be Ag, sometimes soldered either completely or in designated areas. The front contact stack for Si is usually TiPdAg although CrAnAg has been used. The back contact stack is usually TiPdAg but often a highly reflective layer (Al) is used to enhance IR reflectance and reduce solar absorptance - so called BSR cells. These cells are combined with a back surface of high reflectance.

The grid design varies widely from planar to concentrator cells, and also within each category. The back contact may be gridded, either to reduce bowing in thin cells or to allow most of the unabsorbed IR radiation to pass through the cell, again reducing solar absorptance - so called BST cells. For this latter cell, usually an AR coating is applied to the back surface to enhance IR transmission.

The contact configuration most used is called "top/bottom," but both wraparound and wrapthrough contact configurations are gaining popularity.

Internally, Si cells may use a range of resistivities (1 to 14 ohm-cm). In some cases, especially for thinner cells, a back surface field is used, and this must also be formed to retain any BSR or BST features.

Finally the specified cell thickness can vary widely. Mostly for larger cells, 8-10 mils is adequate. However, for weight reduction and increased radiation resistance, Si is often thinned to the range of 2 to 6 mils. GaAs (and Ge) are both over twice as dense as Si. Therefore, for weight reduction, the starting substrate is often thinned. Because Ge is stronger than GaAs but allows good MOCVD growth of active GaAs layers, large area GaAs cells are usually grown on thin Ge substrates.

Critical Manufacturing Areas

Although there are many combinations possible with the above described variations, it is important that the basic cell properties are maintained. These properties include

- maximum efficiency, for the resistivity range used. This often involves trade-off between EOL and BOL efficiency, and may be dictated by the orbit selected;
- reasonably high radiation resistance;
- good contact strength and good ruggedness under temperature cycling;
- good performance when exposed to the short wavelength UV in space;
- good performance in the environmental stress tests specified;
- controlled solar absorptance;
- good mechanical strength, perhaps combined with redundant contact placement.

The critical manufacturing steps with most influence on the final cell properties are

- ingot growth and polishing (ingot size must be compatible with good yield of final cell size). The surface finish helps control the solar absorptance;
- contact deposition, usually by evaporation. The surface cleanliness controls the contact adhesion. Photoresist technology is usually used to produce fine grid patterns;
- AR coatings are deposited usually by evaporation;
- sintering treatments are used to enhance contact or coating adhesion;
- the in-process handling and fixturing must often be adjusted to accommodate large and/or thin wafers;
- if wraparound contacts are used, the cell edges must be polished and coated with an impregnable dielectric layer to support the contact layer;

- if wrapthrough contacts are used, smooth surface holes must be formed and also coated with dielectric to support the contact layer.

Complexities in Production Runs

It can be appreciated from the above list of possible cell properties, that to make limited but possibly large volume production runs of any particular cell type requires maintaining a wide range of processing technology, fixturing and equipment in readiness. For each new run, there is usually a short period required to confirm that all the processes can be combined (under production conditions) to meet all the cell requirements.

In addition, the scheduling of space cell runs is unpredictable, and stockpiling has not been possible. Thus, often several different cell types may have to be processed in parallel, each cell type being optimized with its own particular requirements. For each given materials (Si, GaAs), all the cells produced must share the same general processing facilities and this too makes control of the production run more complex.

Conclusion

We have discussed the factors which make it necessary to have available a wide range of cell processing technologies, and to deploy these technologies as required for theoretical cell runs. There is always the need for parallel processing for "keeping-alive" a set of finely tuned processes, to cope with a mostly unpredictable blend of cell types.

Production conditions require that a set of highly optimized process techniques be applied to meet a complete set of demanding cell properties, and there is little time to perform empirical tests of the type used in laboratory scale development work.

Also the in-line characterization and process controls must provide prompt feedback to allow the line conditions to be monitored and controlled.

We hope we have presented reasons why present space cell production lines require great flexibility.

Large Area Silicon Cells

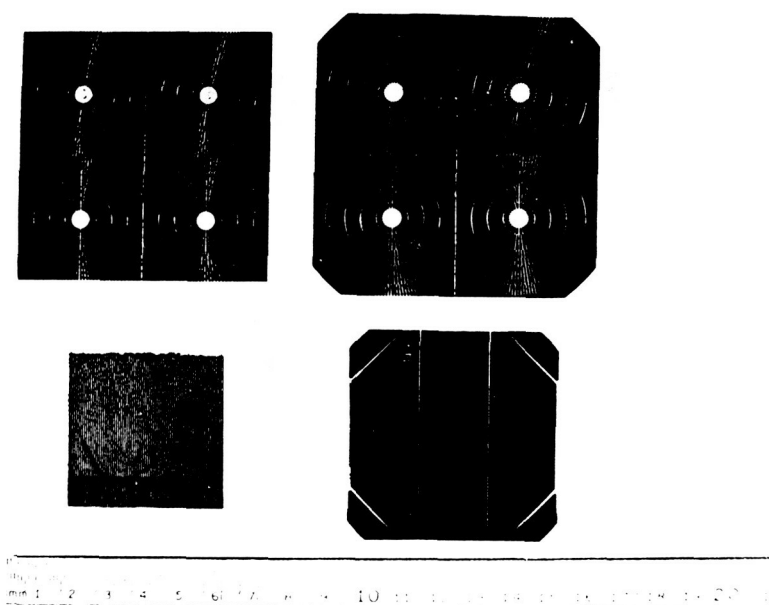


Figure 1

Various Space Cell Size

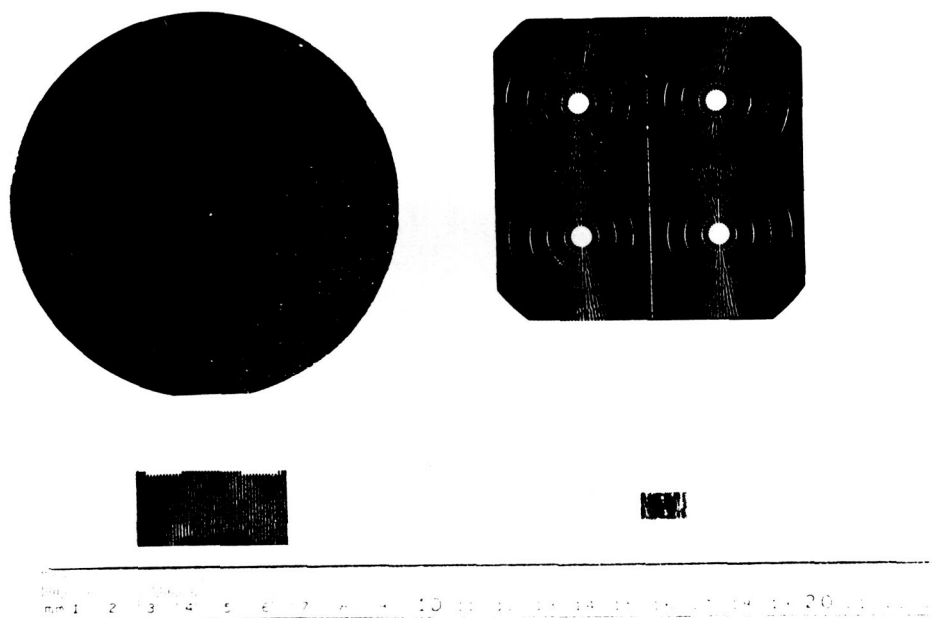


Figure 2

ORIGINAL PAGE
BLACK AND WHITE PHOTOGRAPH

2x4 and 4x2 Silicon Cells

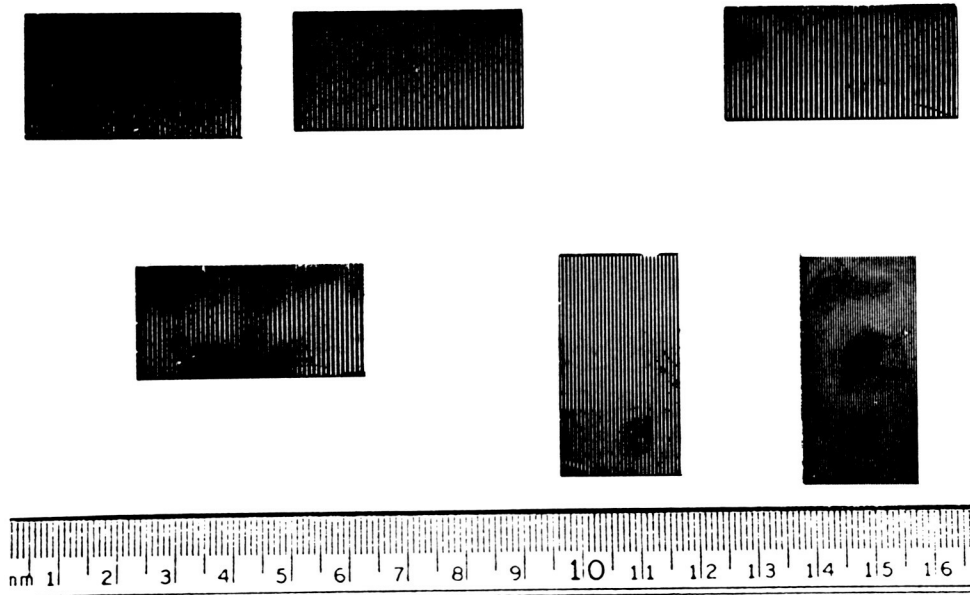


Figure 3

GaAs Wafers and Cells of Different Sizes

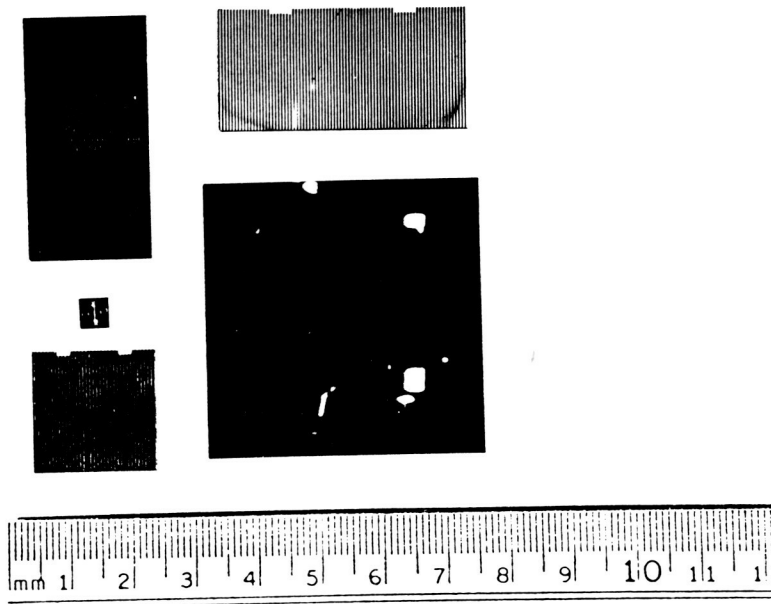


Figure 4

Gallium Arsenide Welded Panel Technology for Advanced Spaceflight Applications

D.R. Lillington, M.S. Gillanders, G.F.J. Garlick,
B.T. Cavicchi and G.S. Glenn
Spectrolab, Inc.

S. Tobin
Spire Corporation

Abstract

A significant impediment to the widespread use of GaAs solar cells in space is the cost and weight of the GaAs substrate. In order to overcome these problems, Spectrolab is pursuing thin cell technologies encompassing both LPE GaAs on GaAs and MOCVD GaAs on Ge cells.

In this paper we describe Spectrolab's experience in the manufacture of 4-6 mil 2 cm x 4 cm GaAs cells on our LPE production line. By thinning the cells at a late stage of processing, production yields comparable to 12 mil cells have been achieved. Data are presented showing that GaAs cells can be welded without degradation and have achieved minimum average efficiencies of 18% AM0, 28°C with efficiencies up to 20%.

Spectrolab, in conjunction with Spire Corporation has also been pursuing GaAs on Ge cell technology in support of larger area lighter weight power systems. Data are presented showing that individual 2 cm x 2 cm, 8 mil cell efficiencies up to 21.7% have been achieved. Efficiencies up to 24% AM0 will be possible by optimizing the GaAs/Ge interface. Cells have been welded without degradation using silver interconnects and have been laid down on an aluminum honeycomb/graphite facesheet substrate to produce a small coupon. The efficiency was 18.1% at AM0, 28°C.

Thin 2 cm x 4 cm GaAs Cells

Spectrolab's 12 mil LPE GaAs manufacturing process has been modified to accommodate processing of 5 mil GaAs cells at high yield. The cross sectional cell construction which has been described in detail elsewhere [Ref. 1] is shown in Figure 1. The cell also utilizes the Hybrid Etch-Through (HET) front contact structure (shown in Figure 2) to allow assembly by welding or soldering without degradation [Ref. 2].

Initially substrates were etched from 12 mil to 5 mil prior to LPE growth and subsequently processed at that thickness. However, significant component losses due to breakage at all stages of processing led us to investigate an alternate route to cell thinning.

In Figure 3 we show the baseline process, modified to include thinning after frontside processing. Thinning at this late stage of processing resulted in only marginal losses during back contact metallization, sintering, dicing and test.

In Figures 4, 5, 6 and 7 we show the distribution of V_{oc} , I_{sc} , FF and efficiency for over 100 thin cells recently produced. High open circuit voltages with a tight distribution in FF and efficiency are achieved by statistical control of all growth parameters and front contact sintering conditions. The latter has been found to be particularly important in controlling V_{oc} and FF since over sintering of structures with thin radiation hard emitters can significantly increase the second diode saturation current I_{o2} . The average efficiency of bare cells shown in Figure 7 is 17.7%. It should be noted that a coverglass gain of approximately 2-3% is observed when CMX or fused silica covers are attached using DC93-500 adhesive resulting in average efficiencies of approximately 18% AM0 28°C.

Spectrolab has parallel gap welded solid silver interconnects to both the front and back of 5 mil GaAs cells without any electrical degradation being observed. However, some cracking during backside welding of glassed cells has been experienced. Similar problems have also been observed on 12 mil cells. Breakage is largely independent of weld tip pressure which implies that the cracking is induced by thermal stress rather than by tip pressure alone. This problem is currently being addressed.

During April 1988 a coupon of fifty 5 mil GaAs cells on an aluminum honeycomb substrate with graphite facesheets will be assembled using welded silver interconnects. Based on measured efficiencies of cells already fabricated for this project it is expected that the coupon efficiency will be greater than 18% AM0.

8 Mil GaAs/Ge Cells

In order to address issues relating to the cost, size and weight limitations of GaAs cells [Ref. 3] Spectrolab, in conjunction with Spire Corporation has been developing GaAs on Ge solar cells. These cells offer substantial increase in power due to the bandgap matching between GaAs and Ge which allows two terminal monolithic dual junction cells to be fabricated.

It is believed that 3 mil thick cells up to 7 cm x 7 cm or even 8 cm x 8 cm can ultimately be achieved due to the excellent mechanical properties of Ge substrates.

In Figure 8 we show the computed internal spectral response of a GaAs/Ge cell in which the Ge substrate is active. The parameters used for modeling both the GaAs and Ge cells are shown in Table 1. Due to the low bandgap of Ge (0.67 eV) the cell response extends out to 1.87 microns wavelength. Provided the back surface recombination velocity at the back of the Ge substrate can be kept below 100 cm sec⁻¹ the current in the Ge base is approximately 30 mA cm⁻² and a current matched cell is produced. In Figure 9 we show the projected AM0 I-V characteristic of such a cell. We estimate that a 24.4% efficiency cell is achievable with approximately 5.5% being contributed from the Ge cell.

In Figure 10 we show the illuminated AM0 I-V characteristic of a 2 cm x 2 cm 8 mil GaAs/Ge cell fabricated by Spire Corporation and measured at NASA LeRC. An AM0 25°C efficiency of 21.7% was achieved. It is believed that the present efficiency is limited by a recombination velocity of approximately 10⁶ cm sec⁻¹ there. Reduction in these states by optimization of the growth conditions should allow efficiencies up to 24% to be achieved.

We have also demonstrated the assembly hardness of GaAs/Ge cells by fabricating and testing a small 3 cell welded coupon. The substrate material was 0.75 inch aluminum honeycomb with

graphite facesheets. The cells were filtered using 6 mil CMX coverglass and DC93-500 adhesive. A glassing loss of approximately 2% was observed. Cells were interconnected by parallel gap welding using solid silver interconnects. No electrical degradation was observed after welding. Pull tests on other sample cells indicated excellent pull strengths of over 3 newtons on both sides of the cell. In Figure 11 we show the AM0, 28°C characteristic of the coupon. An overall efficiency of 18.1% was achieved. The small amount of shunting seen in the characteristic was attributed to leakage paths at the GaAs/Ge interface rather than to welding assembly degradation which was not observed on any cells.

Conclusion

Thin 5 mil 2 cm × 4 cm GaAs solar cells have been fabricated by a high yield process. The cells had an average efficiency (bare) of 17.7% with a projected average efficiency after glassing of 18%.

GaAs/Ge cells up to 21.7% efficiency were also fabricated and have been shown to be easily assembled by welding into an 18.1% efficiency coupon. Pull strengths of the front and back contact metallizations were excellent and exceeded 3 newtons. These cells show promise of achieving efficiencies of up to 24% AM0 in 7 cm × 7 cm or 8 cm × 8 cm form for future high power, radiation hard missions.

Acknowledgements

The authors wish to thank Russell Hart of NASA Lewis Research Center for making AM0 cell measurements on GaAs/Ge cells.

References

- [1] M. Gillanders, B. Cavicchi, D. Lillington and N. Mardesich, *Proc 19th IEEE PVSC*, New Orleans, p289 (1987).
- [2] B.T. Cavicchi, H.G. Dill and D.K. Zemmrich, *Proc 19th IEEE PVSC*, New Orleans, p67 (1987).
- [3] K.I. Chang, Y.C. Yeh, P. Iles, J. Tracy and R.K. Morris, *Proc 19th IEEE PVSC*, New Orleans, p273 (1987).

LAYER	THICKNESS	DIFF.L	DIFF.CFT.	SURFACE REC.		
				VELOCITY	DOPING CONC.	DAMAGE CFT.
	(uM)	(uM)	(cm ² /s)	(cm/s)	(1/cm ³)	(1/e)
TOP CELL : AlGaAs Windowed GaAs Cell						
Window	.1	.2	.27	1E6	2E18	--
Emitter	.5	5	90	1E4	2E18	3.5E-8
Base	5	2	5	1E2	2E17	1.8E-7
BOTTOM CELL : Ge						
Emitter	.1	50	24	5E3	1E19	1E-10
Base	75	200	15	1E2	4E17	1E-10

Table 1 Parameters Used in Cell Modeling

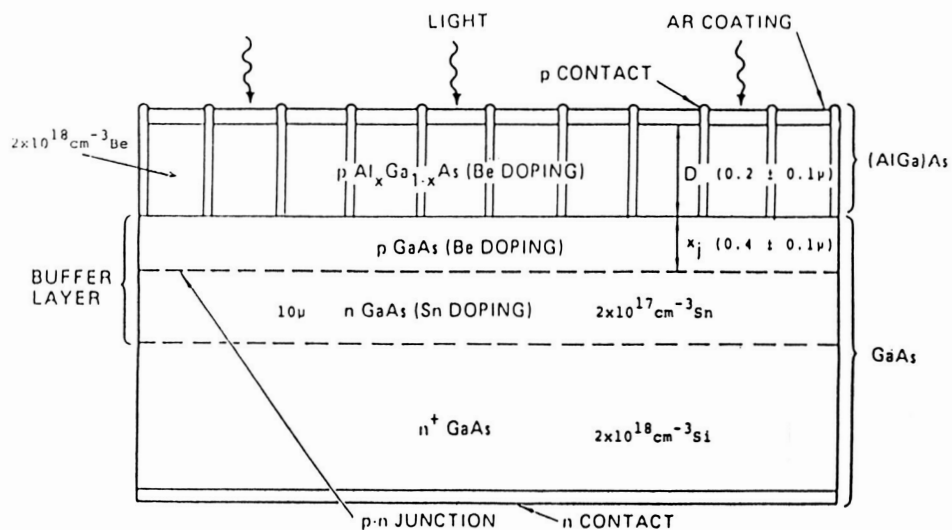


Fig 1 GaAs Cell Cross-Section

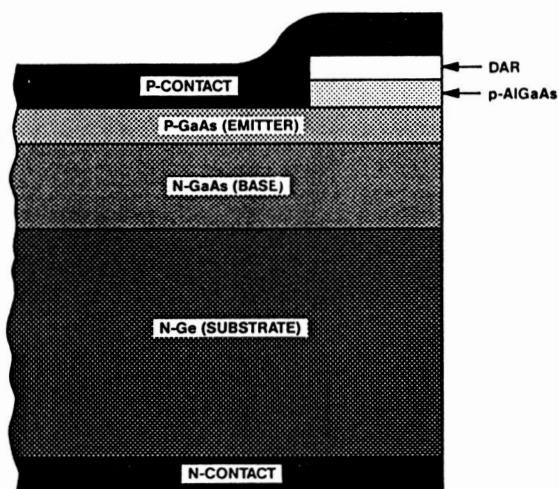


Fig 2 Hybrid Etchthrough Contact

ORIGINAL PAGE
BLACK AND WHITE PHOTOGRAPH

ETCH
 BUFFER/BASE GROWTH
 WINDOW GROWTH
 ANNEAL
 DAR COAT
 PHOTOLITHOGRAPHY
 ETCH
 FRONT CONTACT METALLIZATION
 LIFT-OFF
 FRONT MASK
 ETCH TO 5 MILS
 BACK CONTACT METALLIZATION
 SINTER
 DICE

Fig 3 Thin Cell Process Sequence

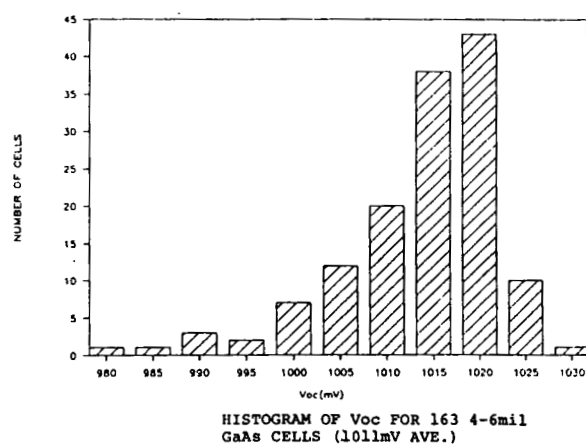


Fig 4 5 mil GaAs Cell V_{oc} Distribution

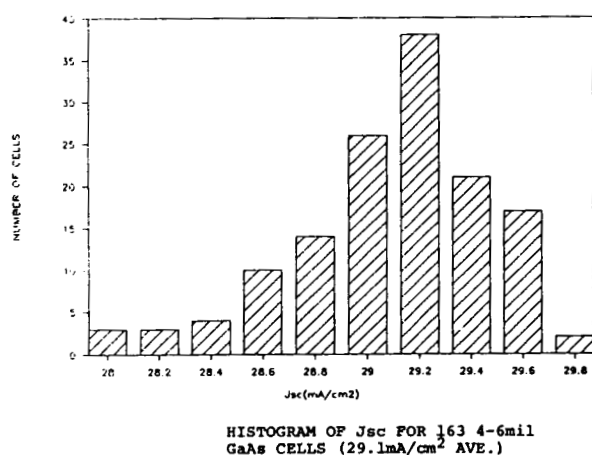


Fig 5 5 mil GaAs Cell J_{sc} Distribution

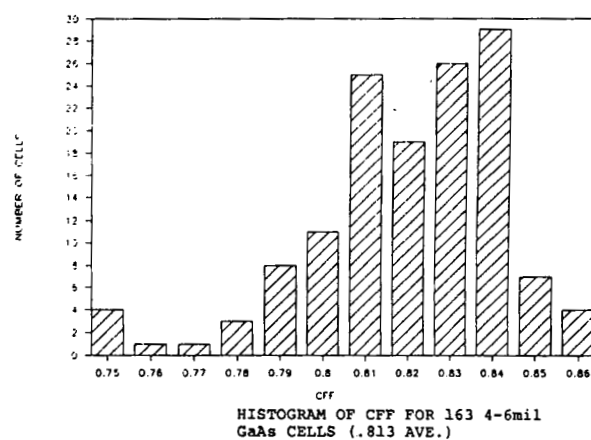
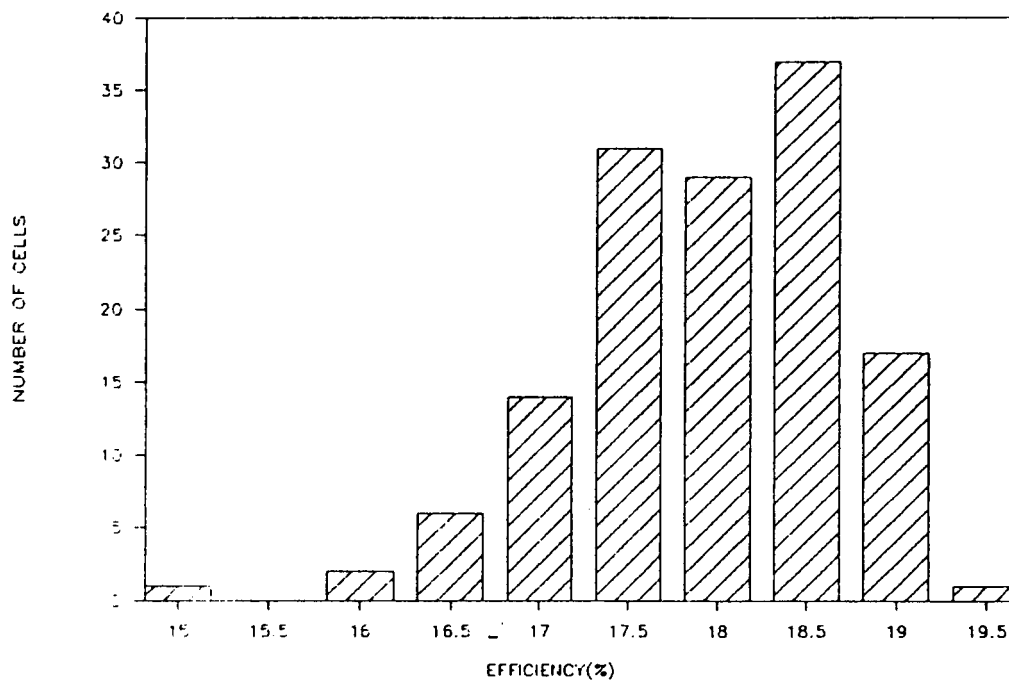


Fig 6 5 mil GaAs Cell CFF Distribution



HISTOGRAM OF EFFICIENCY FOR 163
4-6mil GaAs CELLS (17.7% AVE.)

Fig 7 5 mil GaAs Cell Efficiency Distribution

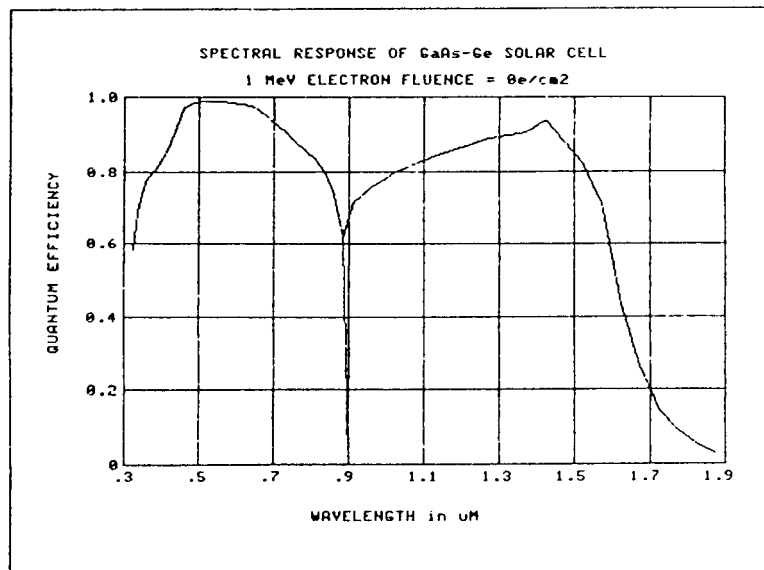


Fig 8 GaAs/Ge Cell Internal Q.E.

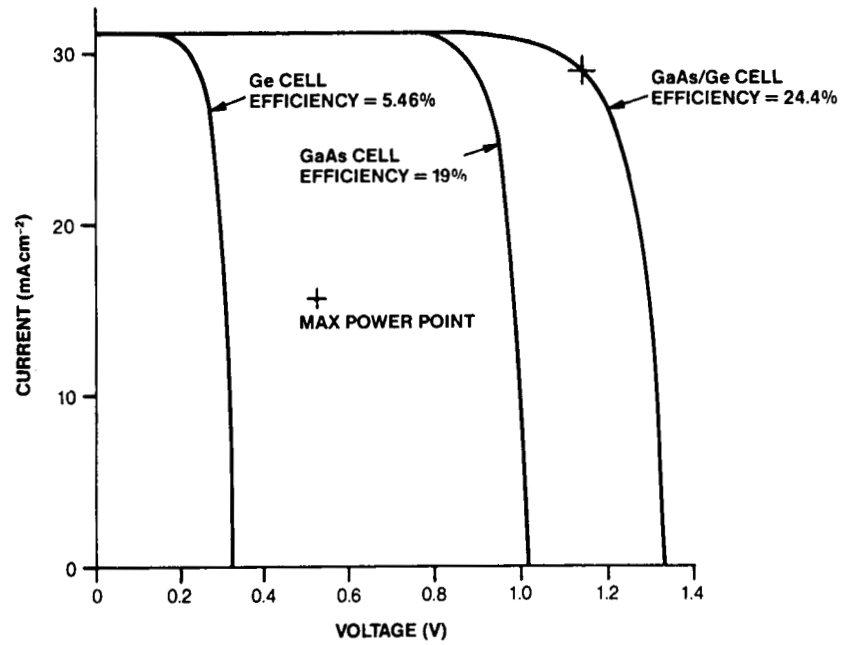


Fig 9 Predicted GaAs/Ge Cell Performance

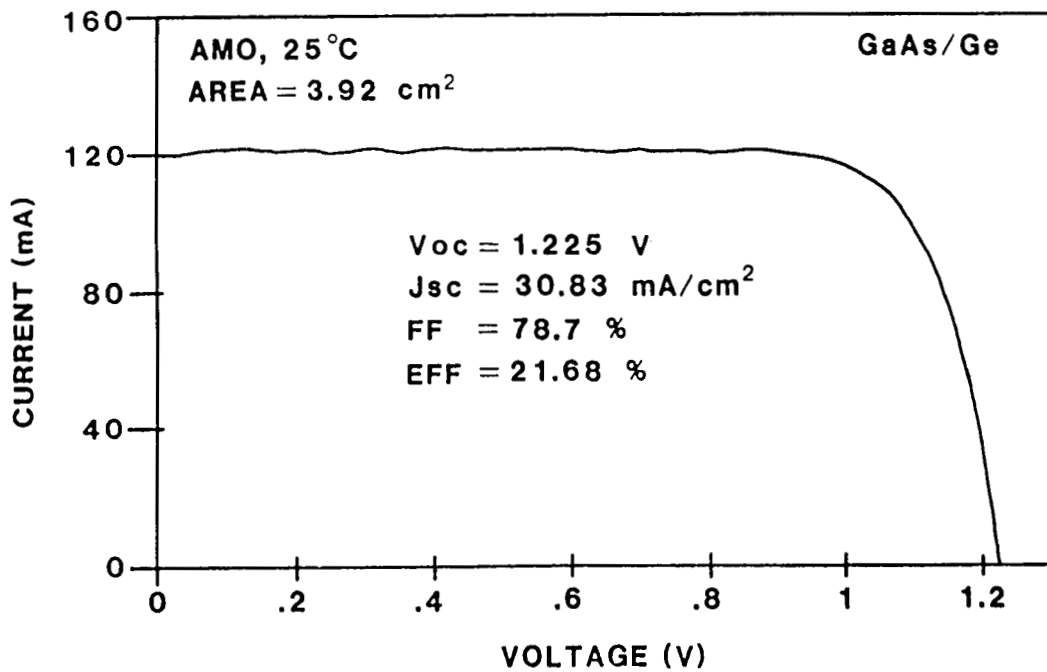


Fig 10 Measured I-V curve of $2\text{ cm} \times 2\text{ cm}$ GaAs/Ge Cell

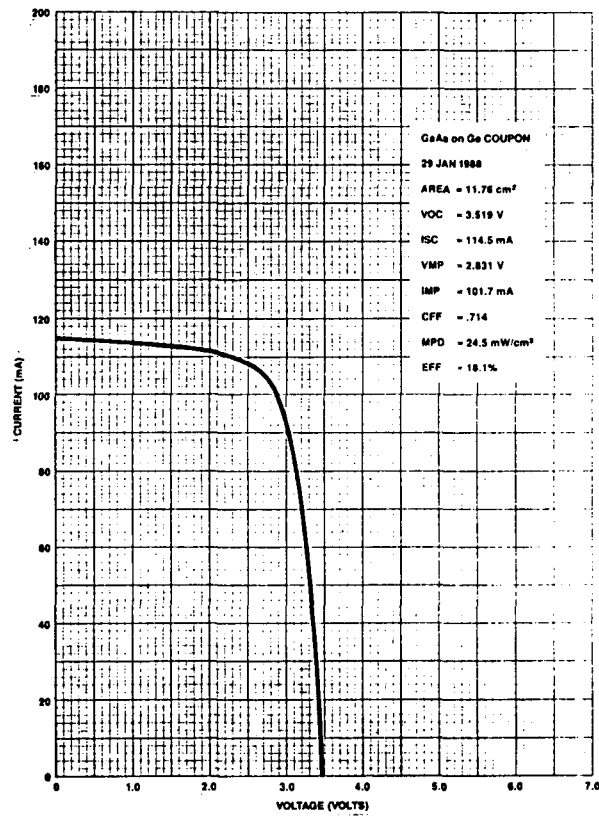


Fig 11 Measured I-V Curve of GaAs/Ge Coupon

ORIGINAL PAGE IS
OF POOR QUALITY

Domed Fresnel Lens Concentrator Technology for Space Application

Michael F. Piszczor, Jr.
NASA Lewis Research Center
Cleveland, Ohio 44135

Mark J. O'Neill
Entech, Inc.
Dallas, Texas 75261

Over the past three years, NASA Lewis and Entech, Inc. have been investigating the use of high efficiency refractive photovoltaic concentrators for use in space. The design currently under investigation uses a square domed Fresnel lens to focus light on a GaAs concentrator cell. A prismatic cell cover, which directs light away from the front contacts and thus eliminates metalization losses, is applied to the top of the GaAs cell to further enhance array efficiency. This paper will present the latest experimental results based on testing the GaAs cell/prism cover assembly at standard and operating conditions.

Introduction

Under a Small Business Innovative Research (SBIR) contract, NASA Lewis has been working with Entech, Inc. to develop a highly efficient, relatively lightweight refractive concentrator array which would be applicable to a wide variety of missions. The selection of the domed Fresnel lens design is based on the results of studies conducted during the Phase I SBIR contract [refs. 1,2]. The design uses a gallium arsenide cell with a 4 millimeter diameter active area, which is designed to operate at conditions of 100 suns, 100 C. Based on the preliminary studies, an array performance of 240 watts per square meter and 80 watts per kilogram is possible in the near term. Improvements in lens and cell efficiency as well as weight optimization could further improve future system performance. A Phase II contract, currently under way, will develop hardware and enable further testing of the concept.

Figure 1 shows a conceptual design of the the domed Fresnel lens concentrator module. The domed Fresnel lens uses a curved shape as well as individually designed Fresnel facets along the inner surface. The design maximizes the lens optical efficiency by minimizing reflection losses within the lens by providing equal angles of incidence and emergence from the lens [ref. 3]. Initial optical analysis studies indicate that a net lens optical efficiency of 91.5% is reasonable without an antireflection coating. Use of a good antireflection coating could further improve the lens efficiency to 96%. The domed Fresnel lens can be cut into a square to increase the packing factor of the individual modules and further decrease losses. In Figure 2, the individual lens and cells are incorporated into a panel and illustrate this point.

GaAs Cell/Prism Cover Measurements

The domed Fresnel lens concentrator concept uses a prismatic cell cover to minimize losses due to metalization. The prism cover directs incoming light away from the metalized surface of the the cell. An optimized prism cover design is shown in Figure 3. The design can accommodate light coming within the 30 degree rim angle of the domed Fresnel lens and can essentially eliminate losses due to gridline obscuration up to a metalization coverage of 21%. This not only increases the system efficiency by eliminating metalization losses, but also improves the operating cell efficiency by reducing series resistance, which becomes important under higher concentration ratios.

The visual effects of the prism cover can be seen in Figure 4. This figure shows two gallium arsenide concentrator solar cells side-by-side on a dime. Each cell has a circular active area with a 4 mm. diameter surrounded by gold metalization. The cells are identical, with the exception that a prismatic cell cover has been attached to the cell on the right. The prismatic cell cover directs incoming light away from the front grid fingers toward the open active areas of the cell. Note that since light is not reflected from the gridlines of the cell with the prism cover, the top grid lines essentially disappear on the cell on the right.

A number of GaAs concentrator cells with the proper front metalization configuration were provided by Varian. Four of the cells were covered with a prismatic cell cover. The cells were measured under AM0 conditions at a concentration of $100\times$, 25 C both before and after prism cover application. Three of the cells were also measured at $100\times$, 100 C, which is the expected operating condition of the cell in the domed Fresnel lens concentrator array. The results of the tests are shown in Table I.

After prism cover application, each cell measured over 23% at $100\times$, 25 C, with the highest efficiency being 24.3%. At an operating temperature of 100 C, the best cell achieved an efficiency over 22%. These results represent the highest efficiencies ever measured under space conditions at NASA Lewis.

The increase in short circuit current, after application of the prism cover, is a direct measure of the effectiveness of the prism cover in eliminating reflection losses from the front surface. Increase in current for the four cells ranged from 9% to 12%. Given the amount of front metalization, a maximum current increase of 13% would be expected. Since the method of applying the prism cover to individual cells is still being perfected, the results of these tests are encouraging.

Program Status and Further Development

The goal of the SBIR Phase II program is to produce two prototype panels and a number of individual lens/cell modules for continued testing. To date, only the gallium arsenide cell/prism cover component of the domed Fresnel lens concentrator array has been tested. Efforts are currently under way to manufacture the domed Fresnel lens. Figure 5 shows the lens design being used for this Phase II contract. The domed shape of the lens is supplied by a microglass superstrate. The Fresnel facets are made from a silicone RTV and then bonded to the inside of the glass dome. Should another lens material prove more appropriate for the space environment, the array design is flexible enough to accomodate such changes. Efforts are also under way on developing a lightweight version of the domed Fresnel lens concentrator array.

Summary

The domed Fresnel lens concentrator array is currently being investigated at NASA Lewis as an approach to get high efficiency, relatively light weight concentrator arrays. This concept uses a prismatic cell cover to reduce reflection losses from the top gridlines. A GaAs cell/prism cover assembly was recently measured at 24.3% and 22.1% under conditions of 100× AM0, 25 C and 100 C respectively. Future work will concentrate on development of the domed Fresnel lens itself.

References

- [1] M.F. Piszczor and M.J. O'Neill, "Development of an Advanced Photovoltaic Concentrator System for Space Applications," *Proceedings of the 22nd IECEC*, August 10-14, 1987.
- [2] M.J. O'Neill and M.F. Piszczor, "Development of a Dome Fresnel Lens/Gallium Arsenide Photovoltaic Concentrator for Space Applications," *Proceedings of the 19th Photovoltaic Specialists Conference*, May 4-8, 1987.
- [3] M.J. O'Neill, "Solar Concentrator and Energy Collection System," U.S. Patent No. 4,069,812, January 24, 1978.

Table 1 GaAs/Prism Cover Cell Performance

Cell #	Before Prism Cover 100×, 25°C	With Prism Cover 100×, 25°C	With Prism Cover 100×, 100°C*
3	21.4%	23.1%	—
18	21.7%	24.0%	21.9%
25	21.8%	24.3%	22.1%
26	21.7%	23.8%	21.8%

* Expected Array Operating Conditions

ORIGINAL PAGE IS
OF POOR QUALITY

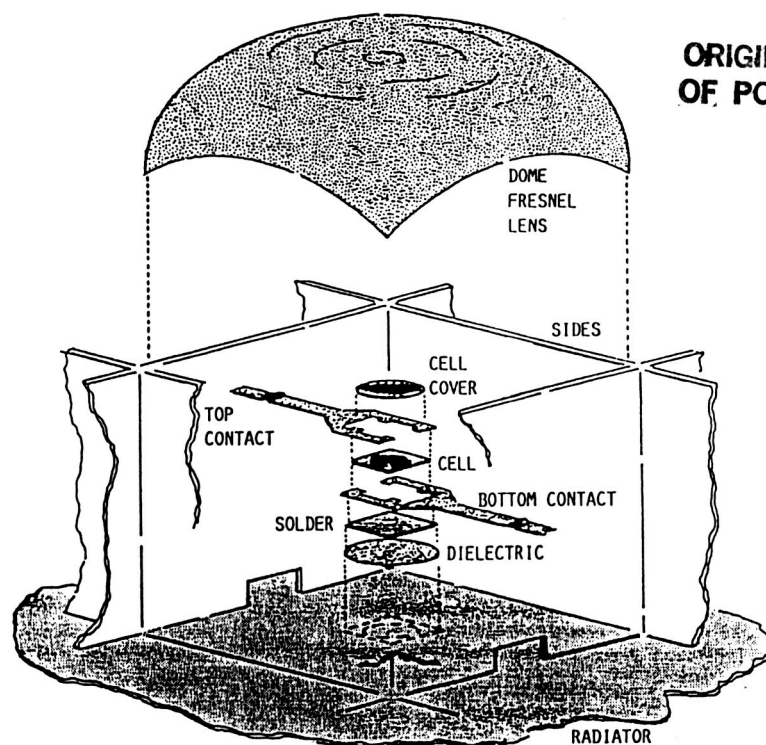


Figure 1 Domed Fresnel Lens Module Conceptual Design

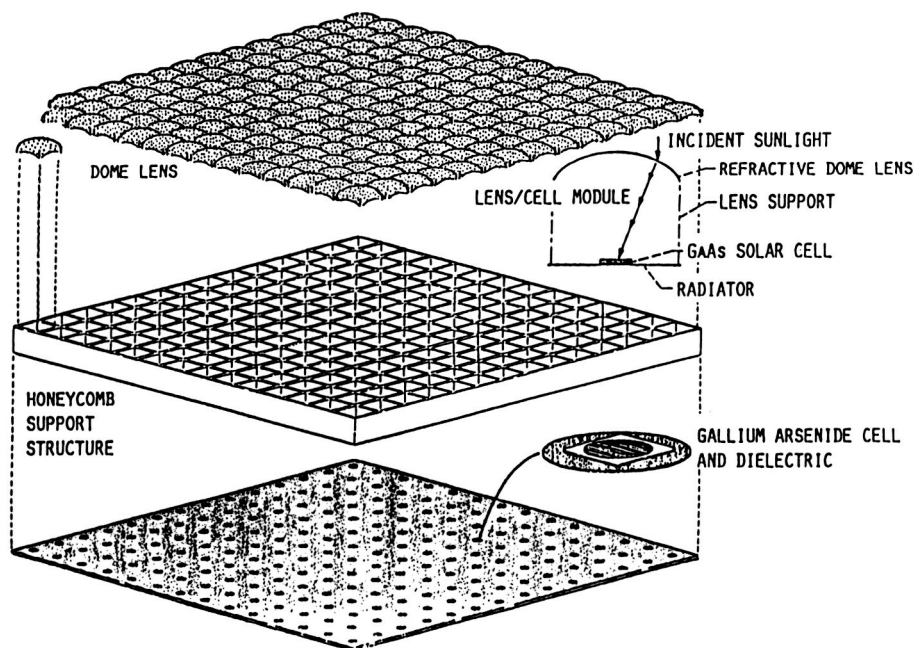


Figure 2 Domed Fresnel Lens PV Concentrator Panel Design

ORIGINAL PAGE
BLACK AND WHITE PHOTOGRAPH

Thickness Tolerance: ± 13 microns (0.5 mil)
Allowable Metallization: 21%
Actual Metallization: 20%

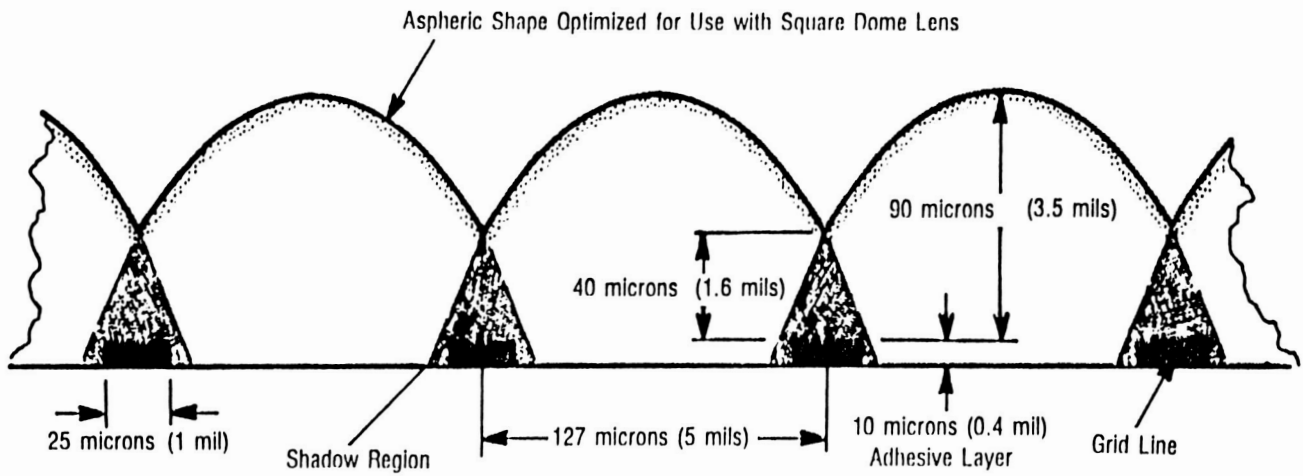


Figure 3 Optimized Prism Cover Design

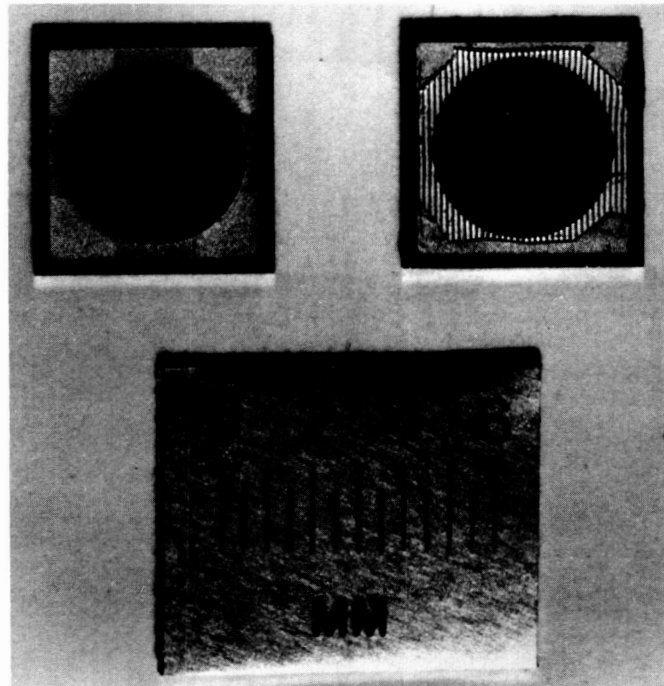


Figure 4 Gallium Arsenide Concentrator Cells With and Without a Prismatic Cell Cover Applied to the Top Contacts

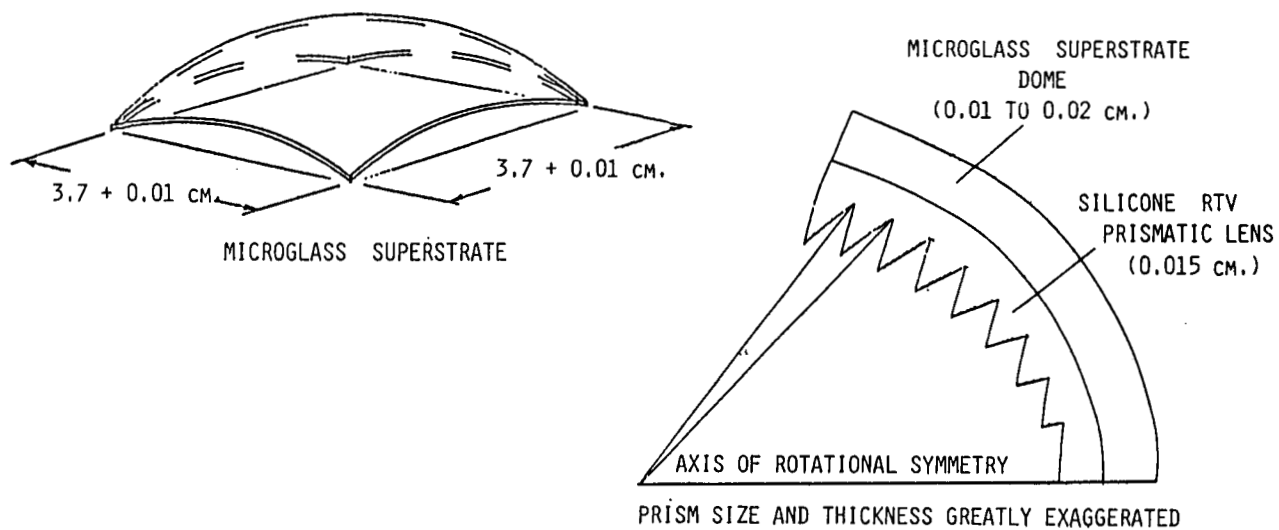


Figure 5 Current Domed Fresnel Lens Development

25%-Efficient GaAs Cassegrainian Concentrator Cell

H. C. Hamaker, M. Grouner, N. R. Kaminar, M. S. Kuryla, M. J. Ladle,
D. D. Liu, H. F. MacMillan, L. D. Partain, G. F. Virshup and J. G. Werthen

*Varian Research Center
Palo Alto, California 94303*

J. M. Gee
*Sandia National Laboratories
Albuquerque, New Mexico 87185*

Very high-efficiency GaAs Cassegrainian solar cells have been fabricated in both the *n-p* and *p-n* configurations. The *n-p* configuration exhibits the highest efficiency at concentration, the best cells having an efficiency η of 24.5% (100X, AM0, temperature $T = 28^\circ\text{C}$). Although the cells are designed for operation at this concentration, peak efficiency is observed near 300 suns ($\eta = 25.1\%$). To our knowledge, this is the highest reported solar cell efficiency for space applications. The improvement in efficiency over that reported at the previous SPRAT conference is attributed primarily to lower series resistance and improved grid-line plating procedures. Using previously measured temperature coefficients, we estimate that the *n-p* GaAs cells should deliver approximately 22.5% efficiency at the operating conditions of 100 suns and $T = 80^\circ\text{C}$. This performance exceeds the NASA program goal of 22% for the Cassegrainian cell. One hundred Cassegrainian cells have been sent to NASA as deliverables, sixty-eight in the *n-p* configuration and thirty-two in the *p-n* configuration.

Introduction

Solar energy systems using GaAs cells in concentrator arrays offer the potential for very high conversion efficiency along with low array costs. Several concepts for light-weight, radiation-resistant space concentrators have been proposed, such as the point-focus miniature Cassegrainian array [ref. 1] and the parabolic trough design [ref. 2]. The advantages of higher cell efficiency and reduced array costs in a concentrator system are balanced against optical losses of the reflecting mirrors and the need for greater accuracy in aiming the arrays at the sun. Since the cell comprises such a small fraction of the weight and area of the array, the most important of the cell parameters — cost, weight, *etc.* — is the conversion efficiency η . GaAs devices have a greater potential for this application than their Si counterparts due to their more optimal band gap, superior radiation resistance and lower temperature coefficient. The last factor enables the GaAs cells to operate efficiently at moderate to extreme solar concentrations, for which the operating temperatures T of the solar cells are higher than observed in flat-plate systems. In this paper, we report on improved performance of Varian's $\text{Al}_x\text{Ga}_{1-x}\text{As}/\text{GaAs}$ heteroface solar concentrator cells grown by metalorganic chemical vapor deposition (MOCVD) for use in Cassegrainian arrays.

Cell Design and Fabrication

The structure of the concentrator cells described in this paper is very similar to that reported at the previous SPRAT conference [ref. 3]. The design conditions for the Cassegrainian cells were

defined to be 100 suns, AM0 at $T = 80^\circ\text{C}$, with a circularly illuminated area of 0.126 cm^2 (4-mm diameter) on a $5 \times 5\text{ mm}^2$ die. As before, the cells were designed with the aid of a computer model simulating the performance of $\text{Al}_x\text{Ga}_{1-x}\text{As}/\text{GaAs}$ heteroface solar cells [ref. 4]. The structure of a typical p - n cell is shown in Fig. 1. In addition to the emitter and base, the devices include a highly doped buffer layer to minimize surface recombination effects at the back of the base and to provide a smooth surface upon which the overlying structure is grown. The $\text{Al}_{0.9}\text{Ga}_{0.1}\text{As}$ window layer passivates the front surface of the emitter and, in combination with the single-layer antireflection (AR) coating, minimizes the reflectance. Finally, the GaAs cap layer enables excellent ohmic contact by the top grid pattern while simultaneously minimizing the possibility of the grid metallization diffusing into the p - n (or n - p) junction during processing. The cap layer is selectively etched away between the grid lines prior to the application of the AR coating. For n - p cells, the emitter thickness is approximately $0.2\text{ }\mu\text{m}$.

The multilayer structure was grown in a horizontal rf-heated MOCVD reactor at 730°C , as described in Reference 5. Growth rates were $0.1\text{ }\mu\text{m}/\text{min}$, and zinc and selenium were used as the p - and n -type dopants, respectively. Conventional photolithographic techniques were used to lay down the top grid pattern. Metallizations, which were deposited by evaporation, were Pd/Au and Au/Ge/Ni/Au for p - and n -type GaAs ohmic contacts, respectively. The SiO_xN_y AR coating was deposited by plasma deposition at 300°C .

To raise the cell conversion efficiency, improvements were sought in the grid-line quality and the series resistance R_s of the cell. To accomplish the first task, a superior technique for electroplating the front grid metallization was developed. This procedure, which uses thick photoresist as a plating mask, significantly reduced the mushrooming effects associated with plating. Since the Cassegrainian mask requires numerous narrow grid lines ($\sim 3\text{ }\mu\text{m}$ wide) for optimal efficiency, the reduction in the amount of mushrooming greatly lowered the obscuration and raised the spectral response.

The series resistance problem is a more difficult matter, however. The primary factors contributing to R_s are the contact resistance R_c , the sheet resistance R_{\square} , and the grid-line resistance R_g . With the good ohmic contact afforded by the highly doped GaAs cap layer, R_c does not significantly influence η , even for concentrations ≥ 1000 suns. Any improvement in R_s , therefore, must come from lowering either R_{\square} or R_g . Recently, we have attempted to lower the value of R_{\square} by reexamining the effects of the doping level in the emitter. Using the original material parameters included in the computer model, the calculated value for the optimal doping level in the emitter N_E was approximately $1 \times 10^{18}\text{ cm}^{-3}$ in both the p - n and n - p configurations. This value resulted from the conflicting objectives of maximizing the diffusion length L in the emitter for high quantum efficiency (low doping condition) and lowering R_{\square} (high doping). Recent data [ref. 6] for L in GaAs indicate that the values originally used in the computer model [ref. 4] were unduly pessimistic. As a result, the optimum value for N_E is higher than the computer model predicted, since satisfactory quantum yield may be attained at higher doping levels. Consequently, in the cells presented here, we have empirically increased the value for N_E in both the p - n and n - p configurations until the optimal value was obtained.

Testing

One-sun efficiencies were determined using Spectrolab XT-10 simulators both at Varian and Sandia National Laboratories. For AM0 measurements, the simulator intensity was set using balloon-flight-calibrated GaAs solar cells which had similar spectral responses to the appropriate concentrator

cells. A xenon-lamp flash tester was used to determine device performance under concentration. The incident power upon the cell in the flash tester was determined by assuming that the short-circuit current I_{sc} was linearly dependent upon the solar concentration. The exposed sawing streets at the edges of the cell were masked off from any light to assure the accuracy of the measurements. Efficiency calculations were based on the total illuminated area, and no correction was made for obscuration.

Results and Discussion

Figure 2 plots the external quantum yield of an n - p spectral response sample, in which the grid obscuration has been eliminated. In this case, $N_E = 2 \times 10^{18} \text{ cm}^{-3}$, and at this doping level, the sheet resistance of the emitter is not a significant factor in limiting cell performance, *i.e.*, the power loss associated with R_{\square} is much smaller than that associated with R_g . It is readily apparent that in spite of the increased doping level in the emitter, the cell still has excellent quantum efficiency. Nearly unity quantum yield is observed at the center of the spectrum, and most of the losses in the red and blue are due to a less-than-optimal AR coating on this particular sample. This demonstrates that the material quality is sufficiently high that low series resistance and high values for I_{sc} are not mutually exclusive. For p - n cells, $2 \times 10^{18} \text{ cm}^{-3}$ also appears to be the optimal value for N_E . Due to the lower mobility of the holes in this structure, R_{\square} is not negligible. At the solar concentrations relevant to the Cassegrainian module, however, the series resistance problem is not serious, as will be shown below.

Figure 3 shows the current-voltage (I - V) characteristics of an n - p Cassegrainian cell at a solar concentration of 333 suns and $T = 28^\circ\text{C}$. Although the cell is intended for use at 100 suns, the efficiency remains very high ($\eta = 25.1\%$). The open-circuit voltage $V_{oc} = 1.18 \text{ V}$, and the current density J_{sc} corresponds to $33.6 \text{ mA/cm}^2/\text{sun}$. The high value for the fill factor ($\text{FF} = 0.862$) indicates that series resistance is not a significant parameter limiting cell performance. Curve fitting of the I - V data yields an estimate of $R_s \sim 3 \text{ m}\Omega$. Figures 4–6 plot the dependence upon concentration of η , V_{oc} and FF, respectively. The efficiency peaks near 300 suns with a value of 25.1%; at 100 suns, $\eta = 24.5\%$. The drop in efficiency above ~ 400 suns results from the increasing importance of losses due to series resistance, as indicated by the decreasing fill factor. The p - n cells show slightly lower efficiencies, primarily due to lower values of I_{sc} . The advantages of the n - p configuration may be attributed to tenfold higher values of mobility for electrons *vs* holes in GaAs. By making electrons the majority carrier in the emitter, lower sheet resistance R_{\square} may be obtained without the disadvantages of either overdoping or thickening the emitter. The lower value of R_{\square} leads directly to the generally higher values for FF in the n - p case. The higher values for I_{sc} are the result of the thinner emitter coupled with the long diffusion length in the p -type base.

Comparing these results with those which were presented at the previous SPRAT conference [ref. 3], it is plain that the improvements in the plating procedures and sheet resistance have significantly improved cell performance. The more recent cells exhibit better values for I_{sc} (33.6 *vs* 32.4 mA/cm^2), presumably due to the reduced obscuration due to mushrooming. The series resistance is also less of a problem, as indicated by the increase in the concentration for which the efficiency peak is observed (300 *vs* 180 suns). Even higher efficiencies may be attained by lowering R_g , since this is the only remaining source of significant series resistance. This may be accomplished by widening and thickening the grid lines or lowering the resistivity of the grid-line metallization. Since increasing the grid-line width decreases I_{sc} , improvements must come from the latter two

factors. At this time, we are developing an improved metallization process to address this minor problem.

Although we have not yet measured the temperature behavior of the cell examined in Figs. 3-6, we can use the previously determined value for the temperature coefficient [ref. 3] ($-0.036\%/^{\circ}\text{C}$ for a 23.4%-efficient cell at $T = 28^{\circ}\text{C}$ and 90 suns) to estimate the performance of the cell under the intended operating conditions of 100 suns and $T = 80^{\circ}\text{C}$. Such an estimate predicts that the most recent cell would be 22.5%-efficient under these conditions, which exceeds the NASA-program goal of 22%. The program also calls for the delivery of 100 Cassegrainian cells to NASA, so we have delivered sixty-eight n - p cells and thirty-two p - n cells.

Summary

Cassegrainian cells with a conversion efficiency near 25% have been fabricated in both the n - p and p - n configuration. To our knowledge, this is the highest reported cell efficiency for space applications. The improved performance is the result of new grid-line plating procedures and lower series resistance associated with higher doping in the emitter. Under the probable operating conditions of 100 suns and $T = 80^{\circ}\text{C}$, the estimated efficiency is 22.5%. To meet program goals, we have delivered sixty-eight n - p cells and thirty-two p - n cells to NASA.

References

- [1] R. E. Patterson, H. S. Rauschenbach and M. D. Cannady, *Conference Record of the 16th IEEE Photovoltaic Specialists Conference*, IEEE, New York, 1982, p. 39.
- [2] T. G. Stern and E. W. Hayes, *Conference Record of the 17th IEEE Photovoltaic Specialists Conference*, IEEE, New York, 1984, p. 326.
- [3] J. G. Werthen, G. F. Virshup, H. F. MacMillan, C. W. Ford and H. C. Hamaker, *Space Photovoltaic Research and Technology 1986*, NASA Conference Publication 2475, 1986, p. 25.
- [4] H. C. Hamaker, *J. Appl. Phys.* **58**, 2344, 1985.
- [5] C. R. Lewis, W. T. Dietze and M. J. Ludowise, *J. Electron. Mater.* **12**, 507, 1983.
- [6] R. K. Ahrenkiel, D. J. Dunlavy, D. Greenberg, J. Schlupmann, H. C. Hamaker and H. F. MacMillan, *Appl. Phys. Lett.* **51**, 776, 1987.

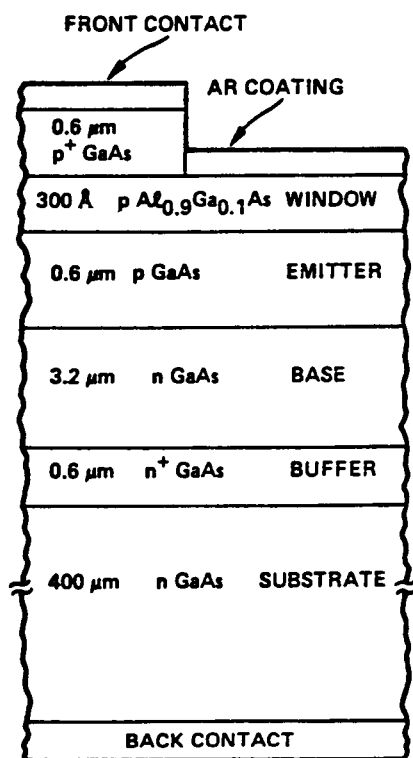


Fig. 1. Schematic structure of a typical p - n GaAs concentrator cell.

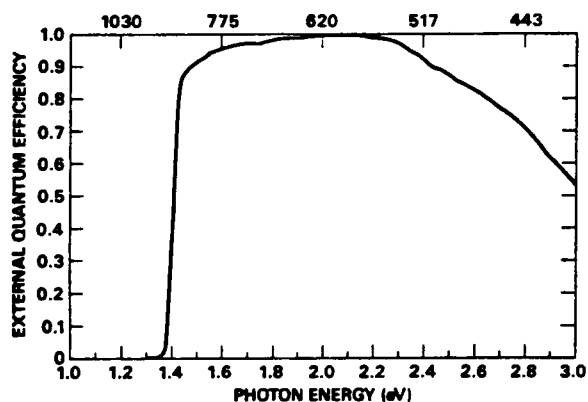


Fig. 2. External quantum efficiency *vs* photon energy for an n - p GaAs spectral response sample. The scale on the top axis shows the wavelength in nm.

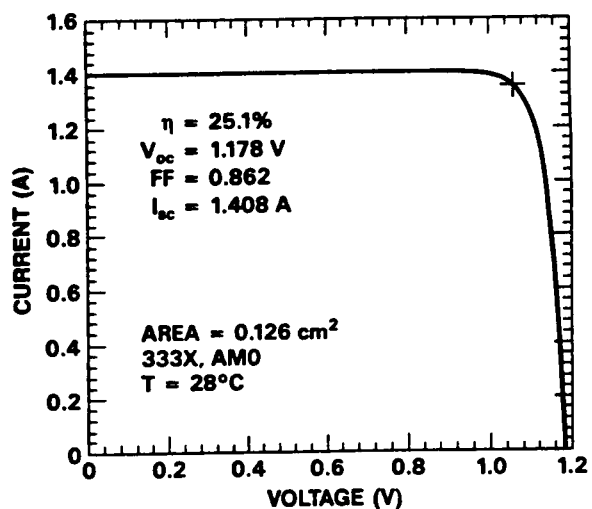


Fig. 3. Current *vs* voltage for an n - p GaAs Cassegrainian cell under a simulated 333 \times , AM0 spectrum. The cross indicates the maximum power point.

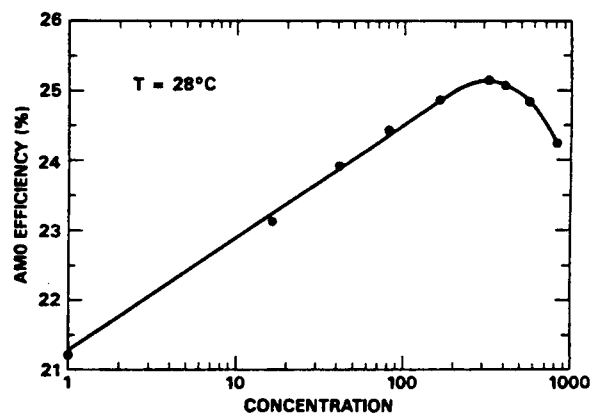


Fig. 4. AM0 efficiency *vs* solar concentration for the n - p GaAs cell shown in Fig. 3.

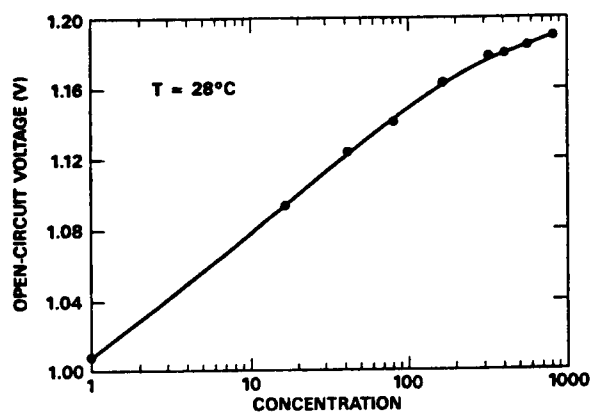


Fig. 5. Open-circuit voltage *vs* solar concentration for the *n-p* GaAs cell shown in Fig. 3.

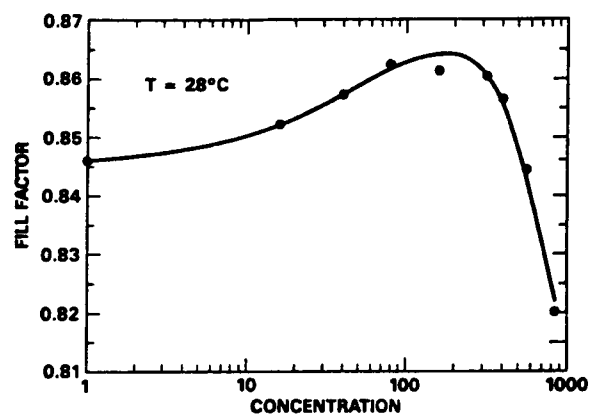


Fig. 6. Fill factor *vs* solar concentration for the *n-p* GaAs cell shown in Fig. 3.

Session 6
Environmental Effects and Measurements

PRECEDING PAGE BLANK NOT FILMED

Contamination Effects of GPS Navstar Solar Array Performance

Dean C. Marvin and Warren C. Hwang
The Aerospace Corporation
Los Angeles, CA 90009

Summary

The solar arrays on Navstars 1-6 have been limiting the electrical power capabilities in the extended life (beyond the 5 year design life). The departure from predicted performance consists of an extra 2.5% per year degradation beyond the radiation model estimates. This degradation is unusual in showing a linear rather than exponential decay with time. The performance of the arrays on these satellites has been examined in order to predict future behavior and to make refined projections on the Navstar 7-11 solar arrays. Evidence obtained from flight experiments on Navstar 5 and 6, and from laboratory experiments, suggests that contamination of the solar arrays while on orbit may be responsible. In this paper the evidence for photo-induced contamination of spacecraft surfaces is presented, and the effect on solar array output in the case of the GPS satellites is shown to be consistent with the observed anomalies.

Background

The Block I Navstar satellites have a design life of 5 years, and utilize silicon solar cells which are essentially the K4 1/2 type. For several of these satellites there is now 9 years of flight data, from which the solar panel output may be estimated. These data contrast sharply with the predicted output calculated from radiation models. In particular the degradation is more rapid than expected and is nearly linear with time rather than exponential. The data from five spacecraft are plotted in Figure 1 along with the predicted degradation. All of the spacecraft in this group show the same trend, with power losses of 23% and 37% at 5 and 10 years, respectively. The predicted losses are 18% and 21% for these same times. A discrepancy of this magnitude has strong implications for the end of life of the spacecraft and subsequent generations of satellites of similar design.

Approach to the Problem

Initial attempts to explain the flight data included consideration of several scenarios. One of these was the possibility that the radiation environment used to predict performance was inadequate. The GPS orbit is half-synchronous and no published data are available for solar cell performance on other vehicles in this orbit. The JPL Solar Cell Radiation Handbook [ref. 1] shows that for cells of this type, the radiation fluence would have to be in error by more than an order of magnitude to account for the observed degradation at the 10 year point. Therefore the knowledge of the environment was assumed to be accurate. The possibility was also considered that the solar cells

were substandard. However, the cells used on these vehicles were manufactured by several vendors over a 5 year period, and it is highly improbable that they would all be flawed in the same way.

The possibility of physical damage to the cells was also considered. Micrometeoroid impacts on the coverglasses could roughen the surface and lead to a small reduction in short circuit current, but not a reduction of the observed magnitude. Actual mechanical failures such as interconnect detachments or cell breakage were also considered, however these would have led to abrupt changes in power output rather than the smooth decrease which was observed. Also it would be unlikely that all 5 spacecraft in this study would be affected in the identical fashion that has been observed.

Attention was then turned to the possibility that the solar cells themselves were not degrading, but that less light was reaching them. Recent work [ref. 2] on photo-enhanced contamination of spacecraft thermal control surfaces was examined. Observation of thermal radiator properties on a number of spacecraft (DSCS, FLTSATCOM, INTELSAT, DSP, SCATHA) had shown that contamination of these surfaces occurs over time. This contamination leads to increases in the solar absorptance, which in turn results in higher radiator temperatures. Figure 2 shows the increase with time on orbit of the radiator solar absorptance for a variety of spacecraft, as inferred from observed temperature increase [ref. 2]. The absorptance is defined as

$$\Delta\alpha = (I_0 - I_r)/I_0 - \alpha_0$$

where I_0 is the incident solar intensity, I_r is the reflected intensity, and α_0 is the absorptance of the radiator in the absence of any contaminant film. The curve labeled GPS Navstar refers to data taken from a second surface mirror mounted on the solar array of Navstar 5. This sensor was therefore exposed to the same environment as the solar panels.

Two curves from the DSP program provide direct evidence that contamination emanating from the spacecraft body is redepositing on the thermal control surfaces. The "DSP AVG" data are averages over several early vehicles, on which the sensitive surfaces had a direct field of view of spacecraft body vents. DSP "FLT-10" is a later vehicle in which the vents were relocated to eliminate the field of view. The improvement is obvious, and lends support to the contamination scenario.

Additional flight and laboratory experiments [refs. 2,3] have determined that the contamination of thermal control surfaces is a photo-assisted deposition process. The essence of the process is that organic films which condense on, and evaporate from surfaces become polymerized on UV exposed surfaces and cannot re-evaporate. Under illuminated conditions the temperature of the surface becomes relatively unimportant (up to at least 60°C), as demonstrated by a SCATHA flight experiment which utilized a temperature controlled quartz crystal microbalance. This experiment also showed that the net contaminant deposition rate is approximately an order of magnitude higher on a sunlit surface than on a dark one. Polymerized films produced by this process on fused silica second surface mirrors and silverized teflon have been characterized [ref. 3]. In particular the wavelength dependence of the film absorption coefficient $\epsilon(\lambda)$ has been estimated from 3 sets of data, and using this information and the measured $\Delta\alpha$ for Navstar 5, the expected degradation of solar array output power can be computed.

Contaminated Solar Array Calculation

The procedure for calculating the loss in solar array power is straightforward once the necessary input data is available. The measured value of $\Delta\alpha$ vs. time from Figure 2 is combined with the estimated $\Delta\alpha$ per unit film thickness from reference 3, equation 8 to obtain the film deposition rate. The wavelength dependent absorption of this film is convolved with the spectral response characteristic of the silicon solar cell and the AM0 solar spectrum to estimate the power loss as a function of time.

From the Navstar 5 calorimeter flight experiment, the measured $\Delta\alpha$ is 0.06/year. The dependence of $\Delta\alpha$ on film thickness is obtained from equation 8 of reference 3 as $\Delta\alpha = 0.0034/100 \text{ \AA}$. Combining these parameters gives a deposition rate $L(t) = 0.176 \text{ }\mu\text{m/year}$. The spectral absorption $\epsilon(\lambda)$ for contaminant films on silica surfaces was obtained from reference 3. The spectral response of the silicon solar cells $S(\lambda)$ is taken from Figure 4.7 of reference 4. The degradation factor for output current of the solar cell is thus

$$F(t) = \int \exp(-\epsilon(\lambda) L(t)) S(\lambda) I_0(\lambda) d\lambda / \int S(\lambda) I_0(\lambda) d\lambda$$

where $I_0(\lambda)$ is the AM0 solar spectrum.

Figure 3 shows the power system output for Navstar 4 (squares), the original radiation induced degradation predictions (solid line) and a new prediction based on the product of this original model and the $F(t)$ term just evaluated. Although the uncertainty in the contamination contribution is substantial, the shape of the flight data curve is well represented by the combined effects, and the magnitude of the total degradation is much closer to that actually observed on the five Block I vehicles.

Conclusion

Evidence for the effects of contaminant films on spacecraft radiator surfaces have been applied in a study of anomalous solar array degradation on the GPS Navstar satellites. Data from flight experiments on Navstar 5 have been used to demonstrate that this degradation is consistent with photo induced contaminant deposition on the solar array surface.

References

- [1] *JPL Solar Cell Radiation Handbook*, publication 82-69.
- [2] D. F. Hall and T. S. Stewart, AIAA-85-0953.
- [3] D. F. Hall, *Intl. Symposium on Spacecraft Materials in Space Environment*, ESA SP-178, June 1982, Toulouse, France.
- [4] Fahrenbruch and Bube, "Fundamentals of Solar Cells", Academic Press, 1983.

NAVSTAR 1-6 Solar Array Output (Lower Bound)

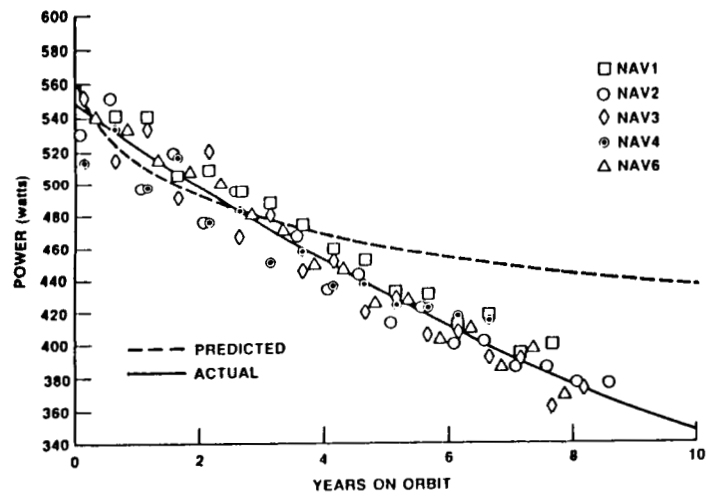


Figure 1

Thermal Control Surface Degradation

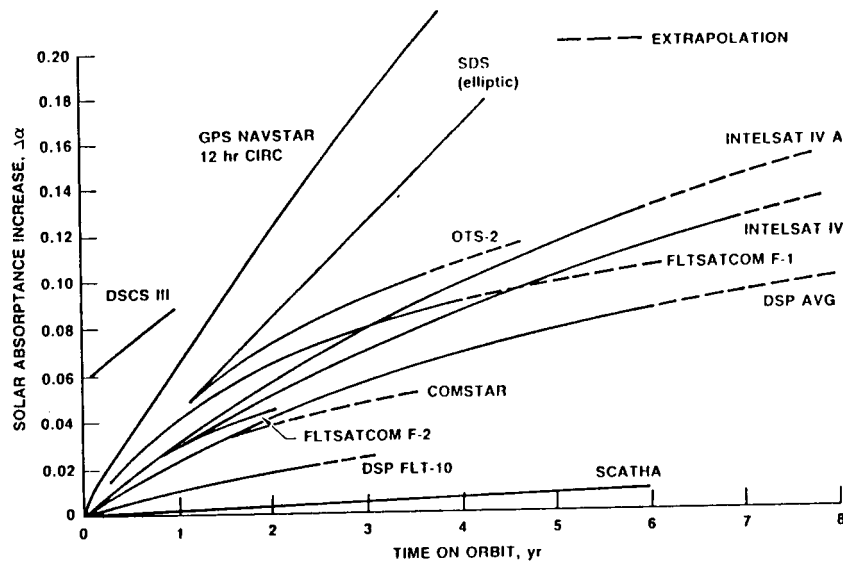


Figure 2

NAVSTAR 4 Power Output

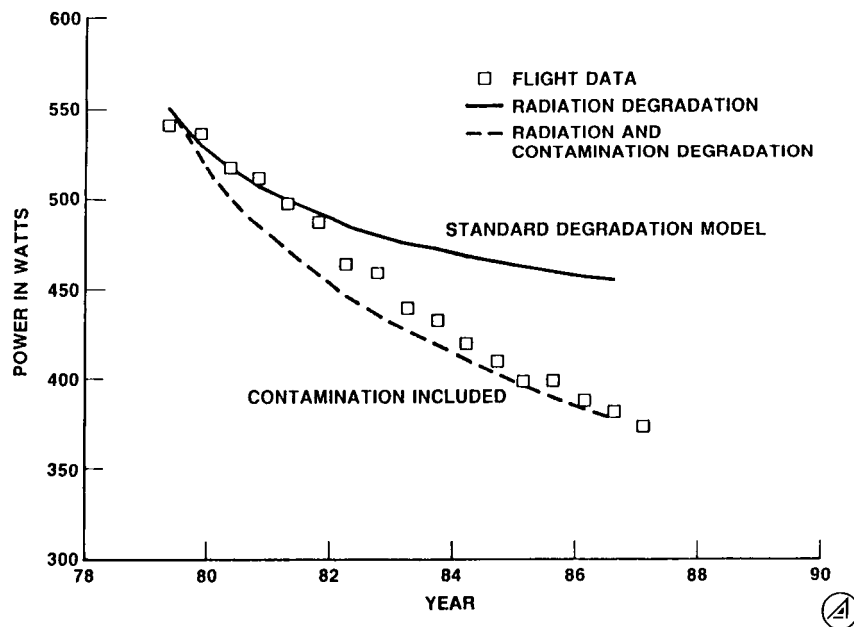


Figure 3

The Experiments of LIPS III

J. G. Severns, R. M. Hobbs, N. P. Elliott and R. H. Towsley
Naval Research Laboratory
Washington, D. C. 20375

G. F. Virshup
VARIAN Associates
Palo Alto, California

LIPS III is a member of the "Living Plume Shield" series of spacecraft. In each LIPS project the plume shield, a simple sheet metal cone, was structurally stiffened, and an active satellite was then built around it. The original purpose of the plume shield was to prevent the plume from solid propellant engines, which are fired outside the atmosphere after the aerodynamic shroud is jettisoned, from reaching the primary payload. The surface of LIPS III facing the plume also functioned in this manner, but the anterior surfaces were unaffected, and it was there that all solar arrays, sensors, and experiments were mounted.

The purpose of LIPS III was to provide a test bed for new space power sources. With the long delays projected for schedules of the STS and other major launch systems, it appeared that a decade might pass before long term flight data could be obtained on many new and innovative power sources. The fact that a launch scheduled for early in 1987 required a plume shield was seen as a unique opportunity to obtain some of this data in a timely manner. The paragraphs below will describe the LIPS III system, the experiments placed aboard, and the experiment data acquisition subsystem. Various problems were encountered during integration and after launch; those which appear to effect the accuracy of experimental results will be discussed. The paper will conclude with a preliminary description of the accuracy of the flight experiment data.

The LIPS III System

LIPS III was injected into a nearly circular orbit of 1100 kilometer altitude with inclination slightly in excess of 60° late in the spring of 1987. The planned mission life of LIPS III is 3 years, with hopes of attaining 5 years. As shown in Figure 1, the structure is very shallow, with an outside diameter of 74 inches and a height of only 4 inches. The paddles shown were folded over the annular spacecraft body during launch and subsequently deployed as shown. The spacecraft is spin stabilized with the spin axis pointed toward the sun so that all experiments receive constant illumination. The concentrator experiments on LIPS require both accurate alignment to the sun and the means to optimally radiate waste heat to space. To meet the sun pointing requirement the error between the spin vector and the sun vector was limited to $\pm 0.5^\circ$. These sun pointing needs also required careful alignment of the paddles, on which the concentrators were mounted, so that in their deployed configuration they would remain perpendicular to the spin vector. The waste heat rejection requirement was met by mounting the concentrator experiments over holes cut in the paddles for this purpose, allowing a clear view of space for radiation from the back (nonilluminated) surfaces. The shallowness of the LIPS structure was a distinct advantage here, since it eliminated any radiative interaction between the spacecraft body and the concentrator waste heat radiators.

The spacecraft EPS is powered by five silicon solar panels generating 25 watts (BOL). This solar array drives an unregulated bus operating at $14.5\text{v} \pm 2\text{v}$ with a 6 A-H NiCd battery for storage. The telemetry system encodes an analog voltage of 0.0 - 5.1 volts into an 8-bit word. This data is transmitted via an L band downlink at a rate of 2441 bits/second, and includes both housekeeping information and experimental data. The telemetry frame rate, the time required for every quantity in the telemetry list to be sampled once, is 0.2228 seconds. No provision was made for on-board data storage, so data can only be obtained in real time when the spacecraft is in view of a tracking station.

The thermal control system is an all passive design, with multilayer thermal blankets covering most of the satellite surface. The paddles were not blanketed, but were coated with silver-teflon tape. The blanket on the non-illuminated side of LIPS provided freedom for thermal properties of the outer blanket surface to change markedly during impingement of the plume without affecting subsequent thermal performance. A number of experiments were mounted on standoffs over the blanket on the illuminated (clean) body surface, thus limiting their ability to radiate thermally from their back surfaces. For this reason, many of the body mounted panels are operating at higher temperatures in sunlight ($80^\circ - 100^\circ\text{C}$), compared to those on the paddles which operate at lower temperatures ; i.e., $20^\circ - 50^\circ\text{C}$.

The operation of the attitude control system (ACS) will now be sketched. For a detailed survey of the design and operation of the ACS, see Ref. 1. This system was designed to operate in two modes. At orbit injection, the spacecraft was expected to be spinning at 30 RPM with its spin vector pointed 120° from the sun vector. A hydrazine thruster was designed to be pulsed each time the spacecraft rotation put it in the appropriate position to reduce the angle between sun and spin vectors. The pulse timing is determined from a wide angle sun sensor with a "fan shaped" field of view ($\text{FOV} = 4^\circ \times 180^\circ$). This sun sensor was mounted on the outer edge of the spacecraft with the plane of the "fan" containing the spin axis. As LIPS rotates the fan sweeps across the entire celestial sphere and when the sun crosses the field of view, the angle between the spin and sun vectors is measured. From the time between consecutive measurements, the next hydrazine pulse time is calculated. Once the spin vector was brought within five degrees or less of the sun, the second mode of operation began which relies on a magnetic interaction to control attitude. A solenoid [ref. 2] was mounted in the spacecraft so that when a pulse of current flowed through its windings the resultant dipole moment was perpendicular to the spin axis. This dipole couples to the earth's magnetic field to generate a torque on the spacecraft which will change the spin rate if the torque is parallel to the spin vector, or change the spin vector direction if the torque and spin vector are perpendicular. Thus, depending upon the instantaneous direction of the earth's field, either spin rate or direction (or both) can be changed, and thus controlled. To implement this magnetic control system, a three axis fluxgate magnetometer and a fine angle sun sensor were placed aboard the spacecraft. The design ensured that measurements of the earth's magnetic field are accepted from the magnetometer only when the solenoid is not energized. The fine angle sun sensor has a useful field of view of 5° with a resolution 0.05° . Since this magnetic control system is currently operating with errors $\leq 0.1^\circ$, we plan to rely on this mode of operation for the remainder of the mission.

The Experiments

With the exception of a study of material properties of selected thin films submitted by Martin Marietta Company, all of the experiments aboard LIPS III were photovoltaic in nature. It is unfortunate that the small size of the spacecraft and very tight schedule precluded integration of

other types of energy conversion experiments, such as solar dynamic systems. As can be seen from Table 1, experiments were submitted by 18 laboratories involving cells of silicon (both crystalline and amorphous), GaAs, AlGaAs, InGaAs, and CuInSe₂. One of the primary goals of the LIPS III effort was to realistically test photovoltaic concentrators in space; there are three concentrator concepts represented on LIPS III. In all, 140 separate I-V characteristics are measured. These span short circuit current values of 1.2×10^{-3} amps up to 2.0 amps, with open circuit voltages varying from 0.35 volts to 6.0 volts. Temperatures are sensed by measuring the resistance of a sensor, and including resistance values of the non-photovoltaic thin film experiment from the Martin Company, resistances from 40 ohms to 24 megohms are measured. These experiments are housed on some 30 panels or fixtures, nearly all manufactured by the experimenters and integrated by NRL.

It should be pointed out that the LIPS experimenters met an extremely tight schedule, building and testing their experiments in a time so short that many had no chance to obtain official support for their efforts from their respective managers before starting work. Integration meetings were usually held by telephone and telecopier. Throughout this hectic time, high standards of workmanship were adhered to as evidenced by the almost complete success (to date) of the experiments.

Data Acquisition Plan

Provision was made for measuring the current-voltage (I-V) characteristics of each experiment both in sunlight, and the forward characteristic in darkness for those experimenters requesting it. A four terminal measurement was planned so that only very small currents would flow in the pair of wires monitoring voltage. Due to the large number of experiments, the grounding scheme became quite complex, so that one half of the experiment current is inadvertently permitted to flow in the voltage ground lead. Since this is a short (length ≤ 2 ft.) AWG#22 wire, the resulting underestimation of cell voltage was deemed unimportant. A given I-V curve is measured by varying a dynamic load through 24 points, measuring current and voltage values of each point. One value each of voltage, current, and temperature sensor resistance are measured simultaneously during each telemetry frame. The illuminated measurements were made in the following way:

- a. First, the open circuit voltage of the cell is measured and the value is stored.
- b. Next, the short circuit current is measured by driving the dynamic load to zero. The cell is slightly back biased to compensate for line losses between the cell and dynamic load.
- c. Once I_{sc} is measured, values of voltage are selected at which the current is to be measured. The voltage points were planned to form an ascending array of values which steps out across the I-V curve from short circuit to open circuit. The target voltages are chosen in the following way: V_{oc} is divided into three parts, as shown in Figure 3, corresponding to three regions of the I-V curve; region one runs from 0.0 volts to $0.4 V_{oc}$, and corresponds to the low voltage region of approximate constant current operation. Region two runs from $0.4 V_{oc}$ to $0.65 V_{oc}$, well into the "knee" of the curve. The third region, running from $0.65 V_{oc}$ to V_{oc} , represents the region of rapidly falling current as the open circuit condition is approached. Region I is divided into four equal segments, region II into five equal segments, and region III into fourteen. The ends of these segments are the voltage values targeted for measurement. After each desired voltage value is calculated, the dynamic load is varied until the experiment operating voltage is equal to the calculated value. To improve resolution of the voltage measurement, two possible gain settings are provided, and the most appropriate setting is automatically selected for each measurement.

d. With the voltage value set, the current is measured. Since the experiment currents span such a wide range, there are seven possible gain settings for current measurement. An autorange circuit selects the gain giving the best resolution, and this gain setting with the analog values of current, voltage, and voltage gain are then available for telemetry.

e. The resistance of the appropriate temperature sensor is measured for every current-voltage point. This much temperature data is overkill, but it was quite inconvenient to do this any other way. In this way, 24 points (including I_{sc}) are measured for each I-V curve, the last point being V_{oc} , according to plan at least. Actual operation in orbit will be described in the next section.

The dark forward I-V characteristic is measured in a very similar way, except that the maximum voltage was chosen by the experimenter and stored in a ROM on the spacecraft. The 24 points are evenly spaced between $V=0$ and V_{max} .

There are three data channels each of which make the above measurements independently. These can each be turned on or off by ground command. Each channel has a compliment of up to 64 experiments through which it steps and a counter to indicate which experiment is being measured at any given time. Unfortunately, the values of these three counters were not included in the telemetry list. A master counter is included however, which can indicate the current status of each multiplexer. When this master counter runs through its complete sequence, it resets and issues a reset pulse that forces all of the data channel counters to reset, so thereafter, they are all in sync with the master counter. This causes some operational complexity since when a data channel is commanded on, the master counter must then be reset before any of the data is meaningful. As discussed in the next section, considerably more serious problems result from unreliable master counter readings.

Problems Encountered With LIPS III

Several problems effecting the collection of experimental data appeared during final integration and after launch. Some of the more serious difficulties which have not yet been completely resolved will be discussed below:

a. Dust Buildup: During final integration LIPS was mechanically attached to the primary payload with the axis of symmetry vertical, LIPS on the bottom, and the body mounted experiments looking upward. This configuration was maintained throughout transport to the launch site, mating with the launch vehicle, and subsequent launch. Now after complete assembly at the launch pad, the finished vehicle waited for a number of weeks before launch, and during this time a robust stream of cooled and filtered air flowed down over the primary payload and LIPS. LIPS was below a very complex spacecraft structure so that gravity, assisted by the air flow, would bring any loose particles to the LIPS surface on which experiments were mounted. A considerable buildup of dust was observed on this surface shortly before launch, but a comprehensive cleaning would have required removal of the aerodynamic shroud, causing an intolerable launch delay. Samples of the dust were collected through a small access door and studied. The particle size varied widely from a few up to several hundred micrometers, and because of this wide variation, obtaining reliable particle counts was complicated. The samples were studied under a low power microscope producing counts of particles 10 micrometers and up. Densities of these larger particles were between $5/cm^2$ and $100/cm^2$. Among the debris there were bits of thread, particles of a red substance resembling RTV, and a few metallic appearing species which might have been chips of solder. The difficulty of sample collection precludes making a meaningful quantitative estimate of density, but observers reported

that the dust layer appeared thick enough to allow "writing a name in it with one's forefinger." The effects of this dust coverage might well be partially mitigated by several factors. First, the paddles were folded during accumulation so that dust would have collected on the paddle surface not illuminated after deployment. During launch, the entire spacecraft is subjected to vibration. After the aerodynamic shroud is jettisoned, the entire assembly is spinning at approximately 30 RPM when the third propulsion stage is fired. After separation, the paddles are deployed producing a mild shock, once again while the spacecraft is spinning. Since the dust did not appear oily and was seen to brush off easily in the small areas available through the access doors, it is hoped that centrifugal force, in conjunction with vibration, removed many of the particles. Those experiments which were mounted on the LIPS body (instead of one of the paddles), and which were not covered by a paddle in the folded, pre-launch position are the most likely to be affected by the dust. Some of these experiments do show low short circuit currents which might be attributed to this problem. However, several other experiments mounted in this way show no adverse effects.

b. Voltage Offset Problem: Twenty-four hours before final integration of the LIPS spacecraft with the primary payload, it was discovered that voltages as reported by telemetry occasionally varied by up to 10%, as if a very low frequency signal of unknown origin was present. This effect was unmistakable during a test of experiments with all three data channels turned on simultaneously. The data taken during this test was essentially gibberish. This effect is greatly reduced when only one data channel is turned on, so it is in that mode that experimental data has been gathered ever since. The effect can be seen from Figure 4 where bus voltage (which is equal to solar array voltage) is plotted with solar array current. It is seen that both the current and the voltage fall simultaneously, which cannot happen for a photovoltaic device. At the same time, temperatures of large components such as the battery vary with identical time dependence. All this could be explained if a ground potential were varying, but considerable analysis has not produced a plausible explanation for such a variation.

Though the effect on housekeeping data can be severe, it is most fortunate that the effect on the quality of experimental data is small or zero when only one data channel is on. The measurement of small resistance values does seem to be effected occasionally, but overall the values returned for currents and voltages do not seem to drift when the effect is evident in housekeeping data. Recall, however, that only a small amount of flight data has been studied to date.

c. Spacecraft Attitude Determination: A primary requirement was the collection of as much experimental data as possible during the first week after launch, especially in the first 24 hours, for the purpose of firmly establishing an initial operating point for each experiment. Now when the spacecraft first came in view of the tracking station shortly after launch, we expected to see an attitude error of about ten degrees and the ACS operating in mode 1 with the hydrazine thruster continuing to reduce that error. Instead, we observed a nutation of the spin vector in excess of twenty degrees which made the hydrazine thruster ineffective or occasionally detrimental in reducing the error. It required almost two weeks to solve this problem and achieve stable, high accuracy sun pointing of the spin vector. During the first week of operation considerable experimental data was gathered, but to sensibly reduce it, accurate knowledge of the rapidly varying spacecraft attitude was needed. Much effort has been expended to achieve this, without, as yet, producing suitable results. We have two sun sensors aboard, neither of which are useful for attitude determination with a large nutation angle. The small angle sun sensor saturates at approximately 5° , as shown in Figure 5. The wide angle sensor with the "fan" shaped field of view records the sun angle, but the time of that measurement is not known, and as the following paragraph shows, ignorance of the time of measurement makes this data nearly useless.

The solar array was designed to operate at voltages considerably less than that for maximum power at BOL. In fact, the array closely approximated a constant current source during the first week in orbit. With knowledge of the array temperature (which was measured and included in telemetry), variations of the current due to changes in sun angle can be isolated. In short, we have a crude sun angle sensor in the solar array, the current being proportional to the cosine of the desired error angle. The period of the LIPS spin rotation is denoted by T_{spin} in Figure 6, which shows solar array current as a function of time. The nutation of the spacecraft is obvious, and turns out to have a period almost exactly $1/2$ that of the spinning motion. The information from telemetry will determine that some time during T_{spin} a measurement of sun angle was made by the wide angle sensor, and it will report the value of that angle. It is clear from Figure 6 that the spacecraft motion is far too rapid for the wide angle sensor to be of use. It should be noted that no evidence of the voltage offset phenomenon was seen in the data of Figure 6. What is seen there is due only to the complexity of the LIPS motion. The solar array current itself could provide an estimate of the angle, except that this variable is susceptible to the voltage offset problem (see Figure 4). There are numerous statistical means for detecting a variation of this type, a number of which were tried. The difficulty in isolating (and hopefully algebraically removing) the offset signal results from the fact that we have only four data points per nutation period. This is close to the nyquist limit, making data recovery uncertain. The magnetic field measurement could be included with the solar array current to improve an estimate, but these measurements of the earth's field are themselves affected by the offset problem, though to a smaller degree than the solar array current. The combination of solar array and magnetic data still offer some hope of satisfactory attitude determination.

Taking a different approach, the data was searched for points during the spacecraft gyrations at which the fine angle sensor was not saturated. If these occurred often enough, they might well be used to recalibrate the solar array current to provide useful data. The fine angle sensor gives no indication when it is in saturation, however, as shown from the high angle "wings" in Figure 5. A telemetry voltage of, say, three volts could indicate an angle of -2° , or -10° or less. Upon discovery of this fact from study of the telemetered data, the effort to reduce experimental data from the first week of operation was postponed.

Several other problems have occurred but have been suitably resolved. The most worrisome of these was the occasional unreliability of the master telemetry counter. Recall that, after the experiment counters in the data channels are forced into synchronization with the master, it is the value of this master counter from which we infer the identity of the experiment currently being measured. If the master counter "jumps" rather than incrementing its count by one at each reading, identification of all subsequent data in that run can be confused. It is most fortunate that the types of errors experienced are not too numerous, so that a program can be written to test for all of them. This has been satisfactorily implemented without the loss of great amounts of data.

Preliminary Assessment of Data Quality

Approximately fifteen percent of the data gathered to this point has been analyzed, but already some generalizations can be made. First, the goal of measuring the entire I-V curve from short circuit to open circuit conditions was not achieved, since a measurement of V_{oc} is almost never made and I_{sc} is rarely obtained. It seems that the data acquisition system has stability problems when either the voltage or current of the cell operating point is driven to zero. Secondly, the accuracy of current and voltage measurements seem to be more accurate for those experiments with larger short circuit currents. Short circuit and open circuit conditions are also more nearly approached for the larger

current experiments. A method has been devised by G.F. Virshup [ref. 3] for estimating V_{oc} from the raw data. Recall that target voltage values for measurement were calculated from V_{oc} . By observing the differences between actual voltages measured and comparing them with the scheme described in Figure 3, the starting value of V_{oc} can be estimated. As pointed out in the next paragraph, caution should be exercised since the process of target voltage selection is often unstable. Shown in Figures 7-10 are results for the silicon witness cells of LIPS. These figures depict early flight data adjusted to 135.3 mw/cm^2 and 27°C compared to the results of preflight measurements made with an X-25 solar simulator before the experiments were integrated with the spacecraft. These figures show a fair representation of the data quality and its variation among experiments.

If the voltage offset problem were seriously affecting the current vs voltage data, it would be of much lower quality than what is shown here. The offset problem, along with other noise sources does appear to have a serious effect on the selection of target voltages at which current is to be measured. Recall from Figure 3 that the target voltages should have started at 0.0 and increased monotonically up to V_{oc} . The values actually selected by the data acquisition system are often out of order, and do not show the regular progression of values as planned. We believe, however, that once a voltage is selected, the resulting current measurement is not effected by this noisy environment, and that the values reported are of reasonably high quality.

The measurement of temperature is, unfortunately, not as accurate in some cases. First, the digital quantization noise is quite high for some experiments, and disastrously high for one, indicating a failure in integration of the experiment with LIPS. This effect can be seen in Figure 8, where there is a considerable difference in voltage between the flight and preflight data. A change of the least significant bit here amounts to a temperature difference of 15°C . Thus, our knowledge of that temperature is imprecise and the adjustment of flight data back to 27°C is inaccurate. This is the most likely reason for the voltage discrepancy in Figure 8. It also appears that the offset problem does occasionally effect the measurement of resistances, especially the small values. This is most pronounced whenever the current or the voltage that is simultaneously being measured is zero. Figure 9 shows what may be evidence of the dust problem. Observe that flight values of current at lower voltages are uniformly low, but the flight data and preflight measurements approach each other as we approach V_{oc} .

Conclusion

The discussion above has dealt in some detail with the problems of LIPS III. Although mistakes were made and satellite operation is not according to plan, the quality of the flight data is, in general, quite good. Almost all photovoltaic technologies for space (circa 1987) are represented on LIPS and, with the exception of four temperature sensors and two cells, the large number of experiments here survived integration, launch, and the first six months of flight operation. Thus, a preliminary assessment can be made that, overall, LIPS III with its compliment of experiments, is a success.

The effort to design, fabricate, and test LIPS III was made difficult by the short time available for the task. Many people made outstanding efforts under the most trying of circumstances, without which success would have been impossible. All of the coauthors of this paper played essential roles in this project and are due much credit. The long list of those who contributed experiments is one of true distinction. Of particular importance to the spacecraft in general were the contributions of experimenters Ted Stern, Micky Cornwall, Allan Dollery, Christopher Goodbody, and especially

Gary Virshup. Members of the NRL staff whose efforts were exemplary are far too numerous to be listed here, but, aside from the coauthors, this paper would be incomplete without expressing special thanks to Robert Burdett, command system design and flight computer "Guru", Christopher Herndon, AGE design, Mark Johnson, telemetry design, David Hastman, thermal design, George Gregory, mechanical layout and design, Robert Morris, RCS design, Christopher Garner and Wilbert Barnes, NiCd Battery, Charles Morgan, ordinance design, William Webster, RF design, Joseph Valsi, wiring layout, Eric Eisler, RCS valve control design, Michael Mook, ACS system, Robert Conway, tracking station operations, Robert Grant and James Mills, system test conductors, and Joseph Delpino, launch integration specialist.

References

- [1] Robert H. Towsley, David A. Hastman, and Michael Mook, "LIPS III: An Effective and Existing 'Lightsat' ", AIAA/DARPA Meeting on Lightweight Satellite Systems, August 4-6, 1987, Monterey, CA.
- [2] The solenoid used was a "TORQROD", a lightweight, flight qualified unit manufactured by Ithaco Corporation, Ithaca, NY.
- [3] G.F. Virshup, and J. Werthen, To be published in the proceedings of the Twentieth IEEE Photovoltaic Specialists Conference.

Table 1

GaAs, AlGaAs, InGaAs

Applied Solar Energy Corp	2cm x 2cm and 4cm x 4cm GaAs Cells: GaAs cells on Ge substrate - four cells in series
AFWAL/POOC-2	CRRES Ambient Panel (Backup) - 10 four-cell strings comparing coverslips, coatings, and adhesive
Boeing	Small Area "Concentrator" Cells: LPE (Spectrolab); MOCVD (ASEC); MOCVD (Kopin)
CNRS (France)	MBE GaAs - two cells; LPE InGaAs - two cells
MBB (Munich, FRG)	Two cells (MELCO)
Royal Aircraft Estab. (Farnborough, Hants, UK)	Four cells in series (MARCONI)
Spectrolab	Two GaAs (Spectrolab) and two AlGaAs/GaAs (HRL)
VARIAN	GaAs, AlGaAs - nineteen cells in all: InGaAs under inactive AlGaAs; AlGaAs grown on inactive InGaAs
Martin Marietta Astronautics Group	MOCVD GaAs - compares welded and soldered interconnects

Single Crystal Silicon

AEG (Wedel, FRG)	Bifacial Cell Array - four 5cm x 5cm cells; Two very light weight support structures tested
Applied Solar Energy Corp	2 mil Cells (2cm x 4cm)
AFWAL/POOC-2	Integral Coverslip covering eight cells; Gallium Doped Silicon Cells
Boeing Co.	Four cells with high temperature contacts ("Burst" Annealable)
MBB (Munich, FRG)	Five advanced design cells
NRL/Solarex	Six Vertical Junction Cells (Comparing various coverslips & adhesives); Advanced Design Planar Cells
Royal Aircraft Estab. (Farnborough, Hants, UK)	Four cells comparing coverslips & coatings; Two designs for high radiation resistance
Spectrolab	Two advanced design cells

InP

Royal Aircraft Estab. (Farnborough, Hants, UK)	Four cells fabricated by Newcastle University
NASA-LeRC	Four cells fabricated by Rensselaer Polytechnic

Thin Film Cells - CuInSe₂ and Si

Boeing Co.	Three series strings of four CuInSe ₂ cells each
Sovonics	Two α Si Cells
Solarex	Two α Si Cells

Concentrators

Boeing Co.	Six light funnels
General Dynamics	Three Slats Modules, Six I-V curves
TRW MiniCassegrainian	Three Lightweight Modules (NASA); Two Hardened Modules (AFWAL)

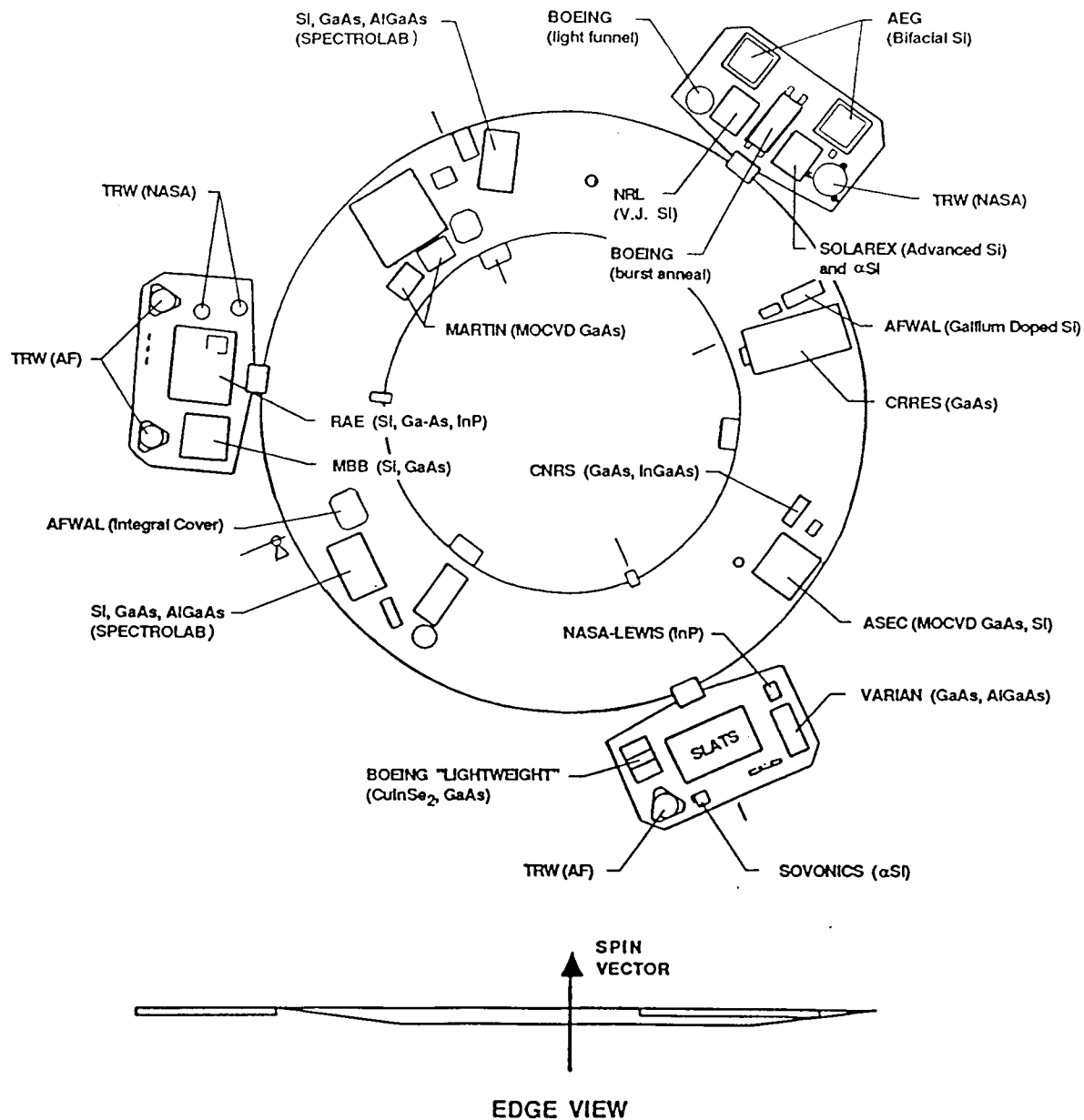


FIGURE 1
LIPS III EXPERIMENT LAYOUT

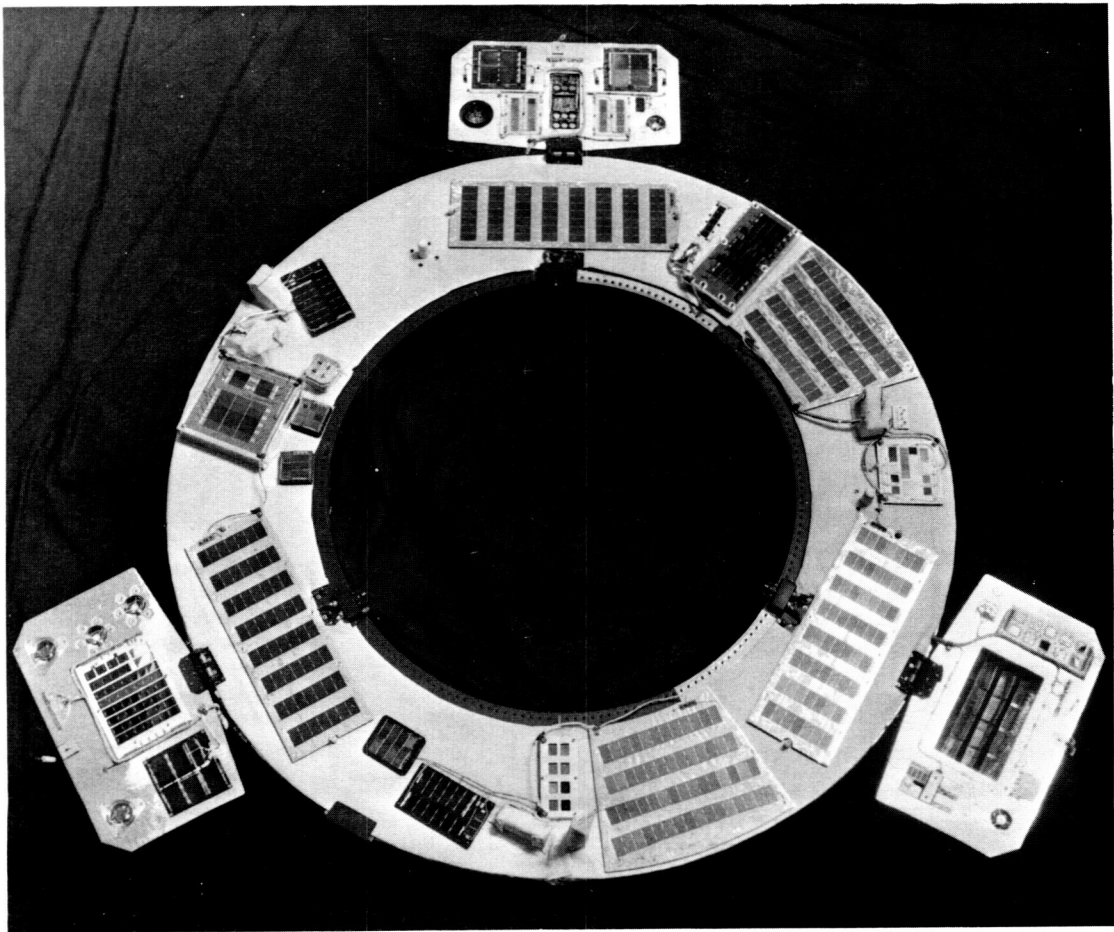


FIGURE 2
LIPS III PADDLES IN FLIGHT CONFIGURATION

ORIGINAL PAGE
BLACK AND WHITE PHOTOGRAPH

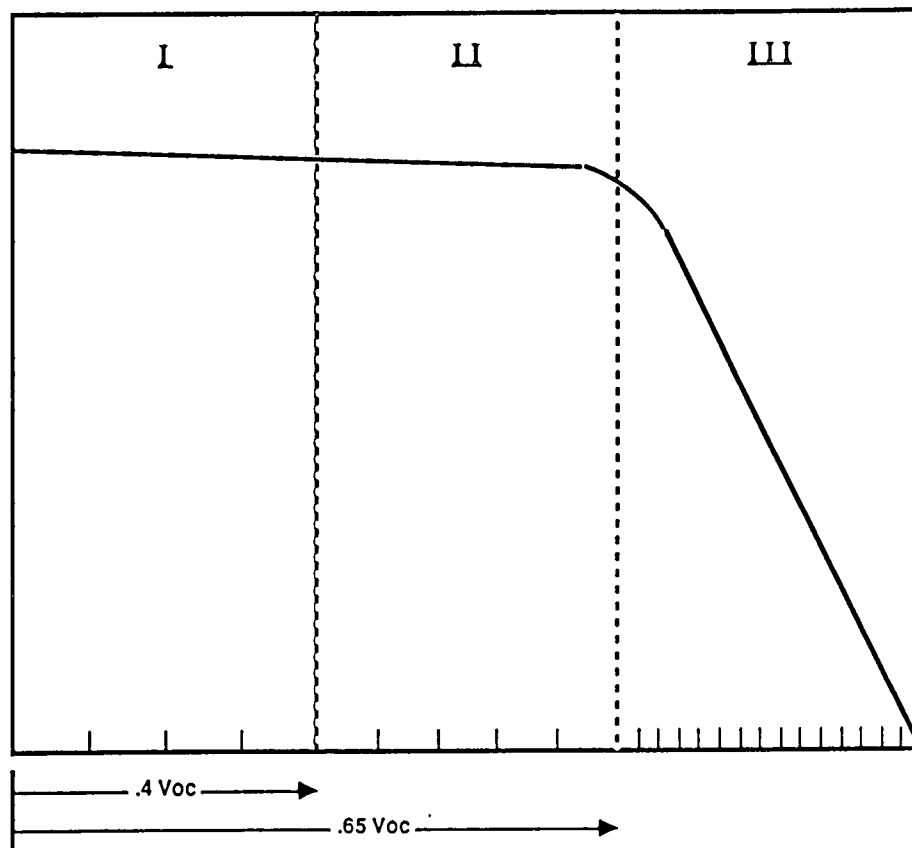


FIGURE 3
TARGET VOLTAGE POINT SELECTION

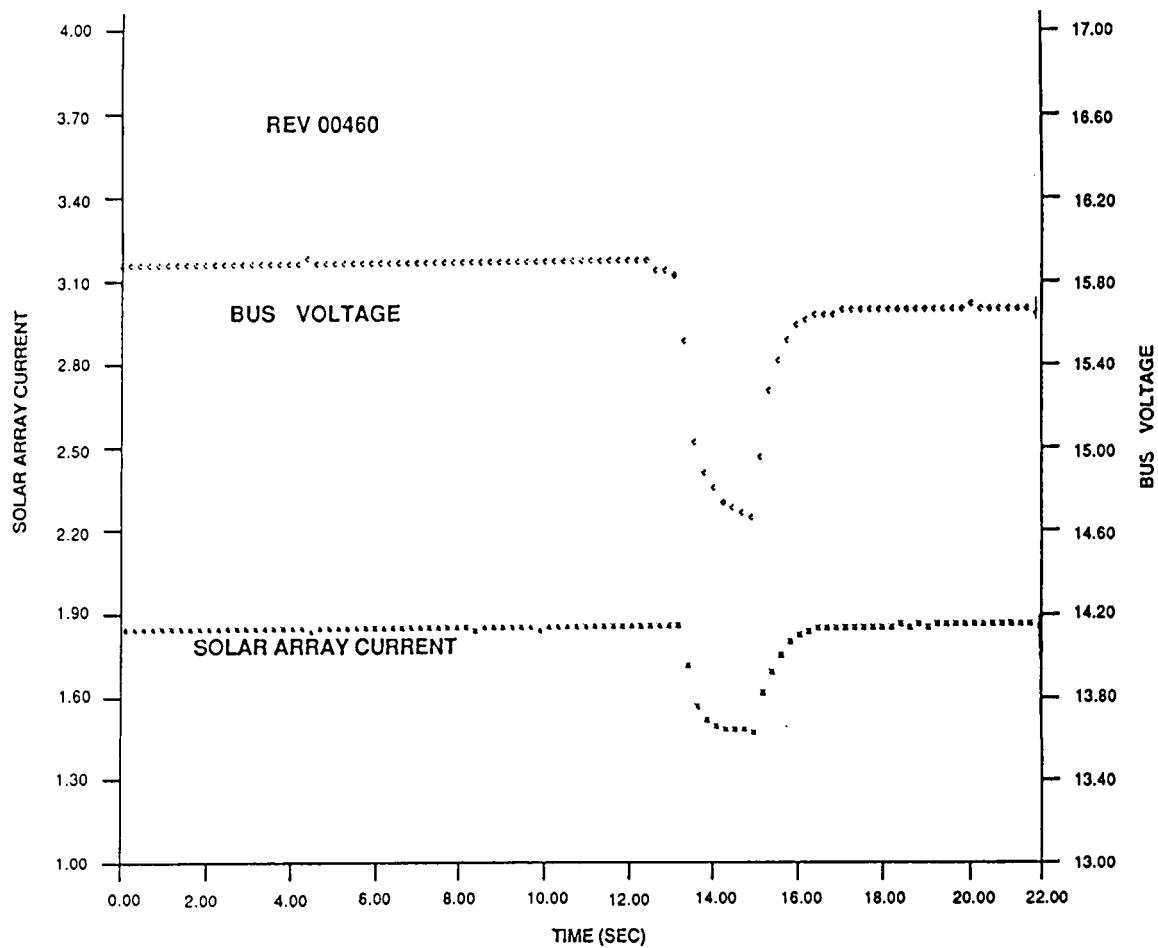


FIGURE 4
BUS VOLTAGE and SOLAR ARRAY CURRENT SHOWING VOLTAGE OFFSET
SPACECRAFT ATTITUDE VERY STABLE

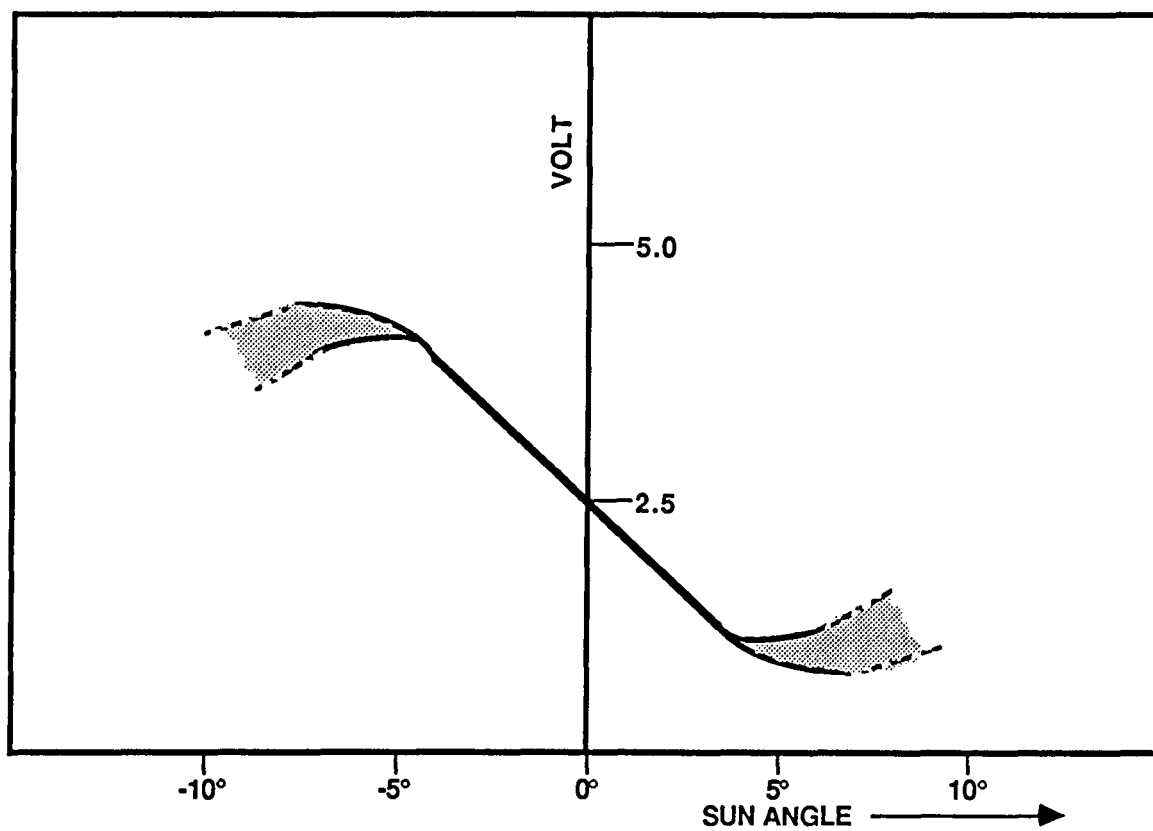


FIGURE 5
FINE ANGLE SUN SENSOR RESPONSE

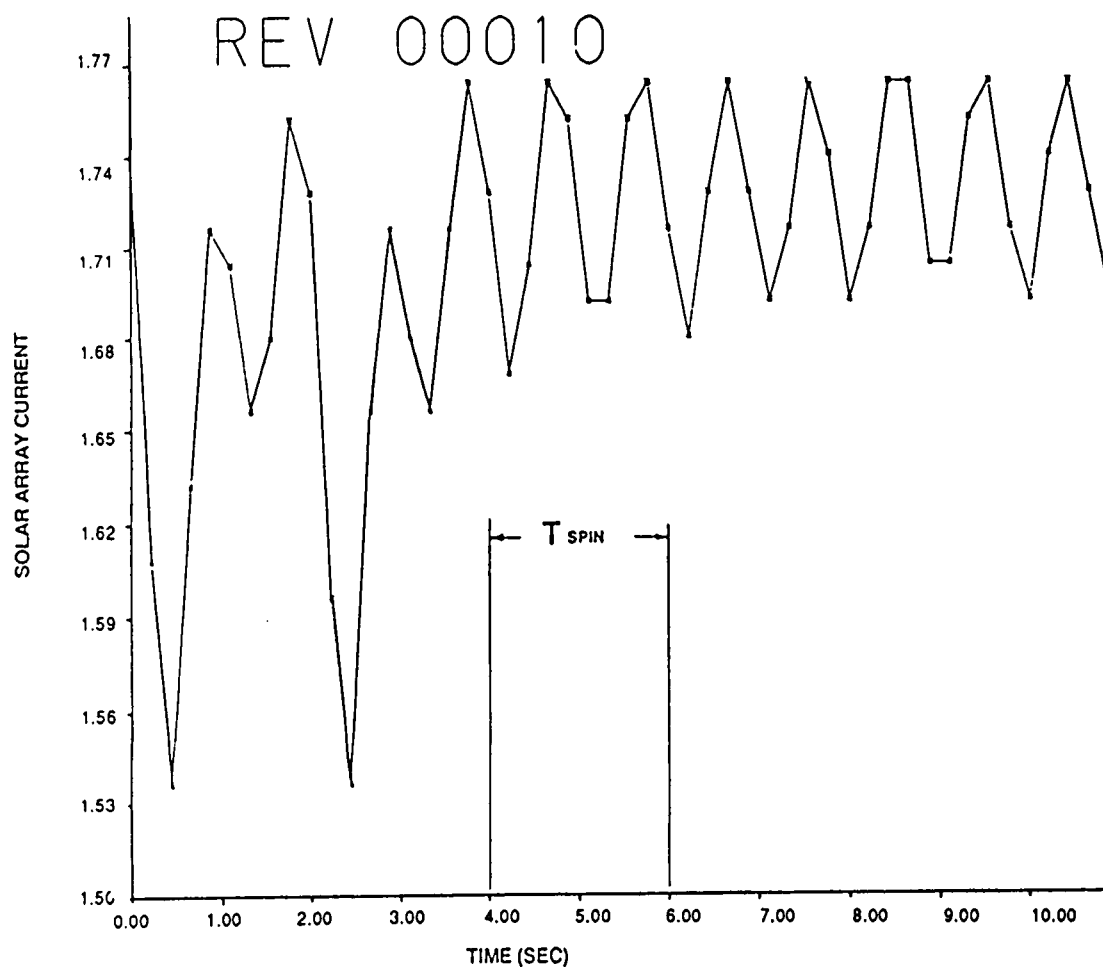


FIGURE 6
SOLAR ARRAY CURRENT WHEN NUTATION IS HIGH

LIPS III FLIGHT DATA

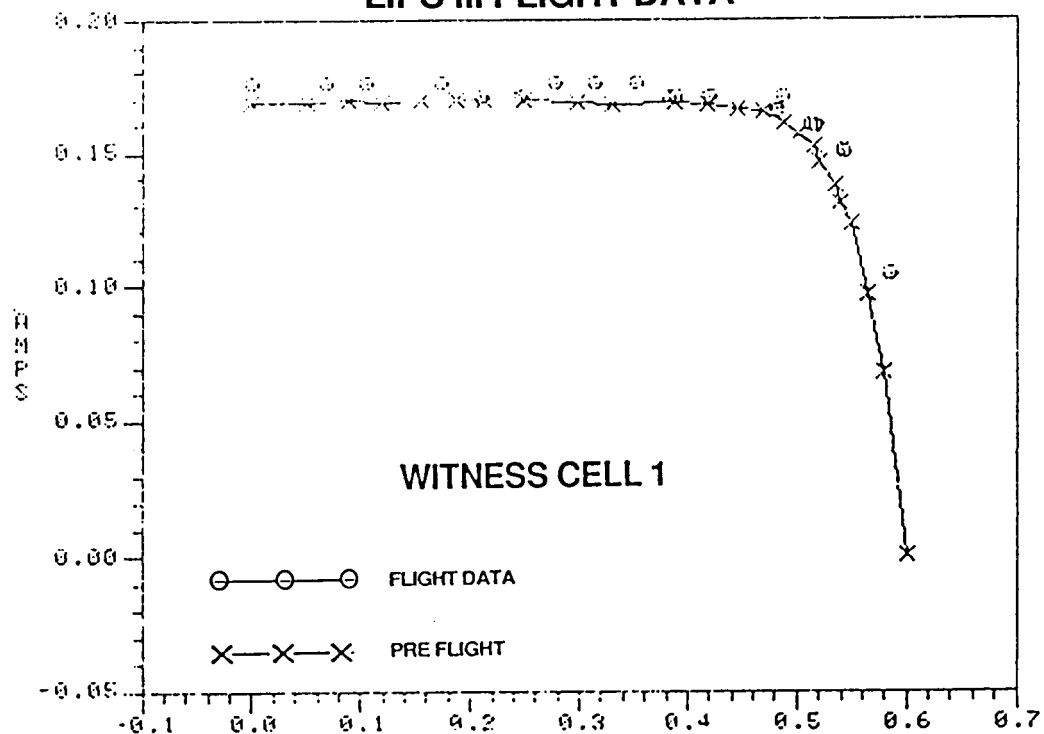


FIGURE 7

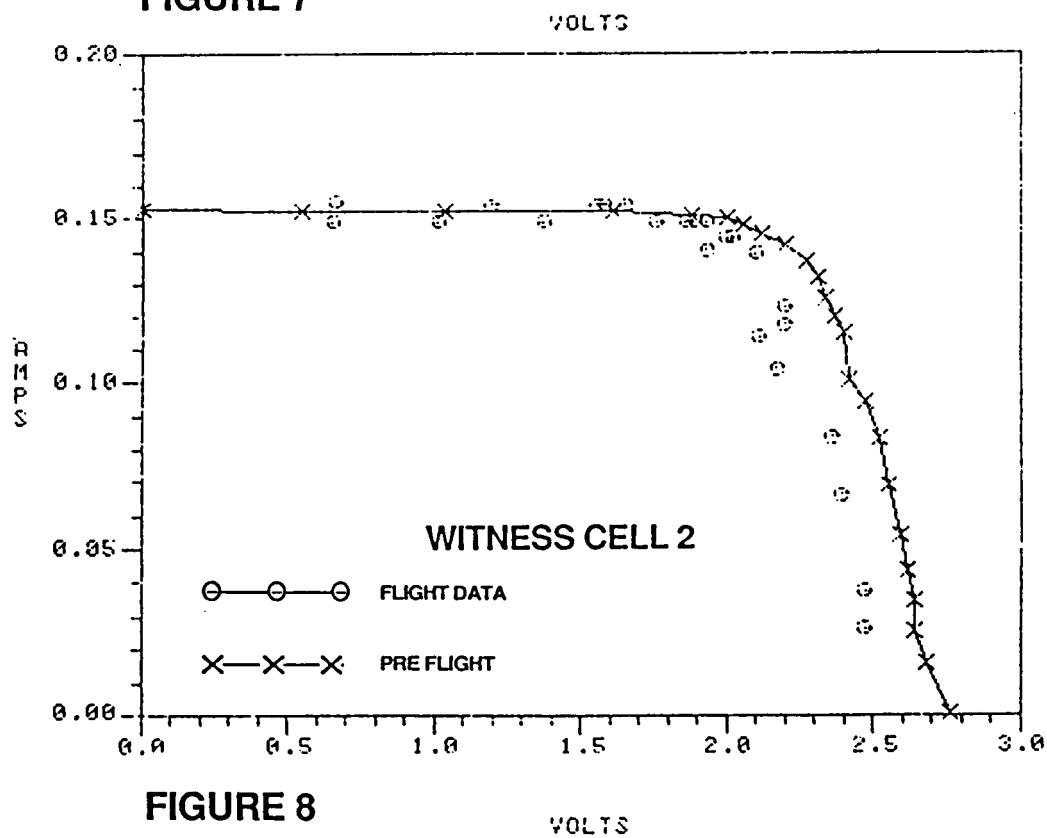


FIGURE 8

LIPS III FLIGHT DATA

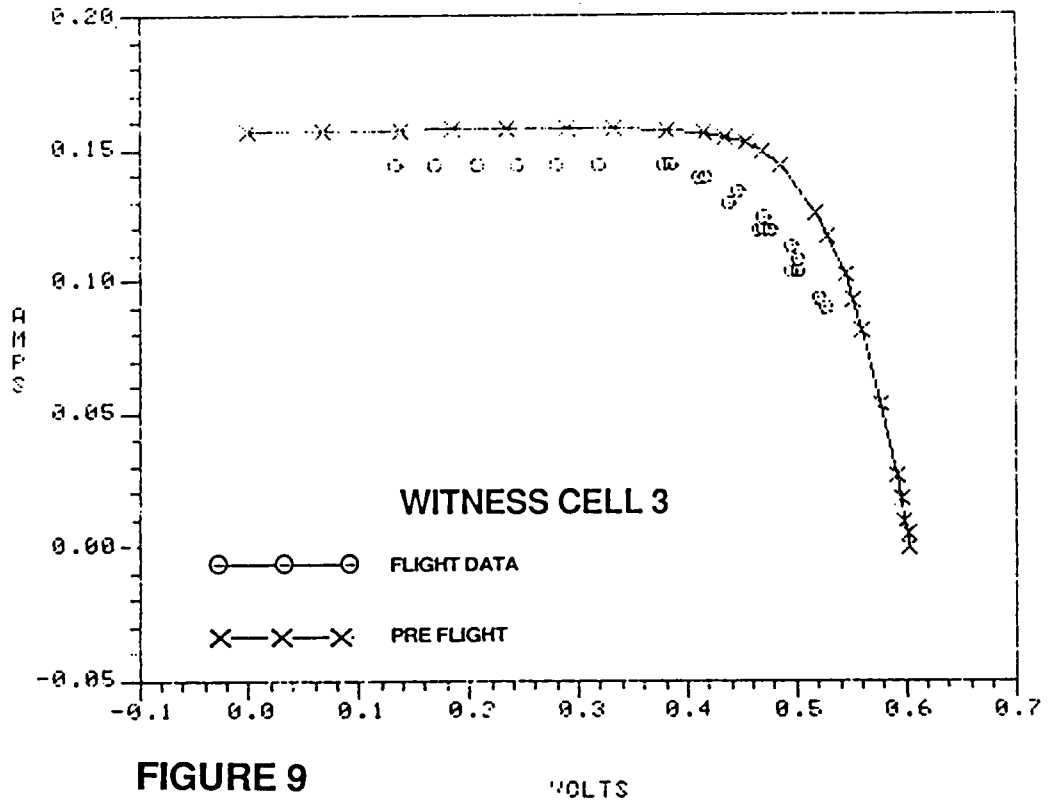


FIGURE 9

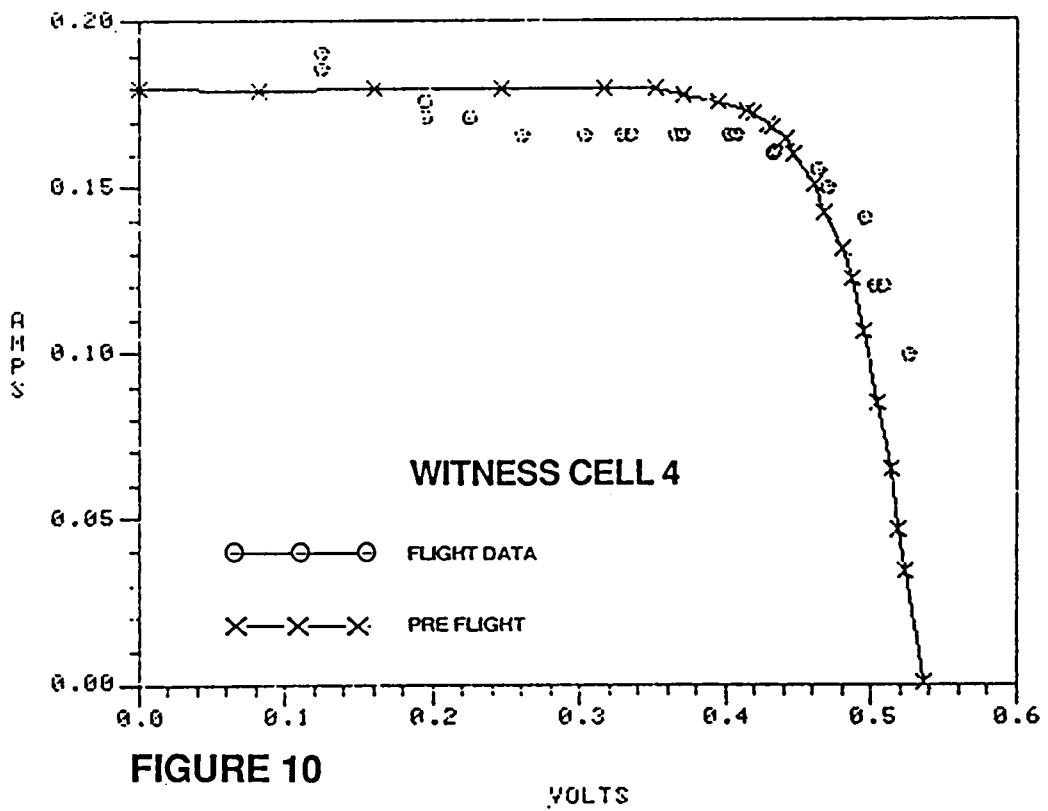


FIGURE 10

AM0 Efficiency Measurements

Keith Emery and Carl Osterwald
Solar Energy Research Institute
 1617 Cole Blvd.
 Golden, CO 80401

Summary

Procedures for measuring the AM0 current versus voltage characteristics and calculating the efficiency are discussed. The various factors influencing the determination of the efficiency includes the I-V measurement system, reference cell calibration, standard reporting conditions, area measurement, light source characteristics, temperature measurement and control, and the measurement procedures. Each of these sources contribute to the precision index and bias limit which is combined to obtain the total uncertainty in the efficiency. This paper discusses these factors and how to minimize differences in the reported AM0 efficiency of a given PV cell between various laboratories.

Introduction

In measuring the current versus voltage (I-V) characteristics with respect to standard reporting conditions, the reference total and spectral irradiance must be established along with a reference temperature and device area definition. For AM0 efficiency measurements, the total and spectral irradiance are defined as the extraterrestrial solar output at 1 astronomical unit (AU) distance from the sun. The reference temperature is 25° or 28°C (depending on the laboratory) while a total cell area definition which, including the area covered by grids and contacts, is generally accepted. The AM0 standard reporting conditions have not been formalized by consensus standards but have been informally adopted by NASA, JPL, and the European Space Agency (ESA) and published in various reports. The AM0 efficiency in percent is normally expressed as:

$$\eta = \frac{100 \cdot P_{\max}}{A \cdot E_{\text{ref}}} = \frac{100 \cdot V_{\max} \cdot I_{\max}}{A \cdot E_{\text{ref}}} \quad (1)$$

where V_{\max} and I_{\max} are the voltage and current at the maximum power P_{\max} , A is the device total area, and E_{ref} is the reference total irradiance. A value of 1353 Wm^{-2} is often used for E_{ref} [ref. 1,2]. However, measurements of the solar constant since 1980 suggest that 1367 Wm^{-2} is a much better value [ref. 3]. In computing η using (1), the assumption is made that the device is illuminated by a "perfect" solar simulator. Since the only location where this is true is in space at 1 AU from the sun, the simulator is set using a primary AM0 reference cell whose short-circuit current ($I_{\text{sc}}^{\text{R,R}}$) at 1 AU has been determined by high altitude aircraft, balloon, or spacecraft flight. The irradiance of the solar simulator is adjusted until the fractional error F , in the measured current of the test cell is unity using [ref. 4]

$$F = \frac{I_{\text{sc}}^{\text{T,S}}}{I_{\text{sc}}^{\text{T,R}}} = \frac{I_{\text{sc}}^{\text{R,S}}}{I_{\text{sc}}^{\text{R,R}}} \cdot M \quad (2)$$

where the first superscript refers to the test device (T) or to the reference cell (R), and the second superscript refers to the source spectrum (S) or to the reference spectrum (R). M is called the spectral mismatch parameter and can be expressed [ref. 4-6] as

$$M = \frac{\int_{\lambda_1}^{\lambda_2} E_{\text{sor}}(\lambda) R_{\text{T}}(\lambda) d\lambda}{\int_{\lambda_1}^{\lambda_2} E_{\text{ref}}(\lambda) R_{\text{T}}(\lambda) d\lambda} \cdot \frac{\int_{\lambda_3}^{\lambda_4} E_{\text{ref}}(\lambda) R_{\text{R}}(\lambda) d\lambda}{\int_{\lambda_3}^{\lambda_4} E_{\text{sor}}(\lambda) R_{\text{R}}(\lambda) d\lambda} \quad (3)$$

The spectral irradiance of the light source is $E_{\text{src}}(\lambda)$, the spectral irradiance of the reference spectrum is $E_{\text{ref}}(\lambda)$, the spectral response of the test device is $R_T(\lambda)$, and the spectral response of the reference cell is $R_R(\lambda)$. The limits of integration λ_1 and λ_2 should at least equal the spectral response limits of the test device, and λ_3 and λ_4 should at least be equal to the spectral response limits of the reference cell. Notice that if the test device and reference cell have identical spectral responses, the M is unity. Most AM0 measurement groups assume M is unity since the reference cell is normally of the same type as the test device.

Reference 7 reports that when M is with 0.005 of unity (spectral mismatch error < 0.5%), the uncertainty in computing M can exceed the error in assuming M is unity. Dividing (1) by (2) gives η for a non-ideal simulator using the reference cell method

$$\eta = \frac{100 \cdot V_{\text{max}} \cdot I_{\text{max}} \cdot I_{\text{sc}}^{\text{R,R}}}{A \cdot E_{\text{ref}} \cdot M \cdot I_{\text{sc}}^{\text{R,S}}} \quad (4)$$

These seven quantities account for all sources of difference in the efficiency. We neglect any errors in V_{max} due to the spectral and total irradiance (F different from unity) because they are normally small.

Uncertainty Analysis

A standard method has been developed to estimate the uncertainty interval for a given quantity such as the efficiency [ref. 8-10]. Using this method, the uncertainty limit (sometimes used synonymously with the terms total error or accuracy) which is expected to include 99% of all results can be written as

$$U_{99} = B + t_{95} \cdot S \quad (5)$$

with

$$B = \left[\sum_{i=1}^J (\theta_i \cdot b_i)^2 \right]^{(1/2)} \quad (6)$$

and

$$S = \left[\sum_{i=1}^J (\theta_i \cdot s_i)^2 \right]^{(1/2)} \quad (7)$$

where t_{95} is the student's t value for 95% confidence ($t_{95} \sim 2$ for more than 30 degrees of freedom or replications), and J is the total number of elemental error sources. Each error source has an individual bias limit (b_i) precision index (s_i) that is associated with random sources. The precision index is usually associated with the standard deviation of an individual error source. The precision index (S) is often incorrectly taken to be the accuracy or total error but neglects the bias errors (B) which often dominate the contribution to the uncertainty limit. The sensitivity coefficient (θ_i) is obtained by partial differentiation of the result with respect to one of the parameters in the result. For example, in (4) the result is η and the parameters are P_{max} , A , and E_{ref} , each with their elemental error sources. If the elemental errors in (4) are expressed as percentages the θ_i is unity. Assuming that M is unity will introduce a bias error as will assuming that a 2 by 2cm cell is actually 4cm². An uncertainty analysis of PV efficiency measurements is summarized in reference 7.

I-V Measurement System

The I-V measurement system needed for the determination of V_{\max} , I_{\max} , and $(I_{sc}^{R,S})$ will introduce errors because of the instrumentation used for data acquisition. A summary of typical precision indexes and bias limits for common instrumentation in measuring voltage and current is given in reference 7. In general, most groups use instrumentation that have a negligible contribution to the uncertainty limit ($<0.1\%$). Also, the contacting method can cause substantial errors (100%) in the I-V characteristic [ref. 11]. The voltage and current contacts should be in close proximity to prevent unrealistically large fill factors [ref. 11]. The resistance between the voltage and current contact should be monitored to ensure a good Kelvin connection (resistance \times device area $< 1W \bullet cm^2$). For devices with multiple current contact pads on the grid, a separate Kelvin contact to each pad should be used with the current contacts connected together and the voltage contacts connected together. Some devices can change their I-V characteristics depending upon the voltage bias rate, bias direction, illumination time, and time at a fixed voltage prior to the I-V measurement [ref. 11]. For these devices the important factor to remember is that P_{\max} in (1) is only defined for steady-state conditions.

Temperature Measurement and Control

Because V_{\max} , I_{\max} , and $(I_{sc}^{R,S})$ all vary as function of temperature, any deviation of the device temperature from the reference temperature will introduce an error in the efficiency. The error in the temperature can be minimized by controlling the temperature but cannot be eliminated because of imperfect temperature control, temperature sensor calibration errors, and temperature gradients between where the temperature is measured and the junction temperature. Typically, the best that can be obtained is a $1^\circ C$ bias limit and a $0.1^\circ C$ precision index in the device junction temperature.

Area Measurement

The device area can be a source of large errors if it is not carefully considered [ref. 7]. If the standard area definition is not used errors over 100% are possible (active area). More subtle errors can and do occur from sources which include light trapping, poor mesa etches, irregular edges, and other fabrication related artifacts (a small perimeter to area ratio minimizes edge related errors). Errors in the actual measurement of the total device area also occur. For example, a 2 by 2cm device measured on a X-Y translation stage with a $1\mu m$ resolution and a $10\mu m$ bias error would contribute $\sim 0.1\%$ to the total uncertainty. The same device measured with vernier caliper with a $0.01mm$ resolution and a bias error of $0.1mm$ would add $\sim 1\%$ to the total uncertainty. Worse yet is to simply assume that a 2 by 2 cm device is actually $4cm^2$.

Light Source

Spatial uniformity and temporal stability of the source illumination will affect the measurement of I_{\max} and $(I_{sc}^{R,S})$. The error due to temporal instability (lamp flicker) can be minimized if I_{\max} and $(I_{sc}^{R,S})$ in (4) are measured during the same time period. The error η because of spatial nonuniformity of the light source can be minimized if the primary AM0 reference cell has the same geometry as the test device and the calibration of primary reference cell is transferred to a monitor cell in the test

plane, thereby allowing the test device to be measured in the same location as the primary reference cell. This procedure will not correct for the spatial uniformity changing with time but does allow the current of the test device to be measured with a precision error of less than 0.05% [ref. 11,12].

The spectral mismatch parameter (3) can be a major source of uncertainty in η measurements. The AM0 community has minimized this bias error resulting from the assumption that M is unity by obtaining a primary reference cell of the same type as the test device. This may not always be possible in a research environment where the quantum efficiency is being altered by changing fabrication processes, antireflection coatings, radiation damage, and energy gap, making the cost and time of obtaining a new primary AM0 reference cell for each change prohibitive. Table 1 demonstrates that the same short-circuit current ($I_{sc}^{T,R}$) can be obtained using equation 2, independent of the primary AM0 (Fig. 1) or terrestrial (Fig. 2) reference cell used. Figure 3 compares the AM0 spectral irradiance in reference 13 with the measured Spectrolab X-25 solar simulator spectral irradiance used in Table 1. The primary terrestrial reference cells were calibrated in Golden, CO using the tabular method [ref. 12]. The primary AM0 reference cells were calibrated by R. Hart of NASA Lewis Research Center. This procedure (equation 4) has been used successfully (<1.5% error) for terrestrial and AM0 reference cells for a wide variety of test cell-reference cell combinations [ref. 7, 12, 14, 15]. An uncertainty analysis of this procedure found that a 5% random error in the measurement of the relative spectral response of the test and reference cell and spectral irradiance of the light source gave a 0.4% error in M for a wide variety of test cell-reference cell combinations and light sources [ref. 7]. The limiting factor in using M in (4) is not the error in M but the calibration error in the reference cell itself and the ability to correct for spatial nonuniformity and temporal instability.

Tandems

Perhaps the most difficult challenge facing the PV efficiency measurement community today is how to measure the efficiency of multi-junction devices with respect to standard reporting conditions [ref. 16]. For tandems where the cells are independent of each other (mechanically stacked or monolithic multi-terminal) the efficiency of each device can be separately measured using (4) and then added to obtain the tandem efficiency. The only problem with this procedure is the cost and difficulty in obtaining primary AM0 reference cells for each cell in the stack as the structure is being optimized. The requirement of "matched" AM0 reference cells for each cell in the stack can be relaxed if spectral mismatch corrections are applied to each cell in the tandem structure.

Two-terminal multi-junction cells pose a unique problem because even if a "matched" primary reference cell can be obtained allowing the short-circuit current of the test device ($I_{sc}^{R,R}$) to be determined the fill factor P_{max} , and η may be in error [ref. 16,17]. The fill factor is determined by the spectral irradiance of the light source even when the short-circuit current is correct. This is because the fill factor is affected by the current mismatch between the individual component cells in the multi-junction device and this current mismatch is determined by the spectral irradiance of the light source. A multi-source simulator has been proposed as a method of ensuring that the multi-junction device is being measured with respect to standard reporting conditions [ref. 17]. This method requires the computation of F in (2) for each of the light-source-reference cell combinations that selectively illuminate each of the junctions in the multi-junction device. Each of the light sources should be filtered so that only one of the junctions responds to the light (e.g., a 640nm cut off filtered light source for an AlGaAs top cell and a separate light source with a 660nm cut on filter for the bottom cell). The uncertainty of this technique has been estimated to be $\pm 3\%$ based upon comparing measurements under a single-source simulator with measurements made under a

multi-source simulator that used this single-source simulator's spectral irradiance as the reference spectral irradiance [ref. 17].

Summary

A large number of procedural and measurement related artifacts can and do occur when determining the efficiency of a PV device with respect to standard reporting conditions. A variety of procedures have been discussed for reducing the uncertainty in efficiency measurements. When careful attention is paid to what is actually being measured and care is taken to minimize artifacts, then a total uncertainty of less than $\pm 2\%$ in efficiency is possible. The uncertainty in the reference cell calibration which has been established at $\pm 1\%$ is only a part of the uncertainty in the efficiency. The measurement of tandem efficiencies will pose a challenge to many groups that do not have the resources to apply spectral mismatch corrections and build a multi-source solar simulator.

References

- [1] H. Tada, J. Carter, B. Anspaugh, and R. Downing, "Solar Cell Radiation Handbook", JPL Tech. Rep. 82-69, 1982.
- [2] "Standard for Solar Constant and Air Mass Zero Spectral Irradiance Tables", ASTM Standard E490.
- [3] R. Wilson, H. Hudston, C. Frolich, and R. Brusa, "A Long-term Downward Trend in Total Solar Irradiance", *Science*, **234**, pp 1114-1117, 1986.
- [4] C.R. Osterwald, "Translation of Device Performance Measurements to Reference Conditions", *Solar Cells*, **18**, pp 269-279, 1986.
- [5] C.H. Seaman, "Calibration of Solar Cells by the Reference Cell Method- the Spectral Mismatch Problem," *Solar Energy*, **29**, pp 291-298, 1982.
- [6] "Standard Practice for Determination of the Spectral Mismatch Parameter Between a Photovoltaic Device and Photovoltaic Reference Cell", ASTM Standard E973.
- [7] K.A. Emery, C.R. Osterwald, and C.V. Wells, "Uncertainty Analysis of Photovoltaic Efficiency Measurements", *Proc. 19th IEEE PV Spec. Conf.*, pp 153-159, 1987.
- [8] R.B. Abernathy and R.P. Benedict, "Measurement Uncertainty: A Standard Methodology", *Instrument Soc. of America*, **24**, pp 75-79, 1985.
- [9] "Instruments and Apparatus Part 1: Measurement Uncertainty", ANSI/ASME standard PTC 19.1, 1985.
- [10] "Fluid Flow Measurement Uncertainty", ISO draft standard ISO DIS 5168 for the International Organization for Standardization Committee ISO TC30 SC9, 1987.
- [11] K. Emery and C. Osterwald, "Measurement of PV Device Current as a Function of Voltage, Temperature, Intensity, and Spectrum", *Solar Cells*, **21**, pp 313-327, 1987.
- [12] K.A. Emery and C.R. Osterwald, "Solar Cell Efficiency Measurements", *Solar Cells*, **17**, pp 253-274, 1986.
- [13] C. Wehrli, "Extraterrestrial Solar Spectrum", Physical-Metrological Observatory and World Radiation Center, publication No. 615, Davos-Dorf, Switzerland, July 1985.

- [14] K.A. Emery, C.R. Osterwald, T.W. Cannon, D.R. Myers, J. Burdick, T. Glatfelter, W. Czuby, and J. Yang, "Methods for Measuring Solar Cell Efficiency Independent of reference Cell or light Source", *Proc. 18th IEEE PV Spec. Conf.*, pp 623-628, 1985.
- [15] K.A. Emery, C.R. Osterwald, L.L. Kazmerski, and R. Hart, "Calibration of Primary Terrestrial Reference Cells - Comparison with Primary AM0 Reference Cells", *Proc. 8th European Community PV Solar Energy Conf.*, Naples, Italy, 1988.
- [16] K.A. Emery, C.R. Osterwald, T. Glatfelter, J. Burdick, and G. Virshup, "A Comparison of the Errors in Determining the Conversion Efficiency of Multijunction Solar Cells by Various Methods", *Solar Cells*, **24**, 1988, Special issue of papers presented at the SERI 8th PV AR&D project review meeting, Denver, CO, 1987.
- [17] T. Glatfelter and J. Burdick, "A Method for Determining the Conversion Efficiency of Multiple Cell Photovoltaic Devices", *Proc. 19th IEEE PV Spec. Conf.*, pp 1187-1193, 1987.

Table 1. A GaAs cell with a primary AM0 calibration at 25°C of 113.0 mA had an uncorrected short-circuit current under the Spectrolab X-25 solar simulator (Figure 3) of 120.2 mA. The corrected short-circuit current $I_{sc}^{T,R}$ is independent of the quantum efficiency of the primary AM0 (Figure 1) or primary terrestrial (Figure 2) reference cell within $\pm 2\%$, even though the spectral mismatch error varied from -1% to +6%, and the uncertainty of the reference cell calibration was $\pm 1\%$.

Primary AM0 Reference Cell					
sample number	type	current under X25 $I_{sc}^{R,S}$ (mA)	AM0 Current $I_{sc}^{R,R}$ (mA)	M	GaAs test cell $I_{sc}^{T,R}$ (mA)
4606	Silicon	176.1	175.0	1.0400	114.9
3	Silicon	112.7	110.2	1.0426	112.7
D13dd	poly-Si	162.3	157.8	1.0339	113.0
248	InP	8.40	8.035	1.0351	111.1
B25	CuInSe ₂	47.20	45.18	1.0378	110.9
mean =					112.5 mA
std. deviation =					1.3%

Secondary AM0, Primary Terrestrial Reference Cell					
S01	Silicon	155.0	154.75	1.0476	114.6
S02	Silicon	169.4	168.95	1.0609	113.0
S03	Silicon	156.4	155.91	1.0536	113.7
DSET31	poly-Si	113.2	108.92	1.0221	113.2
S09 KG5	filtered Si	64.20	58.67	0.9903	110.9
S10 KG5	filtered Si	60.74	55.50	0.9856	111.4
S05	CuInSe ₂	41.45	40.22	1.0427	111.9
S25	GaAs	111.5	106.95	1.0103	114.1
S26	GaAs	112.2	107.43	1.0207	112.8
mean =					112.8 mA
std. deviation =					1.0%

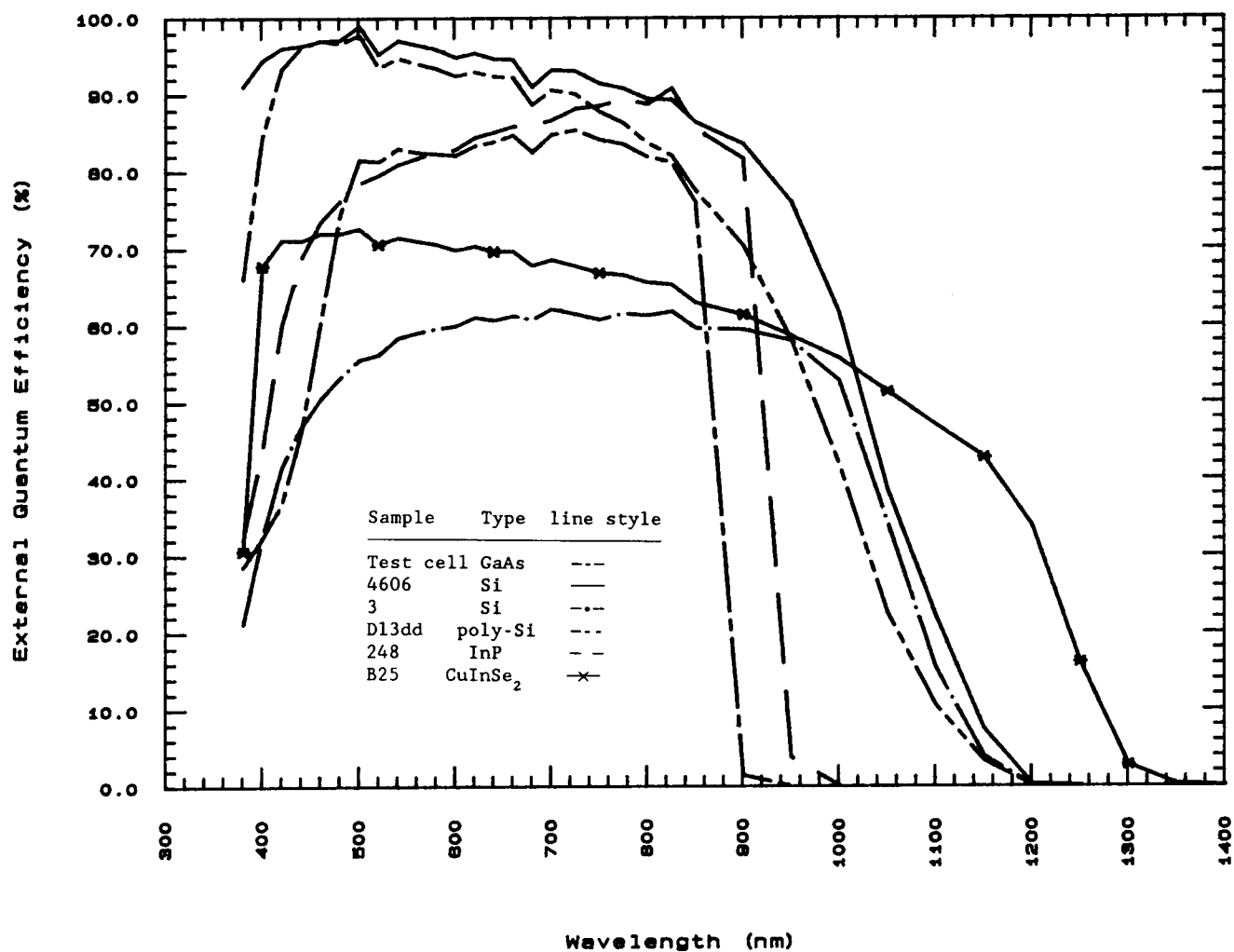


Figure 1. Measured external quantum efficiencies (electron per photon) for the primary AMO GaAs reference cell used as a test cell in table 1 and the other high altitude aircraft flown primary AMO reference cells.

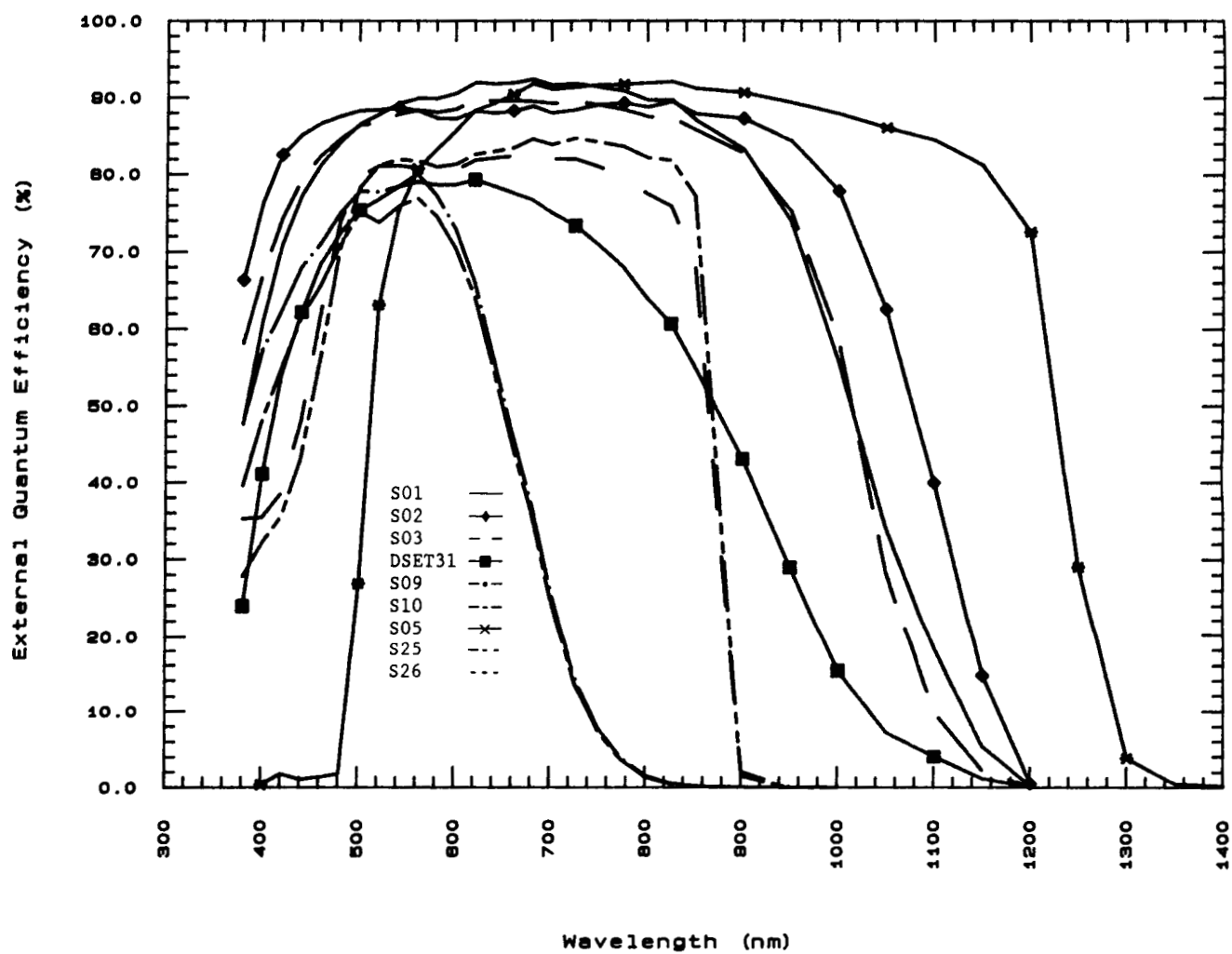


Figure 2. Measured external quantum efficiencies for the primary terrestrial reference cells given in table 1.

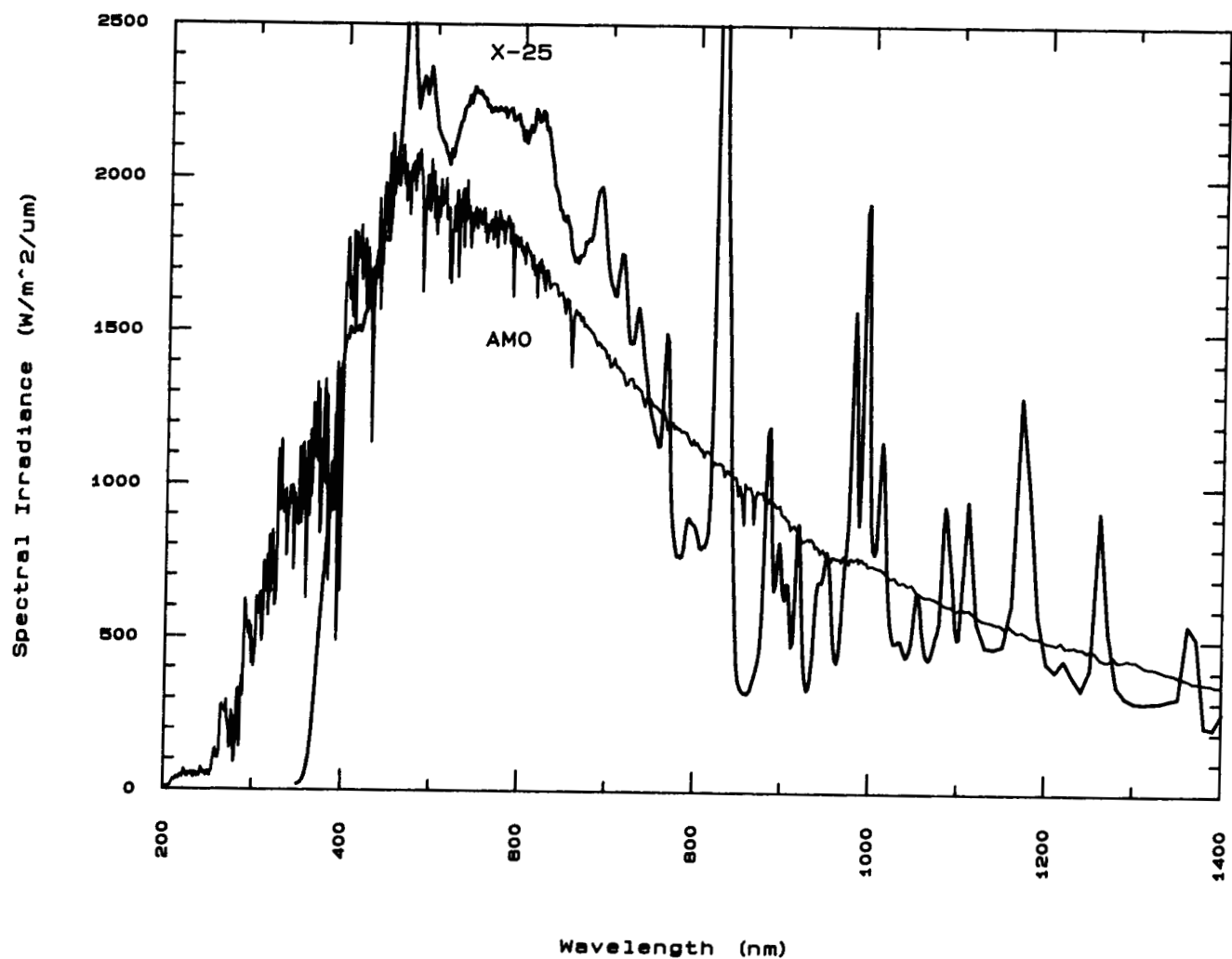


Figure 3. The AMO reference spectral irradiance recommended by the World Radiation Center [13] (1367Wm^{-2}) compared with the SERI Spectrolab X-25 spectral irradiance used calculating the spectral mismatch error in table 1.

A Comparison of the Radiation Tolerance Characteristics of Multijunction Solar Cells with Series and Voltage-Matched Configurations*

James M. Gee
*Sandia National Laboratories
Albuquerque, NM*

Henry B. Curtis
*NASA Lewis Research Center
Cleveland, OH*

Summary

The effect of series and voltage-matched configurations on the performance of multijunction solar cells in a radiation environment was investigated. It was found that the configuration of the multijunction solar cell can have a significant impact on its radiation tolerance characteristics.

Introduction

Multijunction (MJ) solar cells have the potential for extremely high efficiencies ($>30\%$). Such cells consist of several photovoltaically active junctions (subcells) with different bandgaps stacked in optical series. This arrangement essentially splits the broad solar spectrum into portions to which the individual subcells are better matched. MJ cells are under consideration for space applications where high efficiency is important. In order to be useful for space applications, the radiation tolerance of MJ cells needs to be addressed.

The radiation tolerance of an MJ solar cell is determined by several factors. The first factor is the radiation characteristics of the individual subcells. The degradation characteristics of an individual subcell are expected to be similar (after accounting for the shielding of any overlying material) to a single-junction cell fabricated from the same material and with the same cell structure. The radiation tolerance of single-junction solar cells has been extensively studied and documented [ref. 1].

A second factor that influences the radiation tolerance characteristics of an MJ cell is its module configuration. Module configuration refers to the electrical circuit in which the subcells of the MJ cell are wired. The degradation characteristics of one subcell may affect the power available from the other subcells through limitations imposed by the electrical circuit. In this paper, we report results of a study concerning the effect of the module configuration on the radiation tolerance of an MJ cell.

* This work was partially supported by the U.S. Department of Energy under contract DE-AC04-76DP00789.

MJ Cell Configurations

The simplest module configuration for an MJ cell has the subcells connected in series. This cell requires only two terminals. The current from a series string of cells is limited by the cell with the lowest current. The bandgaps of the subcells for a series-configured MJ cell should therefore be chosen for matched photocurrents. In a radiation environment, the bandgaps should be chosen for matched currents at end-of-life (EOL). Since many cells degrade more rapidly in current rather than voltage, series operation could impose severe limitations to the radiation tolerance of MJ cells with a series configuration.

MJ cells whose subcells can be wired in various series/parallel circuits have been recently described [ref. 2]. The voltage of cells in parallel is limited by the cell with the lowest voltage. Hence, these MJ cells require matched voltages between subcell circuits for efficient operation and are referred to as having a voltage-matched (VM) configuration. An example of a two-junction, four-terminal tandem cell wired in a voltage-matched configuration is given in figure 1. VM circuits have also been described for both two- and three-junction tandem cells with three terminals, so that the VM configuration may be used with monolithic MJ cells [ref. 2]. Figures 2 and 3 show the effect of the module configuration on the efficiency versus bandgap relationship for series and VM configurations. (These efficiencies were calculated using the model of reference 2.) An advantage of the VM configuration compared to the series configuration is that it allows a wider selection of bandgaps for a given efficiency.

Experiment and Calculations

In general, the voltage and current of a solar cell degrade at different rates with irradiation. Hence, the radiation tolerance is expected to be influenced by the module configuration. For this study, we used the measured radiation characteristics of AlGaAs (1.72 eV), GaAs, and InGaAs (1.15 eV) concentrator cells presented in reference 3. The AlGaAs and InGaAs cells have appropriate bandgaps for use with both the series and VM configurations. The initial device characteristics are presented in table 1 and the degradation characteristics under 1-MeV electron irradiation are presented in figures 4, 5, and 6. Note that the maximum power (P_{\max}) of the InGaAs cell degrades very rapidly due to the rapid degradation of the current.

The expected performance of an AlGaAs/InGaAs tandem cell was calculated using the following procedure. Each illuminated current-voltage (IV) curve was fitted to a lumped parameter model consisting of a current source, two diodes ($n=1$ and $n>1$), and a shunt and series resistance. No physical interpretation was attached to these fitted parameters; the purpose of the exercise was to allow addition of IV curves for tandem cell modeling. Next, the tandem cell performance for independent, series, and VM configurations was calculated using the lumped parameter model for the AlGaAs and InGaAs subcells. ("Independent" configuration refers to operation of each subcell independently.) For this calculation, the photocurrent of the InGaAs subcell was set equal to the photocurrent of the AlGaAs subcell at beginning-of-life (BOL); i.e. we have assumed that the photocurrents are matched at BOL for an optimized cell. The photocurrents from the AlGaAs and InGaAs cells were assumed to degrade at the measured rates given in figures 4 and 6. The data of figure 6 was taken with full spectrum illumination while the InGaAs cell in an AlGaAs/InGaAs tandem cell will only be illuminated by a filtered spectrum. Our spectral response data indicates that the InGaAs cell degrades more rapidly in the blue, so that our calculations may overestimate slightly the current degradation expected from an InGaAs cell in the stacked configuration.

Results of the calculations are presented in figure 7. The rapid degradation in I_{sc} for the InGaAs cell is seen to have a substantial effect on the series-configured MJ cell. The P_{max} of the series-configured tandem cell, in fact, becomes less than that of a single-junction GaAs cell at high fluences despite the much higher BOL efficiency. The P_{max} degradation of the VM configuration is much less than that of the series configuration for the AlGaAs/InGaAs tandem concentrator cell since voltage degrades much less rapidly than current for these particular subcells. Initially, the VM configuration produces about 3% less power at BOL than the series or independent configurations because the voltages of the subcells are slightly mismatched. However, the subcell voltages become better matched as they degrade with irradiation. In fact, P_{max} of the VM configuration is nearly the same as the independent configuration and 39% greater than the series configuration at EOL.

Conclusions

We have calculated the expected performance of an AlGaAs/InGaAs tandem cell as a function of 1-MeV electron fluence with series and voltage-matched configurations. It was shown that the module configuration can have a significant impact on the radiation tolerance of an MJ cell due to the different rates of degradation for voltage and current of the individual subcells.

References

- [1.] H. Y. Tada, et al., *Solar Cell Radiation Handbook, 3rd Ed.*, JPL Publication No. 82-69 (November 1982).
- [2.] James M. Gee, "Voltage-Matched Configurations for Multijunction Solar Cells," *Proc. 19th IEEE Photo. Spec. Conf.*, pg. 536 (1987).
- [3.] H.B. Curtis, C.K. Swartz, and R.E. Hart, Jr., "Radiation Performance of AlGaAs and InGaAs Concentrator Cells and Expected Performance of Cascade Structures," *Proc. 19th IEEE Photo. Spec. Conf.*, pg. 727 (1987).

Table 1. Initial IV data at 100 suns, AM0 and 25°C.

	AlGaAs	GaAs	InGaAs
J_{sc} (A/cm ²)	1.961	3.174	3.579
V_{oc} (volts)	1.367	1.139	0.859
Fill Factor	0.835	0.799	0.794
Efficiency (%)	16.5	21.3	18.1

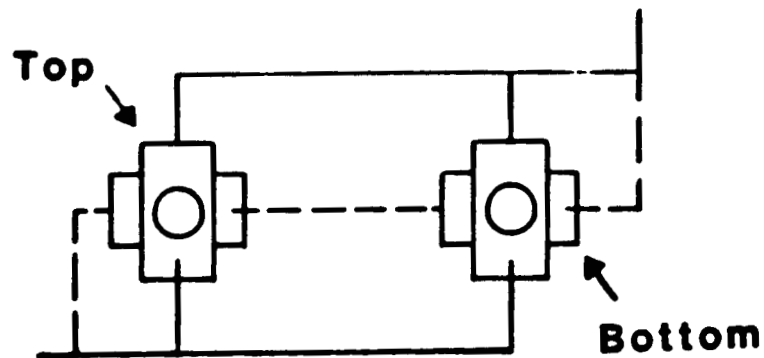


Figure 1. A voltage-matched circuit for a four-terminal, two-junction tandem cell. In the above circuit, the top subcells are wired in parallel with two series-connected bottom subcells.

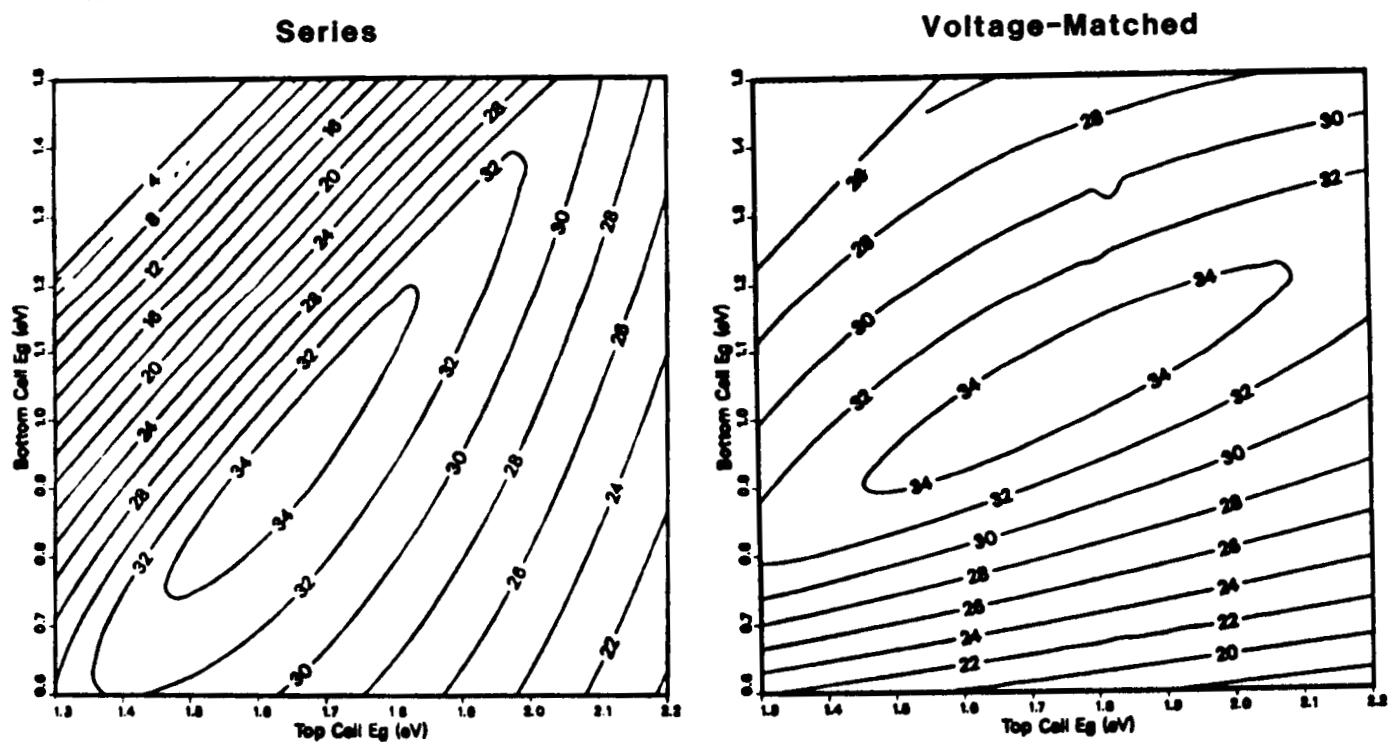


Figure 2. Iso-efficiency curves for a two-junction tandem cell as a function of top and bottom subcell bandgaps (1X, AM0).

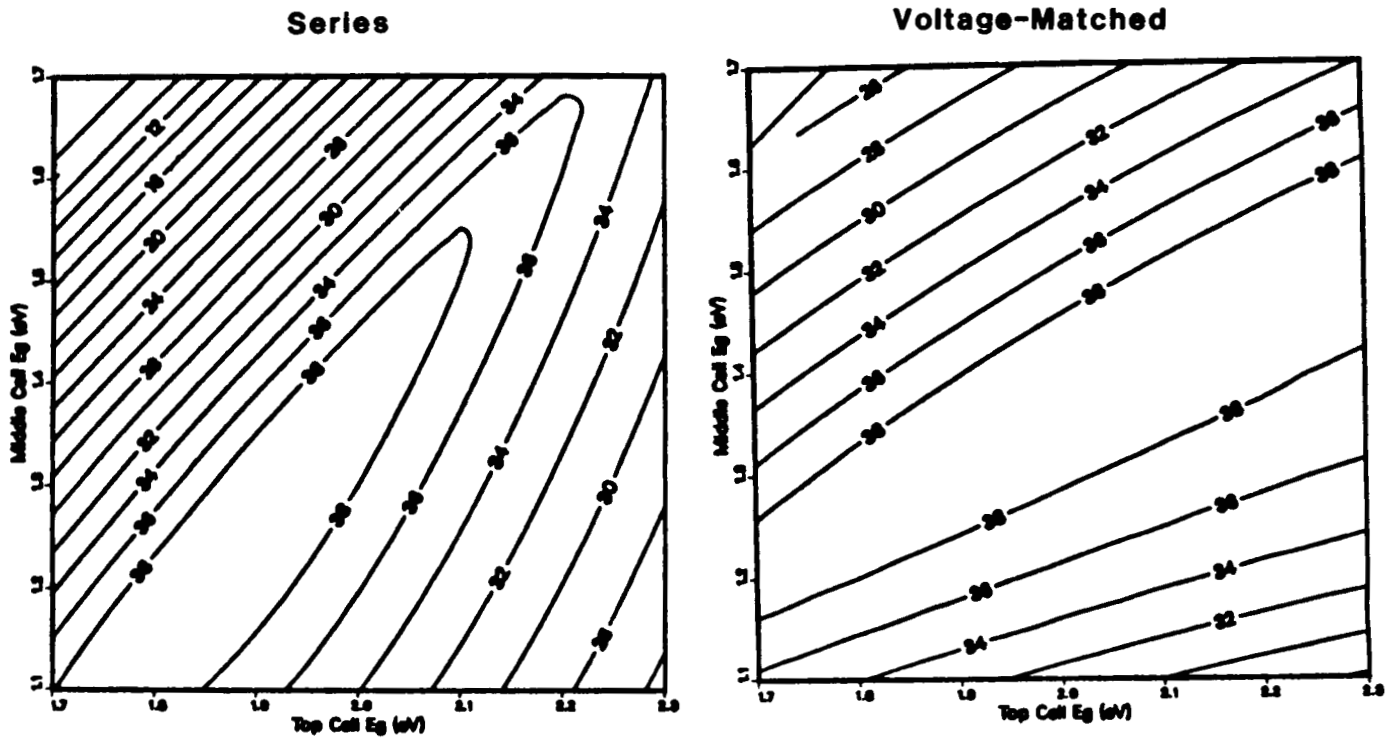


Figure 3. Iso-efficiency curves for a three-junction tandem cell as a function of top and middle subcell bandgaps (1X, AM0). The bandgap of the bottom subcell is optimized each pair of top and middle subcell bandgaps.

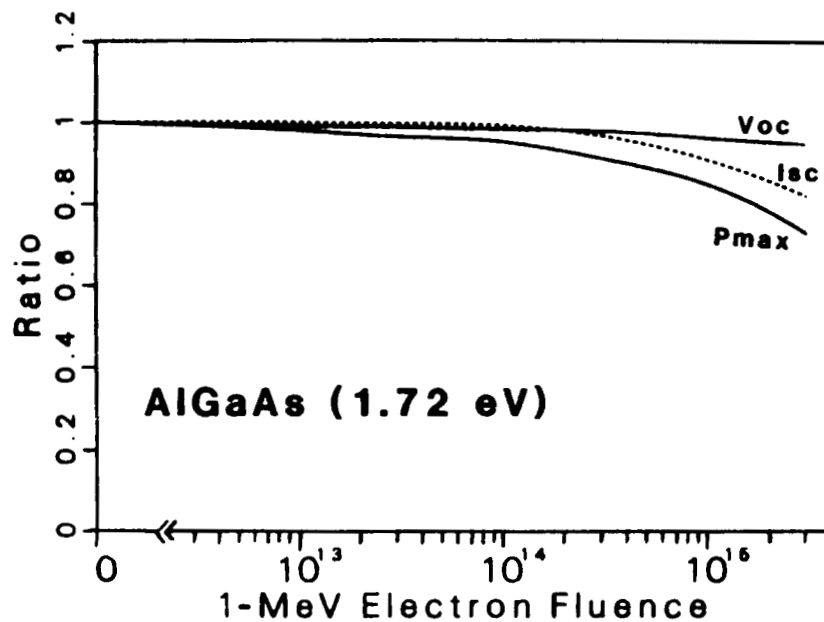


Figure 4. Ratio of degraded/initial values for V_{oc} , I_{sc} , and P_{max} of an AlGaAs (1.72 eV) concentrator cell as a function of 1-MeV electron fluence (100X, AM0, 25°C). (The units of fluence are cm^{-2} .)

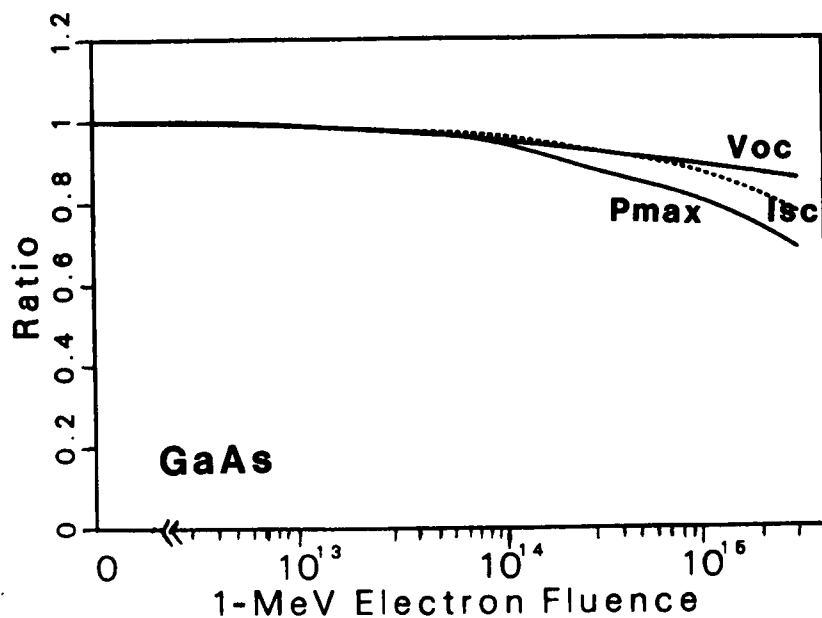


Figure 5. Ratio of degraded/initial values for V_{oc} , I_{sc} , and P_{max} of a GaAs (1.42 eV) concentrator cell as a function of 1-MeV electron fluence (100X, AM0, 25°C). (The units of fluence are cm^{-2} .)

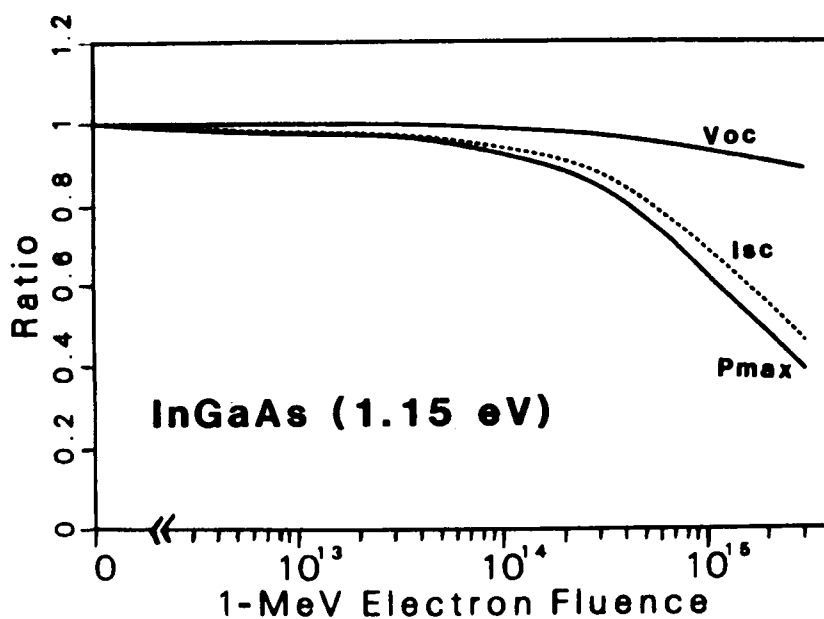


Figure 6. Ratio of degraded/initial values for V_{oc} , I_{sc} , and P_{max} of an InGaAs (1.15 eV) concentrator cell as a function of 1-MeV electron fluence (100X, AM0, 25°C). (The units of fluence are cm^{-2} .)

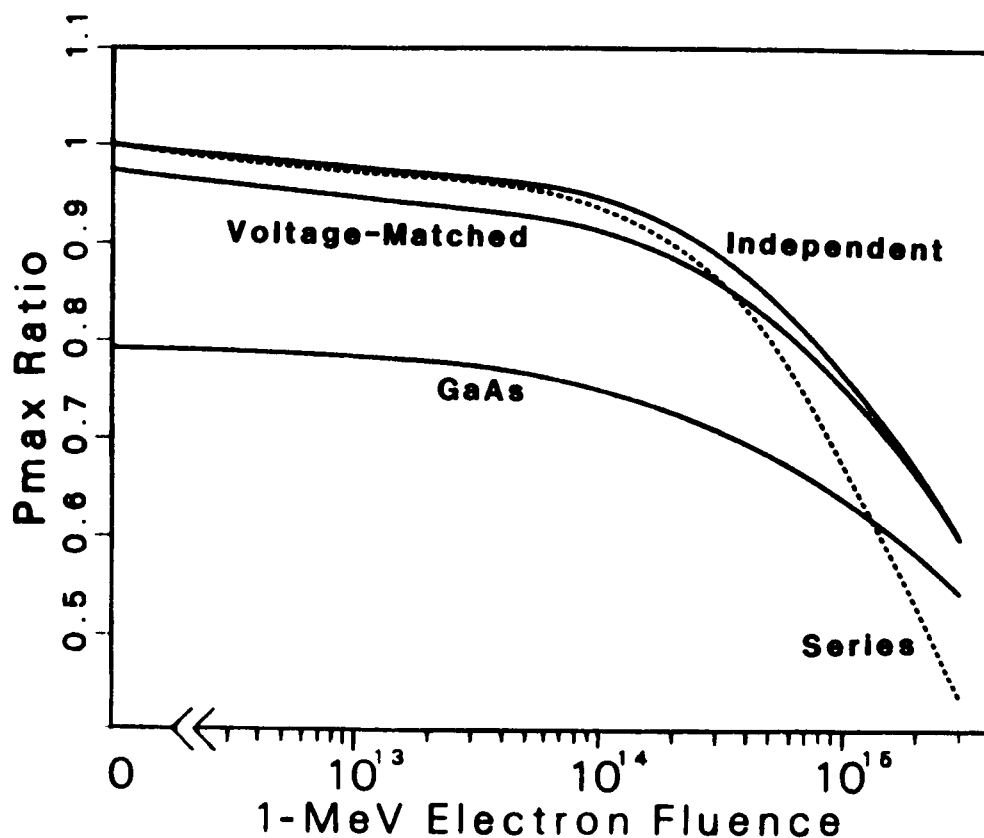


Figure 7. P_{max} at as a function of 1-MeV electron fluence for a GaAs concentrator cell and an AlGaAs/InGaAs tandem concentrator cell with a series, an independent, and a VM configuration (100X, AM0, 25°C). P_{max} is normalized with respect to the initial P_{max} of the AlGaAs/InGaAs tandem cell with an independent configuration. (The units of fluence are cm^{-2} .)

Radiation Resistance Studies of Amorphous Silicon Films*

James R. Woodyard and J. Scott Payson
Wayne State University

Summary

Hydrogenated amorphous silicon thin films were irradiated with 2.00 MeV helium ions using fluences ranging from $1\text{E}11$ to $1\text{E}15\text{ cm}^{-2}$. The films were characterized using photothermal deflection spectroscopy and photoconductivity measurements. The investigations show that the radiation introduces sub-band-gap states 1.35 eV below the conduction band and the states increase supralinearly with fluence. Photoconductivity measurements suggest the density of states above the Fermi energy is not changing drastically with fluence.

Introduction

Hydrogenated amorphous silicon alloy (a-Si) thin film photovoltaic devices have been identified for cell module design and development [ref. 1]. The attractiveness of a-Si alloy solar cells for space application is clearly documented and is based on the material's potential for high specific power density, stability and radiation resistance; investigations of a-Si cells show that the radiation resistance is 50 to 100 times more radiation resistant than c-Si, the damage anneals at about 430 K, and that the defect mechanism is probably nuclear knock-on of Si in the intrinsic layer [ref. 2-5]. The earlier radiation resistance studies of a-Si thin films is reviewed in reference 4.

Much work remains to be done to develop a basic understanding of the detailed mechanisms involved in radiation resistance, thermal properties, and stability of a-Si based cells. Additionally, the factors limiting cell efficiency must be explored, and a host of engineering and testing activities developed. The work reported herein is concerned with the radiation resistance of a-Si and is a continuation of investigations reported earlier.

This work shifts from the study of devices to thin films because of our need to develop techniques which complement device investigations. Examples of such techniques are photothermal deflection spectroscopy (PDS) and electron spin resonance which are powerful for characterizing thin films, but they are not useful for device structures. We irradiated the films with helium ions instead of protons because of the need to develop techniques with other bombarding ions in order to elucidate the defect generation mechanisms; electronic and nuclear cross section ratio are useful in the identification of defect generation mechanisms. PDS and photoconductivity measurements are carried out to determine the effect of 2.00 MeV helium radiation fluence on the sub-band-gap density of states.

* This work was supported under NASA contract NAG 3-833 and the Wayne State University Institute for Manufacturing Research.

Experimental

The a-Si films used in this study were fabricated at Energy Conversion Devices, Inc. using the plasma enhanced chemical vapor deposition method. The films were deposited at a temperature of 543 K on 25.8 cm² Corning 7059 glass substrates. The deposition was done at a pressure of 0.25 Torr with a R.F. power of 0.22 Watts cm⁻². Pure Silane was used as the feed gas and the films were deposited to a thickness of one micron. Twelve samples were cut to an area of 1.5 by 1.0 cm², mounted on a sample manipulator, and loaded into a target chamber. The target chamber was evacuated to about 1E-7 Torr. The samples were irradiated with a 2.00 MeV singly ionized helium beam which was 1.0 by 0.6 cm² in area and had a uniform current density. Ten samples were irradiated with two at each of the following fluences: 1E11, 1E12, 1E13, 1E14 and 1E15 cm⁻². Currents between 20 and 120 nanoamperes were used during the irradiations.

The sub-band-gap optical absorption was measured using PDS [ref. 6,7]. The pump source was a 650 W tungsten-halogen lamp chopped at 10 Hz. and coupled to the samples through a double monochromator. A thermopile detector was used to monitor the intensity. A laterally-sensitive photo-detector was used as a detector; the probe beam was Spectra-Physics model SP-117 laser. The signal was amplified using a Princeton Applied Research model 5301 lock-in amplifier, and the data were collected and averaged using a HP 71B computer. The entire optical system was enclosed in a plastic cabinet to reduce noise due to convection currents in the ambient air. The measurements were done at room temperature and the deflecting fluid was carbon tetrachloride. The PDS data were normalized by matching the spectra to absorption coefficients obtained by standard transmission and reflection techniques in the region where the absorption coefficient was between 1E3 and 1E4 cm⁻¹.

Figure 1 shows the sub-band-gap absorption coefficient plotted as a function of photon energy for fluences ranging from 1E11 cm⁻² to 1E15 cm⁻². There is no change in absorption between the virgin sample and the sample with a fluence of 1E11 cm⁻². The sub-band-gap absorption increases for fluences greater than or equal to 1E12 cm⁻². For fluences of 1E14 and 1E15 cm⁻², a pronounced shoulder appears in the sub-band-gap absorption for photon energy of approximately 1.4 eV. For lower photon energies, the spectra appear to merge. No change was observed in the above-band-gap absorption as a function of irradiation fluence.

The temperature dependence of the dark conductivity was measured on a virgin sample in the temperature range of 308 to 453 K; it was not possible to measure the irradiated samples as annealing of the defects occurs in this range. The measurements were done in a vacuum of 1E-6 Torr, with an applied bias of 100 v. in the co-planar configuration. Silver paint formed the contacts, and the sample was ohmic for applied biases between 0 and 150 v. The activation energy for the dark conductivity was found to be 0.75 eV.

The room temperature photoconductivity and dark conductivity were measured for all the samples. The measurements were made using white and red illumination sources. An ELH lamp with an infrared absorbing filter was used as the white illumination source; a red color glass filter, which passes wavelengths greater than 600 nm, was used for the red illumination source. Measurements of the photoconductivity as a function of intensity for white and red illumination were performed in air and vacuum in order to separate out any effects due to surface band bending. A vacuum of 1E-6

Torr and 2.0 mm silver paint contacts were employed. A 2.0 by 6.0 mm² area was scribed in the irradiated area to isolate it from the remainder of the sample area in order to eliminate the effect of the non-irradiated area on the measurements. The contacts were placed within the irradiated area.

The photoconductivity measurements with white and red illumination were essentially the same when corrected for the integrated photon flux. Figure 2 shows the dependence of the photoconductivity on optical density (OD) for red illumination. It is apparent that the photoconductivity decreases as the irradiation increases. Note however, that even though the PDS spectra show no change between the virgin sample and the sample with fluence of 1E11 cm⁻², there is a pronounced decrease in the photoconductivity for this fluence. It should also be emphasized that the slope of the photoconductivity versus intensity does not change with fluence, but the photoconductivity decreases monotonically with fluence. The dark conductivity as a function of fluence decreases only slightly with increasing fluence, from approximately 3E-10 to 1E-10 S/cm. For a fluence of 1E15 cm⁻² the photoconductivity is, for the largest intensity, only a factor of ten above the dark conductivity.

Discussion

The optical absorption coefficient is derived from a convolution of the states below the Fermi level and the states above the Fermi-level. In order to derive information about the density of states in the gap, simplifying assumptions must be made about the density of states. In accordance with earlier work [ref. 6,8,9], we have assumed that the matrix element for transitions from a localized state to an extended state is constant and independent of photon energy. For photon energies less than the band gap we assume that only transitions from occupied localized states below the Fermi level to unoccupied extended states in the conduction band are allowed. This implies that the conduction band tail is steeper than the valence band tail, and consequently transitions from extended valence band states to localized conduction band tail states are ignored. Under these conditions the optical absorption is given by [ref. 10]

$$\alpha = \frac{\text{const}}{\hbar\omega} \times \int N_v(E)N_c(E + \hbar\omega)dE \quad (1)$$

where $N_c(E)$ corresponds to the density of extended conduction band states, and $N_v(E)$ to the occupied localized states below the Fermi-level.

The optical absorption can be modeled with various functions. As shown previously [ref. 12], for high quality amorphous silicon the sub-band-gap absorption is relatively insensitive to the exact form of the deep states and these deep states may be modeled equally well using a peaked mid-gap distribution or an exponential distribution. We chose to model the absorption of the virgin sample with two exponentials. Under these conditions the optical absorption is given by

$$\alpha = \frac{K}{\hbar\omega} \int_0^{E_F + \hbar\omega} A(E + E')^{1/2} \left[N_v \exp \frac{(-E - E_g + \hbar\omega)}{E_{0v}} + N_m \exp \frac{(-E - E_g + \hbar\omega)}{E_1} \right] dE \quad (2)$$

where K is a constant. E_{0v} is the slope of the valence-band tail, E_1 is the slope of the mid-gap distribution, and E_g is the band gap. The form of the conduction band extended states is assumed to be parabolic with the form $A(E-E')^{1/2}$, with $E' = 0.15$ eV, as cited in references 11 and 12.

The effect of irradiation on the absorption is modelled by adding to equation 2 a peak in the density of states in the form used by Wronski et al. [ref. 8]. The excess absorption due to the irradiation is given by

$$\alpha' = \frac{K}{\hbar\omega} \int_0^{E_r + \hbar\omega} A(E - E')^{1/2} N_r \text{sech} \left[\frac{(-E - E_r + \hbar\omega)}{E_{r0}} \right] dE \quad (3)$$

where N_r is the peak value of the distribution, E_r is the position of the peak with respect to the conduction band, and E_{r0} is the width of the distribution. K , A and E_0 are the same as was defined earlier. This distribution was chosen in order to fit the absorption data by changing only the peak value of the distribution and not varying the width. The total absorption is then given by

$$\alpha_T = \alpha + \alpha' \quad (4)$$

It was found that if we model the density of states with a single exponential and a peaked mid-gap distribution that the width of the mid-gap distribution changed by more than a factor of two in going from the virgin sample to the most highly irradiated sample. It is found that a good fit to the data is achieved placing the peak in the density of states at 1.35 eV below the conduction band. The position of this peak in the density of states agrees well with the position of the defect peak reported by Jackson et al. [ref. 13], but disagrees with the work of Vanáček et al. [ref. 9] who places the defect peak at 1.0 eV below the conduction band. Since there was no change in the optical absorption for the sample irradiated with $1E11 \text{ cm}^{-2}$, we cannot derive any information about the increase in the density of states from absorption measurements.

The increase in the density of states due to the irradiation, n_r , is easily calculated from the integration of the $\text{sech}(x)$ in equation 2. This is plotted versus fluence in figure 3. For fluences larger than $1E13 \text{ cm}^{-2}$ the defect density follows a power law with exponent equal to ~ 1.5 . The optical absorption data were examined within the model proposed by Jackson et al. [ref. 6,13]. The defect density in this model is calculated by subtracting the Urbach edge absorption from the total absorption and integrating this excess absorption, α_{ex} . The number of defects is given by

$$N_s = 7.9 \times 10^{15} \int \alpha_{ex}(E) dE \quad (5)$$

This is also plotted in figure 3. Note that the number of defects does not obey the same functional form, and seems to be saturating at higher fluences. At low fluence the two models give the same results.

An indication of the disorder in the amorphous silicon alloy is seen in the slope of the Urbach edge [ref. 14]. We find that the slope of the Urbach edge increases only slightly from $E_0=0.055 \text{ eV}$ for low fluence to $E_0=0.070 \text{ eV}$ for a fluence of $1E15 \text{ cm}^{-2}$, as shown in figure 4. If these same data are examined within the model of Jackson et al. [ref. 6,13], the slope increases dramatically with fluence, reaching a value of $E_0=0.117 \text{ eV}$ for the maximum fluence. This would seem to indicate a substantial change in the structure of the material with fluence, whereas the slope as calculated in our model would indicate only slight changes.

In summary, our model indicates that the result of irradiation is to increase the density of states near $E_c - E = 1.35$ eV, and even for the highest fluence, indicates only a slight increase in the disorder of the system as revealed by the slope of the Urbach edge. The increase in the defect density follows a power law with exponent of ~ 1.5 . A comparison with Jackson's model [ref. 1,8], would indicate that the irradiation also increases the density of defects, but not in the same way, and that the disorder in the system, as modeled by the slope of the Urbach edge of the absorption coefficient, indicates a large change in the disorder with increasing fluence, as compared to a relatively small change for our model.

One may also obtain information about the gap-states in a-Si:H through analysis of the steady-state photoconductivity. Unlike the sub-band-gap optical absorption, the steady-state photoconductivity probes the region in the band-gap from the Fermi level towards the conduction band. It has been shown that if the trap distribution is exponential between the Fermi level and the trap quasi-Fermi level [ref. 15], the intensity dependence of the photoconductivity obeys the relation $\sigma_{ph} \propto I^\gamma$, where γ is determined by the logarithmic slope of the distribution of states. Referring to figure 2 we note that the value of γ for the virgin sample is 0.82. A fluence of $1E11$ cm $^{-2}$ results in γ increasing to 0.87. Increasing the fluence results in very little change in the logarithmic slope of the photoconductivity versus intensity curves. This indicates that the form of the trap distribution is not changing drastically with fluence. The values of the photoconductivity are, however, seen to decrease with fluence. Using the generalized Shockley-Read-Hall analysis of Taylor and Simmons [ref. 16], we note that the recombination rate for an arbitrary distribution of states in the band gap is proportional to the number of states that lie between the trap quasi-Fermi level for holes and the trap quasi-Fermi level for electrons, and for an n-type material most of the recombination takes place between the Fermi level and the trap quasi-Fermi level for holes. If we associate the increase in the optical absorption due to irradiation with an increase in the density of states below the Fermi level, then one would expect the photoconductivity to decrease dramatically for fluences of $1E13$ cm $^{-2}$ and above, which is indeed observed as shown in figure 4. However, note that even for a fluence of $1E11$ cm $^{-2}$, there is a decrease in the photoconductivity of almost a factor of 10. This might be due to an increase in the density of states above the Fermi level, which is not probed by the sub-band-gap absorption. One possible method to confirm this conjecture would be to fabricate n+-i- n+ devices and measure the space-charge-limited conduction as a function of fluence, which gives information about states in the gap from the Fermi level towards the conduction band [ref. 17,18]. We should like to note that the decrease in the photoconductivity with increasing fluence can not be due to the de-sensitization of the photoconductivity [ref. 19] when the Fermi level falls towards mid-gap, because the dark conductivity changed by less than a factor of ten with even the highest fluence. We therefore conclude that the increase in the sub-band-gap absorption is due to an increase in the density of states below the Fermi level and these states act as recombination centers causing an increase in recombination and thus a decrease in the photoconductivity.

Preliminary annealing measurements indicate that the thin film defects anneal at about the same temperature as devices. This fact along with the measurements reported herein suggests that studies of thin films are useful in the elucidation of the mechanisms which lead to the degradation of devices subjected to irradiation.

Conclusion

Our model indicates that irradiation increases the density of states near $E_c - E = 1.35$ eV and there is only a slight increase in the disorder of the system as revealed by the slope of the Urbach

edge. The increase in the sub-band-gap absorption is due to an increase in the density of states below the Fermi level and these states act as recombination centers causing an increase in recombination and thus a decrease in the photoconductivity. Thin film studies appear to be important for learning the basic aspects of device degradation.

References

- [1] Joseph Wise and Cosmo Baraona, *Proc. of the Space Photovoltaic Research and Technology Conference*, Nasa Conference Publication 2475, 1986, page 355.
- [2] Joseph J. Hanak, Art Myatt, Prem Math and James R. Woodyard, *Proc. of the Eighteenth IEEE Photovoltaic Specialists Conference*, 1985, page 1718.
- [3] J. J. Hanak, Englade Chen, C. Fulton, A. Myatt and J. R. Woodyard, *Proc. of the Space Photovoltaic Research and Technology Conference*, NASA Conference Publication 2475, 1986, page 99.
- [4] J. J. Hanak, E. Chen, Art Myatt and James R. Woodyard, *Proc. of the Nineteenth IEEE Photovoltaic Specialists Conference*, 1987, page 630.
- [5] James R. Woodyard and J.J. Hanak, "Amorphous Silicon Semiconductors-Pure and Hydrogenated", *Materials Research Society Symposia Proceedings*, Edited by D. Adler, A. Madan, Y. Hamakawa and M. Thompson, 1987, Volume 95, page 533.
- [6] N.M. Amer and W. B. Jackson, *Appl. Phys. A.* **32**, 141 (1983).
- [7] J. S. Payson and S. Guha, *Phys. Rev. B* **32**, 1326 (1985).
- [8] C. R. Wronski, B Abeles, T.Tiedje and G. B. Cody, *Solid State Commun.* **44** 1423 (1982).
- [9] M. Vanecek, J. Kocka, J. Stuchlik, Z. Kozisek, O. Strika, and A. Triska, *Sol. Energy Mater.* **8** 411 (1983).
- [10] N. F. Mott and E. A. Davis, *Electronic Processes in Non-Crystalline Solids* (Clarendon, Oxford, 1979).
- [11] C.-Y. Huang, S. Guha, and S. J. Hudgens, *Phys. Rev. B* **27**, 7460 (1983).
- [12] W. E. Spear, D. Allan, P. G. LeComber and A. Ghaith, *J. Non-Cryst. Solids* **35-36**, 357 (1980).
- [13] W. B. Jackson and N. M. Amer, *Phys. Rev. B* **25**, 5559 (1982).
- [14] G. D. Cody, T. Tiedje, B. Abeles, B. Brooks and Y. Goldstein, *Phys. Rev. Lett.* **47**, 1480 (1981).
- [15] A. Rose, *Concepts in Photoconductivity and Allied Problems* (Krieger, New York, 1978).
- [16] J. G. Simmons and G.W. Taylor, *Phys. Rev. B* **4**, 502 (1971).
- [17] W. den Boer, *J. Physique* **42**, C4, 451 (1981).
- [18] K. D. Mackenzie, P. G. LeComber, and W. E. Spear, *Phil. Mag.* **B 46**, 377 (1982).
- [19] M. Hack, S. Guha, and M. Shur, *Appl. Phys. Lett.* **45**, 467 (1984).

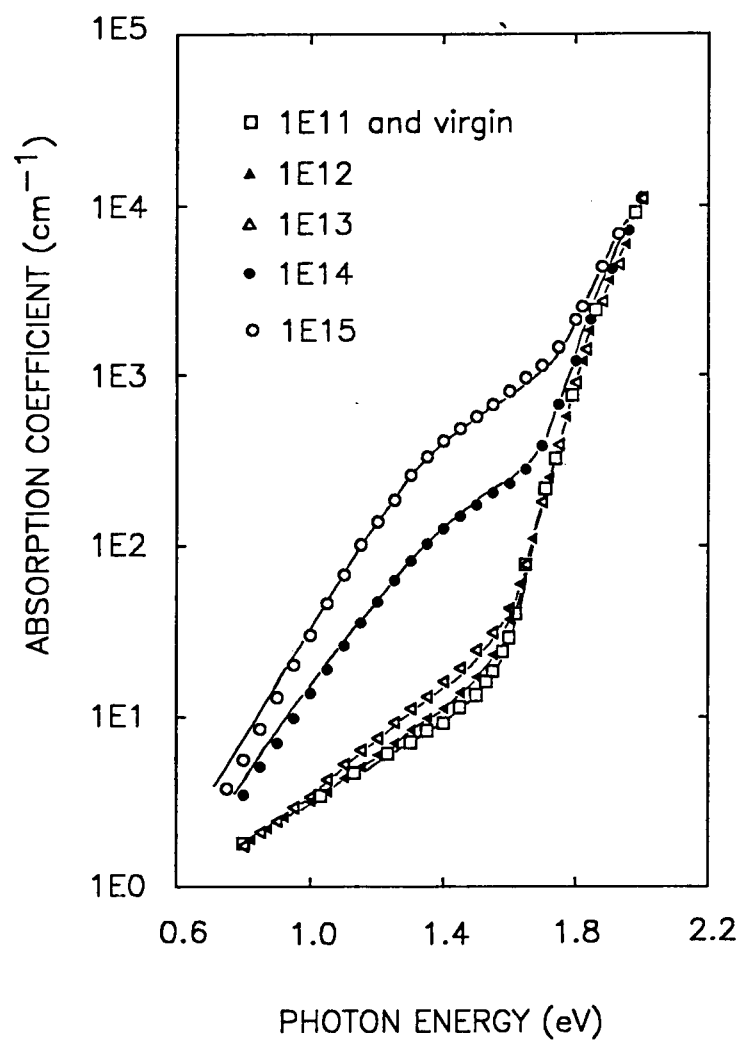


Figure 1. The optical absorption coefficient as a function of incident photon energy for various fluence, where the open circles correspond to a fluence of $1 \times 10^{15} \text{ cm}^{-2}$, closed circles $1 \times 10^{14} \text{ cm}^{-2}$, open triangles $1 \times 10^{13} \text{ cm}^{-2}$, closed triangles $1 \times 10^{12} \text{ cm}^{-2}$, and the open squares $1 \times 10^{11} \text{ cm}^{-2}$ and the virgin sample. The solid lines are absorption coefficients calculated from the density of states model.

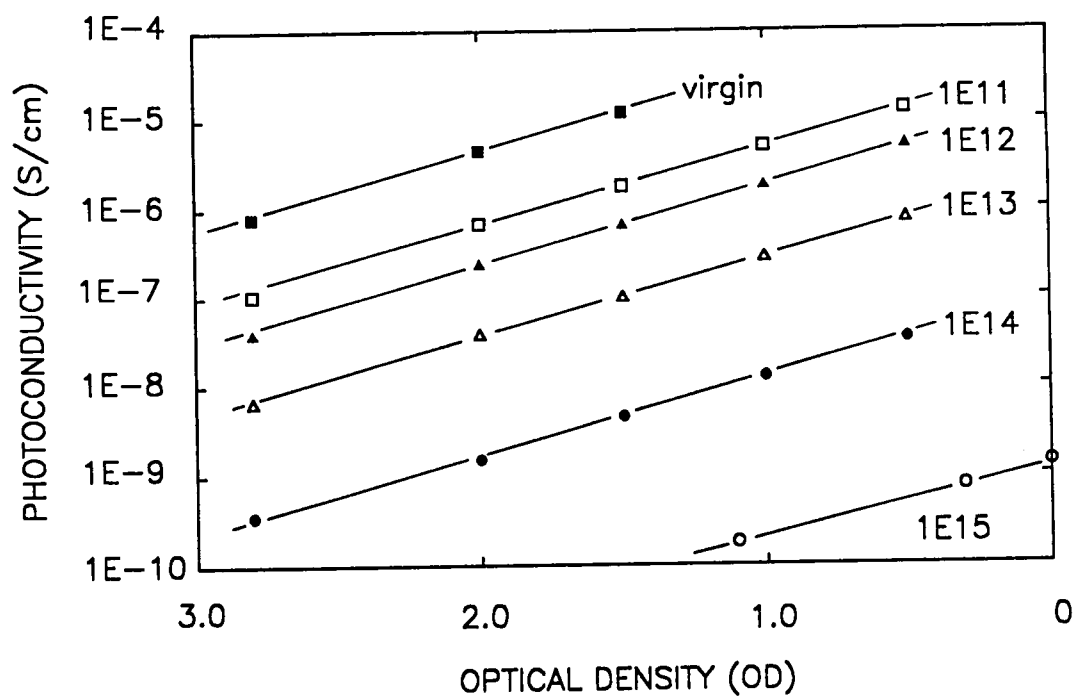


Figure 2. The steady-state photoconductivity as a function of intensity for various fluences ranging from the open circles-- $1\text{E}15\text{ cm}^{-2}$, closed circles-- $1\text{E}14\text{ cm}^{-2}$, the open triangles-- $1\text{E}13\text{ cm}^{-2}$, the closed triangles-- $1\text{E}12\text{ cm}^{-2}$, the open squares-- $1\text{E}11\text{ cm}^{-2}$, and the closed squares corresponding to the virgin sample.

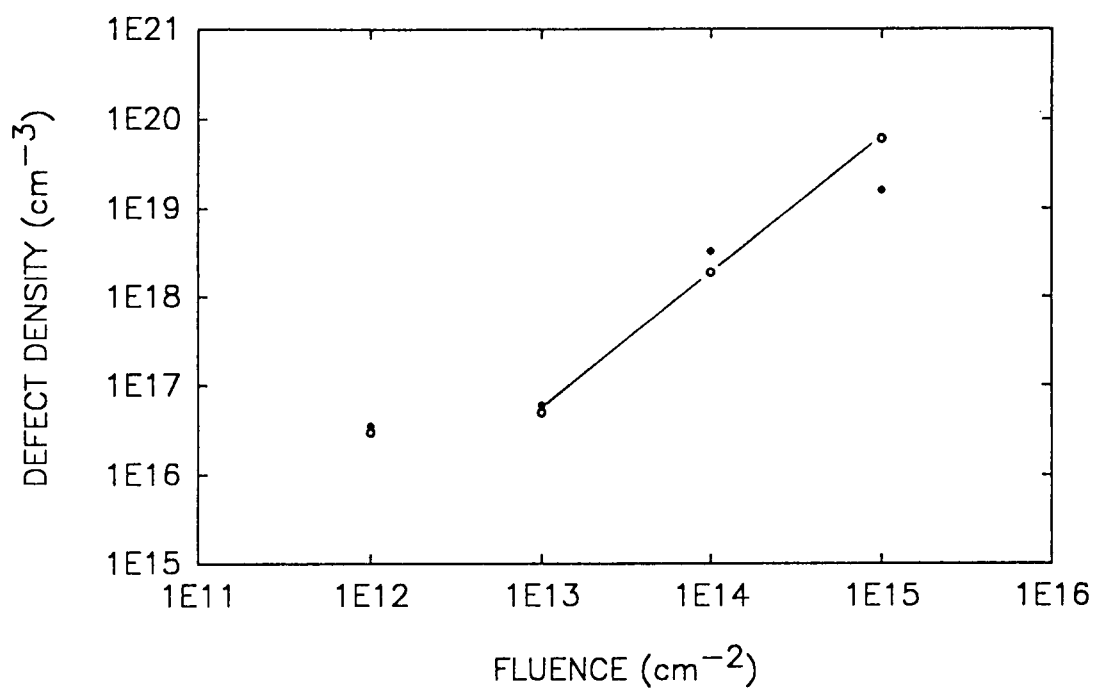


Figure 3. The ion-induced defects versus ion fluence. The open circles were calculated using our model, whereas the closed circles were calculated using the model of Jackson et al. (ref. 6,13).

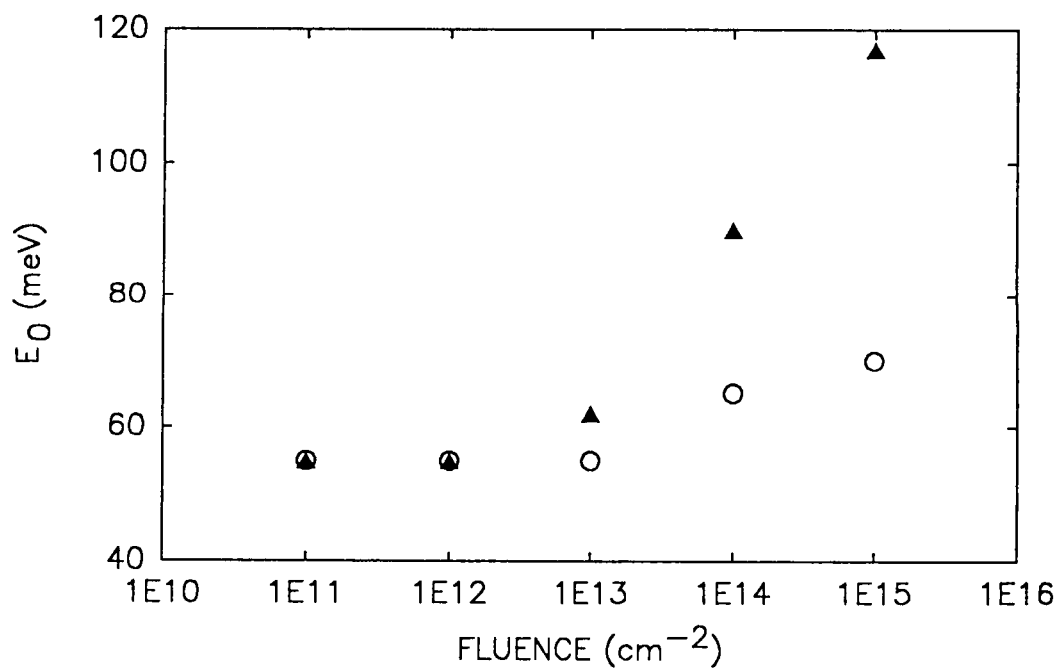


Figure 4. The logarithmic slope of the Urbach edge of the density of states as calculated using our model (open circles) and the model of Jackson et al. (ref. 6,13), (diamonds).

Workshop Summaries

PRECEDING PAGE BLANK NOT FILMED

Workshop Summary Indium Phosphide Cells

Mark B. Spitzer
Kopin Corporation
Taunton, MA

Stan M. Vernon
Spire Corporation
Bedford, MA

The InP workshop considered first the identification of research priorities in this area. The consensus of the group is that the most important goal at this time is the attainment of an InP cell with an AM0 efficiency of 20%. This was considered to be a reasonable goal, based on the modelling presented at this conference, which indicates that an efficiency of 22% is possible with present designs. Although this efficiency goal is the most important priority, the attainment of cells with larger area was also considered to be important.

The device modelling and characterization were discussed. Better minority carrier data are needed for more accurate modelling. In particular, some disagreement is noted regarding the actual value of front surface recombination velocity. While reports in the literature suggest values of the order of 10^3 to 10^4 cm/sec, modelling of actual devices suggests higher values (10^6 to 10^7 cm/sec). The InP solar cell, of course, is covered by an AR coating and contacts, and may not be strictly equivalent to the free surfaces discussed in the literature. The AR coated and metallized surface may indeed have a high surface recombination velocity. Better data for the modelling is important to obtaining an understanding of this question. The workshop also considered the related question of whether surface passivation is necessary for InP. It was the consensus of the group that the available data is insufficient to answer this question.

The subject of n-on-p versus p-on-n structures was addressed. It was noted that p-on-n cells have yielded relatively high performance on early devices and that modelling predicts a high efficiency. The workshop participants agreed that it is too soon to make a determination in this area, and that more radiation testing is necessary for both types of cells.

It was noted that unlike GaAs, fairly good cells can be formed from bulk wafers, using either ion implantation or diffusion for junction formation. This surprising attribute may have certain advantages in production; however, it was generally agreed that the most efficient cells would probably be formed by epitaxy.

Concentrator cells appear to be an interesting application of the InP technology, since the high substrate cost may be partially offset by the concentration factor. The operating temperature may be high enough to permit continuous annealing. In addition, if light-induced annealing is effective, the concentrated light may also provide a further advantage. It will be necessary to investigate the radiation resistance of the dopant concentrations required for highly efficient concentrators.

The use of larger cell areas and alternative substrates requires further research. Approaches to reduce the cost of the substrates are required. Possible approaches include heteroepitaxial deposition

of InP on GaAs, on GaAs-on-Si or directly on Si, or on Ge. Removable substrate approaches such as CLEFT are also candidates.

It is the consensus of the group that it is premature to consider manufacturing issues; however, stability and reliability of the contacts should be addressed. It is recommended that NASA organize an InP solar cell workshop that would involve InP specialists from other fields; this might provide the community with ideas and experience from which we can benefit.

Workshop Summary New Cells--Barriers to Use

Gene Ralph, Chairman
Hughes Aircraft Company

R. E. Hart, Jr., Liaison
NASA Lewis Research Center

The purpose of this workshop was to examine the spectrum of space solar cells that are presently known to assess their level of technology readiness, and to identify those steps that must be undertaken before a given cell type would be considered for a flight program. A summary of the workshop conclusions has been prepared in bullet format, and is given on the following pages. At present, only three cell types are considered to be ready for actual flight programs. All others are in need of continued development and/or space performance verification and, most importantly, must have their producibility established through a space qualified manufacturing demonstration program.

The workshop also recommended that a central database be established which would allow rapid and accurate assessment of the current status of any space cell type by potential users, and that such a database should be updated on a regular basis at each succeeding SPRAT meeting. It was also agreed that more user feedback is needed to the R&D community to help guide the direction and scope of space photovoltaic R&D activities, and to help assure that resources will be applied where they can have maximum impact.

0 WHAT CELLS!

SILICON:	THICK *
	THIN *
GaAs:	THICK *
	THIN
	ULTRA-THIN
GaAs/Ge:	THIN
/Si:	THIN
AlGaAs/GaAs	
InP:	THICK
	THIN
CuInSe ₂ /GaAs	
CuInSe ₂	
SILICON	
TRIPLE J.	
VERTICAL J.	

* PRODUCTION READY

0 WHAT CRITERIA USED TO SELECT CELLS?

EFFICIENCY
COST
WEIGHT
RADIATION DAMAGE
RELIABILITY
MANUFACTURABILITY

0 WHERE DOES TECHNICAL DATA COME FROM?

LABORATORY TESTS
LITERATURE/REPORTS
MANUFACTURES INFORMATION
MINI QUALIFICATION TESTS
FULL QUAL.

0 WOULD CENTRAL DATABASE BE USEFUL?

YES, A SPREADSHEET COULD LIST ALL CELL PROPERTIES

MUST BE UPDATED REGULARLY!

MUST BE UPDATED REGULARLY!

WARNING: IT COULD BE LIMITING!

SPRAT WOULD BE GOOD PLACE TO UPDATE

0 WHAT PREJUDICES EXIST?

USERS CONSERVATIVE? NOT EXCESSIVE!

SOME USERS MORE WILLING TO USE NEW TECHNOLOGY

USUALLY FAIR TRADE-OFFS PERFORMED

0 OTHER BARRIERS SUGGESTED

MORE USER FEEDBACK NEEDED (CELL NEEDS)

MORE TRADE-OFF INFORMATION NEEDED

NEED PROGRAMS TO COMMIT TO NEW TECHNOLOGY

NEED GOVERNMENT MANTECH SPONSORSHIP - NASA AS WELL AS DOD

THIS IS IMPORTANT

NEED MORE CONSISTANT FUNDING OF NEW TECHNOLOGY THAT IS PROMISING.

Workshop Summary Ultralightweight (ULW) Photovoltaic Technology

Paul M. Stella
*Jet Propulsion Laboratory
California Institute of Technology
Pasadena, California*

The initial activity of the ULW Photovoltaic Technology Workshop was to assess the composition of the workshop attendees with respect to technology background. Approximately 20% had an array technology background, with the remainder involved in cell development or system evaluation. The small number of array technologists was felt to limit the scope of the discussions since the majority were not familiar with array details. However, the combination of cell developers' optimism and array developers' pragmatism created a useful interaction. In order to facilitate the subsequent discussions a value of 150 W/kG was set as a lower threshold for ULW technology. This value is actually within range of the present APSA development and represents a nearly 5-fold improvement over conventional array technology.

Applications of ULW Technology

Potential applications for ULW arrays were discussed and a set of generic mission types were proposed. These fell into a number of categories relating to overall power system levels. Figure 1 lists the various types of missions. Most applications fall into the 3-25 kW power level with low mass density clearly beneficial for very high power levels. The interplanetary power levels listed refer to both the power at the mission objective (moderate-low) and power at earth required (high) to achieve the moderate power levels at great solar distances. Electric propulsion has always matched well with lightweight technologies. The low thrust propulsion system benefits greatly from reduced spacecraft mass through decreased flight times and increased payload allowance.

Geosynchronous and interplanetary spacecraft typically have strict mass limitations due to the high energy requirement of achieving operational orbit. A novel potential application includes military spacecraft where additional stowed ULW arrays could be included which would deploy to replace those damaged by natural or manmade occurrences. Lightsats are an area where ULW arrays will enable higher power levels than can be obtained from body mounted arrays. Since lightsats are expected to be small in overall dimensions a compactly packaged deployable array design will also be required. Planetary/lunar base power systems will need to be low mass due to the high propulsion energy levels required for achieving rendezvous. In view of their large power levels they too, will need to package into small volumes for the transit. A new application, enabled by very low mass and small package volume, would be as emergency power supplies either at low power levels for individuals, or high power levels for spacecraft or bases. Photovoltaic power systems have demonstrated long term storage capabilities and could be unfurled quickly to provide power if other power sources failed.

ULW Array Specific Power Goals

Specific power goals were proposed for three time periods, near term (1990), mid term (1994-1998), and far term (2005-2010+). These are shown in figure 2. Although not a rigorous analysis, an attempt was made to mitigate the optimism of the cell technologists somewhat by factoring in an appreciation of the difficult transition to array applications. Even so it is to be appreciated that realization of the following goals is based on the availability of reasonable resources. Comments at this SPRAT conference however, indicated that future funding for PV technology is likely to decrease and fall short of needs resulting in the delay or derailment of these advances. The near term goal is based on the present APSA array design, allowing for some additional optimization of the thin silicon cell. As such it represents the upper limit of LW (lightweight) technology and the lower bound of ULW array technology. By the mid nineties it is possible that some of the impressive performance gains demonstrated for research cells may be translated to pilot line performance and allow for initial array integration. It is anticipated that the structure for such an array would be based on the present APSA configuration. For the period beyond the year 2005, the ULW array design would represent a combination of cell advances (thin, with efficiencies up to 25%) and advances in structure design. The contribution of cell blanket specific mass and the array structure mass need to be balanced in order to fully realize ULW benefits/performance.

ULW Array Requirements

Although the BOL (beginning-of-life) specific performance (W/kG) is a useful parameter for guiding advanced array technology development, a number of other features can be of equal or greater importance depending on the specific mission. Consequently many concerns must be answered before an advanced array design can actually be considered for an application. The workshop addressed a number of these. They include:

- a. Cost- Competitive cost is always key, but must be viewed at the system level.
- b. Reliability/Predictability- High reliability is difficult to define but a necessary attribute. Of equal importance is the ability to predict array behavior under environmental exposure. This implies a high level of manufacturing control and the existence of a data base sufficient to support predictive analysis.
- c. EOL performance- The end-of-life performance generally establishes the initial power system design. Consequently, although BOL specific performance is useful for goal setting it is critical to maintain high specific power at the mission end, particularly for high radiation environments.
- d. Efficiency- In some situations array area limitations will create a need for maximum cell efficiencies.
- e. Ruggedness- Lightweight arrays should not become so fragile as to require extreme handling conditions.

f. Array/Spacecraft dynamics- A concern arose that ULW arrays may become so flexible as to adversely impact spacecraft maneuvering and pointing. Array stiffness and modes must be compatible with spacecraft requirements.

g. Stowed volume- For large power systems in particular, limited launch vehicle volume will put a premium on minimizing array stowed volume.

Maximum Array Power/Size Limitations

The question of what the maximum size of ULW arrays might be was briefly discussed. It was clear that in fact, no such size limitation has been demonstrated. Size can obviously be increased by increasing wing area and also by increasing the actual number of wings utilized. In practice, pragmatic reasons will define a maximum usable size for a particular application. For example mass, available launch volume, solar cell production capacity, structural stiffness and strength, spacecraft dynamics, fields of view requirements, and wiring harness conduction losses, are a few of the more obvious limitations that can exist for any specific mission. At this point in time array technology is in general far from pushing these limits. Examining existing or planned array power systems can only indicate a lower limit for an array maximum power level. For space applications, Skylab was designed to provide 23 kW (two wings providing 12.5 kW, and four wings providing 10.5 kW), and the space station is presently planned for approximately 200 kW. For lunar/planetary bases terrestrial experience may be instructive. In such a case then there exists a number of solar photovoltaic systems providing power in the megawatt level. Although these existing large power systems do not use ULW technology they should provide a guide to what might be possible inasmuch as fundamental limits have not been identified.

Thin Film Cell Technology

A key element in the development of ULW array technology is the solar cell. As the active component in the system, improvements in the cell, particularly conversion efficiency, impact the array performance considerably. At present a number of thin film cell technologies exist in varying states of development. It is premature to select any one device as a preferred cell for development. In fact, it is not clear that "thin film" can be restricted to non single crystal materials. Although present results show single crystal devices to be somewhat more massive and of greater efficiency than other materials, this has not been proven to be a fundamental difference. Due to the diverse cell material experiences of the members of the workshop, there was no real consensus on preferred materials. The III-V family, CuInSe₂, amorphous silicon, and combinations of these, were all considered viable components for future ULW arrays. It was felt that a device should demonstrate a minimum of 5% efficiency over the near term, with negligible radiation sensitivity, to be considered competitive. This value was chosen based on the present EOL performance of some silicon arrays. For true competitiveness with non photovoltaic power sources a value of 10% minimum efficiency was considered more reasonable. Even higher efficiencies are certainly desirable, but it was shown earlier in the conference presentation session that a thin film cell with 10% efficiency could yield up to 200 W/kg on an APSA type array. Beyond low mass and acceptable efficiency, other factors that will govern use at the panel level will require involvement of the array manufacturers. This will allow development of assembly and repair procedures and a performance and environmental

behavior data base. This in turn will require that the cell manufacturer have a well established manufacturing process and be in a position to supply a few thousands of cells for evaluation.

Conclusions

Figure 3 summarizes the conclusions of the Ultralightweight Photovoltaic Technology Workshop session.

POTENTIAL APPLICATIONS - ULW ARRAYS

	POWER LEVEL			
	LOW <1 kW	MED. (1-3 kW)	HIGH (3-25 kW)	VERY HIGH (25-100+ kW)
ELECTRIC PROPULSION		X	X	X
GEOSYNCHRONOUS (VARIOUS)			X	X
INTERPLANETARY		X	X	
MILITARY (REPLACEABLE)		X	X	
LIGHT SATS	X			
MARTIAN/LUNAR BASE			X	X
EMERGENCY POWER (ASTRONAUT/SATELLITE/BASE)	X	X	X	X

Figure 1.

ULW ARRAY SPECIFIC POWER GOALS*

• NEAR TERM	1990	150 W/kg	APSA
• MID TERM	1994 - 1998	300 W/kg	ADVANCED CELLS/ APSA STRUCTURE MOD.
• FAR TERM	2005 - 2010*	500 W/kg	ADVANCED THIN FILM CELLS ADVANCED STRUCTURE

- * MED. TO HIGH POWER ARRAYS WITH MULTIPLE APPLICATIONS

Figure 2.

CONCLUSIONS

- ULW PHOTOVOLTAIC ARRAY TECHNOLOGY BEST ADDRESSED AT SYSTEM LEVEL
- APSA CAPABLE OF AT LEAST 50% IMPROVEMENT OVER 130W/kg
- LOW MASS IS ONLY ONE OF MANY IMPORTANT FACTORS
- MANY ADVANCED AND PROMISING CELL CANDIDATES
- ULW ARRAY CONCEPTS WILL REQUIRE NEW GENERATION OF STRUCTURES (NUTS & BOLTS)
- FUNDING STABILITY FOR REQUIRED ULW CELL DEVELOPMENT QUESTIONABLE
- FUNDING FOR TRANSFER OF CELL TO ARRAY NOT IDENTIFIED (AMOUNT/SOURCE)

Figure 3.

Workshop Summary Space Concentrator Photovoltaic Technology

James M. Gee
Sandia National Laboratories
Albuquerque, NM

Robert W. Francis
The Aerospace Corporation
Los Angeles, CA

This report summarizes the discussions held in a workshop on space photovoltaic (PV) concentrators that was organized as part of the 9th Space PV Research and Technology Conference. Approximately 20 people attended the workshop. The purpose of the workshop was to assess the status of space PV concentrator technology in order to identify critical issues and future prospects for the technology. An oral report of this workshop summary was presented at the conference; the vu-graphs from this report are enclosed as Appendix A.

Advantages of Space PV Concentrators

The first item discussed in the workshop was identification of possible advantages for using concentrators in space. For commercial space power applications, the appropriate technological parameters are areal and specific power densities (W/m^2 and W/kg). It was felt that a reasonable near-term (<2 years) goal is $250 \text{ W}/\text{m}^2$ and $100 \text{ W}/\text{kg}$, while a reasonable far term goal is $300 \text{ W}/\text{m}^2$ and $150 \text{ W}/\text{kg}$. There was a discussion on whether a light-weight concentrator could maintain an acceptable rigidity due to alignment requirements for the individual concentrator elements. Most of the participants felt that due to the structural requirements, concentrators would never be able to compete with the ultra-light-weight flat-plate arrays that were discussed in a separate workshop. The relatively modest specific power density goal suggests that concentrators will need significant mission-specific advantages in other areas in order to be considered.

Two significant advantages were identified for space PV concentrators. The first advantage of a concentrator is that it allows use of advanced high-efficiency solar cells sooner. Concentrators were felt to be a first application area for such advanced cells as multi-bandgap and InP solar cells due to the high cost of such cells and the limited production quantities that would initially be available. Also, the superior radiation shielding of concentrators may allow use of radiation-sensitive advanced cells. For example, both low- and high-resistivity silicon cells have been developed under terrestrial solar energy programs that have achieved much higher efficiencies than the designs typically used for space applications. However, the high-efficiency silicon solar cells are also known to be more sensitive to radiation than the conventional space silicon solar cells. Some of the workshop participants felt that concentrators have an areal power density advantage relative to flat-plate arrays in the near term due to their ability to use the advanced high-efficiency devices sooner.

The second advantage for concentrators, which was alluded to above, is the superior radiation tolerance characteristics of a concentrator array. The mass of the concentrator optics provides shielding to the solar cell. Because cell area is reduced by the geometric concentration ratio, more

shielding may be applied around each cell with less weight penalty than in a flat plate array. Note, however, there still remains a mass versus shielding tradeoff. Finally, it was noted that concentrators allow for use of in-situ annealing for high-radiation missions due to the higher intensity illumination and to the higher operating temperatures. Due to the superior radiation tolerance characteristics and to a limited acceptance angle, concentrators are particularly attractive for military applications requiring survivability to various threats. Some of the workshop participants felt that documentation of the shielding characteristics to natural radiation would be helpful for array designers who would like to consider concentrators.

Technological Issues for Space PV Concentrators

Several technological issues regarding implementation of PV concentrators were discussed. Two items that are always discussed regarding concentrators are the requirements for 2-axis tracking and for array pointing accuracy. While none of the participants were directly involved with satellite structural engineering, those who had discussed these issues with satellite system designers were informed that 2-axis tracking and pointing accuracies of better than 1° are available with present technologies. It was also mentioned that 1-axis may be easier to implement than 2-axis tracking.

While tracking is well understood, the pointing accuracy requirement is more of a concern for fabrication of the array due to the resultant rigidity requirements. The rigidity requirements are due to the alignment tolerance required for the individual concentrator elements on the array. A large array may require a greater rigidity in order to maintain alignment over the greater area. A large array may also be more difficult to move due to a larger moment of inertia. In terrestrial concentrators, this problem is alleviated by dividing an array field into smaller units (typically 1 to 10 kW) that are individually tracked. The same technique may be possible with space arrays for some missions.

Many of the discussions were about structural requirements and deployment. From the presentation on the PV power for the space station, it is clear that the SAFE experiment's demonstration of a flexible-blanket technology was very influential in the decisions regarding the space station array design. It was suggested that a similar experiment for concentrators may alleviate many of the concerns of array designers.

Also briefly discussed was the relative advantages of using a central-receiver approach (reflective dish collector with active cooling) versus a distributed approach with many small collectors. The biggest advantage of using a distributed approach is thermal management - passive cooling may be used with distributed collectors since the power to be dissipated at each PV receiver is much smaller. The biggest advantage for using a central receiver is that much more sophisticated receivers may be used since they are fewer in number. For example, the receiver may use a beam-splitter for higher efficiencies and the active cooling may be controllable to provide short annealing periods ("bursts").

One of the most critical technological issues regarding concentrators involves reliability. It was pointed out that the increased ΔT , particularly if in-situ annealing is desired, may lead to long-term reliability problems. The durability of optical materials to the space environment is also unknown and needs to be addressed before concentrators can be fielded. It should also be noted that the optical performance of concentrators is probably more sensitive to radiation than the optical performance of coverglasses, since only the the specular component is optically concentrated. Degradation that

increases the diffuse relative to the specular component of transmissivity of a coverglass does not affect flat-plate arrays since these cells have a field-of-view of 180°.

Summary

The workshop felt that due to the increased complexity and relatively modest specific power densities available with PV concentrators, they would only be used for specific missions. These missions include high radiation orbits (e.g. orbital transfer vehicles), military missions with survivability requirements, and missions requiring high areal power densities. Possible cost advantages (\$/W) were not discussed. It should be noted that for terrestrial solar energy, concentrators are less expensive than flat-plate arrays for utility-scale (>1MW) applications in high-insolation areas.

Specific recommendations for the workshop include the following:

1. consider IR rejection filters to reduce the thermal load,
2. document the radiation shielding that is available with published concentrator geometries,
3. research and document the in-situ annealing characteristics of advanced III-V concentrator cells,
4. investigate and document the durability of concentrator materials, and
5. initiate a structural deployment experiment similar to SAFE to demonstrate the deployment of a concentrator structure.

Items 2 and 3 are necessary since these are areas where concentrators are felt to have an advantage, while items 4 and 5 are necessary in order to demonstrate the flight-readiness of concentrators.

Appendix A

SPACE CONCENTRATOR PV TECHNOLOGY

SUMMARY

**JAMES GEE
SANDIA NATIONAL LABS**

**ROBERT FRANCIS
AEROSPACE CORPORATION**

QUESTIONS FOR THE SPRAT WORKSHOP ON SPACE CONCENTRATOR PHOTOVOLTAIC TECHNOLOGY

1. WHAT ARE THE ADVANTAGES AND DISADVANTAGES OF REFLECTIVE AND REFRACTIVE CONCENTRATORS IN SPACE RELATED TO ONE ANOTHER AND TO FLAT PLATE ARRAYS?
2. WHAT ARE THE SPECIFIC POWER LIMITS OF CONCENTRATOR ARRAYS?
3. WHAT ARE THE TOTAL POWER LIMITS OF CONCENTRATOR ARRAYS?
4. WHAT ARE THE MOST PROMISING APPLICATIONS OF CONCENTRATOR ARRAYS IN SPACE?
5. WHAT ARE THE CRITICAL ISSUES IN CONCENTRATOR TECHNOLOGY -
 CELLS?
 OPTICAL ELEMENTS?
 THERMAL MANAGEMENT?
 DEPLOYMENT STRUCTURES?
6. IS POINTING ACCURACY REALLY A PROBLEM?
7. WHAT ABOUT DISTRIBUTED ELEMENT ARRAYS (i.e., THE MCC) VERSUS DENSE ARRAYS WITH LARGE AREA, HIGH POWER CONCENTRATORS AND ACTIVE COOLING?

• PERFORMANCE GOALS

	W/kg	W/m ²	η (%)
NEAR TERM (<2 YRS)	100	250	22
FUTURE	150	300	26

• PRIMARY ADVANTAGES

- FIRST APPLICATION FOR ADVANCED CELLS
 - COST
 - QUANTITY
 - PROVIDES PROTECTION FOR SENSITIVE CELLS
- RADIATION SHIELDING/SURVIVABILITY
 - NATURAL & ENHANCED RADIATION
 - ALLOWS INCREASED SHIELDING W/LESS WEIGHT PENALTY VS. FP.
 - SHIELDING VS. WEIGHT TRADEOFF
 - IN-SITU ANNEALING

- **CRITICAL ISSUES**
 - DURABILITY OF OPTICAL ELEMENTS
 - RIGIDITY OF THE PANEL VS. SIZE
 - INCREASED ΔT HAS RELIABILITY CONCERNS
 - DISTRIBUTED VS. CONTROL RECEIVER - THERMAL MGMT.
- **NON-ISSUES**
 - 2-AXIS TRACKING
 - ARRAY POINTING ACCURACY"
- **HORSE RACE - NEVER A CLEAR CHOICE - ALWAYS MISSION SPECIFIC**
- **MOST LIKELY APPLICATION AREAS:**
 - HIGH RADIATION MISSIONS
 - ENHANCED SURVIVABILITY
 - HIGH AREAL POWER DENSIBLY AVAILABLE SOONER THAN FP
- **RECOMMENDATIONS:**
 - IR REJECTION FILTERS
 - DOCUMENT RADIATION SHIELDING OF CONCENTRATORS
 - DURABILITY OF CONCENTRATOR MATERIALS - ASAP

Workshop Summary Space Environmental Effects

**R. L. Statler, Chairman
Naval Research Laboratory
Washington, DC 20375-5000**

The Workshop consisted of approximately 40 people. The discussion was guided by a list of topics, which are grouped in the following format along with the collective thinking of the Workshop participants.

Solar Cell Radiation Damage Data Base

On the question of a radiation damage equivalence for gallium arsenide cells, a main source for radiation damage experimental data can be found in papers published by JPL authors, who have studied GaAlAs/GaAs solar cells made by ASEC on a Manufacturing Technology Program. Proton damage data exists at some energies for both unidirectional and omnidirectional monoenergetic proton radiation. There was expressed an urgent need for electron damage data over the range of 0.5 to 10 MeV electrons.

The status of a radiation damage data base for other advanced cells elicited the comments that thin silicon should be studied in more detail, and the belief that thin GaAs will have a different structure, and therefore a different damage equivalence, than the thick GaAlAs/GaAs cells for which data does exist. The new composite structure of GaAs/Ge should begin to be examined in 1989, as the cells become more available and their processing reaches a greater maturity of development. Also, InP solar cells should be continually studied as the cells are developed, and the structure is modified, because of the very unique radiation hardness of this material.

It is commonly believed that in 1989, amorphous silicon cells could be compared with single crystal space cells for both electron and proton damage coefficients.

An important point to be made in almost all these studies is that the data be made publicly accessible as, for example, in the manner of the JPL Solar Cell Radiation Handbook.

Radiation Damage Annealing

The point was emphasized that radiation damage annealing is of very great experimental interest from the viewpoint of deducing physical mechanism behavior. However, the concept of using annealing as an engineering accomplishment on solar arrays in space is recognized as introducing possible complexities and weight or cost factors which may not be acceptable to a space mission manager. Of course, the AFWAL solar cell experiment for the CRRES spacecraft will contain active annealing experiments which will yield first-time valuable information on space annealing effects in solar cells.

It is an obvious statement that photon and thermal annealing studies be made a part of any serious InP solar cell development, in view of the already published data on photon annealing of Japanese n-on-p InP cells.

Thermal Management of Solar Arrays

This topic can be briefly summarized by stating that adequate technology and thermal modeling exists for solar array design, and no new interest was indicated for exploring more advanced technologies. The present solar solar cell technology would normally be directed to the use of Back Surface Transmitting cells for applications such as the Space Station baseline solar array with Kapton blankets, and the use of Back Surface Reflector cells on rigid panels.

The chart in Table 1 summarizes the state of the amount of available data of various kinds for several types of present day solar cells.

Other Space Environmental Effects

Atomic oxygen is a materials-damaging factor which is most significant at low earth orbit (LEO). For example, a recovered Solar Max spacecraft showed erosion of the silver interconnects between cells. The simulation of atomic oxygen in test chambers leaves much uncertainty about the actual concentrations to be encountered in space. In fact, the ground testing in some cases may be too severe. Nevertheless, the Space Station solar array blanket will be coated with an organic material to protect it against atomic oxygen.

Space plasma and corona effects have received attention from the NASA centers and from the AFWAL. A flight experiment by the AFWAL, AFGL, and JPL to measure and study corona effects is awaiting launch in June 1990. NASA Lewis Research Center has recommended limiting high voltage on solar array terminals to 160 volts to eliminate corona discharge. NASA Goddard Space Flight Center requires the use of conductive coated coverglass on solar arrays of plasma-experiment spacecraft. They are investigating better interconnecting techniques for the indium-tin oxide (ITO) coated coverglass. In general, there was an expressed need for more and better data from large power systems with respect to corona effects.

Orbital debris has been considered as a possible source of progressive or catastrophic damage to solar arrays. The Johnson Space Flight Center has made studies of micrometeoroid damage, and may have data available. It is to be noted that the North American Defense Command (NORAD) tracks over 6400 pieces of debris at all altitudes. Specific evidence was obtained from a WESTAR satellite which was recovered after 8 months at an orbit of 800 N.M. The coverglass showed etching, but no cracking.

Most participants in this Workshop did not show strong concerns for these other environmental effects. Most concern is still expressed for radiation damage, thermal cycling, and solar cell and material stability in space environmental exposure.

Ultraviolet radiation and contamination are linked together because of their unfavorable synergism in solar array degradation. The outgassing of volatile materials from the interior of the

spacecraft in the high vacuum of space leads to deposition of contaminant layers in coverglass. The formation of the layers is enhanced in the presence of solar ultraviolet light. A study by Aerospace of the Global Positioning System (GPS) Block 1 spacecraft led to the conclusion that over several years in orbit, enough material is deposited on the coverglass surface to cause substantial transmission loss, and consequent solar array power degradation. The exact physical mechanism may not be known; it is possible that a mechanical change in the spacecraft design, i.e., adding field-of-view baffles might protect the solar array from contaminants streaming through open ports in the spacecraft structure. In new spacecraft designs, this potential problem should be addressed by geometrical design and materials selection.

Concentrator Solar Arrays

The surface contamination issue for concentrators may be even more serious because of multiple reflective or refractive surfaces involved in the collection of solar illumination. The minicavities which are a design feature in some structures may also pose a problem as a trap leading to higher concentrations of contaminants on small areas. The effect of higher operating temperatures on GaAs and InP concentrator cells may lead to enhanced annealing of radiation damage, or may, on the other hand, create conditions for long term aging and degradation of cell outputs. These are unresolved questions which need to be answered very soon.

Need for Space Experiments

There was unanimity among the Workshop participants that all opportunities for space experiments should be exploited to the fullest, and continual effort be made to develop and plan for new solar cell experiments in space.

The two most recent experiments to study radiation damage in solar cells are, first, the Naval Research Laboratory LIPS-3 satellite which carries more than 140 separate solar cell experimental circuits, and second, the AFGL Combined Release and Radiation Effects Satellite (CRRES) with a launch date of 30 June 1990. On the CRRES, the AFWAL has a large solar cell experiment comprised of GaAs, GaAs/Ge, and thin silicon cells with various coverglass thicknesses from 2 to 70 mils. Some cells will undergo thermal annealing at 150°C with forward bias. The CRRES spacecraft is also fully instrumented with particle detectors so the radiation environment throughout its orbital history can be measured and recorded.

An experiment to study plasma and corona effects is jointly planned by the AFWAL, AFGL, and JPL.

An experiment to study atomic oxygen effects on spacecraft materials is designed for the EOIM3 spacecraft by the Johnson Space Flight Center. The launch is scheduled for June 1990.

It was the emphatic opinion that space flight tests will be needed in the future as far as can be imagined, because of the inadequacy of simulating the complex combined environment of space.

Table 1 - Status of Environmental Dependent PV Parameters

Cell Type	Thick Silicon	Thin Silicon	Thick GaAs	Thin GaAs	GaAs Ge	InP	α - Si
Radiation Effects	G	F(1)	F(2)	F(3)	P	P	P
Temperature Coefficients	G	F	G	P	P	F	P(4)
Thermal Cycling Stability	G	G	G		?	?	?
Photon Effects and Stability	G	G	?	?	?	?	?

Quantity of available data: G (good), F (fair), P (poor)

- 1 - Need more data for 2 mil silicon cells
- 2 - Need more electron damage data
- 3 - May be very similar to thick GaAs
- 4 - Temp. coeff. data for 15 to 60°C
- ? - Unknown, not tested

Workshop Summary Heteroepitaxial Cells for Low Cost, High Performance

D. B. Lillington
Spectrolab, Inc.
12500 Gladstone Avenue
Sylmar, CA 91342

John Tracy
Applied Solar Energy Corp.
15251 E. Don Julian Road
Industry, CA 91746

- O WHAT DOES LOW COST MEAN?
 - LOW CELL COST
 - LOW POWER SYSTEM LIFE CYCLE COST
- O WHAT DOES HIGH PERFORMANCE MEAN?
 - HIGH EFFICIENCY
 - LOW WEIGHT
- O MOST PROMISING LONG TERM
 - NO CONSENSUS
- O VERY LITTLE FUNDING FOR GaAs/Si, AlGaAs/Si, InP/Si
 - WHAT ABOUT InP/Ge?
 - SHOULD WE RIDE ON BACKS OF IC INDUSTRY FOR GaAs/Si? PROBABLY. YES
- O DO WE NEED OTHER WINDOW MATERIALS FOR GaAs?
 - SUCH AS ZnS, NaCl, GAP, etc?
 - GAP - NO COMPELLING ARGUMENTS
 - OXYGEN REACTIVITY WITH THIN AlGaAs?
 - NO PROBLEM
 - MARGINAL INCREASE - BLUE RESPONSE
 - TWEAKING ONLY
- O FEASIBILITY OF InP FRONT SURFACE PASSIVATION
 - IS IT REALLY NECESSARY?
 - FIRST NEED TO DETERMINE WITH GREATER ACCURACY THE RECOMBINATION VELOCITY
- O STATUS OF ISOTYPE HETEROFACE TO Si (ZnS, GAP)
 - GAP vs SiO₂ PASSIVATION
 - HIGH TEMPERATURE CAN BE LIFETIME KILLER
 - ADVANTAGES OVER BORON BSF?
 - MUST BE LOW COST
- O RADIATION, STABILITY
 - RADIATION MEASUREMENTS IMPORTANT BUT ON MATURE SAMPLES ONLY

GaAs/Ge

KEY ISSUES REMAINING:

- O CONTROL OF AND OPTIMIZATION OF GaAs/Ge INTERFACE AND TUNNEL JUNCTION (IF REQUIRED)
- O ELECTRICAL MEASUREMENTS ARE COMPLICATED BY PRESENCE OF Ge CELL.
 - NO CLEAR APPROACH TO UNIVERSAL MEASUREMENT TECHNIQUE.
 - MULTISOURCE SIMULATOR SUGGESTED, BUT HOW TO SET 'DEPENDS ON DETAILS OF SPECTRAL RESPONSE.
 - SOME CONCERN OVER WHETHER ROOM TEMPERATURE MEASUREMENTS CAN ADEQUATELY SIMULATE PERFORMANCE AT OPERATING TEMP.
 - SHOULD VERIFY MEASUREMENTS BY FLIGHT TESTS, BUT PROVISION OF STANDARDS WILL BE DIFFICULT.
 - HOW CAN QUICK ELECTRICAL TEST FOR PRODUCTION BE DEFINED?
- O SUBSTRATES: SCALE UP TO 4-INCH DIAMETER WILL BE REQUIRED. LOW COST AND HIGH QUALITY MUST BE MAINTAINED.

WHAT HETEROEPITAXIAL CELLS ARE NEAR PRODUCTION

- O GENERAL AGREEMENT THAT ONLY GaAs/Ge IS ONLY TYPE NEAR PRODUCTION. SOME DISPUTE OVER HOW NEAR.
 - GaAs/Ge PROVIDES THIN, RUGGED, HIGH EFFICIENCY, RADIATION-HARD, LOWER COST
- O GaAs/Ge - SUBSTRATE CAN BE ACTIVE OR PASSIVE. USE OF Ge AS ACTIVE SUBSTRATE ADDS POTENTIAL COMPLICATION IN RADIATION HARDNESS AND TEMPERATURE COEFFICIENT, BUT RESULTS IN HIGHER EFFICIENCY. THERE WAS NO CONSENSUS ON WHICH APPROACH SHOULD BE USED.